Minnesota Department of Transportation

RESEARCH SERVICES

Office of Policy Analysis, Research & Innovation

Instrumentation, Monitoring, and Modeling of the I-35W Bridge

Catherine E. French, Principal Investigator
Department of Civil Engineering
University of Minnesota

August 2012

Research Project
Final Report 2012-24

Your Destination...Our Priority

Technical Report Documentation Page

1. Report No.	2.	3. Recipients Accession No.	
MN/RC 2012-24			
4. Title and Subtitle Instrumentation, Monitoring, and Modeling of the I-35W Bridge		5. Report Date August 2012 6.	
7. Author(s) Catherine E.W. French, Carol K. Shield, Henryk K. Stolarski, Brock D. Hedegaard, and Ben J. Jilk		8. Performing Organization Report No.	
9. Performing Organization Name and Address Department of Civil Engineering University of Minnesota 500 Pillsbury Drive SE Minneapolis, MN 55455		10. Project/Task/Work Unit No. CTS #2009051 11. Contract (C) or Grant (G) No. (C) 89261 (WO) 131	
12. Sponsoring Organization Name and Address Minnesota Department of Transportation Research Services 395 John Ireland Blvd., MS 330 St. Paul, MN 55155		13. Type of Report and Period Covered Final Report 14. Sponsoring Agency Code	
15. Supplementary Notes http://www.lrrb.org/pdf/201224.pdf			

16. Abstract (Limit: 250 words)

The new I-35W Bridge was instrumented incorporating "smart bridge technology" by Figg Engineering Group in conjunction with Flatiron-Manson. The purpose of the instrumentation was to monitor the structure during service, and to use this information to investigate the design and performance of the bridge. Instrumentation included static sensors (vibrating wire strain gages, resistive strain gages and thermistors in the foundation, bridge piers, and superstructure, as well as fiber optic sensors and string potentiometers in the superstructure) and dynamic sensors (accelerometers in the superstructure). Finite element models were constructed, taking into account measured material properties, to further explore the behavior of the bridge. The bridge was tested using static and dynamic truck load tests, which were used, along with continually collected ambient data under changing environmental conditions, to validate the finite element models. These models were applied to gain a better understanding of the structural behavior, and to evaluate the design assumptions presented in the Load Rating Manual for the structure. This report documents the bridge instrumentation scheme, the material testing, finite element model construction methodology, the methodology and results of the truck tests, validation of the models with respect to gravity loads and thermal effects, measured and modeled dynamic modal characteristics of the structure, and documentation of the investigated assumptions from the Load Rating Manual. It was found that the models accurately recreated the response from the instrumented bridge, and that the bridge had behaved as expected during the monitoring period.

17. Document Analysis/Descriptors		18. Availability Statement	
Bridge monitoring, Bridge testing, Finite element modeling		No restrictions. Document available from: National Technical Information Services, Alexandria, Virginia 22312	
19. Security Class (this report) Unclassified	20. Security Class (this page) Unclassified	21. No. of Pages 352	22. Price

Instrumentation, Monitoring, and Modeling of the I-35W Bridge

Final Report

Prepared by:

Catherine E.W. French
Carol K. Shield
Henryk K. Stolarski
Brock D. Hedegaard

Department of Civil Engineering
University of Minnesota

Ben J. Jilk

Minnesota Department of Transportation

August 2012

Published by:

Minnesota Department of Transportation
Research Services
395 John Ireland Boulevard, Mail Stop 330
St. Paul, Minnesota 55155

Acknowledgments

The authors would like to acknowledge the support of the Minnesota Department of Transportation. Numerical computations were performed using resources provided by the University of Minnesota Supercomputing Institute.

Table of Contents

List of Tables

List of Figures

Executive Summary

Following the collapse of the steel truss bridge crossing the Mississippi River on August 1, 2007, the I-35W St. Anthony Falls Bridge was constructed by the joint venture of Flatiron-Manson with engineering provided by Figg Engineering Group. The construction followed a design-build approach, and the new bridge was completed in September of 2008. The new bridge was constructed as two parallel structures for northbound and southbound traffic. Each structure was composed of post-tensioned concrete box girders. The river span used precast segmental construction, while the remaining three spans were fabricated with cast-in-place concrete.

Construction of the bridge incorporated a "smart bridge" system, equipped with instrumentation for monitoring the behavior of the structures. The University of Minnesota (UMN) was responsible for the collection and interpretation of the data gathered by the system to better understand the behavior of post-tensioned concrete box girder structures with the potential to impact future designs. Finite element models were constructed to further investigate the behavior of the structure and to aid the assessment of the assumptions presented in the Load Rating Manual for the structure.

The bridge was instrumented with over 500 sensors to collect data pertaining to structural behavior. Structural deformations were measured by a number of different instruments, including vibrating wire strain gages (198), resistive strain gages (24), and fiber optic strain gages (12). Temperatures in the bridge were measured by thermistors (246, including those integrated into the vibrating wire strain gages). Structural vibrations were measured by accelerometers (26). Linear potentiometers (12) were located at the expansion joints to measure the overall expansion and contraction of the bridge. Sensors that monitored electrochemical activity and concrete resistivity (4) were located in the deck to provide an indication of the potential for corrosion.

The vibrating wire strain gages (VWSGs) could only measure static strain changes, and so were limited to investigations of static truck load tests or thermal effects. All instrumented sections included gages in the top and bottom flanges at a minimum to determine the longitudinal curvature. Locations at the midspans of the river span and the south span of the southbound bridge were more heavily instrumented to better investigate local behavior at those sections including transverse bending, deformation of the box, and load distribution. Additional thermistors were installed at midspan of the river span in the southbound and northbound bridges to measure thermal gradients through the section.

Resistive strain gages, vibrating wire strain gages, and thermistors were installed in both columns and two of the drilled shafts of the southern piers of the southbound structure as part of a Federal Highway Administration funded study performed by the University of South Florida with supplemental instrumentation provided by UMN.

Fiber optic sensors were installed in pairs on the top and bottom flanges in the exterior box of the river span of the southbound bridge. These sensors were used to determine the overall longitudinal curvature of the river span. The data from the fiber optic sensors were typically collected statically, but had the potential to be collected dynamically through periodic attachment to a dynamic data acquisition system. The dynamic data acquisition system was supplied by the manufacturer twice during the first two years of monitoring to collect data during live traffic and dynamic truck load tests.

Accelerometers were installed in both the northbound and southbound structures to investigate modal behavior of the bridge due to dynamic loading. Many of the accelerometers were mounted to facilitate repositioning.

Linear potentiometers (LPs) were installed in each box of both structures at the expansion joints. Data from the LPs was used to investigate thermal expansion and time-dependent effects.

Sensors used to monitor corrosion activity were installed in the decks of both structures. Each corrosion sensor unit consisted of a humidity sensor unit and a corrosion current unit. The humidity sensor units measured the resistivity of the concrete between adjacent probes at four different depths to estimate the humidity throughout the deck. The corrosion current sensor units used the measured current between four rebars located at different depths to track possible corrosion initiation and corrosion rate with respect to depth.

Three-dimensional and two-dimensional models of the bridge were constructed to explore the structural response associated with gravity loading, thermal effects, and dynamic effects. Parameters assumed for the concrete properties in the models were determined from material tests performed on concrete samples taken during the construction of the I-35W Bridge. Material tests included measurement of the concrete compressive and tensile strength, modulus of elasticity, time-dependent properties (i.e., creep and shrinkage), and coefficient of thermal expansion.

Truck tests were performed on the bridge to gain a baseline understanding of the instrumented bridge, as well as to provide information for validation of the finite element models. Static tests were performed by stationing eight loaded sand trucks in various configurations at a number of locations on the structure. These tests were performed to investigate longitudinal deformation (shear and bending), torsional load cases, and local bending of the box cross section. Dynamic truck tests consisted of driving the same trucks across the bridge in a variety of configurations. The trucks were run both with ambient traffic and without traffic (that is, on a closed bridge). The dynamic truck tests created sufficient vibrations to facilitate modal analysis of the bridge.

The finite element models were validated with the static truck test data. The models were found to correlate well with respect to the longitudinal behavior of the bridge. The three-dimensional model was also checked with regard to the torsional and local deformation measurements, where it was also found to reasonably predict the response of the structure, with typical error magnitudes between measured and modeled results less than ±6 με for measured strains on the order of 15 με in the top and bottom flanges, though larger errors were occasionally observed in the webs. Of particular note was that modeled strain results showed that, for some of the truck test configurations, the maximum local transverse and vertical strains were of similar magnitude as the longitudinal strains produced by the test that produced the most bending. Large transverse strains were observed at the centerlines of the boxes and between the two boxes. Large vertical axial strains were seen at the top of the box webs where they met the deck. Because box girder structures typically do not have post-tensioning installed vertically, the structure would be expected to behave as a mildly reinforced concrete member in the vertical direction. Therefore, some controlled cracking might be expected in order to engage the mild steel reinforcement. Sufficient mild steel reinforcement was provided to resist the combination of shear, torsion, and flexure in the webs.

The finite element models were validated considering thermal effects, particularly thermal gradients (distributions of temperature through the cross section). The largest thermal gradients measured during the three years of monitoring were selected for validation in the model, and the model was shown to perform well at predicting the thermal response of the structure. The shapes of the measured gradients through the depth of the cross section substantially differed from the AASHTO design recommendations. Maximum gradients were best approximated by using a fifth-order curve and assuming a top surface temperature equal to that for solar radiation Zone 2 from the AASHTO LRFD recommendations.

The long-term strains (VWSGs) and expansion joint (LPs) measurements were examined for the three years of data collection. It was found that the LP measurements were strongly correlated with the

approximate uniform structural temperature. From the VWSGs, it was noted that the daily and seasonal changes in mechanical strain (i.e., strain related to changes in stress), exceeded those observed during the truck tests, implying that the thermal variations had a substantial impact on the behavior of the bridge.

The dynamic modal characteristics of the bridge were computed from the measured accelerometer data using the NExT-ERA/DC procedure. This method used vibration data to calculate the dynamic properties of the bridge. The method was used to characterize the modal characteristics (natural frequencies and mode shapes) from both ambient traffic vibrations and larger excitations induced by the dynamic truck load tests, and proved to be successful for both forms of data. The dynamic modal frequencies were found to be temperature dependent, which complicates the use of modal properties as a metric for detection of structural deterioration.

Using the validated finite element models and the measured bridge data, the assumptions as presented in the original Load Rating Manual (LRM) for the behavior of the I-35W Bridge were investigated. For the longitudinal live load behavior of the bridge, the original LRM did not provide guidance regarding the live load distribution of moments between boxes, and instead investigated only the total moment in the section. Barring considerations for live load moment distribution, it was found that the procedure employed by the original LRM for longitudinal live load moments was conservative with respect to the modeled bridge. Live load moment distribution was later added in an updated LRM, but was not investigated in detail for this study. Some moment restraint provided by the bearings was not considered in the LRM methodology, but the magnitude of this restraint was insignificant. The maximum longitudinal tensile stresses due to vehicular live load under the Service III limit state were investigated using the three-dimensional finite element model, and it was found that the maximum service tensile stresses were notably larger than those associated with the truck tests but only marginally larger than stresses caused by extreme measured positive thermal gradients.

For exploration of thermal effects, it was noted that the design recommendations for thermal gradients presented in the AASHTO LRFD produced deformations and stresses that were only 60% of the maximums measured from the bridge. As was consistent with the measured thermal gradient shapes, the structural response was best predicted by assuming a fifth-order gradient curve through the depth of the cross section with the top surface gradient temperature equal to that specified in Zone 2 from the AASHTO LRFD. The Inspection and Maintenance Manual methodology for estimating the overall elongation of the structure due to uniform temperature changes was found to be sufficient.

In exploration of the LRM methodology for transverse stresses in the top flange, it was found that the LRM procedure was conservative in the loaded box, but did not accurately predict stresses in the deck between the boxes due to differential displacement of the boxes. The live loading case for maximum transverse stresses between the boxes was examined in the finite element model, and it was found that the induced stresses were less than the live-load service capacity and therefore safe.

Stresses in the webs and bottom flanges of the box were not documented in the LRM, so finite element results for these locations were instead compared to design stress limit states. The bottom flange always performed within bounds. Web stresses nearly reached the limit for two-way bending under the examined load cases, but were never exceeded.

The shear and torsion methodology from the original LRM was investigated. This methodology was substantially reworked in the updated LRM but only the original LRM methodology was investigated in detail for this study. The original LRM method assumed that vertical and torsional shear were only carried by the loaded box, with vertical shear divided evenly between the webs of the box and torsional shear being calculated using the theory for closed thin-walled sections. This method produced reasonable approximations for the shear force in the exterior webs of the boxes, but failed to accurately calculate the

shear in the interior webs. Despite some discrepancies, the maximum shear force per web over all webs for each of the examined load cases was greater from the original LRM results than from the finite element model method. Therefore, it was concluded that the methodology employed by the original LRM for shear and torsion was reasonable and conservative.

By monitoring and testing the I-35W St. Anthony Falls Bridge, and through investigation of the Load Rating Manual, it was concluded that the bridge has been behaving according to expectations.

Chapter 1. Introduction

1.1 Background

Reconstruction efforts for the I-35W Bridge crossing the Mississippi River commenced immediately after the August 1, 2007 collapse. On August 4, 2007, MnDOT began searching for a contractor by issuing a Request for Qualifications (RFQ) which gave a description of the design concept, how the construction team would be selected, and the need for a team with design-build experience. Five construction teams were pre-qualified based on the RFQ, and four teams submitted proposals: Ames/Lunda, C.S. McCrossan, Flatiron/Manson, and Walsh Construction/American Bridge. The technical proposals submitted by the teams were evaluated by MnDOT based on quality, aesthetics and visual quality, enhancements, and public outreach and involvement.

Based on the results of the evaluation, on October 8, 2007, the joint venture of Flatiron Constructors, Inc. and Manson Construction Co. was awarded the project. The design firm on the project specified in the Flatiron-Manson proposal was Figg Bridge Engineers, Inc. In finalizing some of the aesthetic details of the bridge, the design team held a series of charettes to give the community an opportunity to provide input on aspects of the bridge including the color, pier shape and lighting.

1.2 Bridge Description

The bridge proposed and constructed by Flatiron-Manson and Figg was a post-tensioned concrete box girder bridge. There were two separate bridges that comprised the I-35W Bridge (St. Anthony Falls Bridge) built adjacent to each other: the northbound bridge (Br. 27410) and the southbound bridge (Br. 27409). Figure 1.1 shows an elevation view of the bridges, which each contained four spans numbered in ascending order from south to north, with the main span (Span 2) crossing the entire river. The span lengths for each bridge are shown in Figure 1.1. The main span was constructed using precast segmental construction while the other spans were constructed with cast-in-place concrete. In total, each bridge was 90 ft-4 in. (27.5 m) wide, each carrying five 12-ft (3.7 m) lanes of traffic and a 13-ft (4.0 m) wide shoulder on the exterior side of the bridge and a 14-ft (4.3 m) wide shoulder on the interior side of the bridge. The bridge was designed to accommodate future contingency dead and live loads, such as light-rail train along the interior shoulder and a pedestrian bridge hanging beneath the superstructure.

The first three spans of the bridge were continuous, with the fourth span separate. The bridge design included an expansion joint at the south end of Span 1, pins at Piers 2 and 3 (i.e., at either end of the main span), and another expansion joint at the north end of Span 3 (south side of Pier 4). Span 4 was pinned on the south end (north side of Pier 4) and built integrally with Abutment 5 at the north end.

The main span (Span 2) of the bridge was constructed of precast concrete box girders. In Span 2, as well as in Spans 1 and 3, each bridge design consisted of two boxes with varying depth, which were approximately 25 ft (7.6 m) deep near the pier and approximately 11 ft (3.4 m) deep at the midspan. The dimension between the inner sides of the webs at the top of the boxes was 21 ft-2 in. (6.5 m). The thinnest portion of the top flange across the width of the section had a nominal thickness of 11.5 in. (0.29 m) and remained constant along the entire length of Spans 1, 2, and 3. The bottom flange was 9 in. (0.23 m) thick at midspan of Span 2 and increased to 4 ft-10 in. (1.5 m) thick near each pier in Span 2. The bottom flange of Span 1 and Span 3 varied similarly. The webs were 1 ft-4 in. (0.41 m) thick in Spans 1 and 2, and 2 ft (0.61 m) thick in Span 3. Each precast box was 43 ft-2 in. (13 m) wide, tip-to-tip. The boxes were transversely post-tensioned together with a 4-ft (1.2 m) closure pour between them, such that the total section width from the tip of one box to the opposing tip of the other box was 90 ft-4 in. (27.5

m). Figure 1.2 shows a cross section of the southbound bridge exterior box at midspan of Span 2 (the other box being symmetric across the closure pour). Figure 1.3 shows a cross section of Span 2 near Pier 2. The thickened diaphragm section shown in Figure 1.3 extended 5 ft (1.5 m) on either side of the centerline of the piers. The northbound and southbound bridge designs had similar cross sections for Spans 1 and 2, but differed in Span 3 where the north end of northbound Span 3 widened to allow for exiting traffic onto University Avenue. The widening of Span 3 was gradually introduced starting near midspan, such that a total section width was equal to 95 ft-4.375 in. (29.1 m) at Pier 4. The widening of the bridge was accomplished by increasing the width of the box section geometry while keeping the distance between the two boxes constant.

Span 4 varied from the other three spans. This span design consisted of two multi-celled boxes for each bridge. The northbound bridge contained three cells per box while the southbound bridge contained two cells per box in Span 4. The multi-celled box geometries are shown in Figure A.14. Northbound Span 4 continued to widen from Pier 4 to Abutment 5, where the total width of the section was 104 ft-11.125 in. (32.0 m).

Major construction of the bridge started in early November 2007. The first precast segment was cast on February 14, 2008, and the first segment was erected on May 25, 2008. The final precast segment was erected on July 5, 2008. Table 1.1 shows the date that each precast segment was cast and the date on which they were erected. After all segments were erected, the two halves of the northbound and southbound bridges were each jacked apart with a force of approximately 1120 kips (5000 kN) to compensate for future creep and shrinkage. An approximately 7-ft (2.1-m) long closure pour was then cast between the cantilevered half-spans. The jacks were subsequently released, which put the closure pour in compression. Table 1.2 shows casting dates of the cast in place (CIP) spans and dates that the tendons in these spans were stressed. Table 1.3 shows significant events, other than erection of precast segments, during construction that induced loads on the bridge. The bridge opened to traffic on September 18, 2008 with just minor work left to be done.

1.3 Project Description

The original design of the I-35W Bridge included instrumentation, termed the “smart-bridge” system, as prescribed by the Figg Flatiron-Manson joint venture. The “smart-bridge” system included sensors to support the construction process, as well as sensors to investigate the long-term structural behavior. Sensors were also included to provide security and to control the automated anti-icing and lighting systems. The University of Minnesota (UMN) became involved in the project to assist in refining the choice of instrumentation to investigate the structural behavior, and to interpret and evaluate the collected data. To assist in the data interpretation, the UMN developed detailed finite element models (FEM) to investigate the static and dynamic properties of the bridge including time-dependent effects. The effects of loads due to vehicle traffic and environmental effects due to temperature changes and thermal gradients in the structure were investigated. The UMN also collected and instrumented concrete samples obtained from the bridge during construction to investigate the coefficient of thermal expansion and creep and shrinkage of the concrete, which were important to deciphering some of the collected data.

This report provides a description of the instrumentation used to investigate the structural behavior, including gage types, locations, and purposes for selecting the types and locations. A description of the concrete samples collected, test methods and results are included. The truck load tests conducted prior to bridge opening and two years afterwards that were used to verify the instrumentation and bridge behavior are also described. The structural response to thermal and environmental effects is discussed. Dynamic properties of the bridge were computed and are presented herein. Finally, validation of the assumptions presented in the Load Rating Manual for the I-35W Bridge is covered.

The report is organized as follows: Chapter 2 contains a description of the instrumentation types, gage locations, and data collection; Chapter 3 contains material testing procedures and results; Chapter 4 contains information on construction of the finite element models; Chapter 5 presents information on the truck load testing procedure; Chapter 6 contains static truck test results and validation of the finite element models with respect to gravity loading; Chapter 7 presents thermal and environmental factors and their impact on the bridge, as well as validation of the finite element models with respect to thermal effects; Chapter 8 presents the dynamic properties measured from the bridge for both ambient and dynamic truck test data; Chapter 9 presents an investigation of the assumptions presented in the Load Rating Manual; Chapter 10 summarizes the conclusions from the report.

Chapter 2. Instrumentation

2.1 Overview

Over 500 sensors were installed in the I-35W St. Anthony Falls Bridge to investigate the structural behavior. This chapter presents a brief description of each of the sensor types, their purpose, and their locations in the bridge. In addition, the data collection systems used to acquire the static and dynamic data are described.

The types of sensors included: vibrating wire strain gages (VWSGs), thermistors, fiber optic (SOFO) sensors, resistance strain gages, accelerometers, linear potentiometers, and corrosion monitoring sensors. The VWSGs and thermistors were wired to a slow-rate data acquisition system, henceforth referred to as the "static" system. Resistance strain gages, accelerometers, and the linear potentiometers were wired to a system capable of high data acquisition rates, henceforth termed the "dynamic" system. The SOFO sensors were delivered with a slow-rate data acquisition system; however, these same gages could be attached to a data processing system capable of dynamic rates. The SOFO dynamic data acquisition system was supplied by the manufacturer twice during the first two years of monitoring to collect data during live traffic and dynamic truck load tests.

Linear potentiometers were placed inside the boxes of the superstructure to monitor the movement of the bridge at the expansion joints. In addition, corrosion sensors were installed in the deck to give an indication when resurfacing the bridge might become necessary due to the ingress of chlorides. Each of the boxes in each span contained a nominal amount of instrumentation to monitor the behavior of the bridge. This included two to nine VWSGs to measure curvatures near midspan and near the piers and an accelerometer located below the deck near the center of the box at midspan for calculating dynamic modal properties of the structure.

The exterior box of the southbound bridge was more heavily instrumented to provide more detailed information. Near midspan of Spans 1 and 2, 26 and 38 VWSGs, respectively, were provided to measure the deformation of the boxes in the longitudinal and transverse directions. This included local transverse curvature measurements of the top and bottom flanges of the box and out-of-plane curvature of the webs to investigate local distortions. Longitudinal gages were spaced across the width of the top flange to investigate load distribution across the deck. Near the southern end of Span 2 (near Pier 2) and the northern end of Span 1, the box was instrumented using VWSGs installed in the web oriented as a rosette to investigate shear near the support. The rosettes consisted of three strain gages: one gage oriented longitudinally, one oriented vertically, and one oriented at a 45° angle relative to the other two gages. These rosettes enabled the determination of the principal stress directions. The longitudinal gage in the rosette was also used in determining longitudinal curvatures of the bridge.

The SOFO sensors were installed in the exterior box of southbound Span 2. Six pairs of SOFO gages were placed along the span to measure the curvatures in an average sense. The average curvatures provided by the SOFO sensors could be compared to the local curvature data provided by the VWSGs, which facilitated evaluation of the relative benefits of the two types of instruments. Near midspan of Span 2 of the southbound bridge, 42 thermistors were placed to provide an indication of the thermal gradient through the section while the location near midspan of Span 2 of the northbound bridge contained six thermistors to allow for comparison of thermal gradients between the two bridges. Fourteen moveable accelerometers were installed in the exterior box of southbound Span 2. These accelerometers could be positioned to monitor the distributed dynamic behavior of the bridge as well as local behavior (e.g., positioning multiple gages at a cross section to monitor accelerations across the deck within the box, or oriented to investigate torsional modes of vibration, etc.).

In addition to the data collected in the superstructure, additional gages were located in the substructure and foundation of the bridge. This instrumentation was installed as part of a Federal Highway Administration (FHWA) study conducted by the University of South Florida (USF) and included gages installed by USF and UMN to monitor the construction loads in the foundation as well as the axial deformations and curvature of the southbound Pier 2.

Table 2.1 denotes the general location and quantity of each type of gage in the bridge. The following sections describe each instrumentation system in greater detail, including the static system in Section 2.2, the SOFO fiber optic system in Section 2.3, the dynamic system in Section 2.4, and the corrosion monitoring system in Section 2.5. Data sheets for the sensors, dataloggers, and other monitoring equipment is available on request.

2.2 Static System: VWSGs and Thermistors

The static system contained all VWSGs and thermistors located in the superstructure of both northbound and southbound bridges, and also the VWSGs located in the piers and caissons (i.e., drilled shafts) of Pier 2 of the southbound bridge. The majority of the gages within the bridge were collected by the static system, including 148 VWSGs and 48 thermistors between both northbound and southbound superstructures and an additional 50 VWSGs in the piers and drilled shafts of southbound Pier 2. Each VWSG had an integral thermistor to measure the temperature at the location where the strain was read. These gages were used to monitor strain in the concrete which could be used to compute changes in curvatures and estimate changes in stresses in the bridge.

2.2.1 Superstructure VWSGs

2.2.1.1 Naming Scheme

Numbers were assigned to each of the locations instrumented with VWSGs. The numbers increased going from south to north, and were similar for both northbound and southbound structures. Location 3 was near the midspan of Span 1. Location 4 was just to the south of Pier 2, Location 5 was 10.5 ft (3.2 m) north of the centerline of Pier 2, and Location 6 was 20 ft (6.1 m) north of the centerline of Pier 2. Location 7 was near the midspan of Span 2, Location 8 just south of Pier 3, and Location 9 was near the midspan of Span 3. Location 14 was near the midspan of Span 4 and Location 15 was just to the south of Abutment 5. Figures 2.1 through 2.5 show these locations on the elevation view of the bridge along with the stations.

The gages were installed by Polyphase, an electrical contractor hired by Flatiron/Manson, which used their own naming scheme when documenting the installation. Roctest, hired by Flatiron/Manson to connect the VWSG gages to the dataloggers, used a different naming scheme in setting up the data loggers. After determining the final locations of the gages, the UMN assigned a new name to the gages to better associate the gage with its type and location.

The VWSG label assigned by the UMN consisted of eight characters. The first character denoted whether the strain (V) or temperature (T) of the gage was being measured. In other words, each VWSG gage had two labels, one for strain and one for temperature. The second character in the label denoted whether the gage was located in the northbound (N) bridge or southbound (S) bridge. The third and fourth characters denoted the location of the gage along the length of the bridge. The possible locations corresponded to those shown in Figure 2.1 (i.e., 03, 04, 05, 06, 07, 08, 09, 14, or 15). The fifth character in the label specified whether the gage was located in the interior (I) box or the exterior (E) box. The sixth character specified whether the gage was located within the top flange (T), the bottom flange (B), the east web (E) (i.e., on the interior side of the bridge for the southbound bridge and exterior side for the northbound

bridge), the west web (W) (i.e., on the exterior side of the bridge for the southbound bridge and interior side for the northbound bridge), or the middle web (M) (i.e., in the case of Span 4) of the box. The seventh character denoted whether the orientation of the gage was longitudinal (L), transverse (T), vertical (V), or at 45˚ (A). Finally, the eighth character was a number assigned to the gage to separate it from the other gages with the same first seven characters in their label. The eighth character typically increased from exterior to interior and from the top of the section down. For example, the gage labeled "VS07EEA1" represented the vibrating wire strain gage located near midspan of Span 2 of the southbound bridge (i.e., location 7), in the exterior (west) box, in the east (interior) web, oriented at 45˚ in the rosette. If a sensor's first seven digits were unique to that sensor, the eighth digit was "1" by default.

All of the assigned labels are provided in Figures A.2 through A.14 in Appendix A which show the gage locations corresponding to the labeling. The labels are shown as "UMN gage label (installation gage number) (connection gage number)". The installation gage number refers to the number assigned by Polyphase during construction of the bridge. The connection gage number refers to the number assigned by Roctest during the connection of the system to the dataloggers. The assigned labels are also given in Table 2.2 along with associated locations of the gages within the bridge. Listed X and Y gage locations are coordinates in inches relative to the nominal top deck surface at the centerline of the box in which the gage was installed. For both structures, X-coordinates are positive to the east and negative to the west, and Y-coordinates are positive up and negative down. Further details regarding the gage coordinates are discussed in Section 2.2.1.4.

2.2.1.2 Gage Models

Two types of VWSGs were used in the bridge superstructure. Most of the VWSGs were Roctest EM-5 gages cast within the concrete. Figure 2.6 is a photograph of an installed Roctest EM-5 VWSG.

The second type of VWSG used was the Roctest SM-5A. These gages were installed externally on the interior face of the exterior box at southbound Location 6. The segment to which they were attached was cast before determining the final gage locations, so the external SM-5As were used in lieu of the EM-5s to instrument this section. Roctest SM-5A gages were also installed externally for replacements of malfunctioning embedded Roctest EM-5 strain gages. A list of gage replacements is given in Section 2.2.6.1.

The Roctest EM-5 VWSGs had a specified range of 3000 με. The resolution of these gages was a minimum of 1 με, and their specified operating temperatures were -4˚F (-20˚C) to 176˚F (80˚C). The Roctest EM-5 VWSGs contained a 3 kΩ thermistor with a range of -58˚F (-50˚C) to 302˚F (150˚C) and a resolution of 0.18˚F (0.1˚C). Based on the temperature range of the cable, the range of the thermistor was limited to -4˚F (-20˚C) to 176˚F (80˚C). The Roctest SM-5A VWSGs and thermistors had the same ranges and resolutions as those associated with the Roctest EM-5 VWSGs. Datasheets from the manufacturer are available on request for each of the gages. Both the Roctest EM-5 and Roctest SM-5A VWSGs were approximately 6.75 in. (0.17 m) in length.

2.2.1.3 Gage Locations and Behaviors of Interest

The majority of the VWSGs were located in just a few sections of the bridge to provide a more thorough understanding of the behavior of the bridge at those locations. It was assumed that if the behavior of the bridge at the few critical sections could be well understood and modeled with the finite element model, then that model might be used to infer the behavior of the bridge at the other locations.

The gage locations were chosen to provide information on the following behaviors of interest: deformation of the flange connecting the two boxes of each bridge (of interest especially for the case of

only one box loaded, and for loading between boxes); shear of the boxes under various loadings; deformation of the sections under thermal gradients (especially of interest as the deck would try to expand due to solar radiation while the sides of the box and bottom surface of the deck would have much lower temperatures).

VWSGs were placed in at least the top and bottom flanges at southbound structure Locations 3, 4, 5, 6, 7, 8, 9, 14 and 15 and northbound structure Locations 3, 5, 7, 8, 9, 14, and 15. Most of the VWSGs were oriented longitudinally within the bridges. To provide redundancy for the longitudinal curvature measurements, gages were placed longitudinally above, below, and in the webs of the section. Typical installation details of these gages are shown in Figures 2.7 through 2.9.

The bulk of the instrumentation was located within the exterior box of the southbound bridge. The heavily instrumented sections included Location 3 (near midspan of Span 1), Location 4 (negative moment region just to the south of the Pier 2 diaphragm section), Location 5 (negative moment region just to the north of the Pier 2 diaphragm section), and Location 7 (near midspan of Span 2 within the precast segment adjacent to the closure pour). The majority of the VWSGs were placed near the midspan of the river span section because this was where the largest deformations were anticipated due to thermal gradient effects. Both boxes of the southbound bridge were instrumented at Location 7 in order to capture more information on the behavior across the section.

The following sections summarize some of the behaviors of interest for the instrumented sections.

2.2.1.3.1 Location 7: Near Midspan of Span 2

Figures 2.10 and 2.11 show the VWSG layout for Location 7 near midspan of Span 2 for the southbound and northbound bridges, respectively. Thirty-eight gages (twenty longitudinal, ten transverse, two vertical, and six oriented in two rosettes) were installed in the southbound bridge at this section. Five longitudinal gages were installed at this location in the northbound bridge. The rationale for the distribution of the sets of gages in Span 2 of the southbound bridge is described below:

- Three gages were oriented longitudinally in each web of the exterior box. By providing three strain gages in the longitudinal direction in the webs (gages at top, approximately mid-depth, and bottom), the longitudinal curvature at the section could be measured using a best-fit line through the data. The middle longitudinal gage in each of these webs was part of a rosette. These rosettes were installed in order to investigate the direction of principal stresses at the section.
- Gages were placed longitudinally in the top and bottom flanges at the centerline of each box for both northbound and southbound structures so that measured curvatures at Location 7 might be compared among all boxes.
- The gages oriented in the transverse direction between the boxes were used to investigate the behavior of the deck (i.e., top flange) as it spanned transversely between the webs while under loading of a single box, loading between the two boxes, or some other local load positioning. Pairs of transverse gages were located on either side of the east web of the west (exterior) box and on the west side of the west web of the east (interior) box to investigate the distribution of transverse moments. A pair of VWSGs was installed vertically near the top of the east web of the west (exterior) box to investigate the out-of-plane bending of the web and the distribution of moments at the top flange and web intersection.
- Gages oriented in the transverse direction were also placed in two locations of the bottom flange of the west (exterior) box to investigate distortions of the bottom flange.
- A series of 15 gages were oriented longitudinally and distributed across the deck to investigate the load distribution across the section due to gravity loading and thermal effects. Previous studies performed in Texas by Davis et al. (1999), Roberts et al. (1993), and Thompson et al.

(1998) found increased stresses above the webs in box girder bridges due to the thermal gradient effects. It was stated that this increased stress (larger than design stress) was caused by warping of the section. The thermal gradient played a significant role in this warping. The longitudinal gages in the deck (as well as other gages in the section) were provided to enable strain measurements in the deck due to warping caused by the thermal gradient.

2.2.1.3.2 Location 3: Midspan of Span 1

Figures 2.12 and 2.13 show the VWSG layout at Location 3 near midspan of Span 1 for the southbound and northbound bridges, respectively. Twenty-six gages (eleven longitudinal, ten transverse, two vertical, and three oriented in a rosette) in the southbound bridge at this section, and five longitudinal gages at this location in the northbound bridge.

Location 3 of the southbound bridge was instrumented similarly to Location 7 of the southbound bridge, with the exclusion of the dense distribution of longitudinal gages across the deck. In addition, there was no rosette in the exterior web of the exterior box at this section. Also, VWSGs located near the centerline of the box in the top and bottom flanges of both boxes were offset transversely 4 ft (1.2 m) from the centerline of the box to allow for an access opening in the bottom flange. This differed from all other sections, for which gages in the top and bottom flanges were located at the centerline of the box.

2.2.1.3.3 Negative Moment Regions near Pier 2

Because of the increased stiffness of the sections at the piers due to the nearly solid diaphragm within the boxes over the piers, the expected deformations at these sections were small. Consequently, fewer gages were used at these locations. Figures 2.14 and 2.15 show the VWSG layout at the negative moment regions on the southbound bridge for Location 4 (20 ft (6.1 m) south of centerline of Pier 2) and Location 6 (20 ft (6.1 m) north of centerline of Pier 2), respectively. As the figures show, the instruments were distributed similarly in both sections, except that the gages just to the north of Pier 2 were externally mounted to the interior of the box because this section was cast before determining the final gage locations. Nine gages (three longitudinal and six oriented in two rosettes) were installed in the exterior box of the southbound bridge at each of these locations.

- The thickened diaphragm section above the piers ran 10 ft (3.0 m) along the length of the bridge, 5 ft (1.5 m) on either side of the centerline of pier. In order to prevent the data from being affected by the internal diaphragm located within the boxes over the pier, the gages were located 15 ft (4.6 m) away from the face of the thickened section on each side of the pier (i.e., 20 ft (6.1 m) from centerline of the pier). This was approximately two-thirds the height of the box and was expected to be far enough to reduce the impact of local effects due to the thickened section.
- To measure the longitudinal curvatures, gages were placed in the top and bottom flanges at (or near) the center of the box sections of the exterior box of the southbound bridge.
- Rosettes were placed in both webs of the exterior box of the southbound bridge at these sections. The combination of these gages was expected to provide information on the directions of the principal stresses, as well as information regarding shear of the boxes.

In addition to the gages located 20 ft (6.1 m) south and north of southbound Pier 2, VWSGs were placed at Location 5 (10.5 ft (3.2 m) north of centerline of Pier 2) of the southbound and northbound bridges as shown in Figure 2.16 and Figure 2.17, respectively. As the figures show, there were five gages in each bridge at these sections. Each box had a gage in the top and bottom flange near the center of the box in the longitudinal direction. The fifth gage was placed near mid-depth in the interior web of the exterior box. These gages provided information for calculating longitudinal curvature of the section.

2.2.1.3.4 Directly Over Pier 3, Near Midspan of Span 3 and Span 4, and Near Abutment 5

Besides the locations discussed above for the VWSGs, additional sections were instrumented less heavily. These sections included Location 8 located 10.5 ft (3.2 m) south of centerline of Pier 3 (Figures 2.18 and 2.19), Location 9 near the midspan of Span 3 (Figures 2.20 and 2.21), Location 14 near the midspan of Span 4 (Figures 2.22 and 2.23), and Location 15 in Span 4 near Abutment 5 (Figures 2.24 and 2.25). With the exception of Location 8 of the southbound bridge, all of these sections had the same gage layout as Location 5, with five gages in each bridge at the section. Each box had a gage oriented longitudinally in the top and bottom flange near the centerline of the box. For boxes with two webs, a third gage was placed near mid-depth in the interior web of the exterior box. In the case of Span 4 with more than two webs, the extra gage was placed in the exterior box in the web nearest the center of the box on the interior side of the box, near mid-depth of the section. These gages provided information for calculating longitudinal curvature of the sections. Location 8 of the southbound bridge over Pier 3 was instrumented identically to the sections discussed for Locations 4 and 6 of the southbound bridge with the rosettes in each web of the exterior southbound box, but also including gages located in the top and bottom flange near the center of the interior box. Location 8 of the northbound bridge had the typical five gage layout as discussed previously.

2.2.1.4 Discussion of Sources of Uncertainty in VWSG Installation

Because the gages were not installed by UMN personnel, some uncertainties were associated with the exact gage locations. The UMN was present at one of the early installations but was not present during all gage installations. As a consequence, the exact X- and Y-coordinates of the gages in the cross section and the reference from which these measurements were taken was a source of uncertainty. The UMN was provided with tables of gage location measurements assuming several different, unstated origins. This required the data to be interpreted and discussed between the UMN and the contractor which left some uncertainties as to the accuracy of the coordinates.

Additionally, because the location of the gages was measured using a tape measure, there was some error associated with the measurement procedure which varied for each gage location. For gages in the webs of each box, the Y-coordinate of the gage was typically measured from the bottom formwork or the bottom of the box. The measurement was taken as a vertical measurement; therefore, for gages located higher in the web, larger measurement errors were likely as a result of the outward flare of the webs. Based on how difficult it was to interpret the tape-measure reading (i.e., how far the tape measure was from the gage when taking the reading), the measurement was likely to be within ± 0.5 in. (±13 mm) for gages near the bottom flange, or within a few inches for gages near mid-height or the top of the web. For gages in the top and bottom flanges, the Y-coordinate was measured up from the formwork of the corresponding flange, resulting is short measurements which were likely within ±0.5 in. (±13 mm) of the true value. The X-coordinate for gages in the web was likely to be within ±0.5 in. (±13 mm) of the true value because the measurement was taken from the exterior wall of the web, resulting in a relatively small measurement (around 18 in. (0.45 m) or less) and correspondingly small error. The X-coordinate measurement of gages in the top and bottom flanges were taken from a corner of the formwork, resulting in errors likely within ±0.5 in. (±13 mm) for the bottom flange and within ±1 in. (±25 mm) for the top flange.

In order to create a common set of origins between the VWSGs, the coordinates given to the UMN were adjusted such that the origin of the X-coordinate was the centerline of either the interior or exterior box (depending on the box in which the gage was located), and the origin of the Y-coordinate was the top of the deck assuming section dimensions from the as-built drawings (Minnesota Department of Transportation, 2008). The X-coordinate was always taken as positive to the east for consistency. This corresponded to positive towards the interior of the bridge for the southbound bridge and positive towards the exterior of the bridge for the northbound bridge. The Y-coordinate was taken as negative in the

downward direction. Coordinates presented in Table 2.2 represent the adjusted X- and Y-coordinates for each gage; the raw measurements are not given.

Another source of uncertainty that affected the exact X- and Y-coordinates of the VWSGs and their expected measurement was the thickness of the deck. The coordinates of gages given in Table 2.2 were taken from the nominal top of deck as specified in the as-built drawings. This, however, was not necessarily equivalent to the final top of deck elevation as constructed. The deck thickness had a tolerance of 0.375 in. (9.5 mm) for the precast segments (i.e., Span 2), and the cast-in-place sections had a higher deck thickness tolerance. The goal was to achieve 4 in. (100 mm) of cover to the top mat of rebar after planing, and the pours were typically setup for 4.5 in. (110 mm) of cover. The actual pours may have provided up to 5.5 in. (140 mm) of cover (from email correspondence with Dustin Thomas, MnDOT, July 30, 2009). After casting, the deck of the bridge was planed to achieve the desired ride quality. This required the deck to be planed by varying amounts along the bridge. In general, 0.25 to 0.5 in. (6 to 13 mm) of concrete was removed during planing. Ground penetrating radar was used to determine rebar cover after planing. The majority of the scanned length had cover in the range of 4 to 5 in. (100 to 130 mm) with the most likely cover at any particular location being approximately 4.25 in. (110 mm). Due to the tolerance in deck thickness and the planing operation, the final thickness of the deck varied throughout the bridge, resulting in actual vertical dimensions of the gages from the top of deck different than those given in Table 2.2. Ultrasonic tomography performed on April 14, 2011 (31 months after bridge opening) at midspan of Span 2 (Location 7) in the southbound bridge revealed that the thickness of the deck at the centerline of the box was, to an accuracy of ±0.25 in. (±6 mm), 10.6 in. (270 mm), which was 0.9 in. (23 mm) thinner than specified.

Some uncertainty was also associated with the exact orientation of each gage. Gages typically were installed by attaching the gage to two pieces of rebar attached to the main reinforcement in the box as shown in Figure 2.6. The exact orientation of the gage was dependent on the orientations of the main rebar and the additional two pieces of rebar used to attach the gage. For example, if the rebar was not aligned perfectly longitudinally along the bridge, the attached gages might not have been aligned perfectly longitudinally as intended.

Additionally, in some cases the small pieces of rebar were not placed on the same side of the main rebar which resulted in the gage being tilted slightly up and down as shown in Figure 2.26. These slight variations in orientation could result in readings that would be slightly off that which would be expected at the gage location for the desired gage orientation.

Another issue that arose from gage installation was that not all initial data was recorded. Strain readings from the gages were recorded at the time of installation of gages and typically at a “24 hour” reading around a day after the concrete at the gage location had been poured. The temperature associated with this strain reading, however, was not recorded. Without the reference temperature, the initial strain reading was of no value. Because the temperature was not known in association with the strain reading, the total strain could not be determined from the gages, and only changes in strain from times with paired strain and temperature readings were usable.

2.2.2 Superstructure Thermistors

2.2.2.1 Naming Scheme

The labels assigned to the thermistors by the University of Minnesota had eight characters. The first character denoted that the thermistor measured temperature (T). The second character in the label specified whether the thermistor was in the northbound (N) bridge or southbound (S) bridge. The third character denoted whether the thermistor was in the interior (I) box or exterior (E) box. The fourth

character specified whether the thermistor was located within the top flange (T), the bottom flange (B), the East web (E), or the West web (W) of the box. The fifth character in the label specified to which set of thermistors the gage belonged (i.e., the set with the same first four characters). A set of gages consisted of thermistors measuring a gradient through a thickness (e.g., top flange, bottom flange, etc.) in the section. Sets consisted of one to six thermistors. The thermistors used to measure thermal gradient through the depth of the web (i.e., gradient from the top flange to the bottom flange through the depth of the web) were not labeled as a single set of gages, and instead consisted of gages from multiple sets. The sixth, seventh, and eighth characters denoted the location of the thermistor within the set with the numbering starting at one and increasing from the exterior surface of the box to the interior surface or from the top of the deck to the bottom of the deck in the case where the thermistor was in the deck. Although only one digit was required to number the gages, three digits were used in order to keep the entire label eight digits in length. This was consistent with the VWSG labels and was required for data collection purposes because the thermistors and VWSGs were connected to the same datalogger. Thermistor names, channels and positions are summarized in Table 2.2 in the same manner as was done for the VWSG system in Section 2.2.1.1.

2.2.2.2 Gage Model

All thermistors installed independently from the VWSGs were Roctest Model TH-T. These were 3 kΩ thermistors with an operating temperature range of -4˚F (-20˚C) to 176˚F (80˚C) limited by the cable. The datasheet provided by the manufacturer for the thermistors is available on request.

2.2.2.3 Gage Locations and Behaviors of Interest

Of the 48 total individual thermistors installed in both structures, 42 were located at midspan of Span 2 (Location 7 as shown in Figure 2.1) of the southbound bridge. The remaining six thermistors were located in the exterior box at midspan of Span 2 (Location 7) of the northbound bridge. These thermistors were used in conjunction with the VWSG thermistors to provide information on the thermal gradient through the section.

The thermistors were grouped into sets of one to six gages. At locations with multiple thermistors, the gages were installed at different depths to obtain the thermal gradient through the thickness of the web or flange. In some cases, the VWSG thermistors located in the section were used to add an additional data point to a set of thermistors in obtaining the thermal gradient. The thermal gradients were to be investigated through the thickness of the webs, through the thickness of the bottom flange of the box, through the thickness of the top flange of the box at multiple locations, and through the depth of the webs.

The thermistors were placed primarily in the exterior box of the southbound bridge, but some were also placed in the interior box of the southbound bridge in order to investigate the effect of the shade provided by the flange and the northbound bridge on the thermal gradient. The northbound bridge was only instrumented with thermistors in the east (exterior) web and bottom flange of the exterior box. Because dense thermistor instrumentation was provided at only one location of each bridge, temperatures obtained from the VWSG thermistors at other instrumented locations along the length of the bridge were required to investigate the consistency of the measured thermal gradients along the length of the structure.

Cross sections showing the layout of the thermistors in the southbound and northbound bridges are shown in Figures 2.27 and 2.28, respectively. Figure 2.29 shows a typical installation of six thermistors through the thickness of the top flange. For all thermistor sets within the top flange, including the three-gage installation just below the roadway crown, the topmost thermistor was nominally (i.e., according to the as-built construction documents (Minnesota Department of Transportation, 2008)) located 1.75 in. (44 mm) below the top surface of the deck, the lowest thermistor was nominally 9.75 in. (250 mm) below the

top surface of the deck, and the remaining thermistors were spaced evenly between the two. It was found that gage position measurements (performed in a similar manner as was discussed for the VWSG in Section 2.2.1.4) did not agree with the nominal thermistor positions as stated above for the top flange. On average, the topmost thermistor was measured to be approximately 2 in. (51 mm) below the top surface of the deck instead of 1.75 in. (44 mm). Also, the thermistors in the three-thermistor set below the roadway crown were recorded to be 6.75 in., 8.25 in, and 9.75 in. (170 mm, 210 mm, and 250 mm) below the top surface of the deck. From comparison with the temperature profiles obtained from the other sets of thermistors through the depth of the top flange, it was determined that the temperature values from this set of gages were not consistent with these recorded depths. However, no other position records were available. Thermistors above the east web of the interior box (gage numbers TSITC001 through TSITC006) were recorded to be 2.8 in., 4.3 in., 4.8 in., 5.3 in., 5.3 in., and 5.8 in. (71 mm, 110 mm, 130 mm, 130 mm, and 150 mm) below the top surface of the deck (the two gages located at the same depth is not a typographical error in this report, it is representative of the gage position records received). Again by comparison of the temperature profiles obtained by the other sets of thermistors in the deck, it was concluded that temperature readings from this set of gages were not consistent with the provided depth measurements, rendering this set of gages unusable for investigation of thermal gradients.

For three-thermistor installations in the webs, the exterior and interior thermistors were installed with 2.25 in. (57 mm) of cover, with the center thermistor placed at the midpoint between the two. For single thermistors in the web, the sensor was placed at the center of the web. Location measurements confirmed that the positions of the web gages were consistent with the nominal locations, with the exception of the innermost thermistor in the set of three gages in the east web of the southbound interior box (gage number TSIEB003). This gage provided temperature readings approximately equal to those from the topmost deck gages, which was deemed impossible given that this gage, if in its specified location, would be subject to no heating from solar radiation. It was suspected that this gage may have been mislabeled in connection to the multiplexer.

Installation of the thermistors in the bottom flanges were spaced such that the local VWSGs at the same sections were effectively added to the set. For the three-thermistor installations in the bottom flange, the topmost thermistor was nominally 1.75 in. (44 mm) below the top of the bottom flange, with the second thermistor 2.75 in. (70 mm) below the first, then the VWSG located 2.75 in. (70 mm) below the previous thermistor, and the bottommost thermistor located 2.75 in. (70 mm) below that (nominally 1.75 in. (44 mm) above the bottom of the bottom flange). For the two-thermistor installation, the topmost and bottommost thermistors were located as described above, with the VWSG at the midpoint between the two thermistors. Figure 2.30 shows a typical two-thermistor installation with a single VWSG in the bottom flange. Location measurements confirmed that the positions of the bottom flange thermistors were consistent with the nominal locations.

2.2.2.4 Discussion of Sources of Uncertainty in Thermistor Installation

Similar to the VWSGs as described in Section 2.2.1.4, there was some inherent uncertainty in the exact location of each thermistor. As was the case with the VWSGs, the X- and Y-coordinates had some uncertainty associated with the particular reference point used for measurement and a certain amount of error associated with visually estimating the measurement with a tape measure. The X- and Y-coordinates for each thermistor, adjusted using the same procedure as used for the VWSGs, are given in Table 2.2.

2.2.3 Pier and Caisson VWSGs

2.2.3.1 Naming Scheme

Vibrating wire strain gages in the piers and caissons (i.e., drilled shafts) were given "VW_GK" numbers ranging from 1 through 48 translating to the channel connections used in the long-term static system configuration. Table 2.3 shows the serial number and location of each of the vibrating wire strain gages. Seven of the VWSGs were not connected to the datalogger in the final instrumentation layout, and were consequently not assigned a number (refer to Section 2.2.6.3 for problems encountered with connection of the VWSGs in the data collection vault). Pier and caisson gages installed by the USF were identified according to their serial number. The ten gages installed by the UMN in Pier 2 were identified by a unique label UofMN1 through UofMN10.

2.2.3.2 Gage Model

Geokon 4911A vibrating wire gages were installed by the USF, and Geokon 4200 vibrating wire gages were installed by the UMN. Geokon 4911A were rebar strainmeter “sister bars” tied to the rebar cages and embedded into the concrete, whereas the Geokon 4200 gages were concrete embedment strain gages (similar to the Roctest EM-5 VWSGs used in the superstructure). In addition to measuring strain, each of the installed vibrating wire gages included a thermistor to measure temperature.

The Geokon 4911A VWSGs had a specified range of 2500 με and a resolution of 0.4 με. Their specified operating temperatures were -4˚F (-20˚C) to 176˚F (80˚C). The Geokon 4200 VWSGs had a specified range of 3000 με and a resolution of 1.0 με. Gage length was equal to 6.0 in. (152 mm). Their specified operating temperatures were also -4˚F (-20˚C) to 176˚F (80˚C). Datasheets from the manufacturer are available on request for each of the gages.

2.2.3.3 Gage Locations and Behaviors of Interest

Geokon 4911A gages were installed in the drilled shafts (i.e., caissons) by the USF to investigate the effect of the construction loads within the foundation. These gages were installed in two shafts below the southbound bridge Pier 2 exterior column. Figure 2.31 shows the shafts (Shaft 1 and Shaft 2) instrumented in a cross-sectional view of the southbound bridge Pier 2 footing. Each drilled shaft contained 16 vibrating wire strain gages, for a total of 32 vibrating wire strain gages in the caissons. Elevation and cross section views showing the locations of the gages in Shafts 1 and 2 are presented in Figures 2.32 and 2.33, respectively. The gages were placed at four levels in each shaft, with level 1 being the topmost layer and level 4 being the bottom. Four Geokon 4911A gages were installed in each level. All the gages within the shafts were oriented vertically.

To monitor axial deformations and curvature of Pier 2 of the southbound bridge, gages were oriented vertically about the perimeter and at the center of the columns. The instruments in the southbound bridge Pier 2 were distributed evenly between the interior and exterior columns (i.e., four Geokon 4911A, and five Geokon 4200 gages were installed in each the interior and exterior column of Pier 2 of the southbound bridge). The Geokon 4911A gages were installed at the midheight of the columns (i.e., 39.88 ft (12.2 m) above the base of the southbound bridge Pier 2 interior column and 39.27 ft (12.0 m) above the base of the exterior column), while the Geokon 4200 gages were installed nominally 23.21 ft (7.07 m) above the base of the southbound bridge Pier 2 as shown in Figure 2.34. Geokon 4911A gages were placed in each of the four corners of the cross section (northwest, northeast, southwest, southeast) while Geokon 4200 gages were placed in each of the four corners of the cross section with a fifth gage near the center of the cross section. Field measurements taken when the Geokon 4200 gages were installed are given in Table 2.4, and Figures 2.35 and 2.36 describe the measured dimensions. Figure 2.37 shows the

layout the gages with respect to the pier reinforcement for the Geokon 4200 gages. Field measurements for the Geokon 4911A gages were not available.

2.2.4 Connectivity and Wiring of the Static System

Sensors in the static system of the bridge (e.g., VWSGs and thermistors) were connected to multiplexer boards in the static junction boxes (Roctest model RTX-248) within the bridge. There were a total of six static junction boxes in the northbound bridge superstructure and eight in the southbound bridge superstructure. Additionally, there were static junction boxes used to connect the gages in the southbound bridge Pier 2 columns and caissons. The static junction boxes were connected in series over the length of both northbound and southbound structures, with the final static junction boxes being connected to dataloggers (Campbell Scientific CR1000) in Span 4. Using the Campbell Scientific Model NL115 ethernet interface, the dataloggers were connected to fiber optic converters (B&B Electronic Media Converter). The fiber optic cables were connected to a second set of fiber optic convertors in the control room, and connected to the bridge server by ethernet cables.

The static junction boxes and dataloggers were all connected to the interior side of the interior web in the exterior box of each bridge. The locations of the static junction boxes and dataloggers along the length of the bridges are shown in Figure 2.38. The channel and junction box to which each VWSG and thermistor in the superstructure was connected is documented in Table 2.2. The boxes used to connect the gages within the pier and caissons were located in an instrumentation vault, shown in Figure 2.39. The boxes labeled Roctest Box 1 through Roctest Box 4 were used to connect the VWSGs within the pier and shafts and the thermistors associated with the VWSGs. The connections for the VWSGs in southbound bridge Pier 2 and caissons are given in Table 2.3.

2.2.5 Data Collection for the Static System

2.2.5.1 Construction

During construction of the St. Anthony Falls Bridge, data was collected from only a portion of the static gages. The gages located in the southbound Pier 2 and associated caissons that were installed by the University of South Florida (USF) and the University of Minnesota were monitored by USF throughout the construction process. In addition to this data, USF had a camera setup on the University of Minnesota West Bank Office Building (WBOB) monitoring the construction process to facilitate correlation of the gage readings to the estimated construction load applied to the piers.

For the VWSGs located in the superstructure, strain readings were taken at the time of installation to ensure that the gages were reading near the middle of their range. The day after the concrete was cast around a given gage, a “24 hour” strain reading was recorded. Temperature readings from the “24 hour” reading were not obtained, thus strain measurements can only provide relative strains; without the temperature readings, absolute strain measurements were not possible, and only relative strain measurements between any two readings were possible. Individual thermistors (i.e., those not integrated into the VWSGs) were also recorded with a “24 hour” reading.

In addition to the initial readings, some of the VWSGs in the southbound bridge exterior box were recorded for a brief period of time during the construction process. Selected gages were read using three Campbell Scientific CR10 dataloggers connected at midspan of Span 2, midspan of Span 1, and near Pier 2 in Span 1. The CR10 data collection times and sensors are summarized in Table 2.5. A maximum of 16 channels were available for each CR10, and gages were chosen for collection such that the wires connecting to the dataloggers would not cross the walking paths or work areas within the bridge (due to safety concerns). Sensor labels for collection at Pier 2 were improperly recorded, and it is therefore

unknown which gages were collected at that time. The entire construction process could not be recorded using the CR10 dataloggers because the contractor had to remove the wires in order to connect them to the permanent multiplexers in the bridge. Construction data is not presented in this report.

2.2.5.2 Truck Tests prior to Bridge Opening

Prior to opening the bridge, UMN coordinated a series of truck tests that took place on September 14 and 17, 2008 (discussed in Chapter 5). At the time the truck tests were performed, the permanent data acquisition systems were not fully completed. Gages within the piers and caissons had not yet been connected to the permanent system; consequently, USF used a temporary datalogger to record data during the truck tests. The vendors who supplied the static system participated in the truck tests by temporarily setting up their systems to record when prompted. For the second set of truck tests performed in October of 2010, the long-term monitoring system was in place and used instead.

2.2.5.3 Long-Term Monitoring Setup

In the permanent data acquisition setup, the server to which the dataloggers were connected was used to command and download the data from the dataloggers. The system was set up to be accessed remotely by authorized users who could copy data files to their local computers for further analysis. The sampling rate and other factors could be adjusted remotely.

Data acquisition for the static system was controlled on the server by a program called *LoggerNet*, which interfaced with the dataloggers installed inside Span 4 of each structure. During data collection, the dataloggers effectively acted independently from *LoggerNet*, and interfacing was only required when downloading data off the dataloggers' onboard storage space or when sending out new information (routines, time synchronization, etc.). Datalogger times were independent from server times, did not account for daylight savings time adjustments, and could only be synchronized with the server time manually. Even if communication between the server and the dataloggers was temporarily lost, the dataloggers would still continue to collect data until the onboard memory was full, at which point they would begin to overwrite the oldest data. As long as *LoggerNet* was running and the server was able to communicate with the dataloggers, the server would automatically download all new data points at regular intervals throughout the day. Downloaded data was saved to three separate comma-delimited files: one for the northbound bridge (labeled NB), one for the southbound superstructure (labeled SB), and another for the southbound substructure (labeled SB_GK, the GK standing for Geokon).

The long-term monitoring setup for the static system was instituted on the southbound bridge beginning on September 1, 2008. Prior to the truck tests performed on September 14 and 17, 2008, a single sample was collected from each VWSG in the southbound superstructure every hour. During the truck tests, as noted in Section 2.2.5.2 above, data was collected from the northbound and southbound superstructures only when prompted by the system. Following the truck tests, the northbound superstructure was also integrated into the long-term monitoring setup, and data was sampled once every six hours (at midnight, 6:00 AM, noon, and 6:00 pm) from both superstructures until noon on March 26, 2009. At that time, the substructure static system gages in Pier 2 of the southbound bridge were integrated into the long-term monitoring setup, thus including all static system gages into the long-term setup. Also, in order to better quantify average strains and to be able to detect anomalous or spurious readings, five readings were taken from every static system gage every six hours. For the vast majority of measurements, all five readings were very similar, and spurious readings were rare in most gages. All five readings for one given set of measurements were taken within 15 minutes of initiating the reading routine. Beginning at 2:00 PM on September 17, 2009, the routine was changed such that five readings would be taken every hour instead of every six hours. This was done in order to better quantify daily thermal changes given that maximum temperature or thermal gradients would not necessarily occur at the six-hour interval times (refer to

Chapter 7 for more discussion regarding thermal behavior). Following this change, the routine remained consistent, excepting the occasional short-duration changes during system repairs and other investigations when the time between readings was decreased for sake of convenience (i.e., so workers did not need to wait a full hour before ensuring that the system was collecting properly). The ability to manually prompt the dataloggers to read all the gages was still available in the long-term setup, and was used during the truck tests conducted in October of 2010. The collection interval and number of readings per measurement set can be changed by modifying the program file sent to the dataloggers.

On July 1, 2010, a Matlab routine was implemented on the server to streamline the daily collection of static system data. The routine was set to run every morning at 1:20 AM central standard time. The routine would average together all the readings from each measurement set in order to simplify data handling. No anomaly detection was included in the Matlab routine other than removing infinite or non-number readings (i.e., gage errors), so anomalous strain readings were not removed before averaging. However, it was found that anomalous readings were extremely rare in the functioning gages. Upon successful completion of the routine, the system would send an email to the user. If the static system had not collected any new data since the previous day, a warning email would be sent to notify the user that there was likely an error in the collection. If no email was sent, then the user would know that the Matlab routine either erred during analysis or was never initiated, and that efforts would need to be made to rectify the mistake. All averaged data was saved into comma-delimited files for downloading from the server onto a local computer for analysis.

2.2.6 Repairs and Difficulties

2.2.6.1 Superstructure Static System Repairs

Of the 148 VWSGs installed in the superstructure, 134 (about 90%) survived installation and casting of the concrete. Four of the fourteen VWSGs that did not survive provided strain measurements, but did not provide temperature readings. Twelve of the nonoperational VWSGs were replaced with externally mounted Roctest SM-5A VWSGs on May 11, 2010 and June 18, 2010. Of those replaced, nine gages provided reasonable data values (VS15EML1, VS09EEL1, VS08ETL1, VS04EBL1, VN15EBL1, VN14ITL1, VN14IBL1, VN07EWL1, and VN05IBL1). Five gages were deemed unrecoverable due to either multiplexer connection problems (VN08IBL1 and VS07EBT3), impossibility of replacement (VS07ETT4 and VS04EEL1 were in positions unreachable from inside the boxes), or anchorage difficulties (VS06ETL1, originally installed as an external VWSG, was removed and re-epoxied into place, but still provided unreliable data). Although gages VS07ETT4 and VS04EEL1 were not replaced, only the thermistors of these VWSGs were broken. Therefore, these gages were still able to provide data if it was assumed that temperatures could be extrapolated from other gages.

No repairs were performed on any thermistors, as it was not feasible to embed new gages, and external gages would not provide the information necessary for investigating thermal gradients through the concrete. Four thermistors did not survive installation: TSITB002, TSITB005, TSITB006, and TSEBA003. As discussed in Section 2.2.2.3, gages TSITC001, TSITC002, TSITC003, TSITC004, TSITC005 and TSITC006 located above the east web of the interior box that had inconsistent coordinates were not used for investigation of thermal gradients.

2.2.6.2 Wiring Difficulties

Through inspection of the collected data during the truck tests (Chapter 5) and thermal variations (Chapter 7), it was determined that certain gages, particularly thermistors, were wired incorrectly and that channels were swapped among gages. Strain gages were confirmed to have their wiring swapped if clear sign errors or unrealistic magnitudes were observed during the truck tests (Chapters 5 and 6).

Thermistors were found to be swapped by noting that during the peak of the thermal gradients (discussed in Chapter 7) through the deck, the temperature should always decrease with depth. Other gages which did not provide obvious signs of swapped wires were left unaltered, and therefore other unknown wiring issues may be present. Table 2.2 and Appendix A represent the correct channel assignments to the best of the authors' knowledge.

2.2.6.3 Substructure Static System Difficulties

Six gages (USF serial numbers 28059 and 1994, and UMN gages UofMN1, 2, 3 and 5) in the interior column and one gage (USF serial number 1987) in the exterior column of southbound Pier 2 were never identified in the instrumentation vault at the base of the pier. Two gages (assigned VW_GK numbers of 14 and 34 according to the multiplexer channels to which they were connected) had no wire labeling, and could not be assigned to any gages installed in the superstructure. Therefore five of the gages listed above were never connected inside the instrumentation vault. It was believed that the unconnected gages were lost because their cable lengths were not long enough to reach to vault, and were therefore abandoned inside the piers.

A number of gages either did not survive construction and concrete casting, or did not provide usable data for monitoring. These gages were not able to be replaced. For gages in the drilled shafts, USF gage 28038 (VW_GK number 12) did not survive casting and USF gage 28049 (VW_GK number 25) output erratic strain data. In the exterior column, four of the five UMN gages (UofMN9, 10, 7 and 8, assigned respectively to VW_GK numbers 35, 37, 39, and 41) output nonphysical erratic strain data.

Strain data from the drilled shafts was not believed to provide results relevant to monitoring the structure after construction was complete. Therefore, data from the drilled shaft gages are not presented in further detail in this report.

2.2.6.4 Static System Failure

On October 28, 2010, the power supply that converted AC power to 12V DC for the fiber optic converters (B&B Electronic Media Converter) inside the control shed failed. This failure cut off connection between the server and dataloggers located inside the bridge. The dataloggers continued to run and collect data without continuous connection to the server. The power supply was replaced on January 4, 2011. It was found that the northbound bridge datalogger did not lose any data; the onboard hard disk had enough storage space such that none of the data collected during the outage was overwritten. The datalogger in the southbound bridge, which collected from far more sensors but had the same size of hard disk as the northbound datalogger, overwrote data from November 8, 2010 to December 15, 2010. This data was not recoverable.

2.3 SOFO System: Fiber Optic Strain Gages

The SOFO (Surveillance d'Ouvrages par Fibres Optiques) system was supplied by Smartec and contained all fiber optic strain gages located in the exterior box of the southbound bridge. A total of 12 sensors were installed along Span 2. These gages were used to monitor global strains and curvature of the southbound bridge either statically or, with the proper datalogger, dynamically.

2.3.1 Naming Scheme

Labels consisting of three characters followed by an underscore and another four characters were assigned to each of the SOFO sensors. The first two characters denoted the location of the gage along the length of Span 2 of the southbound bridge exterior box with the exception of two sensors (7gT_7011 and

7gB_7009) which were mislabeled and located at Location 7f. The third character denoted whether the gage was at the top (T) or bottom (B) of the box. The four-digit numbers were uniquely assigned to each sensor, but had no relevant meaning. The gage label associated with each SOFO sensor is given in Figure 2.40. Table 2.6 shows the stationing associated with each of the SOFO sensor locations. Because of the long gage length, stations refer to the location at the midlength of the gage.

2.3.2 Gage Model

The SOFO standard deformation sensors had a nominal 13.1 ft (4.0 m) gage length, which was the distance between the SOFO mounting points inside of the southbound exterior box of Span 2. Compared to the gage length of the Roctest EM-5 VWSGs (Section 2.2.1.2) equal to 6.75 in. (0.17 m), the SOFO sensors provided a global average strain over relatively long gage lengths. The SOFO standard deformation sensors had a measurement range of 0.5% in shortening and 1.0% in elongation. The operating temperature range of the passive zone of the SOFO sensors (i.e., the parts of the sensors not directly used for strain measurement, and instead used for connection of the gage to the reading unit) was -40˚F (-40˚C) to 176˚F (80˚C), and the operating temperature range of the active zone (i.e., the part of the sensors with the measurement and reference fibers over which the deformation was measured) was -58˚F (-50˚C) to 230˚F (110˚C). The datasheets from the manufacturer are available on request.

Each SOFO gage had two parallel optic fibers of the same length, one that was mechanically attached to the structure (i.e., the measurement fiber) and one that was not attached (i.e., the reference fiber). The purpose of the second fiber was to enable compensation for any changes in length of the optical fiber due to temperature, and therefore making the sensor insensitive to temperature changes.

2.3.3 Gage Locations

The SOFO gages were installed in pairs, one on the top and one on the bottom of the box, at six locations along the length of Span 2. These sensors were used to compute average strains and curvatures of the bridge over the length of the sensor (i.e., 13.1 ft (4.0 m)). Sensors were offset from the centerline of the exterior box to the east by a distance of 2.5 ft (0.76 m). A cross section of the gage placement is shown in Figure 2.41. The gages were placed such that the midlength of the gage was 33.5 ft (10 m) from each pier, and the midlength-to-midlength distance between two adjacent SOFO sensors ranged from 73.5 ft (22.4 m) to 106.5 ft (32.5 m). The locations for each pair of SOFO sensors are shown in Figure 2.40, with stations documented in Table 2.6.

2.3.4 Connectivity and Wiring of SOFO System

2.3.4.1 Static SOFO Connectivity

The default collection system used for the SOFO gages used the SOFO Bee static datalogger. All SOFO sensors were connected to a single optical junction box near the midspan of the southbound bridge Span 2 exterior box, as shown in Figure 2.38. The optical junction box was connected to the SOFO Bee datalogger in the control room. Then, through a switch, the datalogger was connected to the server.

2.3.4.1 Dynamic SOFO Connectivity

The supplier of the SOFO system (Smartec) committed to providing a dynamic data acquisition system a total of four times over the course of the monitoring project. Thus far, the system has been used twice: the first time during July of 2010 and the second time during the truck tests performed in October of 2010. Connectivity of the dynamic acquisition system was largely the same as for the SOFO Bee static datalogger. No wiring changes were necessary inside the bridge. Instead of attaching the optical junction

box cables to the SOFO Bee, they were connected to the dynamic acquisition system, which was then attached to the computer. Out of convenience during both uses of the dynamic acquisition system, a separate laptop computer was used for data collection instead of the bridge server. One issue with the dynamic collection unit was that only eight channels could be simultaneously attached to the acquisition system. Therefore, for any given test, four of the sensors were excluded from measurements. Collecting from two separate acquisition systems separately so that a total of 16 channels might be recorded did not appear to be feasible.

For future uses of the dynamic SOFO system, if it is desired to compute curvatures from all locations, all six bottom flange sensors and the two top flange sensors at locations 6a and 7b should be connected to the acquisition system. Computing curvatures according to an assumed neutral axis and only bottom flange strains was found to be only marginally less reliable than computing curvatures using both top and bottom measured strains for all locations except those near the pier at locations 6a and 7j. However, it was further found that the top flange sensor 7jT_7015 provided occasionally unreliable data when connected to the dynamic acquisition system. Therefore, the top sensor at location 7b (7bT_7008) should be connected to provided redundancy for the bottom flange sensor at the same location (7bB_7006). It was found that local deck deflections from live loading made computing global longitudinal curvature difficult from only top sensors. If it is desired to compute the most reliable curvatures from fewer sections, all top and bottom flange sensors at locations 6e, 6i, 7b, and 7f should be connected to the system.

2.3.5 Data Collection for the SOFO System

2.3.5.1 Static SOFO Data Collection

Static data collection for the SOFO system was handled by the SOFO SDB program on the server. Schedules (known as "agendas" in the program) were defined to collect data from each sensor every hour. Data could also be collected from all sensors on prompt from the user. During the truck tests in September of 2008, data was collected from each sensor manually be prompt from the server. The long-term collection system was started on October 30, 2008, and until February 11, 2010, one reading from each sensor was collected every hour. From February 11, 2010 until the present, the agenda was modified such that three readings would be collected from every sensor each hour. Data was saved to an SBD database file, which can be opened in either the SOFO SDB program or with Microsoft Access. Unlike the data from the static system (Section 2.2.5), the SOFO data required the SOFO SDB program on the server to be continuously running during collection. If the server were shut down, if the program were closed for any reason, or if the agenda running within the program were stopped, then data would not be collected (and would never be recoverable) until all these issues were rectified. Unlike the static system, collection times were intrinsically bound to the server clock times, and the SOFO Bee datalogger did not keep its own clock.

Similar to the static system, a Matlab routine was established on the server on July 1, 2010 to run every night and parse the collected SOFO data. The routine averaged together all readings from a single set of measurements and saved the data to a comma-delimited file for ease of file transfer and analysis. The program would send an email alerting the user whether or not any new SOFO data was collected, and no email was indicative that the Matlab routine either erred during analysis or was never initiated, and that efforts would need to be made to rectify the mistake.

2.3.5.2 Dynamic SOFO Data Collection

Dynamic data was collected through a SOFO Dynamic program independent from the SOFO SDB program used for static collection. The SOFO Dynamic program was incapable of automatically collecting data for given intervals of time; the program required constant user supervision to initiate and

save data. Consequently, the system was only used for short-term data collection, such as five-minute data blocks collected during ambient traffic, or data blocks encompassing individual dynamic truck tests, and only when research personnel were available. Because the cables from the optical junction box inside the bridge were connected to the dynamic acquisition unit instead of the SOFO Bee, static and dynamic measurement could not be taken simultaneously.

The SOFO Dynamic program allowed for modification of the frequency of data collection. During both times when the dynamic acquisition system was used, data was collected at 100 Hz (the same sampling rate as used for the accelerometer data, discussed in Section 2.4). Just after the acquisition system was powered on, the system required approximately an hour of "warm-up time." If data was collected before the system had "warmed-up," then a strong linear drift unrelated to deformations of the bridge would be seen in the collected strain readings. Also, the dynamic acquisition system always began collection of the strain readings for each data block at zero (regardless of the absolute level of sensor deformation) and thus was only used to measure the changes in strain over the measurement block.

Analysis of the dynamic SOFO data is not considered within this report.

2.3.6 Repairs and Difficulties

From October 30, 2008 until January 9, 2010, the data collection from the static system was often erratic. The system would randomly miss data readings. Although the system was scheduled to read every hour, it would occasional skip sensors. Occasionally, these skips would be chronic, and one sensor would appear to be down for several days at a time, and these chronic problems were not necessarily unique to any particular sensor. When the system did manage to read the sensors, the strain values appeared to be reasonable. This issue was resolved by Smartec (the system supplier) on January 9, 2010 with an update to the data collection software and data-logger firmware.

Whenever the database for the SOFO static system became too large, typically approximately 2 GB in size, the system would fail to collect data, usually with an error noting that "operation is not allowed in this context." This issue was solved simply by creating a copy of the database file (preferably renaming to South_Bound_exterior_backupYYMMDD.sdb), then creating a new database for South_Bound_exterior.sdb (the default collection name used for the system). The data not collected while this error occurred was permanently lost.

2.4 Dynamic System: Accelerometers, Linear Potentiometers, and Resistive Strain Gages

The dynamic system contained all accelerometers, linear potentiometers, and resistive strain gages installed in the bridge. The system was provided by Dataq, and Minnesota Measurements was in charge of the installation and service of the system. A total of 26 accelerometers were included in the superstructure of the bridge, and 12 linear potentiometers were included at the bridge expansion joints. A total of 24 resistive strain gages were installed in the southbound bridge Pier 2 columns and drilled shafts as part of the FHWA study performed by the USF.

2.4.1 Accelerometers

2.4.1.1 Naming Scheme

Accelerometers that were permanently attached at a specific location were named in accordance with their location. For example, “Accelerometer NB SP 2 Ext” was attached to the northbound bridge, Span 2, in

the exterior box. Permanently attached accelerometers were always located near midspan of their respective span and attached to the top flange at the centerline of the box (described in more detail in Section 2.4.1.3). Movable accelerometers were either named "Acc#", where # varied from 1 to 13 (excluding 9), or by their serial number. Names for the movable accelerometers had no relation to their position within the bridge. Accelerometer names, locations, and channels in the data acquisition system are summarized in Table 2.7.

2.4.1.2 Gage Models

The model of accelerometer used in the bridge was the Kistler 8310B2. The accelerometers had a range of ±2 g, a frequency response of zero to 250 Hz (± 5%), and noise of 380 μg. The datasheet for the accelerometers is available on request. The selected sensor was a DC-coupled accelerometer as opposed to an AC-coupled accelerometer, meaning that the installed sensors were able to measure "static" (i.e., gravity) acceleration at zero hertz. This was chosen so that the installed sensors would have the potential to be used for deflection measurements. Upon inspection of the data after installation, it was found that noise and low-frequency sensor drift made deflection measurements unachievable, and therefore the purpose of the acceleration data was narrowed to that of dynamic modal analysis (i.e., identification of modal frequencies, damping ratios, and mode shapes).

2.4.1.3 Gage Locations

Permanent accelerometers were attached to the bottom of the top flange at the center of each box near midspan of Spans 1, 2, and 3 of both the northbound and southbound structures. In addition, 14 movable accelerometers were placed within the exterior box of the southbound bridge in Span 2.

To facilitate rearrangement of the movable accelerometers within the southbound exterior box of Span 2, small aluminum angles to which the accelerometers could be mounted were installed at permanent locations within the box. Holes were drilled into both legs of the aluminum angles in order to allow the accelerometer to be bolted to it in either the vertical or horizontal position. The angles were then epoxied to the interior surface of the bridge at the desired locations, allowing gages to be repositioned relatively easily. Figure 2.42 shows a typical accelerometer installation. The permanently installed angles ensured that information obtained from the gages reinstalled at the same locations could be repeatable, even after repositioning the gages at various locations in the bridge. This was important to investigate changes in the behavior of the bridge subjected to repeated load tests in the future.

Dynamic truck tests, described in Chapter 5, were performed in September of 2008 prior to opening the bridge to investigate the dynamic properties of the bridge. To this end, the 14 movable accelerometers in the exterior box of Span 2 of the southbound bridge were oriented in two different configurations during these tests. The first orientation, also known as the short-term configuration and shown in Figures 2.43 and 2.44, was intended to capture the torsional modes of the bridge under dynamic loads. Figure 2.43 shows the location and orientation of accelerometers for the first orientation near Pier 3 (located 62 ft (19 m) from the thickened section). Figure 2.44 shows the location and orientation of the accelerometers for the first orientation near midspan of Span 2. As the figures show, the accelerometers were placed to read both vertical and horizontal movements, thus capturing torsional modes.

The second orientation, also known as the long-term configuration and shown in Figure 2.45, was used from September 17, 2008 until May 10, 2010. The accelerometers were attached to the top flange of the bridge adjacent to the east (interior) web of the box to exclude the local deck vibrations of the top flange from the measurements. On May 11, 2010, two accelerometers were moved and reoriented so that horizontal accelerations might be measured. This modified long-term configuration, shown in Figure 2.46, has been used to the present. For both long-term configurations, two of the 14 additional

accelerometers (ACC 1 and ACC 3) were located near midspan: one adjacent to the web and one attached to the top flange near the centerline of the box. For the first configuration (Figure 2.45), the remaining 12 accelerometers were spaced approximately evenly along the length of Span 2, with the exception of ACC 8, which was placed 10 ft (3.0 m) from ACC 9 because of cable length limitations. Accelerometers nearest the piers were 30 ft (9.1 m) from centerline of the piers. For the second configuration (Figure 2.46), ACC 8 was moved to midspan and oriented horizontally (in the transverse direction) on the same aluminum angle as ACC 1, and ACC 10 was moved and oriented horizontally (in the transverse direction) to the same aluminum angle as ACC 11.

The purpose for these long-term orientations of accelerometers was to investigate the modal frequencies and mode shapes of the bridge. The data from the accelerometers were to be used in the future to investigate potential deterioration of the bridge. Assuming that deterioration would be accompanied by a change in the structural stiffness, modal frequencies and mode shapes of the bridge would change accordingly. Although the frequency change might provide an indication of the occurrence of damage or deterioration, it does not provide sufficient information to determine the location of the damage. The determination of the higher mode shapes of the bridge has been suggested to be a potential means to better locate the sources of damage. Location and detection of damage are complicated by the temperature dependence of modal properties, which has been noted by Peeters et al. (2001), Sohn et al. (1999), and Kim et al. (2004). The identification of changes in bridge behavior may be useful in providing an early warning of bridge deterioration that could signal the need for bridge inspection, and repair if necessary.

2.4.2 Linear Potentiometers

2.4.2.1 Naming Scheme

Linear potentiometers were named according to the box, expansion joint, and superstructure region to which they were attached. They were named in the form of (A)(B)(C), where (A) was either NB or SB denoting to which structure the sensor was attached, (B) was SP 1 (LP was attached to Span 1 at the Abutment 1 expansion joint), SP 3 (LP was attached to Span 3 at the Pier 4 expansion joint), or SP 4 (LP was attached to Span 4 at the Pier 4 expansion joint), and (C) was either Ext or Int denoting whether the LP was attached to the exterior or interior box, respectively. Linear potentiometer names and positions are summarized in Table 2.8.

2.4.2.2 Gage Model

The overall longitudinal movement of the bridge at the expansion joints due to thermal effects was measured by a total of 12 Unimeasure HX-P420 Series linear potentiometers, which had a measurement range of 20 in. (0.51 m) and an operating temperature range of -40˚F (-40˚C) to 203˚F (95˚C). The datasheets for the linear potentiometers provided by the manufacturer are available on request.

2.4.2.3 Gage Locations

The linear potentiometers were located in both boxes of the northbound and southbound bridges attached to the south end of Span 1 at Abutment 1, the north end of Span 3 at Pier 4, and the south end of Span 4 to Pier 4. Figure 2.47 shows a cross section depicting the location of these instruments at the south end of Span 1 and north end of Span 3. Figure 2.48 shows the cross section depicting the location of the instruments at the south end of Span 4 for the southbound bridge, and Figure 2.49 shows the location of the instruments at the south end of Span 4 for the northbound bridge.

The potentiometers were installed similarly at all locations. They were all attached to the inside surface of the box and connected to a horizontal extension tube, as shown in Figure 2.50. At Abutment 1, this tube was attached directly to the abutment wall, and at Pier 4, the horizontal extension tube was attached to a vertical extension tube connecting down to the top of the pier.

Potentiometers attached at the south end of Span 1 measured the expansion joint movement at Abutment 1. Potentiometers attached to Span 3 and Pier 4 measured to relative displacement between the superstructure at Span 3 and the top of Pier 4. Because the superstructure of Span 4 was pinned to the top of Span 4, the expansion and contraction of Span 4 due to thermal changes would deflect the top of Pier 4. The potentiometers attached to Span 4 and Pier 4 were expected to measure virtually no relative movement between Span 4 and Pier 4 because of this pinned connection. The absolute deflection of Pier 4 was not able to be measured, and could only be assumed. Because of the vertical positions of the LPs, rotations of the superstructure would alter the measured expansion joint movements. Also, for LPs attached to Span 3 and Span 4, rotation of the top of Pier 4 would move the extension tubes and further alter the expansion joint measurements. Because the length of the tubes and gages were small compared to the length of the structures being measured, thermal expansion and contraction of the gages and tubes were assumed to be negligible compared to total measured bridge movements.

2.4.3 Resistive Strain Gages

2.4.3.1 Naming Scheme

The resistive strain gages installed in the columns and drilled shafts of southbound Pier 2 by the USF were connected to the dynamic data acquisition system. Gages were recorded according to their assigned "Windaq Serial Number," ranging from 1 to 24. These serial numbers corresponded to the acquisition channels used by the USF prior to connection of the resistive strain gages to the Dataq system. Table 2.9 shows serial numbers, acquisition and output channels, and associated locations within the shafts of the resistive strain gages.

2.4.3.2 Gage Model

Geokon 3911A resistive rebar strain gages were installed by the USF. These gages had a specified range of 2500 με and accuracy of 0.25% full-scale range. Their specified operating temperatures were -40˚F (-40˚C) to 200˚F (90˚C). Datasheets from the manufacturer are available on request for each of the gages. Resistive strain gages tend to drift with time, and thus were considered unsuitable for long-term monitoring.

2.4.3.3 Gage Locations

Geokon 3911A gages were installed in the drilled shafts (i.e., caissons) by the USF to investigate the effect of the construction loads within the foundation. These gages were installed in two shafts below the southbound bridge Pier 2 exterior column. Figure 2.31 shows the shafts (Shaft 1 and Shaft 2) instrumented in a cross-sectional view of the southbound bridge Pier 2 footing. Each drilled shaft contained 8 resistive strain gages, for a total of 16 resistive strain gages in the caissons. Elevation and cross-sectional views showing the locations of the gages in Shafts 1 and 2 are presented in Figures 2.32 and 2.33, respectively. The gages were placed at four levels in each shaft, with level 1 being the topmost layer and level 4 being the bottom. Two resistive strain gages were installed in each level. All the gages within the shafts were oriented vertically.

Resistive strain gages were installed to monitor the curvature of the columns. The Geokon 3911A gages were installed at the midheight of the columns (i.e., 39.88 ft (12.2 m) above the base of the southbound

bridge Pier 2 interior column and 39.27 ft (12.0 m) above the base of the exterior column) adjacent to the vibrating wire strain gages as described in Section 2.2.3.3 and shown in Figure 2.34. Resistive gages were placed in each of the four corners of the cross section (NW, NE, SW, SE) amounting to a total of 8 resistive gages in the columns. Field measurements for the Geokon 3911A gages were not available.

2.4.4 Connectivity and Wiring

The dynamic system setup consisted of eight dynamic junction boxes (i.e., nodes). Of the eight junction boxes, three were located in the northbound bridge, and five were located in the southbound bridge. Three repeaters were placed in the northbound bridge to minimize the cable length between any two junction boxes. The junction boxes and repeaters were connected in series starting at the control room and going south on the northbound bridge, then crossing over to the south end of the southbound bridge, and then heading north on the southbound bridge. The junction boxes were named "Node X", where X was a number ascending from 1 for the first node in the series (northbound bridge Span 3) up to 8 for the final node in the series (southbound bridge Span 3). Figure 2.38 shows the location of dynamic junction boxes and repeaters within the bridges. Tables 2.7 and 2.8 show the channel and node to which each accelerometer and linear potentiometer were connected, respectively. The resistive strain gages were directly connected to the resistive gage box in the instrumentation vault at the base of the southbound bridge Pier 2 shown in Figure 2.39. Channels from the resistive gage box were then wired up the pier and connected to Node 5 of the dynamic system, with the gages being assigned to the channels as given in Table 2.9.

2.4.5 Data Collection for the Dynamic System

Data collection was controlled by the Dataq TCP/IP Manager on the server. This program connected to all the junction boxes in series and opened a DI-720 Acquisition window for each node. At the end of each day, the daily dynamic data would be saved for each node as a binary file (with format either .wdq or .wdh) that could be opened by the Windaq Waveform Browser (WWB). These binary files could also be opened using ActiveX controls made available by Dataq. A new set of files (one file for each node) was saved each day. These files represented time series data, and did not apply timestamps to each collected data point. Instead, a timestamp was collected at the initiation of measurement at the beginning of the day and after each interruption in data collection. This time stamp was taken from the server time and saved as a UTC timestamp. Whenever the data was viewed using the WWB or ActiveX controls, the UTC timestamp would automatically be converted to the time zone of the computer used to view data. Times of points after data initiation were able to be computed using the sampling rate and the number of samples after data initiation.

Initial readings from the dynamic truck test data collected in September of 2008 prior to opening the bridge to traffic indicated there was too much noise to meaningfully interpret the data. In order to reduce the amount of noise for data collected after these truck tests, the collection sample rate was set to 1,000 Hz with a gain of 4 on a ±5V full scale, and then filtered by a resistance capacitance low-pass filter with cutoff frequency of 159 Hz. The data was then low-pass filtered using a Kaiser window with cutoff frequency of 23 Hz and decimated by a factor of 5 to 200 Hz. The final data was digitized to 14 bits (and saved as a .wdq binary file) until October 20, 2009, at which point the data was digitized to 16 bits (and saved as a .wdh binary file). Increasing the data to 16 bits increased the resolution of the digitized data by a factor of four.

Dynamic data used up a vast amount of hard disk space on the server, and it was periodically necessary to manually move all the dynamic data from the server onto an external hard drive. One reason for the disk space difficulties was the necessity of saving all data from a single node at the same sampling frequency. High frequency data collection was necessary for the dynamic accelerometer data, but high frequency

measurements were not important for linear potentiometers and resistive strain gages, for which the measured behaviors were largely "static." Every node had at least one accelerometer attached, and therefore in order to preserve the acceleration data, all nodes were recorded at the high sample rate of 200 Hz. On May 15, 2009, the two accelerometers attached to Node 5 were saved to a separate "virtual node" (i.e., a file for a node not physically existing on the bridge), thus leaving the file for Node 5 with channels only pertaining to resistive strain gage data. After this point, Node 5 was resampled down to 20 Hz to save disk space, while the accelerometer data saved to virtual Node 9 was continued at 200 Hz. To save even more disk space, beginning on September 1, 2009, the decimation of the accelerometer data following the Kaiser window filtering described above was increased to a factor of 10 down to a sample rate of 100 Hz. The resistive strain gage data at this time still remained at a sample rate of 20 Hz. On February 1, 2010, more virtual nodes were introduced to the system, separating out all accelerometer channels from the linear potentiometer channels. Accelerometer data was moved to virtual Nodes A, B, C, and D, which were saved at a sample rate of 100 Hz. Linear potentiometer data, now the exclusive sensors saved to Nodes 1, 3, 4 and 8, were reduced to a sample rate of 4 Hz, greatly saving disk space. The resistive strain gage data from Node 5 was reduced from a sample rate of 20 Hz down to 4 Hz on April 1, 2010.

No changes were made to the data collection procedure after April 1, 2010. A summary of the present state of the dynamic data collection system is as follows:

- All data digitized as 16-bit data files (using .wdh suffix).
- All data collected from all instruments at 1000 Hz with a gain of 4 on a ±5V full scale.
- All data filtered by a resistance capacitance low-pass filter with cutoff frequency of 159 Hz, then passed through a low-pass filter using a Kaiser window with cutoff frequency of 23 Hz.
- All accelerometer data decimated by a factor of 10 to a sample rate of 100 Hz and saved to Nodes 2, 6 and 7, and virtual Nodes 9, A, B, C, and D.
- All linear potentiometer data decimated by a factor of 250 to a sample rate of 4 Hz and saved to Nodes 1, 3, 4, and 8.
- All resistive strain gage data decimated by a factor of 250 to a sample rate of 4 Hz and saved to Node 5.

On July 1, 2010, a Matlab routine was implemented on the server to streamline the daily collection of the "static" data (i.e., the linear potentiometer and resistive strain gage data) on the dynamic system. The routine would extract hourly readings averaged over 100 points (for a sample rate of 4 Hz, this was equivalent to 25 seconds) from the continuously collected linear potentiometer and strain gage data, and would send an email to the user upon successful completion of the routine. If the dynamic system had not collected any new data since the previous day, a warning email would be sent to notify the user that there was likely an error in the collection. If no email was sent, then the user would know that the Matlab routine either erred during analysis or was never initiated. The hourly readings were saved into comma-delimited files for each node.

2.4.6 Repairs and Difficulties

2.4.6.1 Dynamic System Failures

The entire dynamic system was shut down on three separate occasions. The first outage occurred on August 15, 2009, and persisted until September 28, 2009 (1.5 months of no system). The second outage occurred on June 25, 2010. Approximately half of the system (Nodes 1 through 5) was brought online on August 28, 2010 (about 2-months downtime). Nodes 6, 7 and 8 were brought online on September 19, 2010. The third outage occurred on May 7, 2012 and has persisted to the present.

The timing for these outages appeared to coincide with electrical storms in the area. Repairs for this system have always involved replacement of the data-logger boards or repeater nodes (which connect data-logger nodes together): rarely have the instruments themselves had issues, excepting the linear potentiometer issues noted in Section 2.4.6.2.

On June 25, 2011, difficulties were encountered when attempting to collect data from Nodes 5-8 simultaneously with Nodes 1-4. Collecting Nodes 5-8 without Nodes 1-4 worked, as did collecting Nodes 1-4 without 5-8, but collecting both sets at the same time was not possible. The problem was discovered to be a poor synchronization signal between Nodes 4 and 5. On September 13, 2011, Node 5 was replaced and the issue was resolved. Nodes 5-8 were not collected for approximately 3 months.

During the repairs performed on September 13, 2011, an additional wire was tied from a point near the accelerometer channels of Node 5 to ground. Josh Sebasky from Minnesota Measurements stated that this was to "augment" the ground. It was noted that Ken Spikowski from Dataq found manifestations of a weak ground in the Node 5 accelerometer data (the accelerometers would occasionally and temporarily lose their 1g stable point). Josh Sebasky mentioned that the grounds used for all the Dataq nodes were tied into the lighting system, for which the electrical work was supplied by Polyphase. He believed that the ground had been weak for Node 5 ever since installation, but it would not be possible to rectify this situation short of tying to a new ground outside the lighting system. It was not clear if the weak ground at Node 5, or the grounding scheme in general, had any implications regarding the cause of the aforementioned failures, nor was it clear whether the annual summer system failures would continue in the future.

2.4.6.2 Linear Potentiometer Repairs

The four LPs attached to the southbound bridge at Pier 4 were not collecting data at bridge opening. It was found that the LPs were operational, but were not powered properly. This issue was resolved on September 28, 2009, and approximately one full year of data was lost since bridge opening.

It was discovered that the LP braces extending down to the top of Pier 3 from the interior box of southbound bridge Span 3 were colliding with the vermin guard across the expansion joint. This caused erroneous LP readings during the winter of 2009-2010. On June 18, 2010, the vermin guard was sufficiently trimmed back for all LP braces extending down to Pier 3.

After the second dynamic system outage on August 28, 2009, it was found that four of the linear potentiometers had failed during the outage. The two LPs attached to the northbound bridge at Abutment 1 were replaced September 21, 2010, and the two LPs attached to Span 4 of the southbound bridge at Pier 4 were replaced September 30, 2010. For these replacements, the new LPs were mounted on the same concrete embedded bolts as were used to mount the replaced LPs.

2.4.6.3 Accelerometer Integration Difficulties

The accelerometer data could not be accurately integrated to determine bridge deck displacement at the locations of the accelerometers. It was found that noise and low-frequency sensor drift made deflection measurements unachievable. The signal-to-noise ratio of the acceleration data would need to be increased by several orders of magnitude before this type of calculation would be feasible, or vastly different methods for integration of acceleration signals would need to be developed and tested. Computing displacement from acceleration data is not discussed in further detail in this report.

2.4.6.4 Time Gaps in Dynamic Data

The dynamic system will occasionally, and seemingly randomly, stop recording for a few minutes and leave time gaps in the readings. These time gaps can cause problems for analysis of the accelerometer data. Discussions with Dataq have revealed that development of proper ActiveX controls could circumvent the problem in the analysis (although time gaps would still remain present in the data, it would be possible to avoid to data gaps in analysis without encountering processing errors). Development of these ActiveX controls is presently ongoing.

2.4.6.5 Usability of Resistive Strain Gage Data

Six of the resistive strain gages were not collected in the dynamic system. Four gages (Windaq serial numbers 2, 3, 17 and 21) were connected in the pier instrumentation vault, but were not collected in the dynamic system. It was unclear why these channels were never collected. Furthermore, the two gages at the bottom layer of Shaft 2 were never connected in the pier instrumentation vault, and consequently also never collected on the dynamic system. It is unclear why these gages were never connected.

The resistive strain gages were not well suited for long-term monitoring due to signal drift unrelated to structural deformation changes. Furthermore, the dynamic strains of the piers were not considered to be of particular value to overall monitoring of the structure. Therefore, the resistive strain gage data is not further discussed in this report.

2.5 Corrosion Monitoring System

The corrosion monitoring system, also known as the Corsensys, was installed by Smartec to monitor the corrosive environment of the bridge deck. Sensors were installed to measure the concrete resistivity, related to the moisture in the concrete, and to measure the corrosion current indicating the rate of corrosion of plain (i.e., non-epoxied) reinforcing bars in the concrete.

2.5.1 Naming Scheme

Gages were named according to the number assigned to the datalogger. Each logger had attached a single resistivity sensor (CS-402 in Section 2.5.2) and a single corrosion current sensor (CS-040 in Section 2.5.2), so the datalogger numbers were also unique descriptors for the attached sensors.

The Corsensys dataloggers are summarized in Table 2.10. The dataloggers originally installed into the system were all found to be defective (discussed in greater detail in Section 2.5.6). These dataloggers (corresponding to the "old logger numbers" in Table 2.10) were all replaced, and therefore the names assigned to the sensors were changed to the "new logger numbers."

2.5.2 Gage Models

To monitor the susceptibility of the bridge to corrosion, Corsensys CS-040 and CS-402 sensors were used. Datasheets from the manufacturer for these sensors are available on request. These sensors consisted of a series of four short pieces of reinforcement which were connected to a bar in parallel layers.

The CS-040 sensors used ordinary rebar, according to the data sheets, to obtain corrosion initiation and corrosion propagation information. The sensors worked by measuring the current (i.e., corrosion current) between two adjacent layers of rebar. As long as the steel was passive, the corrosion current was zero. If corrosion initiated, the current would increase, indicating that the critical chloride content had reached the

reinforcement. The corrosion propagation could be measured over time by measuring the current. The measurements were used to indicate when it was time to replace the deck (i.e., when the corrosion susceptibility reached a certain depth within the concrete.

The CS-402 sensors used stainless steel bars to measure electrical resistivity. The AC impedance of each sensor (i.e., the four parallel bars) was measured against the surrounding reinforcement (ground) and between the adjacent sensors. The resistance was dependent on concrete moisture, pore volume, and temperature. Temperature was measured with temperature sensors at two different depths. The temperature effects could then be compensated using an Arrhenius equation:

$$R_{T1} = R_{T0} \cdot e^{b\left(\frac{1}{T_1} - \frac{1}{T_0}\right)} \qquad (2\text{-}1)$$

where R_{T1} and R_{T0} are the resistivity at absolute temperatures T_1 and T_0 (specified in Kelvin), respectively, and b is a fitting parameter estimated from the measured data. The fitting parameter can be computed by plotting the logarithm of resistivity measurements with respect to the absolute temperature. Then using this fitting parameter, all resistivity measurements can be converted to a reference temperature (for example, T_1 = 276 K) from the measured temperature T_0.

Figure 2.51 shows the typical installation of the Corsensys CS-040 sensors while Figure 2.52 shows the typical installation of the Corsensys CS-402 sensors. These photos were obtained from the Corsensys data sheets, not from the I-35W installations.

2.5.3 Gage Locations

A total of four of each of these units (i.e., four CS-040 and four CS-402 sensors) were installed in the bridge. The gages were located in the deck above the exterior box of each bridge near the midspan of Span 1 and Span 3. The sensors were installed such that the first bar was 1.75 in. (44 mm) below the nominal top of slab. The remaining three bars were then located in 1-in. (25-mm) increments below the top bar.

2.5.4 Connectivity and Wiring

Each set of CS-040 and CS-402 corrosion potential sensors was connected to a datalogger at the location of each sensor (i.e., in the exterior box near the midspan of Span 1 and Span 3 of both bridges) as shown in Figure 2.38. The two dataloggers in each bridge were connected in series and then connected to the CU-100 Corsensys Central Unit in the control room. The Corsensys Central Unit was then connected to the server through a switch.

2.5.5 Data Collection for the Corsensys

Data collection for the Corsensys was handled by the Corsensys Online-Monitor. This program connects to each datalogger within the bridge and saves the data to semicolon-delimited files. Each datalogger is saved to a separate file named by the number of the datalogger: 401.csv, 402.csv, 403.csv, and 404.csv. Data was read hourly from each sensor. Each datalogger has some onboard hard disk space for storing data when the Corsensys Online-Monitor is not running.

This program has not been configured to run automatically on server startup and must be started manually. When the program is started, the button labeled "Start Communication" must be pressed before the Online-Monitor connects to the dataloggers. Once pressed, the program will continue to run until shutdown. No Matlab routine has been developed for analysis of the Corsensys data.

2.5.6 Repairs and Difficulties

The Corsensys has never been fully operational since the system was installed. No user's manual has been provided by the suppliers, and the collected data has never been fully analyzed or understood. Prior to April 14, 2011 none of the dataloggers provided data usable for any sort of monitoring. On April 14, 2011, two of the dataloggers were replaced (503 was replaced by 402, and 504 was replaced by 401). These dataloggers appear to provide data that might be usable for monitoring, but because no user's manual has been provided, interpretation of the data has proven impossible. The two remaining dataloggers were replaced on September 13, 2011 (505 was replaced by 403, 506 was replaced by 404). Again the new dataloggers appear to provide data that might by usable, but without a user's manual, interpretation has been impossible. Because of these problems, the Corsensys data is not discussed in more detail in this report.

Chapter 3. Mechanical and Time Dependent Concrete Properties

To interpret the data from the bridge using finite element modeling, it was important to determine the material properties to be included in the model. Over the course of the construction, concrete samples were taken from the bridge for material testing. The properties of interest included the concrete compressive strength, tensile strength, elastic modulus, creep and shrinkage, and coefficient of thermal expansion.

The entire superstructure of the bridge was built using the same concrete mix. However, this was a massive structure with concrete coming from many trucks and many batches of concrete, cast over the course of eleven months during a variety of environmental conditions with extreme temperature ranges. In order to obtain a better representation of the concrete within the bridge, samples were collected by the University of Minnesota from different pours over the course of construction. MnDOT also provided the research team with more than 300 cylinders that had been cast but were not needed for their testing purposes. The samples from MnDOT came from various areas of the bridge including the superstructure and piers. The piers and other areas of the bridge used different concrete mixes than that used in the superstructure. The samples used for the results presented in this report are summarized in Table 3.1.

All samples collected by the University of Minnesota (except those used to measure coefficient of thermal expansion) and tested in this project were stored in the laboratory in an environmental chamber. The room automatically maintained a relatively constant temperature and relative humidity. For these tests, the room was kept at 73.4°F (23°C) and 40% relative humidity as per ACI 209R-92 standard for measuring creep and shrinkage. The temperature and relative humidity of the room were read from a digital readout displayed outside the room and recorded each day shrinkage and creep measurements were taken. The temperature of the room varied from 70.3 to 79.0°F (21.3 to 26.1°C) while the relative humidity varied from 30.2% to 40.1%. The additional samples collected by MnDOT and donated to the UMN were not stored in temperature and humidity controlled rooms, and were instead placed on pallets located in the UMN Structures Laboratory or in storage rooms in the UMN Civil Engineering Building.

The coefficient of thermal expansion samples were stored in several locations. Some were stored in the same environmental chamber as the creep and shrinkage specimens, and some were stored in a room that did not have controlled temperature or relative humidity. Once testing started on these samples, they were moved into a temperature controlled room that did not include humidity control.

The following sections describe the sample preparation, instrumentation, testing procedures, results of the tests, and general comments about the tests. The chapter is organized starting with a discussion of compressive strength and modulus of elasticity of the concrete, followed by tensile strength, then shrinkage and creep, followed by coefficient of thermal expansion of the concrete.

3.1 Compressive Strength and Modulus of Elasticity

3.1.1 Sample Preparation

The concrete compressive strength, f'_c, and modulus of elasticity, E_c, were measured using standard 4 x 8 in. (100 x 200 mm) cylinders. The specimens tested came from deck pours on Span 4 of the southbound and northbound bridges on August 8 and August 9, 2008 (the same pour of concrete from which the shrinkage and creep samples were collected), with the majority from the southbound bridge pour. To ensure that the source of the specimen was known after the samples were moved, the cylinder molds were labeled at the time of casting. The samples from the Span 4 deck pours were allowed to cure at the bridge site for one day, and were then brought to the University of Minnesota and placed in the environmental

chamber in the laboratory. The final step in preparing these specimens for testing was to cap the ends with sulfur compound and label the source of each sample on the cylinder.

3.1.2 Instrumentation

A Forney concrete testing machine was used to conduct the compressive strength and modulus of elasticity tests. A compressometer was used to measure the modulus of elasticity of the samples. Before fastening the compressometer to the cylinder, side bars were mounted to maintain an initial undeformed configuration. Once the compressometer was slid over the cylinder and tightened into place using screws, the side bars were removed, allowing the apparatus to pivot about a hinge when the cylinder was under loading. Displacement of the specimen was measured by a linear variable differential transformer (LVDT) attached to the compressometer frame. The pivoting associated with the frame amplified the vertical deformation of the concrete cylinder by a factor of two to enhance the resolution of the measurements. Figure 3.1 shows a photograph of a modulus sample in the Forney machine with steel plates used to position the cylinder, and the LVDT and frame attached.

3.1.3 Testing

The concrete compressive strength and modulus of elasticity of the concrete were measured using the Forney concrete testing machine on the days that the creep frames (refer to Section 3.3) were initially loaded (i.e., at ages of 56, 93, and 130 days). The 7-day compressive strength was not tested for the samples collected. The testing machine was inadvertently metered at approximately 16 psi/s (110 kPa/s) for these tests while ASTM C39/C39M specifies a rate of 35±7 psi/s (240±48 kPa/s). Aside from the loading rate, the testing procedure followed ASTM C39/C39M. MnDOT provided compressive strength test data for samples that were tested according to MnDOT manuals and procedures which were set per the ASTM specifications.

Three specimens were used to establish the concrete compressive strength, f'_c, at each age. After determining the failure load from the first cylinder, the compressometer was attached to the second and third samples to measure the modulus of elasticity. In measuring the elastic modulus, the initial reading of the LVDT was noted with no load applied to the cylinder. The modulus tests were performed according to ASTM C469 except that the load rate was inadvertently metered at approximately 16 psi/s (110 kPa/s) while ASTM called for a loading rate of 35±5 psi/s (240±34 kPa/s). Load was then applied, and the load at which the LVDT reading first changed was recorded. The loading rate was monitored to ensure that it remained constant until the load reached 40 percent of the load required to fail the first cylinder tested, and the LVDT reading was recorded. Several intermediate loads and LVDT readings were also manually recorded while loading the specimen. After the load reached 40 percent of the failure load, the test was repeated. After the last repeat, the compressometer was removed and the cylinders were then loaded to failure.

For measurements at 56 days, the cylinders tested for modulus of elasticity were loaded to 40% of their failure load twice, as described above, before being loaded to failure. For measurements at 93 and 130 days, modulus measurements were performed in the same manner as noted above, but the cylinders were loaded to 40% of failure three times before loading to failure.

3.1.4 Results

The specified 28-day compressive strength of concrete, f'_c, for the superstructure was 6.5 ksi (45 MPa). Based on this concrete compressive strength, the predicted modulus of elasticity according to the AASHTO LRFD Bridge Design Specifications 4th Edition (2007) Eqn. (C5.4.2.4-1) was

$$E_c = 1820\sqrt{f_c'} = 4640 \text{ ksi } (32 \text{ GPa}) \quad (3\text{-}1)$$

The concrete compressive strength and modulus of elasticity were tested on the days that creep specimens were loaded. The results of these tests are given in Table 3.2. The average measured 56-day, 93-day, and 130-day compressive strengths were 7.1 ksi, 6.7 ksi, and 6.2 ksi (49 MPa, 46 MPa, and 43 MPa), respectively. The average measured moduli at 56, 93, and 130 days were 4400 ksi, 4700 ksi, and 4200 ksi (30 GPa, 32 GPa, and 29 GPa), respectively. The expected modulus computed using the measured compressive strengths in Eqn. (3-1) ranged from 4550 to 4850 ksi (31.4 to 33.4 GPa). As noted in Section 3.1.1, these measured samples were all taken from the same pour of concrete (i.e., the southbound bridge Span 4 deck pour). It was unclear why the measured concrete strength and modulus generally decreased with age.

Concrete strength tests were also performed by MnDOT. A summary of MnDOT's test results for concrete taken from Span 4 deck concrete of both the northbound and southbound bridges is presented in Table 3.3. The average 7-day, 28-day, and 56-day strengths of the southbound bridge Span 4 deck concrete from MnDOT's results were 5.8 ksi, 7.6 ksi, and 7.2 ksi (40 MPa, 52 MPa, and 50 MPa), respectively. The modulus of elasticity associated with these measured strengths and computed using Eqn. (3-1) was 4360 ksi, 5000 ksi, and 4880 ksi (30.1 GPa, 34.5 GPa, and 33.6 GPa), respectively. Although concrete compressive strengths are typically assumed to increase with age, this was not observed in the results collected after 28 days. MnDOT's data indicated the mean compressive strength reduced from 28-day strength to 56-day strength for the southbound bridge Span 4 deck concrete. The samples tested by the UMN also had a reduction in mean compressive strength as age increased. The mean compressive strength obtained by MnDOT and the UMN at 56 days was within one percent between the two groups. One possible explanation for the unexpected results was the number of samples tested at each age. The 7-day and 28-day MnDOT test results each consisted of 30 or more test specimens while the 56-day and older results consisted of three to four samples.

3.2 Tensile Strength

3.2.1 Sample Preparation

Concrete cylinders with dimensions of 6 x 12 in. (150 x 300 mm) were prepared for testing tensile strength. Two of these samples were collected from the deck pour of Span 4 of the northbound bridge and three samples were collected from the deck pour of Span 4 of the southbound bridge. These samples were taken from the same pours from which the creep and shrinkage specimens were collected. The samples were stored in the same environmental chamber as the creep and shrinkage cylinders, as noted in the Chapter 3 introduction, at a constant temperature and relative humidity.

3.2.2 Instrumentation and Testing

The Forney concrete testing machine was used to measure the tensile strength of the concrete in the bridge using the split cylinder method on 6 x 12 in. (150 x 300 mm) cylinders. These tests were performed on October 6, 2008. Five samples were tested, three from Span 4 of the southbound bridge (58 days old) and two from Span 4 of the northbound bridge (59 days old). The tests were performed on this date to be close to the 56-day tensile strength. The tests were performed according to ASTM C496/C496M.

3.2.3 Results

For concrete with specified compressive strength of 6,500 psi (45 MPa), the average splitting tensile strength can be estimated from section R8.6.1 of the ACI 318-08 (2008) as

$$f_{ct} = 6.7\sqrt{f_c'} = 540 \text{ psi } (3.7 \text{ MPa}) \quad (3\text{-}2)$$

The results of the split cylinder tensile strength tests of the concrete specimens tested at 58 and 59 days old are given in Table 3.4. For the specimens from the southbound bridge, the overall average tensile strength was 395 psi (2.7 MPa) with a maximum tensile strength of 469 psi (3.2 MPa) and a minimum tensile strength of 328 psi (2.3 MPa). The average tensile strength of the northbound bridge samples was 410 psi (2.8 MPa). The tensile strengths computed using Eqn. (3-2) and the average measured compressive strengths measured each day for the UMN and MnDOT cylinders are shown in Table 3.2 and Table 3.3, respectively. The measured tensile strengths were low in comparison with the tensile strength expected using Eqn. (3-2). One possible explanation for this was the low number of samples tested with a relatively large coefficient of variation.

3.3 Shrinkage and Creep

3.3.1 Sample Preparation

Special forms were created for the shrinkage and creep specimens using 4 in. (100 mm) diameter PVC pipe. The pipe was cut into pieces 11.5 in. (290 mm) in length which allowed for an 11 in. (280 mm) long specimen after the cap was placed on the end of the pipe (the cap extended 0.5 in. (13 mm) into the pipe). Care was taken to ensure that the ends of the pipe pieces were cut flat and perpendicular to the lengthwise direction of the pipe. The pipe pieces were then placed in the fixture shown in Figure 3.2 which had three holes at 120° increments around the circumference of the two metal rings (i.e., three holes per ring). The two rings were set 7.75 in. (200 mm) apart, center-to-center. The holes were aligned vertically between the two rings and served as a template for drilling three sets of two holes through the PVC pipe in straight lines parallel to the length of the pipe. Brass inserts were attached to the inside of the PVC pipe at each of these locations using a screw from the outside that was tightened by hand.

The forms were completed using PVC cement to attach a PVC cap to the bottom of each form. Duct tape was used to help secure the cap to the pipe to ensure that it did not come loose while casting the samples. Just prior to casting, motor oil was applied to the inside of the forms with care taken to avoid application to the brass inserts so the concrete would be able to adhere to the inserts. Figure 3.3 shows images of the completed mold used for the shrinkage and creep specimens.

The concrete for the shrinkage and creep tests was taken from two pours during construction. The first set of samples (three shrinkage cylinders) came from concrete used in Span 4 of the northbound bridge and was collected on August 8, 2008. The second set of samples (six shrinkage cylinders and eight creep cylinders) came from concrete used in Span 4 of the southbound bridge collected on August 9, 2008. Samples from the northbound bridge were inadvertently left uncovered at the bridge site where they were stored for one day before being brought to the University of Minnesota and placed in the environmental chamber in the structural engineering laboratory. The samples from the southbound bridge were covered and allowed to cure for one day at the bridge site before being brought to the University of Minnesota and placed in the environmental chamber in the laboratory. On August 12, 2008, the concrete was removed from the molds by removing the screws and then sawing off the PVC shell. DEMEC (demountable mechanical strain gage) points were recovered from previously used shrinkage and creep specimens and placed in the brass inserts for measuring.

To finalize the preparation of the shrinkage and creep specimens, a sulfur cap was added to the end of the specimens that would be used for the creep measurements, and epoxy was applied to the ends of the specimens to be used for shrinkage measurements in order for both sets of specimens to have the same area exposed to the air. To apply epoxy, duct tape was attached to the edge of the concrete specimen with half of its width sticking past the end of the concrete. The epoxy was then poured on the end; the tape prevented the epoxy from spilling over the edge and produced an even layer of epoxy on the specimen. The epoxy was allowed to harden for a day before removing the tape. The samples were labeled to indicate their source and uniquely identify each cylinder. The label consisted of five figures. The first figure denoted whether shrinkage (S) or creep (C) would be measured with the sample. The second figure specified from which span the sample came. The third and fourth figures showed whether the specimen came from the southbound (SB) or northbound (NB) bridge. The final figure was a numerical value to differentiate between samples that came from the same span of the same bridge and were being used to test the same property. Each set of points was labeled as either "A", "B", or "C" on each cylinder to keep track of which side was being measured.

3.3.2 Instrumentation

3.3.2.1 Shrinkage

As mentioned earlier, brass inserts were placed in the shrinkage specimens and DEMEC points were inserted into them. The DEMEC points that were installed in the specimens had a conical dimple with a very fine point at the center of the head. A Whittemore gage was used to measure the distance between two DEMEC points along the length of the specimen. The Whittemore gage, shown in Figure 3.4, had a fine point at each end which was inserted into the dimple. The gage used was a Mitutoyo Absolute Model ID-C112TB. It had a digital readout that measured the offset of the reading from 8 in. (200 mm).

In addition to the gage, an Ohaus Explorer Pro Model EP12001 balance was used to weigh the specimens each time the Whittemore gage readings were recorded.

3.3.2.2 Creep

The creep specimens had brass inserts and DEMEC points in them as well, thus the same Whittemore gage used for measuring the shrinkage samples was also used for measuring the creep specimens.

In order to measure creep, the cylinders were subjected to load. To do this, spring-loaded creep frames were used, which required periodic adjustment to maintain relatively constant load. The creep frames were constructed using 10 x 10 x 1.5 in. (250 x 250 x 38 mm) thick plates, 1.25 in. (32 mm) diameter by 48 in. (1.2 m) long steel tension rods, and disk springs. Each plate had four holes just large enough for the rods to slide through. The holes were oriented in an approximately 7.25 in. (180 mm) square pattern, center-to-center. Additionally, nuts and washers to match the rod were used to assemble the frames.

To build the frames, the nuts and washers were placed at the bottom of each of the four tension rods. A plate (lower base plate) was then slid down the rods to rest on the washers and nuts. Attached to the lower base plate over the tension bars were four pairs of disk springs. The springs were placed in series (one pair at each corner of the base plate). Above the springs, another plate (upper base plate) was placed. Two creep specimens in series sat on this plate. A bearing block rested on the top creep specimen and a plate (lower jack plate) was placed on the tension bars above the bearing block. A load cell rested on this plate. A hydraulic jack was placed above the load cell, and above this, the final plate (upper jack plate was placed). Nuts and washers were placed above the upper jack plate in order to load the frame. Nuts were placed above the lower jack plate and tightened after the frame was loaded in order to sustain the load after releasing the jack. Additionally, nuts were placed below each of the jack plates to

prevent the plates from falling and crushing fingers while installing specimens and the load cell and jack. Figure 3.5 shows a picture of the frame used for loading the creep specimens. The load in the frame was monitored using a Wheatstone bridge created with four 120-Ω electrical resistance strain gages applied to each tension bar. The resistance gages were hooked up to a switch and balance unit (two frames per switch and balance unit) and each switch and balance unit was hooked up to a strain indicator box, which displayed the load in each tension bar.

In order to ensure that the correct load was obtained from the resistive gages in the tension bars, the frames had to be calibrated. The load cell was calibrated using a Forney concrete testing machine. An additional 10 x 10 x 1.5 in. (250 x 250 x 38 mm) thick plate was then used between the load cell and the jack in the creep frame. Nuts and washers were used above this plate to allow the load to be sustained and read by the load cell after the jack was released. Instead of using concrete samples, a 4 x 4 x 0.5 in. (100 x 100 x 13 mm) thick hollow steel member 1 ft-8 in. (0.5 m) in length was used for the calibration. The steel calibration member is shown in Figure 3.6. By having the load cell placed under the additional plate, it was easy to compare the load being read from the load cell with the sum of the loads obtained from the gages in the tension bars. The gage factor in the strain indicator box was adjusted and the frame reloaded until the two values matched closely.

3.3.3 Testing

3.3.3.1 Shrinkage

Shrinkage measurements began shortly after the specimens were cast because this was when the largest shrinkage effects were expected to occur. To ensure that the correct value was measured each day, each set of points was measured four times. First, an invar bar was measured before each sample. This bar allowed for measurements taken one day to be compared with readings taken on another day in case the Whittemore gage changed length (e.g., due to variations in temperature in the room), as the invar bar did not change length with temperature changes. Initially, measurements taken with the invar bar were difficult to keep consistent. It was discovered that the initial inconsistency in readings was due to the surface (i.e., the floor) on which the invar bar was placed. To prevent the inconsistency in the readings, the invar bar was placed on a thick, flat piece of steel for taking measurements. After the invar bar length was recorded, side “A” of the cylinder was read. The cylinder was then rotated, and side “B” was measured. This process of rotating the cylinder and measuring was continued until sides “A”, “B”, and “C” of the cylinder had each been measured four times, then the invar bar was measured again. This process was performed for every shrinkage specimen. In order to obtain consistent results, the same person performed the measurements each day. In addition to measuring the change in length, the shrinkage samples were also weighed every day that DEMEC measurements were taken. The temperature and relative humidity of the environmental chamber were recorded each day the shrinkage measurements were taken.

Shrinkage samples were measured once a day for 11 days. The measurements then became less frequent; typically three times per week until the creep specimens were loaded. Several months after beginning to take the measurements, the measurements were taken approximately once per week, with increasing duration between measurements as more time passed.

3.3.3.2 Creep

The samples used to measure creep were stored in the environmental chamber until loading. The ages at which the specimens were loaded were chosen to approximate the loading ages experienced by the precast segments in the bridge. The youngest concrete age at loading during construction of the bridge was from one of the segments nearest midspan (segment 15) of the northbound bridge exterior (east) box,

which was loaded at an age of 48 days. The oldest concrete age at loading was from the precast segment nearest Pier 2 on the southbound bridge interior (east) box, which was loaded at an age of 124 days.

Two different stress levels were chosen to be investigated with the creep tests: 275 ksf (13.2 MPa) and 420 ksf (20.1 MPa). The 275-ksf (13.2 MPa) stress level was equivalent to the maximum compressive stress experienced by most of the bridge, with the exception of the precast segments nearest the midspan of Span 2 which experienced a larger compressive stress for a short amount of time while the cantilevers were jacked apart to cast the closure pour at the midspan of Span 2. Some portions of the bridge never had a compressive stress level as large as this. For this stress level, the load applied to the 4-in. diameter cylinders was 24.0 kips (106 kN). The 420-ksf (20.1 MPa) stress level corresponded to the maximum allowable sustained compressive stress level for concrete according to ACI and AASHTO (i.e., $0.45*f'_c$). The load applied to the cylinders to achieve this stress level was 36.8 kips (164 kN). The original plan called for using the 24.0-kip (106-kN) load for one frame (two samples) at each of the ages and the 36.8-kip (164-kN) load for the youngest age of concrete loaded.

The first specimens labeled C4SB1 and C4SB2 (in Frame #1) were loaded on October 4, 2008 at an age of 56 days, approximately corresponding to the youngest age at which any segment of the bridge was first loaded. These samples were loaded to approximately 24.0 kips (106 kN). The second set of samples labeled C4SB3 and S4SB3 (in Frame #2) was loaded the following day at an age of 57 days. Frame #2 was loaded one day after loading Frame #1 because while attempting to load Frame #2 during the first day, the load became larger than expected, and one of the original samples (C4SB4) failed in compression. The overload occurred due to the following sequence of events: The samples were initially loaded to the desired 36.8-kip (164-kN) load, and the nuts tightened. Upon releasing the jack, the load was read using the strain indicator box. It was found that the load had reduced upon releasing the jack as a result of not tightening the nuts enough and that the load was not evenly distributed amongst the tension bars. Upon reloading, the nuts were not loosened, but the load was being read using the load cell. The actual load being applied to the samples was that being measured using the load cell plus that being sustained by the tightened nuts, thus the load was increased too much by using the load cell reading, and the sample failed. One of the shrinkage samples (S4SB3) was subsequently capped and used on the second day, and the samples were loaded to approximately 36.8 kips (164 kN). For both Frames #1 and #2, only two of the three sides of DEMEC points were measured due to interference with the vertical rods of the creep frame.

The creep samples were measured every day for the first week. The measurements were then reduced to typically three times per week for a few weeks before reducing to a couple of times per week. Finally, the samples were read only once per week after it was determined that the load was not reducing very quickly. Because the creep frames were spring loaded, creep and shrinkage of the concrete between readings would result in decreased load on the specimens (due to the spring deformations). After each set of measurements if the loading was observed to have dropped by more than 1.0 kip (4.4 kN) from the target load, loading was reapplied to the cylinders until the initial loading levels were achieved. After reloading the specimens in this manner, cylinder measurements were immediately repeated to account for the elastic deformation from the increased load application.

After reviewing the initial results from the samples, it was determined that significant bending was occurring in Frame #1, so the samples (subjected to 24.0-kip (106-kN) load) were unloaded on October 31, 2008 at an age of 83 days.

On November 10, 2008, the third set of samples labeled C4SB5 and C4SB6 (in Frame #4) was loaded to approximately 24.0 kips (106 kN) at the age of 93 days, corresponding to a median age of concrete at first loading during construction of the bridge. Again, these samples were initially measured frequently, with the number of measurements taken decreasing over time.

After reviewing the data from Frames #1 and #2, it was determined that it was more important to measure the third set of points than to position the cylinders in the exact center of the frame. The reason for this was that an average creep could be measured if readings were taken from all three sides, even if bending occurred. If readings were only taken at two locations along the length, it was not possible to discern the effect of bending on the results. Great care was taken to try and get the cylinders as close to the center of the frame as possible while still being able to measure the third set of points. Care was also taken to try and ensure that the cylinders were vertical in the frames (i.e., ensure the caps were normal to their length) to help eliminate bending from the results.

The final samples labeled C4SB7 and C4SB8 (in Frame #3) were loaded to approximately 24.0 kips (106 kN) on December 17, 2008 at the age of 130 days, corresponding to the oldest age at which any segment of the bridge was first loaded. Similar to the other three frames, these samples were initially measured more frequently, and over time, the frequency of measurements decreased as the load in the frame stayed more constant.

To compare results, the first set of samples labeled C4SB1 and C4SB2 (in Frame #1) were reloaded to approximately 24.0 kips (106 kN) on the same day that Frame #3 was loaded.

For both Frames #1 and #3, care was taken to position the cylinders as close to the center of the frame as possible while still being able to read the third set of gage points. Cylinders were capped to try to get the capped surface normal to the length of the cylinder. Setting up Frame #1 for the reloading went well, with the cylinders appearing to be straight (i.e., capping surfaces normal to length of the cylinders) and near the center of the frame. Setting up Frame #3 did not go as well because the cylinders needed to be offset more in order to read the third set of points on the cylinders, likely resulting in some bending. Table 3.5 shows the date that each set of creep samples was loaded or unloaded and the magnitude of the load applied.

Similar to the shrinkage samples, each side (“A”, “B”, and “C”) of the creep cylinders was measured four times in order to get accurate readings. Invar bar readings were taken before and after each set of cylinder readings. In order to calculate the creep, shrinkage had to be subtracted from the measurements, thus the shrinkage specimens were measured on the same days as the creep specimens. The average shrinkage among all shrinkage specimens was subtracted from the creep measurements to obtain the pure creep measurements. The coefficient of variation between the shrinkage measurements among all the specimens was typically near 10% at any given time, and therefore the average shrinkage was believed to be indicative of typical shrinkage strains in the creep specimens.

Measurements were typically taken on a schedule (e.g., Monday, Wednesday, and Friday of each week) and reloading was done if necessary. Load in the frames was not allowed to reduce more than one kip below the target value which was approximately 5% of the lesser load (24.0 kips (106 kN)). To reload the frame loaded at 36.8 kips (164 kN), a jack had to be used to increase the load. The nuts were retightened after load application, the jack was released, and then the load was read. If the load did not match the desired load, the process was repeated until the load was correct. By this method, it was difficult to uniformly distribute the load in the specimen, because if the jack was not perfectly centered above the creep specimens, then a bending moment would be introduced to the cylinders. The frames loaded to 24.0 kips (106 kN) were comparatively easy to reload. This load was light enough that the jack was not required and just a large wrench was needed to tighten the nuts on the tension bars, increasing the load. This also made it easier to evenly distribute the load and to reach the desired total load. Creep measurements were taken before and after reloading the frames.

3.3.4 Results

3.3.4.1 Shrinkage

The results obtained for the shrinkage specimens at the time of this report are shown in Figure 3.7 through Figure 3.18 through the first approximately 600 days of specimen age. Figure 3.7 through Figure 3.12 show the shrinkage results for each side of the individual specimens collected from the southbound bridge. The cause of the jump in the Side C strain of sample S4SB4 as shown in Figure 3.10 was unknown. Changes such as this might be indicative of problems with the DEMEC points on the anomalous side, but this could not be confirmed. Figure 3.13 shows the average shrinkage strain for each of the individual specimens from the southbound bridge. Figure 3.14 through Figure 3.16 show the shrinkage strain results for each side of the individual specimens collected from the northbound bridge. The sudden drop in the Side B strain of sample S4NB2 as shown in Figure 3.15 was, like the S4SB4 readings, again unclear, though possibly due to problems with the DEMEC points. Figure 3.17 shows the average shrinkage strain for each of the individual specimens from the northbound bridge.

3.3.4.1.1 AASHTO LRFD Shrinkage

The results obtained from testing the concrete samples for shrinkage were compared to theoretical results obtained by applying equations found in the AASHTO LRFD Bridge Design Specifications 5th Edition (2010). AASHTO uses the following parameters for calculating shrinkage:

- H = relative humidity in percentage (%)
- k_s = factor for the effect of the volume-to-surface ratio of the specimen
- k_f = factor for the effect of concrete strength
- k_{hs} = humidity factor for shrinkage
- k_{td} = time development factor
- t = Maturity of the concrete in days. This was taken as the time from the end of curing to the time considered for the analysis of shrinkage effects. End of curing was assumed to be the first time shrinkage measurements were taken (i.e., at 3.5 days old).
- V/S = volume-to-surface ratio of the specimen in inches

Coefficients k_f and k_{td} required knowledge of the initial concrete compressive strength, f'_{ci}, specified in ksi. The concrete strength at the end of curing was unknown, so f'_{ci} was assumed to be equal to the average 7-day strength from the MnDOT strength results (Table 3.3), equal to 5.65 ksi (39 MPa). The AASHTO LRFD (2010) equations (Eqns. 5.4.2.3.2-2, 5.4.2.3.2-4, 5.4.3.2-5 and 5.4.3.3-2) and resulting values are as follows:

H = 37.5% (was taken as the average relative humidity over all the total duration of testing)

$$V/S = \left(\pi R^2 L\right)/\left(2\pi RL\right) = 0.5R = 1.0 \text{ in.}$$

$$k_s = 1.45 - 0.13\left(V/S\right) = 1.32 \geq 1.0 \qquad \text{(AASHTO Eqn. 5.4.2.3.2-2)} \qquad (3\text{-}3)$$

$$k_f = \frac{5}{1 + f'_{ci}} = 0.752 \qquad \text{(AASHTO Eqn. 5.4.2.3.2-4)} \qquad (3\text{-}4)$$

$$k_{hs} = 2.0 - 0.014H = 1.475 \qquad \text{(AASHTO Eqn. 5.4.2.3.3.-2)} \qquad (3\text{-}5)$$

$$k_{td} = \frac{t}{61 - 4f'_{ci} + t} \qquad \text{(AASHTO Eqn. 5.4.2.3.2-5)} \qquad (3\text{-}6)$$

The code-predicted shrinkage strain in the sample was then calculated using

$$\varepsilon_{sh} = k_s k_{hs} k_f k_{td} \cdot 0.48 * 10^{-3} \qquad \text{(AASHTO Eqn. 5.4.2.3.3-1)} \qquad (3\text{-}7)$$

3.3.4.1.2 CEB/FIP Model Code (1978) Shrinkage

For the design of the I-35W St. Anthony Falls Bridge, time-dependent behavior was investigated using the 1978 CEB/FIP Model Code (Minnesota Department of Transportation, 2008). Concrete shrinkage behavior as presented here is documented in Appendix B, Annex E of the 1978 CEB/FIP Model Code.

The shrinkage strain ε_s beginning at time t_0 until time t (both specified in days since the beginning of shrinkage) for concrete was assumed to follow Eqn. (3-8):

$$\varepsilon_s = \varepsilon_{s1}\varepsilon_{s2}\left[\beta_s(t) - \beta_s(t_0)\right] \quad (3\text{-}8)$$

where ε_{s1} and ε_{s2} are the shrinkage constants dependent on humidity and shape, respectively, and β_s is the shrinkage progression as a function of time and shape. The humidity dependence of constant ε_{s1} is listed in Table 3.6. The positive value for ε_{s1} for concrete in water indicates that the specimen will swell instead of shrink. Shape dependency was quantified in terms of the effective thickness h, specified in millimeters and defined by

$$h = \frac{2\lambda A_c}{u} \quad (3\text{-}9)$$

where λ is a humidity dependent parameter as specified in Table 3.6, A_c is the area of the cross section, and u is the perimeter of the section.

Times t and t_0 were corrected by the Model Code correction procedure for temperature:

$$t_{corrected} = \frac{\alpha}{30}\sum_{0}^{t_m}(T+10)\Delta t_m \quad (3\text{-}10)$$

for which t_m is the total uncorrected time, T is the mean ambient temperature in degrees Celsius, Δt_m is the time increment over which the ambient temperature is averaged, and α is a factor accounting for the type of cement. For shrinkage computations, the α parameter is always set equal to 1 regardless of cement type.

The 1978 CEB/FIP time-dependent procedure is primarily graphical, and Model Code plots for shape-dependent constant ε_{s2} and shrinkage function β_s are presented in Figures 3.18 and 3.19, respectively.

Values used for computing the 1978 CEB/FIP estimates of shrinkage strain for the tested cylinders are as follows:

Relative humidity = 40%
λ = 1 (see Table 3.6)
ε_{s1} = -0.00052 (see Table 3.6)
h = 50.8 mm
ε_{s2} = 1.2
T = 20°C (assumed constant)
α = 1

3.3.4.1.3 Comparison of Measured to Design Shrinkage

This AASHTO and CEB/FIP 1978 relations for shrinkage are shown plotted in Figure 3.20 relative to the overall average shrinkage strains measured for both the southbound and northbound bridges. Samples S4SB4 and S4NB2 have been removed from their respective averages due to the anomalous readings as noted in Section 3.3.4.1. As shown in the figure, the experimental results for the samples from the southbound and northbound bridge were comparable (they were both taken from the deck concrete poured on consecutive days). At early ages (less than approximately 100 days old), the measured results indicated larger shrinkage strains than predicted by the AASHTO equation. Long-term shrinkage strain values were over-predicted by the AASHTO results by approximately 5% compared to the average

southbound bridge shrinkage and 12% compared to the average northbound bridge shrinkage. The 1978 CEB/FIP Model Code provisions predicted the measured shrinkage strains well throughout the entire duration of measurement, with the long term measured strains from the northbound specimens very nearly matching the Model Code results. It was concluded that the 1978 CEB/FIP Model Code shrinkage procedure was a superior predictor of measured shrinkage strains for these specimens compared to the AASHTO LRFD (2010) method.

3.3.4.2 Creep

To obtain the experimental creep strain, the average southbound bridge experimental shrinkage strains (excluding sample S4SB4 which was determined to be anomalous as discussed in Section 3.3.4.1) were subtracted from the total strain measured in the creep specimens that were stored in the same environmental control room as the shrinkage specimens. The average southbound bridge shrinkage strains were used because they came from the same batch of concrete as the creep specimens, thus they had the same reference or "zero" strain date.

As the samples remained in the creep frames, the applied load was reduced by the continued deformation of the cylinders. This reduced load caused a reduction in the elastic strain of the cylinder by an amount equal to the difference between the initial and current stress divided by the modulus of elasticity of the concrete. Furthermore, the reduction in load allowed some of the creep to recover according to the superposition principle. To correct for the reduced elastic strain, all creep readings were corrected by adding back the "lost" elastic deformation assuming a nominal concrete modulus as presented in Section 3.3.4.2.1. This correction had the effect of smoothing the presented creep curves at the times of reloading. No corrections were performed to account for the creep recovery that occurred due to the temporarily reduced load.

3.3.4.2.1 AASHTO LRFD Creep

Similar to the shrinkage strains, the results obtained from testing the concrete samples for creep were compared to the predictions obtained by applying equations found in the AASHTO LRFD Bridge Design Specifications 5th Edition (2010). AASHTO uses the following parameters for calculating creep:

- H = relative humidity in percentage (%)
- k_s = factor for the effect of the volume-to-surface ratio of the specimen
- k_f = factor for the effect of concrete strength
- k_{hc} = humidity factor for creep
- k_{td} = time development factor
- t = Maturity of the concrete in days. This was taken as the difference between the time of loading and the time being considered for the analysis of creep effects.
- t_i = age (in days) of the concrete when the specimen is loaded
- V/S = volume-to-surface ratio of the specimen in inches
- f'_{ci} = strength of the concrete at the time of loading, specified in ksi

Coefficients k_f and k_{td} required knowledge of the initial concrete compressive strength at the time of loading, f'_{ci}, specified in ksi. For creep predictions, the average compressive strength among all samples measured by the UMN on the day of loading was used (Table 3.2). Therefore, strengths were 7.12 ksi (49 MPa) at 56 days (Frame #2), 6.70 ksi (46 MPa) at 93 days (Frame #4), 6.24 ksi (43 MPa) at 130 days (Frames #1 and #3). The average measured modulus of elasticity at each day was also used, equal to 4450 ksi (30.7 GPa) at 56 days (Frame #2), 4730 ksi (32.6 GPa) at 93 days (Frame #4), and 4190 ksi (28.9 GPa) at 130 days (Frames #1 and #3).

The relative humidity, H, was taken as the average relative humidity over all the time the samples were tested (i.e., approximately 36.5% for each sample, slightly lower than the humidity-controlled room set point of 40%, and varying slightly by specimen depending on the time of loading). Other parameters were determined from AASHTO Eqns. (5.4.2.3.2-2) through (5.4.2.3.2-5):

$$V/S = \left(\pi R^2 L\right)/\left(2\pi RL\right) = 0.5R = 1.0 \text{ in.}$$

$$k_s = 1.45 - 0.13\left(V/S\right) = 1.32 \geq 1.0 \qquad \text{(AASHTO Eqn. 5.4.2.3.2-2)} \qquad (3\text{-}11)$$

$$k_f = \frac{5}{1+f'_{ci}} = 0.752 \qquad \text{(AASHTO Eqn. 5.4.2.3.2-4)} \qquad (3\text{-}12)$$

$$k_{hc} = 1.56 - 0.008H \qquad \text{(AASHTO Eqn. 5.4.2.3.2-3)} \qquad (3\text{-}13)$$

$$k_{td} = \frac{t}{61 - 4f'_{ci} + t} \qquad \text{(AASHTO Eqn. 5.4.2.3.2-5)} \qquad (3\text{-}14)$$

The creep coefficient was calculated using

$$\psi(t,t_i) = 1.9 k_s k_{hc} k_f k_{td} t_i^{-0.118} \qquad \text{AASHTO Eqn. (5.4.2.3.2-1)} \qquad (3\text{-}15)$$

The AASHTO-predicted creep strain was then calculated as

$$\varepsilon_{cr} = \frac{Load/\pi R^2}{E_c}\psi(t,t_i) \qquad (3\text{-}16)$$

3.3.4.2.2 CEB/FIP Model Code (1978) Creep

Concrete creep behavior as presented here is documented in Appendix B, Annex E of the 1978 CEB/FIP Model Code.

The creep strain ε_c for concrete under stress σ_0 applied at time t_0 was assumed to follow

$$\varepsilon_c = \frac{\sigma_0}{E_{c28}}\varphi(t,t_0) \qquad (3\text{-}17)$$

where E_{c28} is the modulus of elasticity of the concrete at 28 days and $\varphi(t,t_0)$ is the creep coefficient at time t. The current time t and the loading start time t_0 are to be specified as age of the concrete in days after casting. The creep coefficient is a function of a series of parameters including ambient humidity, dimensions, concrete rate of hardening, and concrete composition. Specifically, the 1978 CEB/FIP Model Code defines the creep coefficient as

$$\varphi(t,t_0) = \beta_a(t_0) + \varphi_d\beta_d(t-t_0) + \varphi_{f1}\varphi_{f2}\left[\beta_f(t) - \beta_f(t_0)\right] \qquad (3\text{-}18)$$

The first term, $\beta_a(t_0)$, represents the partially irreversible rapid deformation during the first day of loading. This term is specified as

$$\beta_a(t_0) = 0.8\left[1 - \frac{f_{cm}(t_0)}{f_{cm}}\right] \qquad (3\text{-}19)$$

where f_{cm} is the mean concrete compressive strength measured at t_0 or, if no argument is specified, 28 days. The second term, $\varphi_d\beta_d(t\text{-}t_0)$, represents the recoverable portion of the long-term deformation. The final term, $\varphi_{f1}\varphi_{f2}[\beta_f(t)\text{-}\beta_f(t_0)]$, is the irreversible "flow" long-term deformation.

With the exception of the $\varphi_d\beta_d(t\text{-}t_0)$ term, all times specified should be corrected based on the ambient mean temperature and the type of concrete according to Eqn. (3-10). For creep, the Model Code specifies that α should be equal to 1 for normally or slowly hardening cements, 2 for rapid-hardening cements, and 3 for rapid-hardening high-strength cements, but provides no specific criteria for classifying the cement type.

The 1978 CEB/FIP Model Code employs graphical-based approaches to calculating the long term recoverable and irrecoverable deformations. For the recoverable deformation, φ_d represents the coefficient of delayed elasticity, and is always taken as 0.4. The deformation coefficient $\beta_d(t\text{-}t_0)$ is given in graphical format as a function of the time after initial loading. The plot for the recoverable deformation coefficient is shown in Figure 3.21. Note that this definition of recoverable deformation does not vary by section shape; the coefficient of delayed elasticity is assumed constant, and the recoverable deformation coefficient only depends on the uncorrected duration of loading.

The unrecoverable long-term deformation is dependent on the corrected total time and time of loading, the ambient humidity, and the shape of the specimen. The creep flow coefficient φ_{f1} is a function of the ambient humidity and is documented in Table 3.6. The creep flow coefficient φ_{f2} depends of the shape of the specimen, characterized by the effective thickness *h*, which is computed according to Eqn. (3-9). The plot for coefficient φ_{f2} as a function of *h* is shown in Figure 3.22. The Model Code plot provided for β_f is given in Figure 3.23.

3.3.4.2.3 Comparison of Measured and Design Creep

Figure 3.24 through Figure 3.27 show the experimental creep strains obtained for each of the four creep frames compared to predictions using the AASHTO LRFD (2010) and 1978 CEB/FIP Model Code methods. Figure 3.24 shows the plots of experimental and predicted creep strains for the samples loaded in Frame #2 at an age of 57 days under a stress of $0.45*f'_c$ (36.8-kip (164-kN) load), though only two of the three DEMEC point sides were used for computing the experimental strains in samples C4SB3 and S4SB3. The plots of experimental and predicted creep strains for the samples loaded in Frame #4 at an age of 93 days under a stress of 275 ksf (13.2 MPa) (24.0-kip (106-kN) load), about $0.30*f'_c$, are shown in Figure 3.25. Experimental and predicted creep strains for the samples loaded in Frame #3 at an age of 130 days under a stress of 275 ksf (13.2 MPa) (24.0-kip (106-kN) load) are shown in Figure 3.26. Finally, the results obtained for experimental and predicted creep for the samples reloaded in Frame #1 at an age of 130 days under a stress of 275 ksf (13.2 MPa) (24.0-kip (106-kN) load) are shown in Figure 3.27. Results of the Frame #1 specimens for the initial loading at an age of 56 days and during creep recovery after unloading at an age of 83 days are not presented. Results from the first loading suffered from significant bending of the cylinders and were recorded for only two sides of DEMEC points. The elastic response to unloading was unknown because, although all three sides of DEMEC points were measured after the cylinders were removed from the frame, only two sides were measured before the load was removed. The impact that any continuing creep recovery or other effects associated with the first loading and unloading process had on the presented data for the reloaded Frame #1 was unknown, and thus no effort was made to correct for the loading and unloading procedure. The results for Frame #3 and Frame #1 (each loaded at 130 days and to a stress of 275 ksf (13.2 MPa)) are compared to the predictions in Figure 3.28.

Figure 3.24 shows that AASHTO LRFD (2010) greatly underestimated the long-term creep for samples C4SB3 and S4SB3 stressed to $0.45*f'_c$ in Frame #2 at 57 days. The 1978 CEB/FIP Model Code estimates predicted the long-term creep strains measured from Frame #2 well. The experimental procedure used for collection of data from Frame #2 contained a number of discrepancies that may have contributed to errors in the measured data. For the first two weeks of creep measurements, only two of the three sides (Sides "A" and "B") of the samples in Frame #2 were measured because one of the four rods in the creep frame was obstructing Side "C" such that the Whittemore gage could not be made to reach the DEMECs. After the first two weeks, data was gathered from Side "C" by orienting the Whittemore gage nearly perpendicular to the DEMEC points, which introduced possible error in the strain readings. However, because the elastic compression of cylinders from the initial loading was not measured, further measurements along Side "C" were of little value for creep measurements. Furthermore, because of problems with the sulfur capping process, it was expected that the capped ends were not orthogonal to the

axis of the cylinder. The apparatus used to cap the cylinders required the molten sulfur material to be poured into a mold, after which the concrete cylinder was then lowered into place. This procedure required the cylinder to be placed in the apparatus hastily before the sulfur was allowed to cool and solidify. In addition, the DEMEC points should have been removed prior to capping to ease the alignment of the cylinder in the apparatus. These issues made it quite difficult to consistently make caps square with the length of the cylinder. Several attempts were made to perfect the cap, but the final caps were not perfectly orthogonal to the length of the specimen, thus inducing bending in the cylinder once it was loaded. By measuring from only two of the three sides, it was not possible to average out the bending strains from the axial creep, making the results from Frame #2 suspect. Upon reloading the cylinders on January 19, 2010 (528 days after casting), the specimens cracked and spalled, causing a steep rise in the measured strain. Strain readings were discontinued for these specimens thereafter. The cracking either indicated that more load had been applied to the cylinders than was recorded by the strain gage readouts, or that the specimens were under significant bending stresses.

The experimental creep strain results of the samples loaded in Frame #4 (i.e., C4SB5 and C4SB6) correlated to the AASHTO LRFD (2010) predictions for specimen C4SB6, and to 1978 CEB/FIP Model Code predictions for specimen C4SB5 as shown in Figure 3.25. As noted earlier, these samples had a 275 ksf (13.2 MPa) (i.e., $0.30*f'_c$) stress applied at 93 days. The caps on these specimens were oriented more orthogonally to the length of the specimens than the caps of the specimens in Frame #2, which helped to eliminate the effects of bending.

Figure 3.26 through Figure 3.28 show the AASHTO LRFD (2010) and 1978 CEB/FIP Model Code predictions and experimental results of creep strain for the samples in Frame #3 (i.e., C4SB7 and C4SB8) and Frame #1 (i.e., C4SB1 and C4SB2). These samples had a 275-ksf (13.2-MPa) stress applied at 130 days. The AASHTO predicted creep strain overestimated the measured creep strain at an age of 600 days for both Frames #1 and #3 by approximately 27%, while the 1978 CEB/FIP Model Code creep strain overestimated the measured creep strain at an age of 600 days by approximately 20%.

Judging from all four creep frames, it was concluded that the 1978 CEB/FIP Model Code creep strain was consistently a better, or at least equivalent, predictor of the measured creep strains for these specimens than the AASHTO LRFD (2010) procedure.

3.3.5 Comments

3.3.5.1 Creep

The largest difficulty encountered with the creep specimens was in eliminating bending in the specimens under loading. One source of this error was in capping the specimens. A future possible solution to this difficulty would be to grind the end of the cylinder normal to the axis of the cylinder. A second possible solution would be to use an apparatus to hold the cylinder in place while the molten sulfur is poured around the end.

Another source of the bending, and probably the biggest contributor, was due to eccentric loading of the cylinders in the creep frame; the cylinders were offset from the center of the frame in order to provide access to the three sets of DEMEC points. This resulted in the load not being concentrically applied to the cylinders which increased the difficulty in maintaining the same load in each of the four tension bars. A possible remedy to this problem would be to use four sets of DEMEC points as opposed to three, as it would enable easy access to the lines of DEMECs that could be centered between the rods.

3.4 Coefficient of Thermal Expansion

3.4.1 Sample Preparation

The coefficient of thermal expansion of the concrete was important for both modeling purposes and data reduction. One of the primary roles of some of static sensors in the bridge was to measure the effect of changes in temperature and thermal gradients on the strains in the bridge, as thermal gradients were expected to have a large effect on the behavior of the bridge. In addition to this, the coefficient of thermal expansion of the concrete was required to determine the mechanical strains from the VWSGs (i.e., to account for the strain differential due to the differences in the coefficient of thermal expansion of the steel wire in the gage versus the coefficient of thermal expansion of the concrete).

Samples for measuring the coefficient of thermal expansion were collected from several locations in order to get a good representation of the concrete used in the bridge. Samples were collected from the southbound bridge Span 1 deck (upper portion of the box), near Pier 2 on Span 1 of the southbound bridge, the deck of Span 4 of both the northbound and southbound bridges (from the same pours as the creep and shrinkage samples), the 2nd Street bridge deck, and from Pier 2 under the southbound bridge. All of these locations used the same nominal concrete mix with the exception of Pier 2. Table 3.7 lists information (e.g., sample type, sample location, etc.) for each coefficient of thermal expansion sample.

Two different sample sizes and shapes were used to investigate the coefficient of thermal expansion to determine whether there was any effect of specimen shape on the results. They included six 6 x 6 x 24 in. (150 x 150 x 610 mm) beams and two 6 x 12 in. (150 x 300 mm) cylinders. To measure the strain in the concrete, a Roctest EM-5 VWSG was installed in four of the eight forms (three beams and one cylinder) prior to casting the concrete. A Geokon Model 4200 VWSG was installed in the remaining four samples (three beams and one cylinder) prior to casting the concrete. The gages used were the same type as those used within the bridge. Data sheets for these gages are available on request.

In the case of the six beam specimens, the VWSG was tied to plastic chairs to keep the VWSG level and centered in the beam. The VWSG was zip-tied to the chairs which were cut so they fit tightly in the form. After installing, the VWSG was read to ensure that it was still near the center of its range. After the concrete was poured, the gage was read again to make sure it was still reading and to determine the zero strain reading. This reading was recorded. A picture of a completed 6 x 6 x 24 in. (150 x 150 x 610 mm) form ready for concrete to be cast is shown in Figure 3.29.

The VWSG placed in each of the 6 x 12 in. (150 x 300 mm) cylinders, was fixed in place by securing it to wire that crossed transversely through the form. Holes were drilled into the sides of the forms to accommodate placement of the wire. Again, the gage was read before and after casting the concrete to ensure that it was near the center of its range and the final readings were recorded. One of these 6 x 12 in. (150 x 300 mm) samples was collected from the same pour as most of the creep and shrinkage specimens (i.e., the deck pour of Span 4 of the southbound bridge), and one 6 x 12 in. (150 x 300 mm) sample was collected from Pier 2 of the southbound bridge.

In addition to data from the laboratory specimens, the coefficient of thermal expansion for concrete was computed using in situ results from the bridge instrumentation. This procedure is described in further detail in Section 3.4.2.2.

3.4.2 Instrumentation and Testing

3.4.2.1 Laboratory Testing Procedure

The coefficient of thermal expansion laboratory specimens contained either a Roctest EM-5 VWSG or a Geokon Model VCE-4200 VWSG as discussed in Section 3.4.1. The Roctest EM-5 VWSGs were attached to a CR10 datalogger to record temperature and strain values over time. One additional Roctest EM-5 VWSG was not embedded into any specimen, and was connected to the same CR10 to monitor air temperature. The Geokon Model VCE-4200 VWSGs were attached to a second CR10.

The specimens were stored in a temperature-controlled room, where the temperature was varied between 5°F (-15°C) and 77°F (25°C) over 6 weeks. The full temperature range was cycled twice during the testing duration. The temperature was changed by increments of approximately 9°F (5°C). Each temperature was held for at least 24 hours to allow the specimens to achieve thermal equilibrium with the surrounding air temperature. Temperature and strain readings from the vibrating wire strain gages were taken every 30 minutes. The tests took place later than 16 months after casting such that shrinkage strains were assumed to be negligible during the test. Direct superposition of measured shrinkage strains from the shrinkage samples could not be performed on the specimens for measuring coefficient of thermal expansion due to differences in specimen geometry, age, and environmental conditions. However, it was noted that strains of the shrinkage specimens were only 15 με over the course of the coefficient of thermal expansion tests, as compared to the measured thermal strain ranges over the testing duration on the order of 400 με.

To calculate the coefficient of thermal expansion, ten readings over five hours were sampled from each temperature increment after the measured concrete temperatures had stabilized. This was done to eliminate readings for which the concrete was not yet in thermal equilibrium and, given that the duration of stabilized concrete temperature varied for each increment, to ensure that each temperature increment contained the same number of samples. The total strain for the vibrating wire strain gages was given by:

$$\varepsilon_{total} = B(R - R_0) + \alpha_{gage}(T - T_0) \quad (3\text{-}20)$$

where R and T were the current gage reading and temperature, respectively, R_0 and T_0 were the reference reading and temperature, respectively, B was the batch gage factor with a typical value of 0.96 for Geokon Model VCE-4200 (not specified for Roctest Model EM-5, assumed equal to 1) and α_{gage} was the coefficient of thermal expansion of the vibrating wire strain gage, given as 6.39 με/°F (11.5 με/°C) for Roctest Model EM-5 and 6.78 με/°F (12.2 με/°C) for Geokon Model VCE-4200. Values of B and α_{gage} are specified in Geokon Installation Manual (2004) for vibrating wire strain gages models VCE-4200/4202/4210, and Roctest Instrumentation Manual (2006) for embedded strain gage model EM-5.

The total strain measured from each gage was plotted with respect to temperature, and a least-squared fit line was passed through the data. The slope of this line represented the coefficient of thermal expansion for the concrete.

3.4.2.2 In Situ Testing Procedure

The coefficient of thermal expansion of the superstructure concrete was estimated through inspection of the VWSG data over temperature changes. Strains due to traffic loading were impossible to quantify using the vibrating wire strain gages, so the total measured change in strain was necessarily assumed to be equal to

$$\Delta\varepsilon_{total} = \Delta\varepsilon_{temp} + \Delta\varepsilon_{constraint} + \Delta\varepsilon_{time} \quad (3\text{-}21)$$

where $\Delta\varepsilon_{temp}$ is the temperature related strain given by

$$\Delta\varepsilon_{temp} = \frac{\alpha}{A}\int b(y)\Delta T dy + \frac{\alpha}{I_x}\int b(y)\Delta T y dy \quad (3\text{-}22)$$

and $\Delta\varepsilon_{constraint}$ and $\Delta\varepsilon_{time}$ are due to the boundary condition constraints to expansion and time-dependent effects, respectively.

In theory, the total strain measurements from the VWSG data can be used to back calculate the coefficient of thermal expansion, α. In order to simplify the calculation, however, particular conditions were imposed on the data used for this calculation. First, only measurements with very low thermal gradient were considered, meaning the data was limited to times with approximately constant temperature throughout the entire section. Any measurement for which the magnitude of the difference between top and bottom measured temperatures (taken from thermistors TSETB003 and TWESC001, respectively) was greater than 1°F (0.5°C) was omitted from consideration. In order to reduce the impact of the boundary condition constraints, only gages at the midspans of Spans 1, 2 and 3 were considered. The expansion joints at Abutment 1 and Pier 4 were assumed to remove any axial restraint felt within Spans 1 and 3, and Piers 2 and 3 were assumed to be sufficiently flexible such that axial restraint on Span 2 was minimal. Bending restraint was still present due to the continuity of the structure, but this was factored out by considering strains either at the neutral axis, or from gages oriented vertically or transversely. Data was used over a six-month period, but it was assumed that time-dependent effects on the strains were minimized by only considering data points taken at least two years after bridge opening.

Assuming that the temperature is constant throughout the section and that constraint and time-dependent effects are negligible, then Eqn. (3-21) simplifies to

$$\Delta\varepsilon_{total} = \alpha\Delta T \quad (3\text{-}23)$$

meaning the coefficient of thermal expansion can be estimated by

$$\alpha = \frac{\Delta\varepsilon_{total}}{\Delta T} \quad (3\text{-}24)$$

The procedure for estimating the coefficient of thermal expansion was as follows:

1. Gather temperature and strain readings for the time period of interest.
2. Find the change in total strain from the readings, as given by
$$\Delta\varepsilon_{total} = (R - R_0) + \alpha_{gage}(T - T_0) \quad (3\text{-}25)$$
where R and T were the current gage reading and temperature, respectively, R_0 and T_0 were the reference reading and temperature, respectively, and α_{gage} was the coefficient of thermal expansion of the vibrating wire strain gage, given as 6.39 με/°F (11.5 με/°C) per Roctest Instrumentation Manual (2006) for embedded strain gage model EM-5. The gage factor B from Eqn. (3-20) was assumed to be equal to 1 for Roctest Model EM-5, and is therefore not shown in Eqn. (3-25).
3. Consider only the measurements where the top and bottom strain gages in the section of interest were within 1°F (0.5°C) of each other.
4. Plot the change in total strain (y-axis) versus temperature (x-axis).
5. Perform a least-squared linear fit on the total strain versus temperature plot.
6. For gages that were oriented longitudinally at the neutral axis, or vertically or transversely anywhere in the section, the slope of this line was equal to the coefficient of thermal expansion. For longitudinal gages not located on the neutral axis, the gage also measures the curvature of the box (due to the bending restraint provided by the adjacent continuous spans). In order to remove the curvature, corresponding top and bottom gages were used to interpolate the coefficient of thermal expansion to the location of the neutral axis.

The coefficient of thermal expansion was also estimated using the linear potentiometers (LPs) located at the expansion joints at Abutment 1 and Pier 4 of both the northbound and southbound structures. These LPs were attached to the webs of the boxes above the centerline of the slide plate of the bearing pad assemblies, as shown in Figure 2.50. Shop drawings for the bearing pad assemblies are presented in Appendix B.

The LP data was plotted as the total extension of the LP in inches with respect to a representative bridge temperature. For this case, temperatures were taken from gage TSEWB002 located 81 in. (2.1 m) below the top deck surface in the west (exterior) web of the exterior box of the southbound bridge at Location 7, considered as representative of the uniform temperature for the structure (that is, the temperature in absence of any thermal gradient temperatures). The same measurements that were considered for the VWSG analysis (those with negligible thermal gradient) were plotted. The movement measured by the LPs attached to Span 1 at Abutment 1 represented the distance between the centerline of the bearing pad and the abutment backwall. The movement measured by the LPs attached to Span 3 at Pier 4 represented the differential movement between the centerline of the Span 3 bearing pad and the top of Pier 4. Span 4 was pinned to the top of Pier 4 and integral at Abutment 5; therefore, the thermal movement in Span 4 caused deflections at the top of Pier 4 or Abutment 5. Because the top of Pier 4 deflected under thermal loading, the Span 3 LPs measured the elongation of the three-span structure plus the movement of Pier 4. There was no method for measuring the absolute deflection of the top of Pier 4; it was assumed that the integral abutment did not deflect, and that all the thermal movement of Span 4 was transferred to Pier 4. Preliminary finite element analysis indicated that Pier 4 was highly flexible and did not sufficiently restrain longitudinal deformation of the superstructure, and thus it was assumed that the top of Pier 4 deflected according to

$$\Delta L_{Pier\,4} = \alpha \Delta T L_4 \tag{3-26}$$

where L_4 was the length of Span 4, equal to 1743 in. (44.3 m) for both southbound and northbound structures. This change in length was subtracted from the measured change in length from the Span 3 LPs to represent the elongation of the three-span continuous portion of the superstructure.

A least-squares linear fit was performed on the Span 1 data as well as the Span 3 data minus the assumed Pier 4 deflection from Eqn. (3-26), and the slopes of these lines were calculated. Restraint of Span 2 to axial elongation applied by Piers 2 and 3 was assumed to be minimal. Therefore, the above values were taken to be equal to the total elongation of all three spans. The coefficient of thermal expansion was calculated by the following equation:

$$\alpha = \frac{m_1 + m_3}{L} \tag{3-27}$$

where m_1 was the slope of the least-squares linear fit line for the LP attached to Abutment 1, m_3 was the slope of the least-squares linear fit line for the LP attached to Span 3 minus the longitudinal deflection of Pier 4, and L was the length of bridge measured between the two LPs. For the southbound bridge L was taken to be 12780 in. (324.6 m), and for the northbound bridge L was taken to be 12870 in. (326.9 m).

The solution procedure followed an iterative approach. First, the coefficient of thermal expansion for Span 4 was assumed. Slopes m_1 and m_3 were computed, noting that slope m_3 was dependent on the assumed value of α. The coefficient of thermal expansion was then calculated using Eqn. (3-27) and compared to the assumed value. The elongation of Span 4 was recalculated from Eqn. (3-26) using the computed α, and the process was repeated until the computed α converged with the assumed Span 4 α.

3.4.3 Results

3.4.3.1 Laboratory Results

Table 3.8 summarizes the measured coefficients of thermal expansion (CTE) for each laboratory specimen over the entire measured temperature range. Table 3.9 summarizes the averaged coefficients of thermal expansion for the two mix designs constituting the measured specimens from Table 3.7.

To determine whether the coefficient of thermal expansion varied by temperature, the incremental CTE values were calculated for each 9°F (5°C) temperature increment. The incremental CTE was estimated to be equal to the slope of the least-squares fit line using only the data points from one temperature increment and the following increment. These CTE values are plotted for the superstructure laboratory specimens against the average temperature between the two increments in Figure 3.30. In general, the CTE values appeared to be invariant with temperature. However, when the temperature stopped increasing and began decreasing, the CTE appeared to spike up to a considerably higher value. This effect seemed to be related to the reversal of the direction of the strain, and occurred regardless of the temperature at which this reversal occurred. Thus, it was assumed that this disturbance was mechanical in nature, and it followed that the CTE remained relatively invariant with temperature.

3.4.3.2 In Situ Results

Total strain and temperature data from the southbound bridge was filtered such that only data with thermal gradients less than 1°F (0.5°C) was considered, as described in Section 3.4.2.2. All coefficient of thermal expansion calculations used only the filtered data. The thermal gradient was calculated using a linear fit to all of the filtered data from January 1, 2011 until June 30, 2011. This data was assumed to have little creep or shrinkage, as the bridge was opened in September of 2008.

Gages were selected at the midspans of each span (i.e., Location 3 for Span 1, Location 7 for Span 2, and Location 9 for Span 3). The coefficient of thermal expansion was calculated individually for each gage. The top flange gages were averaged together for each location, as were the bottom flange gages.

An example of the data used for this calculation from gage VS03ETL2 is presented in Figure 3.31 (other gages provided similar results). The linear fit was found to be very robust, indicating that time-dependent strains and thermal gradients were not significant over the examined duration. The resulting CTE values from this method at the various locations in the bridge are presented in Table 3.10. As can be noted from the results, the top and bottom flange gages include the curvature of the bridge under uniform temperature changes. To factor out bending strains, the averaged CTE values from the top and bottom flange longitudinal gages as presented in Table 3.10 were interpolated at the location of the neutral axis. Then the results of the vertical gages (for which no correction was necessary) and the interpolated longitudinal gages were averaged. These averaged CTE values per instrumented location are presented in Table 3.11.

This method was repeated on the VWSG data from the northbound bridge. The methods for filtering the northbound data and calculating and averaging the coefficients of thermal expansion were identical to that described for the southbound bridge. Table 3.12 summarizes the measured CTE values using the in situ VWSG method. Between results from both the northbound and southbound bridges, the CTE values computed at each instrumented location were found to be consistent along the length of the structures, with minimum and maximum estimates being 5.39 με/°F (9.70 με/°C) and 5.53 με/°F (9.95 με/°C), respectively, representative of a 2.6% relative difference.

A procedure analogous to that described above for the VWSG data was applied to the LP data. The LP data was filtered in the same fashion as the VWSG data. The LP data was plotted as superstructure

elongation against average structure temperature from January 1, 2011 until June 30, 2011. An example of the data used for this calculation from the exterior box of the southbound structure at Abutment 1 is presented in Figure 3.32 (other LPs exhibited similar results).

The slopes measured at each end of the bridge were averaged between the two boxes. Slopes measured from each individual box at either end of the bridge (that is, before any averaging) were noted to be different by no more than 0.1 με/°F (0.2 με/°C), or approximately 2% relative difference, and therefore the average was believed to be representative for both boxes. Eqns. (3-26) and (3-27) were then applied in the iterative procedure as described in Section 3.4.2.2 until the CTE converged. The results are summarized in Table 3.13.

3.4.3.3 Results Summary

The coefficient of thermal expansion was measured using both the installed vibrating wire strain gages and instrumented concrete specimens placed in a temperature-controlled room. The superstructure average CTE computed from the laboratory specimens was 5.72 με/°F (10.3 με/°C). From the superstructure VWSGs, it was found that the CTE was constant along the length of the bridge, with maximum relative difference between any two investigated locations being 2.6%. The overall average CTE using the in situ VWSG method from the three investigated sections on both the southbound and northbound structures was equal to 5.46 με/°F (9.83 με/°C). Using the linear potentiometer data, it was found that average CTE from both structures was equal to 5.60 με/°F (10.1 με/°C). Considering each method with equal weight, the recommended thermal expansion value for modeling purposes was an overall average superstructure CTE of 5.60 με/°F (10.1 με/°C). For the piers, only laboratory specimens were used to estimate the CTE; this result gave an average pier CTE equal to 4.85 με/°F (8.73 με/°C). Results are summarized in Table 3.14.

Chapter 4. Finite Element Modeling

Finite element models of the bridge, validated using measured data, were created for two primary purposes. The first was to provide a comparison of the performance of the bridge relative to design requirements and load rating assumptions, including verification of the structural performance under live loading, thermal effects, long-term deflections, and post-tensioning losses. The second purpose was to provide a tool through which predictions of bridge performance could be made. This included predicting time-dependent effects, dynamic modal properties, checking the bridge response under extreme loading conditions, and predicting the response after possible damage. Measured data obtained from truck tests and daily readings from thermal effects were used to validate the models. This chapter focuses on the construction methodology used for the finite element models. Model validation against static truck load tests and thermal effects are discussed in Chapters 6 and 7, respectively.

4.1 Development of Three-Dimensional Finite Element Model

4.1.1 Modeling Methodology

The three-dimensional model, created using Abaqus (Dassault Systèmes, 2010), was limited to Spans 1 through 3 of the southbound bridge, as shown in Figure 4.1. This choice was made because Span 4 was separated from the end of Span 3 by an expansion joint, and was thus assumed to act independently; the southbound bridge was modeled because most of the instrumentation was concentrated in the southbound superstructure and piers (refer to Chapter 2 for instrumentation). Piers 2 and 3 supporting the river span were modeled and assumed to be fixed at the base.

A consistent system of units was decided upon to guarantee the consistency of the finite element model. Lengths were specified in inches (in.), forces in pounds (lbs), temperatures in degrees Fahrenheit (°F), time in seconds (sec), and masses in slug-feet per inch (slug-ft/in.). The choice of units for mass, which was equivalently equal to lb-sec^2/in., was necessary to enforce dimensional consistency with the acceleration due to gravity (necessarily specified as 386.4 in./sec^2 according to the length and time units as noted).

The concrete was modeled using 20-node three-dimensional quadratic continuum elements with reduced integration (element type C3D20R), which were found to provide superior results to linear continuum elements, but were computationally more efficient than quadratic formulations not using reduced integration. The characteristic element size was approximately 24 in. (610 mm), such that the structure consisted of approximately 500 elements along the length of the three spans, ranging from 8 to 15 elements through the depth. Most box flanges and webs were thin sections, and were only meshed with a single element through the thickness, which, because of the particular element choice, was found to not cause any issues. The top flange was meshed with two elements through the thickness so that temperature distributions in the deck could be more accurately modeled. Thicker sections such as the diaphragms above the piers and the thickened bottom flanges near the piers were, naturally, meshed with more elements through the thickness.

To simplify the meshing of the superstructure, the bridge was divided into segments where the bridge geometry changed dramatically. The segments were as follows:

1. The expansion joint and diaphragm in Span 1 above Abutment 1.
2. The main body of Span 1.
3. The ten-foot diaphragm above Pier 2.
4. The cast-in-place transition from the Pier 2 diaphragm to the precast construction.
5. The main body of Span 2.

6. The cast-in-place transition from the precast construction to the Pier 3 diaphragm.
7. The ten-foot diaphragm above Pier 3.
8. The main body of Span 3.
9. The expansion joint and diaphragm in Span 3 above Pier 4.

Each segment was meshed independently and then tied together using surface-to-surface constraints. Consequently, the meshes did not necessarily match at the interfaces between two segments. It was observed, however, that for the C3D20R elements the surface-to-surface constraints performed as expected, and the mesh discontinuities had negligible effect on the overall model.

With the exception of the external draped tendons within the boxes, the prestressing strands were smeared and approximated as 4-node linear shell elements embedded within the top and bottom flanges of the concrete box. These shell elements were given negligible bending stiffness and appropriate axial stiffness to emulate the stiffness of the strands. This was done via a preprocessing option in Abaqus known as "rebar layers" which were used to generate the unidirectional strength of the tendons. First, the shell was defined with no stiffness in any direction. Then, by specifying the area of steel per tendon, the spacing of the tendons, and the direction of the tendons, the rebar layers assigned the proper axial stiffness in the direction of the tendon to the shell. The final stiffness of shell was the sum of the stiffness induced by the shell itself (specified as zero) and the unidirectional stiffness of each rebar layer. A straight-forward preprocessing option was available for the rebar layers so that the amount of post-tensioning in the tendons could be input as initial conditions into the model. The stiffness provided by the external draped tendons was negligible, and was not modeled. In order to model the post-tensioning from the draped strands, nodal forces were applied at the tie-down and anchorage points of the draped strands.

Mild steel was not explicitly modeled, and was instead assumed to be uniformly distributed throughout the sections by artificially adjusting the modulus of elasticity of the concrete. An overall reinforcement ratio was used to adjust the modulus of elasticity,

$$E_{eff} = E_c\left(1+\frac{E_s A_s}{E_c A_g}\right) \tag{4-1}$$

where A_s is the total area of mild reinforcement in the section, A_g is the gross area of the section, E_s is the modulus of elasticity of the steel (assumed to be 29,000 ksi (200 GPa)), and E_c is the modulus of elasticity of the concrete. Because the sections are not uniform, an average reinforcement ratio was calculated between the least reinforced and most reinforced sections of each structural entity.

Boundary conditions were chosen to approximate the physical constraints on the bridge, as determined from the as-built documents (Minnesota Department of Transportation, 2008) and the bearing manufacturer's shop drawings (R.J. Watson, Inc., 2008). Shop drawings for the bearing pad assemblies are presented in Appendix B. At Abutment 1 and Pier 4, the ends were supported by a combination of multidirectional and guided bearings. This meant that the bridge was constrained to have only longitudinal deflection at Abutment 1 and Pier 4. Modeling the as-built bearing assemblies in the three-dimensional model was found to be computationally taxing, so simplifying approximations were made regarding the bearing pad geometries. To account for the dimensions and locations of the pads, boundary conditions were specified along one-element wide patches across the bottom of the boxes (about 26 in. (0.66 m) wide), with the center of the patches at about 40 in. (1.0 m) from the end of the bridge. These dimensions were chosen as convenient approximations to the as-built drawings, where Abutment 1 bearing pads were 24.5 in. (0.62 m) diameter and centered about 4.05 ft (1.24 m) from the face of the stemwall, and Pier 4 bearing pads were 21.25 in. (0.55 m) diameter and centered 2.33 ft (0.71 m) from the centerline of Pier 4. Transverse and vertical deflections were specified as zero along these locations. Any frictional restraint to longitudinal deflection was neglected, but some restraining moment was

induced by the width of the boundary condition region. The physical geometries of Abutment 1 and Pier 4 were considered unnecessary for computations, and were consequently not modeled.

At Piers 2 and 3, the superstructure was tied to the piers by nodal constraints. The model at first used surface-to-surface constraints to tie the superstructure to the top of the pier over the dimension of the bearing pads, similar to the procedure described above for the Abutment 1 and Pier 4 boundary conditions. However, it was found that preliminary results using the surface-to-surface constraints were virtually no different from nodal constraints emulating pin connections between Piers 2 and 3 and the superstructure. Therefore, in the final model, the nodal (pin) constraints were adopted for computational simplicity. The nodal constraint was applied in a line across the entire width of the bottom flanges of both boxes, thus restraining all deflections between superstructure and piers, but allowing rotation about the axis of the line of nodes (i.e., rotation that would be expected under longitudinal bending). The bottoms of the piers were fixed, meaning that all displacements and rotations were specified as zero. Any soil-structure interaction was assumed negligible with respect to the overall structural response.

The construction staging procedure was not modeled for any analysis performed in this report. Furthermore, time-dependent effects for the concrete (creep and shrinkage) or steel (relaxation) were not included in this model. In any case where "total stresses" were approximated using this model, the post-tensioning forces at release were applied unless otherwise noted.

4.1.2 Adjustments to Methodology during Model Generation

During the initial generation of the model, a variety of iterations were made to the model methodology to better capture the behavior of the physical bridge. A discussion of the critical adjustments is presented below. The discussion from Section 4.1.1 presents only the final model state used to generate the results found in this report.

Of the iterations made to the methodology, adjustment of the boundary conditions had the most significant impact on the model behavior. The initial model included only the superstructure of the southbound bridge from Spans 1 through 3. It was immediately discovered that the flexibility of Piers 2 and 3 were necessary to accurately represent the behavior of the physical structure. Initial boundary conditions for the model of the superstructure and piers were chosen such that all bearing pad assemblies were treated as perfect pins or rollers, as would typically be assumed for design, with the piers fixed at the base. From comparisons of the truck test data (Chapter 6) with modeled results, the measured response of the physical bridge for loading in Span 1 or 3 was found to be notably less than the modeled response. This was more clearly evident from comparison of the measured temperature response (Chapter 7) with the model behavior. It was concluded that the perfect roller supports did not accurately capture the restraint at the expansion joints. Iterations on boundary conditions altered the amount of restraint by adjusting the length constrained under the boundary conditions. At Pier 2 and Pier 3, the connection between the superstructure and the top of the pier was found to be modeled equally well with a pin or moment-restrained connection, and therefore the pin connection was adopted for ease of modeling. At the Abutment 1 and Pier 4 expansion joints, adding moment restraint significantly changed the modeled response for the better with respect to the measured truck test and thermal responses. The final restraint, whereby the length of the boundary condition constraint corresponded to the size of the bearing pads, was chosen because the application of such a boundary condition was justified by the geometry of the bearings, and also accurately conveyed the restraint observed from the measured data.

Other alterations to the modeling methodology, including the adjustment of the concrete modulus using Eqn. (4-1) and changing truck load applications from patch loads to point loads (as discussed in Section 6.2), had a relatively minor impact on the model behavior when compared to changes to the boundary conditions.

4.1.3 Material Properties

4.1.3.1 Elastic Properties

The concrete moduli used in the finite element model were derived from experimental results. As discussed in Section 3.1, concrete strength at 28, 56, 93, and 130 days was measured from a total of 46 cylinders taken from the southbound bridge superstructure mix that had a nominal 28-day design strength of 6.5 ksi (45 MPa). The measured average concrete strength for all southbound specimens from both UMN and MnDOT results (excluding 7-day strengths), equal to 7.4 ksi (51 MPa), was used to compute the modeled superstructure concrete's modulus according to Section 5.4.2.4 of the AASHTO LRFD Bridge Design Specifications (2010):

$$E_c = 1820\sqrt{f_c'}\text{, where } f_c' \text{ is in ksi} \qquad \text{(AASHTO Eqn. C5.4.2.4-1)} \qquad (4\text{-}2)$$

Strength data was not available for pier and railing concrete, so the concrete strength used in Eqn. (4-2) for these areas was assumed to be 4.4 ksi (30 MPa), equivalently 10% higher than the nominal 28-day design strength of 4.0 ksi (28 MPa). All concrete moduli were modified proportionally by the mild steel reinforcement ratio using Eqn. (4-1). Table 4.1 summarizes the calculations for the effective modulus of elasticity. Table 4.2 describes the sections chosen for evaluation.

The modulus of elasticity for the post-tensioning steel was assumed to be equal to 28,500 ksi (196 GPa), as presented in the Saint Anthony Falls Bridge Stressing Summary (Minnesota Department of Transportation, 2008). Poisson's ratio was assumed to be 0.2 for all concrete and 0.3 for all steel. All materials were assumed to remain in the linear-elastic range. Material moduli were converted to pounds per square inch (psi) for input into Abaqus for dimensional consistency.

4.1.3.2 Mass Properties

Abaqus requires that densities (mass/volume) be specified for all materials as opposed to unit weights (force/volume). All reinforced concrete was assumed to be normal weight with unit weight equal to 150 lbs/ft^3 (2,400 kg/m^3), which is equivalently a density of 0.00270 slugs/in.^{3}. One slug equals one lb-sec^2/ft, but for dimensional consistency, the density was input into Abaqus using units of lb-sec^2/inch (or slug-ft/inch) for the mass.

For post-tensioning steel, the weight of the strands was given as 0.74 lbs/ft (1.1 kg/m) of 0.6-in. (15-mm) diameter strand according to Appendix C of the St. Anthony Falls Bridge Erection Manual (Figg, 2008). Strand cross-sectional area was given as 0.223 in.^{2} (144 mm^2) in the Saint Anthony Falls Bridge Stressing Summary (Minnesota Department of Transportation, 2008). This corresponded to a unit weight of 0.28 lbs/in.^{3} (7,700 kg/m^3), and a density of 0.0086 slugs/in.^{3}. This density was divided by 12 in./ft for dimensional consistency, resulting in a post-tensioning steel density of 0.00072 slug-ft/in^4.

4.1.3.3 Thermal Properties

Material coefficients of thermal expansion used in the model were averaged from the available test methods as described in Section 3.4 and summarized in Table 3.13. A coefficient of thermal expansion of 5.60 με/°F (10.1 με/°C) was chosen for the superstructure concrete and 4.85 με/°F (8.73 με/°C) was chosen for the piers. No tests were performed on the concrete in the barrier rails, but because the mix design was identical to that of the piers, it was assumed to also have an identical CTE of 4.85 με/°F (8.73 με/°C). The CTE of steel was assumed to be a typical value of 6.78 με/°F (12.2 με/°C).

4.1.3.4 Material Summary

Material properties used in the finite element analysis for the concrete and post-tensioning steel are presented in Table 4.3.

4.2 Development of Two-Dimensional Model

4.2.1 Modeling Methodology

A two-dimensional model was created in Abaqus as a computationally efficient alternative to the three-dimensional model. Due to the nature of the modeled geometry, the two-dimensional model was limited to investigations of longitudinal behavior.

The two-dimensional model was limited to the continuous spans, Spans 1 through 3, of the southbound bridge. Piers 2, 3 and 4 were included. The concrete was modeled using 8-node quadratic shell elements with reduced integration. Individual elements were typically 24 in. (610 mm) in length, meaning that the superstructure contained approximately 500 elements along the length of the bridge. In order to more accurately model the shape of the temperature gradient, the mesh was refined in the top flange with minimum element lengths of 4 in. (100 mm). Between 10 and 18 elements were modeled through the depth of the section. Elements were assumed to have out-of-plane thickness corresponding to the geometry of the section. Thus, while the box geometry was not explicitly captured, the modeled section moment of inertia was consistent with the physical structure. The post-tensioning strands were approximated as 2-node linear truss elements embedded within the top and bottom flanges of the concrete box. These truss elements had appropriate axial stiffness and no bending stiffness to emulate the stiffness of the strands. Mild steel was not explicitly modeled, but was instead assumed to be uniformly distributed throughout the sections and taken into account by adjusting the modulus of elasticity of the concrete in the same manner as was performed for the three-dimensional model (refer to Eqn. (4-1)). The concrete barrier rail on the interior edge of the bridge was not modeled, as instrumentation was not provided to investigate possible changes in the temperature distribution in and around the rail, and the stiffness provided by the rail was assumed to not greatly contribute to the global stiffness of the structure. The metal guard rail and curbing on the exterior edge of the bridge were also excluded for similar reasons.

For the boundary conditions, all parts of the bearing pad assemblies, including the elastomeric pads and the steel bearing plates, were modeled using 8-node quadratic shell elements. Bearing assembly dimensions were taken from the bearing manufacturer's shop drawings (R.J. Watson, Inc., 2008), as shown in Appendix B.

For the Abutment 1 (shown in Figure 4.2) and Pier 4 (shown in Figure 4.3) bearing assemblies, parts for the sole plate, slide plate, top bearing plate, and elastomeric bearing pads were modeled. The bottom bearing plate and masonry plate below the elastomeric bearing pad were not modeled. The steel plates were assumed to have material properties equal to that from the post-tensioning steel (see Table 4.3). The elastomeric bearing pad was modeled using an incompressible elastic material. The sole plate (top plate) was perfectly bonded to the base of the superstructure. The slide plate was perfectly bonded to the bottom of the sole plate. Although the field bearings would normally leave the slide plate free to move longitudinally on top of the bearing plate, this too was perfectly bonded in the FEM. This was done to avoid performing contact analysis for the boundary conditions. The bearing plate was then perfectly bonded to the elastomeric bearing pad. The base of the elastomeric bearing pad was fixed in the vertical direction. The longitudinal direction of this boundary condition was released to ensure that the structure was free to expand without friction in the longitudinal direction.

For the Pier 2 and 3 bearing assemblies (shown in Figure 4.4), parts for the sole plate, top bearing plate, and elastomeric bearing pad, bottom bearing pad, and masonry plate were modeled. Material properties were identical to those used for the Abutment 1 and Pier 4 bearings pad assemblies. According to the bearing assembly shop drawings (R.J. Watson, Inc., 2008) as shown in Appendix B, these bearing plates were fixed against all translational motion. Therefore each plate or pad in the assembly was modeled to be perfectly bonded to the adjacent plates or pads in the assembly, such that no translational motion would be allowed between any two pieces. The sole plate at the top of the assembly was attached to the block-out structure at the Pier 2 and Pier 3 diaphragms, and the masonry plate at the bottom of the assembly was fixed to the block-out located at the centerline of the tops of the piers.

Out-of-plane deflection of the entire model was constrained, such that the shell formulation emulated a plane-stress problem.

The construction staging procedure was not modeled for any analysis performed in this report. Furthermore, time-dependent effects for the concrete (creep and shrinkage) or steel (relaxation) were not included in this model. In any case where "total stresses" were approximated using this model, the post-tensioning forces at release were applied unless otherwise noted.

4.2.2 Material Properties

Material properties used in the two-dimensional model were identical to those used in the three-dimensional model as presented in Table 4.3.

The elastomeric bearing pad material was the only material used in the two-dimensional model not specified for the three-dimensional model. The elastomeric bearing pad was assumed to be perfectly elastic, with modulus of elasticity equal to 10 ksi (69 MPa) (per discussion with Paul Bradford from R.J. Watson, Inc.). Poisson's ratio was specified as 0.499 to enforce that the material was nearly incompressible. The bearing pad was not assigned a density or coefficient of thermal expansion, meaning that it would apply no gravity loading, that it would not have inertia in dynamic computations, and that it would not expand under thermal changes.

Chapter 5. Description of Truck Tests

5.1 Purpose and General Information

Truck tests were conducted on the bridge for two primary reasons. The first was to establish a baseline regarding the response of the bridge to known static and dynamic loading. By positioning the trucks with known loads at specific locations, it was possible to capture the effect of the vehicle loads with the static data acquisition system. The truck tests were also used as a means to validate the finite element models used to investigate the behavior of the bridge (discussed in Chapter 4). Two sets of truck tests were performed. Prior to the bridge opening, the bridge was subjected to the first series of truck tests over the course of two evenings, September 14 and 17, 2008. The second set of truck tests was performed two years after bridge completion, on the nights of October 27 and 28, 2010. For both sets of truck tests, a total of eight fully loaded sand trucks were stationed in various patterns across the bridge, both statically and dynamically. Knowing the loads and positions of the vehicles for the static tests and the speeds and orientations of the trucks for the dynamic tests, this information could be applied to the finite element model, and the numerical results could be compared directly to the measured data.

5.2 September 2008 Truck Tests

The truck tests performed in September of 2008 prior to bridge opening formed the basis for model validation and observation of general bridge behavior. To avoid conflicts with the construction schedule, all truck tests were performed at night. Performing the truck tests at night was also beneficial because it minimized the thermal effect on the bridge due to solar radiation. There was still a change in temperature over the course of the evening that affected the measurements, but that temperature change and the thermal gradient through the section was minimal.

Because the truck tests were performed at night, the number of tests that could be performed was limited. The first night that the truck tests were performed, the construction workers were still working on the bridge expansion joints, so it was not possible to conduct dynamic tests that evening. The second night of testing included all of the dynamic tests as well as additional static tests. The bridge opened to traffic a few hours after the second round of truck tests was completed.

To verify that the static and dynamic results were repeatable, tests were performed multiple times with the same truck orientation. Because the majority of gages were located in the southbound bridge exterior box, the majority of truck tests were run on the southbound bridge.

On the first night of truck tests (September 14), the temperature ranged from about 55°F (13°C) at the beginning of the tests to about 45°F (7°C) towards the end of the night of testing. The wind was approximately 5-10 mph (8-16 km/hour). There was a light rain at the beginning of the night of testing which quit a few hours into testing. The sky remained overcast with the humidity remaining high throughout the evening. The temperature on the second night of testing (September 17) was around 60°F (16°C). The wind was calm, and the sky was clear.

5.2.1 Truck Information

For these tests, eight MnDOT sand trucks were used. Trucks of different model years were used, but care was taken to find trucks with similar axle dimensions. The trucks were weighed before and after each night of truck testing in order to verify the load applied by each truck. To ensure that the load used each night was as close as possible to the previous tests, the trucks used on the first night of testing were stored

with the sand in the truck until the second night of testing. The only exception was that one truck used the first night was not used on the second night and was replaced by a different truck filled with sand.

Because repeatability was of interest, when a repeat test was done, the trucks were oriented in the same way. In other words, each truck was in the same location that it had been for the previous test or tests at that orientation.

The typical truck used is shown in Figure 5.1. It had a front axle to center of rear tandem dimension of 17 ft-5 in. (5.3 m), and the out-to-out dimension of approximately 8 ft (2.4 m). Each truck weighed approximately 50 kips (222 kN) with about 35 kips (155 kN) on the rear tandem and about 15 kips (67 kN) on the front axle. The dimensions and weights specific to each truck are given in Table 5.1. Based on each orientation, between six and eight trucks were used for each test. The large number of trucks was used in order to maximize the strains and hence, the strain signal to noise at the instrumented sections.

5.2.2 Static Truck Tests

The first night of truck tests consisted of only static truck tests. These tests involved placing each truck in a specific location and letting them sit while taking readings from the static gages (e.g., VWSGs and SOFO fiber optic gages). In order to ensure that the exact locations of the trucks were known, the contractor, prior to the truck tests, surveyed the bridge and marked the requested locations on the bridge. The possible error in positioning the trucks would have been likely within a foot of the surveyed lines (likely much less). With the large span lengths, this error was deemed negligible for the global behavior of the bridge, but may have impacted strains caused by local deformations near the loads.

The static data acquisition system was programmed to cycle through the VWSG gages in series. As a consequence, it took approximately three minutes to take a set of readings from each of the VWSGs in the southbound bridge, due to the large number of gages, especially in the exterior box of the southbound bridge. For the northbound bridge, it took less than a minute for a set of readings to be taken. For the first test at a given orientation, the trucks were typically stationed long enough to obtain three measurements from each gage; due to time constraints, the repeat tests usually allowed the trucks to sit long enough for just one measurement from each gage.

The trucks for the static tests were typically oriented in the direction that traffic would be flowing. The trucks were then moved from location to location along the bridge until each desired location had been tested. Before tests started and after the measurements for a particular configuration had been completed at each desired location on the bridge, a zero-reading was taken with the trucks completely off the bridge. Zero-readings before and after a set of truck tests were used to correct the measured strain data to eliminate the effects of temperature changes on the structure. After the zero-reading had been taken, the trucks were driven back to the other end of the bridge and the next test configuration began.

Data collection during the static tests was done upon prompt for the VWSGs from the control room (located near the northeast corner of the bridge). Three individuals from the UMN were stationed in the control room to start and stop the data recording during each test, to observe the data, and to label the files with a designation to denote which test was performed. Walkie-talkies were used by the UMN researchers in the control room to stay in contact with the UMN researchers on the bridge. The UMN individuals on the bridge helped to orient the trucks in the proper configuration, and measured the distances between the trucks (transversely and longitudinally) to more accurately determine the location of the vehicles on the bridge. They also notified the UMN researchers in the control room when the trucks were in position and indicated which test was being run. The individuals in the control room started recording the data upon notification and informed the individuals on the bridge when the desired number of data points had been collected. In order to help verify that the data collected was identified

with the correct truck orientation, watches were synchronized with the computer clock, and researchers on the bridge recorded the time, the test, the bridge (southbound or northbound), and any dimensions from marked stations on the bridge.

In addition to the UMN researchers, Smartec representatives collected data during the static truck tests. The Smartec representatives connected to the server and collected data from the SOFO sensors remotely. The data from these sensors were collected continuously during the static truck tests. Labels to signify each different test were not assigned to this data, thus the data had to be compared to that from the VWSGs and to the recorded testing times to determine which SOFO data corresponded to each truck test. This was accomplished by relating the time that each test was started and stopped for the VWSGs with the data collected during that time interval by the SOFO sensors.

A total of five truck orientations were used for the static truck tests. The priority of these tests was selected based on the amount of time available for testing and the potential impact the test would have on analyzing the data in the future. Tables 5.2 and 5.3 give the date, time, location, and orientation of each static truck test performed for the southbound and northbound bridges, respectively. Static truck tests were named in the format ST[a][b][c], where [a] was the truck test orientation roman numeral (I, II, III, IVa, IVb, V, or VI), [b] was the instrumented location at which the trucks were positioned, with numbers in parentheses denoting any offset in feet (positive being north, negative being south) from the specified location, and [c] was either SB or NB to denote whether the test was performed on the southbound or northbound structure. For example, STII3SB referred to orientation ST II (see Section 5.2.2.2) located at Location 3 of the southbound bridge. STI7(+9)NB referred to orientation ST I (see Section 5.2.2.1) located at a 9-ft (2.7-m) offset to the north of Location 7 of the northbound bridge.

5.2.2.1 Truck Orientation ST I

Truck orientation ST I, shown in Figure 5.2, was the configuration for the primary static test performed on the southbound bridge, and the only static configuration performed on the northbound bridge. This test consisted of placing eight trucks side by side across the width of the bridge. Because the bridge was 90 ft-4 in. (27.5 m) wide (87 ft-0 in. (26.5 m) between barriers) and the total width of the trucks was 64 ft-0 in. (19.5 m) out-to-out (i.e., eight trucks at 8 ft-0 in. (2.4 m) out-to-out of tires, thus wider when including side mirrors), this provided for an approximately uniform distribution of load across the width of the bridge with the trucks spaced very closely (less than 1 ft (0.3 m) between the trucks when including side mirrors). The longitudinal curvatures that the eight trucks created (i.e., positive and negative moments) were maximized with this truck orientation. For each test, the readings were taken from every VWSG in the bridge on which the trucks were stationed.

For testing on the southbound bridge, static readings were taken with the trucks positioned with orientation ST I with the rear tandem of the trucks centered near midspan of Span 1 (i.e., instrumented Location 3 as shown in Figure 2.1), just to the south of Pier 2 (i.e., 25 ft (7.6 m) south of Location 4), directly over Pier 2, near the midspan of Span 2 (Location 7), just to the south of Pier 3 (Location 8), near the midspan of Span 3 (Location 9), and near the midspan of Span 4 (Location 14). The trucks were also positioned with this orientation with the front axle of the trucks centered just to the north of Pier 2 (Location 6) and just to the south of Abutment 5 (Location 15) on the southbound bridge. On the first night of testing, truck tests were performed twice per location (i.e., one repeat test was performed) for all locations on the southbound bridge, excepting Locations 14 and 15 for which only a single test was performed. On the second night of testing, an additional repeat test was performed with trucks positioned at both Locations 3 and 7, and two additional repeat tests were performed at Locations 14 and 15.

For testing on the northbound bridge, truck orientation ST I was used near the midspan of each span (Locations 3, 7, 9 and 14) with the rear tandem of the trucks centered on the instrumented location. This

orientation was also applied just to the south of Abutment 5 (Location 15) on the northbound bridge, with the front axle centered on the instrumented location. On the first night of testing, the northbound bridge was tested only once at Locations 3, 7, and 9. During the second night of testing, truck tests were performed twice per location at Locations 14 and 15, and a single repeat test was performed for Locations 3 and 7.

5.2.2.2 Truck Orientation ST II

Truck orientation ST II, shown in Figure 5.3, was performed only on the southbound bridge during the first night of testing. For this test, the trucks were aligned in two columns of four rows of trucks placed as close as practicable. Each row of trucks was located directly over the webs of the exterior southbound box. The purpose of this test was to look at the case of one box being loaded while the other was not. By placing the trucks directly over the web, the local deformation of the top flange was minimized. Specifically, this test was performed in order to look at bending of the flange between the two boxes and at shear and torsion near Pier 2 versus the case of truck orientation ST I. This orientation of trucks was used near the midspan of Spans 1 and 2 (Locations 3 and 7, respectively), just to the north of Pier 2 (Location 6), and directly over Pier 2 on the southbound bridge. The trucks were oriented such that the location being tested was centered between the rear axle of the trucks in the second row and the front axle of the trucks in the third row for all locations excepting Location 6, at which the trucks were oriented with the front axle of the front two trucks located on the specified location and the rows of trucks extending north onto Span 2 on the southbound bridge. These tests were performed twice (i.e., one repeat) per location on the first night of testing.

5.2.2.3 Truck Orientation ST III

Truck orientation ST III, shown in Figure 5.4, was performed only on the southbound bridge during the first night of testing. This test involved a similar truck layout to that of truck orientation ST II. Again, the trucks were aligned in two columns of four rows of trucks placed as close as practicable. Instead of being oriented over the webs of the exterior box, however, the two rows of trucks were both applied over the flange between the two boxes on the southbound bridge. The purpose of this test was to investigate bending of the flange between the two boxes when subjected to load between the boxes. Shear and torsion near Pier 2 were also investigated with this loading condition. This orientation of trucks was used near the midspan of Spans 1 and 2 (Locations 3 and 7, respectively), just to the north of Pier 2 (Location 6), and directly over Pier 2 on the southbound bridge. The trucks were oriented such that the location being tested was centered between the rear axle of the trucks in the second row and the front axle of the trucks in the third row for all locations excepting Location 6, at which the trucks were oriented with the front axle of the front two trucks located on the specified location and the rows of trucks extending north onto Span 2. Measurements were taken with this truck orientation twice per location (i.e., one repeat) on the first night of testing.

5.2.2.4 Truck Orientation ST IV

Truck orientations ST IVa and ST IVb, shown in Figures 5.5 and 5.6, respectively, were performed on the southbound bridge during the first night of testing. These tests again used a similar truck layout to that used for truck orientations ST II and ST III. Trucks were aligned in two columns of four rows of trucks placed as close as practicable. For these tests, the two rows of trucks were located as close to the edge of the bridge as possible. The purpose of these truck orientations was to investigate torsion of the box, bending of the deck, and shear near Pier 2. In truck orientation ST IVa the trucks were positioned near the exterior edge of the bridge while in truck orientation ST IVb the trucks were positioned near the interior edge of the bridge. This orientation of trucks was used near the midspan of Spans 1 and 2 (Locations 3 and 7, respectively), just to the north of Pier 2 (Location 6), and directly over Pier 2 on the

southbound bridge. The trucks were oriented such that the location being tested was centered between the rear axle of the trucks in the second row and the front axle of the trucks in the third row for all locations excepting Location 6, at which the trucks were oriented with the front axle of the front two trucks located on the specified location and the rows of trucks extending north onto Span 2. Truck orientation ST IVa was performed twice (i.e., one repeat) at Locations 3, 6 and 7, and only once (i.e., no repeats) centered above Pier 2. Truck orientation ST IVb was performed only once for each location.

5.2.3 Dynamic Truck Tests

All dynamic truck tests were performed on the second night of testing. On the first night of testing, the crews were still working on the expansion joints which eliminated the possibility of running these tests. The dynamic tests involved running the trucks across the bridge at known speeds (as indicated by the drivers who noted the speedometer readings). The trucks had a relatively short run to accelerate to a near constant velocity across the bridge. The short acceleration distance was the result of the entrance and off ramps. The road was not as wide as the bridge on either end, thus some of the trucks had to accelerate using the approaching roadway while some of the trucks accelerated using the ramp.

The overall purpose for performing these tests was to obtain the baseline dynamic properties of the new bridge (i.e., longitudinal and torsional mode shapes). Three different truck orientations were tested on the southbound bridge and one truck orientation was tested on the northbound bridge. The three different configurations were used on the southbound bridge to attempt to excite torsional as well as longitudinal modes of vibration. The accelerometers in the southbound exterior box were positioned in the "short-term" configuration as shown in Figures 2.43 and 2.44 to capture this information. Time did not permit rearranging the accelerometers and rerunning the dynamic tests in their long-term orientations. Other than the dynamic Dataq system, no other dynamic monitoring system, including the SOFO dynamic acquisition system, was in place during these tests. Tables 5.4 and 5.5 list the dynamic truck tests performed, the approximate speed, time of the test, and any notes that were taken for tests on the southbound bridge and northbound bridge, respectively.

The dynamic truck test data gathered with the accelerometers during the September 2008 tests were found to be unusable for analysis due to the low signal-to-noise ratios (which were resolved shortly after by changing the analog filtering of the accelerometers, as described in Section 2.4.5). Therefore, the results of these tests are not discussed further in the remainder of his report. The testing procedure is presented below for completeness.

5.2.3.1 Truck Orientation ST IVa

For this set of tests, the trucks were oriented the same as they were for the case of truck orientation ST IVa for the static tests, except in this case the trucks were moving. The trucks, as noted earlier for this orientation, were aligned in two rows of four trucks as close as practicable as shown in Figure 5.5. These tests were performed only on the southbound bridge because it had multiple accelerometers configured in the southbound box of Span 2 to investigate the dynamic properties of the bridge. All other boxes in the other spans had only single accelerometers oriented in the vertical direction, attached to the underside of the deck near midspan of the boxes. In truck orientation ST IVa, the trucks drove as close to the exterior edge of the box as the drivers felt comfortable. This truck orientation focused on finding the torsional dynamic properties of the bridge. This truck orientation was applied four times with the truck speed varying between 30 and 45 mph (48 and 72 km/hour) with the trucks running from north to south.

5.2.3.2 Truck Orientation ST V

Truck orientation ST V was similar to the static test configuration ST I in that the trucks were lined up across the width of the bridge. However fewer trucks were used in the dynamic tests because there was insufficient room to stage and operate eight trucks for the dynamic tests due to the tight spacing. In fact, the original test configuration for truck orientation ST V called for seven trucks, but this was changed to six trucks as shown in Figure 5.7 to accommodate for driver comfort (seven trucks was a tight fit at the speeds driven). The purposes for running this dynamic test were to obtain the longitudinal frequencies and mode shapes of the new bridge. This test was run four times on the southbound bridge and three times on the northbound bridge. For the southbound bridge tests using the ST V truck orientation, the trucks were run from south to north three of the four times and from north to south one of the four times. For the northbound bridge, the trucks were run from south to north for all of the tests. For the southbound bridge, the three tests run from south to north were run at approximately 45 mph (72 km/hour) while the test run north to south was run at approximately 20 mph (32 km/hour). The average speeds during the tests on the northbound bridge ranged from about 35 to 40 mph (56 to 64 km/hour).

5.2.3.3 Truck Orientation ST VI

The final truck orientation run for the dynamic tests was ST VI shown in Figure 5.8. For this test the trucks were oriented in groups of four. Two rows of two trucks positioned as close as practicable were driven across the bridge over the center of each box (one group of four trucks over the southbound exterior box and one group of four trucks over the southbound interior box) between the webs. This test was run twice on the southbound bridge with the trucks running from north to south. These tests were performed in order to obtain longitudinal modes of the bridge. The trucks were driven at approximately 40 mph (64 km/hour) for these tests.

5.3 October 2010 Truck Tests

The truck tests performed in October of 2010 two years after completion of the bridge were done to provide an evaluation of the evolution of the structure's behavior, and to provide additional dynamic truck test data. To avoid disruptions to traffic, the tests were performed at night. Timing for the tests was constrained between 10:00 PM and 5:00 AM the next morning to ensure that the interstate closure did not significantly impact the travelling public.

During the first night of truck tests (October 27), the northbound bridge was closed to all traffic from 10:00 PM until approximately 12:30 AM the next morning. During the closure period, static truck tests were performed on the northbound bridge. After the bridge was reopened, dynamic truck tests were performed with traffic on both structures. Weather conditions during the first night were a constant 32°F (0°C) with approximately 20 mph (32 km/hour) winds.

During the second night of truck tests (October 28), the southbound bridge was closed to all traffic from 10:00 PM until 5:00 AM the next morning. While the structure was closed, dynamic truck tests without traffic were performed on the southbound structure, followed by static truck tests on the southbound structure. Weather conditions during the second night were a constant 32°F (0°C) with winds typically less than 5 mph (8 km/hour).

5.3.1 Truck Information

Trucks used for the October 2010 truck test were selected to be comparable to the trucks used for the September 2008 tests. Trucks were weighed only the first night of testing (October 27) and were left loaded until the completion of the tests on the second night (October 28). It was assumed that the trucks

did not significantly change weight between the testing days. Only total truck weights, and not the individual axle weights, were measured. It was assumed the trucks distributed the weight among the axles in a similar fashion observed for the September 2008 tests. Details for the trucks used during the October 2010 tests are provided in Table 5.6.

5.3.2 Static Truck Tests

Truck test configurations for static load tests were identical to those performed during the September 2008 tests. Static configuration ST I (Figure 5.2) was used to investigate longitudinal bending of the structure, as well as load distribution and transverse bending at southbound Locations 3 and 7. This configuration was ultimately performed at eight locations on the northbound bridge (Location 3, Location 3 offset to the north by 9 ft (2.7 m), Location 7, Location 7 offset to the north by 9 ft (2.7 m), Location 9, Location 9 offset to the north by 9 ft (2.7 m), Location 14, and Location 14 offset to the north by 9 ft (2.7 m)) and at seven locations on the southbound bridge (70 ft (21 m) south of Location 3, Location 3, Location 6, Location 7, Location 7 offset to the south by 9 ft (2.7 m), Location 9 offset to the south by 9 ft (2.7 m), and Location 14). The "offset tests," for which the trucks were positioned 9 ft (2.7 m) away from the instrumented section, were performed as an attempt to minimize the impact that local deformations of the top flange under the truck loading had on the measured results. Configuration ST III (Figure 5.4) was planned only for load distribution investigations at southbound Locations 3 and 7, but because of time constraints and instrumentation issues during the testing procedure (specifically, the power supply for the VWSG system fiber optic converters failed during testing, as discussed in Section 2.2.6.4), configuration ST III was not performed. Configurations ST IVa and ST IVb (Figure 5.5 and 5.6) were planned to investigate deformation and torsion of the box at southbound Locations 3 and 7. Again, due to time constraints and the VWSG complications as noted above, configuration ST IVa was only performed at southbound Location 7, and configuration ST IVb was not performed. For each performed test, three readings from all VWSGs and SOFO fiber optic sensors on the loaded structure were captured before repositioning the trucks.

The static truck tests performed on the northbound bridge during the first night of testing are summarized in Table 5.7. The static truck tests performed on the southbound bridge on the second night are summarized in Table 5.8.

Trucks were positioned relative to survey markers (PK Nails) installed prior to the testing. The markers were placed behind the exterior metal guard rail and on top of the interior concrete barrier rail on both the southbound and northbound bridges.

Tests were performed in the same manner as the September 2008 tests (refer to Section 5.2.2). Data collection was performed by two UMN personnel in the control room (representatives from the instrumentation vendors were not necessary for data collection during these tests), with UMN and MnDOT personnel on the bridge deck for positioning and measuring the trucks.

Deflection measurements were taken during the second night of testing for the southbound static tests using the IBIS-S microwave radar sensor provided by Olson Engineering. Representatives from Olson Engineering were onsite to collect this data. The radar station was setup below Span 3, facing south such that all reflectors were within view. Laser distance measurements were taken from the radar station to Pier 4, and from the radar vertically up to the bottom face of the top flange of the superstructure. From these measurements, the radar station was determined to be located at bridge station 224+88.7, and was 89.2 ft (27.2 m) below the bottom face of the top flange. Reflectors were mounted along the exterior guardrail of the southbound structure. Reflector locations are documented in Table 5.9. The horizontal range is the horizontal distance from the radar station to the reflector. The angle of inclination is the angle up from the horizontal measured from the radar station to the reflector. The projection factor is

equal to $1/\sin(\theta)$, where θ is the angle of inclination. The radar system could only measure changes in the range of the reflector from the radar station. In order to calculate the vertical deflections, the measured change in range was multiplied by the projection factor for each reflector.

5.3.3 Dynamic Truck Tests

Because dynamic truck tests were being performed both with and without traffic, the truck configurations used for the September 2008 truck tests were not adopted for the October 2010 tests. By necessity, it was required to keep the moving trucks in traffic lanes when the loaded trucks were moving with traffic, and for consistency, this same policy was adopted for the dynamic tests on the closed bridge. For describing the dynamic tests, lanes were given numbers 1 through 5. Lane 1 was the outermost lane and Lane 5 was the innermost lane for both structures, as shown in Figure 5.9. Through lanes for both structures were Lanes 3, 4 and 5.

Each dynamic test set consisted of two to eight waves of trucks. A wave was defined by a set of trucks that travelled on the bridge as a block. Waves were always separated by at least one minute as they crossed the structure. The configurations were described by the lanes that the trucks occupy. For instance, "345" meant that the trucks for this wave occupied Lanes 3, 4 and 5. For cases where a truck was expected to follow closely behind another truck (as close as safely possible, and thus not constituting a new wave), the number was listed twice in the entry. Therefore, "4455" contained two trucks in Lane 4, and two trucks in Lane 5, forming a 2x2 block of trucks. Some waves were specified as "random." These specifications were always used simultaneously with a second, orderly wave. The trucks assigned to the random wave drove across the bridge individually at random times within 30 seconds before or after the orderly wave, and drove in a randomly assigned lane in no specific configuration. This was done to emulate large amounts of ambient vehicle traffic during the orderly truck tests.

Dynamic tests with traffic did not require traffic control measures. For these tests, the trucks alternated tests between the northbound and southbound structures, turning around and reorienting when necessary.

For with-traffic dynamic testing on the southbound bridge, trucks were limited to driving in Lanes 3 through 5. Lane 1 joined the interstate via the University Avenue ramp, and did not merge with the other four lanes until the start of the structure. Lane 2 originated below the 4th Street overpass. Because the trucks were not allowed to use the 4th Street exit/University Avenue on-ramp, the extra complications and possible hazards associated with using Lanes 1 and 2 were deemed to outweigh the benefits.

For with-traffic dynamic testing on the northbound bridge, trucks were also limited to Lanes 3 through 5. Lanes 1 and 2 exited the bridge to University Avenue. Using the University Avenue exit/4th Street on-ramp was undesirable for testing (trucks would need to decelerate up the ramp or quickly merge into one of the through lanes while still on the bridge), so all tests were planned to avoid these lanes. Furthermore, the dynamic instrumentation was identical within the two northbound bridge boxes, and it was believed that utilizing Lanes 1 and 2 would not provide a significant amount of new information.

Times, configurations, and observed traffic for each of the with-traffic dynamic truck tests are summarized in Table 5.10. With-traffic dynamic tests were named using the format Open [a][b], where "Open" referred to the fact that the bridge was open to traffic, [a] was either N or S depending on whether the test was performed on the northbound or southbound structure, respectively, and [b] was a number sequentially assigned to the tests to ensure each test had a unique name.

Closed-bridge dynamic testing on the southbound structure utilized all lanes of the structure. Trucks lined up for Lane 1 accelerated down the 4th Street on-ramp (when travelling south) or the Washington Avenue on-ramp (when travelling north). Lanes 2 through 5 were all arranged without use of the on-ramp,

although trucks travelling in Lane 2 were required to shift over from/to Lane 3 when the lane was added/removed.

Times and configurations for each of the closed-bridge dynamic truck tests are summarized in Table 5.11. Closed-bridge dynamic tests were named using the format Closed [a][b][c], where "Closed" referred to the fact that the bridge was closed to traffic, [a] was either N or S depending on whether the test was performed on the northbound or southbound structure (for the tests performed, this value was always S), [b] was either N or S describing whether the trucks travelled north or south, respectively, and [c] was a number sequentially assigned to the tests to ensure each test had a unique name.

For all dynamic truck tests performed on October 2010, the long-term accelerometer configuration shown in Figure 2.46 was used. Additionally, the dynamic SOFO fiber optic datalogger was used to collect the dynamic strains. Only eight channels were able to be collected by the dynamic data logger, so all six bottom flange SOFO sensors and two top flange sensors (at Locations 6a and 7b) were selected. Previous experience with the SOFO dynamic system showed that using only the bottom flange sensors provided reasonable accuracy for computing curvatures at the instrumented sections, except at sections near the piers (Locations 6a and 7j), where both top and bottom sensors were necessary. Because the top flange sensor at location 7j (sensor 7jT_7015) was noted to provide occasionally unreliable data when attached to the dynamic datalogger, this channel was switched to the top sensor at location 7b (sensor 7bT_7008) to provide redundant measurements at this section. Data was collected at a sample rate of 100 Hz.

No personnel were allowed to walk on the bridge deck during any of the dynamic tests. Instead, UMN and MnDOT personnel not in the control room or driving the trucks were stationed off the bridge, typically in parking lots overlooking the structure. Groups were positioned at both the north and south ends of the structure to monitor the testing, to record when the trucks had entered and exited the bridge, and to record ongoing traffic in the case of the with-traffic dynamic tests. Communication between the monitoring groups, truck drivers, and control shed personnel was kept through walkie-talkie and radio.

5.4 Discussion of Truck Test Procedures

Both the static and dynamic truck tests were conducted to investigate the behavior of the bridge and to provide data that could be compared to the FEM for validation purposes. The tests also provided benchmark data that could be referenced over the life of the structure to aid in the detection of deterioration.

5.4.1 Static Truck Tests

It took approximately five to ten minutes to set up the static truck tests at each section. Each time a truck configuration was positioned at a new location along the bridge to record the instrument data, the trucks had to be reoriented and aligned. The trucks remained in position while the data was collected. Each gage was read sequentially, and because the bridges, particularly the southbound bridge, were heavily instrumented, data collection took a significant amount of time (anywhere between three and ten minutes to acquire the data as described in Section 5.2.2). With multiple locations on the bridge to position the trucks, and a limited amount of time to conduct the tests, the number of tests that could be performed was restricted, thus limiting the amount of data that could be collected to analyze the bridge behavior. Markers denoting key locations along the bridge were placed by survey prior to the tests. While data was being collected for each test, the positions of the vehicles were measured relative these markers.

The static tests were important for establishing the bridge baseline behavior prior to opening the bridge, and for investigating the performance of the structure after two years of service. Most of the instruments in the bridge provided static measurements, and these sensors could not provide meaningful data with

respect to dynamic vehicular loading. Each VWSG required approximately two seconds to register a reading, and the data acquisition system acquired the data from each gage sequentially. For the southbound structure, this meant that it took a minimum of three minutes to record a measurement from each of the VWSGs. As a consequence, the loads had to be stationary for the readings to correlate with each other. After opening the bridge to traffic, it was not possible to capture meaningful static instrument readings with respect to vehicular loadings because the traffic was moving and the vehicular loads were not known. Therefore, the static truck tests provided relevant data regarding the structural response to vehicle loading that could not have been obtained from monitoring daily traffic data.

5.4.2 Dynamic Truck Tests

The dynamic truck tests did not take a significant amount of time to run, and to further hasten the dynamic tests performed on the bridge (naturally excluding those performed with traffic during the October 2010 tests), trucks were run in both directions across the structures. By the time the trucks were able to get turned around and reoriented, a zero reading of the bridge without any trucks on it had been taken such that the next test could be performed immediately. Because of the limited amount of time available for the truck tests, the accelerometers were not repositioned during the tests. Moving the accelerometers would have required access to the inside of the boxes and would have taken several hours for two people to accomplish.

Unlike the static tests, the trucks were not easy to position for the dynamic tests. During some of the tests, primarily those performed in September of 2008, the trucks were not aligned exactly according to the proposed truck orientation (e.g., some of the trucks lagged relative to others). This was more often the case for the dynamic tests utilizing the onramp lanes, where there was limited space for the trucks to get up to speed and stay in the desired orientation. Limiting the trucks to remain in their respective lanes, as was done for the October 2010 tests, and removing the need to use Lanes 1 and 2 greatly aided truck positioning.

For future dynamic testing, the lane configurations as used for the with-traffic dynamic truck tests could still be performed without the need to close the bridge. For modal analysis (with methods assuming ambient forcing), it is not necessary to know the exact alignment of the trucks, and it is more important to simply induce large excitations in the structure. Therefore, with regards to modal analysis, with-traffic dynamic tests provide just as much information as the closed-bridge tests without the costs associated with full bridge closure. This is discussed in detail in Chapter 8.

5.4.3 General Truck Tests

In general, for the truck tests, there were a number of differences between the proposed tests and the truck tests that occurred. These differences were primarily the result of time constraints and allowances for driver comfort.

Quite a few people were required to perform the static truck tests: two people in the control room to start and stop recording the data and to note the test being performed, and 12-14 people on the superstructure including the eight truck drivers. The individuals on the superstructure included one who directed the tests (including supervising safety aspects) and relayed information to and from the people in the control room; the eight truck drivers, plus another person moving along with the trucks that helped position and align the trucks; two people that measured the truck locations during the static tests and then moved ahead to position the cones for the next static location while the trucks were sitting allowing the gages to be read; another person that recorded information on the bridge during the tests, such as which test was being performed at a particular time and measurements being taken for static truck tests. Security personnel

were also used at each end of the bridge during testing to ensure that no one tried to access the bridge during testing for safety reasons.

Fewer personnel were required for the dynamic tests: two people in the control room that started and stopped measurements, two people overlooking each end of the bridge that monitored the testing progress, and the eight truck drivers. If more time were allowed for the tests and access to the boxes was available, a few people could have been inside the box during the dynamic tests to move the accelerometers in order to have tests performed with gages in both the short-term and long-term orientations.

Chapter 6. Static Truck Test Data and Validation of Finite Element Model

Data from the static truck load tests were used to validate the finite element models. Model construction methodology is detailed in Chapter 4, and the truck test methodology is presented in Chapter 5. Also, it was important to verify that the static behavior of the structures did not change substantially between the truck tests performed on September 2008 and those on October 2010.

All strain data presented from the truck tests represent changes in strain due to the applied load. The "unloaded" reading for each test was linearly interpolated between the zero readings immediately before and after the test according to the temperature change from the zero readings. The change in strain was equal to the loaded measurement minus the interpolated unloaded strain. Positive strains are defined to be tensile, and negative strains are compressive.

This chapter presents investigations only for the static truck tests and finite element model results under static gravity loading. Finite element validation with respect to thermal effects is discussed in Chapter 7. Data from the dynamic truck tests are presented in Chapter 8.

6.1 Comparison of September 2008 and October 2010 Truck Tests

Truck tests from both testing periods were performed in largely the same manner, and with a number of repeat tests between the two sessions, to facilitate comparison of the bridge behavior both before opening and after two years of service.

The most common measurement for bridge behavior comparisons was to calculate the curvature from the measured changes in strain at each instrumented location. Curvature was calculated from the slope of the least-squares line fit to sets of gages through the depth of the cross sections. The measured curvatures represent the average of the curvatures measured through only the web gages where possible; where web gages were not available, the curvatures were obtained using the data measured from the two gages located at the centerlines of the boxes. This was done in an attempt to minimize the effects that local bending of the top flange as it spanned between the webs might have on the measured strains. In each presented curvature plot, local bending effects would be of concern only at the location of the trucks, which typically corresponded to the location of peak measured curvature. Positive curvature has been defined such that the top flange is in compression and the bottom flange in tension.

Northbound curvature plots from the October 2010 truck tests were found to be nearly identical to those from the September 2008 tests, as shown in Figure 6.1. In the loaded spans, minor discrepancies between the two sets of truck tests might be attributed to changes in concrete stiffness over time or small differences in load magnitude and position. The two largest discrepancies (around stations 227+00 and 228+00) for each plot were located in Span 4. It is unclear why the results in Span 4 differed between the two sets of truck tests, the most likely reason being the possibility of unrecorded loads placed on Span 4, especially during the September 2008 tests when work was still being performed on the bridge. Given that this span was separated from the three continuous spans by an expansion joint at Pier 4, these results were inconsequential in validating the three-span finite element model.

Overall, the southbound curvature plots from the October 2010 tests were also found to be nearly identical to those from the September 2008 tests, with the exception of test STI6SB (eight trucks across the width of the bridge at Location 6), as shown in Figure 6.2. In the figure, curvatures measured using the SOFO fiber optic sensors are shown with unfilled symbols, whereas locations with VWSGs are

presented as filled symbols. The SOFO sensors near the midspan of Span 2 gave much higher strains than anticipated during the October 2010 STI6SB test, though curvature magnitudes recorded during STI6SB tests were far less than during tests with the trucks positioned at the midspans. No malfunctions were detected in the gages at that time, and none of the three values that were averaged to obtain these results appeared to be anomalous. It might be expected that this error was caused by positioning the trucks too far north (i.e., upstation). However, moving the trucks would cause an increase in curvature at all locations (specifically at Location 3 at midspan of Span 1) and not just the SOFO sensors located in Span 2. It was therefore unlikely that this was caused by an improper positioning of the trucks. The measured response of the structure due to thermal gradients (discussed in Section 7.1) both before and after the October 2010 truck tests did not exhibit any notable change in the structural response, so it was believed that the differences noted here was not damage related. Ultimately, the cause for this discrepancy was uncertain. For the STI9SB plot in Figure 6.2, the October 2010 line uses the 9-ft offset test from Location 9 (test STI9(-9)SB), whereas the September 2008 line uses the tandem centered over Location 9 (test STI9SB). This comparison was necessary because the STI9SB test was not performed in October of 2010. The comparison confirmed that the load offset did not have a significant impact on the global bending behavior.

Load distribution across the boxes was investigated for all truck configurations common to both sets of truck tests at Locations 3 and 7, these being the sections most heavily instrumented with vibrating wire strain gages. The load distribution was investigated by measuring the longitudinal strain at multiple locations in the top flange across the width of the bridge. It was found that the STI7SB configuration (eight trucks across the width of the bridge at Location 7) from October 2010 produced consistently less strain across the entire width than was measured in September 2008 as shown in Figure 6.3. This could be due to a number of effects including differences in exact truck positions and continued stiffness gain of the concrete over the two year period. The 9-ft (2.7 m) offset test, STI7(-9)SB, appeared to have uniformly reduced the longitudinal strains from the STI7SB configuration. Similarly, longitudinal strains at southbound Location 3 due to truck test STI3SB on October 2010 were slightly less than those from the September 2008, as shown in Figure 6.4.

With the exception of truck test STI6SB as noted above, all comparable truck tests between the two testing sessions were found to be consistent with each other, with the October 2010 results typically 2% to 10% lower than September 2008 results.

6.2 Validation of Three-Dimensional Model

The construction of the three-dimensional finite element model is presented in Section 4.1. The following section will compare data from the truck tests with results from the finite element model in order to validate the finite element model. The investigation was confined to the southbound structure, as this was the modeled structure. Because the northbound bridge was less heavily instrumented, the only behavior of interest under static loading that could be gained from inspection of the northbound bridge was curvature, which was presented briefly in Section 6.1.

Table 6.1 lists the truck positions used in validating the three-dimensional finite element model. Truck tests were named in the format ST[a][b][c] as described in Section 5.2.2. The load from each truck was applied to the model by six point loads, two for each truck axle, idealized as shown in Figure 6.5. Dimensions of the truck were rounded to 2-ft (0.6-m) increments to facilitate application of the point loads to the nodes of the model, for which the typical element dimension was 24 in. (0.6-m) as discussed in Section 4.1.1. The model was used to investigate longitudinal bending, load distribution, shear strains, and cross-sectional deformation in the bridge.

6.2.1 Longitudinal Bending

Truck tests with configuration ST I were used primarily to investigate global longitudinal bending behavior. Figure 6.6 shows a comparison of the measured longitudinal strain through the depth of the section in the webs at Location 7 to the computed strain due to the truck load STI7SB performed during the October 2010 truck tests. The September 2008 truck test results for configuration STI7SB were similar, but were excluded from this plot to facilitate comparison with the offset test STI7(-9)SB performed only in October of 2010, as discussed in the next paragraph. The vertical distance on the y-axis was measured from the top of the deck. Measured and computed results for the strains corresponded well. The computed strain profile showed slight nonlinearity in the top flange region. Figure 6.7 presents the strain profile from the same location and truck test, but shows the strains measured at the centerlines of the two boxes instead of along the webs. The modeled results showed that the strain profile was distinctly nonlinear. However, the instrumentation was unable to capture this because only one strain gage was located through the depth of the top flange. The change in slope in the top flange was likely due to a combination of Poisson's effect from transverse bending in the deck as it spanned between the webs and local longitudinal bending of the deck due to the loading.

The strain profile was also investigated with the loading slightly offset from the instrumented section. Figure 6.8 shows a comparison of the computed and measured longitudinal strains through the centerline of the boxes at Location 7 due to truck test STI7(-9)SB performed during the October 2010 truck tests, representing an identical test to STI7SB except with trucks offset 9.0 ft (2.7 m) down station (south). Between the STI7(-9)SB and STI7SB tests, the measured curvature at the centerlines of the boxes only changed by approximately 0.025 με/in. (0.98 με/m), or approximately 4%. Likewise, the measured curvatures through the webs changed by 0.057 με/in. (2.2 με/m), approximately 10%. Local transverse effects were minimized for the gages at the centerlines of the boxes by positioning the gages at the neutral axis of the deck in the transverse direction as it spanned between the webs. The gages above the webs were located above the neutral axis of the deck, and thus were impacted comparatively more by the small local transverse effects. However, despite the load offset, computed results showed the strain profile through the centerline of the box was still nonlinear. This nonlinearity was attributed to local longitudinal bending of the top deck. This particular local bending mimicked that of an infinite beam on an elastic foundation under a point load, which explains the reversal of the strain profile nonlinearity when compared to results from STI7SB. In order to nearly remove this local bending, it would likely be required to position the trucks at least a distance away from the instrumented section equal to the transverse distance between two adjacent webs, or approximately 22 ft (6.7 m). The computed strain profile through the webs was found to be linear as expected.

Longitudinal curvature was measured at all locations instrumented with vibrating wire strain gages or fiber optic strain gages for the ST I configurations (i.e., the truck loads distributed uniformly across the width of the bridge). As noted above, curvature was calculated from the slope of the least-squares line fit to sets of gages through the depth of the cross sections. The measured curvatures represent the average of the curvatures measured through only the web gages where possible; where web gages were not available, the curvatures were obtained using the data measured from the two gages located at the centerlines of the boxes. The curvatures along Spans 1 through 3 of the southbound bridge for truck tests STI3SB, STI6SB, STI7SB and STI9SB are given in Figure 6.9. In each of the cases, the computed curvatures corresponded well with the measured results. Percent errors at the midspans of each span were less than 4%. The model tended to slightly over-predict the curvature at locations along Span 2 not at the midspan. All these locations were instrumented with SOFO fiber optic strain gages, which had long gage lengths of 13 ft (4.0 m) as opposed to the vibrating wire gages with approximate gage lengths of 6.75 in. (170 mm). This increase in length may have reduced the measured strain, as the fiber optic strains were effectively average strains along a 13-ft (4.0-m) chord along a non-prismatic cross section. This error was minor, and the strain results from the SOFO gages were still considered acceptable for model validation.

Deflection along Spans 1 and 2 due to the truck loading was measured during the October 2010 static truck tests using the IBIS-S microwave radar sensors provided by Olson Engineering. The sensors were only in place for truck tests STI7(-9)SB, STI6SB, STI3SB, and STI3(-70)SB. Only one zero reading was captured at the end of testing; the average displacement during the zero reading was subtracted from the average measured displacements from the truck tests. As a consequence, any temperature-related deflections over the course of the testing were unknown, and were not removed from the measured deflections. The results from these tests are compared to finite element results in Figure 6.10. Error bars indicate one standard deviation of the measured data over the entire time span of the test.

The measured displacements generally compared well with the predicted FEM displacements in Span 2 for truck tests STI7(-9)SB, STI3SB, and STI3(-70)SB. For example, under truck test STI7(-9)SB, measured deflection at Location 7 was approximately 0.75 in. (19 mm) downward, whereas computed deflections were 0.79 in. (20 mm). Other tests showed similar correlation. The Span 2 displacements appear to be slightly under-predicted by the model for test STI6SB. In all cases, however, the deflections in Span 1 matched poorly with the FEM results. It was found that the signal-to-noise ratio of the reflectors placed at these locations was very high, and the standard deviations of the measured data in this span were large. Because the reflectors on Span 1 were distant from the reading unit, and because there was a low angle of inclination between the reading unit and the reflector, potential errors in vertical deflection measurements were greatly magnified. It was also believed that Pier 2 was reflecting the radar back upon the reading unit, causing additional spurious readings near and beyond the pier. Regardless, the deflection readings confirmed that the model was consistent with the measured response of the structure at locations in Span 2 where the measured data was reliable.

6.2.2 Load Distribution

Load distribution across the boxes was investigated for all truck configurations at southbound Locations 3 and 7, these being the sections most heavily instrumented with vibrating wire strain gages. The load distribution was investigated by measuring the longitudinal strain at multiple locations along the top flange across the width of the bridge. Figure 6.11 shows a plot of the measured and computed top flange strains at Location 7 due to truck test STI7SB, which applied nearly uniform loading across the width of the structure. Dotted lines indicate computed strains at 2 in. (51 mm) above and below the assumed vibrating wire gage depth in the section. These bounds emulate the errors expected from gage positioning. Additionally, the uncertain thickness of the top deck could affect the plotted error bounds. According to the I-35W St. Anthony Falls Bridge Inspection and Maintenance Manual (Figg, 2008), a 2.5-in. (64-mm) integral wearing surface was cast on the top flange. The contractors ground approximately 0.5 in. (13 mm) off the top surface to prepare a smooth driving surface, resulting in an additional 2 in. (51 mm) of concrete above the specified as-built top flange thickness. However, ultrasonic tomography at Location 7 in the southbound bridge revealed that the thickness of the deck at the centerline of the box was, to an accuracy of ±0.25 in. (±6 mm), only 10.6 in. (270 mm), which was 0.9 in. (23 mm) thinner than specified. A thicker deck would decrease the error bounds as shown by reducing the local bending in the top flange, whereas a thinner deck would tend to amplify the error bounds. Modeling the top flange thickness as specified in the as-built drawings (Minnesota Department of Transportation, 2008), the measured strains generally fell within the computed strains associated with the ±2 in. (±51 mm) bounds, except at positions away from the webs where greater transverse bending caused larger deviations with depth in the longitudinal strains, as evinced by the bilinear strain profiles from Figure 6.7. The maximum strains occurred in the center of the bridge between the two boxes. The measured longitudinal compressive strains in the top deck ranged from 16 με up to 26 με.

Figure 6.12 shows the load distribution at Location 7 for truck loads STII7SB, STIII7SB, STIVa7SB, and STIVb7SB. For load orientations ST II, ST IVa, and ST IVb, the strain varied approximately linearly across the width of the bridge, from maximum measured compressive strains of approximately 25 με

down to minimum measured strains of approximately 10 με. In addition to the concerns discussed above pertaining to Figure 6.11, it was further noted that measured strains near the loading tended to be less than modeled strains, implying, in some combination, that additional stiffness in the physical bridge was not modeled and that the physical bridge distributed load more evenly between the boxes than was observed in the model. This was likely due, in part, to the approximation of the mild steel into the concrete stiffness properties whereby the resulting concrete was assumed to be homogeneous; locally, the reinforcement ratios may have been greater than the average ratios used to determine the effective modulus of the concrete. For example, in the deck spanning transversely between the two boxes, the reinforcement ratio in the transverse direction ranges from 0.003 near the webs (similar magnitude to the overall reinforcement ratios assumed for adjusting the modulus) up to 0.006 near the centerline of the boxes (nearly double the reinforcement used for the overall modulus adjustment). Assuming a reinforcement ratio of 0.006, the adjusted concrete modulus of elasticity would be approximately 2% higher than what was used in the model. Additionally, post-tensioning anchorage points located at the corners of the webs were not modeled, which would have introduced extra local transverse stiffness. Strain readings at the centerlines of the boxes appeared to be consistently lower than computed values, even where no load was near enough to the gage to induce local effects; this implied that more gage errors beyond those due to deck thickness discrepancies and vertical position were present (e.g., horizontal position errors, gages not oriented perfectly along the longitudinal axis, etc.), although no evidence clearly showed what these issues might be.

Load distribution results from Location 3 were similar to those for Location 7, and are presented in Figure 6.13 for truck test STI3SB and Figure 6.14 for tests STII3SB, STIII3SB, STIVa3SB and STIVb3SB.

6.2.3 Deformed Shape of the Box and Transverse Bending

The deformed shape of the box and transverse bending were investigated for all load configurations at Locations 3 and 7. Deformation was measured by considering the transverse and vertically oriented strain gages throughout the section, as well as the rosettes in the webs. The maximum FEM transverse and vertical strains at Locations 3 and 7 for the investigated truck test configurations are summarized in Table 6.2. For reference, the extreme FEM longitudinal strains at Location 7 under truck test STI7SB were -37 με and 58 με. The largest overall transverse strains were caused by truck configuration ST III, and corresponded to extreme bending of the top flange as it spanned between the boxes. The largest vertical strains were caused by truck configuration ST IVa, which produced large amounts of bending in the webs.

Figure 6.15 shows a depiction of the deformed shape of the cross section at Location 7 due to truck test STI7SB (with the trucks placed approximately uniformly across the width of the bridge). Callouts indicate the locations of vibrating wire strain gages, and how the measured strains compared to the computed strains. Computed strains were always within ±4 με of measured results for this test. Considering the approximations of modeling, such as lumping mild steel in with the concrete and uncertainties of material properties, structural dimensions and truck positions, and the sources of errors in the strain gages, such as installation positional errors and a gage resolution of 1 με, the deformed cross-sectional shapes resulting from the model were found to be reasonable. Other tests, discussed further down in this section, typically had larger errors than those observed for test STI7SB. This was believed to be due, in part, to the more complex behaviors present in the instrumented bridge that might not have been as precisely captured by the simplifications necessary for efficient finite element modeling. However, for the reasons discussed above, differences between modeled and measured results for all tests were found to be acceptable.

For test STI7SB, the maximum computed transverse strains (not limited only to instrumented points) of ±29.5 με were located in the thin portions of the top flange at the centerlines of the boxes and centerline of the bridge. The bottom flanges of both boxes were fully in compression, and also exhibited bending in

triple curvature. The webs did not undergo significant out-of-plane bending in this test; maximum computed vertical strains (not limited only to instrumented points) were approximately ±14 με.

Results for truck test STI3SB at Location 3, presented in Figure 6.16, were similar. For STI3SB, maximum FEM transverse tensile strain was 30.31 με at the bottom fiber of the top flange at centerline of the exterior box. Maximum FEM transverse compressive strain was -29 με at the top fiber of the top flange at centerline of the interior box. Extreme FEM vertical strains were 9.0 με on the outside and -16 με on the inside of the east web of the interior box as it met the top flange.

Truck tests STII7SB and STII3SB were used to investigate truck loading straddling the exterior box's webs at Locations 7 and 3, respectively. Figure 6.17 shows a contour plot of the transverse strains at Location 7 under truck test STII7SB. Maximum FEM transverse tensile strain for STII7SB was 35 με at the bottom fiber of centerline of exterior box. Maximum FEM transverse compressive strain for STII7SB was -29 με at the bottom fiber of the bottom flange where it met the east (interior) web of the exterior box. Extreme FEM vertical strains were 35 με on the outside and -36 με on the inside of the east (interior) web of the exterior box as it met the top flange.

Results were similar for Location 3 under test STII3SB, shown in Figure 6.18. Maximum tensile strain for STII3SB was 31 με at the bottom fiber of the top flange where it met the east (interior) web of the exterior box as it spanned between the two boxes. The maximum compressive strain was -27 με at the top fiber of the top flange where it met the east (interior) web of the exterior box as it spanned between the two boxes. Extreme FEM vertical strains were 33 με on the outside and -36 με on the inside of the east (interior) web of the exterior box as it met the top flange.

Truck test configuration STIII7SB (with trucks centered between the two boxes) exhibited the largest computed transverse strains of all configurations. Figure 6.19 shows a contour plot of the transverse strains at Location 7 under truck test STIII7SB. Transverse strains in the top flange were higher than all other previously discussed truck tests. The bottom flanges of the boxes were bent in double curvature, as was typical for all measured cases except STI7SB. Maximum FEM transverse tensile strain for STIII7SB was 52 με at the bottom fiber of the top flange at the centerline of the cross section. Maximum FEM transverse compressive strain for STIII7SB was -50 με at the top fiber of the top flange at the centerline of the cross section. These transverse strains were approximately as large as the maximum longitudinal strains of all configurations, measured at ~55 με at Location 7 for test STI7SB. Significant bending was seen in the interior webs of both boxes, with extreme FEM vertical strains equal to 27 με on the inside and -29 με on the outside of the west (interior) web of the interior box where it intersected with the top flange.

Results were similar for Location 3 under test STIII3SB, shown in Figure 6.20. Maximum tensile strain for STIII3SB was 46 με at the bottom fiber of the top flange at the centerline of the cross section. The maximum compressive strain was -44 με at the top fiber of the top flange at the centerline of the cross section. Extreme FEM vertical strains were 27 με on the inside and -31 με on the outside of the west (interior) web of the interior box as it met the top flange.

Truck test configuration STIVa7SB (with trucks along the exterior edge of the structure) exhibited the largest computed vertical normal strains among all configurations. Figure 6.21 shows a contour plot of the transverse strains at Location 7 under truck test STIVa7SB. Large bending was observed in the east (interior) web of the exterior box, with extreme FEM vertical strains of 55 με on the outside and -52 με on the inside of the east (interior) web of the exterior box as it met the top flange. These computed vertical normal strains were nearly as large as the maximum longitudinal strains from test STI7SB. For this test configuration, measured vertical normal strains in the web were lower than those predicted by the model, implying that, as was mentioned in the discussion for load distribution, some stiffness in the physical

structure was excluded from the model. Also, given the large amount bending in the cross section, many of the errors were considered reasonable; 1-in. (25-mm) positional error in the gages (either vertically or transversely) could translate to changes in strain readings up to 6 με. The west (exterior) web of the exterior box and east (exterior) web of the interior box did not bend by significant amounts. The bottom flange of the loaded exterior box was in double curvature. Maximum transverse strains in the top flange under test STIVa7SB, with the tensile maximum of 36 με at bottom fiber of centerline of exterior box, were slightly higher than those generated by STI7SB. Compared to test STII7SB (trucks aligned over the webs), STIVa7SB produced similar transverse strains in the top flange as it spanned between the boxes. The bottom flange and the webs of the exterior box underwent less bending during STII7SB compared to STIVa7SB.

Results were similar for Location 3 under test STIVa3SB, shown in Figure 6.22. Maximum FEM transverse tensile strain for STIVa3SB was 40 με at bottom fiber of centerline of exterior box. Maximum FEM transverse compressive strain for STIVa3SB was -42 με at bottom fiber of the bottom flange where it met the east (interior) web of the exterior box. Extreme FEM vertical strains were 51 με on the outside and -50 με on the inside of the east (interior) web of the exterior box as it met the top flange.

Due to additional stiffness provided by the concrete barrier rail on the interior edge of the bridge, strains for STIVb7SB and STIVb3SB (with trucks along the interior edge of the bridge) were invariably lower than those predicted for STIVa7SB and STIVa3SB.

6.2.4 Shear

Shear strain was measured by vibrating wire strain gage rosettes located in the webs of the boxes at Locations 3, 4, 6, 7, and 8. Shear strain from these gages was calculated as

$$\varepsilon_{12} = \pm\left(\frac{1}{2}(\varepsilon_1 + \varepsilon_2) - \varepsilon_{diag}\right) \qquad (6\text{-}1)$$

where ε_{12} is the tensorial shear strain (equal to half the engineering shear strain γ_{12}), and ε_1, ε_2, and ε_{diag} are the longitudinal, vertical and diagonal gage strains, respectively. The plus/minus sign was selected based on the particular orientation of the diagonal gage in the installed rosette, and has already been accounted for in all presented results. All shear strains in this section are reported in tensorial shear strain components.

Figures 6.23 through 6.27 depict the shear strains in Locations 3, 4, 6, 7, and 8 for truck test STI7SB. Measured shear strains in the west web of the exterior box at Location 7 (Figure 6.26) were larger than those predicted by the FEM model, although this was considered acceptable. Due to the point load nature of the rear tandem loading which was located directly over the rosettes, small adjustments in truck or gage position yielded large changes in measured shear strain. FEM results only a few feet away from Location 7 showed shear strains above 6 με, the average measured shear strain at Location 7. Measured shear strains at Location 7 due to the offset truck test STI7(-9)SB were -10.5 με and -8.8 με in the east and west webs, respectively, of the exterior box. Locations 6 and 8 (Figures 6.25 and 6.27) had larger overall shear forces than Location 7, but lower computed maximum shear strains of 2.5 με. Location 4 (Figure 6.24) had an abnormal computed shear profile through the section, but negligible shear strains. This profile was assumed to be caused by the pinned boundary conditions very close to the location. This profile shape was typical for sections near the piers during tests for which the loading was not in the span of the section. Measured readings in each plot include error bars of ±1 με to depict the resolution of the gages at these small strain readings. Error bars including truck positioning errors and other factors were expected to be larger than those depicted.

Figures 6.28 through 6.30 show the shear strains at locations 3, 4, and 7 for test STI3SB. Locations 6 and 8, not shown here, had negligible strain magnitudes with profiles similar to what is shown in Figure 6.24. The maximum computed shear strain for this test was found at location 3 (Figure 6.28) with an FEM magnitude of 4.6 με. Maximum computed shear strains at location 4 (Figure 6.29) and location 7 (Figure 6.30) were 2.75 με and 1.5 με, respectively.

Shear strains were investigated for load cases near the piers, specifically test STI6SB. The maximum FEM shear strain at Location 6 (Figure 6.31) was 5.4 με. Computed shear strains at Location 7 (Figure 6.32) were around 0.5 με, below the resolution of the instrumentation. All other locations yielded similarly negligible strains for this test.

Torsion of the boxes was investigated for truck test STIVa7SB. Truck test STIVb7SB was not specifically investigated in this manner as the majority of the instrumentation was in the unloaded box, and only a single reading was captured for a single run of this test configuration. Tensorial shear strains at Locations 6, 7 and 8 are plotted for STIVa7SB in Figures 6.33, 6.34, and 6.35, respectively. Computed shear strains peaked near 8 με at Locations 6 and 8 in the west web of the exterior box. At the location of loading, computed results indicated that the majority of the shear was carried solely by the west web of the exterior box. However, large positive shear strains were measured in the east web of the exterior box, conflicting with FEM results. This was believed to be due to the large out-of-plane bending in the east web of the exterior box, which may have affected rosette strain readings, or the rapidly changing shear strains due to load position along the length of the bridge, as was discussed for truck test STI7SB above. According to the FEM results, assuming that the webs of each box distributed the non-torsional shear evenly between them (but not necessarily that each box carried equal total shear), the torsional shear strains were about 5 με in the exterior box and 2.5 με in the interior box.

6.2.5 Conclusions

The three-dimensional finite element model was successfully validated using the results from the truck tests. Global curvature results were checked for the ST I configuration truck tests, and it was found that FEM results compared well, typically within 10%, to vibrating wire strain gage data and fiber optic data.

Examining longitudinal load distribution in the top flange showed comparable results for FEM and measured strain data. Due to the local bending effects of the top flange as it spanned between the webs, errors tended to be larger for these tests than from global bending examinations. Strain bounds for positional errors in gages of up to ±2 in. (±51 mm) were plotted from FEM data. The measured results tended to either lie within or occasionally below (i.e., less compressive strain) these bounds. The trends found in both the measured and FEM data were similar, implying that the model accurately captured the bridge behavior despite some discrepancies in strain magnitudes.

Deformation of the cross section was explored at Locations 3 and 7. Under ST I loading, the top flange acted essentially as a continuous beam, while the bottom flange was under a combination of compression and fixed-fixed beam bending (triple curvature) in the transverse direction. The webs did not bend significantly out of plane. The east (interior) web of the exterior box and the west web of the interior box both exhibited significant out-of-plane bending under the asymmetric loading from configuration ST IVa. Asymmetric load case ST II generally produced smaller strains than those exhibited under configuration ST IVa. Load case ST III (with the truck loads placed on the flange between the two boxes) caused large transverse bending in the top flange as it spanned between the two boxes. Configuration ST III produced the largest transverse strains among all investigated configurations, while configuration ST IVa produced the largest vertical strains. The transverse and vertical strains caused by truck configurations ST II, ST III, and ST IVa were often of similar magnitudes to the largest longitudinal strains generated by the extreme longitudinal bending load case, STI7SB.

Shear was investigated along the length of the bridge for a variety of load tests. For most instrumented locations, the shear strain was below 1.0 με, and thus was less than the resolution of the instrumentation. For tests where the trucks were located at midspan of one of the spans, the maximum shear strains were found at the location of the loading. In these cases, shear strains were less at the supports due to the larger cross section able to carry the loads. Loading near the piers naturally yielded higher overall shear strains than loading at midspan. According to FEM results, torsional shear strains were divided unevenly between the two boxes for the STIVa7SB load tests. The torsional test produced the highest shear strains over all considered tests.

6.3 Validation of Two-Dimensional Model

The construction of the two-dimensional finite element model is presented in Section 4.2. This model was validated using strain gage (VWSG and SOFO) data from static truck tests. Table 6.3 lists the truck tests that were checked in the two-dimensional finite element model. The two-dimensional model could only feasibly model the ST I configuration, for which eight trucks were positioned uniformly across the width of the bridge. The total load was applied as three point loads on the top surface of the bridge, each point load representing a line of axles from the eight trucks.

The validation process involved matching the curvature response of the model to the measured results for the truck tests. Comparisons of the averaged curvatures at each of the instrumented sections between the validated FEM results and the measured results are presented in Figure 6.36. Overall, the FEM compared favorably to the measured curvatures, implying that the model provided an accurate representation of the physical structure with respect to gravity loading. Furthermore, the agreement of the two-dimensional model results with the measured, and by extension the three-dimensional model results, verified that the differing assumptions inherent in the construction of both models (namely differing boundary conditions and plane-stress versus continuum formulations) still produced comparable results.

Chapter 7. Measured Thermal Effects

Temperature and strain data were collected over the course of three years using the VWSGs, SOFO fiber optic gages, and thermistors as documented in Chapter 2. Bridge temperatures were investigated for thermal gradients and uniform temperature changes.

This chapter presents a comparison between the measured thermal gradients and design gradients. The behavior of the finite element model was validated with respect to measured results taken during the maximum measured thermal gradients. The long-term thermal behavior, primarily due to uniform temperature changes, was investigated with the linear potentiometer and VWSG data.

7.1 Thermal Gradients

Thermal gradients (i.e., variations in temperature through a cross section) in concrete bridge structures are caused by a combination of solar radiation, conduction, and convection with the surrounding atmosphere. The comparably low thermal conductivity of concrete causes the section to heat or cool non-uniformly during a daily cycle. These gradients are typically most pronounced through the depth of the cross section; the incident solar radiation heats the top surface of the bridge deck, and the heat flows down through the superstructure. Positive thermal gradients, defined as the top surface temperature being higher than the temperature in the webs, are generally observed on clear, sunny, hot afternoons, typically 2:00 to 4:00 PM, with high solar radiation. Negative thermal gradients, defined as the top surface temperature being lower than the temperature in the webs, are generally found during early mornings, usually 5:00 to 8:00 AM, throughout the year. All times listed in this chapter are Central Standard Time and have not been adjusted for daylight savings time.

7.1.1 Literature Review

The heat flow problem in bridge structures was considered computationally by Potgieter and Gamble (1983). The authors constructed a finite difference heat flow model and complemented their numerical study with field measurements from the Kishwaukee River Bridge. The work of Potgieter and Gamble was advanced by Imbsen et al. (1985), in what was later adapted into the AASHTO LRFD Bridge Design Specifications. The AASHTO LRFD (2010) design positive gradient for solar radiation Zone 2 (which includes Minneapolis) is illustrated in Figure 7.1. The design negative gradient for structures with plain concrete decks and no asphalt overlay is found by multiplying the design positive gradient by -0.3.

The design gradient from the New Zealand Code, shown in Figure 7.2, is a fifth-order curve decreasing from maximum gradient temperature T_0 at the top of the deck to zero at a depth of 47.2 in. (1200 mm) defined by

$$T_{grad}(y) = T_0\left(\frac{y}{47.2}\right)^5, \; y \text{ in inches} \qquad (7\text{-}1)$$

where y is defined positive up from the point 47.2 in. (1200 mm) below the top surface regardless of section depth (Priestley, 1978). The specified maximum gradient temperature T_0 for plain concrete decks with no asphalt overlay is equal to 57.6°F (32°C). The fifth-order curve is applied to the section above the webs, through the depth of the webs, and to portions of the deck above unenclosed air. For portions of the deck above enclosed air cells in box girders, a linear gradient is prescribed with a top gradient temperature equal to T_0 and, for plain concrete decks with no asphalt overlay, temperature decreasing at a rate of 1°F per 0.44 in. (1°C per 20 mm). The bottom gradient tail temperature is specified as 2.7°F (1.5°C), decreasing linearly to zero over a height of 7.9 in. (200 mm) measured from the bottom of the section. A design negative thermal gradient is not specified.

A number of investigations regarding the effect of thermal gradients on concrete bridges have been conducted. Potgieter and Gamble's (1983) investigation of the Kishwaukee River Bridge, a segmental five-span continuous box girder bridge with blacktop covering located near Rockford, Illinois, revealed that the shape, but not the top surface magnitude, of the New Zealand gradient matched measured thermal gradients. Shushkewich (1998) investigated the measured thermal gradients of the North Halawa Valley Viaduct, a cast-in-place concrete box girder bridge in Hawaii. Positive and negative thermal gradients were found to correspond well with AASHTO (1998) proposals, which are identical to the thermal gradient provisions in AASHTO LRFD 2010. Thompson et al. (1998) considered the "Ramp P" structure, a curved precast segmental concrete box girder bridge on highway US 183 in Austin, Texas. Gradients were measured both with and without 2-in. (51-mm) blacktop covering. Measured gradients were typically lower than those specified in AASHTO LRFD (1994), which had an identical positive design gradient to AASHTO LRFD (2010) but used a multiplier of -0.5 instead of -0.3 for defining the negative gradient. However, it was stated that more data was needed to construct a sound statistical comparison. Roberts-Wollman et al. (2002) investigated thermal gradients in precast segmental concrete box girders in the San Antonio "Y" Project. They concluded that typical positive gradients could be approximated by a fifth-order curve similar to that presented in Priestley (1978). They also stated that the AASHTO LRFD (1994) positive and negative design gradient magnitudes were conservative for the San Antonio region.

7.1.2 Structure and Instrumentation

Thermal gradients were measured in the I-35W St. Anthony Falls Bridge in Minneapolis, Minnesota. The driving surface had no blacktop covering. Bridge geometry is discussed in Chapter 1. The full bridge instrumentation is documented in Chapter 2.

One segment of the southbound structure near the midspan of the river span (Location 7) was heavily instrumented with thermistors to explore the temperature distribution throughout the cross section. Some characteristic sectional dimensions and the thermistor layout used for the investigation of thermal gradients at this section, including thermistors integral with the vibrating wire strain gages, are presented in Figure 7.3. Insufficient instrumentation prevented detailed investigation of thermal gradients at other locations within the northbound and southbound structures; however, temperatures within the section could be spot checked along the length of the bridge using thermistors associated with the vibrating wire strain gages.

7.1.3 Comparison of Measured and Design Thermal Gradients

Measured thermal gradients from Location 7 of the southbound St. Anthony Falls Bridge superstructure were compared to AASHTO LRFD (2010) and New Zealand (Priestley, 1978) design gradients as presented in Section 7.1.1. A graphical comparison of these two design positive thermal gradients both scaled to the same top surface gradient temperature T_0 is presented in Figure 7.4. Even when the maximum gradient temperature values are equal, the area under the Priestley gradient curve is considerably larger than that under the AASHTO LRFD gradient.

7.1.3.1 Comparison of Gradient Magnitudes

The magnitude of the measured positive thermal gradients was taken as the difference between (1) the average of the operational topmost thermistors of all six-thermistor sets in the top flange and (2) the coldest measured temperature along the centerlines of the webs. Minimum temperatures were captured along the centerlines of the webs to minimize the influences of gradients through the thickness of the webs, which were measured using sets of three thermistors installed through the width of the webs. The thermal gradients through the webs were typically not linear; often the temperature at the centerline of the

web was lower than temperatures from both the outermost thermistor (with 2.25 in. (57 mm) of concrete cover) and the innermost thermistor (with 2.25 in. (57 mm) of concrete cover from the air inside the box). Differences between any two web thermistors rarely exceeded 3.0°F (1.7°C), and thus were negligible compared to gradients through the depth of the box section.

Because top surface temperature measurements were not taken, comparisons made between measured and design gradient magnitudes required that the value of the design gradient at a depth of 2 in. (51 mm) below the top surface of the deck (where the topmost thermistor was located) be used. Consequently, the AASHTO LRFD gradient in Zone 2 (top surface gradient temperature equal to 46°F (25.6°)) would have a magnitude of 29.0°F (16.1°C) at a depth of 2 in. (51 mm), and the Priestley fifth-order gradient scaled to the same top surface gradient temperature (henceforth referred to as the Priestley-Z2 gradient) would have a magnitude of 37.1°F (20.6°C) at that same depth. These design gradient magnitudes at the depth of the thermistors are compared to the measured positive gradient magnitudes from September 1, 2008 until October 26, 2011 in Figure 7.5a.

The measured positive gradients showed a strong seasonal trend, as was expected. Temperature data collected prior to September 19, 2009 was only sampled every six hours (midnight, 6:00 AM, noon, 6:00 PM), and thus the maximum measured gradients appeared to be smaller during this time frame. Temperature data collected after September 19, 2009 was sampled hourly. It was observed that the daily maximum gradients often occurred around 2:00 PM to 3:00 PM (equivalently 3:00 PM to 4:00 PM during Central Daylight Savings Time). The measured gradient magnitudes exceeded the AASHTO LRFD magnitude regularly during the summers, and occasionally approached the Priestley-Z2 levels.

Negative gradient magnitudes were calculated in the same manner as positive gradients, but the warmest temperature at the centerlines of the webs was considered instead of the coldest. Design negative gradients, including the Priestley-Z2 curve for which no negative design gradient was specified, were considered by scaling the positive gradients by -0.3 per AASHTO LRFD (2010) specifications. Again, the design magnitudes were considered at a depth of 2 in. (51 mm) below the deck surface for comparison with measured negative gradients, as shown in Figure 7.5b.

The seasonal dependence of the negative gradient magnitudes was not as pronounced as that observed for the positive gradients, but the overall maximum negative gradients tended to occur during the winter months. Maximum daily negative gradient most often occurred between 5:00 AM and 8:00 AM. The measured negative gradient magnitudes often exceeded both the AASHTO LRFD and the Priestley-Z2 interpolated magnitudes.

Regarding thermal gradients through the thickness of the webs, the measured temperature differences in the webs were extrapolated out to the web surfaces to estimate nominal web gradient magnitudes. Assuming a linear temperature distribution from the outer edge to the web to the centerline, the measured temperature differences between any two web thermistors of 3.0°F (1.7°C) might indicate a reasonable thermal difference of approximately 4.2°F (2.3°C) between outer surface and centerline of the webs (positive meaning that the outer surface was warmer than the centerline). Measurements where the outer surface was observed to be cooler than the centerline were exceedingly rare, and no negative web gradient value can be recommended. Assuming a separate linear temperature distribution from the inner edge of the web to the centerline, measured temperature differences would indicate reasonable web thermal differences of -4.2°F (-2.3°C) and 2.8°F (1.6°C) between the centerline and inner surface (negative meaning that the inner surface was warmer than the centerline). A positive value has been suggested in addition to the negative value because the inner surface was not always warmer than the centerline, though warmer inner surfaces were more common.

7.1.3.2 Comparison of Gradient Shapes

The five maximum measured positive gradients are plotted in Figure 7.6. Weather conditions taken from the Minneapolis-St. Paul Airport (approximately 7 miles (11 km) from the bridge) during the days of maximum measured positive gradients are presented in Table 7.1. The measured gradients were compared to the AASHTO LRFD (2010) design gradient for Zone 2, the Priestley-Z2 curve, and the Priestley linear gradient for decks above enclosed air cells assuming no blacktop and with top temperature equal to 46°F (25.6°C) according to AASHTO LRFD Zone 2. In all cases, the measured gradients were better approximated by the Priestley-Z2 curve than the AASHTO LRFD gradient. The Priestley linear gradient above the enclosed box was a poor fit at the centerline of the boxes. In fact, the gradients at the centerline of the boxes were not largely different from those measured along the webs. Gradient tails in the bottom flange ranged from 0.9 to 2.7°F (0.5 to 1.5°C).

The five maximum measured negative gradients are plotted in Figure 7.7 with corresponding weather conditions taken from the Minneapolis-St. Paul Airport presented in Table 7.2. The measured gradients were compared to the AAHTO LRFD (2010) design negative gradient assuming no blacktop, the Priestley-Z2 curve scaled by -0.3 to remain consistent with the AASHTO LRFD top surface gradient temperature, and the Priestley linear gradient for decks above enclosed air cells as used for positive gradient comparison but scaled by -0.3. The measured negative gradients were noted to be much more diverse in shape than the positive gradients, and were not consistently matched in shape by either design gradient. However, the Priestley-Z2 scaled by -0.3 appeared to produce reasonable negative gradient estimates in the top flange. Again, gradients at the centerline of the boxes were not largely different from those measured along the webs.

To investigate the development of thermal gradients throughout the day, hourly temperatures through the depth of Location 7 were plotted over the course of a single day. These hourly temperatures for July 1, 2011, during which the maximum positive gradient was measured at 3:00 PM, are shown in Figure 7.8. Similar trends were observed during other days with large positive thermal gradients, but the details of the 24-hour development of the temperature profile varied for each day depending on ambient weather conditions and the temperature distribution left in the bridge from the previous day. During all days with large positive gradients, the positive gradients were observed during the afternoon until approximately 5:00 PM to 7:00 PM, at which time the temperature from the topmost thermistor rapidly dropped below that from the second thermistor. After this point, negative gradients began to develop for the next day. Large thermal gradients with magnitudes near the daily peak gradient were regularly observed in the hours immediately before and after the time of the peak gradient.

Hourly temperatures for January 21, 2011, during which the maximum negative gradient was measured at 6:00 AM, are shown in Figure 7.9. Again, similar trends were observed during other days with large negative thermal gradients, but the details of the development of the temperature profile varied strongly depending on the temperature distribution left in the bridge from the previous day. Large negative gradients with magnitudes near the peak daily negative gradient were observed for several hours before and at least one hour after the time of the peak gradient.

Only Location 7 was instrumented in a manner to investigate gradient shapes, but the consistency of thermal gradient magnitudes along the length of the structure was examined by considering the temperature difference between top and bottom flange vibrating wire strain gages at each instrumented section. Regardless of section geometry, the nominal locations of the top flange strain gages were consistently 5.5 in. (140 mm) below the deck top surface and bottom flange gages were 3.0 in. (76 mm) above the bottom fiber. Measured temperatures in the top and bottom flanges along the length of the southbound superstructure corresponding to the maximum measured positive gradient on July 1, 2011 at 3:00 PM are presented in Figure 7.10. It was noted that the top surface temperature was nearly uniform

along the length of the bridge, but the bottom flange temperature dropped significantly near the piers. This was presumed to be caused by the large thermal mass of the pier diaphragms, the increase in thickness of the bottom flange, and possibly the additional shade and cover provided by the decorative fins at the tops of the piers. The top flange temperatures reinforce the idea of consistent thermal gradients along the length of the structure caused by solar radiation, whereas the bottom temperatures indicate the complexities of the heat transfer problem given varying geometry and thermal boundary conditions. Top and bottom flange temperatures during other positive and negative gradients on both southbound and northbound structures showed similar trends.

7.1.4 Finite Element Modeling

For thermal investigations, it was assumed that because thermal gradients could be reasonably approximated as one-dimensional (that is, temperature varied only with depth from the top surface), then a two-dimensional finite element model could accurately predict the structural response. The two-dimensional finite element model is documented in Section 4.2.

Despite changing sectional properties along the length, and especially the great increase in thermal mass at the diaphragms, the gradient shape was assumed constant along the length of the structure. This assumption was consistent with the application of design gradients, but could not be verified in more detail as only Location 7 was instrumented for investigation of thermal gradient shapes. Thermal gradients through the thickness of the webs were ignored, and the "tail" gradient in the bottom flange, found to be less than 2.7°F (1.5°C) for the maximum measured positive gradients as noted in Section 7.1.3.2, was assumed to be negligible (i.e., T3 as shown in Figure 7.1 for the AASHTO LRFD gradient was set equal to zero for simplification).

7.1.5 Validation of Model with Respect to Measured Thermal Gradients

The global behavior of the two-dimensional finite element model was compared to the measured behavior of the bridge under the maximum measured positive thermal gradients as described in Table 7.1 and Figure 7.6. In order to isolate the measured behavior due to the thermal gradient, initial strain readings were selected within a short time interval (less than two months) from the gradient readings to minimize time-dependent creep and shrinkage strains. Initial readings were chosen when the temperature distribution through Location 7 was approximately uniform, and the web temperatures were nearly unchanged between the initial and gradient measurements. It should be noted that due to continual changes in ambient temperature and weather conditions, a perfectly uniform temperature through the section, especially in the top flange, was never realized. Thermal gradients were input into the model by fitting the change in measured gradients (gradient measurement minus initial readings through the depth) with a curve of the form

$$T_{grad}(y) = T_0\left(\frac{y}{47.2}\right)^n, \; y \text{ in inches} \qquad (7\text{-}2)$$

where the values of T_0 and n were chosen to minimize the sum of squares error between modeled and measured thermal gradients. Using Eqn. (7-2), temperatures were specified at each node of the model. Temperatures within each element were computed according to the isoparametric mapping of the quadratic shell elements.

Because the temperature distribution was unknown between the top surface down to the top thermistor 2 in. (51 mm) below the top surface, three variations of the fitted thermal gradient were tested in the finite element model. The baseline fitted gradient used Eqn. (7-2) for the entire cross section. Table 7.3 summarizes the dates and times used for the initial strain readings (i.e., times with approximately uniform temperature) for each maximum measured positive gradient and the fitting parameters T_0 and n required

for Eqn. (7-2) for the baseline fitted gradient. The temperature profiles through the depth of the west web of the exterior box at Location 7 in the southbound structure both at the time of the maximum measured positive gradient and the associated initial (uniform temperature) strain reading are shown in Figure 7.11. The change in the temperature profile at the same location as used for Figure 7.11 between the initial and maximum gradient readings, along with the fitted baseline gradient using Eqn. (7-2), are presented in Figure 7.12. For the two modified gradients, the temperature distribution throughout most of the section was identical to the fitted baseline gradient, and only the gradient in the top 2 in. (51 mm) was changed. For the lower bound estimate, the top surface temperature extrapolated from the best fit curve was decreased by 20%, with a linear temperature distribution between the decreased top surface temperature and the fitted temperature at depth 2 in. (51 mm). Likewise for the upper bound estimate, the top surface temperature extrapolated from the best fit curve was increased by 20%, with a linear temperature distribution between the increased top surface temperature and the fitted temperature at depth 2 in. (51 mm). The area and moment of the area under a bottom flange tail gradient of 2.7°F (1.5°C) were of similar order of magnitude to those associated with the changes in gradient due to the upper- and lower-bound estimates for the top surface temperature, and thus the assumption to not model the tail gradient was validated.

In situ changes in stress were approximated by multiplying the measured change in mechanical strains by the elastic modulus of the concrete (equal to that used for the finite element model, but not corrected according to the mild steel reinforcement ratio). The change in mechanical strain $\Delta\varepsilon_m$, sometimes called load-related strain, does not include strains due to unrestrained thermal expansion, creep and shrinkage as follows:

$$\Delta\varepsilon_m = \Delta\varepsilon - \alpha_{conc} \cdot \Delta T - \Delta\varepsilon_{cr} - \Delta\varepsilon_{sh} \qquad (7\text{-}3)$$

where $\Delta\varepsilon$ is the change in measured total strain, ΔT is the change in temperature, α_{conc} is the coefficient of thermal expansion of the concrete, and $\Delta\varepsilon_{cr}$ and $\Delta\varepsilon_{sh}$ are the change in creep and shrinkage strains over the same time period, respectively. Because the initial readings were chosen to minimize the time-dependent strains, $\Delta\varepsilon_{cr}$ and $\Delta\varepsilon_{sh}$ were assumed to be zero.

Experimentally derived stresses had variations up to 280 psi (2.0 MPa) across the width of the deck for the same gradient. Contrary to the results from Davis et al. (1999), Roberts et al. (1993), and Thompson et al. (1998), stresses above the webs were not necessarily higher than those away from the webs. The observed stress variations might be attributed to errors in the positions of the gage, variations in deck thickness, or cross-sectional issues such as shear lag, and do not necessarily refute or confirm the conclusions from the mentioned studies. Large variations such as these were not unexpected, as stresses in the top flange would vary rapidly with depth in sync with the quickly decreasing temperature distribution though the top flange; thus, small positional errors in gage location were likely to propagate as large errors in the derived stress estimates.

The changes in experimentally derived longitudinal stresses at each of the three instrumented depths were averaged over all gages across the width of the cross section for each of the five maximum measured positive gradients and compared to the computed values of stress from the finite element model (FEM) using the three variations of the fitted gradients as documented above. These comparisons using the baseline fitted gradients for Location 7 of the southbound bridge are presented in Figure 7.13. It was found that the measured and modeled results corresponded well. The FEM results were found to be insensitive to variations in the precise top surface temperature; the upper and lower bound modifications to the input gradient altered the FEM stresses by approximately 2% at all instrumented depths (results not shown).

Measured curvatures were computed by considering the short-term changes in total strains averaged at each of the instrumented depths through the section, and then computing the slope of the least-squares

best fit line of the averaged strains through the section depth. The short-term change in total strain was equal to the change in mechanical strain from Eqn. (7-3) plus the thermal strain equal to $\alpha_{conc}\Delta T$. Measured curvatures along the length of the southbound structure due to the maximum measured positive gradients were compared to FEM-computed curvatures using the three variations of the fitted gradients. These comparisons for the baseline fitted gradients are presented in Figure 7.14. At Location 7 and near Piers 2 and 3, the measured curvatures were typically higher than those predicted by the FEM for all considered gradients, but results at other locations were predicted well by the model. Overall, it was believed that the model reasonably captured the behavior of the physical structure. Similar to the stress results, the FEM curvature results were found to be insensitive to variations of the temperature distribution in the top 2 in. (51 mm) (results not shown).

The presented results do not include the "tail" gradient in the bottom flange. However, it was found that the global FEM behavior was insensitive to the inclusion of a 2.7°F (1.5°C) tail gradient as was typical of the maximum positive gradients shown in Figure 7.6. Changes in the FEM behavior due to the inclusion of the gradient tail were of similar magnitude to changes associated with the upper and lower bound modifications to the top surface temperature as described above. It would be expected that this tail gradient would have a larger impact on the local deformations of the box cross section than on the global response, but this was not investigated for this study with the two-dimensional model.

7.2 Long-Term Thermal Behavior

Long-term thermal behavior and uniform temperature changes in the structure were investigated using the linear potentiometer (LP) data from the expansion joints and from the vibrating wire strain gage (VWSG) data.

7.2.1 Linear Potentiometer Data

Linear potentiometer data was collected since October 31, 2008. Plots of the first three years of data are presented in Figures 7.15 through 7.17. Measurements were zeroed on October 1, 2010. Temperatures were taken from gage TSEWB002 located 81 in. (2.1 m) below the top deck surface in the west (exterior) web of the exterior box of the southbound bridge at Location 7, considered as representative of the uniform temperature for the structure (that is, the temperature in absence of any thermal gradient temperatures, as this gage would not undergo significant changes in temperature from the thermal gradient through the depth of the section or the tail gradient in the bottom flange). Breaks in the data occurred when the system suffered from temporary electrical failures. The two LPs attached to the northbound bridge at Abutment 1 were replaced on September 21, 2010, and the two LPs attached to Span 4 of the southbound bridge at Pier 4 were replaced September 30, 2010. It was not possible to capture new zeroes for the replaced sensors, but LPs measure absolute distances and the new sensors were mounted in the same manner and on the same concrete embedded bolts as the original sensors. In the presented plots, it was assumed that the zero used prior to replacement was still valid to the tolerances of the instrumentation, or approximately 0.05 in. (1 mm). This assumption was not verifiable, and therefore investigations using data both before and after sensor replacement should only be made with particular discretion.

Figure 7.15 presents the LP measurements from the northbound and southbound structures at the expansion joint located at Abutment 1. The behavior of both structures was nearly identical, and trended consistently with temperature. Figure 7.16 presents the LP measurements from the northbound and southbound structures at the expansion joint located at Pier 4 for the sensors attached to Span 3. These LPs measured the differential longitudinal displacement between the superstructure and Pier 4, and as noted in Section 3.4, included both the expansion of the continuous Spans 1 through 3 and the deflection of the top of Pier 4 due to the expansion of Span 4. Again, the behavior monitored from both structures

was nearly identical, and trended consistently with temperature. Figure 7.17 presents the LP measurements from the northbound and southbound structures at the expansion joint located at Pier 4 for the sensors attached to Span 4. Because Span 4 was effectively pinned to the top of Pier 4, very little differential movement was expected between the Span 4 superstructure and the pier. This was found to be the case, with total changes in LP readings of approximately 0.2 in. (5 mm), which would be expected simply from rotation of the superstructure about the bearing.

The total elongation of the three continuous spans for the northbound and southbound structures was approximated by taking the average measured elongation between both boxes at Span 1, plus the average measured elongation between both boxes at Span 3 connected to Pier 4, and subtracting the assumed longitudinal deflection of Span 4. The assumed longitudinal deflection of Pier 4 was calculated as the experimentally measured coefficient of thermal expansion for the superstructure concrete (equal to 5.6 με/°F (10.1 με/°C) per Section 3.4) multiplied by the length of Span 4 (1743 in. (44.3 m)) and the temperature taken from gage TSEWB002 as noted above. This approximate measured elongation was compared to the computed elongation of Spans 1 through 3 assuming no time-dependent effects or thermal gradients, and equal to the experimentally measured coefficient of thermal expansion for the superstructure concrete (5.6 με/°F (10.1 με/°C)) multiplied by the length of Spans 1 through 3 (12780 in. (324.6 m) for the southbound bridge, and 12870 in. (326.9 m) for the northbound bridge) and the temperature taken from gage TSEWB002 as noted above. The total elongation approximated from measured data (named "measured" in the plots) compared to the theoretical elongation assuming only longitudinal expansion from uniform temperatures (named "computed" in the plots) are shown in Figure 7.18 for the northbound bridge and Figure 7.19 for the southbound bridge. Both "measured" and "computed" approximations were zeroed at October 1, 2010. Gaps in the data represent times when both LPs from at least one of the ends of the bridge were not operating; this typically occurred during dynamic system failures. Differences between the "measured" and "computed" approximations are presented in Figure 7.20. A clear long-term drift in the errors was present, and was consistent with the creep and shrinkage strains (which were not included in either approximation). The long-term expansion errors appeared to be stepped every year, which likely reflected seasonal thermal gradient and relative humidity trends. Daily variations were likely due to thermal gradient effects, and due to the fact that the temperature at gage TSEWB002 did not characterize the total uniform expansion of the bridge, as axial elongation would be associated with the gradient temperatures as well. Furthermore, the estimations did not take into account rotation of the boundary conditions, which would occur under both thermal gradients and uniform thermal expansion (due to the continuity of the system). From finite element model results applying the maximum positive thermal gradient measured on June 6, 2011 and a 75°F (41.7°C) uniform temperature increase, rotation of the superstructure at Abutment 1 was found to increase the measured LP extension by 0.04 in. (1 mm), and rotation of the superstructure at Pier 4 plus the rotation of the top of the pier were found to increase the measured LP extension by 0.15 in. (3.8 mm).

7.2.2 Vibrating Wire Strain Gage Data from Superstructure

Mechanical plus creep and shrinkage strains were computed for the vibrating wire strain gage data in the northbound and southbound bridges, where the mechanical strain was defined in Eqn. (7-3). Typical top and bottom flanges gages were chosen for investigation of the long-term longitudinal behavior of the structure. Figures 7.21 through 7.28 depict the measured strains for southbound Locations 3, 4, 5, 7, 8, 9, 14 and 15. Figures 7.29 through 7.35 depict the measured strains for northbound locations 3, 5, 7, 8, 9, 14, and 15. Plotted temperatures, assumed to be representative of the uniform temperature for the structure, were taken from thermistor TSEWB002 (located 81 in. (2.1 m) below the top deck surface in the west web (exterior) of the exterior box of the southbound bridge at Location 7) for plots of gages from the southbound bridge and thermistor TNEEA002 (located 81 in. (2.1 m) below the top deck surface in the east (exterior) web of the exterior box of the northbound bridge at Location 7) for plots of gages from the northbound bridge. Strains were zeroed at the beginning of September 21, 2008.

At Location 7 of both structures, daily mechanical strain variations were often on the order of 100 με. Seasonal variations were just as significant. Bottom flange creep and shrinkage strains at Location 7 were estimated to be around 200 με over the course of the first three years of monitoring, and top flange creep and shrinkage strains were noted to be considerably less, indicating that the structure continued to camber upwards after erection. For most other locations, bottom flange mechanical strain seasonal and daily variations were much lower than those measured at Location 7. Maximum longitudinal strains from the static truck tests were on the order of 55 με, meaning that the daily and seasonal mechanical strain variations were more significant that those induced by nearly 400 kips (1780 kN) of static gravity truck loading.

Figure 7.36 shows the long-term mechanical plus creep and shrinkage strains for the vertical gages located in the east (interior) web of the exterior box of the southbound bridge. Daily mechanical strains due to thermal effects were on the order of approximately 20 με in the web gages, with seasonal mechanical strains typically less than 50 με. Time-dependent strains over the three years were minimal, approximately 50 με, as would be expected from the vertical gages with no vertical post-tensioning present. Maximum measured vertical strains during truck test STIVa7SB (i.e., the test that maximized bending of the webs) were 24 με, which was not substantially different from the daily thermal variations.

Figures 7.37 and 7.38 show the long-term mechanical plus creep and shrinkage strains for the transverse gages located in the top flange and bottom flange, respectively, of the southbound bridge. In the top flange, daily mechanical strains due to thermal effects were typically on the order of 50 με, which was expected due to the rapidly varying temperature with depth observed in the top flange. In the bottom flange, daily thermal variations were on the order of 10 to 15 με. Seasonal thermal variations were approximately 30 με in both the top and bottom flanges. Similar to the vertical gages, time-dependent strains in the transverse gages in both the top and bottom flanges were small, typically less than 50 με over the three years on monitoring. Maximum measured top flange transverse strains during the truck tests were approximately 12 με, which were substantially less than the measured mechanical strains due to daily thermal effects. However, maximum modeled (using the three-dimensional model) truck test top flange transverse strains were on the order of 50 με (located at the centerline of the bridge where no gages were present), which were of similar magnitude to the daily thermal variations. Maximum measured bottom flange transverse strains during the truck tests were approximately 16 με, which were also of similar magnitude to the observed mechanical strains due to daily thermal variations.

None of the superstructure vibrating wire strain gages, including those not plotted in Figures 7.21 through 7.38, showed any clear indications of cracking or other damage.

7.2.3 Vibrating Wire Strain Gage Data from Pier

As discussed in Section 2.2.6.3, a variety of issues during installation and setup resulted in a number of pier gages being effectively lost. In the interior (east) column of the southbound bridge, only three vibrating wire strain gages provided usable data:

1. VW_GK(32) SN 28072 NW corner Interior (east) Pier Midheight
2. VW_GK(43) SN 28060 SW corner Interior (east) Pier Midheight
3. VW_GK(44) SN UofMN4 NW corner Interior (east) Pier Lower height

In the exterior (west) column, four gages provided usable data:

1. VW_GK(36) SN 28073 NE corner Exterior (west) Pier Midheight
2. VW_GK(40) SN 1992 SW corner Exterior (west) Pier Midheight
3. VW_GK(42) SN 1989 SE corner Exterior (west) Pier Midheight
4. VW_GK(38) SN UofMN6 NE corner Exterior (west) Pier Lower height

The remaining gages were either never connected in the instrumentation vault, had unlabeled wires and thus could not be traced to any specific gage, provided null data implying that the gage was damaged, or provided wildly varying and presumably nonphysical data.

Changes in total strains, including time-dependent, load-related, and thermal strains, at midheight of both columns of Pier 2 are plotted with time from March 26, 2009 (when collection of the pier VWSGs was first implemented in the static system) until February 17, 2012 in Figure 7.39. Strains were plotted relative to readings taken at 2:19 PM on March 26, 2009, and the plotted strains do not imply the absolute strain values in the piers. The interior and exterior piers were noted to behave in effectively the same fashion. The north side of the piers showed much larger annual fluctuations than the south side, which can be explained by the deformation of the superstructure in addition to the axial expansion of the pier during seasonal temperature cycles. In the summer, the superstructure expands and Pier 2 is bent towards the south, causing tension (positive strain) on the north side and compression (negative strain) on the south side. Furthermore, the pier expands axially due to the increase in temperature, which adds equal positive strain to both north and south sides. The situation is obviously reversed during the winter months. Therefore, the strains due to pier bending and axial expansion were additive on the north face, and in opposite directions on the south face.

Curvatures were computed by taking the difference in total strain between the north and south faces divided by the distance between the two gages. A positive curvature was arbitrarily assigned such that the top of the pier was deflecting to the south, putting tension on the north face and compression on the south face. Curvatures measured at midheight of the interior and exterior columns of Southbound Pier 2 are plotted in Figure 7.40. The two piers were found to bend nearly identically, as was expected. The annual range of curvature was approximately 4.5 με/in. (177 με/m). Compared to finite element model results using the two-dimensional model (Section 4.2), a 1.8°F (1°C) uniform temperature change over the entire structure resulted in a Pier 2 midheight curvature of approximately 0.1 με/in. (3.9 με/m), meaning that the measured curvature range corresponded to a temperature range of approximately 81°F (45°C). This was nearly 20% less than the measured annual temperature range measured in the superstructure, equal to 99°F (54°C), suggesting that either the modeled piers were less stiff than the physical piers, or that boundary condition assumptions were incorrect. For example, if the base of the pier were modeled as a hinge instead of a perfectly fixed end as was done in the model, then the curvature of the pier at midheight would be equal to zero. Simulating a boundary condition between a hinged at fixed end would result in a midheight curvature less than 0.1 με/in. (3.9 με/m), and would correspond closer to measured data.

Data from the gages installed by the UMN below the midheight of the columns is presented in Figure 7.41. Only one UMN gage from each column was operational (northwest corner of interior column and northeast corner of exterior column), so it was not possible to investigate curvatures or overall deformations in greater detail. Notably, however, the data from the northeast corner of the exterior column appeared to show signs of cracking: the data varied substantially during the course of summer days, but remained consistent during the winter. The fact that the daily variations appear to be reducing in each consecutive years may imply that the crack (if one does exist) is closing due to time-dependent deformations.

7.2.4 Conclusions

Linear potentiometer data at the expansion joints was found to be highly correlated with the approximated uniform bridge temperature. The difference between estimates of the total expansion of the three continuous spans, the first estimate using measured LP data and the second using temperature data and assuming only axial expansion of the structure, showed that axial expansion due to the thermal gradients,

rotation of the boundary conditions, and time-dependent effects will need to be accounted for in order to better predict the structural expansion.

Mechanical plus creep and shrinkage strains from the superstructure showed strong seasonal and daily data trends with magnitudes, for the longitudinal gages, larger than those observed during the truck tests. Continually increasing bridge deformation can be observed in the long-term data. Bottom flange creep and shrinkage strains at Location 7 were observed to be larger than the top flange time-dependent strains, indicating that the structure has continued to camber upwards. Variations of the transverse and vertical vibrating wire strain gages due to thermal and time-dependent effects were considerably less than seen in the longitudinal gages.

Chapter 8. Dynamic Modal Analysis

Dynamic modal data was characterized for the St. Anthony Falls Bridge using the installed accelerometers (refer to Chapter 2 for discussion of the instrumentation). For the analysis documented in this chapter, the two horizontally oriented accelerometers, as noted in the long-term accelerometer configuration shown in Figure 2.46, were not used. For consistency, these two accelerometers, although in different positions, were also removed from the analysis for dates using the first long-term configuration from Figure 2.45.

It is expected that dynamic modal analysis will be a useful tool for continued monitoring of the structure. Changes in measured modal properties may potentially be used to indicate some loss of stiffness or deterioration of the structure.

8.1 Modal Data from Ambient Excitations

8.1.1 Data Selection

Five days of ambient acceleration readings were considered for analysis. These days were selected to capture a representative range of thermal conditions throughout the year. These records, along with the approximate structural temperatures during each day, are summarized in Table 8.1. For each day of ambient traffic, the first 80,400 seconds (22.33 hours) of data was broken into 200 segments of 800 seconds each with 50% overlap between segments.

Dynamic properties of the structure were extracted independently for the northbound and southbound structures for each 800-second segment. In order to focus only on vertical motion in the southbound bridge, only the vertically oriented accelerometers were included in the analyses. For the northbound bridge data, all six accelerometers were used simultaneously.

8.1.2 Data Preprocessing

As described in Section 2.4.5, the raw data was collected at a rate of 1000 Hz and decimated by a factor of 10 to 100 Hz using a Kaiser Window lowpass anti-aliasing filter with a half-amplitude (6 dB down) frequency of 23 Hz. For the analysis conducted, the data was further decimated down to 50 Hz. Accompanying this second decimation, the data was passed through a lowpass, eighth-order Butterworth filter with cutoff frequency at 17 Hz. The data was also passed through a highpass, eighth-order Butterworth filter with cutoff frequency of 0.3 Hz to remove the low frequency (DC) acceleration component.

8.1.3 Analysis Methodology

Dynamic properties were extracted from each 800-second segment using the Natural Excitation Technique (NExT) and the eigensystem realization algorithm with data correlations (ERA/DC). The NExT methodology was introduced by James, et al. (1993) in order to analyze a system's dynamic behavior using only immeasurable ambient forcing. The core of the technique involves formulating the auto- and cross-correlation functions from time history data, and then performing a time-domain modal identification routine as if the correlation functions were the free vibration responses of the system.

The ERA/DC was used as the modal identification method within the NExT framework. The eigensystem realization algorithm (ERA) was proposed by Juang and Pappa (1985). The goal of the ERA was to construct the matrices for the state space problem using only the free response data. Their method

involved using the singular value decomposition of the generalized Hankel matrix constructed from the free response data. For structures under ambient excitation, the free response data is generally not available, but by the NExT procedure, the generalized Hankel matrix can instead be formulated from the correlation functions. The ERA was modified to the ERA/DC by Juang et al. (1988) to reduce bias errors due to noise and to reduce the need for model over-specification. A block correlation matrix is constructed from the generalized Hankel matrices defined in the ERA method. The methodology then continues much like the ERA, except that the singular value decomposition is performed on the block correlation matrix instead of the generalized Hankel matrix. A comparative study by Nayeri, et al. (2009) showed that the ERA and ERA/DC both yielded comparable dynamic results, but the ERA/DC required less modal over-specification in the presence of noise and was computationally faster. Therefore, only the ERA/DC was used for the analyses herein.

The NExT procedure requires that a set of degrees of freedom (i.e., output channels) be specified as the references for the calculation of the correlation functions. The selection of reference channels must consider that any mode for which all the reference channel instruments lie at nodal points cannot be captured by the modal identification procedure. For the northbound structure, all six accelerometers used for analysis were included in the reference channels. However, for the southbound bridge, only the six permanently fixed accelerometers were assigned as reference channels. Additional reference channels might aid in the identification of higher modes with nodal points at each of the permanently fixed accelerometers, but at increasing computational cost. However, higher modes are more difficult to capture consistently regardless of reference configuration due to typically lower signal-to-noise ratio in higher frequencies, and thus using the six permanent accelerometers as reference channels was deemed sufficient.

The model order, equal to twice the number of modes to be extracted, must be prespecified for each run of the ERA or ERA/DC. In general, the number of structural modes that can be accurately extracted is unknown a priori, and therefore the model order must be either assumed or approximated by observation of the data's power spectral density functions or the singular values of the Hankel matrix. The number of extracted modes was varied from 20 to 25 for each 800-second data segment, meaning that the model order was varied from 40 to 50 by increments of 2. Structural modes were separated from noise modes by use of the consistent-mode indicator (CMI). The CMI, proposed by Pappa and Elliott (1993), quantifies the temporal consistency of the identified modes, and varies from 0 to 1, with 1 being a perfectly consistent mode, and 0 being a purely random noise mode. It was assumed that any mode with a CMI greater than 0.7 was a structural mode; all other modes were discarded. In the variation from 20 to 25 extracted modes, duplicate structural modes were inevitably captured (for example, the fundamental mode was likely captured in all iterations). Of the duplicate modes, it was assumed that the output with the highest CMI best represented the structural mode. Thus, for each 800-second data segment, only the most consistent modes were output.

8.1.4 Measured Modal Properties

Summaries of the average modal frequencies extracted from each day of ambient data using the NExT-ERA/DC procedure are presented in Tables 8.2 and 8.3 for the southbound and northbound structures, respectively. The extracted mode shapes associated with each frequency for the southbound and northbound structures are presented in Figures 8.1 through 8.4. The plotted mode shapes represent the mean shapes measured over all 200 data blocks on October 26, 2010. Error bars represent plus or minus one standard deviation in the measured mode shape at each individual accelerometer over the entire day of ambient data. A total of 15 structural modes were captured on the southbound structure, of which 12 modes were captured on all five days. Likewise, 12 modes were captured from the northbound structure, of which 10 were captured on all five days. Generally, modes with frequencies exceeding 6 Hz (above Mode 12) were either inconsistently captured or not detectable at all. Modes 10 and 14, representing

opposed twisting of the two box girders, could not be captured on the northbound structure due to the lack of instrumentation along the webs.

Some difficulties arose in classification of Modes 5 and 6 for the southbound structure. The mode shape associated with Mode 5 was inconsistently captured throughout Spans 2 and 3 of the southbound structure. Examples of the variability of this mode shape from February 1, 2010 and October 26, 2010 are shown in Figure 8.5. For many instances of Mode 5, the excitation in Span 2 appeared to be negligible, and occasionally switched phase with respect to excitations in Span 1. It was discovered that multiple mode shapes were all classified as Mode 6 under the clustering procedure, and manual separation of these modes revealed that three distinct mode shapes were present. Modes 6-1, 6-2, and 6-3 represent the distinct modes all classified as Mode 6 by clustering. Each mode shape had similar shapes over Spans 2 and 3, but divergent responses in Span 1. Modes 6-1 and 6-2 represented torsion mode shapes of Span 1. Mode 6-3 was a bending mode, and typically had a slightly higher average frequency than Modes 6-1 and 6-2. It is likely that Modes 6-1 and 6-2 consisted of misclassifications of Mode 5, or were combinations between the Mode 5 and Mode 6-3 shapes that were unsuccessfully separated by the NExT-ERA/DC procedure. These classification issues with Modes 5 and 6 were not encountered in the data taken from the northbound structure, and of the three modes encapsulated in SB: Mode 6, only the equivalent of Mode 6-3 was found in the northbound data. This was likely related to the reduced quantity of accelerometers used in the classification of the northbound structure. Frequency and damping ratio statistics (mean and coefficient of variation) for October 26, 2010 are summarized in Table 8.4. Damping ratio estimates were found to have a considerably higher scatter than corresponding frequency estimates. The coefficient of variation for frequency estimates throughout the day was typically less than 1%, and never exceeding 3%.

The scatter of the first four estimated modes from each day of ambient data is presented in Figures 8.6 and 8.7 for the southbound and northbound structures, respectively. Histogram plots broken into bins of size 0.0025 Hz depict the variability of the modal frequencies. Compared to Modes 1, 2 and 4, Mode 3 appeared to have the most variability for both the southbound and northbound structure. With the exception of Mode 3, the modal frequencies consistently increased as the ambient temperature decreased. From investigation of the damping ratio against frequency plots, it appeared that damping ratio estimates were not meaningfully altered by changes in ambient temperature. Within the legend on the right, the number in parentheses denotes the number of data blocks in which the mode under question was successfully captured. These four modes were captured in a substantial majority of the analyzed data blocks.

8.1.5 Finite Element Modeling

The three-dimensional finite element method was used to model the southbound structure. Construction of the model is detailed in Section 4.1. The model was previously validated with static truck load testing, as discussed in Chapter 6. This same model was used to extract the frequencies of vibration and corresponding mode shapes. No model updating was performed between validation of the static behavior of the model and the investigation of its dynamic properties.

Due to the nature of the static truck tests, the previous validation of the model by static measurements was only able to investigate the stiffness of the structure, and not the mass. It was therefore assumed that the mass of the structure was entirely due to the density of the reinforced concrete (assumed at 150 lbs_{mass}/ft^3 (2400 kg/m^3)) and post-tensioning steel (assumed at 490 lbs_{mass}/ft^3 (7700 kg/m^3)). Other systems included in the bridge (e.g. electrical, deicing system) were assumed to provide negligible mass. Addition of mass and changes of stress from live loading, such as traffic or wind, were not considered in the analysis. Variation of temperature constitutes a complex process involving changes in structural stresses, material

properties, and effective boundary conditions, and was also not investigated with regard to the dynamic properties of the model.

In order to account for the dead load stress state in the eigenvalue extraction, the model was initially loaded by gravity and the amount of longitudinal and transverse post-tensioning at release as specified by Figg Bridge Engineers (2008). The eigenvalue extraction was carried out for all modes between 0.5 Hz and 10 Hz using the Lanczos method implemented in Abaqus (Dassault Systèmes, 2010).

8.1.6 Finite Element Modeling Results

The 34 modes extracted from the finite element model, of which 16 were matched with their measured mode equivalents, are summarized in Table 8.5. The modeled modes were assigned alphabetical names (A through AH) for purposes of comparison with the modes extracted using the NExT-ERA/DC. Measured mode shapes were given numerical values (i.e., 1 through 16). Modeled modal frequencies were consistently lower than the mean measured frequencies from the ambient data taken from October 26, 2010, but were always within 10% of the expected value. Measured mode shapes 1 through 4 (equivalently, modeled modes A, D, F and G) are presented in Figure 8.8 as extracted from the finite element model. A depiction of one of the opposed twisting modes, SB: Mode 10 (equivalently Mode N from the modeled results), is presented in Figure 8.9. For this and other opposed twisting modes, virtually all the deformation in the top flange took place between the two boxes, while the boxes themselves appeared to individually deform in pure torsion.

The estimated mean mode shapes extracted by the NExT-ERA/DC procedure from the ambient data taken from October 26, 2010, with the exception of Mode 15 for which the measured mode shape and recorded frequency were taken from Truck Test SS9 data (see Section 8.2 for modal analysis on dynamic truck test data), are compared to modeled mode shapes in Figures 8.10 through 8.13. Overall, the measured mode shapes compared well with the modeled mode shapes, with measured SB: Mode 5 and SB: Mode 6-1 being the exception. No equivalent FEM mode was found to match SB: Mode 6-3. It was unclear why measured Mode 16 appeared to have a shape offset from modeled Mode AF, though this was likely related to the fact that the finite element model was never validated for transverse motion, and Mode 16 contained both transverse bending and torsional behavior.

8.1.7 Modal Frequencies using Fast Fourier Transform

Modal frequencies were also extracted from the accelerometer data using a Fast Fourier Transform (FFT). Input averaging was applied to gain greater resolution in the frequencies in the 0 to 5 Hz range where the primary structural modal frequencies resided. The FFT was taken over 16384 points (approximately 27.3 minutes) and utilized Bartlett windowing. The time frame considered was assumed to be a representative sample of daily activity containing an arbitrary number of dynamic events. Figure 8.14 shows one such FFT taken for the permanent accelerometer located at the centerline of the exterior box at midspan of Span 2 in the southbound bridge (i.e., accelerometer SB SP 2 Ext). The plot shows three prominent modal frequencies at 0.8 Hz, 1.5 Hz, and 2.3 Hz. From the NExT/ERA-DC results, it can be surmised that 0.8 Hz corresponds to Mode 1, the primary bending mode, and that 1.5 Hz corresponds to Mode 2, the secondary bending mode. The mode located at 2.3 Hz was either Mode 3 or 4, the tertiary bending mode or the primary torsional mode.

Modal frequencies were calculated using the FFT method bimonthly to further explore variations in the dynamic response. Figure 8.15 plots the three prominent modal frequencies and the temperature variations over an eight-month period from November of 2008 to the end of June of 2009. Figure 8.16 shows the normalized modal frequencies (normalized with respect to the frequencies measured November 2008) plotted against the temperatures for the same period. The modal frequencies all display a nearly

linear correlation to temperature changes. Normalized modal frequencies for the first and second modes decreased at approximately the same rate with respect to temperature, while the normalized third mode decreased at a lesser rate. From this, it was assumed that the third mode from the FFT data corresponded to the primary torsional mode, due to its differing dependence on temperature as compared to the first two extracted modes.

8.1.8 Conclusions

Extracted mode shapes from ambient traffic data using the NExT-ERA/DC method matched well with finite element results. Modeled frequencies were typically lower than those estimated from the ambient data. However, the model was not specifically validated for dynamic results, particularly the density of the materials included in the model, and thus the minor deviation of approximately 10% was considered acceptable. Model updating procedures could be simply employed to adjust the stiffness and mass parameters of the model to more exactly fit the measured data if desired.

The NExT-ERA/DC methodology has been shown to consistently obtain modes with frequencies up to 6 Hz using the long-term accelerometer setup in the I-35W Bridge. Also, the ability to separate out modes with similar frequencies but differing mode shapes (as evinced by Modes 3 and 4 both with frequencies around 2.3 Hz) allows this method to provide much more dynamic system information than could be obtained by a simple Fast Fourier Transform.

Modal frequencies showed a definite trend with temperature. As the temperature increased, the modal frequencies consistently decreased. This phenomenon was observed for both the modes extracted using the NExT-ERA/DC methodology and a Fast Fourier Transform. Damping ratios and mode shapes extracted from the NExT/ERA-DC did not appear to show any temperature dependence.

8.2 Modal Data from Truck Tests

8.2.1 Modal Analysis and Results

The NExT-ERA/DC method (as described in Section 8.1.3) was applied to the accelerometer data collected from the dynamic truck tests conducted on the I-35W Bridge during the nights of October 27 and 28, 2010 (refer to Section 5.3.3). These tests are documented in Tables 5.10 and 5.11. As noted in Section 5.2.3, it was found that the dynamic truck test data gathered during the September 2008 tests were unusable for analysis due to the low signal-to-noise ratios (which were resolved shortly after by changing the analog filtering at the sensors).

The first examined test was Closed SS9. This test represented a single wave of eight trucks positioned in four lines of two trucks placed in Lanes 3 and 4 (lane numbers shown in Figure 5.9). The trucks travelled across the southbound bridge from north to south at 55 mph (88 km/hour), and lines were spaced as close as the truck drivers felt comfortable.

Figure 8.17 shows a plot of the data obtained from the accelerometer located at the centerline of the exterior box at midspan of Span 2 of the southbound bridge. The mean acceleration of the record was subtracted from the data to remove the DC acceleration, but no other filtering was performed. Peak accelerations were approximately 0.008 g for Closed SS9, which was of similar magnitude to maximums generated by large events in the ambient data (typically ranging from 0.006 g to 0.010 g). This record is typical for other vertically oriented accelerometers in the bridge.

The NExT-ERA/DC method was applied to extract the modal properties of the structure. Five accelerometers in the exterior box were chosen as the reference channels for the NExT: Acc 2 at station

220+96.90, Acc 3 at station 221+33.90, Acc 4 at station 221+70.90, SB 1 Ext at station 217+04.58 (Location 3), and SB 3 Ext at station 225+53.17 (Location 9). This set of reference channels differed from that used for the ambient data to investigate the effects of the reference selection process, and to minimize the number of modes that would have nodal points at each of the reference channels. The ERA/DC was attempted for a number of modes ranging from 10 to 60. The data (originally collected at 100 Hz) was decimated by a factor of 5 to 20 Hz to facilitate faster computation. It was found that this did not adversely affect the ability of the algorithm to extract modes with frequencies of interest (typically below 6 Hz).

The aggregated modes from dynamic truck test Closed SS9 are presented in Table 8.6. A total of 12 modes were captured by the analysis (although upon inspection of the mode shapes, it was believed that two of the modes were an erroneous sorting from the ERA/DC procedure). Modes were given numbers corresponding to those assigned during the ambient modal analysis (refer to Table 8.2 for frequencies and Figures 8.1 through 8.4 for mode shapes). Mode shapes obtained from the truck test were similar to those obtained from the ambient excitations, presented in Figures 8.1 through 8.4, and are not presented here.

The NExT-ERA/DC method was also applied to wave 8 of dynamic truck test Closed SS10. This test represents a single truck travelling south across the southbound structure at 55 mph (88 km/hour) in lane 2. The bridge was closed to all other traffic. This test was performed to examine how the NExT and ERA/DC method behaved with minimal excitation (e.g., high-noise data). Figure 8.18 shows a plot of the accelerometer data located at the centerline of the exterior box at midspan of Span 2 of the southbound bridge. The mean acceleration of the record was subtracted from the data, but no other filtering was performed. Peak accelerations were approximately 0.006 g, which was of slightly lower magnitude compared to typical maximums generated by large events in the ambient data. This record is typical for other vertically oriented accelerometers in the bridge.

The ERA/DC analysis was performed using the same constants, reference nodes, decimation factor, and methods as described for test Closed SS9. The aggregated modes from dynamic truck test Closed SS10, Wave 8 are presented in Table 8.7. A total of 6 modes were captured by the analysis. Overall, the modal frequencies and mode shapes compared favorably with those measured from truck test Closed SS9. Some of the modes from Closed SS9 with lower excitation and higher frequencies were either not captured by the ERA/DC procedure, or were simply not excited by the different dynamic load configuration of Closed SS10, Wave 8.

Finally, the NExT-ERA/DC methods were applied to open bridge dynamic truck test Open S4, Wave 2. This test included four trucks travelling south at 55 mph (88 km/hour) across the southbound bridge in two lines of two trucks placed in Lanes 3 and 4. Each line of trucks was spaced as closely as was practicable. The bridge was open to live traffic at the time of the test. Small commercial vehicles and cars were present on the bridge during the entire duration of the test, and four semi-trailers entered the bridge within 30 seconds after the truck block entered. This test presents a good representation of arbitrary heavy traffic on the bridge. Figure 8.19 shows a plot of the accelerometer data located at the centerline of the exterior box at midspan of Span 2 of the southbound bridge. The mean acceleration of the record was subtracted from the data, but no other filtering was performed. Peak accelerations were approximately 0.0075 g. This record was typical for the other vertically oriented accelerometers in the bridge.

The ERA/DC analysis was performed using the same constants, reference nodes, decimation factor, and methods as described for test Closed SS9. The aggregated modes from dynamic truck test Open S4, Wave 2 are presented in Table 8.8. A total of 11 modes were captured by the analysis. Once again, the modal analysis from this test compared well to that from the test Closed SS9. The fact that the loading was unknown is irrelevant to the algorithm. In fact, the irregular loading was thought to be beneficial; if

the loading is pure white noise, it should excite all modes of the structure, whereas well ordered truck loads might not excite particular frequencies.

Variations in frequencies and damping ratios in the captured modes from different truck tests were found to be within the daily scatter of the modes extracted from the ambient data, as presented in Figures 8.6 and 8.7.

8.2.2 Conclusions

The NExT-ERA/DC method was used to calculate modal frequencies and mode shapes of the I-35W St. Anthony Falls Bridge instrumented at various locations with accelerometers. Despite noise within the data, strongly excited structural frequencies were separated from noise modes using the consistent-mode indicator.

The NExT-ERA/DC method shows many benefits over a simple FFT method. Although it is more complex and computationally taxing, the NExT-ERA/DC provides information on not only the modal frequencies, but also the mode shapes and damping ratios. The FFT method is limited to providing only modal frequencies, and cannot separate modes with similar frequencies but different mode shapes (as was seen, for example, between the Mode 3 and Mode 4 near 2.3 Hz).

The algorithm performed well for major traffic events (as simulated by dynamic truck test Closed SS9) and for single vehicles (from dynamic truck test Closed SS10, Wave 8). The data with larger signal-to-noise was able to capture more modes and produced cleaner mode shapes, but both cases were able to reliably extract modal frequencies for many of the lower frequency modes. The NExT was derived assuming that the loading was a wide-sense stationary random process, and it was clear that the method performed well with the random load case presented by truck test Open S4, Wave 2 and also the daily ambient data.

It is expected that the extraction of modal properties will be useful in future monitoring of the structure. Changes in modal properties could indicate a change in the response of the structure, and could possibly be used for damage detection. For example, changes in structural stiffness due to some form of deterioration could alter the modal frequencies and mode shapes of the structure. However, the measured modal properties have been noted to be temperature dependent, which complicates the idealized case of structural monitoring. Future work will be needed in order to evaluate whether changes in modal properties due to structural deterioration can be separated from natural modal variations under normal operating conditions.

Chapter 9. Investigation of Design and Load Rating Assumptions

For the investigation of the design and load rating procedures of the I-35W Bridge, the southbound structure was modeled using the finite element method as described in Chapter 4. The quality of the method was verified using data from static truck load tests (Chapter 6) and thermal effects (Chapter 7). Results from the validated models were compared to results documented in the Load Rating Manual (Figg, 2008). An update was issued for the Load Rating Manual (Figg, 2012) with some modifications to the moment, shear, and torsion methodology. Unless otherwise noted, the discussion presented in the following chapter is concerned specifically with the 2008 version of the Load Rating Manual (Figg, 2008).

9.1 Longitudinal Moment Behavior

The two-dimensional finite element model (Section 4.2) was used to generate influence lines and loading envelopes for various critical sections along the length of the structure. Modeled results were compared to those documented in the Load Rating Manual (Figg, 2008). The model was validated with strain gage data collected during the static truck tests (Chapter 6).

9.1.1 Load Rating Manual Methodology for Computing Longitudinal Moments and Comparison with Modeled Results

The moment response as presented in the Load Rating Manual (Figg, 2008) was for the total cross section in longitudinal bending. Moment influence lines and moment envelopes for HL-93 and light-rail loading were provided in the manual for computation of critical loading cases. According to Section 2.1 of the Load Rating Manual, the strength and service moment capacities of the bridge were given as the total capacity of the interior and exterior box added together. No live load distribution factors were specified for the application of loads to either individual box, meaning all loads were assumed to be evenly distributed between the two boxes.

Podolny and Muller (1982) state that the torsional rigidity of the boxes and the transverse flexural rigidity of the deck typically result in satisfactory load distribution between box girders. The authors report that according to numerical results of a typical post-tensioned twin box girder bridge, a knife-edge load running longitudinally along one curb was distributed 70% to the loaded box and 30% to the opposing box. Similar distributions were confirmed in the truck test data, as discussed in Section 6.2.2, where for eccentric load cases from ST II (Figure 5.3), ST IVa (Figure 5.5), and ST IVb (Figure 5.6) truck configurations, measured longitudinal strains in the deck varied from approximately 25 με at the loaded end down to 10 με at the opposing end. Using the measured data, a conservative estimate of the fraction of the total moment applied to the loaded box was assumed to equal the maximum longitudinal strain (25 με) divided by the sum of the maximum and minimum longitudinal strains (35 με). Thus, 71% of the moment was carried by the loaded box. More conservative estimates for load distribution would be either to apply the total moment to a single box, or to apply the lever rule to distribute loads between the boxes.

Because only the total cross section was considered in the Load Rating Manual (Figg, 2008), the two-dimensional finite element model was used to generate moment influence lines at key locations along Spans 1 through 3. Each point on the influence lines was calculated by applying a single 1000-lb (4.4-kN) downward point load to the top surface of the deck. Given that a two-dimensional model was used, this point load was effectively distributed uniformly along the entire width of the deck. The point load was moved along the length of the bridge in a series of static load positions, each generating a single output point for all of the desired influence lines. Point loads were applied on every other corner node such that the spacing between point loads was approximately 4 ft (1.2 m).

In order to calculate moment at each cross section of interest, the section force in the longitudinal direction was output for each element. Section resultant forces were defined in the Abaqus output in units of force per length (i.e., the stress in the shell element multiplied by the shell thickness). This section resultant force was calculated at the centroid of each element. The output section resultant force was multiplied by the length of the element in the vertical direction, thus converting it to a force, and then multiplied by the distance between the neutral axis of the section and the centroid of the element. The resulting values were summed over the depth of the section to determine the bending moment.

The influence lines calculated by the FEM were compared to those provided by the Load Rating Manual (Figg, 2008). The influence lines in the Load Rating Manual were provided at relatively regular intervals along the length of the bridge, and did not always correspond to the sections with the most extreme moments or shears. Eight cross sections, labeled (a) through (h), were selected from those that were provided in the Load Rating Manual for analysis of the southbound structure's influence lines in the FEM. The positions of these sections are shown in Figure 9.1.

The approximate HL-93 moment envelope was also calculated using the model. A lane load of 0.64 kips/ft (9.3 kN/m) as prescribed by AASTHO LRFD (2010) Section 3.6.1.2.4 was applied to generate the maximum positive and negative moment for each location. A vertical point load of 72 kips (320 kN) was also applied at the location that would cause the maximum positive or negative moment. The 72-kip (320-kN) point load approximated the single HL-93 truck load without accounting for axle spacing, a conservative assumption given that the truck load according to AASHTO LRFD (2010) Section 3.6.1.2.2 uses a 14-ft (4.3-m) spacing between the 8-kip (36-kN) front axle and the 32-kip (142 kN) middle axle, and a 14- to 30-ft (4.3- to 9.1-m) spacing between the middle axle and the 32-kip (142 kN) rear axle. A dynamic impact factor of 1.33 was applied to the 72-kip (320-kN) point load. The HL-93 moment envelope provided in the Load Rating Manual represented a single lane of loading with the dynamic impact factor included on the vehicle load.

The moment influence lines from the FEM calculations are compared to the Load Rating Manual (Figg, 2008) moment influence lines in Figure 9.2. The comparison of the FEM and Load Rating Manual HL-93 live load envelopes is shown in Figure 9.3.

Except for locations near Abutment 1 and Pier 4 (Figures 9.2 (a) and (h)), the moment influence lines provided by Figg were conservative with respect to the finite element model. From Figure 9.3, the Load Rating Manual moment envelopes for HL-93 loading were conservative for both positive and negative moments along the entire length of the bridge, except for regions near Abutment 1 and Pier 4, of which only the moment at Abutment 1 was not negligible. The Load Rating Manual assumed perfect roller supports at these two locations, while the modeled bearing assemblies applied a small amount of restraint to the superstructure. From comparison between the HL-93 moment envelopes provided in the Load Rating Manual and generated by the finite element model, it was concluded that the locations of maximum moment between the two methods were effectively identical.

9.1.2 Critical Live Load Longitudinal Stresses

The maximum longitudinal tensile stress in the southbound structure due to vehicle live loading under service conditions was computed. To this end, the moment influence lines developed in Section 9.1.1 were applied to compute the maximum longitudinal moment due to vehicle live loading under the Service III limit state, and the three-dimensional FEM was used to compute the stresses from the determined critical load cases.

Live loads were applied as combinations of HL-93, permit vehicle, and light-rail live loads. The vehicle loads associated with each type of live load are presented in Figure 9.4. Each lane of HL-93 loading was

accompanied by a lane load of 0.64 kips/ft (9.3 kN/m) positioned to maximize the moment at the location of interest. When permit vehicle loading was considered, one of the three types of permit vehicles (Standard C, MnDOT Standard P413, or the Special Permit Vehicle, as shown in Figure 9.4) was positioned in one of the lanes. When light-rail live loading was considered, one, two, or three light-rail cars were positioned in order to maximize the moment at the location of interest. The proposed light-rail track location was always along the interior edge of the bridge, and so light-rail loads were always assumed to occupy this lane. The additional dead load associated with the addition of the light rail was not included. An impact factor of 1.33 was applied to HL-93 truck and permit vehicle loading, while an impact factor of 1.2 was used for light-rail loading in accordance with the as-built drawings (Minnesota Department of Transportation, 2008). Without light rail, a maximum of seven 12-foot (3.7-m) lanes were applied. When considering load cases with light rail, a maximum of six lanes, including the light-rail lane, were placed on the bridge.

The load combinations considered are summarized in Table 9.1. The multiple presence factors listed in Table 9.1 were taken from the as-built drawings (Minnesota Department of Transportation, 2008). According to Section 2.2 of the Load Rating Manual (Figg, 2008), the multiple presence factor was to be selected according to the total number of loaded lanes (including HL-93, permit vehicle, and light-rail lanes). However, this multiple presence factor was only to be applied to the HL-93 loading. Permit vehicle and light-rail loading were to be given a separate multiple presence factor regardless of the number of loaded lanes, as given in Table 9.1.

When computing moments to find the critical load case, load distribution was assumed such that the loaded box carried 70% of the total moment, as discussed in Section 9.1.1. Moments from HL-93 loads were taken from the moment envelope computed using the FEM. Moments from permit vehicles and light-rail loads were computed using the FEM moment influence lines.

The largest positive live load moments were found to be located at instrumented Location 7 near midspan of Span 2. For load cases without the light rail, the greatest moment was caused by the load case with the exterior lane occupied by the Standard P413 permit vehicle and the remaining six lanes occupied by HL-93 loading. For load cases with light rail, the maximum moment was induced by three light-rail cars in the light-rail lane, the Standard P413 permit vehicle in the interior traffic lane, and four lanes of HL-93 loading. For both cases, the critical position of the P413 permit vehicle was such that the center axle of the second triple-axle set was positioned at instrumented Location 7. The critical position of the light-rail load was such that the center tandem of the second car was centered at instrumented Location 7. For purposes of determining the largest positive live load moments, the HL-93 truck was approximated as a point load as described in Section 9.1.1. The live load moment was maximized when the HL-93 truck point load was directly on instrumented Location 7 and the lane loading was applied only along the entire length of Span 2.

The three-dimensional FEM, as described in Section 4.1, was used to derive the maximum stresses in the bridge as induced by the critical load cases described above. Vehicles, including the HL-93 trucks, were applied as point loads for each tire load as shown in Figure 9.4 but with multipliers accounting for dynamic impact and multiple presence factors. Modeling each of the HL-93 truck tires as a point load provided a more accurate portrayal of the stresses than the single point load per vehicle used to determine the loading conditions of maximum moment as described above. The HL-93 truck loads were applied such that the center axle was positioned at instrumented Location 7, and all other vehicle loads were applied as described above. Dead load and post-tensioning forces were not considered in this analysis.

Under the maximum load case without light rail (P413 permit vehicle in the exterior lane and six lanes of HL-93), the maximum tensile stress computed by the FEM was found to be equal to 850 psi (5.8 MPa) in the west (exterior) corner of the bottom flange of the exterior box at Location 7. Under the maximum

load case with light rail (three light-rail cars, P413 permit vehicle in the interior traffic lane, and four lanes of HL-93), the maximum tensile stress computed by the FEM was equal to 840 psi (5.8 MPa) in the east (interior) corner of the bottom flange of the interior box at Location 7. By comparison, the maximum experimentally-derived longitudinal tensile stress due to the maximum measured positive thermal gradients (presented in Section 7.1.5) was found to be 680 psi (4.7 MPa), and the maximum derived longitudinal tensile stress recorded during the truck tests was 260 psi (1.8 MPa) from configuration STI7SB. The computed live load stresses could not be directly compared to readings collected during daily traffic conditions as no installed instrumentation was capable of measuring this information.

9.1.3 Update to Load Rating Manual Methodology for Computing Longitudinal Moments

The methodology for computing moment in the updated Load Rating Manual (Figg, 2012) was altered to account for load distribution. Verification of the updated methodology with the finite element model was out of scope of the University of Minnesota project. However, a discussion of the changes to the methodology follows.

Strength and service live load moment capacities were no longer provided for the total bridge cross section. Instead, strength and service capacities were specific to only the exterior box girder. Live load capacities for the interior box were not provided. Due to the symmetry of the bridge and the fact that the capacities for the exterior box provided in the updated manual were very nearly half of the total bridge capacity from the original manual, it can be assumed that the live load capacities for the interior box are effectively identical to the exterior box capacities.

The updated manual methodology accounted for live load distribution between the two boxes. However, this was not done using distribution factors. Instead, the manual provided influence lines and moment envelopes for loading in each individual lane and the effects of those loads on only the exterior box. According to Section 2.13 of the updated Load Rating Manual (Figg, 2012), the influence lines and envelopes were developed using a three-dimensional finite element model.

The updated methodology for computing longitudinal moments imposed several restrictions on what types of load cases could be considered. For example, influence lines were given for the moment distributed to the exterior box only due to loading in the exterior painted traffic lane, with no other load cases covered. Thus, the updated manual methodology would be difficult to apply to generic loading on the shoulder or any other traffic lane. HL-93 moment envelopes, on the other hand, were developed for the peak moment in the exterior box due to loading in each painted traffic lane. Additionally, "undistributed" envelopes were provided, assuming equal moment distribution between the boxes, for the peak moments in the total cross section due to light-rail loading and HL-93 loading in an unspecified lane. As expected, these undistributed envelopes were nearly identical to those provided in the original Load Rating Manual (Figg, 2008), with minor differences likely due to minor undocumented changes between the methods in the two manuals. "Undistributed" influence lines were not provided in the updated Load Rating Manual. Because of the restrictions on load positions covered by the provided influence lines and envelopes, loading on the shoulders or otherwise not in designated lanes could not be investigated using the updated methodology.

The Podolny and Muller (1982) assumption, discussed in Section 9.1.1, that moment is distributed 70% to the loaded box appeared to be consistent with the methodology of the updated Load Rating Manual. This was investigated by comparing the "undistributed" influence lines from the original manual with the updated influence line documenting the moment distributed to the exterior box due to loading in the exterior traffic lane. At the location of loading, the updated influence line was typically between 60% and 70% of the undistributed influence line. At locations away from the loading, the updated influence line was approximately half the undistributed influence line, modeling the distribution of the moment between

the boxes as the load travels towards the piers. Due to a lack of provided influence lines, loading on the exterior shoulder, which would be expected to apply larger moment to the exterior box than loading in the exterior traffic lane, could not be investigated.

Because the updated methodology restricted loading to painted traffic lanes, the critical load cases discussed in Section 9.1.2 could not be explored using the updated Load Rating methodology. Furthermore, investigation of the critical loading for the interior box was not possible using the updated method because only the distribution of the load to the exterior box was provided. Combining the undistributed influence lines from the original Load Rating Manual with their equivalent distributed versions in the updated manual would allow computation of moment in the interior box, but would still be necessarily limited by the locations of loading specifically documented in the updated manual.

9.1.4 Summary and Conclusions

Moment influence lines and envelopes were generated from the validated two-dimensional FEM and compared to values presented in the original Load Rating Manual (Figg, 2008). Methodology for moment behavior as presented in the original Load Rating Manual did not include live load distribution factors between the two boxes, and only considered the total cross section. Measured results from the truck tests revealed that applying 70% of the load to the loaded box and the remaining 30% to the unloaded box would reasonably reproduce the transverse distribution present in the structure at the location of loading. For more conservative estimates, either the entire moment could be applied only to the loaded box, or the lever rule could be applied. For the moment behavior of the total cross section, it was found that original Load Rating Manual methodology performed conservatively with respect to the FEM results for all locations except near the expansion joints at Abutment 1 and Pier 4. This result was due to the difference in assumptions of the boundary conditions at Abutment 1 and Pier 4. Figg assumed perfect roller conditions at these locations, whereas the finite element model included some fixity inherent to the more rigorously modeled bearing pad assemblies.

The maximum longitudinal tensile stress due to vehicle live loading under service conditions was derived using the computed influence lines and HL-93 envelope and the three-dimensional finite element model. The critical load cases were found to be one lane of the P413 permit vehicle with six HL-93 lanes or three light-rail cars, one lane of the P413 permit vehicle and four HL-93 lanes. The maximum live-load tensile stress was 850 psi (5.8 MPa) at instrumented Location 7. This was 25% larger than the maximum experimentally derived tensile stress at the same location induced by measured positive thermal gradients, equal to 680 psi (4.7 MPa), and over three times the maximum derived stresses measured during any of the truck tests.

An updated Load Rating Manual (Figg, 2012) was provided to include live load moment distribution between the boxes. A comparison between the undistributed moment influence lines from the original manual and the updated influence lines for the exterior box due to loading in the exterior traffic lane revealed that applying 70% of the moment to the loaded box was a reasonable assumption. However, the updated methodology for computing longitudinal moments was restricted to loads located in specified traffic lanes, and was not general enough to allow exploration of general load cases such as loads on the shoulders. Therefore, although the updated Load Rating Manual methodology would be a useful tool for load rating, it was not general enough to explore the critical service live load cases.

9.2 Thermal Design

The two-dimensional finite element model described in Section 4.2 was used to investigate the response of the St. Anthony Falls Bridge with respect to thermal effects. The model was first validated with strain data resulting from the maximum five measured positive thermal gradients that occurred between

September 1, 2008 and October 26, 2011 (Section 7.1.5). The validated model was subsequently used to investigate the appropriateness of the AASHTO LRFD (2010) thermal design with regards to prestressed concrete box structures in Minnesota. Thermal effects were not discussed in either version of the Load Rating Manual (Figg, 2008, 2012).

9.2.1 Thermal Gradients

9.2.1.1 Modeled Bridge Behavior Using Design Gradients

The changes in experimentally derived longitudinal stresses (as defined in Section 7.1.5) for each of the five maximum measured positive and negative gradients (see Tables 7.1 and 7.2) at Location 7 were compared to the computed values of stress from the finite element model (FEM) using the following design gradients: the AASHTO LRFD (2010) gradient for Zone 2 with top surface temperature equal to 46°F (25.6°C), the Priestley (1978) fifth-order curve with top temperature equal to 57.6°F (32°C) as stated in the New Zealand Code (henceforth called Priestley-NZC), and the Priestley-Z2 gradient as described in Chapter 7. From Section 7.1.3, the shape of the Priestley (1978) fifth-order curve with top surface temperature for AASHTO LRFD (2010) solar radiation Zone 2 was found to best represent the maximum measured gradient magnitudes. Gradient shapes for the AASHTO LRFD (2010) and the Priestley (1978) fifth-order curve are presented in Figures 7.1 and 7.2, respectively. Despite that no negative gradient was specified for the Priestley (1978) curve, all negative design gradients were scaled by a factor of -0.3 from their respective positive design gradient for consistency with the AASHTO LRFD (2010) specifications. These comparisons for Location 7, which was the instrumented location of maximum compressive and tensile longitudinal stresses for each design gradient according to FEM results, of the southbound bridge are presented in Figure 9.5. Considering positive gradients, the changes in experimentally derived stresses in the bottom flange were consistently greater than those predicted by the AASHTO LRFD design gradient applied to the FEM, and always less than the Priestley-NZC gradient. Averaging the experimentally derived longitudinal stresses showed that the Priestley-Z2 gradient was the best fit. For negative gradients, the changes in stresses approximated from measured strains at the neutral axis of the section were typically higher than stresses computed by the FEM using design gradient values. On the contrary, changes in stress from measured strains in the bottom flange were lower than those predicted by the FEM using the design gradients. These discrepancies were believed to be caused by the difference in shape of the measured negative gradients as compared to the design gradients as seen in Figure 7.7b, whereby the measured gradient temperature at a depth of 39.4 in. (1.0 m) far exceeded design values. Modeled results for all presented negative gradients provided reasonable estimates of the experimentally derived stresses.

Measured curvatures along the length of the southbound structure due to the maximum measured positive and negative gradients were compared to FEM-computed curvatures due to the three aforementioned design gradients. These comparisons for the southbound bridge are presented in Figure 9.6. For the positive thermal gradients, the measured curvatures at Location 7 were typically nearest FEM predictions using the Priestley-NZC gradient. At most other instrumented locations, measured curvatures appeared to follow predictions from the Priestley-Z2 gradient. At the majority of the instrumented sections, FEM predictions using the AASHTO LRFD gradient were consistently less than the measured curvatures. For the negative thermal gradients, none of the design gradients appeared to be inherently superior at predicting the measured curvatures. Based on the above discussion, it was decided that the Priestley-Z2 gradient best predicted measured curvature results along the entire structure.

9.2.1.2 Recommendations for Design Gradients

It was concluded that the shape of the Priestley-Z2 gradient best fit the measured positive gradient results from the St. Anthony Falls Bridge, as shown in Section 7.1. While the shape of the negative gradient

could not be consistently captured by the considered design gradients, multiplying the Priestley-Z2 by a factor of -0.3 as suggested in the AASHTO LRFD produced stress results that reasonably approximated the experimentally derived stresses.

In terms of applied stresses and curvatures, the Priestley-Z2 gradient was also found to best approximate the measured response of the St. Anthony Falls Bridge. Notably, as shown in Figure 9.5, the FEM-computed stresses induced by the Priestley-Z2 better matched experimental data and were considerably larger in the bottom flange than those computed using the AASHTO LRFD gradient. In the top flange, changes in stress were dominated by compatibility stresses (i.e., stresses induced in order to satisfy Bernoulli beam theory that plane sections remain plane), and were largely the same among the considered design gradients. FEM-computed compressive stresses at the top fiber of Location 7 using the AASHTO LRFD positive gradient were 8%, or 90 psi (0.6 MPa), greater than those computed using the Priestley-Z2, but were 15%, nearly 170 psi (1.2 MPa), less than those computed from the Priestley-NZC gradient. These differences in compressive top-fiber stresses were not significant for design purposes. FEM-computed tensile stresses at the bottom fiber at Location 7 were 80%, or 250 psi (1.7 MPa), greater for the Priestley-Z2 positive gradient and 126%, or 390 psi (2.7 MPa), greater for the Priestley-NZC positive gradient compared to those computed using the AASHTO LRFD curve. Increases in tensile stress of the stated magnitudes are on the order of the tensile strength of typical concretes, meaning that this increase could be significant if, for example, the post-tensioning was designed to enforce zero tension in the structure. Similarly, the FEM-computed curvatures were 50-95% greater for the Priestley-Z2 and 85-145% greater for the Priestley-NZC gradient than those from the AASHTO LRFD curve. Because negative design gradients were scaled versions of their respective positive gradient, relative percentile differences between the different negative design gradients were the same as for the positive design gradients, and differences in magnitude as presented above were multiplied by -0.3. The design implications of using the Priestley negative gradient curves as opposed to the AASHTO LRFD negative gradient were found to be minor; though comparisons among the differing negative gradients were qualitatively similar to comparisons among the positive gradients, the absolute magnitudes of stresses associated with the negative gradients were far less.

As documented in Section 7.1.3, maximum daily positive gradients typically occurred around 2:00 PM to 4:00 PM CST, which implies a possible correlation between live loading around rush hour and maximum thermal gradient effects. If large live loading and thermal effects are correlated, the thermal gradient load factor equal to 0.5 for service limit states with live load as specified in Section 3.4.1 of the AASHTO LRFD Bridge Design Specifications (2010) might be unconservative. Similarly, the live load factor equal to zero for service limit states with the full design gradient might also be unconservative. Further statistical investigation is required to resolve this topic. Specifically, it cannot be concluded without further investigation that the critical live loads, which consist primarily of heavy trucks, necessarily occur during rush hour.

In the particular case of the I-35W Bridge, the service design live load was very conservative with respect to expected live loads on the structure, due to assumptions such as load application in seven design lanes (five traffic lanes plus the two shoulders) and a minimum multiple presence factor (see Table 9.3) that was greater than required by AASHTO LRFD (2010). Therefore, it is highly likely that the application of the full live load plus half the AASHTO LRFD thermal gradient still produced a conservative design for the service limit state.

9.2.1.3 Summary and Conclusions

Temperature gradients were measured over the course of three years in the I-35W St. Anthony Falls Bridge, a post-tensioned concrete box girder structure in Minneapolis, Minnesota. From Section 7.1.3, the shapes of the thermal gradients through the depth of the section were found to be nearest the shape of

the fifth-order curve found in the New Zealand Code (Priestley, 1978). The maximum measured top surface gradient temperatures for positive and negative thermal gradients were best matched by the top surface temperature specified in AASHTO LRFD (2010) for solar radiation Zone 2.

A two-dimensional finite element model was constructed for the prediction of the structural response subjected to thermal effects. The model was validated using the five maximum measured positive thermal gradients, and was then applied to compute the structural response due to the investigated design gradients. It was found that experimentally derived stresses and curvatures best matched the predictions using the Priestley-Z2 gradient, a fifth-order curve scaled to match AASHTO LRFD Zone 2 top surface temperatures. The predicted curvatures and bottom fiber tensile stresses caused by the Priestley-Z2 positive gradient were nearly 80% larger than those using the AASHTO LRFD (2010) design thermal gradient.

As evinced by the variety of conclusions drawn by various authors in differing studies of thermal gradients, it can be surmised that the thermal response of structures can be highly variable, dependent not only on location and climate, but also on properties of the structure such as blacktop covering and cross-sectional shape. For example, Roberts-Wollman et al. (2002) found that measured gradients in San Antonio could be approximated by a fifth-order curve with top surface gradient temperature less than that presented in the AASHTO LRFD, whereas Shushkewich (1998) stated that gradients in Hawaii were much like the AASHTO gradients. This study showed that the AASHTO LRFD (2010) design thermal gradients are not necessarily conservative for structures in all regions. Specifically, the more rigorous case of the scaled fifth-order gradient was found to best approximate results from the St. Anthony Falls Bridge, was observed multiple times during the three years of monitoring, and was found to cause substantially larger deformations and bottom-flange tension stresses than the AASHTO LRFD (2010) design gradient.

9.2.2 Uniform Temperature Changes

9.2.2.1 Design Bridge Expansion Compared to Measured Expansion

The uniform temperature range used for design as specified in the as-built drawings (Minnesota Department of Transportation, 2008) was from -30 to 120°F (-34 to 49°C). This temperature range was slightly larger than that suggested for Minneapolis from Procedure B in Section 3.12.2.2 of the AASHTO LRFD (2010) specifications, for which concrete girder bridges ranged from -20 to 110°F (-29 to 43°C). Assuming a coefficient of thermal expansion for the superstructure equal to 6.0 με/°F (10.8 με/°C) as specified in the as-built drawings (Minnesota Department of Transportation, 2008), total structural length for Spans 1 through 3 of the southbound bridge equal to 1065 ft (324.6 m), and that the piers and bearings provide no restraint to longitudinal expansion, the overall change in length over the entire temperature range was predicted to be 11.5 in. (290 mm). Using the same assumptions, expansion for the 145.25-ft (44.3-m) southbound Span 4 was predicted to be 1.57 in. (40 mm).

The I-35W Inspection and Maintenance Manual (Figg, 2008) listed the expected thermal motion of the superstructure on the sliding bearing pad assemblies located at Abutment 1 and Pier 4. For the southbound structure, thermal expansion was predicted to be 0.039 in./°F (1.8 mm/°C) at Abutment 1, and 0.046 in/°F (2.1 mm/°C) at Pier 4. These values represented the relative motion between the top and bottom sliding plates of the “roller” type bearing pads at Abutment 1 and Pier 4. Whereas the motion at Abutment 1 was due solely to expansion of the superstructure (that is, the top sliding plate moved with the superstructure while the bottom plate on the abutment was effectively stationary), motion at Pier 4 could be attributed to both expansion of the superstructure and horizontal deflection of the top of Pier 4. Due to the pinned connection of Span 4 to the top of Pier 4, thermal expansion of Span 4 would deflect the top of Pier 4 in the opposite direction that the end of Span 3 was moving. This would effectively

amplify the sliding between the top and bottom sliding plates as they were deflected in opposite directions by any given temperature change.

The Inspection and Maintenance Manual did not separate the motion between the end of Span 3 and the top of Pier 4 into the different motions associated with the shortening of Spans 1 through 3 and the horizontal deflection of Pier 4. Therefore, to facilitate comparison among the Inspection and Maintenance Manual estimates, the estimates from applying unrestrained thermal expansion, and results from the finite element model, it was assumed that Pier 4 was sufficiently flexible compared to the integral abutment at Abutment 5, and the longitudinal deflection of Pier 4 was equal to the total amount of expansion or shortening of Span 4. This was consistent with the assumptions made during the estimation of the concrete coefficient of thermal expansion as presented in Section 3.4.2.2. By application of Eqn. (3-26) and assuming a concrete coefficient of thermal expansion of 6.0 με/°F (10.8 με/°C) as was used for the derivation of the motions from the Inspection and Maintenance Manual, the deflection of Pier 4 due to elongation of Span 4 was assumed to be 0.010 in/°F (0.45 mm/°C). The remaining 0.036 in/°F (1.6 mm/°C) of the total motion at Pier 4 from the Inspection and Maintenance Manual values was therefore assumed to be due to expansion of Spans 1 through 3. According to these estimates, the total expansion of Spans 1 through 3 (0.039+0.036 = 0.075 in/°F (1.8+1.6 = 3.4 mm/°C)) corresponded to a total elongation of 11.25 in. (286 mm) over the 150°F (83°C) uniform temperature range, which was approximately equal to that predicted by direct application of unrestrained thermal expansion which gave a value of 11.5 in. (290 mm).

The linear potentiometer (LP) data from the southbound bridge expansion joints was investigated to verify the assumptions for thermal movement. The LPs were attached to the superstructure and piers or abutments as shown in Figure 2.50. The LP data was examined from January 1, 2011 until June 30, 2011. All measurements for which the magnitude of the thermal gradient in the structure was larger than 1°F (0.5°C) were omitted from the analysis, so that only nearly uniform temperature changes were considered. Time-dependent effects were ignored due to the total time passed since erection. The LP readings were plotted with respect to the uniform temperature changes, and a least-squares linear fit was passed through the data. It was found that for the period considered, the total motion measured at Abutment 1 was equal to 0.039 in/°F (1.8 mm/°C), and the total motion measured at Pier 4 was 0.041 in/°F (1.9 mm/°C). A representative data fit for the LP data at Abutment 1 from January 1, 2011 until June 30, 2011 is provided in Figure 3.27, with linear fits found to be similar for other LPs. Because the linear fit was very strong (R^2 value of 0.99 for the plot in Figure 3.27), it was concluded that assumption to ignore the time-dependent effects was valid. It was not possible to directly measure the longitudinal deflection of Pier 4, so it was again assumed that the deflection of the top of Pier 4 was equal to the estimated expansion of Span 4. Thus, it was estimated that 0.031 in/°F (1.4 mm/°C) of the motion at Pier 4 was due to expansion of Spans 1 through 3 and 0.010 in/°F (0.45 mm/°C) was due to deflection of Pier 4. Note that the total expansion of Spans 1 through 3 under this approximation was found to be equal to 0.070 in/°F (3.2 mm/°C), a 6.7% reduction from the design values. However, field and laboratory studies (refer to Section 3.4) concluded that the coefficient of thermal expansion of the superstructure was 5.6 με/°F (10.1 με/°C), which was 6.7% lower than the design CTE of 6.0 με/°F (10.8 με/°C). Because a larger CTE would imply more structural movement, the design CTE value can be considered as conservative with respect to measured values. Thus these measured results, accounting for the difference in CTE, coincided well with the design assumptions.

9.2.2.2 Finite Element Model Expansion under Uniform Temperature Change

The two-dimensional finite element model (described in Section 4.2) used for thermal gradient modeling was used to investigate uniform temperature changes. The design uniform temperature change of 150°F (83°C) was applied to the model, and the displacement at the locations of the LPs was recorded. The CTE of the modeled superstructure was set equal to the experimentally derived value of 5.6 με/°F (10.1

με/°C). The FEM displacement at Abutment 1 was determined to be 5.67 in. (144 mm), corresponding to 0.038 in/°F (1.7 mm/°C) elongation. The FEM displacement at Pier 4 (only due to expansion of Spans 1 through 3, as Span 4 was not modeled) was found to be 4.92 in. (125 mm), corresponding to 0.033 in/°F (1.5 mm/°C) elongation. The total expansion of Spans 1 through 3 computed in the FEM was 0.071 in/°F (3.2 mm/°C), which was approximately equal to the measured LP expansion assuming that all the expansion of Span 4 caused an equal amount of deflection of Pier 4. The results for uniform temperature changes and the expansion of southbound Spans 1 through 3 are summarized in Table 9.2.

9.2.2.3 Investigation of Total Temperature Range and Total Measured Expansion

The total amount of measured bridge thermal expansion and the uniform temperature design range were investigated using weather station and bridge instrumentation data. Data from weather station KMNMINNE17 located on the University of Minnesota campus approximately one mile from the I-35W Bridge was collected. The maximum and minimum station temperatures from September 1, 2008 until October 23, 2011 were 101°F (38°C) and -16°F (-27°C), respectively. The range of uniform bridge temperatures measured during this time period was consistently less than the range gathered from weather station KMNMINNE17. Assuming that the "uniform" bridge temperature can be reasonably captured from thermistor TSEWB002 located 81 in. (2.1 m) below the top deck surface in the west (exterior) web of the exterior box of the southbound bridge at Location 7, the uniform bridge temperatures over the same period ranged from 90°F (32°C) to -8.6°F (-22°C). The measured temperature ranges from the nearby weather station and from the bridge instrumentation were 22% and 35% less, respectively, than the design temperature range of 150°F (83°C). Using Procedure B for computing temperature range of concrete girder bridges with concrete decks from Section 3.12.2.2 in the AASHTO LRFD (2010), the maximum and minimum design temperatures for Minneapolis were 110°F (43°C) and -20°F (-29°C), respectively, for a total temperature range of 130°C (72°C). Therefore, the temperature range used in design of the St. Anthony Falls Bridge was 15% larger (i.e., more conservative) than the AASHTO LRFD (2010) specifications.

Linear potentiometer readings for the northbound and southbound structures measuring the movement at Abutment 1 and the relative motion between the Span 3 diaphragm and the top of Pier 4 are presented in Figures 7.11 through 7.13. As stated in Section 7.2.1, the two LPs attached to the northbound bridge at Abutment 1 were replaced on September 21, 2010, and the two LPs attached to Span 4 of the southbound bridge at Pier 4 were replaced September 30, 2010, and the zero used prior to replacement was assumed to be valid after replacement and accurate to the tolerances of the instrumentation, or approximately 0.05 in. (1 mm). Again, this assumption was not verifiable, and therefore any conclusions based upon this premise should be considered at the reader's discretion. The northbound and southbound structures behaved largely the same. The total range of Abutment 1 LP measurements from October 31, 2008 to October 23, 2011 was 4.02 in. (102 mm) for the average of the northbound LPs and 3.80 in. (96 mm) for the average of the southbound LPs. The measured ranges, despite including time-dependent effects such as creep and shrinkage, were less than the motion prescribed in the Inspection and Maintenance Manual (Figg, 2008). Due to thermal expansion alone and considering a temperature range of 150°F (83°C), the safe Abutment 1 motions predicted by the Inspection and Maintenance Manual were equal to 6.3 in. (160 mm) for the northbound structure and 5.85 in. (149 mm) for the southbound structure. This indicated that the Inspection and Maintenance Manual provisions for thermal behavior were conservative with respect to the measured results for the first three years of monitoring.

Finally, the design range of uniform temperature changes was investigated in the finite element model for its effect on longitudinal curvature and longitudinal stresses in the superstructure. The model was subjected to uniform temperature changes of positive and negative 150°F (83°C) to capture the full envelope of stress changes dependent on initial temperature. Design assumed that the initial temperature was equal to 45°F (7°C), so that temperature rises and falls were balanced to both equal 75°F (42°C).

The curvatures along the length of Spans 1 through 3 of the southbound FEM over the ±150°F (±83°C) envelope range and the ±75°F (±42°C) design range are plotted in Figure 9.7. Figure 9.8 contains the stress profiles through key instrumented sections of the southbound FEM over the ±150°F (±83°C) envelope range and the ±75°F (±42°C) design range.

The curvature demand for the ±150°F (±83°C) uniform temperature change in Spans 1 and 3 appeared to be much greater than that demanded of all the considered design positive gradients. However, this did not necessarily translate to higher longitudinal stresses: all the positive design gradients caused much higher top fiber stress magnitudes than did the uniform thermal changes. This was not a surprising result, as much of the top stresses caused by the thermal gradient were due to the enforcement of Bernoulli beam bending; where the nonlinear gradient deviated significantly from the linear strain profile, large equilibrating stresses must form to ensure that the section remains planar. The bottom fiber stresses induced by the ±150°F (±83°C) envelope temperature range were more comparable between uniform temperature changes and thermal gradients, which might be of concern as large positive gradients plus large uniform temperature changes together could cause large tensile stresses in the bottom flange. The uniform temperature changes appeared to cause more bottom fiber stress than the examined design gradients at Locations 3, 6 and 9, and comparable bottom stresses at Location 7. The plotted values representative of the ±150°F (±83°C) temperature range envelope the entire expected design response independent of initial structure temperature, and as such represent twice the amount of curvature and stress for design values using ±75°F (±42°C).

9.2.2.4 Summary and Conclusions

Uniform temperature changes were investigated using measured linear potentiometer data and the validated FEM. The design expansion per degree uniform temperature change compared well with the LP and FEM results. However, the total uniform temperature change assumed for design was far larger than what the bridge experienced during the first three years because the bridge had not seen the full design temperature range. As predicted in the finite element model, superstructure curvatures over the ±150°F (±83°C) uniform temperature design range were of similar magnitudes or larger than those caused by the design thermal gradients. However, top fiber stresses caused by the thermal gradients were consistently larger than those caused by uniform temperature changes, largely due to the equilibrating stresses enforcing the section to remain planar despite the nonlinear thermal gradient. Bottom fiber stresses were comparable between the design gradients and uniform temperature changes, with gradients controlling at some locations, and the uniform temperatures controlling at other locations. Generally, high positive gradients will occur when uniform temperatures are also high, so the combination of these stress cases would need to be considered for design. Because the measured air temperature was less than the specified ±75°F (±42°C) uniform temperature range, and the structural temperature range (excluding gradients) were even less still, the computed curvatures and stresses using ±150°F (±83°C) were likely to be between two to three times those experienced by the bridge.

9.3 Transverse Behavior

The three-dimensional continuum finite element model (Section 4.1), validated using static truck test data (Chapter 6), was used to investigate the transverse behavior of the I-35W box girders. The transverse stresses in the examples presented in the Load Rating Manual (Figg, 2008) were compared with those computed using the finite element model. The transverse behavior documented in the original Load Rating Manual (Figg, 2008) was left unchanged in the updated manual (Figg, 2012), and all references to the Load Rating Manual in this section pertain to the original version.

9.3.1 Load Rating Manual Methodology for Computing Transverse Moments

The methodology for computing transverse moments as taken from Chapter 4 of the Load Rating Manual (Figg, 2008) provided the expected transverse moments at several critical points across the width of the top flange. These points of maximum moment were always assumed to lie either at the face of one of the webs or at the midpoint between two webs. The points for Spans 1 through 3 of the northbound and southbound bridges are shown in Figure 9.9. Other possible sections, such as at the top of the web where it met the deck or any section in the bottom flange, were not checked in the Load Rating Manual. Although the Load Rating Manual also contained calculations for Span 4 of both the northbound and southbound structures, this investigation was limited to the sections as shown in Figure 9.9 for the southbound structure.

As stated in the Load Rating Manual, transverse moments were calculated using fixed-end-moment influence surfaces based on the work of Hellmut Homberg (reference details were unspecified in the Load Rating Manual). The fixed-end-moment influence surfaces were generated for each critical section shown in Figure 9.9. Each surface only contained the portion of the top flange where the critical section in question was located (e.g., for Point 1, only the cantilever section starting at Point 1 was examined, and for Point 2, the span from Points 2 to 4 was examined). A sample fixed-end-moment influence surface for Point 2 is shown in Figure 9.10. Moments in one fixed-end region were distributed to other sections by use of "Live Load Moment Summary Tables." Figg calculated the distribution coefficients in these tables by applying a unit moment to each critical section in a two-dimensional frame analysis of the cross section. The provided coefficients were used to calculate the resulting moment at any section based on the fixed-end-moments from the loaded influence surfaces. For example, to calculate the moment at Point 3 due to loading in the left cantilever, the fixed-end moment at Point 1 would be calculated from the cantilever influence surface and then multiplied by the Point 1-to-3 distribution coefficient. The resulting moments were then multiplied by the dynamic impact factor, equal to 1.33, and the multiple presence factor from Table 9.3.

The transverse moments in the manual were provided as the moment over a unit length strip of the top flange. The top flange at Points 1, 2, 4, and 5 was nominally 23.5 in. (600 mm) thick, whereas the thickness at Points 3 and 6 was nominally 11.5 in. (290 mm). An assumption in the Load Rating Manual was that Point 1 would control for negative moments, and Point 6 would control for positive moment.

9.3.2 Sample Problems

The Load Rating Manual documented a series of load cases to illustrate the use of the transverse behavior methodology. For each of these examples, the P413 permit vehicle and up to two HL-93 trucks were applied to the structure to investigate the transverse moment at each of the critical sections. Schematics for the permit vehicle and the HL-93 truck used in the examples are shown in Figure 9.4. Five distinct load cases were examined. Diagrams for each load configuration are presented in Figure 9.11. For each configuration, HL-93 trucks were positioned so that the center axle was along the line of maximum transverse moment. The permit vehicle was positioned such that the center axle of the first set of 10-kip (44-kN) loads (that is, the set of 10-kip (44-kN) loads nearest the 7.5-kip (33-kN) front axle loads) was along the line of maximum transverse moment. All HL-93 and permit vehicles were assumed to be facing the same direction. Each wheel load was treated as a single point load.

9.3.3 Finite Element Modeling

A three-dimensional continuum finite element model (FEM) of Spans 1 through 3 of the southbound structure was used to explore the validity of the assumptions in the Load Rating Manual procedure for

computing transverse moments. Section 4.1 describes the construction of the model and Chapter 6 describes the validation of the model with static truck test data.

The sample load cases documented in Figure 9.11 were modeled using the FEM such that the line of maximum transverse moment was either near midspan (station = 221+37.4) or the south quarter span (station = 219+81.9) of Span 2. Different longitudinal stations were chosen to investigate the possible differences in the transverse response due to the changing box shape. Specifically, the midspan of Span 2 was chosen due to the concentration of instrumentation and number of truck tests performed at the location, and the southern quarter span was chosen because, according to Section 3.2 of the Load Rating Manual, this location was a possible critical section for shear and torsion (investigated in Section 9.5) using similar load cases to those discussed in this section. The geometry and thickness of the top flange were the same along the entire length of Spans 1 through 3, but the total section depth and bottom flange thickness varied along the length. Although the Load Rating Manual assumed that the section was symmetric across the centerline of the roadway, this was not the case with the FEM. The comparatively stiff concrete barrier rail on the interior edge was explicitly modeled with the FEM; the flexible metal barrier rail on the exterior edge was not modeled. All load cases were applied such that the left edge of the bridge as depicted in Figure 9.11 represented the exterior edge of the structure. Each tire load was modeled as a single nodal force.

9.3.4 Results

For each sample load case, the transverse bending moments in the top flange given by the Load Rating Manual were compared to the computed moments from the FEM near midspan and the southern quarter point of Span 2. Plots of these comparisons for each of the five tested load cases are presented in Figures 9.12 through 9.16.

Examination of Figures 9.12 through 9.16 shows that the Load Rating Manual methodology used for computing transverse moments in the top flange was conservative with respect to the elastic FEM solution at the sections where the top flange met the webs. FEM moments at the centerline of the boxes or at the centerline of the bridge compared well to those predicted by the Load Rating Manual. The assumption that Point 1 would control for negative moment and Point 6 would control for positive moment was found to be true for the analyzed load cases.

Of particular note was the moment distribution in the surface spanning between the two boxes. When a single box was loaded, the FEM results showed that the moment distribution through the connecting span was nearly linear, meaning that this moment was caused by differential deflection between the two boxes. This deduction was further reinforced by the fact that the moments between the boxes were smaller for the quarter span loading, for which it would be expected that the differential deflection between the boxes would be less than at midspan. By comparison between the Load Rating Manual and FEM moments at Point 5, it was clear that the Load Rating Manual did not include the effects of differential deflection in its prediction, which was a potentially unconservative assumption.

Although the Load Rating Manual did not explicitly check the moments at Point 5' (the section at the mirrored point from Point 5 as shown in Figure 9.11), it was deduced from the FEM results reported in Figures 9.12 through 9.16 that the maximum negative moment at this point would be due to loading in the exterior box and the span between the boxes. The particular loading case is shown in Figure 9.17. Trucks were positioned at midspan in the same manner as they were for the loads cases examined above. Although lane loading was not originally considered for the transverse procedure in the Load Rating Manual, it was added here in order to maximize the differential displacement between the boxes. Four lanes of HL-93 lane loading of 640 lbs/ft (9.3 kN/m) each were applied along the entire length of Span 2. The total 2,560 lbs/ft (37.4 kN/m) distributed load was applied as a vertical pressure over a width of 50.66

ft (15.4 m), such that the boundary normal traction was specified as 0.35 psi (2.4 kPa). The transverse moments for this load case were only checked at midspan where the differential displacement between boxes was maximized. Vehicle loads were multiplied by an impact factor of 1.33. The multiple presence factor of 0.75 was applied to all loads, including the lane loading. The Load Rating Manual methodology for computing transverse moments as used for the previously examined load cases did not contain the information necessary for calculating the effects of lane loading and large differential deflections at Point 5'. Instead, the FEM results from this particular load case were compared to the service live-load moment capacities from the Load Rating Manual. This comparison is presented in Figure 9.18. The moments at all sections, and critically at Point 5', were below the service live-load transverse moment capacity. However, the assumption that Point 1 would control for negative moment was found to be true only if differential deflection between the boxes was ignored. Considering for differential deflection and lane loads, Point 5' controlled for negative moment.

9.3.5 Summary and Conclusions

A series of load cases were tested in a validated three-dimensional finite element model. Transverse moments in the top flange were computed using the model, and were compared to those using the methodology documented in the Load Rating Manual. It was found that the moments calculated from the Load Rating Manual were higher than those from the finite element model in sections near the webs, and similar for sections near the centerlines of the boxes of the bridge. The results showed that differential deflection between the boxes was not accounted for in the Load Rating Manual. This was not necessarily a conservative assumption for moments in the deck spanning between the boxes, so an extreme case was considered which maximized the differential deflection and the moments in the span between the boxes. Results were compared to the live-load transverse moment capacity from the Load Rating Manual. It was found that even for the extreme case, the computed moments were less than the service live-load transverse moment capacity.

9.4 Local Behavior

Specific procedures for computing local deformations and stresses of the I-35W box girder cross sections were not documented within either the original or updated Load Rating Manuals (Figg, 2008, 2012). These local behaviors were investigated in the validated three-dimensional continuum finite element model and compared to design stress limits.

9.4.1 Objective for Analyzing Local Stresses

Sections outside the top flange were not analyzed for local behavior or deformation of the cross section in the Load Rating Manual; nevertheless, investigation of other key sections was considered with the validated finite element model. Additional critical sections for local behavior included the tops of the webs where they met with the top flange, and sections at both ends of the bottom flanges. The additional critical sections for northbound and southbound Spans 1 through 3 not discussed in the Load Rating Manual but analyzed in the finite element model are presented and labeled in Figure 9.19.

As no assumptions were presented in the Load Rating Manual concerning these locations, it was decided to check the stress values at these critical points under particular load conditions with respect to design stress limits. These stress limits were documented in the as-built drawings for Bridges 27409 and 27410 (Minnesota Department of Transportation, 2008). The allowable transverse tension at the service limit state was specified as $0.0948\sqrt{f'_c}$, where f'_c is specified in ksi. For superstructure concrete with 6.5 ksi strength, this transverse tensile limit was 240 psi (1.7 MPa). This transverse tensile limit was also applied to the webs, for which the behavior under investigation was out-of-plane bending of the webs, and the

critical stresses were the vertical axial stresses on the interior and exterior faces of the web. The compression limit for all points was specified as $0.45f'_c$ for dead and permanent loads only, or $0.6\varphi_w f'_c$ for cases including transient loads, where φ_w is the section shape factor defined in Section 5.7.4.7 in the AASHTO LRFD specifications (2010). The shape factor was conservatively assumed to be equal to 0.75 (the minimum specified in the AASHTO LRFD), so that the compressive limit was 2920 psi (20.2 MPa) both for permanent loading cases and transient loading cases.

These design stress limits were checked under dead loads and post-tensioning and the live load cases presented in Figure 9.11 from Section 9.3. Post-tensioning amounts applied in the model were assumed to be equal to the strand forces just after immediate losses upon release, using design jacking forces from the Erection Manual (Figg 2008) and computed immediate losses according to ACI 318-08. Load Cases 1/4, 2, 3/8, 5, 6/7 and the load case maximizing differential displacement between the two boxes used for checking the transverse design were similarly applied towards investigation of the local behaviors not documented in the Load Rating Manual. These load cases are documented in Figures 9.11 and 9.17. Vehicle placement was near midspan (station = 221+37.4) or the south quarter span (station = 219+81.9) of Span 2. HL-93 trucks were positioned so that the center axle was located on the documented station. The permit vehicle was positioned such that the center axle of the first set of 10-kip (44-kN) loads (that is, the set of 10-kip (44-kN) loads nearest the 7.5-kip (33-kN) front axle loads) was located on the documented station. Loads were modified by the appropriate multiple presence factors and a dynamic impact factor of 1.33.

9.4.2 Modeling

The three-dimensional finite element model was used to investigate local behavior where the webs met the top flange, and in the bottom flanges. Section 4.1 and Chapter 6 discuss the model description and validation.

9.4.3 Results

For sections in the web, vertical axial stresses were computed at the interior and exterior web faces. For sections in the bottom flange, transverse stresses were computed on the top and bottom faces. Stresses at these critical sections at midspan and quarter span are documented in Tables 9.4 and 9.5, respectively. The "PT+DL Only" load case represents the stresses caused by application of the dead load, longitudinal post-tensioning, and transverse post-tensioning in the top flange. Post-tensioning forces were taken as the values at release considering for immediate losses. The stresses recorded for each load case reflect the combination of the dead loading plus the vehicle loads with the appropriate impact and multiple presence factors applied.

For bottom flange stresses, the transverse tensile stress limit of 242 psi (1.7 MPa) was not exceeded for any of the locations in the bottom flanges for the examined load cases. However, the transverse tensile stress limit was exceeded in at least one of the webs at midspan under load cases 2 (maximum vertical axial stress of 273.6 psi (1.88 MPa)), 3/8 (351.3 psi (2.42 MPa)), 5 (358.6 psi (2.47 MPa)), 6/7 (312.2 psi (2.15 MPa)), and the maximum differential deflection case (391.8 psi (2.70 MPa)). This limit was exceeded in at least one of the webs for the quarter span loading under load cases 2 (370.0 psi (2.55 MPa)), 3/8 (407.9 psi (2.81 MPa)), 5 (420.4 psi (2.90 MPa)), and 6/7 (326.0 psi (2.25 MPa)).

Considering the less restrictive limit listed in Table 5.9.4.2.2.1 of the AASHTO LRFD Bridge Design Specifications (2010) for stresses in other areas with sufficient bonded steel in segmentally constructed bridges, the allowable tensile stress in the web could be increased to $0.19\sqrt{f'_c}$, where f'_c is specified in ksi. For 6.5 ksi (45 MPa) concrete, this limit was equal to 484 psi (3.34 MPa). This limit was equal to

the service limit for Class U structures in two-way bending as specified in ACI 318-08, for which the maximum allowable tensile stress is $6\sqrt{f_c'}$, where f'_c is specified in psi. Vertical axial stresses in the web satisfied this limit for all examined load cases.

All compressive stresses throughout the midspan and quarter span sections (including points not discussed here) were well below the compressive limit of 2925 psi (20.2 MPa).

9.4.4 Summary and Conclusions

Although not specifically discussed in the Load Rating Manual, the validated finite element model was also used to check vertical stresses in webs caused by out-of-plane bending and transverse stresses in the bottom flange. The same load cases considered for the top flange bending were applied to assess the stresses in these remaining cross-sectional elements. Computed stresses were compared to service stress limits prescribed in the as-built drawings. It was found that the bottom flange stresses always met the service tensile limits. However, the vertical axial stresses in the webs were found to exceed the tensile stress limits found in the as-built drawings. These stresses, however, did meet the criteria specified in Table 5.9.4.2.2-1 of the AASHTO LRFD Bridge Design Specifications (2010) for stresses in other areas with sufficient bonded steel in segmentally constructed bridges. All locations were found to meet the compressive stress limits.

Because the bridge did not contain post-tensioning in the vertical direction, it is more meaningful to consider the structure as a mildly reinforced member in the vertical direction. Therefore, some controlled cracking would be expected in order to engage the mild steel reinforcement. Per discussion with Figg Bridge Engineers, Inc., the bending of the webs was considered under this assumption, and ample mild reinforcement was provided for the combined effects of bending, shear, and torsion.

9.5 Torsion and Shear Behavior

The two-dimensional and three-dimensional finite element models, validated with static truck test data, were used to investigate the behavior of the I-35W box girders in shear and torsion. The two-dimensional model was used to compute shear influence lines and envelopes, while the three-dimensional model was used to compute torsional effects and the distribution of shear between the boxes. In the original Load Rating Manual (Figg, 2008), torsion was considered as a distribution of the shear stresses in the webs of the boxes. The load cases presented in Section 9.3 were investigated with the finite element models, and the shear forces in the webs were compared to those obtained from the original Load Rating Manual procedure. The updated Load Rating Manual (Figg, 2012) used a completely different methodology for shear and torsion behavior. Comparison of the new methodology presented in the updated Load Rating Manual with the finite element models was out of scope of the University of Minnesota project.

9.5.1 Original Load Rating Manual Methodology for Computing Shear and Torsion

The shear and torsion procedure was described in Chapter 3 of the original Load Rating Manual (Figg, 2008). This chapter considered the vertical (bending) shear and torsion together. Vertical shear forces were assumed to be divided equally among the webs of the loaded box. Torsion was considered as an addition or subtraction of shear force in each web of the loaded box based on the eccentricity of the load relative to the centerline of the box. An inherent assumption in the methodology was that only the loaded box carried shear and torsion, with no shear or torsion being transferred to the unloaded box.

In both versions of the Load Rating Manual (Figg, 2008, 2012), shear forces were only investigated in the webs; vertical shearing of the deck in transverse bending, horizontal shearing of the top and bottom

flanges in torsion, and other shear forces resulting from deformation of the boxes were not considered. From three-dimensional modeled results (discussed in Sections 9.5.3 and 9.5.4), these other shear forces were observed with magnitudes less than 100 psi (0.7 MPa) for all examined load cases.

Vertical (bending) shear forces at a critical section due to vehicle loads anywhere on the structure were calculated from the shear influence diagrams provided in the Load Rating Manual (Figg, 2008). The provided influence lines were assumed to be undistributed, meaning that only the total sectional shear forces were reported and the lane in which the load was located and the manner of distribution of the shear between the boxes was irrelevant. These shear influence lines were compared to two-dimensional finite element model results in much the same manner as were moment influence lines in Section 9.1.1. The same sections selected for comparison of moment influence lines, as shown in Figure 9.1, were used for comparison of shear influence lines. Instead of computing the longitudinal section forces, the shear section force in the x-y (longitudinal-vertical) plane was output. Similar to the longitudinal axial section forces, the shear section resultant forces were also provided as the shear stress multiplied by the shell thickness and output at the centroid of each element. In order to calculate the total shear force through the section, the shear section resultant force for each element was multiplied by the length of that element in the vertical direction, and then summed over all elements in the section. The FEM shear influence lines are compared to those found in the original Load Rating Manual (Figg, 2008) in Figure 9.20.

Shear envelopes for HL-93, light-rail, and potential pedestrian bridge loadings were provided in the original Load Rating Manual (Figg, 2008). The approximate HL-93 shear envelope was calculated using the two-dimensional finite element model. A lane load of 0.64 kips/ft (9.3 kN/m) as prescribed by AASTHO LRFD Section 3.6.1.2.4 was patterned to generate the maximum positive and negative shear for each location. A vertical point load of 72 kips (320 kN) (a conservative assumption, as explained for the moment envelope in Section 9.1.1) was also applied at the location that would cause the maximum positive or negative shear. The HL-93 shear envelope provided in the original Load Rating Manual represented a single lane of loading with the dynamic impact factor of 1.33 included for both the vehicle load and the lane load. This disagrees with AASHTO LRFD (2010) Section 3.6.2.1; the impact factor is not traditionally applied to lane loading. The shear envelopes as provided in the original Load Rating Manual were given in terms of shear force per web, for which the total shear was divided equally among all four webs of the section. However, Section 3.2 of the original Load Rating Manual specified that the total shear should have been divided between two webs in Spans 1 through 3. This was because shear and torsion effects were assumed to be carried only by the loaded box, and thus only two webs could contribute to carrying the shear stresses. Despite these inconsistencies in the original Load Rating Manual, the FEM envelope was generated such that the resulting FEM envelope and Load Rating Manual envelope were comparable. For the FEM envelope, both the lane load and the vehicle load were multiplied by the dynamic impact factor of 1.33, and the total shear was divided among all four webs to remain consistent with the Load Rating Manual envelopes. The comparison of the Load Rating Manual HL-93 live load shear envelope and the FEM results incorporating the inconsistencies as listed above, namely the application of the impact factor to both the lane load and vehicle load and the division of the shear among all four webs in the section, is shown in Figure 9.21. The comparison of the FEM results using assumptions consistent with AASHTO LRFD (2010), namely that the impact factor was not used with the lane loading and that the total shear was only divided between two webs instead of all four, and the HL-93 shear envelope as provided in the original Load Rating Manual is shown in Figure 9.22.

As shown in Figure 9.21, when comparable assumptions were made, the finite element model predicted nearly identical results to those presented in the original Load Rating Manual (Figg, 2008). However, as shown in Figure 9.22, applying assumptions consistent with the AASHTO LRFD (2010) and Section 3.2 of the Load Rating Manual to the FEM shear envelope yielded results 50% to 100% higher than what was provided in the Load Rating Manual.

Using the original Load Rating Manual methodology (Figg, 2008), shear forces in the webs were calculated as a combination of vertical shear and torsion. Total vertical shear was calculated from the shear influence diagrams and envelopes in accordance with the desired loading, and was divided equally among the webs of the loaded boxes. The torsion caused by a given load was assumed to be equal to the associated vertical shear force contribution at the investigated section (that is, the same value calculated from the corresponding shear influence diagram or envelope for the load in question, as described above) multiplied by the eccentricity of the load from the centerline of the loaded box. For vehicle loading, the eccentricity was measured to the center of the vehicle and not for each individual tire or point load. The sign convention for eccentricity used in the original Load Rating Manual is presented in Figure 9.23. The torsion was converted to a vertical web shear by the equation found in Step 6 of Section 3.2 of the original Load Rating Manual:

$$V^{T}_{web} = \pm V_{web}\, e\, \alpha\, n_w \qquad (9\text{-}1)$$

where V^{T}_{web} was the web shear cause by torsion, V_{web} was the vertical shear force contribution per web at the investigated section due to the load in question, e was the eccentricity of the load from the centerline of the loaded box, α was a sectional property of the investigated section listed in Table 3.1 of the original Load Rating Manual (a discussion of the derivation and inconsistencies of α as presented in the Load Rating Manual is provided in Section 9.5.2), and n_w was the number of webs per box at the investigated section (a necessary term only because the shear V_{web} was given as the shear per web).

The dynamic impact factor of 1.33 for vehicle loads and the appropriate multiple presence factor, as documented in Table 9.3 were included in both the torsion and vertical shear estimates.

Regarding the service live load shear force capacity of the webs, the original Load Rating Manual assumed a maximum principal tensile stress at the neutral axis equal to $0.1107\sqrt{f'_c}$, where f'_c was specified in ksi. This tensile limit was 280 psi (1.9 MPa) for design 28-day concrete strength of 6.5 ksi (45 MPa). This was equivalent to the principal stress limit for web shear cracking in ACI 318-08 equal to $3.5\sqrt{f'_c}$, where f'_c was in psi. After accounting for dead loads and post-tensioning, the remaining available shear stress for live load capacity was calculated using Mohr's circle. The Load Rating Manual methodology then converted the remaining shear stress to an allowable service shear force V using the equation for vertical shear in bending:

$$V = \frac{\tau I b}{Q} \qquad (9\text{-}2)$$

where τ was the shear stress, I was the section moment of inertia, b was the section width, and Q was the first moment of the area above the location of τ. By using this equation to derive the vertical shear force, the Load Rating Manual presumed that the distribution of shear stresses through the depth of the section was parabolic, as if the total shear stress was due only to beam bending. Typically, the magnitude of the shear stress at the neutral axis is due to both vertical shear and torsion. The vertical shear distribution in beam bending along the height of the web is parabolic. However, the torsional shear flow around any closed section is constant. Therefore, if a vertical shear force V_1 (integral of the parabolic vertical shear over the web area) and torsional shear force V_2 (integral of the constant torsional shear over the web area) act along a web, the maximum shear stress in the web would be at the same location but lower in magnitude than if a single vertical shear force V_1+V_2 with parabolic stress distribution were applied. Thus, the allowable service shear force calculated by $V = \tau Ib/Q$ was less than the section capacity under some combination of vertical shear and torsion, and so calculating the allowable service shear force capacity by this method was considered conservative.

The original Load Rating Manual procedure was as follows:

1. Consider independently the loads on each box. Assume that loads in one box have no impact on the shear in the adjacent box.

2. For each load on the structure, calculate the vertical shear contribution at the section of interest using the provided influence lines (for permit vehicles) or envelopes (when available). Results computed using the influence lines were total shear forces throughout the cross section, and so needed to be divided by the number of webs per box to arrive at the shear force per web. Results derived from envelopes were previously converted to shear force per web, and required no correction (barring the noted inconsistency documented above).
3. Apply dynamic impact factor and multiple presence factor as appropriate. The resulting value is V_{web} for the specified load.
4. Apply Eqn. (9-1) above to find the torsional shear component for each load. Use the positive sign for the webs where the torsion adds to the vertical shear, and the negative sign for the webs where the torsion is opposed to the vertical shear direction. Typically, negative torsional shears will be ignored and only the critical case of positive vertical shear and positive torsional shear will be considered. Use Table 3.1 in the Load Rating Manual for calculating α (a discussion of the derivation and inconsistencies of α as presented in the Load Rating Manual is provided in Section 9.5.2).
5. For each web, sum the vertical shear and torsional shear components of all the loads.
6. Compare shear demand to shear service capacity estimated from Eqn. (9-2). Strength capacity was also presented in the rating manual, but not discussed in detail for this report.

9.5.2 Inconsistencies in the Original Load Rating Manual Methodology

Several inconsistencies in the original Load Rating Manual (Figg, 2008) prevented direct comparison between the Load Rating Manual procedure documented above and results from the finite element models. The first such inconsistency, documented in Section 9.5.1, was that the Load Rating Manual's derivation of the HL-93 envelope included the dynamic impact factor in the lane loading, and divided the resulting shear among all the webs of both boxes, rather than only the webs of a single loaded box as assumed in the development shown above. To prevent further propagation of this inconsistency throughout the checks performed in this report, all shear envelopes provided in the original Load Rating Manual were ignored and vertical shear forces for all loads were estimated directly from the provided shear influence lines, which gave the total shear force in the cross section due to the load. This total shear stress was then divided by the number of webs per box, following the assumption that the shear was carried only by the loaded box, to convert to shear force per web.

Some inconsistencies in the original Load Rating Manual first required inspection of the derivation for the shear and torsion stresses in accordance with the theory of torsion of thin-walled closed sections. According to this theory, the torsion in a cross section is given by $T = 2qA_0$, where q is the shear flow around the closed section along the centerlines of the webs and top and bottom flanges, and A_0 is the area of the closed section bounded by the centerlines of the webs and top and bottom flanges. The shear force due to torsion along a single web is equal to $V^T_{web} = q\,L_{web}$, where L_{web} is the length measured along the centerline of the web from the centerline of the top flange to the centerline of the bottom flange. Therefore, $V^T_{web} = TL_{web}/2A_0$, or equivalently $V^T_{web} = VeL_{web}/2A_0$, where V is the total vertical shear force at the section calculated from the shear influence diagrams and e is the eccentricity of the load. Combining the shear due to torsion with the vertical shear component gives the total shear force in a single web equal to

$$V_{web}^{total} = V_{web} + V_{web}^{T} = \frac{V}{n_w} \pm \frac{VeL_{web}}{2A_0} \qquad (9\text{-}3)$$

where n_w is equal to the number of webs for a single box. For convenience in comparison to Eqn. (9-1), this equation can be rewritten in terms of the vertical shear force per web, V_{web}, as follows:

$$V_{web}^{total} = V_{web} + V_{web}^{T} = V_{web} \pm \frac{V_{web} e n_w L_{web}}{2A_0} \qquad (9\text{-}4)$$

From the above derivation, it is clear from Eqn. (9-4) that the section property α defined in Eqn. (9-1) is given by $\alpha = L_{web}/2A_0$.

A similar derivation to that shown above was documented in Section 3.12 of the original Load Rating Manual (Figg, 2008), but revealed several inconsistencies. The derivation in the Load Rating Manual culminated with Eqns. (9-5) (LRM Eqn. (7)) and (9-6) (LRM Eqn. (8)) below:

$$\alpha_{LRM} = L_{web} / 2A_0 \tag{9-5}$$

$$V_{web}^{LRM} = V_{web} + V_{web}^{T} = \frac{V}{n_w}\left(V \pm e\alpha_{LRM}\right) \tag{9-6}$$

From inspection of these two equations, it was clear that although Eqn. (9-5) was consistent with its definition from the first derivation provided above, Eqn. (9-6) had several inconsistencies. First was the quadratic V term, and second was the omission of n_w from the $e\alpha$ term. It was presumed that the inconsistencies present in Eqn. (9-6) were typographical in nature, because the procedure proposed in Section 3.2 of the Load Rating Manual encountered neither of these issues. In the remainder of this report, the inconsistently presented Eqn. (9-6) was ignored, and the procedure set out by Eqns. (9-1) and (9-4) were followed instead.

Another inconsistency in the original Load Rating Manual procedure was discovered in the documentation of the torsional-section property α in Table 3.1 of the original Load Rating Manual (denoted here as $\alpha_{T3.1}$, and named as such to contrast with α_{LRM} derived in Section 3.12 of the original Load Rating Manual). From inspection of the cross section geometry from the as-built drawings (Minnesota Department of Transportation, 2008), it was discovered that $\alpha_{T3.1}$ was, at all locations, documented as L_{total}/A_0, where L_{total} was the total height of the box section. Because L_{total} was always greater than L_{web}, and by omission of the factor of two, $\alpha_{T3.1}$ was more than twice as large as those derived by $\alpha_{LRM} = L_{web}/2A_0$. Using the values from Table 3.1 in the original Load Rating Manual was therefore a conservative assumption when compared to the theory of torsion of thin-walled closed sections. In the remainder of this report, the α factor was assumed to be equal to that provided in Table 3.1 of the Load Rating Manual divided by two. This would yield a slightly conservative estimate of α, while still holding true to the assumptions of torsion of thin-walled closed sections.

Furthermore, none of the above calculations in either the theoretical derivation or the original Load Rating Manual derivation considered the increased torsional stiffness due to multiple box cells. The presented Eqns. (9-1) and (9-4) for V^{T}_{web} were correct for single-cell boxes (Spans 1 through 3) and double-cell boxes where the two cells were symmetric (southbound Span 4). However, in the three-celled sections from northbound Span 4, the two additional webs provided extra torsional rigidity and reduced the expected value of α. For the section geometries from northbound Span 4, inclusion of the extra webs in calculation of the torsional stiffness reduced the shear stresses due to pure torsion in the outer webs by approximately 5%. This difference was negligible, and ignoring the contribution of the interior webs to the torsional stiffness was conservative, so the above derivation for V^{T}_{web} was deemed acceptable for all sections of the structure.

Investigations regarding the live load shear force capacity of the webs were not directly considered beyond what was discussed for the original Load Rating Manual shear and torsion procedure presented above.

With respect to the inconsistencies in the Load Rating Manual methodology detailed above, shear and torsion values presented in the remainder of this report used the following procedure:

1. Consider independently the loads on each box. Assume that loads in one box have no impact on the shear in the adjacent box.

2. For each load on the structure, calculate the vertical shear contribution at the section of interest using the provided influence lines (ignoring the provided shear envelopes). Ensure that this shear is given as the shear force per web by dividing by the number of webs per box in the span of interest (two webs for Spans 1 through 3, three webs for southbound Span 4 and four webs for northbound Span 4).
3. Apply dynamic impact factor and multiple presence factors as appropriate. The resulting value is V_{web} for the specified load.
4. Apply Eqn. (9-1) above to find the torsional shear component for each load. Use the positive sign for the webs where the torsion adds to the vertical shear, and the negative sign for the webs where the torsion is opposed to the vertical shear direction. Use Table 3.1 in the original Load Rating Manual to determine α, but divide the result by two such that the value is consistent with Eqn. (9-5) and the theoretical development of the α factor.
5. For each web, sum the vertical shear and torsional shear components of all the loads.

9.5.3 Modeling for Combined Shear and Torsional Behavior

The three-dimensional finite element model of the southbound bridge was applied for comparison to the shear and torsion methodology presented in the original Load Rating Manual (Figg, 2008), with the proper adjustments to the methods as discussed in Section 9.5.2. Section 4.1 contains the model description and Chapter 6 contains information on validation of the model with static truck test data.

9.5.4 Results

Shear forces were calculated for the webs of the southbound structure at station 219+65.4 near the south quarter span on Span 2 using the finite element model and the methodology presented in Section 9.5.2 correcting for the inconsistencies in the original Load Rating Manual process (henceforth called the "rating" results). This station was documented in the Load Rating Manual as one of the likely critical locations for shear and torsion in the southbound structure. Load Cases 1/4, 2, 3/8, 5 and 6/7 used for checking the transverse and local behavior were applied towards investigation of shear and torsion. These load cases are documented in Figure 9.11. Vehicle placement was near midspan (station = 221+37.4) or the south quarter span (station = 219+81.9) of Span 2. HL-93 trucks were positioned so that the center axle was located on the documented station. The P413 permit vehicle was positioned such that the center axle of the first set of 10-kip (44-kN) loads (that is, the set of 10-kip (44-kN) loads nearest the 7.5-kip (33-kN) front axle loads) was located on the documented station. Loads were modified by the appropriate multiple presence factors and a dynamic impact factor of 1.33. Because comparisons between the rating methodology and the finite element model were performed only on changes in behavior due to loading, and not for absolute stress values, dead loads and post-tensioning forces were not considered in the finite element analysis.

For the rating results, the total shear forces caused by the loading were taken from the original Load Rating Manual shear influence diagram for Southbound Span 2 - Abscissa 83.5 ft, which was equivalently station 219+65.4. This influence diagram is shown in Figure 9.24. Eccentricities for each vehicle were calculated from the centerline of the loaded box to the center of the vehicle, and not for each individual wheel-line load. The α-value for calculating the torsional shear component taken from Table 3.1 of the original Load Rating Manual was equal to 0.055/ft (0.18/m) for station 219+65.4, and was halved to 0.0275/ft (0.09/m) to correct for original Load Rating Manual inconsistencies as noted in Section 9.5.2. The total shear force per web V_{web}, eccentricity e, and torsion distribution factor α were applied to Eqn. (9-1) to calculate the torsional shear force per web by the rating methodology. This torsional shear force per web was added to (or subtracted from, depending on the direction of the torsion and the web under investigation) the vertical shear force per web to estimate the total rating shear force per web.

Three-dimensional finite element shear forces were calculated by integrating the vertical shear stress over the area of each web individually. The elements in the top and bottom flanges directly above and below the webs were included in the area of integration, but all other flange elements were ignored. Shell and truss elements for modeling the prestressing strands were not able to carry shear forces by design. The results for the total shear force carried per web for the examined load cases using both the rating methodology and finite element method are tabulated in Tables 9.6 through 9.10. Figures inset into Tables 9.6 through 9.10 indicate the load configuration used to compute the tabulated results.

The rating methodology predicted the shear forces in the west (exterior) web of the exterior box and the east (exterior) web of the interior box (hereafter referred to as the exterior webs) of the southbound bridge with reasonable accuracy compared to FEM results. The rating method produced slightly conservative results in all cases except for Load Case 6/7, for which the shear forces in the west web of the exterior box were negligible anyway. The greatest absolute error between the rating and FEM shear forces in the west (exterior) web of the exterior box was 16.0 kips (71.2 kN), a relative error of approximately 6%, from Load Case 1/4 at midspan. Shear forces in the east (exterior) web of the interior box (the web furthest from any loading) were in all cases small. Due to the symmetry of the section, it would be reasonable to extend the conclusions for the west (exterior) web of the exterior box to the east (exterior) web of the interior box for load cases mirrored across the centerline of the bridge, although the concrete barrier rail on the interior edge of the bridge would likely reduce the amount of shear carried in the webs.

Upon inspection of the FEM results for the east (interior) web of the exterior box and the west (interior) web of the interior box (hereafter referred to as the interior webs) of the southbound bridge, it was found that the assumption that the shear stresses were fully carried by the loaded box in vertical shear and torsion was not substantiated. For all load cases where the load was positioned in a single box (i.e., all load cases except 6/7), the shear force computed in the east (interior) web of the exterior box using the Load Rating Manual method was effectively equal to the sum of the shear forces between both interior webs in the FEM results. For Load Case 1/4 at quarter span and Load Cases 1/4, 2 and 5 at midspan, the FEM-computed forces in the east (interior) web of the exterior box were the opposite sign from those computed using the Load Rating Manual. For Load Case 1/4 at both load positions and Load Case 2 at midspan loading, the shear force calculated in the west (interior) web of the interior box from the FEM results was greater than the shear force in the east (interior) web of the exterior box from the Load Rating Manual method.

For Load Case 6/7, representing loading between the two boxes, the rating method applied each vehicle to a single box without regard to the connectivity of the two box sections, meaning that all the shear was transferred to the box to which the load was nearest. The FEM results from Load Case 6/7 were more intuitive: the shears due to the loads between boxes were divided nearly equally between the interior webs. The division proposed by the rating results produced nearly twice the maximum shear force in any web than the FEM results.

For all the load cases tested, the maximum shear forces in each web were tabulated for both the rating methodology and FEM results. A summary of the maximum shear forces in each web over all load cases is presented in Table 9.11. In every web except for the east (exterior) web of the interior box of the southbound bridge, the maximum rating shear forces were greater than the maximum FEM shear forces. For the examined load cases, shear forces in the east (exterior) web of the interior box were much lower than those in all other webs. Furthermore, the critical load case for shear in the east (exterior) web of the interior box would be Load Case 1/4 mirrored across the centerline of the structure. This would produce stresses in the east (exterior) web of the interior box similar to those found in the west (exterior) web of the exterior box due to Load Case 1/4, stresses which were conservatively predicted by the rating methodology with respect to FEM results. The overall maximum shear force was recorded for Load Case 1/4 positioned at station 219+81.9 (south quarter span of Span 2), for which the rating method produced

287 kips (1280 kN) and the FEM yielded 271 kips (1200 kN) in the west web of the exterior box. From these results, it was concluded that the rating methodology was conservative with respect to the finite element model.

The two major inconsistencies found in the original Load Rating Manual, if applied towards the rating procedure, would have opposite effects on the shear rating estimates. The first major inconsistency concerning the construction of the HL-93 shear envelope with inconsistent application of the dynamic impact factor to lane loading and division of the shear among all webs in the section instead of only the webs of the loaded box, would overall underestimate the shear, and would thus be unconservative with respect to the rating methods discussed herein. However, the second major inconsistency, that being the amplification of the α value by more than a factor of two, would always overestimate the shear, and would thus be conservative compared to the investigated methods. Typographical inconsistencies from Eqn. (9-6) (LRM Eqn. (8)) were ignored for this exercise.

9.5.5 Updated Load Rating Manual Methodology for Computing Shear and Torsion

To address the inconsistencies in the original Load Rating Manual (Figg, 2008) as discussed in Section 9.5.2, the shear and torsion methodology was significantly modified for the updated Load Rating Manual (Figg, 2012). Similar to the changes in the moment rating procedure discussed in Section 9.1.3, the updated shear and torsion procedure incorporated load distribution between the boxes and investigated the live load strength and service shear capacities in only the exterior box.

Shear influence lines for loading in the exterior lane and its effect on the exterior box girder were included in the updated Load Rating Manual. Like the updated methodology for longitudinal moments, only the exterior box was specifically documented. The computations for live load strength and service shear capacities were effectively identical to those used for the original Load Rating Manual as discussed in Section 9.5.1.

The updated shear and torsion methodology accounted for live load distribution between the two boxes by providing shear influence lines and envelopes for loading in each individual lane and their effect on only the exterior box. Torsion in the exterior box could be computed using torsional influence lines, a new addition to the updated manual, instead of multiplying the shear by the load eccentricity. Torsional envelopes for HL-93 or other types of loading, however, were not provided. According to Section 3.12 of the updated Load Rating Manual (Figg, 2012), the influence lines and envelopes were developed using a three-dimensional finite element model.

Much like the updated moment methods, the updated shear and torsion methodology imposed several restrictions on what load cases could be considered. For example, shear and torsional influence lines were given only for the shear distributed to the exterior box due to loading in the exterior painted traffic lane. HL-93 shear envelopes, on the other hand, were developed for peak vertical (bending) shear in the exterior box due to HL-93 loading in each painted traffic lane. Additionally, “undistributed” shear envelopes were provided, for informational purposes only, for peak shear in the cross section assuming equal load distribution among all four webs for light-rail loading or HL-93 loading in an unspecified lane. A comparison between the undistributed HL-93 shear envelope in the updated Load Rating Manual and the HL-93 envelope developed from the two-dimensional model is presented in Figure 9.25. The updated manual HL-93 shear envelope was slightly conservative with respect to the FEM results, though the cause of this conservatism was unknown. “Undistributed” shear influence lines were not provided in the updated Load Rating Manual. Because the updated influence lines and envelopes were provided only for loading in the painted traffic lanes, loading on the shoulders or otherwise not in designated lanes cannot be investigated using the updated methodology.

Distribution of shear load between the boxes was explored by comparing the undistributed shear influence lines from the original manual with the updated influence lines for the effects of loading in the exterior traffic lane on the exterior box girder as taken from the updated manual. Near the location of loading, the distributed shear influence line for the exterior box only was nearly equal to that of the undistributed influence line. This implied that, near the location of loading, the loaded box carried virtually all the shear force. Far from the location of loading, the shear was divided more evenly between the two boxes.

The full updated shear and torsion procedure as presented in the updated Load Rating Manual (Figg, 2012) is performed as follows:

1. Apply permit vehicle in the exterior painted traffic lane and use influence lines to determine shear and torsion in exterior box. Presented shear and torsion influence lines in the updated manual only consider loading in the exterior painted traffic lane and its effect on the exterior box girder, and therefore other load positions for the permit vehicle cannot be explored. Influence lines are not given for loading in other lanes or for the effects of load on either the interior box girder or total section. Apply impact factor of 1.33 to the permit vehicle.
    a. The shear factors taken from the influence line are multiplied by the Resal factor, *R*. The Resal factor is a sectional property which adjusts the total shear by accounting for the arching action in the bottom flange as the section depth changes along the length of the bridge. For a prismatic section, the Resal factor is equal to 1.0. The Resal factors are found in the updated manual on the same pages as their respective influence lines, though the influence lines as plotted do not account for the correction (i.e., it must be manually incorporated by the user).
    b. The torsion factors taken from the influence lines are converted to an equivalent vertical shear component. This is accomplished by multiplying the torsion factors by L_w/A_0, where L_w is the depth of the section measured along the centerline of the web from the centerline of the top slab to the centerline of the bottom slab and A_0 in the area bounded by the centerlines of the webs and top and bottom slabs. This derivation is consistent with theoretical torsion of closed sections, as discussed in Section 9.5.2. The shear along a single web according to the theory of torsion of closed sections would be $V = TL_w/2A_0$. However, to convert this to an equivalent vertical shear applied across the entire exterior box (not just one web), this value is multiplied by two. For single-celled boxes, this assumes that the equivalent vertical shear is divided evenly between both webs of the exterior box. For multi-celled boxes, the torsional shear is assumed to be held by only the outermost webs, and therefore the multiplication by a factor of two is still allowable. This method accurately represents the maximum shear in any given web of the exterior box, though the predicted shears in each individual web may not equal those expected from the combination of shear and torsional loading.
    c. If no other loads are considered concurrently with the permit vehicle (e.g., no HL-93 lanes or LRT, etc.), then the longitudinal shear and the equivalent shear from the torsional effects are summed to compute the effective permit vehicle shear in the exterior box. If other concurrent loading is considered alongside the permit vehicle, only the longitudinal shear induced by the permit vehicle is considered, and the torsion induced by the permit vehicle is ignored. The equivalent shear from the torsional effects of the permit vehicle is excluded in this case because, due to the restrictions on vehicle positioning inherent in the updated shear and torsion procedure, the concurrent loads will always be positioned in such a way to produce opposite torsional effects from those generated by a permit vehicle in the exterior traffic lane. Therefore under load scenarios combining a permit vehicle with other concurrent loads, instead of computing the difference between the permit vehicle torsional effects and the concurrent loading torsional effects, the updated LRM methodology simplifies the computations by requiring concurrent loading torsional effects to always be added and permit vehicle torsion to be

always ignored. This is conservative assuming that the torsional effects caused by the concurrent loading are at least half the torsional effects caused by the permit vehicle in the exterior traffic lane.

2. Determine concurrent loading upon the exterior box using the provided shear envelopes and torsional factors. Impact factors have already been appropriately applied to the vehicle loading in derivation of the shear envelopes.
    a. HL-93 lanes can be applied to the painted traffic lanes B, C, D, and E (lane labeling increases alphabetically from the exterior Lane A to the interior Lane E). Separate plots are provided documenting the shear envelope for the exterior box given HL-93 loading in each individual lane.
    b. Light-rail loads have both dead load and live load shear envelopes for the exterior box girder. LRT loads can only be located in the designated LRT lane, and the presence of LRT loading excludes the use of Lane E for other loads.
    c. Proposed pedestrian bridge dead load shear envelopes are also included.
    d. To compute the effective shear at the location under investigation caused by the lane of concurrent loading, the shear values taken from the respective shear envelopes are multiplied by the appropriate torsional α-factor. These α-factors summarize the Resal and torsional effects for the given load cases as follows:

$$\alpha = R + \frac{e_{eff} L_w}{A_0} \qquad (9\text{-}7)$$

    where R is the Resal factor at the cross section under investigation, e_{eff} is the effective transverse eccentricity of the load, and L_w and A_0 are defined above and represent the sectional properties at the cross section under investigation. Note that each load case (e.g., HL-93 loading in Lane B, LRT loading, and so on) has distinct α-factors along the entire length of the structure. Therefore, the defined α-factors are associated with the one particular load case that causes the maximum effective (longitudinal plus torsional) shear at the location under investigation, and each lane of loading will have a separate α-factor. In the updated Load Rating Manual, these α-factors are tabulated individually for each shear envelope. Similar to the torsion factors used for the influence lines (part 1.b), the $e_{eff}L_w/A_0$ term contains an inherent multiplication and division by two in accordance with torsion of closed thin-walled sections and the conversion from the shear in a single web to an effective vertical shear in the box.
3. Apply load factors (for the strength limit case) and multiple presence factors as appropriate.
4. Compare the computed effective shear in the exterior box girder with the remaining live load shear capacity. Capacities are provided for both strength and service conditions.

The presented methodology addresses all the inconsistencies of the original shear and torsion rating methodology as noted in Section 9.5.2. However, as was noted for the updated methodology for longitudinal moments, the limitations on the positions of loads that can be checked using this method prevented further exploration of the method with respect to the sample load cases considered in Section 9.5.4.

9.5.6 Summary and Conclusions

A number of assumptions were employed in the methodology for the determination of shear and torsion presented in the original Load Rating Manual (Figg, 2008). It was assumed that shear and torsion were only carried by the loaded box, and that the torsion was equal to the eccentricity of the load from the centerline of the loaded box. The shear forces were divided among the webs of the loaded box by application of the theory of thin-walled closed sections in torsion. The original Load Rating Manual provided values for the sectional geometry term α that converted the total vertical shear force to torsional

shear forces in the webs. In calculating the live-load shear force capacity in a given web under service conditions, the original Load Rating Manual assumed that shear stress distribution through the depth of the web was due entirely to vertical shear forces from bending. However, the maximum vertical shear stress in a box with both bending shear and torsional shear will be due to a combination of parabolic and uniform shear stress distributions, whereas for pure bending the maximum shear stress will use only the parabolic distribution. Therefore, the original Load Rating Manual, by assuming a stress distribution associated with pure bending shear, conservatively underestimated the service live-load capacity of the webs in shear.

A number of inconsistencies were discovered in the original manual methodology. Barring trivial issues which appeared to be typographical errors, two major inconsistencies were found. First, the HL-93 shear envelope in the Load Rating Manual was developed by applying the dynamic impact factor inconsistently to lane loading and also by dividing the shear among all webs of the section, as opposed to only the webs of the loaded box. Second, the α factor as documented in Table 3.1 of the Load Rating Manual was found to be conservative by a factor greater than two. It was reasoned that the first inconsistency would cause an underestimation of the Load Rating Manual shear, and that the second inconsistency would overestimate the Load Rating Manual shear.

Correcting for these inconsistencies, the original Load Rating Manual method produced reasonable approximations for the shear force in the exterior webs, but failed to accurately calculate the shear in the interior webs. For cases of loading between the two boxes, the original manual method predicted vastly conservative maximum shears in comparison to the FEM results. However for loading in one box, and particularly for highly eccentric loading in the cantilevered top flange, the interior web forces calculated by the original rating method were neither accurate nor necessarily conservative with respect to FEM results. Despite these discrepancies, the maximum shear force per web over all webs for each of the examined load cases was greater from the original Load Rating Manual results than from the FEM method. Therefore, it was concluded that the methodology employed by the original Load Rating Manual for shear and torsion, correcting for inconsistencies, was in fact conservative.

The updated Load Rating Manual (Figg, 2012) corrected for the inconsistencies found in the original manual. Shear distribution was handled by developing influence lines or envelopes for the shear distributed to the exterior box girder due to loading in the marked traffic lanes. Similar to the updated moment procedure, the updated shear rating procedure was limited to investigation of loading specifically in designated traffic lanes, with the permit vehicle always positioned in the exterior traffic lane.

Chapter 10. Summary and Recommendations

10.1 Summary and Conclusions

The I-35W St. Anthony Falls Bridge was constructed by the joint venture of Flatiron-Manson with engineering provided by Figg Engineering Group. Construction of the bridge incorporated a "smart bridge" system, equipped with instrumentation for monitoring the behavior of the structures. The University of Minnesota (UMN) was responsible for the collection and interpretation of the data gathered by the system to better understand the behavior of post-tensioned concrete box girder structures with the potential to impact future designs.

The bridge was instrumented with over 500 sensors to collect data pertaining to structural behavior. Structural deformations were measured by a number of different instruments, including vibrating wire strain gages, resistive strain gages, and fiber optic strain gages. Temperatures in the bridge were measured by thermistors. Structural vibrations were measured by accelerometers. Linear potentiometers were located at the expansion joints to measure the overall expansion and contraction of the bridge. Sensors that monitored electrochemical activity and concrete resistivity were located in the deck to provide an indication of the potential for corrosion.

Concrete samples were tested for strength, modulus of elasticity, time-dependent properties (i.e., creep and shrinkage), and coefficient of thermal expansion. Average superstructure concrete strength among all strength tests taken at or after 28 days was found to be 7.4 ksi (51 MPa), compared to the nominal 28-day strength of 6.5 ksi (44.8 MPa). Measured modulus results were found to be, on average, about 6% less than would be predicted by AASHTO LRFD Bridge Design Specifications 5th Edition (2010) Eqn. (C5.4.2.4-1). Creep and shrinkage properties were, on whole, well predicted by the 1978 CEB/FIP Model Code recommendations.

Results from the material testing were incorporated into finite element models. Three-dimensional and two-dimensional models of the bridge were constructed in Abaqus (Dassault Systèmes, 2010) to explore the structural response associated with gravity loading, thermal effects, and dynamic effects.

Truck tests were performed on the northbound and southbound bridges to obtain baseline data which could be used over the life of the structure as a benchmark to which subsequent truck tests might be compared as a means of detecting changes in behavior. In addition, the truck tests provided data used to validate the finite element models. Static tests were performed by stationing eight loaded sand trucks in various configurations across the length of the structures. These tests were performed to investigate longitudinal deformation (shear and bending), torsional load cases, and local bending of the box cross section. Dynamic truck tests consisted of driving the same trucks across the bridge in a variety of configurations both with and without ambient traffic.

The finite element models were validated using the static truck test data. The results of the models were found to correlate well with the measured longitudinal behavior of the bridge. The three-dimensional model was also compared to the torsional, transverse, and vertical deformation measurements, and again the model accurately predicted the response of the structure. Modeled strains showed that, for some of the truck test configurations, the maximum local strains in the deck due to transverse bending of the deck and in the webs due to out-of-plane bending of the webs were of similar magnitude as the longitudinal strains produced by the test that produced the most bending (i.e., 8 trucks positioned across the width of the bridge at the center of Span 2). In the finite element results, large transverse strains were observed at the centerlines of the boxes, and in the centerline of the bridge between the two boxes. Large vertical strains were seen at the top of the box webs where they met the deck.

The finite element models were also validated with regard to environmental (thermal) effects. The largest thermal gradients measured during the first three years of monitoring were selected for validation in the model. The model was shown to well predict the thermal response of the structure. Maximum measured thermal gradients were best approximated by using the Priestley (1978) fifth-order curve and assuming a top surface temperature equal to that for solar radiation Zone 2 from the AASHTO LRFD (2010) recommendations.

The long-term strains (VWSGs) and expansion joint (LPs) measurements were examined for the first three years of data collection. It was found that the LP measurements were strongly correlated with the approximate uniform structural temperature, with deviations due to thermal gradients, rotation of the superstructure on the bearings due to uniform and gradient temperature changes, and time-dependent effects over the course of measurement. From the VWSGs, it was noted that the daily and seasonal changes in mechanical strain (i.e., strain related to changes in stress), exceeded those observed during the truck tests, implying that the thermal variations had a substantial impact on the behavior of the bridge. For example, at midspan of Span 2 under truck test STI7SB (maximizing longitudinal bending), maximum measured bottom flange strains were on the order of 55 με, whereas daily thermal changes caused variations in mechanical strain of nearly 100 με. Over the course of the monitoring, no VWSG data was clearly indicative of damage except for one gage in the northeast corner of the exterior column of southbound Pier 2, which showed signs of crack opening during the summer months. The strains associated with the potential crack were decreasing over time, implying that if a crack was present, it was closing due to the time-dependent strains in the pier.

Modal properties were computed from both ambient traffic vibrations and larger excitations induced by dynamic truck tests using the NExT-ERA/DC procedure and Fast Fourier Transforms (FFTs). The NExT-ERA/DC, although more complex and computationally less efficient than FFTs, provided information on modal frequencies, mode shapes, and damping ratios, whereas the FFT method was limited to only frequency information. Furthermore, the NExT-ERA/DC was able to successfully separate modes with similar frequencies but different mode shapes, while the FFT was very limited in this regard. Modal properties computed from the measured data were found to compare well with results from the finite element model. Damping ratios computed using the NExT-ERA/DC were found to have high standard deviation; mode shapes and modal frequencies typically had lower scatter. Modal frequency measurements from a single day typically had a coefficient of variation less than 1%, whereas damping ratio estimates had coefficients of variation ranging up to nearly 70%. The dynamic modal frequencies were found to be temperature dependent, which complicates the idealized use of modal properties as a metric for detection of structural deterioration.

The assumptions presented in the original Load Rating Manual (Figg, 2008) were examined using the finite element model. Longitudinal behavior, thermal effects, transverse bending of the top deck, local stresses throughout the cross section, and torsion and shear were all investigated. An updated Load Rating Manual (Figg, 2012) was provided with changes to the longitudinal behavior and shear and torsion. The updated methodology was not specifically investigated for this study, but a discussion of the changes and their implications has been presented.

The original Load Rating Manual procedure for longitudinal bending assumed perfect pinned and roller connections for a three-span continuous beam. The original Load Rating Manual contained no mention of distribution factors for moments between the boxes. For distribution of longitudinal moments, applying the moment only to the loaded box or using the lever rule would provide conservative estimates, though a more realistic estimate, judging from truck test data, would be to apply 70% of the moment to the loaded box and 30% to the unloaded box. The rating methodology was found to be conservative with respect to finite element results at all locations except near the expansion joints, where the finite element model results showed a small moment restraint applied by the bearing assemblies. This moment restraint was

believed to not negatively impact the rating of the bridge. The updated Load Rating Manual included methodology for distributing live load moment between the two boxes. However, the methods employed in the updated manual restricted the ability to explore any arbitrary load scenario, and allowed only for computation of specific load cases. Upon cursory examination, the live load moment distribution method presented in the updated manual agreed reasonably well with the assumption to apply 70% of the moment to the loaded box.

The finite element model was used to explore the structural response under the AASHTO LRFD (2010) design thermal gradient and the Priestley (1978) thermal gradient. As noted above, maximum measured gradients were best approximated by the Priestley fifth-order curve. For both gradient shapes with top surface temperatures scaled to the AASHTO LRFD solar radiation Zone 2 value, the fifth-order curve induced far greater tensile stresses (80% larger or 250 psi (1.7 MPa)) at the midspan of the river span than did the AASHTO LRFD bilinear gradient. For uniform temperature changes, the design expansion per degree of temperature change as listed in the I-35W Bridge Inspection and Maintenance Manual compared well with finite element predictions and measured results. The design temperature range of 150°F (83.3°C) was much larger than was observed from the instrumentation over a three-year period, and total expansion joint movements were well within the bounds predicted by this range.

The methodology presented in the Load Rating Manual for computing transverse moments in the deck was compared to results from the finite element model using a number of sample load cases. The original and updated Load Rating Manuals contained identical procedures for transverse behavior. The Load Rating Manual procedure was found to be conservative in all cases except where significant differential deflection between the boxes was predicted by the finite element model. To further investigate this scenario, the load case maximizing differential deflection between the boxes was tested in the model, and the resulting transverse moments were found to be less than the service live load transverse moment capacity of the deck.

Local stresses in the bottom flange and the web were examined in the finite element model and compared to stress limits as presented in the as-built drawings (Minnesota Department of Transportation, 2008). Stresses in the bottom flange were found to always meet the limit state for transverse bending, but stresses at the tops of the webs due to out-of-plane bending of the webs were found to exceed this limit state. However, stresses in the webs did meet the criteria specified in Table 5.9.4.2.2-1 of the AASHTO LRFD Bridge Design Specifications (2010) for stresses in other areas with sufficient bonded steel in segmentally constructed bridges. Because no vertical post-tensioning was provided, the webs for the I-35W Bridge were designed as mildly reinforced members accounting for the combination of web flexure, shear, and torsion. Thus, the webs would be expected to undergo controlled cracking in order to engage the mild steel. These checks were only investigated using post-tensioning values at release with immediate losses, and therefore might not hold for long-term post-tensioning stresses considering all losses. Investigation of post-tensioning losses was deferred for future study.

The load cases tested for transverse bending of the deck were again examined for shear and torsion of the structure. The original Load Rating Manual procedure did not necessarily accurately predict the shear forces distributed to each web for the tested load case. However, for each load case the maximum shear force among all webs as predicted by the original Load Rating Manual was larger than the maximum shear force from finite element results, and thus the rating method was deemed conservative. The shear and torsion methods employed by the updated Load Rating Manual accounted for shear distribution between the boxes. However, much like the updated methodology for longitudinal moments, the updated shear and torsion methods were restricted to examination of specific load cases.

Over the course of the monitoring and testing of the I-35W St. Anthony Falls Bridge, and through investigation of the Load Rating Manual, it was concluded that the bridge has been behaving according to expectations.

10.2 Evaluation and Recommendations for Instrumentation

The measurements collected over the three years of monitoring, with the aid of the truck tests and finite element model, provided insight regarding the relative strengths of the instrumentation systems installed in the I-35W Bridge.

For static measurements, both the vibrating wire strain gages and the SOFO fiber optic gages were used to characterize the deformation of the superstructure. It was found that both instruments provided some benefits, along with some drawbacks. Due to the long gage length of the SOFO fiber optics gages, these instruments were not feasible for collection of local deformations, such as transverse bending of the top flange or out-of-plane bending of the webs. Because these transverse and vertical strains were found to be of similar magnitudes to the longitudinal bending strains, as seen in the truck tests, instrumentation with shorter gage length (such as the VWSGs) were required to characterize all relevant aspects of the bridge response. The length of the fiber optic sensors could have been reduced to as short as 10 in. (0.25 m), but because the gage resolution was associated with a change in sensor length, the strain resolution would have dropped as the gage length decreased (e.g., a gage length of 10 in. (0.25 m) would have had a strain resolution of 8 με, which was of the same order of magnitude as the measured strains). However, the SOFO gages were versatile in that both static and dynamic data could be collected from the same gages, whereas VWSGs were limited only to static data. Although it is not specifically discussed in this report, the dynamic data from the SOFO gages can, in theory, be used with the NExT-ERA/DC procedure to characterize modal properties.

Initial strain and temperature readings (i.e., taken before the concrete pour) are required in order to compute the absolute strains, and by extension, estimate the absolute stresses. These were not available for the instrumentation installed in the I-35W St. Anthony Falls Bridge, but should be considered with high importance for future monitoring efforts.

For installing instrumentation on existing structures, both VWSG and SOFO gages could be externally mounted by drilling anchors into the concrete. In so doing, the additional temperature information gained from embedded gages would necessarily be lost. The setup used for both static and dynamic SOFO data required a computer or server to be located onsite and running continuously during collection (which could be difficult depending on the nature of the bridge site), whereas the VWSG system ran more autonomously and only required computer connection for downloading the data or changing the collection routine.

Regarding positioning of the vibrating wire gages, longitudinally-oriented gages implemented for global structural observations should be positioned to minimize local effects. If a single gage in the top flange is to be used, then it should ideally be positioned at the transverse neutral axis of the deck. Multiple longitudinal gages through the depth of the top flange, especially at the centerlines of the boxes, would provide useful information on quantifying local bending of the deck. For measurements of longitudinal curvature, gages above the webs avoid the strain profile nonlinearity seen at the centerline of the box so long as the loading is offset from the instrumentation by an adequate distance. The largest computed transverse normal strains were often located at the “midspans” of the top flange between webs or boxes, which should be high-priority positions for future instrumentation schemes. The largest computed vertical normal stresses were located just below the top flange in the interior webs of either box, and were primarily caused by out-of-plane bending of the webs. Because the walls of box girder structures are typically not post-tensioned, these tensile stresses, on the order of concrete tensile strengths, could be of

concern in some bridges. Sets of two vertically-oriented gages should be included at the top of the webs to measure this local bending behavior. The quantity of instrumented sections along the length of the southbound structure was found to be sufficient in exploring the overall behavior of the bridge, with the exception that more instrumentation near the boundary conditions, such as inclinometers, would have proved useful in capturing the restraints applied by the bearings. Additionally, inclinometers at the bearings would provide the necessary conditions for estimating the static deflection of the structure by using the strain measurements (i.e., from SOFO and VWSG sensors) along the length of the bridge. These recommendations for static instrumentation are shown graphically in Figure 10.1.

The accelerometers, despite their large range of ±2 g, were found to be able to provide serviceable data for the characterization of modal properties. The increase from 14-bit data to 16-bit data on October 20, 2009 was helpful for better characterization. It was found to be difficult to obtain higher frequency modes from the installed instrumentation, particularly local vibrations of the deck. It is unclear at this time if different methods will need to be employed to compute higher frequency modes, or if the provided accelerometers simply do not have enough resolution. However, it should be noted that the DC-component of the accelerations (i.e., the 1 g offset of the gages to measure "static" gravity acceleration and other low frequency accelerations) was unnecessary for modal analysis. Given that peak measured accelerations were on the order of 0.01 g, AC-coupled accelerometers could be used with a much smaller range than ±2 g, and would likely provide superior results.

Dynamic instrumentation was found to be sufficient for characterizing the global modal behavior. As evinced by the ability of the northbound accelerometer network, only a minimum number of accelerometers were required to characterize the lower frequency modes. However, the greater sensor density did aid in the characterization of the southbound structure. Additional sensors in the interior box of the southbound bridge (particularly at the quarter points of Span 2) would be helpful in better characterizing torsional modes. Also, higher resolution accelerometers attached to the decks would likely be useful in characterizing higher-frequency local modes.

The thermistor layout was valuable for understanding the thermal response of the structure. Because virtually all monitored quantities (e.g., strains, dynamic characteristics, longitudinal expansion) were temperature dependent, it was important to obtain accurate portrayals of the temperature distribution throughout the structure. For better characterization of thermal effects, additional thermistors through the section at other locations along the structure, particularly those with largely different cross-sectional shape from the midspan section (e.g., the diaphragms at the piers), would be useful.

The linear potentiometers were found to be valuable additions to the bridge monitoring scheme. They provided a simple measure for overall thermal elongation and time-dependent response.

The corrosion sensors did not provide data until near the end of the three years of data collection, and at the writing of this report, it was unclear whether the sensors were operating as expected.

10.3 Evaluation and Recommendations for Structural Design

Daily and seasonal environmental variations were found to have a more pronounced impact on the global behavior of the bridge than the truck tests. From measurement of the thermal gradients, it was found that measured gradients were best fit by the Priestley (1978) gradient scaled to the top surface gradient temperature equal to that for Zone 2 of the AASHTO LRFD (2010). Furthermore, the deformations and stresses produced by the scaled Priestley gradient (and by extension, the measured values) were considerably larger than those from the AASHTO LRFD (2010) design gradient. Therefore, it can be concluded that the AASHTO LRFD (2010) design gradient is not necessarily conservative for this particular structure.

The maximum daily gradients typically occurred around 2:00 PM to 4:00 PM Central Standard Time during the summer months, and would likely overlap with rush hour traffic live loading. This implies that some correlation may exist between maximum live load and maximum thermal effects. For service limit states in the AASHTO LRFD recommendations (2010), a load factor of 0.5 is applied to thermal gradient effects when simultaneously applying live load. If maximum gradients and large live loads are found to be correlated, then this factor of 0.5 might be statistically unconservative. Furthermore, because the thermal gradient effects were found to have similar maximum tensile stresses as those induced by service state vehicular live loading (and much larger impact on the structural behavior than the 400-kip truck test loadings), and because the design gradient values were realized several times within the three years of monitoring, a case could be proposed by which the controlling load scenario might be the vehicular live load multiplied by some factor less than one plus the full thermal gradient. However, further statistical investigation regarding this topic is warranted before load factor design recommendations can be provided. Specifically, it cannot be necessarily concluded that the critical live loads occur during rush hour traffic. Furthermore, because the service design live loads for the I-35W Bridge included significant conservative assumptions, it is highly likely that for this bridge the combination of the full live load plus half the AASHTO LRFD thermal gradient still produced a conservative design under service conditions. Thermal gradients are not considered under strength and extreme limit cases, and therefore this discussion is only applicable to the service limit state.

Local stresses due to out-of-plane bending of the webs were found to be significant, with magnitudes nearing the tensile strength of concrete. Under the load cases considered in the finite element model, the transverse tensile stress limit of $0.0948\sqrt{f_c'}$, where f'_c is specified in ksi, was regularly exceeded. As box girders are not typically post-tensioned in the vertical direction, it would be expected that these stresses might cause cracking of the webs. For the design of the I-35W St. Anthony Falls Bridge, the webs were considered as mildly reinforced members and contained sufficient mild steel reinforcement to account for bending, shear, and torsion.

References

1. ACI Committee 209 (1992). *ACI 209R-92 Prediction of Creep, Shrinkage, and Temperature Effects in Concrete Structures*, American Concrete Institute, Detroit, MI.
2. American Association of State Highway and Transportation Officials (1989). *AASHTO Guide Specifications for Thermal Effects in Concrete Superstructure*, Washington, DC.
3. American Association of State Highway and Transportation Officials (1994). *AASHTO LRFD Bridge Design Specifications*, First Edition, Washington, DC.
4. American Association of State Highway and Transportation Officials (1998). *Guide Specifications for Design and Construction of Segmental Concrete Bridges*, Proposed Second Edition, Washington, DC.
5. American Association of State Highway and Transportation Officials (2007). *AASHTO LRFD Bridge Design Specifications*, Fourth Edition, Washington, DC.
6. American Association of State Highway and Transportation Officials (2010). *AASHTO LRFD Bridge Design Specifications*, Fifth Edition, Washington, DC.
7. American Concrete Institute (2008). *Building Code Requirements for Structural Concrete (ACI 318-08) and Commentary*, Second Printing, Farmington Hills, MI.
8. ASTM International (2002). *C469 Standard Test Method for Static Modulus of Elasticity and Poisson's Ratio of Concrete in Compression*, West Conshohocken, PA.
9. ASTM International (2002). *C512 Standard Test Method for Creep of Concrete in Compression*, West Conshohocken, PA.
10. ASTM International (2004). *C496/C496M Standard Test Method for Splitting Tensile Strength of Cylindrical Concrete Specimens*, West Conshohocken, PA.
11. ASTM International (2009). *C39/C39M Standard Test Method for Compressive Strength of Cylindrical Concrete Specimens*, West Conshohocken, PA.
12. Bažant, Z.P., Yu, Q., and Li, G.-H., (2009). *Excessive long-time deflections of prestressed box girders. Structural Engineering Report No. 09-12/ITI*, Infrastructure Technology Institute, Northwestern University.
13. Comité Euro-International du Béton (CEB) and the Fédération International de la Précontrainte (FIP) (1978). *CEB-FIP model code 1978.*
14. Dassault Systèmes (2010). "Eigenvalue extraction," *Abaqus Theory Manual*, version 6.10.
15. Dassault Systèmes (2010). Abaqus version 6.10, *SIMULIA*. Providence, RI.
16. R.T. Davis, M.K. Thompson, B.A. Wood, J.E. Breen, and M.E. Kreger (1999). *Measurement-Based Performance Evaluation of a Segmental Concrete Bridge*, FHWA Report 1404-3F, Center for Transportation Research, University of Texas at Austin.
17. Figg Bridge Engineers (2008). *I-35W St. Anthony Falls Bridge Inspection and Maintenance Manual*.
18. Figg Bridge Engineers (2008). *I-35W St. Anthony Falls Bridge Load Rating Manual*. Original version.
19. Figg Bridge Engineers (2008). *St. Anthony Falls (I-35W) Bridge Erection Manual*, Figg Project Number 1665.
20. Figg Bridge Engineers (2012). *I-35W St. Anthony Falls Bridge Load Rating Manual*. Updated version.
21. Geokon (2004). *Installation Manual: Models VCE-4200/4202/4210 Vibrating Wire Strain Gages*, Lebanon, New Hampshire, USA.
22. R.A. Imbsen, D.E. Vandershaf, R.A. Schamber, and R.V. Nutt (1985). *Thermal effects in concrete bridge superstructures. NCHRP Report 276*, Transportation Research Board, National Research Council, Washington, DC.
23. G.H. James, T.G. Carne, and J.P. Lauffer (1993). *The natural excitation technique (NExT) for modal parameter extraction from operating wind turbines. SAND 92-1666*, Sandia National Laboratories, Albuquerque, NM.

24. J.-N. Juang, and R.S. Pappa (1985). “An eigensystem realization algorithm for modal parameter identification and model reduction,” *Journal of Guidance, Control, and Dynamics*, Vol. 8, No. 8, pp. 620-627.
25. J.-N. Juang, J.E. Cooper, and J.R. Wright (1988). “An eigensystem realization algorithm using data correlations (ERA/DC) for modal parameter identification,” *Control-Theory and Advanced Technology*, Vol. 4, No. 1, pp. 5-14.
26. J.-T. Kim (2004). "Thermal effects on modal properties and frequency-based damage detection in plate-girder bridges." *Proceedings of SPIE--the international society for optical engineering*, Vol. 5391, pp. 400-409, San Diego, CA.
27. Minnesota Department of Transportation (2008). *As-built Construction Plan for Bridge Nos. 27409 and 27410*, St. Paul, MN.
28. Minnesota Department of Transportation (2008). *Saint Anthony Falls Bridge Stressing Summary 35W*, St. Paul, MN.
29. R.D. Nayeri, F. Tasbihgoo, M. Wahbeh, J.P. Caffrey, S.M. Masri, J.P. Conte, and A. Elgamal (2009). “Study of time-domain techniques for modal parameter identification of a long suspension bridge with dense sensor arrays,” *Journal of Engineering Mechanics*, Vol. 135, No. 7, pp. 669-683.
30. R.S. Pappa, and K.B. Elliott. (1993), “Consistent-mode indicator for the eigensystem realization algorithm,” *Journal of Guidance, Control, and Dynamics*, Vol. 16, No. 5, pp. 852-858.
31. B. Peeters, J. Maeck, and G. De Roeck (2001). “Vibration-based damage detection in civil engineering: excitation sources and temperature effects,” *Smart Materials and Structures*, Vol. 10, pp. 518-527.
32. W. Podolny and J.M. Muller (1982). *Construction and Design of Prestressed Concrete Segmental Bridges*, John Wiley and Sons, New York.
33. I.C. Potgieter, and W.L. Gamble, (1983). *Response of highway bridges to nonlinear temperature distributions*, Report No. FHWA/IL/UI-201, University of Illinois at Urbana-Champaign.
34. M.J.N. Priestley (1978). “Design of concrete bridges for temperature gradients,” *ACI Journal*, Vol. 75, No. 5, pp. 209-217.
35. R.J. Watson, Inc. (2008). *St. Anthony Falls (I-35W) Bridge Replacement Project No. S.P.2783-120, E.R.MN07(300)*. Amherst, NY.
36. C.L. Roberts, J.E. Breen, and M.E. Kreger (1993). *Measurement Based Revisions for Segmental Bridge Design and Construction Criteria*, FHWA Report 1234-3F, Center for Transportation Research, University of Texas at Austin.
37. C.L. Roberts-Wollman, J.E. Breen, and J. Cawrse (2002). “Measurements of thermal gradients and their effects on segmental concrete bridge,” *Journal of Bridge Engineering*, Vol. 7, No. 3, pp. 166-174.
38. Roctest (2006). *Instruction Manual: Embedded Strain Gage Model EM-5*, Saint-Lambert, Quebec, Canada.
39. K.W. Shushkewich (1998). “Design of segmental bridge for thermal gradient,” *PCI Journal*, Vol. 43, No. 4, pp. 120-137.
40. H. Sohn, M. Dzwonczyk, E.G. Straser, A.S. Kiremidjian, K.H. Law, T. Meng (1999). “An experimental study of temperature effect on modal parameters of the Alamosa Canyon Bridge,” *Earthquake Engineering and Structural Dynamics*, Vol. 28, pp. 879-897.
41. M.K. Thompson, R.T. Davis, J.E. Breen, and M.E. Kreger (1998). *Measured behavior of a curved precast segmental concrete bridge erected by balanced cantilevering*, FHWA Report 1404-2, Center for Transportation Research, University of Texas at Austin.

Tables

Table 1.1: Casting and erection dates of the precast segments

NB Bridge West Box Segment	Concrete Placed Segment	Segment Erected	Age at Erection (days)	Segment Weight (kips)
1'-6" CLOSURE	6/10/2008			
3NB-1	3/27/2008	6/5/2008	70	378.6
3NB-2	4/5/2008	6/16/2008	72	357.2
3NB-3	4/16/2008	6/18/2008	63	336.4
3NB-4	4/21/2008	6/21/2008	61	316.5
3NB-5	4/26/2008	6/22/2008	57	361.5
3NB-6	4/30/2008	6/25/2008	56	336.2
3NB-7	5/5/2008	6/26/2008	52	314.2
3NB-8	5/8/2008	6/28/2008	51	296.3
3NB-9	5/12/2008	6/29/2008	48	283.6
3NB-10	5/15/2008	6/30/2008	46	286.3
3NB-11	5/20/2008	7/1/2008	42	281.8
3NB-12	5/24/2008	7/2/2008	39	292.8
3NB-13	5/30/2008	7/3/2008	34	269.9
3NB-14	6/3/2008	7/4/2008	31	267.6
3NB-15	6/5/2008	7/5/2008	30	213.8
CLOSURE	7/16/2008			
2NB-15	5/3/2008	7/3/2008	61	378.6
2NB-14	4/30/2008	7/2/2008	63	357.2
2NB-13	4/25/2008	6/28/2008	64	336.4
2NB-12	4/19/2008	6/27/2008	69	316.5
2NB-11	4/14/2008	6/26/2008	73	361.5
2NB-10	4/10/2008	6/19/2008	70	336.2
2NB-9	4/7/2008	6/17/2008	71	314.2
2NB-8	4/1/2008	6/15/2008	75	296.3
2NB-7	3/27/2008	6/14/2008	79	283.6
2NB-6	3/24/2008	6/12/2008	80	286.3
2NB-5	3/19/2008	6/9/2008	82	281.8
2NB-4	3/17/2008	6/7/2008	82	292.8
2NB-3	3/10/2008	6/4/2008	86	269.9
2NB-2	3/1/2008	6/1/2008	92	267.6
2NB-1	2/19/2008	5/26/2008	97	213.8
1'-6" CLOSURE	5/30/2008			

NB Bridge East Box Segment	Concrete Placed Segment	Segment Erected	Age at Erection (days)	Segment Weight (kips)
1'-6" CLOSURE	6/10/2008			
3NB-1	4/2/2008	6/5/2008	64	378.6
3NB-2	4/10/2008	6/16/2008	67	357.2
3NB-3	4/17/2008	6/18/2008	62	336.4
3NB-4	4/23/2008	6/21/2008	59	316.5
3NB-5	4/29/2008	6/22/2008	54	361.5
3NB-6	5/2/2008	6/25/2008	54	336.2
3NB-7	5/6/2008	6/26/2008	51	314.2
3NB-8	5/9/2008	6/28/2008	50	296.3
3NB-9	5/14/2008	6/29/2008	46	283.6
3NB-10	5/17/2008	6/30/2008	44	286.3
3NB-11	5/21/2008	7/1/2008	41	281.8
3NB-12	5/28/2008	7/2/2008	35	292.8
3NB-13	5/31/2008	7/3/2008	33	269.9
3NB-14	6/4/2008	7/4/2008	30	267.6
3NB-15	6/6/2008	7/5/2008	29	213.8
CLOSURE	7/16/2008			
2NB-15	5/2/2008	7/3/2008	62	378.6
2NB-14	4/29/2008	7/2/2008	64	357.2
2NB-13	4/25/2008	6/28/2008	64	336.4
2NB-12	4/17/2008	6/27/2008	71	316.5
2NB-11	4/12/2008	6/26/2008	75	361.5
2NB-10	4/8/2008	6/19/2008	72	336.2
2NB-9	4/5/2008	6/17/2008	73	314.2
2NB-8	3/29/2008	6/15/2008	78	296.3
2NB-7	3/26/2008	6/14/2008	80	283.6
2NB-6	3/21/2008	6/12/2008	83	286.3
2NB-5	3/18/2008	6/9/2008	83	281.8
2NB-4	3/12/2008	6/7/2008	87	292.8
2NB-3	3/6/2008	6/4/2008	90	269.9
2NB-2	2/26/2008	6/1/2008	96	267.6
2NB-1	2/14/2008	5/25/2008	101	213.8
1'-6" CLOSURE	5/30/2008			

SB Bridge West Box Segment	Concrete Placed Segment	Segment Erected	Age at Erection (days)	Segment Weight (kips)
1'-6" CLOSURE	6/18/2008			
3SB-1	3/26/2008	6/16/2008	82	378.6
3SB-2	4/4/2008	6/21/2008	78	357.2
3SB-3	4/18/2008	6/22/2008	65	336.4
3SB-4	4/18/2008	6/23/2008	66	316.5
3SB-5	4/23/2008	6/24/2008	62	361.5
3SB-6	4/29/2008	6/25/2008	57	336.2
3SB-7	5/5/2008	6/29/2008	55	314.2
3SB-8	5/7/2008	7/1/2008	55	296.3
3SB-9	5/10/2008	7/4/2008	55	283.6
3SB-10	5/14/2008	7/5/2008	52	286.3
3SB-11	5/19/2008	7/6/2008	48	281.8
3SB-12	5/23/2008	7/7/2008	45	292.8
3SB-13	5/30/2008	7/8/2008	39	269.9
3SB-14	6/1/2008	7/9/2008	38	267.6
3SB-15	6/4/2008	7/10/2008	36	261.3
CLOSURE	7/24/2008			
2SB-15	5/3/2008	7/9/2008	67	378.6
2SB-14	4/30/2008	7/8/2008	69	357.2
2SB-13	4/25/2008	7/7/2008	73	336.4
2SB-12	4/21/2008	7/6/2008	76	316.5
2SB-11	4/15/2008	6/28/2008	74	361.5
2SB-10	4/11/2008	6/19/2008	69	336.2
2SB-9	4/7/2008	6/17/2008	71	314.2
2SB-8	4/2/2008	6/16/2008	75	296.3
2SB-7	3/28/2008	6/14/2008	78	283.6
2SB-6	3/25/2008	6/13/2008	80	286.3
2SB-5	3/20/2008	6/11/2008	83	281.8
2SB-4	3/15/2008	6/9/2008	86	292.8
2SB-3	3/11/2008	6/7/2008	88	269.9
2SB-2	3/5/2008	6/3/2008	90	267.6
2SB-1	2/21/2008	5/29/2008	98	261.3
1'-6" CLOSURE	6/1/2008			

SB Bridge East Box Segment	Concrete Placed Segment	Segment Erected	Age at Erection (days)	Segment Weight (kips)
1'-6" CLOSURE	6/18/2008			
3SB-1	3/29/2008	6/16/2008	79	378.6
3SB-2	4/9/2008	6/21/2008	73	357.2
3SB-3	4/16/2008	6/22/2008	67	336.4
3SB-4	4/21/2008	6/23/2008	63	316.5
3SB-5	4/28/2008	6/24/2008	57	361.5
3SB-6	5/1/2008	6/25/2008	55	336.2
3SB-7	5/6/2008	6/29/2008	54	314.2
3SB-8	5/9/2008	7/1/2008	53	296.3
3SB-9	5/13/2008	7/4/2008	52	283.6
3SB-10	5/16/2008	7/5/2008	50	286.3
3SB-11	5/20/2008	7/6/2008	47	281.8
3SB-12	5/27/2008	7/7/2008	41	292.8
3SB-13	5/31/2008	7/8/2008	38	269.9
3SB-14	6/3/2008	7/9/2008	36	267.6
3SB-15	6/5/2008	7/10/2008	35	261.3
CLOSURE	7/24/2008			
2SB-15	5/1/2008	7/9/2008	69	378.6
2SB-14	4/28/2008	7/8/2008	71	357.2
2SB-13	4/25/2008	7/7/2008	73	336.4
2SB-12	4/18/2008	7/6/2008	79	316.5
2SB-11	4/14/2008	6/28/2008	75	361.5
2SB-10	4/9/2008	6/19/2008	71	336.2
2SB-9	4/5/2008	6/17/2008	73	314.2
2SB-8	3/31/2008	6/16/2008	77	296.3
2SB-7	3/27/2008	6/14/2008	79	283.6
2SB-6	3/24/2008	6/13/2008	81	286.3
2SB-5	3/18/2008	6/11/2008	85	281.8
2SB-4	3/13/2008	6/9/2008	88	292.8
2SB-3	3/7/2008	6/7/2008	92	269.9
2SB-2	2/29/2008	6/3/2008	95	267.6
2SB-1	2/16/2008	5/29/2008	103	261.3
1'-6" CLOSURE	6/1/2008			

Table 1.2: Casting dates of CIP spans

Element	Casting date	Bottom flange tendons stressed	Age	Draped tendons stressed	Age
Segment 1-Bed 1	1/31/2008				
Span 1 NB Super Structure Exterior (1/3)	4/2/2008				
Span 1 NB Super Structure Interior (1/3)	4/3/2008				
Span 1 SB Super Structure (1/3) Interior	4/4/2008				
Span 1 SB Super Structure (1/3) Exterior (1/3)	4/7/2008				
Span 1 NB Superstructure (2/4) Interior Barrel	4/12/2008				
Span 1 SB Superstructure (2/4)	4/15/2008				
Span 1 NB Superstructure (3/4) Exterior Barrel	4/18/2008				
Span 1 SB Superstructure (3/4) Interior Barrel	4/21/2008				
Span 1 SB Superstructure (3/4) Exterior Barrel	4/22/2008				
Span 1 NB Superstructure (4/4)	4/24/2008	5/22/2008	28	5/25/2008	31
Span 3 NB Exterior Barrel	4/29/2008				
Span 3 NB Interior Barrel	4/30/2008				
Span 1 NB Exterior Barrel	4/30/2008				
Span 1 SB Superstructure (4/4)	5/1/2008	5/25/2008	24	5/28/2008	27
Span 3 NB Interior and Exterior Soffit and Stems (To 2nd CJ)	5/3/2008				
Pier 2 NB Diaphragm 3rd Lift	5/7/2008				
Span 1 NB Top Deck (To 1st CJ)	5/7/2008				
Pier 2 SB Diaphragm 1st Lift	5/8/2008				
Span 1 SB Top Slab (1st CJ)	5/11 and 5/12/2008				
Span 1 NB Top Slab (2nd CJ)	5/12/2008				
Span 3 NB Soffit through Pier Diaphragm	5/13/2008	6/1/2008	19	6/7/2008	25
Span 1 NB Top Slab (Final Pour)	5/16/2008	5/22/2008	6	5/25/2008	9
Pier 3 NB Diaphragm 1st Lift	5/17/2008				
Span 1 SB Deck 2nd Pour	5/18/2008				
Span 3 SB Interior Soffit and Stems (1st CJ)	5/18/2008				
Span 1 SB Top Slab Final Pour	5/19/2008	5/25/2008	6	5/28/2008	9
Span 3 SB Exterior Soffit and Stems (1st CJ)	5/20/2008				
Pier 3 NB Diphragm 2nd Lift	5/20/2008				
Pier 3 NB Diaphragm 3rd Lift	5/21/2008				
Span 3 SB Interior Stem and Soffit (2nd CJ)	5/23/2008				
Span 3 NB Top Deck to 1st CJ	5/27 and 5/28/2008				
Span 3 SB Exterior Soffit and Stems (2nd CJ)	5/29/2008				
Span 3 NB Top Deck to 2nd CJ	5/30/2008	6/1/2008	2	6/7/2008	8
Span 3 SB Interior Soffit (through diaphragm)	5/30/2008				
Span 3 SB Exterior Soffit (through diaphragm)	5/30/2008			6/19/2008	20
Pier 3 SB Diaphragm 2nd Lift	6/1/2008				
Span 3 SB Diaphragm	6/4/2008				
Span 3 SB Top Deck	6/8 and 6/9/2008				
Span 3 SB Top Deck (Final Pour)	6/12/2008			6/19/2008	7
Span 4 NB Stems and Soffit	7/17/2008				
Span 4 SB Soffit and Stems	7/24/2008				
Span 4 NB Deck	7/29/2008				
Pier 4 NB Diaphragm	7/29/2008				
Span 4 SB Top Deck	8/2/2008				
Pier 4 SB Diaphragm	8/5/2008				

Table 1.3: Load stages during construction

Date	Loading description
6/27/2008	Partial release of northbound Span 1 falsework bents 1-8, 1-7
6/28/2008	Partial release of northbound Span 1 falsework bents 1-6, 1-5
6/30/2008	Full release of northbound Span 1 falsework
7/4/2008	Partial release of northbound Span 3 falsework bents 3-1 to 3-5
7/5/2008	Full release of northbound Span 3 falsework - bent 3-6
7/4/2008	Hung Span 1 NB falsework deck (3M lbs)
7/7/2008	Lowered Span 1 NB falsework
7/8/2008	Lowered all Span 1 NB falsework
7/8/2008	Placed 60T crane and 24T alignment beams on 2NB cantilever tip
7/9/2008	Hung Span 3 NB falsework deck & poles
7/8/2008	Full release of southbound Span 1 falsework
7/9/2008	Hung Span 1 SB falsework deck (3M lbs)
7/9/2008	Full release of southbound Span 3 falsework
	Aligned NB cantilevers
	Aligned SB cantilevers
7/16/2008	Jacked NB midspan closure apart applying 1120 kips
7/24/2008	Jacked SB midspan closure apart applying 1120 kips

Table 2.1: General gage locations on the bridges

Gage Type	Gage Models	Total # of Sensors	Locations**
Vibrating wire strain gage (VWSG) and associated thermistor	Roctest EM-5 (superstructure)	139 (128*)	SB (Locs 3, 4, 5, 7, 8, 9, 14, 15); NB (Locs 3, 5, 7, 8, 9, 14, 15)
	Roctest SM-5A (superstructure)	8 (19*)	SB (Loc 6 and replacement gages)
	Geokon 4911A (pier, caisson)	40	SB (Pier 2 and Drilled Shafts 1 and 2)
	Geokon 4200 (pier)	10	SB (Pier 2)
Thermistor	Roctest Model TH-T	48	SB (Loc 7); NB (Loc 7)
Fiber optic (SOFO) sensors	SOFO Standard Deformation Sensor (13.12 ft (4 m))	12	Distributed along exterior box of Span 2, SB Bridge
Accelerometer	Kistler 8310B2	26	12 permanently installed near midspans of Spans 1, 2, and 3, both boxes of SB and NB Bridges 14 movable in exterior box of SB Bridge Span 2
Linear potentiometer (LP)	Unimeasure HX-P420	12	Span 1, Abutment 1; Span 3, Pier 4; Span 4, Pier 4; both boxes of SB and NB Bridges
Resistive strain gage	Geokon 3911A-4	24	SB (Pier 2 and Drilled Shafts 1 and 2)
Corrosion monitoring	Corsensys CS-040 corrosion current sensor	4	Near midspans of Spans 1 and 3, exterior box of SB and NB Bridges
	Corsensys CS-402 resistivity (moisture) sensor	4	Near midspans of Spans 1 and 3, exterior box of SB and NB Bridges

* Eleven (11) EM-5 gages replaced by externally mounted SM-5A on May 11, 2010 and June 18, 2010

** Refer to Figure 2.1 for Location numbers

Table 2.2: VWSG and thermistor labeling, locations, and connections

UMN Gage Name	Installation Gage #	Connection Gage #	Serial Number	Gage Type	Bridge	Location	Station	Box Girder	Multiplexer Number	Channel Number(s)	X (in)	Y (in)
VN03EBL1	1	31	114008102	EM-5	NB	3	217+01.79	Exterior	N-06	1,2	-48.0	-141.8
VN03EWL1	2	32	114008094	EM-5	NB	3	217+01.79	Exterior	N-06	3,4	-137.9	-44.0
VN03ETL1	3	33	114008110	EM-5	NB	3	217+01.79	Exterior	N-06	5,6	48.0	-10.0
VN03ITL1	4	34	114008112	EM-5	NB	3	217+01.79	Interior	N-06	7,8	46.5	-8.6
VN03IBL1	5	35	114008095	EM-5	NB	3	217+01.79	Interior	N-06	9,10	48.0	-141.8
VS03IBL1	6	102	114008099	EM-5	SB	3	217+01.79	Interior	S-13	31,32	-48.0	-150.6
VS03ITL1	7	94	114008170	EM-5	SB	3	217+04.58	Interior	S-13	15,16	-140.0	-14.3
VS03ITT1	8	100	114008161	EM-5	SB	3	217+04.58	Interior	S-13	27,28	-140.0	-4.4
VS03ITT2	9	96	114008175	EM-5	SB	3	217+04.58	Interior	S-13	19,20	-140.0	-20.1
VS03ITL2	10	99	114008187	EM-5	SB	3	217+04.58	Interior	S-13	25,26	-48.0	-3.7
VS03ETL3	11	103	114008180	EM-5	SB	3	217+04.58	Exterior	S-14	1,2	48.0	-6.0
VS03ETT1	12	104	114008182	EM-5	SB	3	217+04.58	Exterior	S-14	3,4	121.0	-2.3
VS03ETL4	13	95	114008179	EM-5	SB	3	217+04.58	Exterior	S-13	17,18	131.0	-4.6
VS03ETT3	14	105	114008158	EM-5	SB	3	217+04.58	Exterior	S-14	5,6	141.0	-4.6
VS03ETL5	15	101	114008183	EM-5	SB	3	217+04.58	Exterior	S-13	29,30	220.0	-4.7
VS03ETT4	16	106	114008180	EM-5	SB	3	217+04.58	Exterior	S-14	7,8	141.0	-19.6
VS03ETT2	17	107	114008181	EM-5	SB	3	217+04.58	Exterior	S-14	9,10	121.0	-16.8
VS03EEV2	18	98	114008189	EM-5	SB	3	217+04.58	Exterior	S-13	23,24	131.4	-35.1
VS03EEV3	19	97	114008108	EM-5	SB	3	217+04.58	Exterior	S-13	21,22	141.4	-35.1
VS03EEV1	20	87	114008121	EM-5	SB	3	217+04.58	Exterior	S-13	1,2	130.5	-79.9
VS03EEA1	21	88	114008109	EM-5	SB	3	217+04.58	Exterior	S-13	3,4	130.5	-80.1
VS03EEL1	22	89	114008122	EM-5	SB	3	217+04.33	Exterior	S-13	5,6	131.4	-76.1
VS03EBL3	23	90	114008105	EM-5	SB	3	217+04.58	Exterior	S-13	7,8	112.4	-144.6
VS03EBT3	24	91	114008115	EM-5	SB	3	217+04.58	Exterior	S-13	9,10	97.5	-147.6
VS03EBT4	25	92	114008118	EM-5	SB	3	217+04.58	Exterior	S-13	11,12	98.5	-151.1
VS03EBL2	26	93	114008106	EM-5	SB	3	217+04.25	Exterior	S-13	13,14	48.0	-152.1
VS03EBT1	27	108	114008104	EM-5	SB	3	217+04.58	Exterior	S-14	11,12	-99.0	-148.1
VS03EBT2	28	109	114008120	EM-5	SB	3	217+04.58	Exterior	S-14	13,14	-98.5	-152.1
VS03EBL1	29	110	114008098	EM-5	SB	3	217+04.58	Exterior	S-14	15,16	-108.5	-144.1
VS03ETL1	30	111	114008195	EM-5	SB	3	217+04.58	Exterior	S-14	17,18	-218.0	-5.2
VS03ETL2	31	112	114008181	EM-5	SB	3	217+04.58	Exterior	S-14	19,20	-126.0	-3.6
VS04ETL1	32	86	114008212	EM-5	SB	4	218+61.9	Exterior	S-12	9,10	2.0	-6.5
VS04EEV1	33	79	114008155	EM-5	SB	4	218+61.9	Exterior	S-11	3,4	108.2	-138.3
VS04EEA1	34	80	114008163	EM-5	SB	4	218+61.9	Exterior	S-11	5,6	107.7	-140.4
VS04EEL1	35	85	114008162	EM-5***	SB	4	218+61.9	Exterior	S-12	7,8	108.5	-136.8
VS04EBL2	36	81	114008101	EM-5	SB	4	218+61.9	Exterior	S-11	7,8	79.9	-282.1
VS04EBL1	37	78	114A10206	SM-5A**	SB	4	218+61.9	Exterior	S-11	1,2	48.0	-282.4
VS04EWV1	38	83	114008100	EM-5	SB	4	218+61.9	Exterior	S-12	3,4	-109.9	-130.8
VS04EWA1	39	82	114008160	EM-5	SB	4	218+61.9	Exterior	S-12	1,2	-109.2	-133.8
VS04EWL1	40	84	114008093	EM-5	SB	4	218+61.9	Exterior	S-12	5,6	-109.9	-130.8
VN05ETL1	92	26	114008193	EM-5	NB	5	219+09.1	Exterior	N-05	1,2	3.0	-6.0
VN05EBL1	93	27	114008103	EM-5	NB	5	219+10.1	Exterior	N-05	3,4	-3.5	-290.4
VN05EWL1	94	28	114008194	EM-5	NB	5	219+10.1	Exterior	N-05	5,6	-107.9	-141.1
VN05ITL1	95	29	114008114	EM-5	NB	5	219+09.1	Interior	N-05	7,8	-2.0	-5.8
VN05IBL1	96	30	114A10166	SM-5A**	NB	5	219+10.1	Interior	N-05	9,10	2.0	-290.4
VS05ITL1	97	74	114008154	EM-5	SB	5	218+92.4	Interior	S-10	5,6	0.0	-6.5
VS05IBL1	98	75	114008111	EM-5	SB	5	218+92.4	Interior	S-10	7,8	0.0	-291.4
VS05ETL1	99	76 (77*)	114008188	EM-5	SB	5	218+92.4	Exterior	S-10	11,12	2.5	-6.0
VS05EEL1	100	77 (76*)	114008107	EM-5	SB	5	218+92.4	Exterior	S-10	9,10	108.9	-141.1
VS05EBL1	101	72	114008245	EM-5	SB	Closure 5	218+94.40	Exterior	S-10	1,2	0.0	-299.0
VS06ETL1	102	71	114A10167	SM-5A†	SB	6	219+01.9	Exterior	S-09	15,16	-2.5	-11.5
VS06EEV1	103	68	114008078	SM-5A	SB	6	219+01.9	Exterior	S-09	9,10	108.1	-122.7
VS06EEA1	104	69	114008090	SM-5A	SB	6	219+01.9	Exterior	S-09	11,12	108.8	-119.7
VS06EEL1	105	70	114008080	SM-5A	SB	6	219+01.9	Exterior	S-09	13,14	107.4	-126.2
N/A	106	N/A	N/A	N/A	SB	6	219+01.9	Exterior	N/A	N/A	N/A	N/A
VS06EBL1	107	64	114008082	SM-5A	SB	6	219+01.9	Exterior	S-09	1,2	2.0	-231.2
VS06EWV1	108	65	114008085	SM-5A	SB	6	219+01.9	Exterior	S-09	3,4	-107.5	-125.7
VS06EWA1	109	66	114008094	SM-5A	SB	6	219+01.9	Exterior	S-09	5,6	-108.0	-123.2

* Channel wiring switched. Correct channels shown. Connection gage # in parentheses is the VW gage number in the collected data. Connection gage number before parentheses is number assigned during gage connection.

** Gage replaced and collected data was satisfactory. New gage model and gage serial number shown.

*** Thermistor does not provide readings. Strain measurements only. Never replaced.

† Gage replaced but newly collected data was not satisfactory. New gage model and gage serial number shown.

‡ Thermistor not operational. Never replaced.

@ Gage locations not consistent. Thermistors excluded from thermal gradient analysis.

Table 2.2: VWSG and thermistor labeling, locations, and connections (cont'd.)

UMN Gage Name	Installation Gage #	Connection Gage #	Serial Number	Gage Type	Bridge	Location	Station	Box Girder	Multiplexer Number	Channel Number(s)	X (in)	Y (in)
VS06EWL1	110	67	114008081	SM-5A	SB	6	219+01.9	Exterior	S-09	7,8	-106.9	-128.2
VN07ETL1	111	21	114008217	EM-5	NB	7	221+54.4	Exterior	N-04	1,2	0.0	-6.0
TNEEA003	112	1	133008103	THT	NB	7	221+54.4	Exterior	N-04	12	120.9	-80.2
TNEEA002	113	2	133008068	THT	NB	7	221+54.4	Exterior	N-04	14	126.0	-79.7
TNEEA001	114	3	133008081	THT	NB	7	221+54.4	Exterior	N-04	16	130.4	-79.2
TNEBA003	115	4	133008066	THT	NB	7	221+54.4	Exterior	N-04	18	-2.0	-128.2
TNEBA002	116	5	133008086	THT	NB	7	221+54.4	Exterior	N-04	20	-1.0	-130.7
TNEBA001	117	6	133008062	THT	NB	7	221+54.4	Exterior	N-04	22	-2.0	-133.2
VN07EBL1	118	22	114008216	EM-5	NB	7	221+54.4	Exterior	N-04	3,4	12.0	-133.2
VN07EWL1	119	23	114A10203	SM-5A**	NB	7	221+54.4	Exterior	N-04	5,6	-130.2	-40.2
VN07ITL1	120	24	114008247	EM-5	NB	7	221+54.4	Interior	N-04	7,8	-12.0	-5.0
VN07IBL1	121	25	114008229	EM-5	NB	7	221+54.4	Interior	N-04	9,10	0.0	-131.7
VS07ITL4	122	53	114008230	EM-5	SB	7	221+39.4	Interior	S-08	1,2	0.0	-5.5
TSITB001	123	1	133008087	THT	SB	7	221+39.4	Interior	S-04	2	0.0	-2.0
TSITB002	124	2	133008060	THT‡	SB	7	221+39.4	Interior	S-04	4	0.0	-3.5
TSITB003	125	3	133008104	THT	SB	7	221+39.4	Interior	S-04	6	0.0	-5.0
TSITB004	126	4	133008056	THT	SB	7	221+39.4	Interior	S-04	8	0.0	-6.9
TSITB005	127	5	133008069	THT‡	SB	7	221+39.4	Interior	S-04	10	0.0	-7.8
TSITB006	128	6	133008100	THT‡	SB	7	221+39.4	Interior	S-04	12	0.0	-10.0
VS07ITL5	129	54	114000000	EM-5	SB	7	221+39.4	Interior	S-08	3,4	131.0	-5.5
TSITC001	130	7	133008085	THT	SB	7	221+39.4	Interior	S-04	14	149.0	-5.8 [@]
TSITC002	131	9	133008091	THT	SB	7	221+39.4	Interior	S-04	18	149.0	-5.3 [@]
TSITC003	132	11	133008105	THT	SB	7	221+39.4	Interior	S-05	22	149.0	-5.3 [@]
TSITC004	133	12	133008095	THT	SB	7	221+39.4	Interior	S-05	24	149.0	-4.8 [@]
TSITC005	134	38	133008090	THT	SB	7	221+39.4	Interior	S-08	24	149.0	-4.3 [@]
TSITC006	135	10	133008078	THT	SB	7	221+39.4	Interior	S-04	20	149.0	-2.8 [@]
VS07ITL6	136	55	114008201	EM-5	SB	7	221+39.4	Interior	S-08	5,6	220.0	-6.2
TSIEA001	137	13	133008059	SB	SB	7	221+39.4	Interior	S-05	26	137.0	-31.3
TSIEB001	138	14	133008074	SB	SB	7	221+39.4	Interior	S-05	28	131.3	-74.3
TSIEB002	139	15	133008057	SB	SB	7	221+39.4	Interior	S-05	30	127.6	-73.8
TSIEB003	140	16	133008067	SB	SB	7	221+39.4	Interior	S-05	32	122.2	-73.3
TSIEC001	141	8	133008065	SB	SB	7	221+39.4	Interior	S-04	16	117.0	-119.8
TSIBA002	142	19	133008064	SB	SB	7	221+39.4	Interior	S-06	6	0.0	-128.3
TSIBA001	143	39	133008063	SB	SB	7	221+39.4	Interior	S-08	26	0.0	-133.3
VS07IBL2	144	27	114008220	EM-5	SB	7	221+39.4	Interior	S-04	21,22	0.0	-132.8
VS07IBL1	145	28	114008233	EM-5	SB	7	221+39.4	Interior	S-04	23,24	-116.3	-128.3
VS07ITT2	146	29	114008239	EM-5	SB	7	221+39.4	Interior	S-04	25,26	-142.0	-12.3
TSITA001	147	17	N/A	THT	SB	7	221+39.4	Interior	S-06	1,2	-238.0	-6.8
TSITA002	148	18	N/A	THT	SB	7	221+39.4	Interior	S-06	3,4	-238.0	-8.3
TSITA003	149	20	N/A	THT	SB	7	221+39.4	Interior	S-06	8	-238.0	-9.8
VS07ITL1	150	30	114008218	EM-5	SB	7	221+39.4	Interior	S-04	27,28	-220.0	-4.7
VS07ITL2	151	31	114008225	EM-5	SB	7	221+39.4	Interior	S-04	29,30	-175.5	-4.9
VS07ITT1	152	32	114008232	EM-5	SB	7	221+39.4	Interior	S-04	31,32	-142.0	-7.3
VS07ITL3	153	73	114008227	EM-5	SB	7	221+39.4	Interior	S-10	3,4	-131.0	-6.0
VS07ETL4	154	33	114008199	EM-5	SB	7	221+39.4	Exterior	S-05	1,2	0.0	-5.5
VS07ETL5	155	43	114008208	EM-5	SB	7	221+39.4	Exterior	S-07	1,2	68.5	-5.8
VS07ETT1	156	56	114008204	EM-5	SB	7	221+39.4	Exterior	S-08	7,8	121.0	-5.8
VS07ETL6	157	57	114008209	EM-5	SB	7	221+39.4	Exterior	S-08	9,10	131.0	-5.5
VS07ETT3	158	58	114008223	EM-5	SB	7	221+39.4	Exterior	S-08	11,12	141.0	-6.0
VS07ETL7	159	59	114008206	EM-5	SB	7	221+39.4	Exterior	S-08	13,14	124.0	-8.2
VS07ETL8	160	44	114008153	EM-5	SB	7	221+39.4	Exterior	S-07	3,4	220.0	-5.7
VS07ETL9	161	45	114008175	EM-5	SB	7	221+39.4	Exterior	S-07	5,6	247.0	-5.8
VS07ETT4	162	46	114008207	EM-5***	SB	7	221+39.4	Exterior	S-07	7,8	141.0	-15.0
VS07ETT2	163	47	114008196	EM-5	SB	7	221+39.4	Exterior	S-07	9,10	121.0	-15.3
VS07EEV2	164	48	114008205	EM-5	SB	7	221+39.4	Exterior	S-07	11,12	130.7	-38.0
VS07EEV3	165	49	114008165	EM-5	SB	7	221+39.4	Exterior	S-07	13,14	140.0	-38.0
VS07EEV1	166	50	114008159	EM-5	SB	7	221+39.4	Exterior	S-07	15,16	129.2	-44.6
VS07EEA1	167	51	114008172	EM-5	SB	7	221+39.4	Exterior	S-07	17,18	129.2	-44.6

* Channel wiring switched. Correct channels shown. Connection gage # in parentheses is the VW gage number in the collected data. Connection gage number before parentheses is number assigned during gage connection.

** Gage replaced and collected data was satisfactory. New gage model and gage serial number shown.

*** Thermistor does not provide readings. Strain measurements only. Never replaced.

† Gage replaced but newly collected data was not satisfactory. New gage model and gage serial number shown.

‡ Thermistor not operational. Never replaced.

[@] Gage locations not consistent. Thermistors excluded from thermal gradient analysis.

Table 2.2: VWSG and thermistor labeling, locations, and connections (cont'd.)

UMN Gage Name	Installation Gage #	Connection Gage #	Serial Number	Gage Type	Bridge	Location	Station	Box Girder	Multiplexer Number	Channel Number(s)	X (in)	Y (in)
VS07EEL1	168	52	114008166	EM-5	SB	7	221+39.4	Exterior	S-07	19,20	129.2	-44.6
VS07EBL3	169	60	114008167	EM-5	SB	7	221+39.4	Exterior	S-08	15,16	115.3	-129.3
VS07EBT3	170	61	114A10201	SM-5A†	SB	7	221+39.4	Exterior	S-08	17,18	104.4	-128.8
VS07EBT4	171	62	114008169	EM-5	SB	7	221+39.4	Exterior	S-08	19,20	99.2	-131.5
VS07EBL2	172	63	114008192	EM-5	SB	7	221+39.4	Exterior	S-08	21,22	0.0	-131.8
TSEBA003	173	40	133008082	THT‡	SB	7	221+39.4	Exterior	S-08	28	0.0	-128.3
TSEBA002	174	41	133008099	THT	SB	7	221+39.4	Exterior	S-08	30	0.0	-130.8
TSEBA001	175	42	133008092	THT	SB	7	221+39.4	Exterior	S-08	32	0.0	-133.5
VS07EBT1	176	34	114008235	EM-5	SB	7	221+39.4	Exterior	S-05	3,4	-105.1	-129.3
VS07EBT2	177	35	114008234	EM-5	SB	7	221+39.4	Exterior	S-05	5,6	-104.5	-131.8
VS07EBL1	178	36	114008202	EM-5	SB	7	221+39.4	Exterior	S-05	7,8	-110.9	-128.8
TSEWC001	179	21	133008070	THT	SB	7	221+39.4	Exterior	S-06	10	-115.7	-123.3
TSEWB001	180	22	133008096	THT	SB	7	221+39.4	Exterior	S-06	12	-130.7	-80.3
TSEWB002	181	24	133008097	THT	SB	7	221+39.4	Exterior	S-06	16	-125.5	-81.0
TSEWB003	182	25	133008084	THT	SB	7	221+39.4	Exterior	S-06	18	-120.8	-81.8
VS07EWV1	183	37	114008176	EM-5	SB	7	221+39.4	Exterior	S-05	9,10	-129.4	-43.9
VS07EWA1	184	38	114008171	EM-5	SB	7	221+39.4	Exterior	S-05	11,12	-129.4	-43.9
VS07EWL1	185	39	114008168	EM-5	SB	7	221+39.4	Exterior	S-05	13,14	-129.4	-43.9
TSEWA001	186	23	133008071	THT	SB	7	221+39.4	Exterior	S-06	14	-136.0	-36.9
VS07ETL1	187	40	114008203	EM-5	SB	7	221+39.4	Exterior	S-05	15,16	-220.0	-6.2
TSETA001	188	32	133008073	THT	SB	7	221+39.4	Exterior	S-07	22	-149.0	-2.5
TSETA002	189	33	133008093	THT	SB	7	221+39.4	Exterior	S-07	24	-149.0	-4.0
TSETA003	190	34	133008101	THT	SB	7	221+39.4	Exterior	S-07	26	-149.0	-6.0
TSETA004	191	35	133008077	THT	SB	7	221+39.4	Exterior	S-07	28	-149.0	-7.2
TSETA005	192	36	133008092	THT	SB	7	221+39.4	Exterior	S-07	30	-149.0	-8.5
TSETA006	193	37	133008098	THT	SB	7	221+39.4	Exterior	S-07	32	-149.0	-10.2
VS07ETL2	194	41	114008249	EM-5	SB	7	221+39.4	Exterior	S-05	17,18	-131.0	-19.3
VS07ETL3	195	42	114008198	EM-5	SB	7	221+39.4	Exterior	S-05	19,20	-68.5	-6.0
TSETB001	196	26 (28*)	133008075	THT	SB	7	221+39.4	Exterior	S-06	24	-18.0	-1.7
TSETB002	197	27 (29*)	133008094	THT	SB	7	221+39.4	Exterior	S-06	26	-18.0	-3.3
TSETB003	198	28 (26*)	133008076	THT	SB	7	221+39.4	Exterior	S-06	20	-18.0	-4.9
TSETB004	199	29 (27*)	133008080	THT	SB	7	221+39.4	Exterior	S-06	22	-18.0	-6.5
TSETB005	200	30	133008079	THT	SB	7	221+39.4	Exterior	S-06	28	-18.0	-8.1
TSETB006	201	31	133008089	THT	SB	7	221+39.4	Exterior	S-06	30	-18.0	-9.8
VN08ETL1	202	16	114008241	EM-5	NB	8	223+86.81	Exterior	N-03	1,2	0.0	-8.5
VN08EBL1	203	17 (18*)	114008151	EM-5	NB	8	223+87.41	Exterior	N-03	5,6	0.0	-291.4
VN08EWL1	204	18 (17*)	114008190	EM-5	NB	8	223+87.41	Exterior	N-03	3,4	-99.9	-141.3
VN08ITL1	205	19	114008246	EM-5	NB	8	223+86.61	Interior	N-03	7,8	-2.0	-8.8
VN08IBL1	206	20	114A10164	SM-5A†	NB	8	223+87.41	Interior	N-03	9,10	0.0	-291.4
VS08ITL1	207	24 (25*)	114008250	EM-5	SB	8	223+75.4	Interior	S-03	19,20	-3.0	-6.3
VS08IBL1	208	25 (24*)	114008228	EM-5	SB	8	223+75.4	Interior	S-03	17,18	0.0	-291.6
VS08ETL1	209	26	114A10204	SM-5A**	SB	8	223+75.4	Exterior	S-03	21,22	-1.0	-5.5
VS08EEV1	210	21	114008214	EM-5	SB	8	223+75.4	Exterior	S-03	11,12	106.1	-144.9
VS08EEA1	211	23	114008238	EM-5	SB	8	223+75.4	Exterior	S-03	15,16	106.4	-143.3
VS08EEL1	212	22	114008240	EM-5	SB	8	223+75.4	Exterior	S-03	13,14	105.4	-147.9
VS08EBL2	213	20	114008224	EM-5	SB	8	223+75.4	Exterior	S-03	9,10	83.3	-287.9
VS08EBL1	214	19	114008252	EM-5	SB	8	223+75.4	Exterior	S-03	7,8	0.0	-291.4
VS08EWV1	215	16	114008197	EM-5	SB	8	223+75.4	Exterior	S-03	1,2	-106.2	-142.3
VS08EWA1	216	18	114008243	EM-5	SB	8	223+75.4	Exterior	S-03	5,6	-106.4	-141.3
VS08EWL1	217	17	114008210	EM-5	SB	8	223+75.4	Exterior	S-03	3,4	-105.5	-145.3
VN09ETL1	218	11	114008242	EM-5	NB	9	225+53.17	Exterior	N-02	1,2	0.0	-6.0
VN09EBL1	219	12	114008116	EM-5	NB	9	225+53.17	Exterior	N-02	3,4	0.0	-165.6
VN09EWL1	220	13	114008117	EM-5	NB	9	225+53.17	Exterior	N-02	5,6	-123.1	-63.1
VN09ITL1	221	15	114008236	EM-5	NB	9	225+53.17	Interior	N-02	9,10	0.0	-6.0
VN09IBL1	222	14	114008184	EM-5	NB	9	225+53.17	Interior	N-02	7,8	0.0	-165.6
VS09ITL1	223	14	114008244	EM-5	SB	9	225+35.61	Interior	S-02	7,8	-1.0	-6.0
VS09IBL1	224	13	114008173	EM-5	SB	9	225+35.61	Interior	S-02	5,6	0.0	-170.3
VS09ETL1	225	15	114008226	EM-5	SB	9	225+35.61	Exterior	S-02	9,10	0.0	-6.0

* Channel wiring switched. Correct channels shown. Connection gage # in parentheses is the VW gage number in the collected data. Connection gage number before parentheses is number assigned during gage connection.

** Gage replaced and collected data was satisfactory. New gage model and gage serial number shown.

*** Thermistor does not provide readings. Strain measurements only. Never replaced.

† Gage replaced but newly collected data was not satisfactory. New gage model and gage serial number shown.

‡ Thermistor not operational. Never replaced.

@ Gage locations not consistent. Thermistors exlcuded from thermal gradient analysis.

Table 2.2: VWSG and thermistor labeling, locations, and connections (cont'd.)

UMN Gage Name	Installation Gage #	Connection Gage #	Serial Number	Gage Type	Bridge	Location	Station	Box Girder	Multiplexer Number	Channel Number(s)	X (in)	Y (in)
VS09EEL1	226	12	114A10202	SM-5A**	SB	9	225+35.61	Exterior	S-02	3,4	117.6	-61.8
VS09EBL1	227	11	114008191	EM-5	SB	9	225+35.61	Exterior	S-02	1,2	0.0	-169.8
VN14ETL1	228	6	114008231	EM-5	NB	14	227+11.75	Exterior	N-01	11,12	0.0	-5.8
VN14EBL1	229	5	114008219	EM-5	NB	14	227+11.75	Exterior	N-01	9,10	-2.5	-68.8
VN14EML1	230	4	114008237	EM-5	NB	14	227+11.75	Exterior	N-01	7,8	-50.0	-32.1
VN14ITL1	231	9	114A10205	SM-5A**	NB	14	227+11.75	Interior	N-01	29,30	0.0	-5.8
VN14IBL1	232	10	114A10165	SM-5A**	NB	14	227+11.75	Interior	N-01	31,32	0.0	-72.1
VS14ITL1	233	7	114008346	EM-5	SB	14	227+08.9	Interior	S-01	13,14	-8.0	-5.8
VS14IBL1	234	8	114008358	EM-5	SB	14	227+08.9	Interior	S-01	15,16	0.0	-69.1
VS14ETL1	235	1	114008339	EM-5	SB	14	227+08.9	Exterior	S-01	1,2	-8.0	-5.8
VS14EML1	236	2	114008361	EM-5	SB	14	227+08.9	Exterior	S-01	3,4	0.0	-30.6
VS14EBL1	237	5	114008326	EM-5	SB	14	227+08.9	Exterior	S-01	9,10	0.0	-68.1
VN15ETL1	238	1	114008178	EM-5	NB	15	227+69.82	Exterior	N-01	1,2	0.0	-5.8
VN15EBL1	239	3	114A10200	SM-5A**	NB	15	227+69.82	Exterior	N-01	5,6	0.0	-102.7
VN15EML1	240	2	114008213	EM-5	NB	15	227+69.82	Exterior	N-01	3,4	-54.5	-37.3
VN15ITL1	241	8 (7*)	114008156	EM-5	NB	15	227+69.82	Interior	N-01	13,14	0.0	-5.8
VN15IBL1	242	7 (8*)	114008221	EM-5	NB	15	227+69.82	Interior	N-01	15,16	0.0	-103.7
VS15ITL1	243	9	114008251	EM-5	SB	15	227+69.82	Interior	S-01	17,18	-8.0	-5.8
VS15IBL1	244	10	114008347	EM-5	SB	15	227+69.82	Interior	S-01	19,20	0.0	-102.1
VS15ETL1	245	6	114008357	EM-5	SB	15	227+69.82	Exterior	S-01	11,12	-8.0	-5.8
VS15EML1	246	4	114A10199	SM-5A**	SB	15	227+69.82	Exterior	S-01	7,8	0.0	-35.1
VS15EBL1	247	3	114008344	EM-5	SB	15	227+69.82	Exterior	S-01	5,6	0.0	-102.1

* Channel wiring switched. Correct channels shown. Connection gage # in parentheses is the VW gage number in the collected data. Connection gage number before parentheses is number assigned during gage connection.

** Gage replaced and collected data was satisfactory. New gage model and gage serial number shown.

*** Thermistor does not provide readings. Strain measurements only. Never replaced.

† Gage replaced but newly collected data was not satisfactory. New gage model and gage serial number shown.

‡ Thermistor not operational. Never replaced.

[@] Gage locations not consistent. Thermistors exlcuded from thermal gradient analysis.

Table 2.3: Pier and caisson VWSGs labeling and locations

VW_GK Number	Box Number*	VW Channel	Thermistor Channel	Gage position**	Shaft/Column†	Gage Name/ Serial Number	Geokon gage model
1	1	1	2	GL 3 / 1	Shaft 2	28043	4911A
2	1	3	4	GL 3/3	Shaft 2	28045	4911A
3	1	5	6	GL 2 / 2	Shaft 2	28070	4911A
4	1	7	8	GL 1 / 2	Shaft 2	28067	4911A
5	1	9	10	GL 4 / 1	Shaft 2	28054	4911A
6	1	11	12	GL 2/3	Shaft 2	28046	4911A
7	1	13	14	GL 2/4	Shaft 2	28064	4911A
8	1	15	16	GL 4/4	Shaft 2	28057	4911A
9	1	17	18	GL 1 / 1	Shaft 2	28047	4911A
10	1	19	20	GL 2 / 1	Shaft 2	28051	4911A
11	1	21	22	GL 4 / 2	Shaft 2	28044	4911A
12	1	23	24	GL 4/3	Shaft 2	28038	4911A
13	1	25	26	GL 3/4	Shaft 2	28056	4911A
14	1	27	28	N/A	N/A	Unknown	N/A
15	1	29	30	GL 1/4	Shaft 2	28069	4911A
16	1	31	32	GL 3 / 3	Shaft 1	28039	4911A
17	2	1	2	GL 3 / 2	Shaft 1	28063	4911A
18	2	3	4	GL 1 / 1	Shaft 1	28042	4911A
19	2	5	6	GL 3 / 4	Shaft 1	28068	4911A
20	2	7	8	GL 2 / 1	Shaft 1	28040	4911A
21	2	9	10	GL 1 / 4	Shaft 1	28058	4911A
22	2	11	12	GL 4 / 2	Shaft 1	28062	4911A
23	2	13	14	GL 3 / 1	Shaft 1	26841	4911A
24	2	15	16	GL 4 / 4	Shaft 1	28065	4911A
25	2	17	18	GL 2 / 3	Shaft 1	28049	4911A
26	2	19	20	GL 1 / 2	Shaft 1	28071	4911A
27	2	21	22	GL 2 / 2	Shaft 1	28061	4911A
28	2	23	24	GL 2 / 4	Shaft 1	28066	4911A
29	2	25	26	GL 1 / 3	Shaft 1	28048	4911A
30	2	27	28	GL 4 / 1	Shaft 1	28050	4911A
31	2	29	30	GL 4 / 3	Shaft 1	28041	4911A
32	2	31	32	NW, 39.88 ft	Interior (east) column	28072	4911A
33	3	1	2	GL3 / 2	Shaft 2	28055	4911A
34	3	3	4	N/A	N/A	Unknown	N/A
35	3	5	6	NW, 23.21 ft	Exterior (west) column	UofMN9	4200
36	3	7	8	NE, 39.27 ft	Exterior (west) column	28073	4911A
37	3	9	10	Center, 23.21 ft	Exterior (west) column	UofMN10	4200
38	3	11	12	NE, 23.21 ft	Exterior (west) column	UofMN6	4200
39	3	13	14	SE, 23.21 ft	Exterior (west) column	UofMN7	4200
40	3	15	16	SW, 39.27 ft	Exterior (west) column	1992	4911A
41	3	17	18	SW, 23.21 ft	Exterior (west) column	UofMN8	4200
42	3	19	20	SE, 39.27 ft	Exterior (west) column	1989	4911A
43	3	21	22	SW, 39.88 ft	Interior (east) column	28060	4911A
44	3	23	24	NW, 23.21 ft	Interior (east) column	UofMN4	4200
45	3	25	26	GL1/3	Shaft 2	28052	4911A
46 ‡	3	27	28	N/A	N/A	N/A	N/A
47 ‡	3	29	30	N/A	N/A	N/A	N/A
48 ‡	3	31	32	N/A	N/A	N/A	N/A
Unassigned				NE, 39.88 ft	Interior (east) column	28059	4911A
Unassigned				SE, 39.88 ft	Interior (east) column	1994	4911A
Unassigned				NE, 23.21 ft	Interior (east) column	UofMN1	4200
Unassigned				SE, 23.21 ft	Interior (east) column	UofMN2	4200
Unassigned				SW, 23.21 ft	Interior (east) column	UofMN3	4200
Unassigned				Center, 23.21 ft	Interior (east) column	UofMN5	4200
Unassigned				NW, 39.27 ft	Exterior (west) column	1987	4911A

* Box number corresponding to boxes in instrumentation vault shown in Figure 2.39.

** First number in shaft gage locations refers to level in shaft; second number refers to position within the cross section. Locations for column gages are specified as location with the cross section and approximate height above the base of the pier.

† Shafts are shown in Figure 2.31. Columns are from Pier 2 of southbound bridge.

‡ No gages attached to channels 46 through 48.

Table 2.4: Field measurements of Geokon 4200 gage locations in southbound bridge Pier 2

Gage Name	SB Pier 2 Column	Position	Cover North-South, NS_{cov} (in.)	Cover East-West, EW_{cov} (in.)	Vertical position to bottom, $Vert_{bot}$ (in.)	Vertical position to top of form, $Vert_{top}$ (in.)	Vertical position to cutoff, $Vert_{cutoff}$ (in.)	Computed height from base of pier (ft)
UofMN1	Interior (east)	NE Corner	14	6.125	164 T*	175	14.625	23.85
UofMN2	Interior (east)	SE Corner	14	7.125	163 T*	174	13.5	23.85
UofMN3	Interior (east)	SW Corner	14	7	163	174-175 T*	15	23.67
UofMN4	Interior (east)	NW Corner	13	7.125	164 T*	173-174 T*	14.75	23.84
UofMN5	Interior (east)	Center	Center	85 (east)	163	Measurement not taken	Measurement not taken	23.58
UofMN6	Exterior (west)	NE Corner	14	4.5	162	177.75 (short**)	16.5	23.56
UofMN7	Exterior (west)	SE Corner	17	5.5	162	180.25 (short**)	18	23.50
UofMN8	Exterior (west)	SW Corner	13.25	3.5	162	176	18	23.50
UofMN9	Exterior (west)	NW Corner	13.25	4.5	162.5	174-175	15.5	23.63
UofMN10	Exterior (west)	Center	Center	89 (east), 103.375 (west)	162	Measurement not taken	Measurement not taken	23.50

* Measurements followed by a "T" indicate that the measurement was taken to the end of the gage rather than the center of the gage.

** Forms were 1 in. shorter on one side than the other. Measurements followed by "short" indicate that the measurement was taken to the top of the short side of the form.

Table 2.5: Channel configuration for CR10 data collection during construction

Location	Dates	CR 10 Channel	UMN Gage Name	Installation Gage #	Connection Gage #
Midspan of Span 1 (Location 3)	6/20/2008 to 7/21/2008	1	VS03EBL2	26	93
		2	VS03EBT4	25	92
		3	VS03EBT3	24	91
		4	VS03EBL3	23	90
		5	VS03EEL1	22	89
		6	VS03EEV1	20	87
		7	VS03EEA1	21	88
		8	VS03ETT1	12	104
		9	VS03ETT2	17	107
		10	VS03ETL4	13	95
		11	VS03ETL3	11	103
		12	VS03ETT3	14	105
		13	VS03ETT4	16	106
		14	VS03EEV3	19	97
		15	VS03EEV2	18	98
		16	VS03ETL5	15	101
Midspan of Span 2 (Location 7)	7/11/2008 to 7/21/2008	1	VS07EWV1	183	37
		2	VS07EWA1	184	38
		3	VS07EWL1	185	39
		4	VS07EBL1	178	36
		5	VS07EBT1	176	34
		6	VS07EBT2	177	35
		7	TSEWA001	186	23
		8	TSEWB001	180	22
		9	TSEWB002	181	24
		10	TSEWB003	182	25
		11	TSEWC001	179	21
Midspan of Span 2 (Location 7)	7/22/2008 to 8/4/2008	1	VS07EBL2	172	63
		2	VS07EBT3	170	61
		3	VS07EBT4	171	62
		4	VS07EBL3	169	60
		5	VS07ETT1	156	56
		6	VS07ETL7	159	59
		7	VS07ETL6	157	57
		8	VS07ETT3	158	58
		9	VS07ETL8	160	44
		10	VS07ETL9	161	45
		11	VS07EEV1	166	50
		12	VS07EEA1	167	51
		13	VS07EEL1	168	52
		14	VS07EEV2	164	48
		15	VS07ETL5	155	43
		16	VS07EEV3	165	49
Near Pier 2, Span 1 (Location 4)	7/25/2008 to 8/4/2008	1		Unknown	
		2		Unknown	
		3		Unknown	

Table 2.6: SOFO sensor labeling and locations

SOFO Sensor Name	Location	Station	Location of sensor in box	y-dimension below nominal top of deck (in.)
6aT_7014	6a	219+08.4	Top	-12.722
6aB_7016	6a	219+08.4	Bottom	-227.625
6eT_7012	6e	219+81.9	Top	-12.722
6eB_7010	6e	219+81.9	Bottom	-188
6iT_7007	6i	220+80.9	Top	-12.722
6iB_7005	6i	220+80.9	Bottom	-135.875
7bT_7008	7b	221+86.9	Top	-12.722
7bB_7006	7b	221+86.9	Bottom	-135.875
7gT_7011*	7f	222+85.9	Top	-12.722
7gB_7009*	7f	222+85.9	Bottom	-188
7jT_7015	7j	223+59.4	Top	-12.722
7jB_7013	7j	223+59.4	Bottom	-227.625

* Names not indicative of location in bridge. 7gT_7011 and 7gB_7009 located at Location 7f.

Table 2.7: Long-term accelerometer labeling and locations

Acquisition Node	Acquisition Channel	Serial Number	Sensor Name	Before Feb. 1, 2010*		After Feb. 1, 2010*		Long-term setup 1**		Long-term setup 2**	
				Recording Node	Recording Channel	Recording Node	Recording Channel	Station (ft)	Description	Station (ft)	Description
1	5	2060811	NB SP 3 Ext	1	5	A	1	225+53.17	Vertical at CL of Box	225+53.17	Vertical at CL of Box
1	7	2060793	NB SP 3 Int	1	7	A	2	225+53.17	Vertical at CL of Box	225+53.17	Vertical at CL of Box
2	1	2060803	NB SP 2 Ext	2	1	2	1	221+54.4	Vertical at CL of Box	221+54.4	Vertical at CL of Box
2	3	2060794	NB SP 2 Int	2	2	2	2	221+54.4	Vertical at CL of Box	221+54.4	Vertical at CL of Box
3	3	2060802	NB SP 1 Ext	3	3	B	1	217+01.8	Vertical at CL of Box	217+01.8	Vertical at CL of Box
3	5	2060795	NB SP 1 Ext	3	4	B	2	217+01.8	Vertical at CL of Box	217+01.8	Vertical at CL of Box
4	3	2060796	SB SP 1 Ext	4	3	C	1	217+04.6	Vertical at CL of Box	217+04.6	Vertical at CL of Box
4	5	2060805	SB SP 1 Int	4	4	C	2	217+04.6	Vertical at CL of Box	217+04.6	Vertical at CL of Box
5	28	2060790	SN 2060790	5 / 9 ***	19 / 1 ***	9	1	219+11.9	Vertical at Web	219+11.9	Vertical at Web
5	29	2058713	SN 2058713	5 / 9 ***	20 / 2 ***	9	2	219+48.9	Vertical at Web	219+48.9	Vertical at Web
6	1	2060813	SB SP2 Ext	6	1	6	1	221+39.4	Vertical at CL of Box	221+39.4	Vertical at CL of Box
6	3	2060810	SB SP2 Int	6	2	6	2	221+39.4	Vertical at CL of Box	221+39.4	Vertical at CL of Box
6	17	2060789	ACC 1	6	3	6	3	221+33.9	Vertical at Web	221+33.9	Vertical at Web
6	18	2060791	ACC 2	6	4	6	4	220+96.9	Vertical at Web	220+96.9	Vertical at Web
6	19	2060809	ACC 3	6	5	6	5	221+33.9	Vertical at CL of Box	221+33.9	Vertical at CL of Box
6	20	2060792	ACC 4	6	6	6	6	221+70.9	Vertical at Web	221+70.9	Vertical at Web
6	21	2060807	ACC 5	6	7	6	7	222+07.9	Vertical at Web	222+07.9	Vertical at Web
6	22	2060801	ACC 6	6	8	6	8	220+59.9	Vertical at Web	220+59.9	Vertical at Web
6	23	2060808	ACC 7	6	9	6	9	220+22.9	Vertical at Web	220+22.9	Vertical at Web
6	24	2060799	ACC 8	6	10	6	10	220+12.9	Vertical at Web	221+33.9	Horizontal at Web
7	1	2060797	ACC 10	7	1	7	1	223+55.9	Vertical at Web	222+81.9	Horizontal at Web
7	2	2060798	ACC 11	7	2	7	2	222+81.9	Vertical at Web	222+81.9	Vertical at Web
7	3	2060800	ACC 12	7	3	7	3	223+18.9	Vertical at Web	223+18.9	Vertical at Web
7	4	2060806	ACC 13	7	4	7	4	222+44.9	Vertical at Web	222+44.9	Vertical at Web
8	5	2060804	SB SP3 Ext	8	5	D	1	225+35.6	Vertical at CL of Box	225+35.6	Vertical at CL of Box
8	7	2060812	SB SP3 Int	8	7	D	2	225+35.6	Vertical at CL of Box	225+35.6	Vertical at CL of Box

* Recording node and channel refer to the channel the data was assigned to upon preprocessing. On February 1, 2010, "virtual nodes" were added to separate the accelerometers from the strain gage and LP measurements on the same nodes to better facilitate preprocessing.

** Long-term setup was changed on May 11, 2010. See Figures 2.45 and 2.46 for long-term setups.

*** Accelerometers SN 2060790 and SN 2058713 were originally recorded to Node 5 Channels 19 and 20, respectively. These channels were switched to the virtual Node 9 channels 1 and 2 on May 15, 2009.

Table 2.8: Linear potentiometer labeling and locations

Acquisition Node	Acquisition Channel	Serial Number	Sensor Name (Location)	Before Feb. 1, 2010*		After Feb. 1, 2010*	
				Recording Node	Recording Channel	Recording Node	Recording Channel
1	1	38060484	NB SP 4 Ext	1	1	1	1
1	2	38060489	NB SP 4 Int	1	2	1	2
1	3	38060486	NB SP 3 Ext	1	3	1	3
1	4	38060491	NB SP 3 Int	1	4	1	4
3	1	38060487	NB SP 1 Ext	3	1	3	1
3	2	38060490	NB SP 1 Int	3	2	3	2
4	1	38060482	SB SP 1 Ext	4	1	4	1
4	2	38060482	SB SP 1 Int	4	2	4	2
8	1	38060485	SB SP 3 Ext	8	1	8	1
8	2	38060488	SB SP 3 Int	8	2	8	2
8	3	38060481	SB SP 4 Ext	8	3	8	3
8	4	38060492	SB SP 4 Int	8	4	8	4

* Recording node and channel refer to the channel the data was assigned to upon preprocessing. On February 1, 2010, "virtual nodes" were added to separate the accelerometers from the strain gage and LP measurements on the same channels to better facilitate preprocessing. LPs always kept same Recording information as Acquisition information.

Table 2.9: Pier and caisson resistive gages labeling and locations

Windaq Acquisition Channel	Windaq SN and CR9000X Channel	Windaq Output Channel	Gage Serial Number	Gage Position*	Shaft or Column**	Geokon gage model	Comment
1	17	N/A	28059	NE, 39.88 ft	Interior Column	3911A	Not recorded
2	18	1	1994	SE, 39.88 ft	Interior Column	3911A	
3	19	2	28060	SW, 39.88 ft	Interior Column	3911A	
4	20	3	28072	NW, 39.88 ft	Interior Column	3911A	
5	21	N/A	28073	NE, 39.27 ft	Exterior Column	3911A	Not recorded
6	22	4	1987	NW, 39.27 ft	Exterior Column	3911A	
7	23	5	1989	SE, 39.27 ft	Exterior Column	3911A	
8	24	6	1992	SW, 39.27 ft	Exterior Column	3911A	
9	9	7	28069	GL1/4	Shaft 2	3911A	
10	10	8	28067	GL1/2	Shaft 2	3911A	
11	11	9	28064	GL2/4	Shaft 2	3911A	
12	12	10	28070	GL2/2	Shaft 2	3911A	
13	13	11	28056	GL3/4	Shaft 2	3911A	
14	14	12	28055	GL3/2	Shaft 2	3911A	
15	nc	N/A	28057	GL4/4	Shaft 2	3911A	Never connected
16	nc	N/A	28054	GL4/1	Shaft 2	3911A	Never connected
17	1	13	28058	GL1/4	Shaft 1	3911A	
18	2	N/A	28071	GL1/2	Shaft 1	3911A	Not recorded
19	3	N/A	28066	GL2/4	Shaft 1	3911A	Not recorded
20	4	14	28061	GL2/2	Shaft 1	3911A	
21	5	15	28068	GL3/4	Shaft 1	3911A	
22	6	16	28063	GL3/2	Shaft 1	3911A	
23	7	17	28065	GL4/4	Shaft 1	3911A	
24	8	18	28062	GL4/2	Shaft 1	3911A	

* First number in shaft gage locations refers to level in shaft, second number refers to position within the cross section. Locations for column gages are specified within cross section and approximate height above the base of the pier.
** Shafts are shown in Figure 2.31. Columns are southbound Pier 2 columns.

Table 2.10: Corrosion sensor labeling and locations

New Logger Number*	Old Logger Number*	Location	Station	Date Last Repaired
401	504	Southbound Span 3, Ext Box	225+35.61	4/14/2011
402	503	Northbound Span 3, Ext Box	225+53.17	4/14/2011
403	505	Northbound Span 1, Ext Box	217+06.79	10/21/2011
404	506	Southbound Span 1, Ext Box	217+09.58	10/21/2011

* Old logger numbers were changed to the new logger numbers on the repair dates listed.

Table 3.1: Summary of specimens used for material testing

Collected by:	Test performed	Location	Date Collected	Specimen Type	# of Samples	Notes
UMN	Compressive strength and modulus	SB Span 4	8/9/2008	4" x 8" Cylinder	9	Tested at 56, 93 and 130 days
	Split cylinder tensile strength	NB Span 4	8/8/2008	6" x 12" Cylinder	2	Tested at 59 days; possible problems with ASTM rodding technique.
		SB Span 4	8/9/2008	6" x 12" Cylinder	3	Tested at 58 days
	Creep and shrinkage	NB Span 4	8/8/2008	4" x 11" Cylinder	3	Shrinkage only; left uncovered one day onsite before moving to environmental chamber; possible problems with ASTM rodding technique.
		SB Span 4	8/9/2008	4" x 11" Cylinder	14	Creep and shrinkage measurements
	Coefficient of thermal expansion	SB Pier 2	1/29/2008	6" x 6" x 24" Beam	1	
		SB Pier 2	1/29/2008	6" x 12" Cylinder	1	
		SB Span 1	4/18/2008	6" x 6" x 24" Beam	1	
		SB Span 1 (deck)	5/19/2008	6" x 6" x 24" Beam	1	
		2nd St. Bridge Deck	6/23/2008	6" x 6" x 24" Beam	1	
		NB Span 4	8/8/2008	6" x 6" x 24" Beam	1	
		SB Span 4	8/9/2008	6" x 6" x 24" Beam	1	
		SB Span 4	8/9/2008	6" x 12" Cylinder	1	
MnDOT	Compressive strength	SB Bridge	Unknown	4" x 8" Cylinder	67	Exact location unknown. Tested by MnDOT at 7, 28, and 56 days.
		NB Bridge	Unknown	4" x 8" Cylinder	75	Exact location unknown. Tested by MnDOT at 7, 28, and 56 days.

Table 3.2: Concrete compressive strength and modulus of elasticity determined for samples collected by the University of Minnesota

Date	Age (days)	Sample	f'c (ksi)	Modulus (ksi)	Average f'c (ksi)	Average Modulus (ksi)	Standard Deviation f'c (ksi)	Coefficient of Variation f'c (%)	Modulus calculated with Eqn. 3-1 (ksi)	Tensile strength calculated with Eqn. 3-2 (ksi)
		1	7.068	N/A						
10/4/2008	56	2	7.553	4710	7.119	4450	0.411	5.78%	4890	0.57
		3	6.735	4190						
		1	7.076	N/A						
11/10/2008	93	2	6.587	5000	6.697	4730	0.337	5.04%	4710	0.55
		3	6.429	4450						
		1	6.410	N/A						
12/17/2008	130	2	6.042	4450	6.244	4190	0.187	2.99%	4550	0.53
		3	6.279	3930						

Table 3.3: Summary of MnDOT compressive strength results

Age (days)	Bridge	Number of samples tested	Average f'c (ksi)	Standard deviation (ksi)	Coefficient of variation (%)	Modulus calculated with Eqn. 3-1 (ksi)	Tensile strength calculated with Eqn. 3-2 (ksi)
7	SB	30	5.752	0.417	7.25%	4360	0.51
	NB	34	5.545	0.226	4.08%	4290	0.50
28	SB	33	7.568	0.595	7.86%	5010	0.58
	NB	38	7.354	0.399	5.43%	4940	0.57
56	SB	4	7.193	0.331	4.60%	4880	0.57
	NB	3	7.604	0.460	6.05%	5020	0.58

Table 3.4: Concrete tensile strength

Sample	Sample Origin	Age (days)	Failure Load (lbf)	Tensile Strength (psi)
1	SB Span 4	58	43690	386
2	SB Span 4	58	37110	328
3	SB Span 4	58	53080	469
4	NB Span 4	59	53570	474
5	NB Span 4	59	39230	347
SB average tensile strength:			395	psi
NB average tensile strength:			410	psi

Table 3.5: Creep sample loading and unloading

Date	Frame	Samples	Age	Load Applied	Stress Applied	Notes
10/4/2008	1	C4SB1 C4SB2	56	24.0 kips	275 ksf	Only two of three DEMEC sides measured due to frame difficulties.
10/4/2008	2	C4SB3 C4SB4	56	Unknown	Unknown	Loaded above 36.8 kips, causing sample C4SB4 to fail.
10/5/2008	2	C4SB3 S4SB3	57	36.8 kips	420 ksf	Shrinkage cylinder S4SB3 replacing failed cylinder in Frame #2. Only two of three DEMEC sides measured due to frame difficulties.
10/31/2008	1	C4SB1 C4SB2	83	Unloaded	Unloaded	Frame #1 unloaded because of significant bending of cylinders.
11/10/2008	4	C4SB5 C4SB6	93	24.0 kips	275 ksf	All three DEMEC sides measured.
12/17/2008	1	C4SB1 C4SB2	130	24.0 kips	275 ksf	Frame #1 reloaded at 130 days. All three DEMEC sides now measured.
12/17/2008	3	C4SB7 C4SB8	130	24.0 kips	275 ksf	All three DEMEC sides measured.
1/19/2010	2	C4SB3 S4SB3	528	Unloaded	Unloaded	Specimen cracked and spalled upon reloading.

Table 3.6: Humidity dependent coefficients φ_{f1} , λ, and ε_{s1} from 1978 CEB/FIP Model Code

Environment	Relative Humidity	φ_{f1}	λ	ε_{s1}
Water	--	0.8	30	+0.00010
Very damp atmosphere	90%	1	5	-0.00013
Outside in general	70%	2	1.5	-0.00032
Very dry atmosphere	40%	3	1	-0.00052

Table 3.7: Coefficient of thermal expansion sample information

Gage	Channel	Type	Location	Date Cast
Roctest EM-5	1-1	Beam	Northbound Span 4 deck	8/8/2008
Roctest EM-5	1-2	Beam	Southbound Span 4 deck	8/9/2008
Roctest EM-5	1-3	Open	Open (no specimen)	N/A
Roctest EM-5	1-4	Cylinder	Southbound Span 4 deck (labeled "B3")	8/9/2008
Roctest EM-5	1-5	Beam	2nd St. Bridge deck	6/23/2008
Geokon VCE-4200	2-1	Beam	Southbound Span 1 deck	5/19/2008
Geokon VCE-4200	2-2	Beam	Southbound Span 1 near Pier 2	4/18/2008
Geokon VCE-4200	2-3	Beam	Pier 2 southbound	1/29/2008
Geokon VCE-4200	2-4	Cylinder	Pier 2 southbound	1/29/2008

Table 3.8: Measured coefficient of thermal expansion from laboratory specimens

Location	Channel	Measured CTE (με/°F)
Northbound Span 4 deck	1-1	5.53
Southbound Span 4 deck	1-2	5.57
Southbound Span 4 deck (labeled "B3")	1-4	5.53
2nd St. Bridge deck	1-5	5.70
Southbound Span 1 deck	2-1	6.45
Southbound Span 1 near Pier 2	2-2	5.61
Pier 2 southbound	2-3	4.97
Pier 2 southbound	2-4	4.73

Table 3.9: Summary of coefficient of thermal expansion using laboratory specimens

Mix	Average CTE (με/°F)	Coefficient of Variation (%)
Superstructure (nominal strength = 6500 psi)	5.73	6.28%
Pier (nominal strength = 4000 psi)	4.85	3.51%

Table 3.10: Measured coefficient of thermal expansion using southbound bridge vibrating wire strain gage data

Location	Average (με/°F)
Loc 3, Top Flange	5.24
Loc 3, Bottom Flange	5.97
Loc 3, Web (vertical)	5.43
Loc 7, Top Flange	5.21
Loc 7, Bottom Flange	5.79
Loc 7, Web (vertical)	5.49
Loc 9, Top Flange	5.26
Loc 9, Bottom Flange	5.92

Table 3.11: Averaged coefficient of thermal expansion by location using southbound bridge vibrating wire strain gage data

Location	Average CTE (με/°F)
SB Loc 3, Midspan of Span 1	5.47
SB Loc 7, Midspan of Span 2	5.39
SB Loc 9, Midspan of Span 3	5.49

Table 3.12: Averaged coefficient of thermal expansion by location using northbound bridge vibrating wire strain gage data

Location	Average CTE (με/°F)
NB Loc 3, Midspan of Span 1	5.47
NB Loc 7, Midspan of Span 2	5.53
NB Loc 9, Midspan of Span 3	5.40

Table 3.13: Average superstructure coefficients of thermal expansion using linear potentiometers

Structure	Average CTE (με/°F)
Southbound	5.55
Northbound	5.69

Table 3.14: Summary of concrete coefficient of thermal expansion for I-35W Bridge

Mix	Average CTE (με/°F)
Superstructure (nominal strength = 6500 psi)	**5.60**
- Laboratory VW strain gage	5.72
- In situ VW strain gage	5.46
- In situ linear potentiometer	5.60
Pier (nominal strength = 4000 psi)	**4.85**

Table 4.1: Effective Modulus of Elasticity Calculations

Structural Entity	E_c (ksi)	n (E_s/E_c)	Section	A_g (in^2)	A_s (in^2)	E_{eff} (ksi)	Average E_{eff} (ksi)
Pier	3820	7.60	Least Reinf.	59900	253	3940	4040
			Most Reinf.	18400	205	4140	
Superstructure	4950	5.86	Least Reinf.	5700	13.7	5020	5040
			Most Reinf.	30000	110	5060	
Rail	3820	7.60	All	637	3.07	3960	3960

Table 4.2: Description of Sections Chosen for Modulus of Elasticity Calculations

Section	Description
Pier Least Reinf.	Base of Pier 2 & 3
Pier Most Reinf.	Midheight of Pier 2 & 3
Superstructure Least Reinf.	Southbound Span 1, near pier 2
Superstructure Most Reinf.	Southbound midspan of Span 2, closure segment
Rail all Sections	Similar reinforcing at all sections of concrete barrier assumed

Table 4.3: Material properties used in three-dimensional finite element model

Material Name	Description	Modulus of Elasticity – (psi)	Coefficient of Thermal Expansion – (με/°F)	Poisson's Ratio (nominal)	Density (nominal) – (slug-ft/in.^{4})
Concrete-SS	Concrete in superstructure Nominal 28-day design strength = 6.5 ksi	5,000,000	5.60	0.2	0.000225
Concrete-Pier	Concrete in piers Nominal 28-day design strength = 4.0 ksi	4,000,000	4.85	0.2	0.000225
Concrete-Rail	Concrete in barrier rail Nominal 28-day design strength = 4.0 ksi	4,000,000	4.85	0.2	0.000225
Steel	Post-tensioning steel (axial stiffness only)	28,500,000	6.78	0.3	0.000720

Table 5.1: Truck loads and dimensions for September 2008 truck tests

Truck Number	9/14/08 Total load (lbs)	9/17/08 Front axle load (lbs)	9/17/08 Middle axle load (lbs)	9/17/08 Rear axle load (lbs)	9/17/08 Total load (lbs)	Front axle to rear axle (in.)	Middle axle to rear axle (in.)
2251	49700	15600	17300	15950	48850	236.5	55
2252	50840	16300	16600	17300	50200	236	55
2254	50780	16500	17550	15950	50000	237	56
2255	50820	14950	16600	17650	49200	236	55
2256	50740	14400	17500	17900	49000	236.5	54.5
2257	50940	14800	17750	17650	50200	237	56
2351	50170	16950	16300	16300	49550	237	55
2360	N/A	15400	17800	17700	50900	236	55
1552	50020	N/A	N/A	N/A	N/A	237	N/A

Table 5.2: Southbound bridge static truck test information for September 2008 truck tests

Date	Time Start	Time End	Config.	Test Name	Test Description and Notes
9/14/2008	19:22	19:35	ST I	STI9SB	Trucks Facing South with Rear Tandem Centered on Location 9
9/14/2008	19:39	19:51	ST I	STI8SB	Trucks Facing South with Rear Tandem Centered on Location 8
9/14/2008	19:56	20:08	ST I	STI7SB	Trucks Facing South with Rear Tandem Centered on Location 7
9/14/2008	20:12	20:23	ST I	STI6SB	Trucks Facing South with Front Axle Centered over Location 6
9/14/2008	20:26	20:37	ST I	STI(P2)SB	Trucks Facing South with Rear Tandem Centered over Pier 2
9/14/2008	20:40	20:50	ST I	STI4(-25)SB	Trucks Facing South with Rear Tandem Centered 25' South of Location 4
9/14/2008	20:54	21:04	ST I	STI3SB	Trucks Facing South with Rear Tandem Centered on Location 3
9/14/2008	21:43	21:54	ST II	STII7SB	Trucks Facing South with Location 7 Centered between trucks (i.e. Between Rows 2 and 3 of Trucks)
9/14/2008	22:05		ST II	STII6SB	Trucks Facing South with Front Axle of Front Truck Centered over Location 6
9/14/2008	22:13	22:24	ST II	STII(P2)SB	Trucks Facing South with Pier 2 Centered between trucks (i.e. Between Rows 2 and 3 of Trucks)
9/14/2008			ST II	STII3SB	Trucks Facing South with Location 3 Centered between trucks (i.e. Between Rows 2 and 3 of Trucks)
9/14/2008	23:26	23:36	ST I	STI9SB	Trucks Facing South with Rear Tandem Centered on Location 9
9/14/2008	23:40	23:50	ST I	STI8SB	Trucks Facing South with Rear Tandem Centered on Location 8
9/14/2008	23:53	0:06	ST I	STI8(-21.5)SB	Trucks Facing South with Rear Tandem Centered 21.5' South of Location 8
9/15/2008	0:10	0:20	ST I	STI7SB	Trucks Facing South with Rear Tandem Centered on Location 7
9/15/2008	0:23	0:33	ST I	STI6SB	Trucks Facing South with Front Axle Centered over Location 6 -- One Truck moved at 12:28
9/15/2008	0:36	0:39	ST I	STI(P2)SB	Trucks Facing South with Rear Tandem Centered over Pier 2
9/15/2008	0:42	0:46	ST I	STI4(-25)SB	Trucks Facing South with Rear Tandem Centered 25' South of Location 4
9/15/2008	0:49	0:58	ST I	STI3SB	Trucks Facing South with Rear Tandem Centered on Location 3
No Trucks					
9/15/2008	1:17		ST II	STII7SB	Trucks Facing South with Location 7 Centered between trucks (i.e. Between Rows 2 and 3 of Trucks)
9/15/2008	1:22	1:26	ST II	STII6SB	Trucks Facing South with Front Axle of Front Truck Centered over Location 6
9/15/2008	1:27	1:31	ST II	STII(P2)SB	Trucks Facing South with Pier 2 Centered between trucks (i.e. Between Rows 2 and 3 of Trucks)
9/15/2008	1:31	1:35	ST II	STII3SB	Trucks Facing South with Location 3 Centered between trucks (i.e. Between Rows 2 and 3 of Trucks)
No Trucks					
9/15/2008	1:43	1:54	ST III	STIII7SB	Trucks Facing South with Location 7 Centered between trucks (i.e. Between Rows 2 and 3 of Trucks)
9/15/2008	1:55	2:08	ST III	STIII6SB	Trucks Facing South with Front Axle of Front Truck Centered over Location 6
9/15/2008	2:10	2:14	ST III	STIII(P2)SB	Trucks Facing South with Pier 2 Centered between trucks (i.e. Between Rows 2 and 3 of Trucks)
9/15/2008	2:18	2:27	ST III	STIII3SB	Trucks Facing South with Location 3 Centered between trucks (i.e. Between Rows 2 and 3 of Trucks)
No Trucks					
9/15/2008	2:33	2:36	ST III	STIII7SB	Trucks Facing South with Location 7 Centered between trucks (i.e. Between Rows 2 and 3 of Trucks)
9/15/2008	2:38	2:41	ST III	STIII6SB	Trucks Facing South with Front Axle of Front Truck Centered over Location 6
9/15/2008	2:44	2:47	ST III	STIII(P2)SB	Trucks Facing South with Pier 2 Centered between trucks (i.e. Between Rows 2 and 3 of Trucks)
9/15/2008	2:48	2:52	ST III	STIII3SB	Trucks Facing South with Location 3 Centered between trucks (i.e. Between Rows 2 and 3 of Trucks)
No Trucks					
9/15/2008	3:22	3:33	ST IVa	STIVa7SB	Trucks Facing South with Location 7 Centered between trucks (i.e. Between Rows 2 and 3 of Trucks)
9/15/2008	3:35	3:45	ST IVa	STIVa6SB	Trucks Facing South with Front Axle of Front Truck Centered over Location 6
9/15/2008	3:47	3:51	ST IVa	STIVa(P2)SB	Trucks Facing South with Pier 2 Centered between trucks (i.e. Between Rows 2 and 3 of Trucks)
9/15/2008	3:53		ST IVa	STIVa3SB	Trucks Facing South with Location 3 Centered between trucks (i.e. Between Rows 2 and 3 of Trucks)
No Trucks					
9/15/2008	4:13	4:15	ST IVa	STIVa7SB	Trucks Facing South with Location 7 Centered between trucks (i.e. Between Rows 2 and 3 of Trucks)
9/15/2008	4:17	4:21	ST IVa	STIVa6SB	Trucks Facing South with Front Axle of Front Truck Centered over Location 6
9/15/2008	4:23	4:27	ST IVa	STIVa3SB	Trucks Facing South with Location 3 Centered between trucks (i.e. Between Rows 2 and 3 of Trucks)
No Trucks					
9/15/2008	4:31	4:35	ST IVb	STIVb7SB	Trucks Facing South with Location 7 Centered between trucks (i.e. Between Rows 2 and 3 of Trucks)
9/15/2008	4:36	4:39	ST IVb	STIVb6SB	Trucks Facing South with Front Axle of Front Truck Centered over Location 6
9/15/2008	4:40	4:44	ST IVb	STIVb(P2)SB	Trucks Facing South with Pier 2 Centered between trucks (i.e. Between Rows 2 and 3 of Trucks)
9/15/2008	4:47		ST IVb	STIVb3SB	Trucks Facing South with Location 3 Centered between trucks (i.e. Between Rows 2 and 3 of Trucks)
New Day					
9/17/2008	22:28	22:39	ST I	STI14SB	Trucks Facing North with Rear Tandem Centered on Location 14
9/17/2008	22:42	22:53	ST I	STI15SB	Trucks Facing North with Front Axle Centered on Location 15
No Trucks	Start: 22:55	End: 23:07			
9/17/2008	23:16	23:20	ST I	STI14SB	Trucks Facing North with Rear Tandem Centered on Location 14
9/17/2008	23:22	23:26	ST I	STI15SB	Trucks Facing North with Front Axle Centered on Location 15
No Trucks	Start: 23:27	End: 23:31			
9/17/2008	23:37	23:40	ST I	STI7SB	Trucks Facing South with Rear Tandem Centered on Location 7
9/17/2008	23:43	23:46	ST I	STI3SB	Trucks Facing South with Rear Tandem Centered on Location 3
No Trucks					

Table 5.3: Northbound bridge static truck test information for September 2008 truck tests

Date	Time Start	Time End	Config.	Test Name	Test Description and Notes
9/15/2008	5:13	5:18	ST I	STI3NB	Trucks Facing North with Rear Tandem Centered on Location 3
9/15/2008	5:20	5:25	ST I	STI7NB	Trucks Facing North with Rear Tandem Centered on Location 7
9/15/2008	5:27		ST I	STI9NB	Trucks Facing North with Rear Tandem Centered on Location 9
New Day					
9/18/2008	0:41	0:43	ST I	STI3NB	Trucks Facing North with Rear Tandem Centered on Location 3
9/18/2008	0:45	0:47	ST I	STI7NB	Trucks Facing North with Rear Tandem Centered on Location 7
9/18/2008	0:50	0:56	ST I	STI14NB	Trucks Facing North with Rear Tandem Centered on Location 14
9/18/2008	0:57	1:01	ST I	STI15NB	Trucks Facing North with Front Axle Centered on Location 15
No Trucks	Start: 1:04	End: 1:08			
9/18/2008	1:12	1:13	ST I	STI14NB	Trucks Facing North with Rear Tandem Centered on Location 14
9/18/2008	1:14	1:16	ST I	STI15NB	Trucks Facing North with Front Axle Centered on Location 15

Table 5.4: Southbound bridge dynamic truck test information for September 2008 truck tests

Date	Approx. test time	Truck orientation	Approx. truck speed (mph)	Test Description and Notes
9/18/2008	1:22	ST V (6 Across)	20	Trucks Going South on SB Bridge; Lined up ~ 1/2 way across bridge; trucks entered on ramp, so took a while to line up
9/18/2008	1:36	ST IVa Ext.	30	Trucks Going South on SB Bridge; ~ 1/2 way across before they were assembled
9/18/2008	1:45	ST IVa Ext.	30	Trucks Going South on SB Bridge; Trucks Spaced pretty far out
9/18/2008	1:56	ST IVa Ext.	35	Trucks Going South on SB Bridge; Last 2 Trucks Trailed
9/18/2008	2:03	ST V (6 Across)	45	Trucks Going North on SB Bridge; 2:04, other 2 trucks crossed
9/18/2008	2:13	ST VI	40	Trucks Going South on SB Bridge
9/18/2008	2:19	ST V (6 Across)	45	Trucks Going North on SB Bridge
9/18/2008	2:24	ST VI	40	Trucks Going South on SB Bridge
9/18/2008	2:28	ST V (6 Across)	45	Trucks Going North on SB Bridge; 2:29, other 2 trucks crossed
9/18/2008	2:33	ST IVa Ext.	45	Trucks Going South on SB Bridge; 5 to 6 truck length space between trucks

Table 5.5: Northbound bridge dynamic truck test information for September 2008 truck tests

Date	Approx. test time	Truck orientation	Approx. truck speed (mph)	Test Description and Notes
9/18/2008	1:29	ST V (6 Across)	40	Trucks Going North on NB Bridge
9/18/2008	1:40	ST V (6 Across)	40	Trucks Going North on NB Bridge
9/18/2008	1:50	ST V (6 Across)	35	Trucks Going North on NB Bridge; 1:51 other 2 trucks crossed

Table 5.6: Truck loads and dimensions for October 2010 truck tests

MnDOT Driver Number	Truck Number	Total Weight (lbs)	Rear Axle to Middle Axle (in.)	Middle Axle to Front Axle (in.)	Out-to-out tire width (in.)
1	2257	49340	54	180.5	97
2	2256	49880	55	180.5	98
3	2252	50520	54	180.5	97
4	2360	50460	55	180.25	97.5
5	2353	50460	54	180.5	98
6	2251	48500	55	180.5	98
7	2255	49880	55	180.5	97.5
8	2253	48740	55.5	180.5	95

Table 5.7: Northbound bridge static truck tests during October 2010

Date	Time Start *	Time End *	Config.	Test Name	Test Description:	Dim A Truck 8 (in) **	Dim A Truck 1 (in) **	Notes:
10/27/2010	22:15:00	22:20:00	N/A	NB_Zero_01	Take 3 measurements with no loading			
10/27/2010	22:42:30	22:45:52	ST I	STI3NB	8 trucks across width of bridge facing North, rear tandem centered at Loc 3	-13	-27	Measured from NB Location 3
10/27/2010	22:55:20	22:58:57	ST I	STI3(+9)NB	8 trucks across width of bridge facing North, rear axle 7' north of Loc 3	82	77	Measured from NB Location 3
10/27/2010	23:06:36	23:09:53	ST I	STI7NB	8 trucks across width of bridge facing North, rear tandem centered at Loc 7	-24	-30	Measured from NB Location 7
10/27/2010	23:13:10	23:16:36	ST I	STI7(+9)NB	8 trucks across width of bridge facing North, rear axle 7' north of Loc 7	83	84	Measured from NB Location 7
10/27/2010	23:23:59	23:28:10	ST I	STI9SB	8 trucks across width of bridge facing North, rear tandem centered at Loc 9	-30	-28	Measured from NB Location 9
10/27/2010	23:31:04	23:34:53	ST I	STI9(+9)NB	8 trucks across width of bridge facing North, rear axle 7' north of Loc 9	79	80	Measured from NB Location 9
10/27/2010	23:38:10	23:46:46	ST I	STI14NB	8 trucks across width of bridge facing North, rear tandem centered at Loc 14	-33	-30	Started with truck in wrong position. Ran data twice. Second test name = STI14NB2. Measured from NB Location 14
10/27/2010	23:49:43	23:53:00	ST I	STI14(+9)NB	8 trucks across width of bridge facing North, rear axle 7' north of Loc 14	78	81	Measured from NB Location 14
10/27/2010	23:54:39	23:58:20	N/A	NB_Zero_02	Take 3 measurements with no loading			

* General Notes: Roctest data logger time was 59 minutes behind the synchronized server time (synchronized server time is listed).

** Negative dimensions indicate measuring from the nail SOUTH to the truck axle

** Positive dimensions indicate measuring from the nail NORTH to the truck axle

** Dim A = Distance from marked station (PK Nail) to rear axle.

** Refer to Table 5.6 for Truck Numbers: Truck 1 located on west edge of bridge, Truck 8 located on east edge of bridge

Table 5.8: Southbound bridge static truck tests during October 2010

Date	Time Start	Time End	Config.	Test Name	Test Description:	Dim A Truck 8 (in) *	Dim A Truck 1 (in) *	Notes:
10/29/2010	1:34:50	1:48:16	N/A	SB_Zero_01	Take 3 measurements with no loading			
10/29/2010	1:53:44	2:05:34	ST I	STI14SB	8 trucks across width of bridge facing South, rear tandem centered at Loc 14	31	38	Measured from SB Location 14
10/29/2010	2:10:45	2:22:35	ST I	STI9(-9)SB	8 trucks across width of bridge facing South, rear axle 7' south of Loc 9	-82	-83	Measured from SB Location 9
10/29/2010	2:26:54	2:38:51	ST I	STI7SB	8 trucks across width of bridge facing South, rear tandem centered at Loc 7	28	32	Measured from SB Location 7
10/29/2010	2:42:43	2:54:25	ST I	STI7(-9)SB	8 trucks across width of bridge facing South, rear axle 7' south of Loc 7	-82.5	-79	Measured from SB Location 7
10/29/2010	2:58:49	3:10:50	ST I	STI6SB	8 trucks across width of bridge facing South, front axle centered at Loc 6	480	480	Measured from SB CL of Pier 2
10/29/2010	3:14:30	3:29:30	ST I	STI3SB	8 trucks across width of bridge facing South, rear tandem centered at Loc 3	29	27	Measured from SB Location 3
10/29/2010	3:31:30	3:43:40	ST I	STI3(-70)SB	8 trucks across width of bridge facing South, rear axle 70' south of Loc 3	-840	-840	Measured from SB Location 3
10/29/2010	3:45:15	3:56:44	N/A	SB_Zero_02	Take 3 measurements with no loading			
10/29/2010	4:02:35	4:14:14	ST IVa	STIVa7SB	4 lines of two trucks each on exterior edge of bridge facing South, truck rows 2 and 3 straddle Loc 7	**	**	Measured from SB Location 7
10/29/2010	4:16:35	4:28:00	N/A	SB_Zero_03	Take 3 measurements with no loading			

* Negative dimensions indicate measuring from the nail SOUTH to the truck axle

* Positive dimensions indicate measuring from the nail NORTH to the truck axle

* Dim A = Distance from marked station (PK Nail) to rear axle.

** Measurements for Config ST IVa are as follows:

Distance from marked station (PK Nail) to rear axle of truck number 3 (second line exterior truck) = 64 in.

Distance from outside of tires on exterior trucks to outside of tires on interior trucks = 242 in. (back trucks) and 232 in. (front trucks)

Distance from back axle of front truck to back axle of back truck on the exterior side = 1052 in.

Distance of truck from rail on exterior side = 29.5 in. (back truck) and 23 in. (front truck)

Table 5.9: Reflector setup along exterior guardrail of I-35W southbound structure for October 2010 truck tests

Reflector	Bridge Station (ft)	Horizontal Range (ft)	Angle of Inclination (deg)	Projection Factor
1	224+13.80	74.9	49.99	1.31
2	224+05.50	83.2	47.01	1.37
3	223+65.10	123.6	35.83	1.71
4	223+57.10	131.6	34.14	1.78
5	223+17.50	171.2	27.53	2.16
9	222+40.40	248.3	19.77	2.96
8	222+08.40	280.3	17.66	3.30
7	221+69.00	319.7	15.60	3.72
6	221+36.60	352.1	14.22	4.07
10	220+89.20	399.5	12.59	4.59
14	219+44.30	544.4	9.31	6.18
13	219+04.60	584.1	8.69	6.62
12	218+96.70	592	8.57	6.71
15	218+64.30	624.4	8.13	7.07
16	218+56.20	632.5	8.03	7.16
19	217+98.38	690.32	7.37	7.80
11	217+68.20	720.5	7.06	8.14
18	217+34.78	753.92	6.75	8.51
17	216+87.58	801.12	6.36	9.03
20	216+08.58	880.12	5.79	9.91
21	215+99.58	889.12	5.73	10.01
22*	215+59.78	928.92	5.49	10.46

* Control point – located beyond Abutment 1

Table 5.10: With-traffic dynamic truck tests during October 2010 truck tests

Test Name	Bridge	Total Waves	Wave Number	Configuration	Date	Time Enter Bridge	Time Exit Bridge	Speed	Cars?	Heavy traffic (semi/trailer)? *	Heavy Traffic (dump trucks)? *
Open N0	NB	2	1	4455	10/28/2010	0:40:48	0:41:10	55	yes	none	none
			2	4455	10/28/2010	0:42:44	0:43:07	55	yes	none	none
Open S1	SB	2	1	4455	10/28/2010	0:48:12	0:48:39	55	yes	none	none
			2	4455	10/28/2010	0:50:49	0:51:08	55	yes	none	none
Open N1	NB	2	1	4455	10/28/2010	0:58:59	0:59:10	55	yes	7	-25
			2	4455	10/28/2010	1:01:12	1:01:33	55	yes	none	+5, +5
Open S2	SB	2	1	4455	10/28/2010	1:06:35	1:07:01	55	yes	-5	none
			2	4455	10/28/2010	1:09:24	1:09:44	55	yes	none	none
Open N2	NB	2	1	4455	10/28/2010	1:15:55	1:16:10	55	yes	none	none
			2	4455	10/28/2010	1:19:12	1:19:33	55	yes	+26	none
Open S3	SB	2	1	4455	10/28/2010	1:26:57	?	45	yes	none	none
			2	Random	10/28/2010	Random	Random	45			
Open N3	NB	2	1	4455	10/28/2010	1:37:24	1:37:43	55	yes	none	+5
			2	Random	10/28/2010	Random	Random	55			
Open S4	SB	2	1	3344	10/28/2010	1:44:46	1:45:12	55	no	none	none
			2	3344	10/28/2010	1:46:00	1:46:26	55	yes	-15, -20, -22, -30	none
Open N4	NB	2	1	3344	10/28/2010	1:54:34	1:54:52	55	yes	none	+5
			2	3344	10/28/2010	1:56:02	1:56:25	55	yes	none	none
Open S5	SB	2	1	3344	10/28/2010	2:01:54	2:02:19	55	yes	+20	none
			2	3344	10/28/2010	2:04:10	2:04:37	55	yes	+5	none
Open N5	NB	2	1	3344	10/28/2010	2:12:06	2:12:28	55	yes	+18	none
			2	3344	10/28/2010	2:15:58	2:16:25	55	yes	none	none
Open S6	SB	2	1	3344	10/28/2010	2:23:37	?	55	yes	none	none
			2	Random	10/28/2010	Random	Random	55			
Open N6	NB	2	1	3344	10/28/2010	2:36:44	2:37:20	45	yes	none	none
			2	Random	10/28/2010	Random	Random	45			
Open S7	SB	4	1	45	10/28/2010	2:44:34	2:44:54	55	yes	none	none
			2	45	10/28/2010	2:45:49	2:46:10	55	yes	+20	none
			3	34	10/28/2010	2:46:58	2:47:21	55	yes	none	none
			4	35	10/28/2010	2:48:15	2:48:37	55	yes	-10	none
Open N7	NB	4	1	45	10/28/2010	2:55:25	2:55:45	55	yes	+40	none
			2	45	10/28/2010	2:57:??	2:57:56	55	yes	+50,+14	+20
			3	34	10/28/2010	2:59:37	2:59:57	55	yes	+90,-7,-11	+77
			4	35	10/28/2010	3:01:45	3:02:00	55	yes	-3	-26
Open S8	SB	8	1	5	10/28/2010	3:08:14	3:08:54	55	yes	none	none
			2	5	10/28/2010	3:09:14	3:09:36	55	no	+20	none
			3	5	10/28/2010	3:09:56	3:01:16	55	yes	+15	none
			4	4	10/28/2010	3:11:07	3:11:28	55	yes	none	none
			5	4	10/28/2010	3:12:16	3:12:35	55	yes	none	none
			6	4	10/28/2010	3:13:09	3:13:33	55	yes	+25	none
			7	3	10/28/2010	3:14:52	3:15:14	55	yes	+67, +26	none
			8	3	10/28/2010	3:15:52	3:16:14	55	yes	none	none
Open N8	NB	8	1	5	10/28/2010	3:21:00	3:21:22	55	yes	none	none
			2	5	10/28/2010	3:22:17	3:22:36	55	yes	none	none
			3	5	10/28/2010	3:23:06	3:23:26	55	yes	+9	none
			4	4	10/28/2010	3:24:24	3:24:46	55	yes	+28	none
			5	4	10/28/2010	3:25:27	3:25:50	55	yes	none	none
			6	4	10/28/2010	3:26:30	3:36:52	55	yes	+24	0, -13
			7	3	10/28/2010	3:28:00	3:28:21	55	yes	none	-2
			8	3	10/28/2010	3:29:03	3:29:25	55	yes	none	none
Open S9	SB	1	1	33334444	10/28/2010	3:37:00	3:37:20	55	yes	none	none
Open N9	NB	1	1	33334444	10/28/2010	3:48:35	3:48:57	55	no	+16, -25	none
Open S7B	SB	4	1	45	10/28/2010	3:56:18	3:56:40	55	yes	none	none
			2	45	10/28/2010	3:57:13	3:57:34	55	no	none	none
			3	34	10/28/2010	3:58:20	3:58:41	55	no	-7	none
			4	35	10/28/2010	3:59:25	3:59:46	55	yes	none	-11

* Heavy truck columns: recorded are times in seconds of other vehicles on the bridge relative to the truck blocks.

* Positive numbers mean the non-test truck entered the bridge X seconds before the truck test block.

* Negative numbers mean the non-test truck entered the bridge X seconds after the truck test block.

Table 5.11: Closed-bridge dynamic truck tests during October 2010 truck tests

Test Name	Travel Direction	Total Waves	Wave Number	Configuration	Time Enter Bridge	Time Exit Bridge	Speed	Notes
Closed SS1	South	2	1	4455	22:33:41	22:34:05	55	
			2	4455	22:35:54	22:36:33	30	
Closed SN1	North	2	1	4455	22:44:55	22:45:15	55	Wave 1 left early (redo times are listed)
			2	4455	22:45:52	22:46:26	30	
Closed SS2	South	2	1	3344	22:51:18	22:51:41	55	
			2	3344	22:52:48	22:53:27	30	
Closed SN2	North	2	1	3344	22:56:15	22:56:35	55	Wave not tight
			2	3344	22:57:10	22:57:45	30	
Closed SS3	South	2	1	2244	23:01:33	23:01:56	55	
			2	2244	23:02:41	23:03:21	30	
Closed SN3	North	2	1	2244	23:05:49	23:06:09	55	Missed wave 1 data - redo as SN3B
			2	2244	23:06:40	23:07:16	30	
Closed SS8	South	2	1	2345	23:13:02	23:13:25	55	Lane 2 lagged behind at start
			2	2345	23:14:40	23:15:19	30	
Closed SN8	North	2	1	1245	23:20:01	23:20:21	55	Lane 1 braked and pulled onto shoulder at exit
			2	1245	23:20:47	23:21:23	30	Lane 1 braked and pulled onto shoulder at exit
Closed SS9	South	1	1	33334444	23:26:22	23:26:44	55	
Closed SN9	North	1	1	33334444	23:29:58	23:30:34	30	
Closed SS10	South	8	1	5	23:36:01	23:36:24	55	#2257
			2	5	23:36:53	23:37:16	55	#2256
			3	4	23:37:42	23:38:03	55	#2252
			4	4	23:38:30	23:38:51	55	#2360
			5	3	23:39:21	23:39:45	55	#2353
			6	3	23:40:04	23:40:25	55	#2251
			7	2	23:40:57	23:41:19	55	#2255
			8	2	23:41:43	23:42:05	55	#2253
Closed SN3B	North	2	1	2244	23:45:34	23:45:51	55	Big gap between two lines - wave not tight
			2	2244	23:46:26	23:47:00	30	good

Table 6.1: Truck test positions used in validation of the three-dimensional finite element model

Truck Orientation	Bridge Location	Truck Test Name	Description
ST I	SB Loc. 3	STI3SB	Trucks facing south with rear tandem centered on location 3
ST I	SB Loc. 6	STI6SB	Trucks facing south with front axle centered over location 6
ST I	SB Loc. 7	STI7SB	Trucks facing south with rear tandem centered on location 7
ST I	SB Loc. 9	STI9SB	Trucks facing south with rear tandem centered on location 9
ST II	SB Loc. 3	STII3SB	Trucks facing south with location 3 centered between rows 2 and 3 of trucks
ST II	SB Loc. 7	STII7SB	Trucks facing south with location 7 centered between rows 2 and 3 of trucks
ST III	SB Loc. 3	STIII3SB	Trucks facing south with location 3 centered between rows 2 and 3 of trucks
ST III	SB Loc. 7	STIII7SB	Trucks facing south with location 7 centered between rows 2 and 3 of trucks
ST IVa	SB Loc. 3 Ext.	STIVa3SB	Trucks facing south with location 3 centered between rows 2 and 3 of trucks
ST IVa	SB Loc. 7 Ext.	STIVa7SB	Trucks facing south with location 7 centered between rows 2 and 3 of trucks
ST IVb	SB Loc. 3 Int.	STIVb3SB	Trucks facing south with location 3 centered between rows 2 and 3 of trucks
ST IVb	SB Loc. 7 Int.	STIVb7SB	Trucks facing south with location 7 centered between rows 2 and 3 of trucks
ST I	SB Loc. 3(-70)	STI3(-70)SB	Trucks facing south - STI3SB offset by 70.0 ft south (down station)
ST I	SB Loc. 7(-9)	STI7(-9)SB	Trucks facing south - STI7SB offset by 9.0 ft south (down station)

Table 6.2: Maximum FEM transverse and vertical strains at Locations 3 and 7

Location 7

Test	Transverse (με)		Vertical (με)	
	Maximum Compressive	Maximum Tensile	Maximum Compressive	Maximum Tensile
STI7SB	-29.0	29.5	-14.6	6.3
STIVa7SB	-45.1	35.9	-52.1	54.6
STII7SB	-29.0	34.8	-35.8	35.5
STIII7SB	-50.5	52.0	-29.5	26.7

Location 3

Test	Transverse (με)		Vertical (με)	
	Maximum Compressive	Maximum Tensile	Maximum Compressive	Maximum Tensile
STI3SB	-29.2	30.3	-15.9	8.6
STIVa3SB	-42.0	39.6	-49.9	51.4
STII3SB	-26.6	31.1	-36.2	33.4
STIII3SB	-43.8	46.5	-30.8	26.6

Locations for maximal strains discussed in Section 6.2.3

Table 6.3: List of truck tests used for validation of two-dimensional finite element model

Test	Description	Testing Date
STI3(-70)SB	Trucks facing south, rear axle 70 ft. south of Loc. 3	Oct. 2010
STI3SB	Trucks facing south, rear tandem centered at Loc. 3	Sep. 2008 and Oct. 2010 average
STI6SB	Truck facing south, front axle centered at Loc. 6	Sep. 2008
STI7(-9)SB	Trucks facing south, rear axle 7 ft. south of Loc. 7	Oct. 2010
STI7SB	Trucks facing south, rear tandem centered at Loc. 7	Sep. 2008 and Oct. 2010 average
STI9(-9)SB	Trucks facing south, rear axle 7 ft. south of Loc. 9	Oct. 2010
STI9SB	Trucks facing south, rear tandem centered at Loc. 9	Sep. 2008

Table 7.1: Dates, times, and weather conditions for maximum measured positive thermal gradients

Date	Maximum Gradient Time (CST)	Daily Max Temperature (°F)	Daily Min Temperature (°F)	Daily Mean Wind Speed (miles/hour)	Daily Precipitation (in.)	Weather Events
5/16/2010	14:00	73	54	3	0.00	Mostly cloudy morning, scattered clouds in afternoon
6/17/2010	15:00	90	66	10	0.01	Partly cloudy/scattered clouds in morning and afternoon, thunderstorm at 18:00
6/6/2011	15:00	97	70	4	0.00	Clear morning, partly cloudy afternoon
6/7/2011	14:00	102	79	8	0.00	Clear
7/1/2011	15:00	99	72	5	0.14	Mostly cloudy morning, scattered clouds in afternoon, thunderstorm at 19:00

Table 7.2: Dates, times, and weather conditions for maximum measured negative thermal gradients

Date	Maximum Gradient Time (CST)	Daily Max Temperature (°F)	Daily Min Temperature (°F)	Daily Mean Wind Speed (miles/hour)	Daily Precipitation (in)	Weather Events
1/2/2010	8:00	1	-15	3	0.00	Clear morning, partly cloudy afternoon
1/3/2010	8:00	7	-15	2	0.00	Partly cloudy morning, clear afternoon
1/21/2011	6:00	3	-16	3	0.01	Clear early morning, overcast with light snow in afternoon
2/8/2011	7:00	3	-9	6	0.00	Clear morning, partly cloudy afternoon
9/15/2011	6:00	57	36	2	0.00	Clear early morning, mostly cloudy afternoon, overcast evening

Table 7.3: Initial strain (i.e. uniform temperature) dates and times and fitting parameters from Eqn. (7-2) for maximum measured positive gradients

Maximum Gradient Date	Maximum Gradient Time (CST)	Uniform Temperature Date	Uniform Temperature Time (CST)	Fitting parameter T_0 (°F) for Eqn. (7-2)	Fitting parameter n for Eqn. (7-2)
5/16/2010	14:00	4/14/2010	8:00	48.17	6
6/17/2010	15:00	6/8/2010	16:00	51.53	6
6/6/2011	15:00	8/3/2011	8:00	56.16	6
6/7/2011	14:00	8/2/2011	12:00	51.37	6
7/1/2011	15:00	8/2/2011	12:00	51.45	5

Table 8.1: Information for ambient data used for modal analysis

Date	Operational condition	Note
Feb. 01, 2010	Ambient, i.e. open to traffic	Average temperature in the range of -11°C to -8°C
Mar. 10, 2010		Average temperature in the range of 3°C to 4°C
Jun. 10, 2010		Average temperature in the range of 19°C to 20°C
Jun. 23, 2010		Average temperature in the range of 24°C to 26°C
Oct. 26, 2010		Average temperature in the range of 10°C

Table 8.2: Mean frequency values obtained at different dates for the SB structure using NExT-ERA/DC

Mode	Description	Feb. 01	Mar. 10	Oct. 26	Jun. 10	Jun. 23
SB: mode 1	Bending	0.831	0.814	0.808	0.803	0.803
SB: mode 2	Bending	1.563	1.531	1.519	1.506	1.509
SB: mode 3	Bending	2.269	2.307	2.275	2.259	2.262
SB: mode 4	Torsion	2.368	2.356	2.345	2.325	2.32
SB: mode 5	Torsion - Span 1	3.119	3.086	3.048	2.984	2.996
SB: mode 6-1	Torsion - Span 1	3.087	3.052	3.018	3.057	2.983
SB: mode 6-2	Torsion - Span 1	3.13	3.128	3.076	3.013	3.034
SB: mode 6-3	Bending	3.169	3.118	3.122	3.019	3.042
SB: mode 7	Torsion - Span 3	3.676	3.641	3.617	3.584	3.577
SB: mode 8	Torsion - Span 3	4.264	4.209	4.179	4.139	4.129
SB: mode 9	Bending	4.526	4.496	4.476	4.441	4.441
SB: mode 10	Opposed twisting	4.799	4.697	4.622	4.542	4.524
SB: mode 11	Bending	5.331	5.279	5.263	5.22	5.222
SB: mode 12	Torsion	5.72	5.661	5.666	5.626	5.761
SB: mode 13	Torsion	6.396	6.314	6.295	6.175	--
SB: mode 14	Opposed twisting	--	6.603	6.549	6.449	6.462
SB: mode 15	Bending	--	--	--	--	--
SB: mode 16	Torsion + transverse bending	--	--	9.799	9.614	9.655

Table 8.3: Mean frequency values obtained at different dates for the NB structure using NExT-ERA/DC

Mode	Description	Feb. 01	Mar. 10	Oct. 26	Jun. 10	Jun. 23
NB: mode 1	Bending	0.816	0.799	0.794	0.788	0.788
NB: mode 2	Bending	1.469	1.441	1.432	1.418	1.416
NB: mode 3	Bending	2.323	2.324	2.311	2.294	2.29
NB: mode 4	Torsion	2.383	2.37	2.358	2.34	2.334
NB: mode 5	Torsion - Span 1	2.847	2.808	2.774	2.74	2.73
NB: mode 6-1	Torsion - Span 1	--	--	--	--	--
NB: mode 6-2	Torsion - Span 1	--	--	--	--	--
NB: mode 6-3	Bending	3.268	3.235	3.22	3.204	3.2
NB: mode 7	Torsion - Span 3	3.755	3.72	3.695	3.665	3.567
NB: mode 8	Torsion - Span 3	4.411	4.352	4.311	4.269	4.259
NB: mode 9	Bending	--	4.117	4.108	4.079	4.068
NB: mode 10	Opposed twisting	--	--	--	--	--
NB: mode 11	Bending	5.188	5.151	5.151	5.102	5.086
NB: mode 12	Torsion	6.218	6.137	6.077	6.039	6.026
NB: mode 13	Torsion	--	--	--	--	--
NB: mode 14	Opposed twisting	--	--	--	--	--
NB: mode 15	Bending	--	--	--	--	--
NB: mode 16	Torsion + transverse bending	--	--	9.868	--	9.746

Table 8.4: Frequency and damping ratio estimates identified from ambient data measured on October 26, 2010 using NExT-ERA/DC

Mode	Mode Shape Description	Southbound Bridge				Northbound Bridge			
		Frequency (Hz)		Damping Ratio (%)		Frequency (Hz)		Damping Ratio (%)	
		Mean	CoV	Mean	CoV	Mean	CoV	Mean	CoV
1	Bending	0.808	0.004	0.93%	0.26	0.794	0.004	0.85%	0.29
2	Bending	1.519	0.005	1.05%	0.33	1.432	0.009	0.93%	0.32
3	Bending	2.275	0.006	1.25%	0.29	2.311	0.003	0.78%	0.32
4	Torsion	2.345	0.001	0.43%	0.31	2.358	0.001	0.42%	0.27
5	Torsion - Span 1	3.041	0.009	1.29%	0.39	2.774	0.005	0.98%	0.34
6-1	Torsion - Span 1	3.019	0.013	1.48%	0.44	--	--	--	--
6-2	Torsion - Span 1	3.076	0.016	1.08%	0.61	--	--	--	--
6-3	Bending	3.122	0.011	1.02%	0.69	3.220	0.004	0.67%	0.49
7	Torsion - Span 3	3.617	0.003	0.77%	0.33	3.695	0.002	0.60%	0.30
8	Torsion - Span 3	4.179	0.002	0.71%	0.42	4.311	0.003	0.66%	0.32
9	Bending	4.476	0.006	0.90%	0.34	4.108	0.002	0.93%	0.26
10	Opposed twisting	4.622	0.002	0.73%	0.20	--	--	--	--
11	Bending	5.263	0.004	1.21%	0.34	5.151	0.012	0.66%	0.34
12	Torsion	5.666	0.029	0.57%	0.37	6.077	0.001	0.68%	0.19
13	Torsion	6.295	--	1.05%	--	--	--	--	--
14	Opposed twisting	6.549	0.002	0.60%	0.29	--	--	--	--
15	Bending	--	--	--	--	--	--	--	--
16	Torsion + transverse bending	9.799	0.001	0.29%	0.41	9.868	0.005	0.22%	0.32

Table 8.5: Summary of modeled mode shapes captured from southbound structure finite element model

FEM Mode	Mode Shape Description	FEM Freq. (Hz)	Mean SB Measured Freq, Oct. 10 (Hz)	Percent Error	Measured SB Mode Equivalent
A	Bending	0.750	0.808	7.19%	1
B	Longitudinal Deflection	0.815	-	-	-
C	Transverse Bending	1.158	-	-	-
D	Bending	1.464	1.519	3.60%	2
E	Transverse Bending	2.038	-	-	-
F	Bending	2.143	2.275	5.81%	3
G	Torsion	2.242	2.345	4.38%	4
H	Torsion - Span 1	2.904	3.048	4.72%	5 or 6-1
I	Torsion - Span 1	2.936	3.076	4.55%	6-2
J	Torsion	3.439	-	-	-
K	Torsion - Span 3	3.465	3.617	4.20%	7
L	Torsion - Span 3	4.003	4.179	4.23%	8
M	Bending	4.193	4.476	6.32%	9
N	Opposed twisting	4.527	4.622	2.05%	10
O	Bending	4.967	5.263	5.63%	11
P	Torsion	5.250	5.666	7.34%	12
Q	Transverse Bending	5.351	-	-	-
R	Transverse Bending	5.436	-	-	-
S	Opposed twisting - Span 1	5.511	-	-	-
T	Torsion	5.922	6.295	5.92%	13
U	Opposed twisting	6.472	6.549	1.18%	14
V	Bending	6.903	-	-	15
W	Transverse Bending	7.104	-	-	-
X	Torsion	7.727	-	-	-
Y	Bending - Span 3	7.806	-	-	-
Z	Opposed twisting	7.828	-	-	-
AA	Transverse Bending	7.958	-	-	-
AB	Transverse Bending	8.498	-	-	-
AC	Transverse Bending	8.834	-	-	-
AD	Bending - Span 1	8.850	-	-	-
AE	Opposed twisting	9.135	-	-	-
AF	Torsion + Transverse Bending	9.505	9.799	3.00%	16
AG	Torsion - Span 1	9.650	-	-	-
AH	Bending - Span 2	9.931	-	-	-

Table 8.6: Extracted modes from dynamic truck test Closed SS9 using NExT-ERA/DC

Mode	Frequency (Hz)	Damping Ratio	CMI	Description
SB: mode 1	0.802	0.87%	0.998	Bending
SB mode 2	1.491	1.64%	0.963	Bending
SB: mode 3	2.219	2.56%	0.864	Bending
SB: mode 4	2.327	0.68%	0.716	Torsion
SB: mode 6-3	3.141	0.97%	0.957	Bending
SB: mode 7a*	3.508	0.39%	0.822	Torsion - Span 3
SB: mode 7b*	3.624	1.54%	0.896	Torsion - Span 3
SB: mode 8	4.166	0.82%	0.883	Torsion - Span 3
SB: mode 9	4.480	1.49%	0.899	Bending
SB: mode 10	4.601	0.69%	0.936	Opposed Twisting
SB: mode 14	6.620	0.78%	0.771	Opposed Twisting
SB: mode 15	7.293	0.58%	0.757	Bending

* Appeared to be similar modes, but were split by the NExT-ERA/DC sorting routine.

Table 8.7: Extracted modes from dynamic truck test Closed SS10, Wave 8 using NExT-ERA/DC

Mode	Frequency (Hz)	Damping Ratio	CMI	Description
SB: mode 1	0.810	0.91%	0.990	Bending
SB: mode 2	1.522	0.74%	0.892	Bending
SB: mode 3	2.301	2.10%	0.844	Bending
SB: mode 5	3.052	0.79%	0.880	Torsion - Span 1
SB: mode 6-3	3.210	1.05%	0.807	Bending
SB: mode 7	3.618	0.79%	0.938	Torsion – Span 3

Table 8.8: Extracted modes from dynamic truck test Open S4, Wave 2 using NExT-ERA/DC

Mode	Frequency (Hz)	Damping Ratio	CMI	Description
SB: mode 1	0.823	1.54%	0.970	Bending
SB: mode 2	1.513	0.75%	0.971	Bending
SB: mode 3	2.276	1.00%	0.926	Bending
SB: mode 4	2.333	0.58%	0.976	Torsion
SB: mode 5	3.028	0.75%	0.954	Torsion - Span 1
SB: mode 6-3	3.142	0.32%	0.980	Bending
SB: mode 7	3.621	0.37%	0.937	Torsion - Span 3
SB: mode 9	4.507	0.80%	0.835	Bending
SB: mode 11	5.264	0.57%	0.899	Bending
SB: mode 12	5.613	0.30%	0.931	Torsion
SB: mode 15	7.331	0.22%	0.783	Bending

Table 9.1: Load cases and corresponding multiple presence factors used for investigation of critical Service III live loading

Loading	Permit	LRT	HL-93 (by total loaded lanes)			
			1	2	3	4 or more
Permit + HL-93	1.20	0.00	1.20	1.00	0.85	0.75
Permit + HL-93 + LRT	1.00	1.00	1.20	1.00	0.85	0.75
Permit + LRT	1.20	1.00	0.00	0.00	0.00	0.00
Permit	1.20	0.00	0.00	0.00	0.00	0.00
HL-93	0.00	0.00	1.20	1.00	0.85	0.75
HL-93 + LRT	0.00	1.00	1.20	1.00	0.85	0.75

Table 9.2: Summary of expansion predictions of southbound Spans 1 through 3 due to uniform temperature changes

Scenario	Abutment 1 (in./°F)	Pier 4* (in./°F)	Total (in./°F)
Unrestrained expansion (design CTE values)	N/A	N/A	0.077
Inspection and Maintenance Manual (design CTE values)**	0.039	0.036	0.075
Measured linear potentiometer data**	0.039	0.031	0.070
Finite element model (measured CTE values)	0.038	0.033	0.071

* Only due to expansion of Spans 1 through 3, excluding deflection of Pier 4
** Assuming that deflection of Pier 4 was equal to total expansion of Span 4

Table 9.3: Multiple presence factor using AASHTO LRFD specifications, Section 3.6.1.1.2

Number of Loaded Lanes	Multiple Presence Factor, *m*
1	1.20
2	1.00
3	0.85
>3	**0.75

** Design of structures according to MnDOT specifications uses $m = 0.75$ for more than 3 lanes of loading as opposed to 0.65 as specified in AASTHO LRFD

Table 9.4: FEM computed stresses at critical locations from Figure 9.19 at midspan due to investigated load configurations

Load Case:		PT+DL Only*	1/4	2	3/8	5	6/7	Max. Diff Def.
Section	Face	Stress (psi)						
A	Inside Face	51.2	236.1	38.4	40.0	40.5	41.2	38.5
	Outside Face	133.1	27.5	188.4	**351.3**	**358.6**	154.9	189.4
B	Inside Face	162.1	81.0	28.5	28.3	31.2	**312.2**	27.7
	Outside Face	50.2	111.3	**273.6**	**285.4**	**307.4**	52.0	174.2
C	Top Face	-56.2	-187.0	-69.9	24.6	-2.5	27.2	-1.4
	Bottom Face	80.6	189.1	116.7	41.2	67.7	10.0	59.7
D	Top Face	-120.4	20.3	21.0	-49.6	-15.8	-205.0	-14.9
	Bottom Face	130.7	11.0	36.3	105.3	74.8	199.1	67.8
E	Inside Face	64.1	135.2	176.9	159.8	158.3	223.1	**391.8**
	Outside Face	124.0	53.2	37.8	41.5	42.1	36.2	49.2
F	Inside Face	125.9	134.2	137.1	134.8	135.2	118.9	134.7
	Outside Face	55.6	51.3	50.1	51.2	51.0	61.5	52.5
G	Top Face	-45.0	-73.5	-89.7	-84.2	-83.2	-127.9	-174.0
	Bottom Face	59.7	79.0	90.6	87.0	86.1	123.0	153.1
H	Top Face	-170.3	-143.6	-127.0	-131.2	-132.4	-91.0	-28.3
	Bottom Face	166.7	141.6	126.2	130.3	131.4	95.4	37.6

* Post-tensioning stresses taken at release with immediate losses only. No long-term losses considered.

Bold values exceed transverse tensile stress limit of 240 psi.

Table 9.5: FEM computed stresses at critical locations from Figure 9.19 at quarter span due to investigated load configurations

Load Case:		PT+DL Only*	1/4	2	3/8	5	6/7
Section	Face	Stress (psi)					
A	Inside Face	52.1	193.1	34.2	33.8	34.6	62.6
	Outside Face	188.9	40.0	**261.3**	**388.9**	**403.0**	177.4
B	Inside Face	55.3	43.6	28.1	27.2	29.5	168.7
	Outside Face	213.4	229.0	**370.0**	**407.9**	**420.4**	73.0
C	Top Face	14.3	-59.1	29.0	86.6	77.3	34.2
	Bottom Face	-6.6	57.9	-16.0	-66.6	-57.7	-24.3
D	Top Face	52.1	88.3	111.7	94.0	110.3	-10.4
	Bottom Face	-45.7	-78.5	-94.9	-77.1	-92.3	10.2
E	Inside Face	186.8	222.7	241.8	235.5	231.6	**326.0**
	Outside Face	62.6	48.4	44.9	46.0	46.9	45.6
F	Inside Face	100.8	111.9	119.2	117.8	117.0	118.6
	Outside Face	152.8	140.1	132.6	134.2	135.0	137.5
G	Top Face	-20.6	-30.6	-36.3	-34.4	-32.8	-81.8
	Bottom Face	20.0	28.3	33.0	31.4	30.0	74.1
H	Top Face	39.1	35.8	34.0	34.3	34.0	56.3
	Bottom Face	-35.0	-32.0	-30.4	-30.7	-30.4	-51.2

* Post-tensioning stresses taken at release with immediate losses only. No long-term losses considered.

Bold values exceed transverse tensile stress limit of 240 psi.

Table 9.6: Shear forces carried per web at southbound station 219+65.4 (83.5 ft (25.5 m) north of centerline of Pier 2) due to Load Case 1/4 (Figg 2008, image reproduced with permission from Figg Bridge Engineers, Inc.)

Box Girder	Web	Load at Quarter Span (219+81.9)		Load at Midspan (221+37.4)	
		LRM Shear (k)	FEM Shear (k)	LRM Shear (k)	FEM Shear (k)
Ext (West)	West	286.66	270.66	127.93	113.61
Ext (West)	East	18.30	-49.74	8.17	-50.68
Int (East)	West	0.00	73.69	0.00	56.50
Int (East)	East	0.00	-10.99	0.00	-13.07
Total		304.96	283.62	136.09	106.35

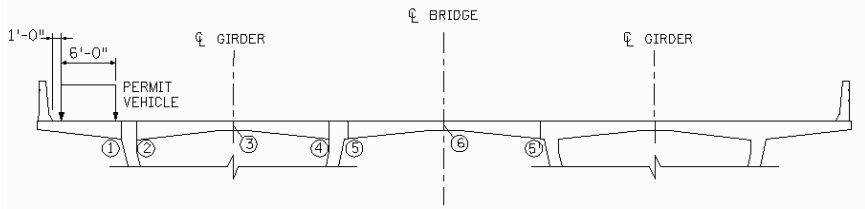

Table 9.7: Shear forces carried per web at southbound station 219+65.4 (83.5 ft (25.5 m) north of centerline of Pier 2) due to Load Case 2 (Figg 2008, image reproduced with permission from Figg Bridge Engineers, Inc.)

Box Girder	Web	Load at Quarter Span (219+81.9)		Load at Midspan (221+37.4)	
		LRM Shear (k)	FEM Shear (k)	LRM Shear (k)	FEM Shear (k)
Ext (West)	West	206.09	201.77	97.34	90.47
Ext (West)	East	144.53	61.85	68.13	-17.74
Int (East)	West	0.00	81.07	0.00	73.89
Int (East)	East	0.00	-11.03	0.00	-14.05
Total		350.62	333.65	165.47	132.57

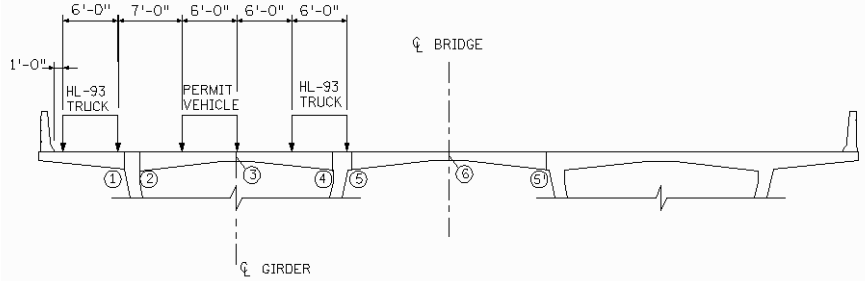

Table 9.8: Shear forces carried per web at southbound station 219+65.4 (83.5 ft (25.5 m) north of centerline of Pier 2) due to Load Case 3/8 (Figg 2008, image reproduced with permission from Figg Bridge Engineers, Inc.)

Box Girder	Web	Load at Quarter Span (219+81.9)		Load at Midspan (221+37.4)	
		LRM Shear (k)	FEM Shear (k)	LRM Shear (k)	FEM Shear (k)
Ext (West)	West	124.27	122.91	58.54	58.02
Ext (West)	East	209.04	119.34	95.50	6.70
Int (East)	West	0.00	86.58	0.00	70.77
Int (East)	East	0.00	-10.68	0.00	-12.19
Total		333.31	318.14	154.04	123.30

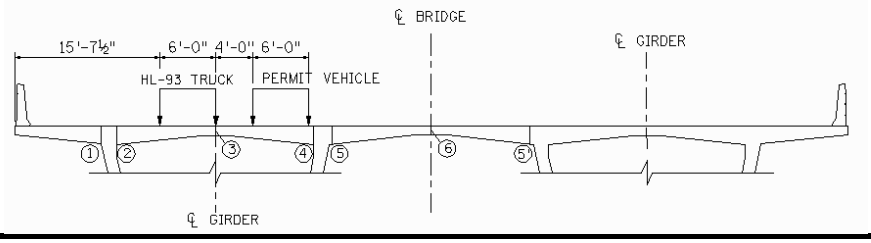

Table 9.9: Shear forces carried per web at southbound station 219+65.4 (83.5 ft (25.5 m) north of centerline of Pier 2) due to Load Case 5 (Figg 2008, image reproduced with permission from Figg Bridge Engineers, Inc.)

Box Girder	Web	Load at Quarter Span (219+81.9)		Load at Midspan (221+37.4)	
		LRM Shear (k)	FEM Shear (k)	LRM Shear (k)	FEM Shear (k)
Ext (West)	West	172.38	168.29	78.56	73.34
Ext (West)	East	160.93	79.20	75.49	-7.22
Int (East)	West	0.00	80.45	0.00	69.80
Int (East)	East	0.00	-11.17	0.00	-12.95
Total		333.31	316.77	154.04	122.97

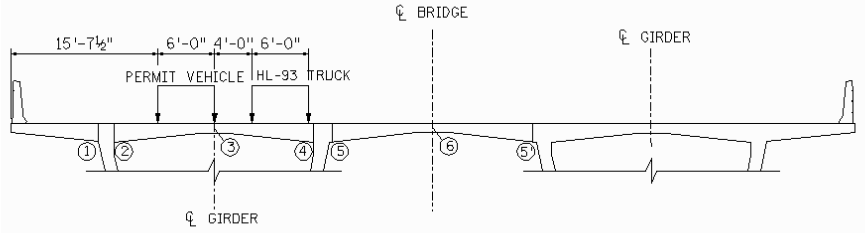

Table 9.10: Shear forces carried per web at southbound station 219+65.4 (83.5 ft (25.5 m) north of centerline of Pier 2) due to Load Case 6/7 (Figg 2008, image reproduced with permission from Figg Bridge Engineers, Inc.)

Box Girder	Web	Load at Quarter Span (219+81.9)		Load at Midspan (221+37.4)	
		LRM Shear (k)	FEM Shear (k)	LRM Shear (k)	FEM Shear (k)
Ext (West)	West	3.48	6.27	1.79	2.05
Ext (West)	East	75.70	152.61	38.84	60.67
Int (East)	West	270.91	144.50	120.90	61.04
Int (East)	East	-16.78	10.01	-7.49	0.57
Total		333.31	313.39	154.04	124.33

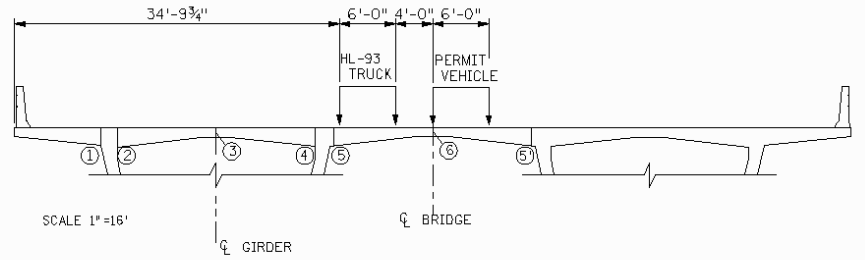

Table 9.11: Summary of maximum shear forces per web from all examined load cases

Box Girder	Web	Load at Quarter Span (219+81.9)		Load at Midspan (221+37.4)	
		LRM Shear (k)	FEM Shear (k)	LRM Shear (k)	FEM Shear (k)
Ext (West)	West	**286.66**	**270.66**	**127.93**	**113.61**
Ext (West)	East	209.04	152.61	95.50	60.67
Int (East)	West	270.91	144.50	120.90	73.89
Int (East)	East	16.78	11.17	7.49	14.05

Figures

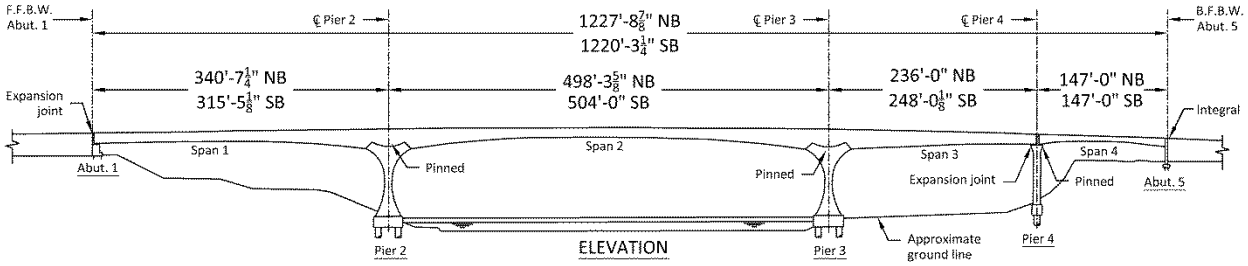

Figure 1.1: Elevation view of the adjacent bridges

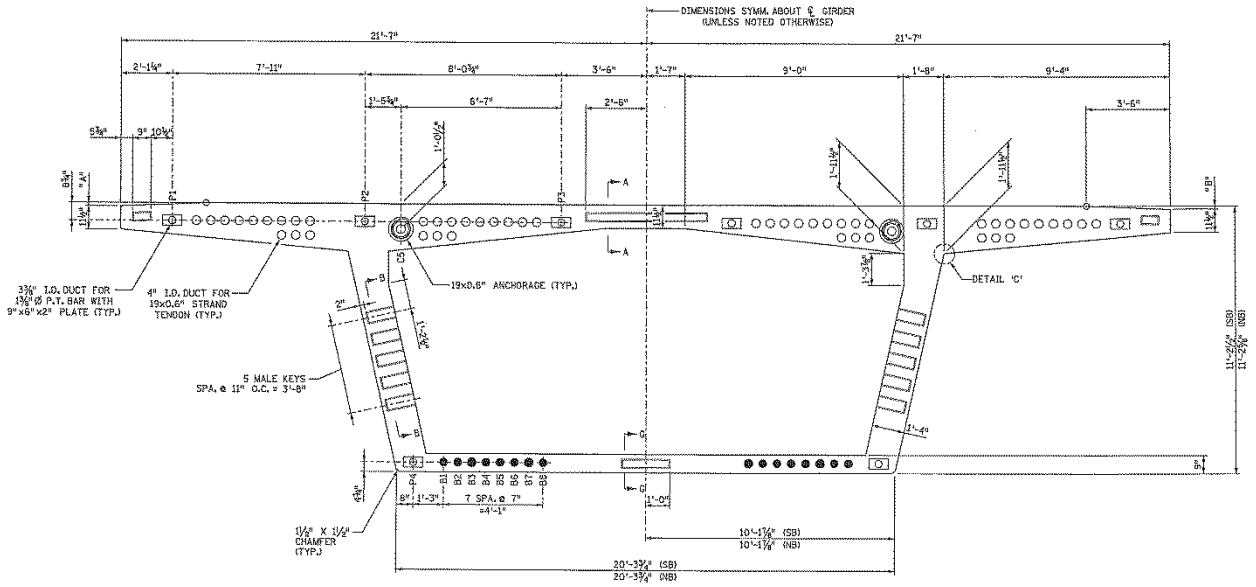

Figure 1.2: Cross section of the southbound bridge exterior box at midspan of Span 2 (other boxes similar)

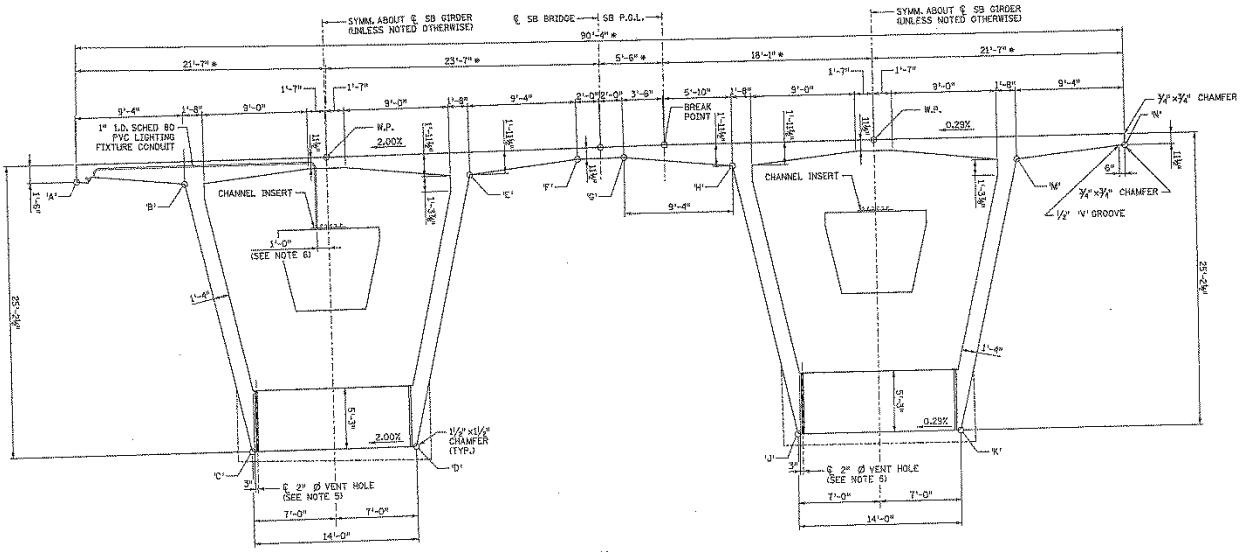

Figure 1.3: Cross section of Span 2 of the southbound bridge near Pier 2 (cross section near Pier 3 similar)

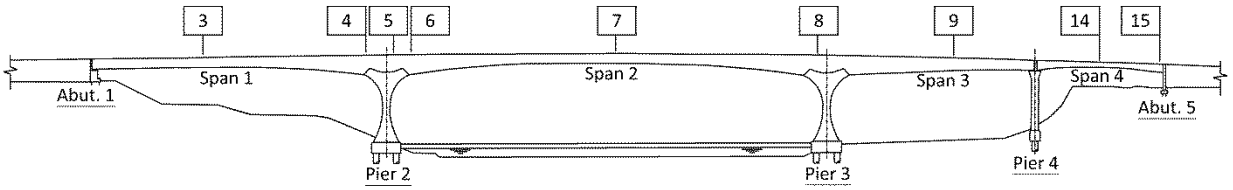

Figure 2.1: Elevation view of the adjacent bridges showing VWSG Locations 3, 4, 5, 6, 7, 8, 9, 14, and 15

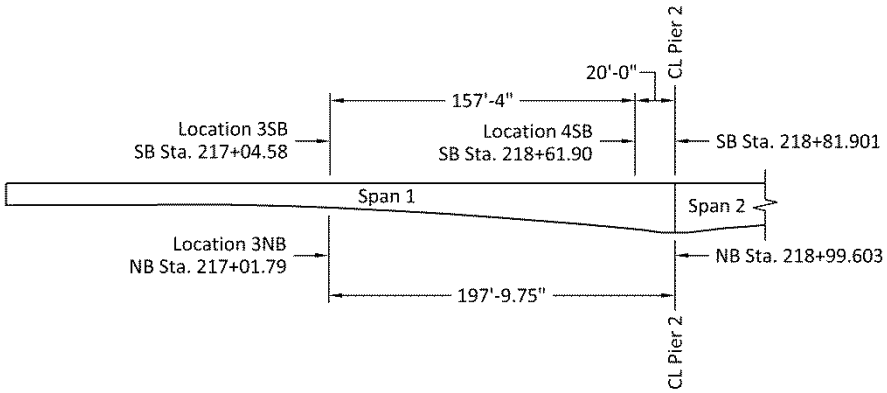

Figure 2.2: Elevation view of Span 1 of the adjacent bridges showing VWSG Locations 3 and 4

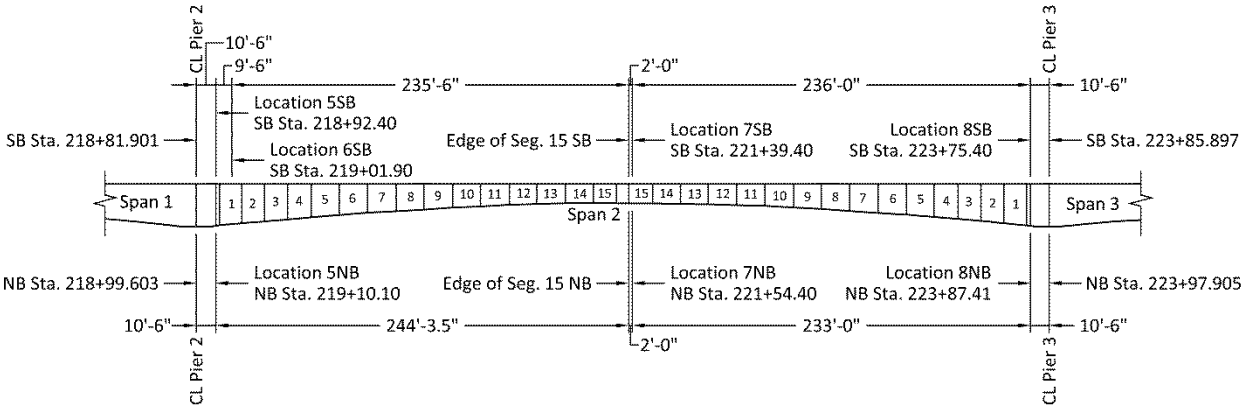

Figure 2.3: Elevation view of Span 2 of the adjacent bridges showing VWSG Locations 5, 6, 7, and 8

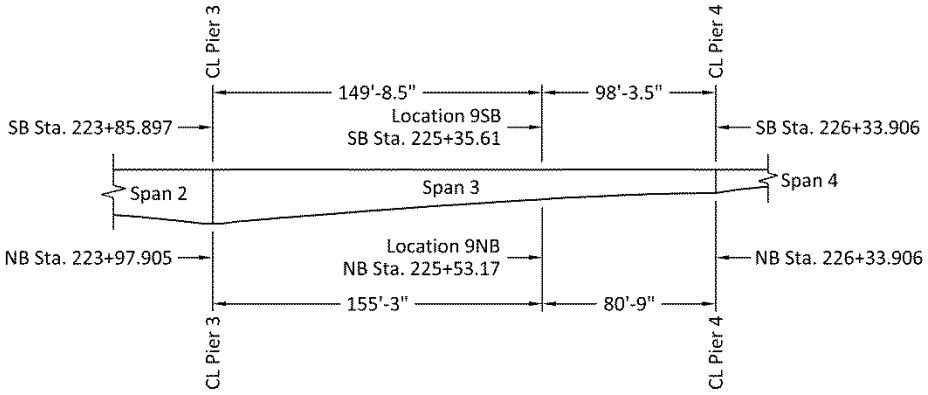

Figure 2.4: Elevation view of Span 3 of the adjacent bridges showing VWSG Location 9

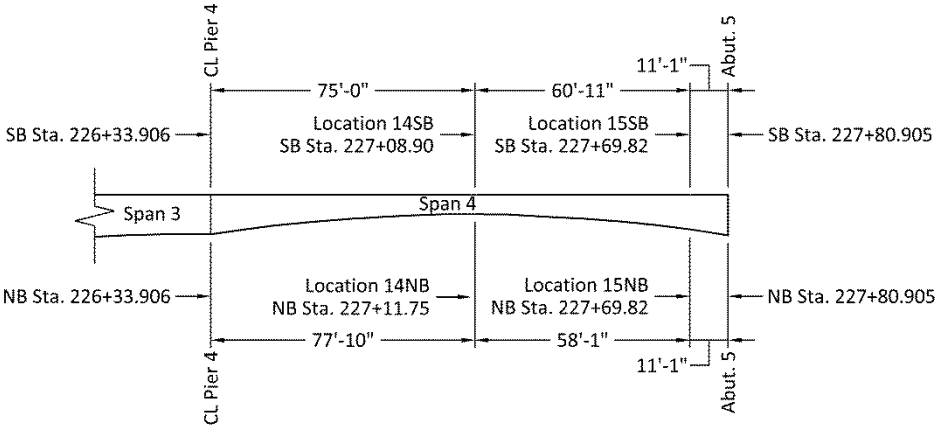

Figure 2.5: Elevation view of Span 4 of the adjacent bridges showing VWSG Locations 14 and 15

Figure 2.6: Installed Roctest EM-5 VWSG

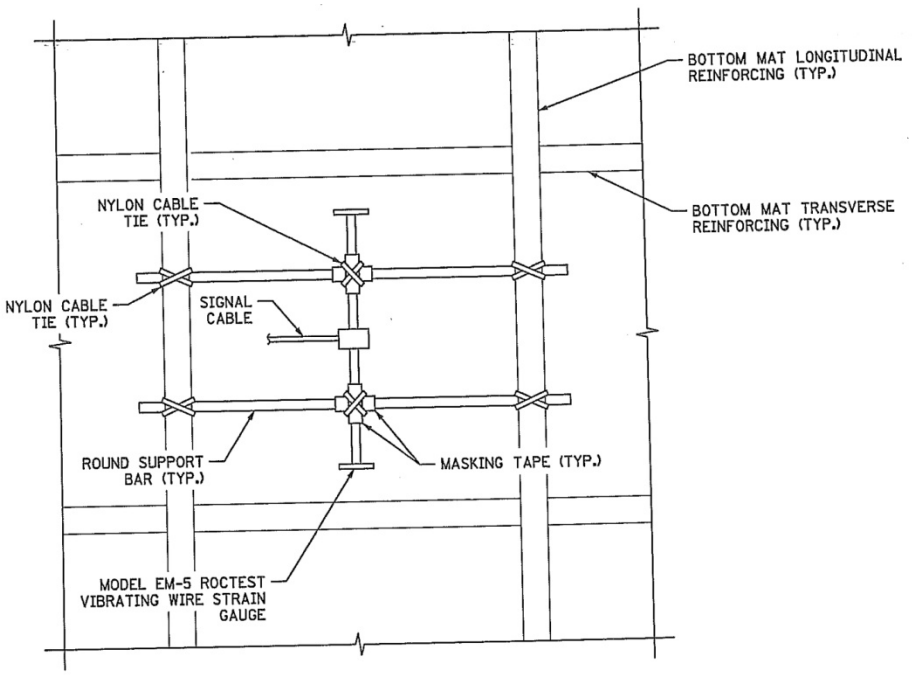

Figure 2.7: Typical installation of a longitudinal VWSG

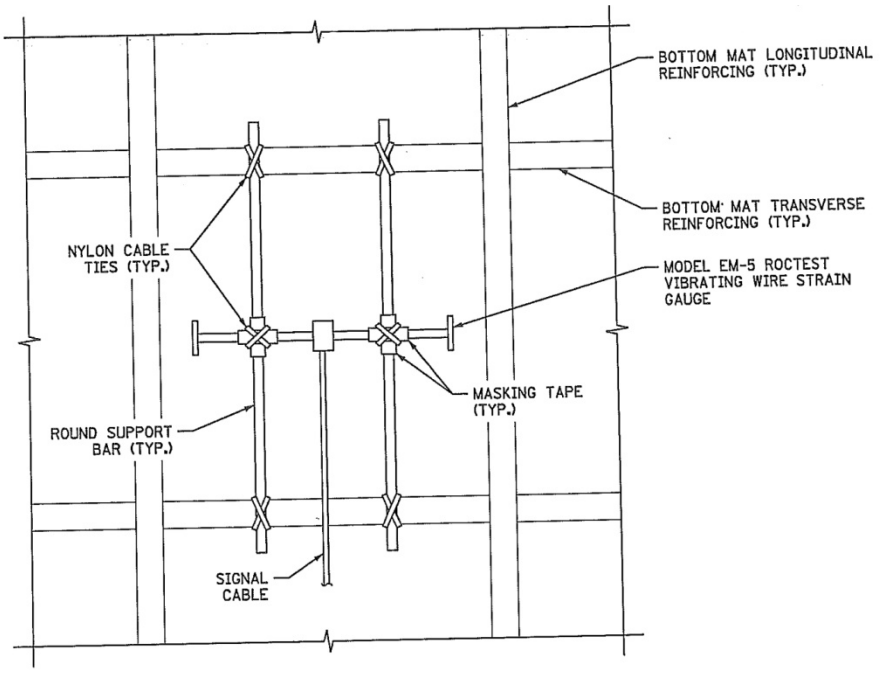

Figure 2.8: Typical installation of a transverse VWSG

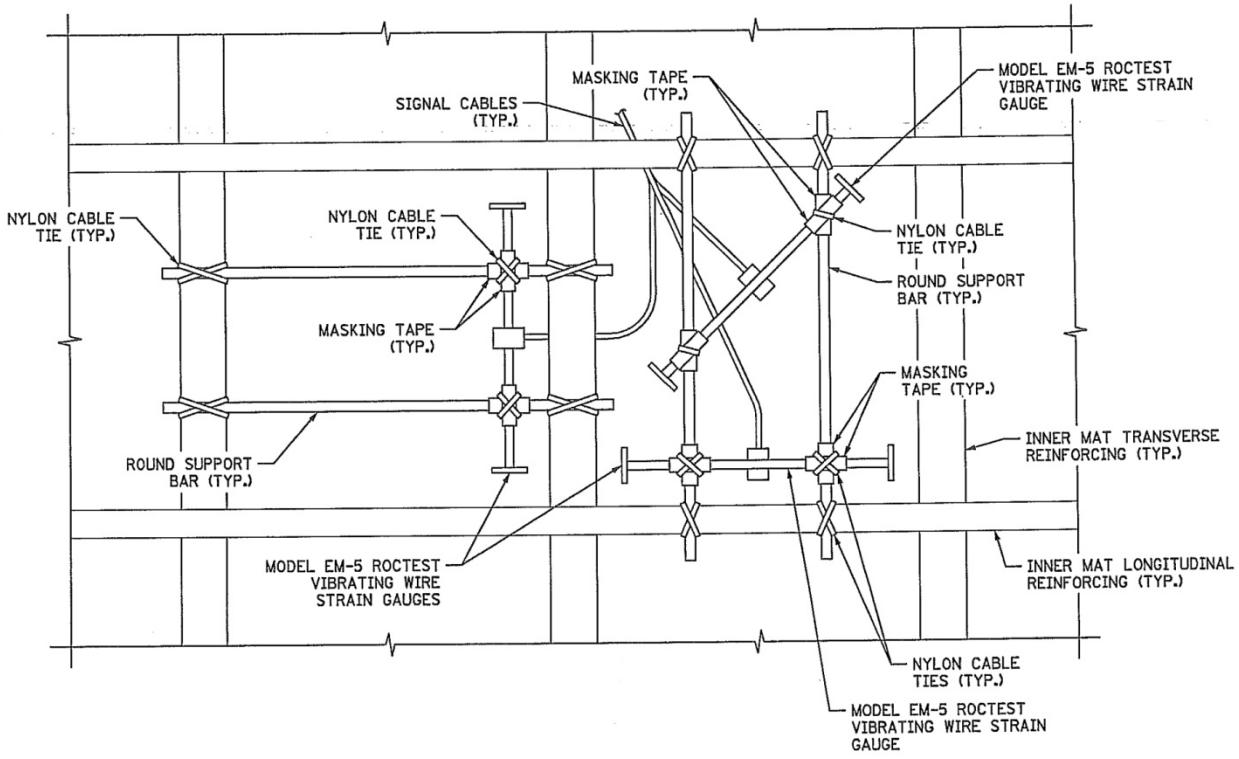

Figure 2.9: Typical installation of a VWSG rosette

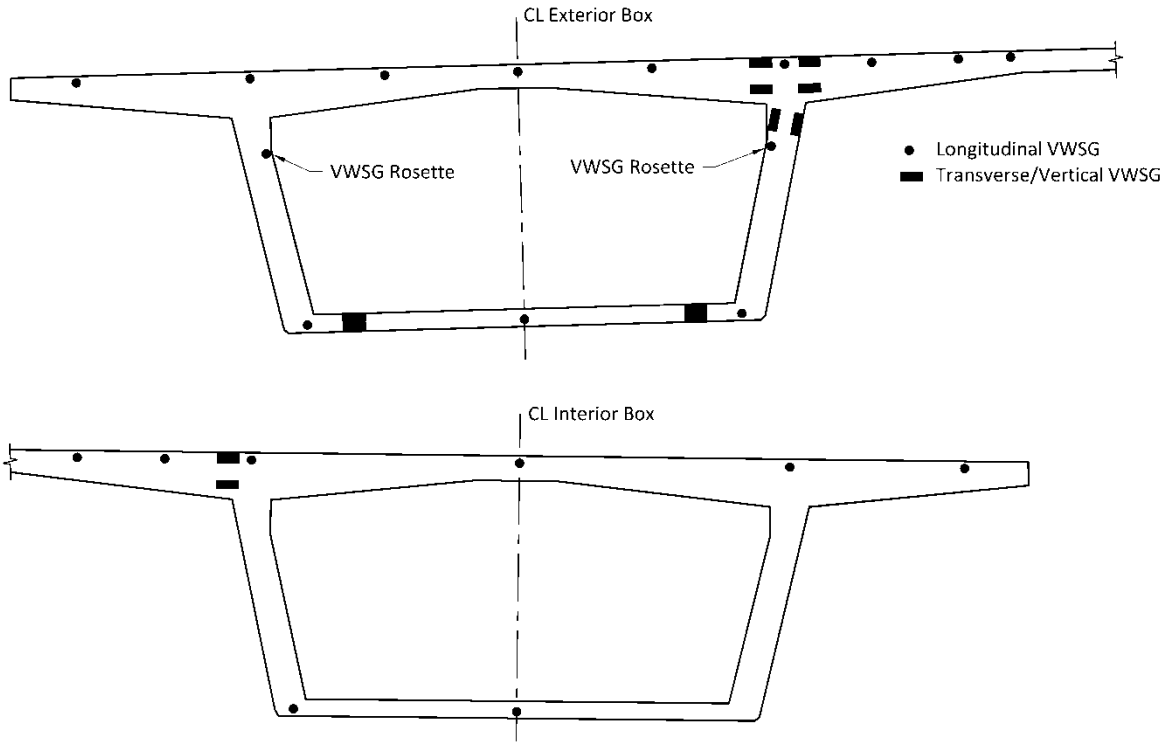

Figure 2.10: VWSG layout near midspan of the southbound bridge Span 2 (Location 7SB) looking upstation (i.e., north).

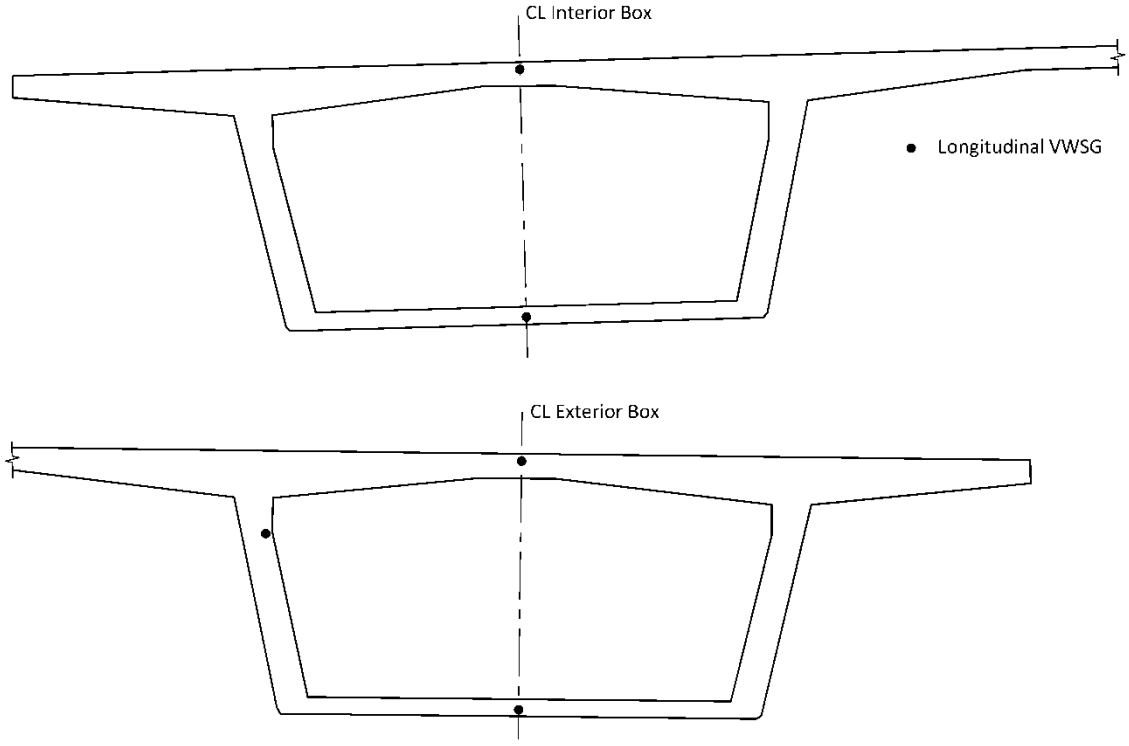

Figure 2.11: VWSG layout near midspan of the northbound bridge Span 2 (Location 7NB) looking upstation (i.e., north).

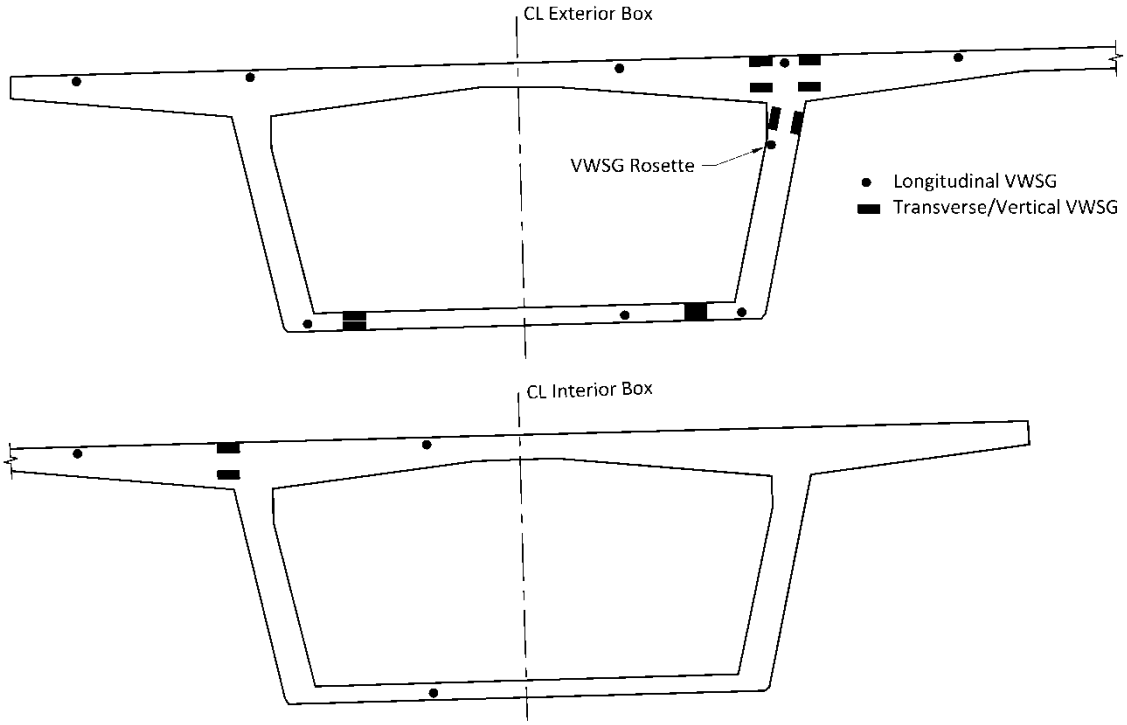

Figure 2.12: VWSG layout near midspan of the southbound bridge Span 1 (Location 3SB) looking upstation (i.e., north)

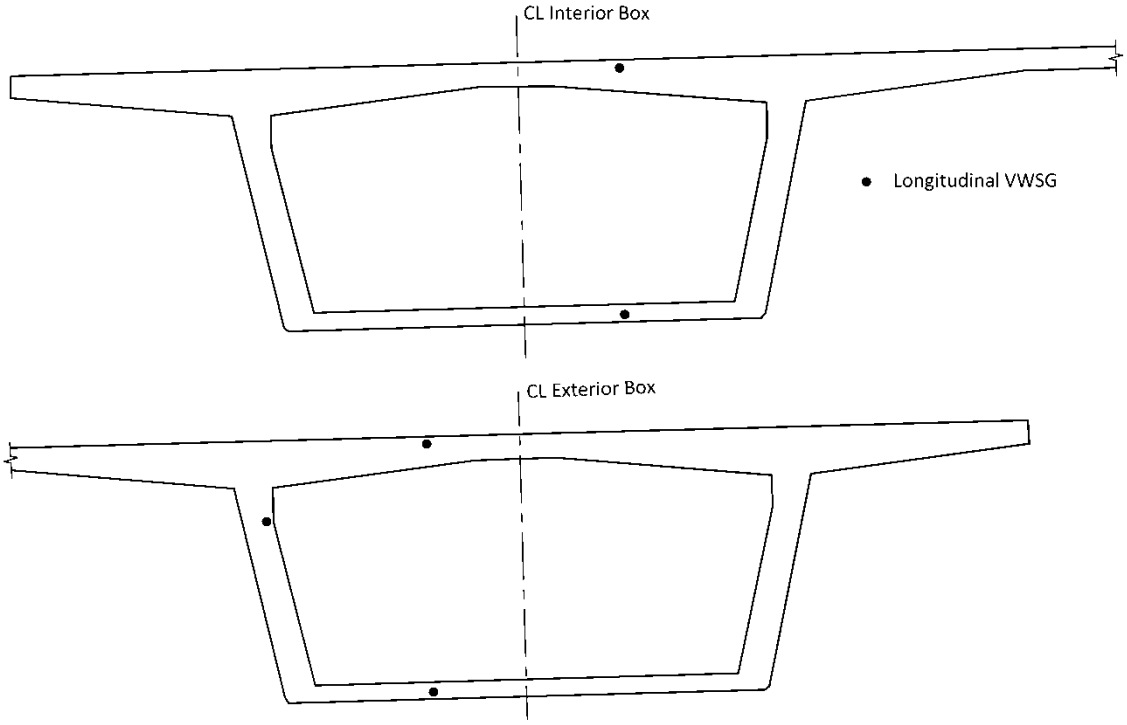

Figure 2.13: VWSG layout near midspan of the northbound bridge Span 1 (Location 3NB) looking upstation (i.e., north)

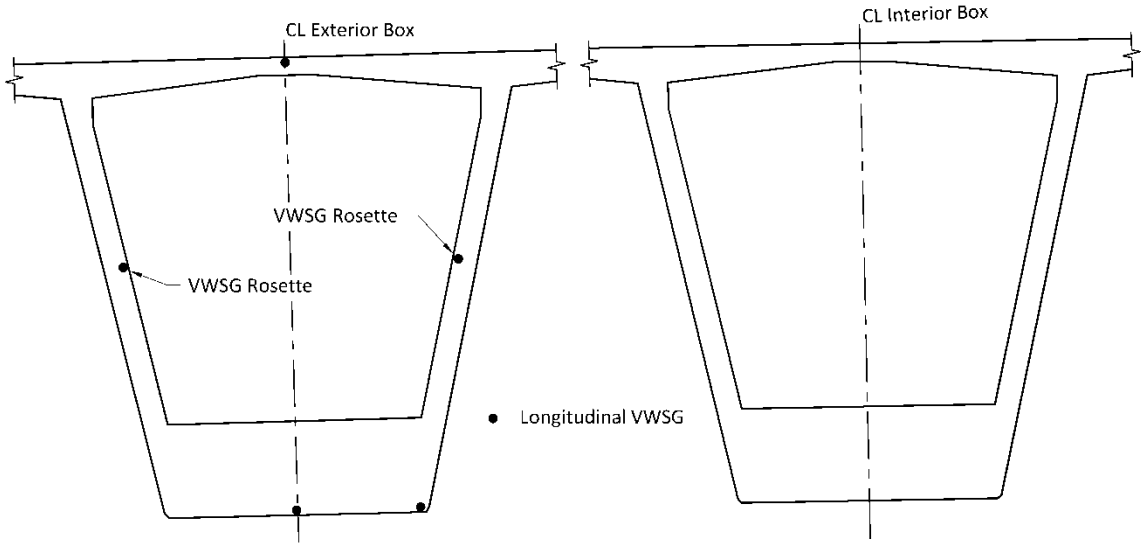

Figure 2.14: VWSG layout 20 ft south of centerline of Pier 2 on Span 1 of the southbound bridge (Location 4SB) looking upstation (i.e., north)

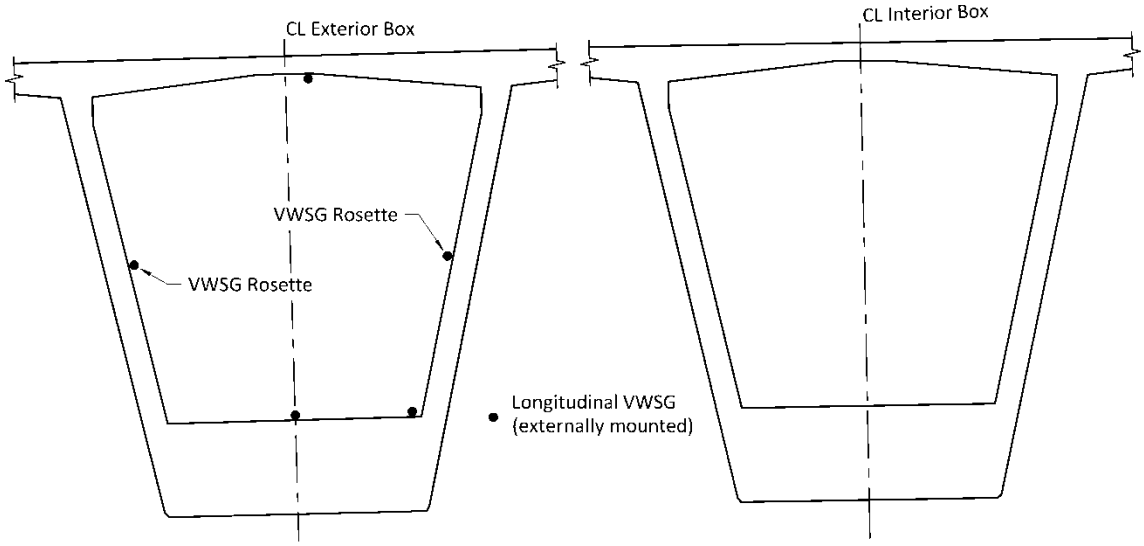

Figure 2.15: VWSG layout 20 ft north of centerline of Pier 2 on Span 2 of the southbound bridge (Location 6SB) looking upstation (i.e., north)

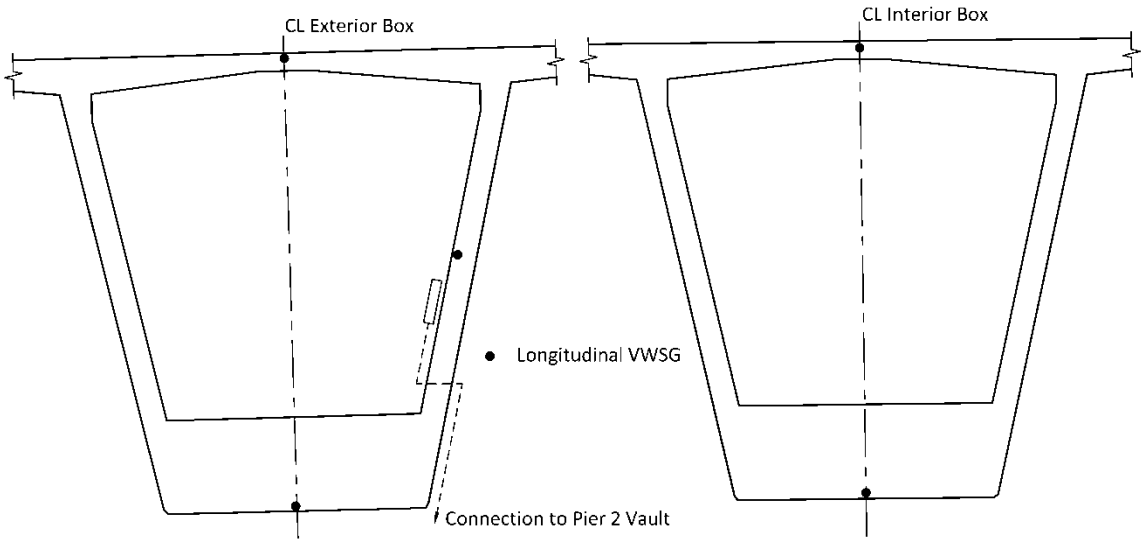

Figure 2.16: VWSG layout 10.5 ft north of centerline of Pier 2 on the southbound bridge (Location 5SB) looking upstation (i.e., north)

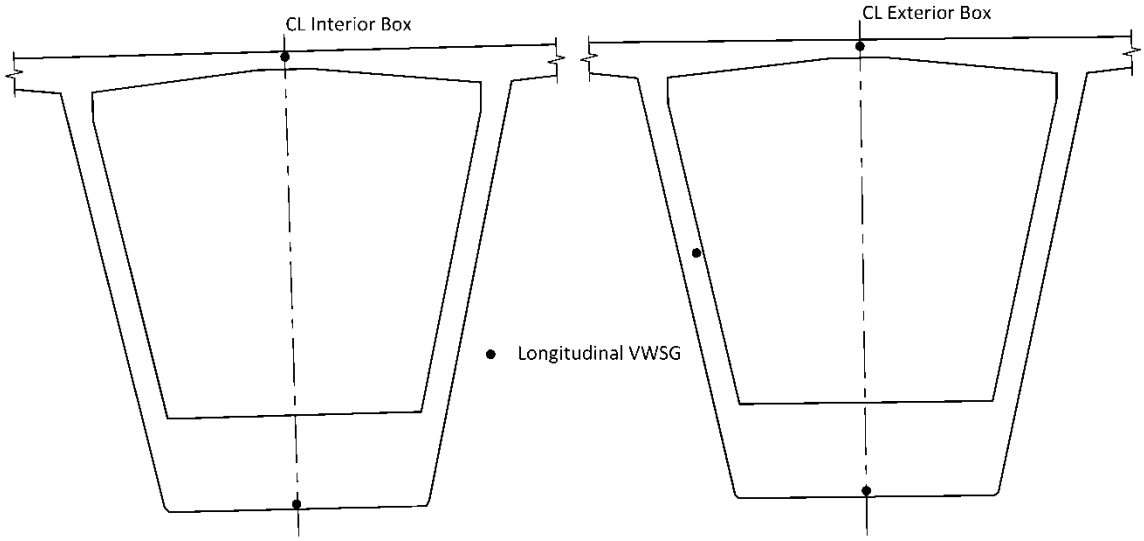

Figure 2.17: VWSG layout 10.5 ft north of centerline of Pier 2 on the northbound bridge (Location 5NB) looking upstation (i.e., north)

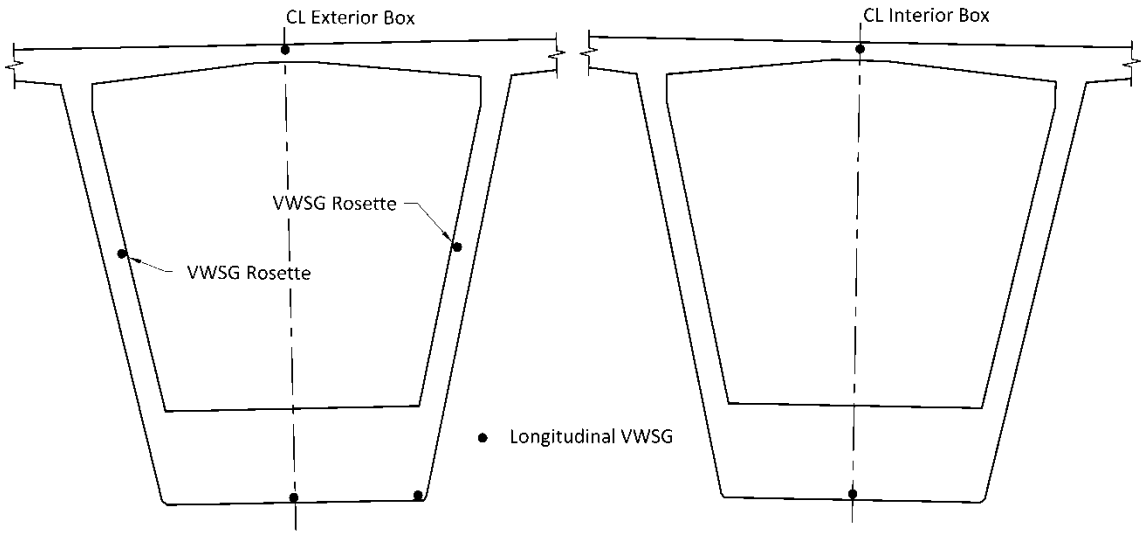

Figure 2.18: VWSG layout 10.5 ft south of centerline of Pier 3 on the southbound bridge (Location 8SB) looking upstation (i.e., north)

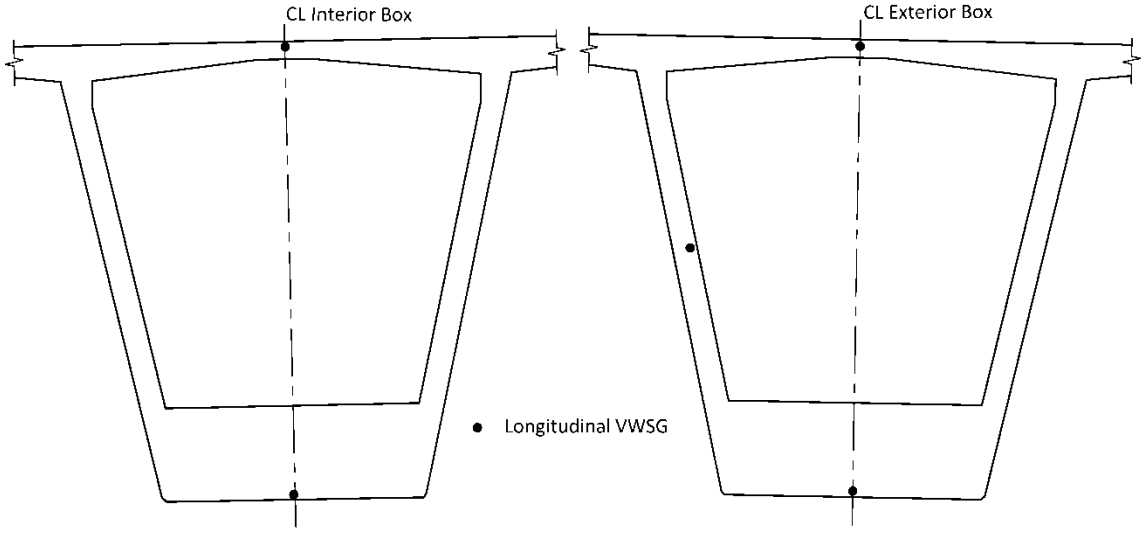

Figure 2.19: VWSG layout 10.5 ft south of centerline of Pier 3 on the northbound bridge (Location 8NB) looking upstation (i.e., north)

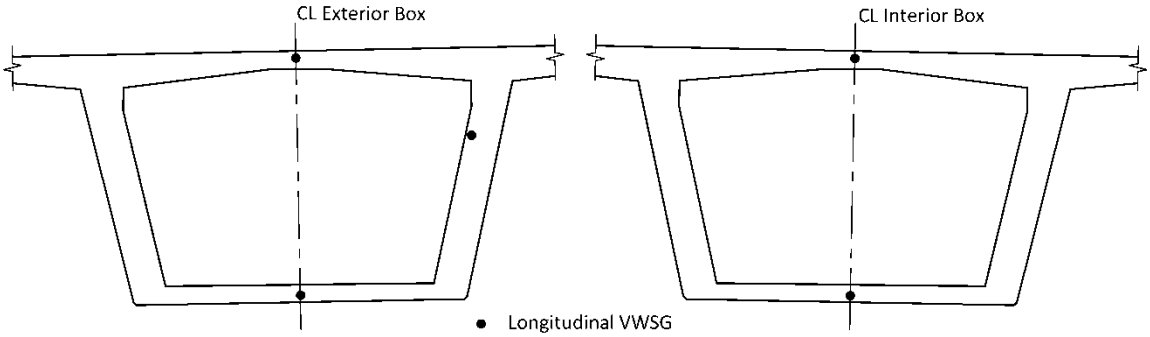

Figure 2.20: VWSG layout near midspan of the southbound bridge Span 3 (Location 9SB) looking upstation (i.e., north)

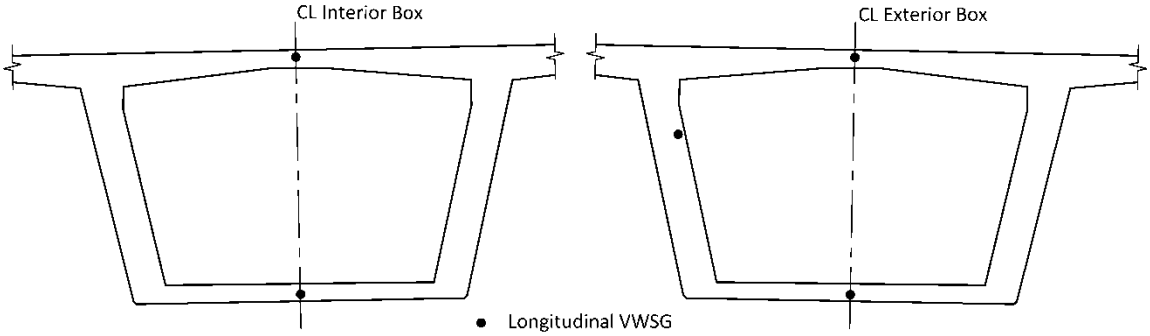

Figure 2.21: VWSG layout near midspan of the northbound bridge Span 3 (Location 9NB) looking upstation (i.e., north)

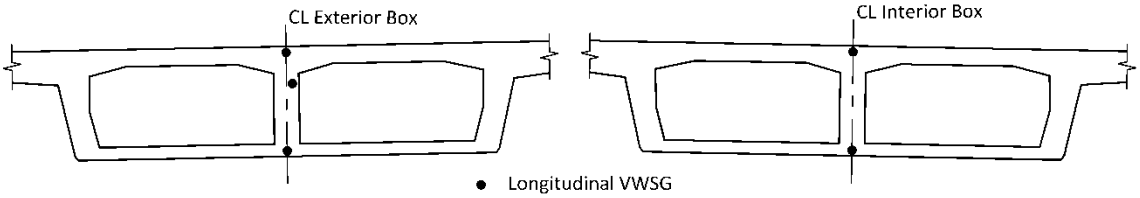

Figure 2.22: VWSG layout near midspan of the southbound bridge Span 4 (Location 14SB) looking upstation (i.e., north)

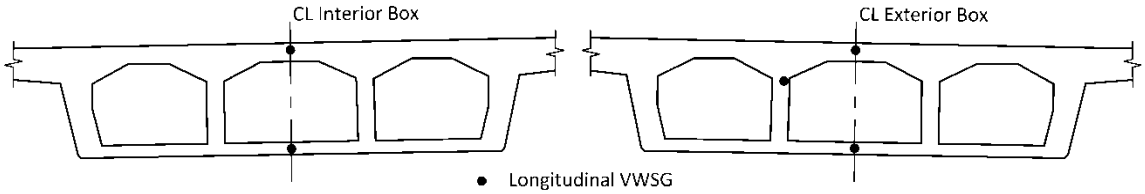

Figure 2.23: VWSG layout near midspan of the northbound bridge Span 4 (Location 14NB) looking upstation (i.e., north)

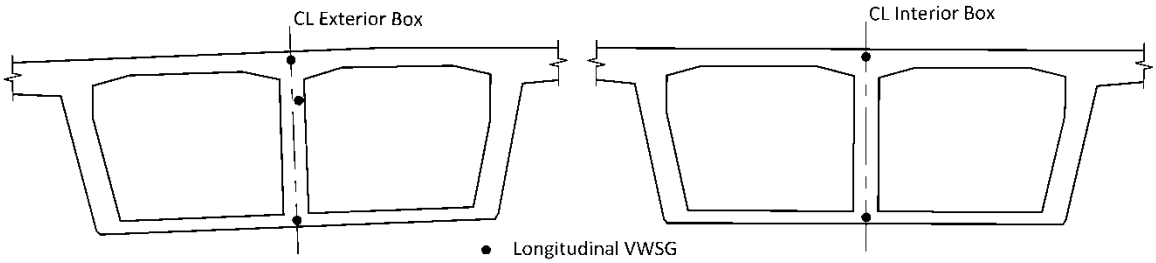

Figure 2.24: VWSG layout just to the south of Abutment 5 on Span 4 of the southbound bridge (Location 15SB) looking upstation (i.e., north)

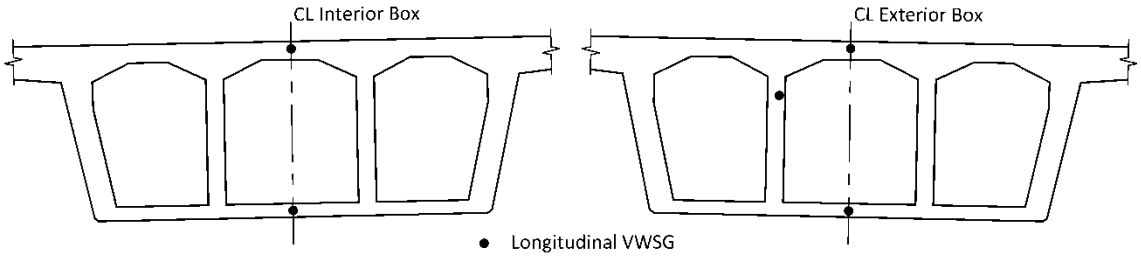

Figure 2.25: VWSG layout just to the south of Abutment 5 on Span 4 of the northbound bridge (Location 15NB) looking upstation (i.e., north)

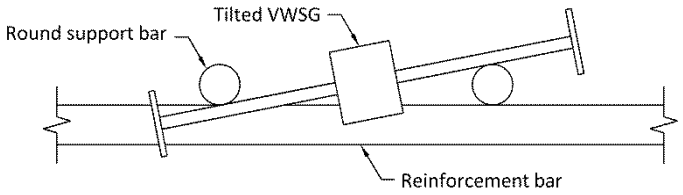

Figure 2.26: VWSG installed incorrectly with tilt

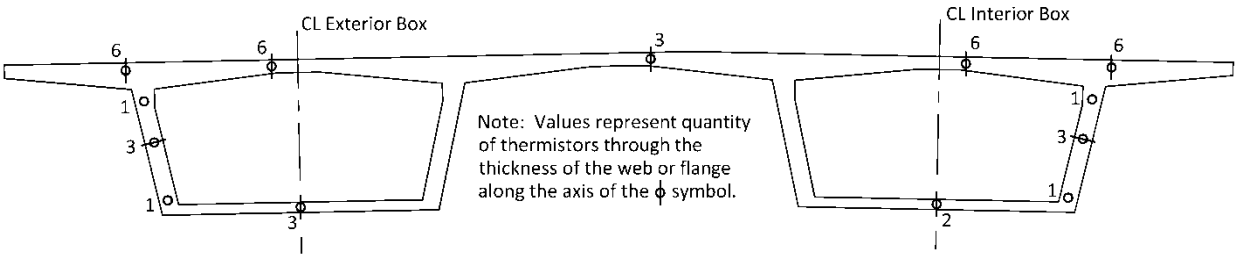

Figure 2.27: Thermistor layout near midspan of Span 2 on the southbound bridge (Location 7SB) looking upstation (i.e., north)

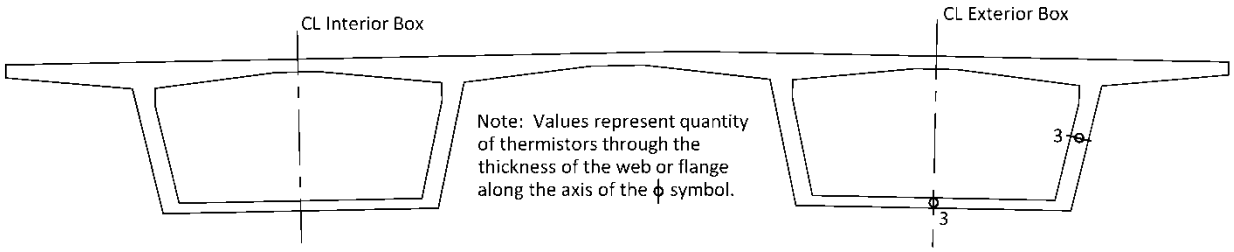

Figure 2.28: Thermistor layout near midspan of Span 2 on the northbound bridge (Location 7NB) looking upstation (i.e., north)

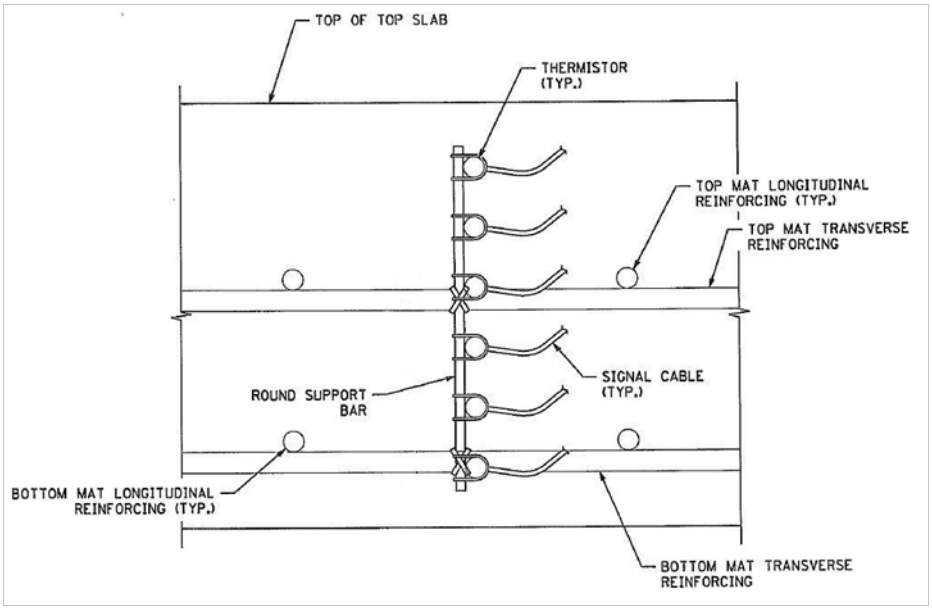

Figure 2.29: Typical thermistor installation for six thermistors in the top flange

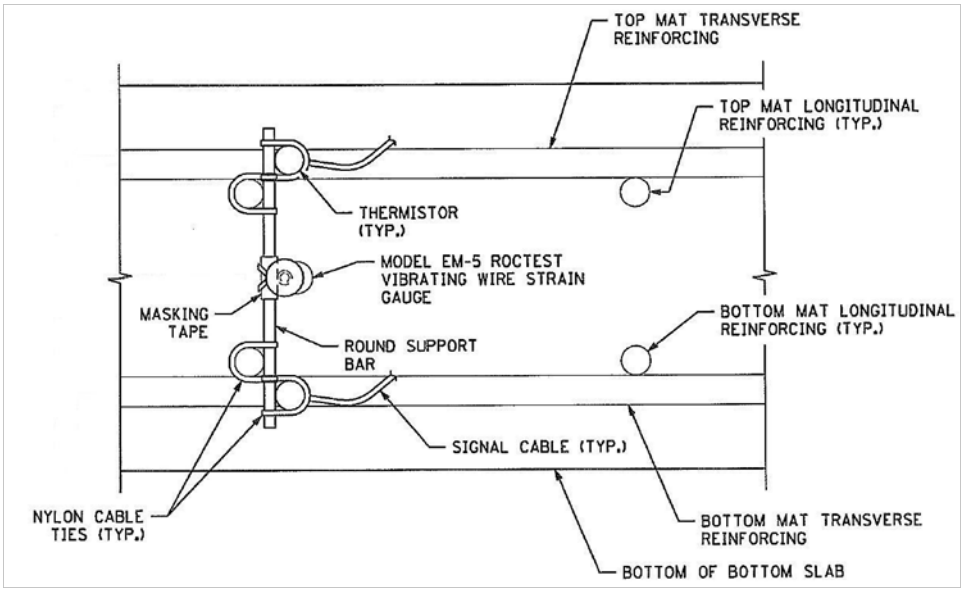

Figure 2.30: Typical two-thermistor installation with VWSG combination

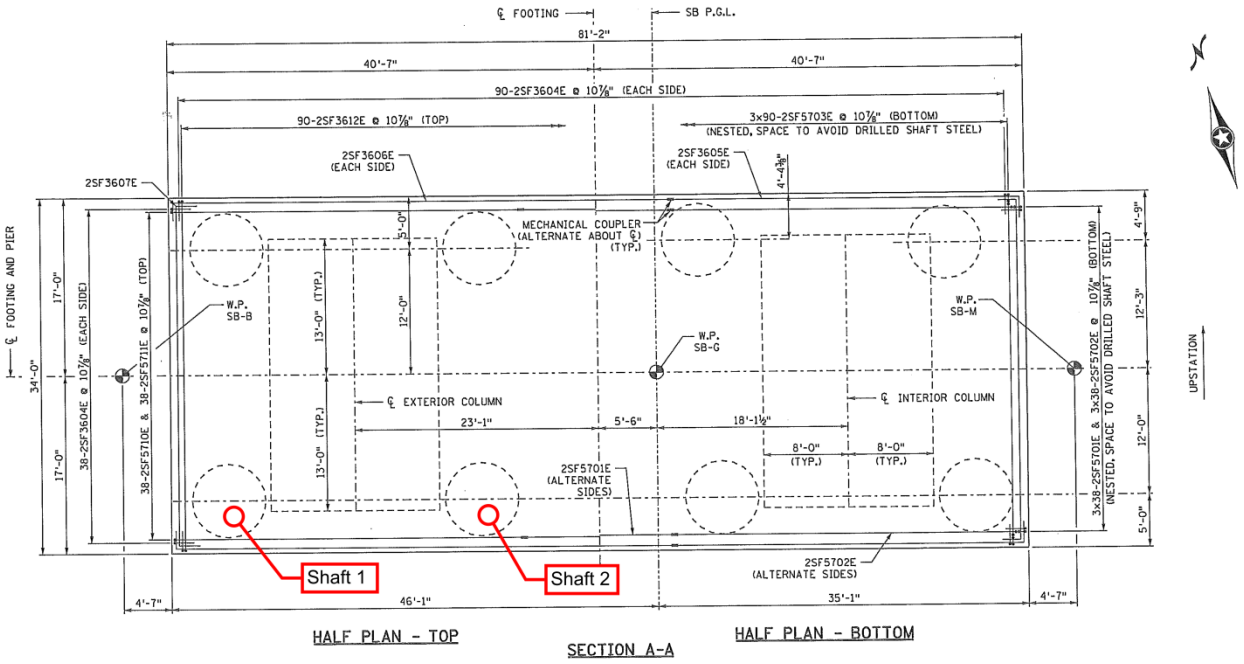

Figure 2.31: Cross section of southbound bridge Pier 2 footing showing location of Shafts 1 and 2

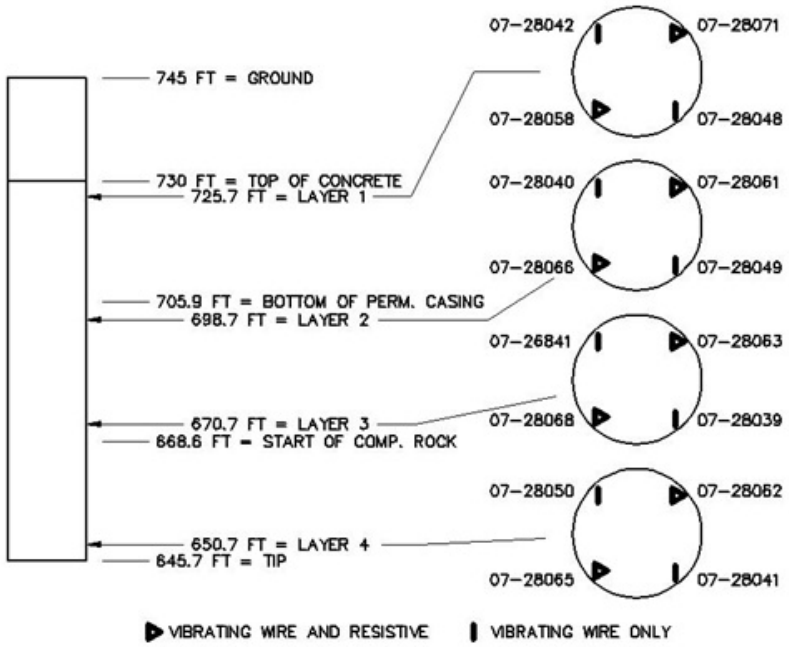

Figure 2.32: Elevation and cross section views of Shaft 1 showing USF/FHWA gage locations

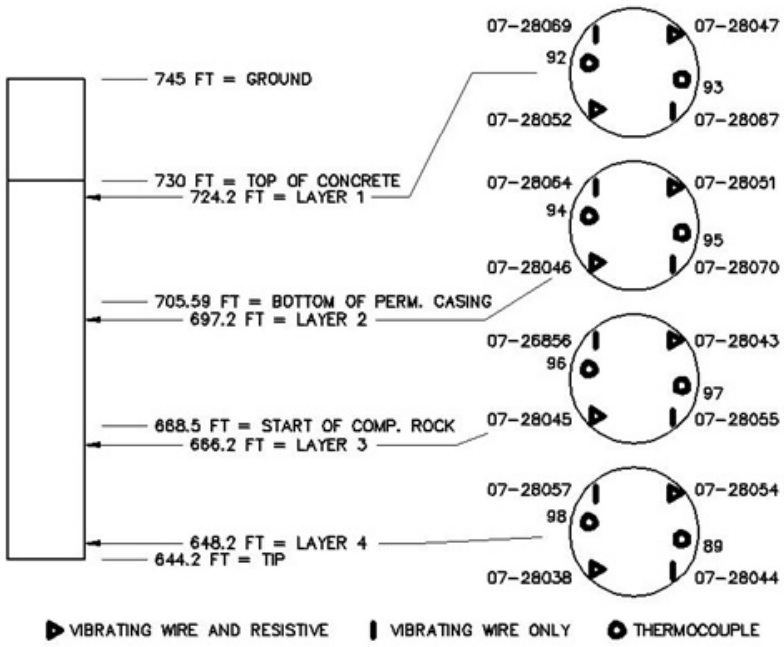

Figure 2.33: Elevation and cross section views of Shaft 2 showing USF/FHWA gage locations

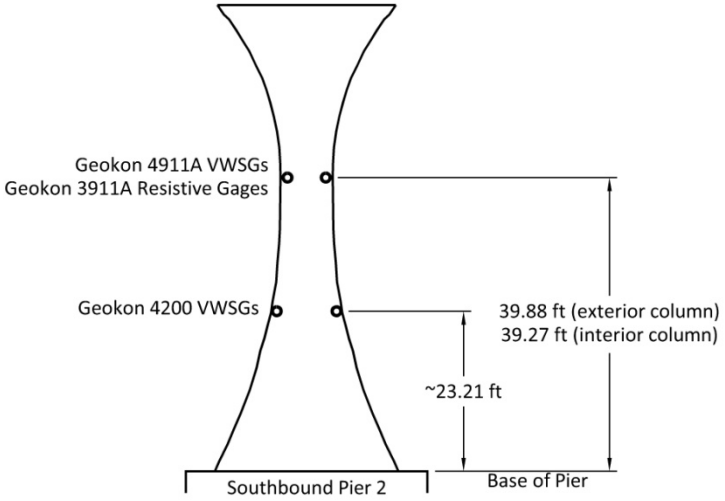

Figure 2.34: Elevation view of southbound bridge Pier 2 showing location of gages

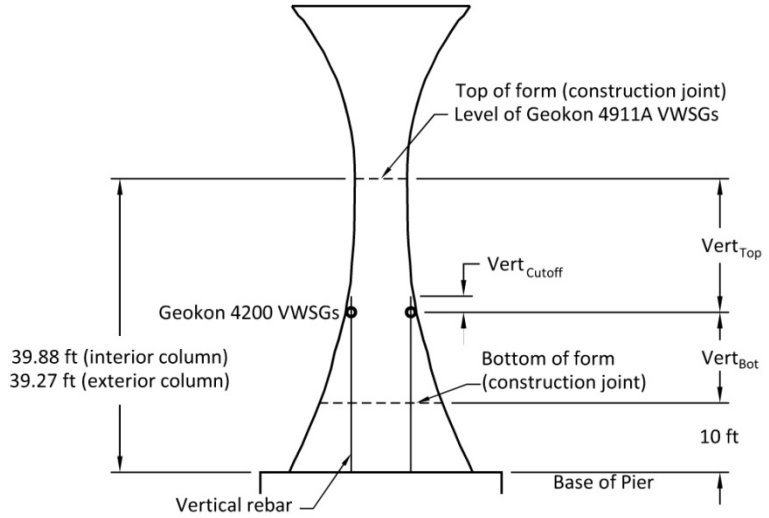

Figure 2.35: Elevation view of southbound bridge Pier 2 showing measured dimensions documented in Table 2.4

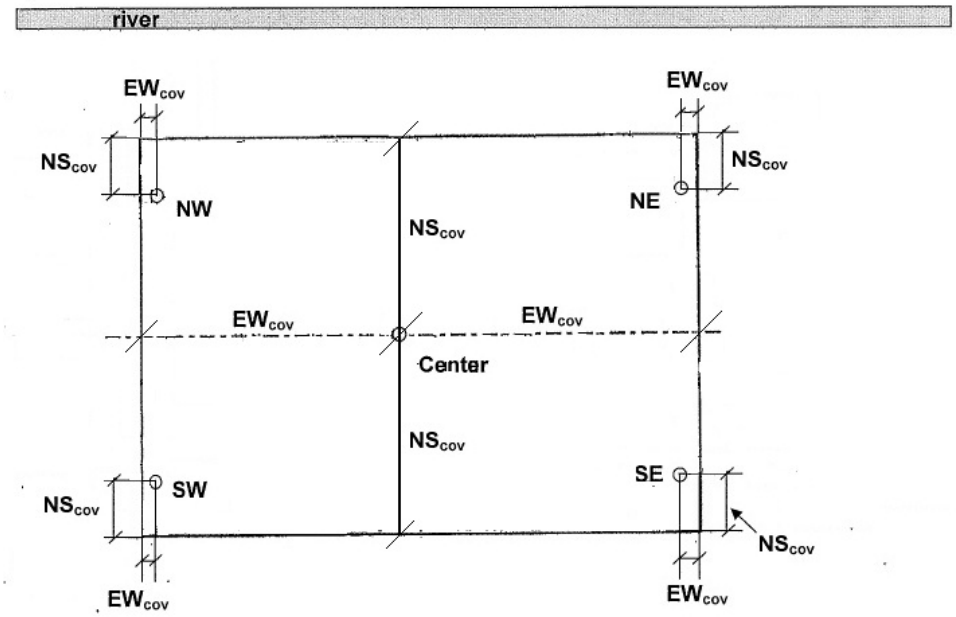

Figure 2.36: Cross section view of southbound bridge Pier 2 showing measured dimensions documented in Table 2.4

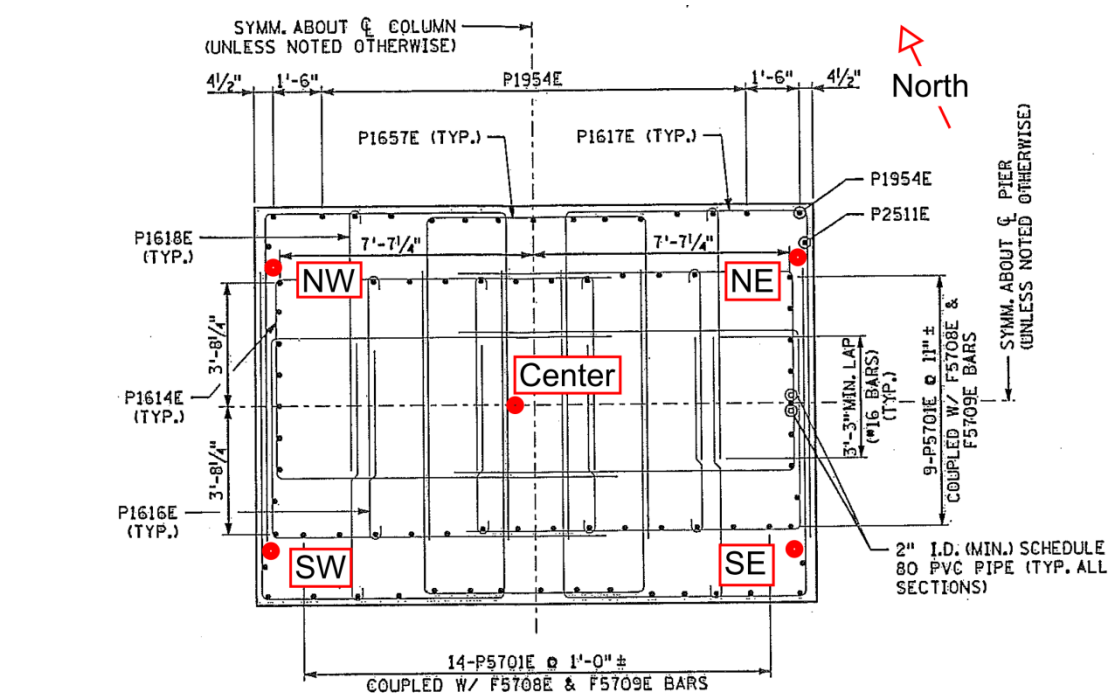

Figure 2.37: Cross section of the gages within southbound bridge Pier 2

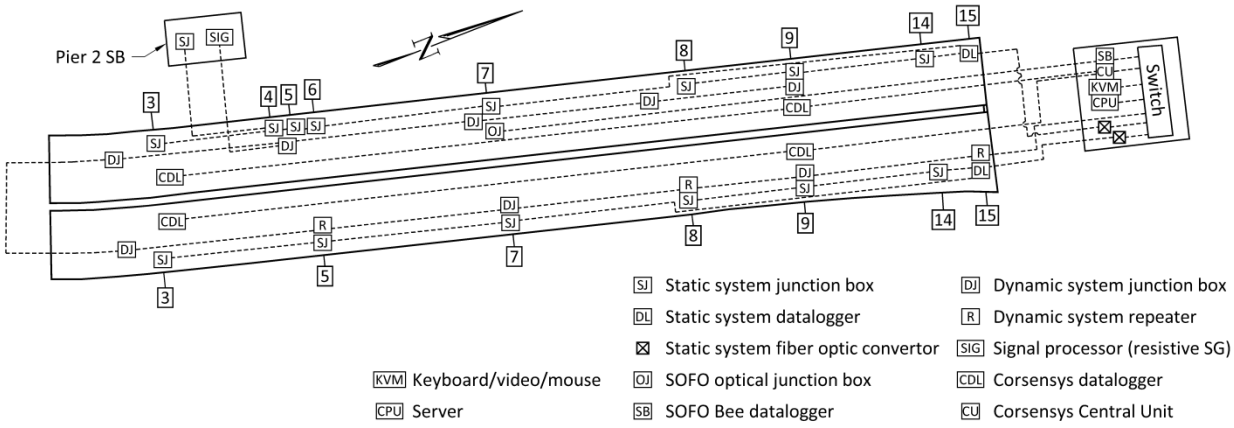

Figure 2.38: Wiring connection locations. VWSG locations shown as reference to location in the span.

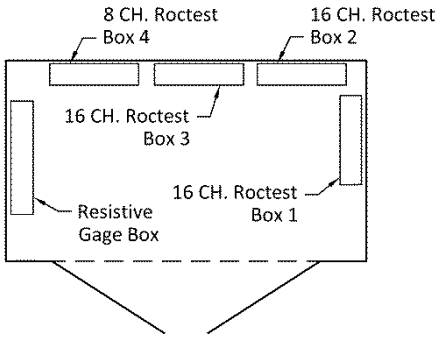

Figure 2.39: Pier and shaft instrumentation vault layout

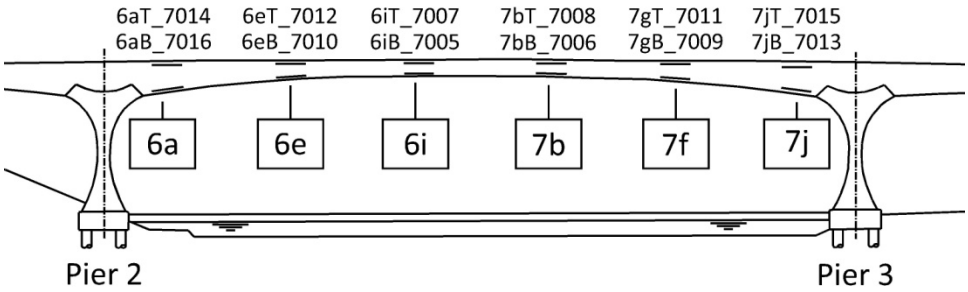

Figure 2.40: Elevation view of Span 2 of the southbound bridge showing SOFO sensor locations and labels

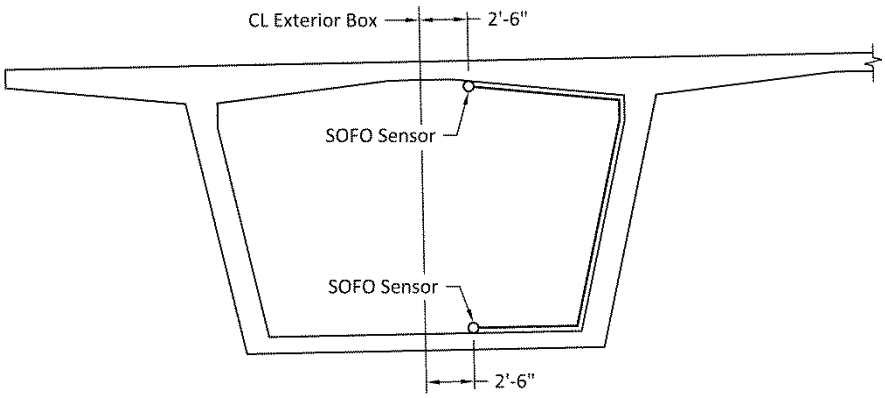

Figure 2.41: Typical SOFO sensor layout

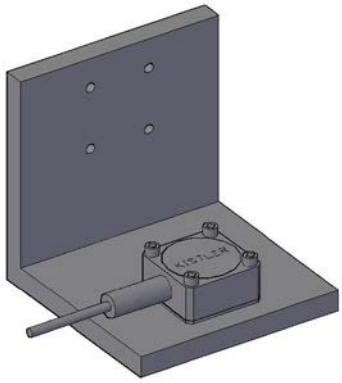

Figure 2.42: Typical accelerometer installation on an aluminum angle

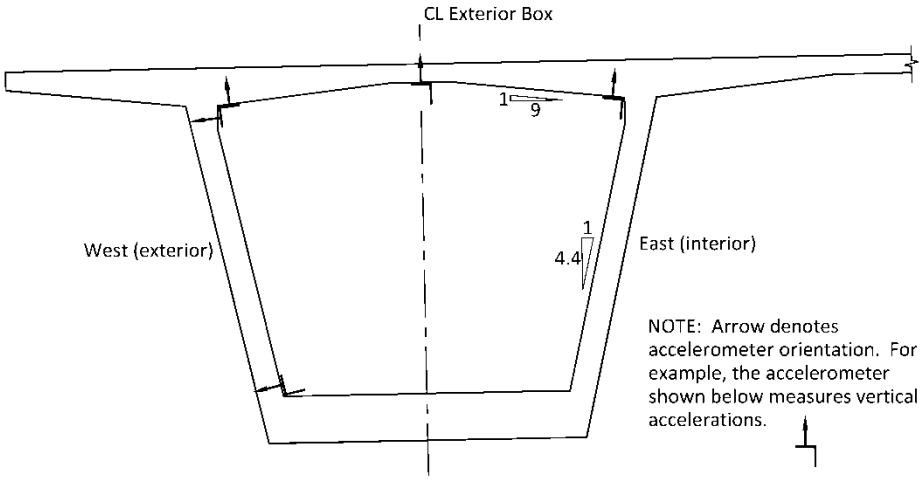

Figure 2.43: Short-term accelerometer layout in the southbound bridge exterior box near Pier 3 at station 223+18.9 looking upstation (i.e., north)

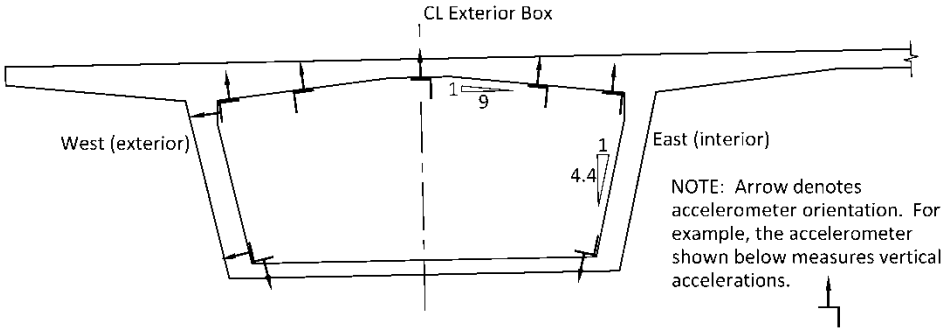

Figure 2.44: Short-term accelerometer layout in the southbound bridge exterior box near midspan of Span 2 at station 221+33.9 looking upstation (i.e., north)

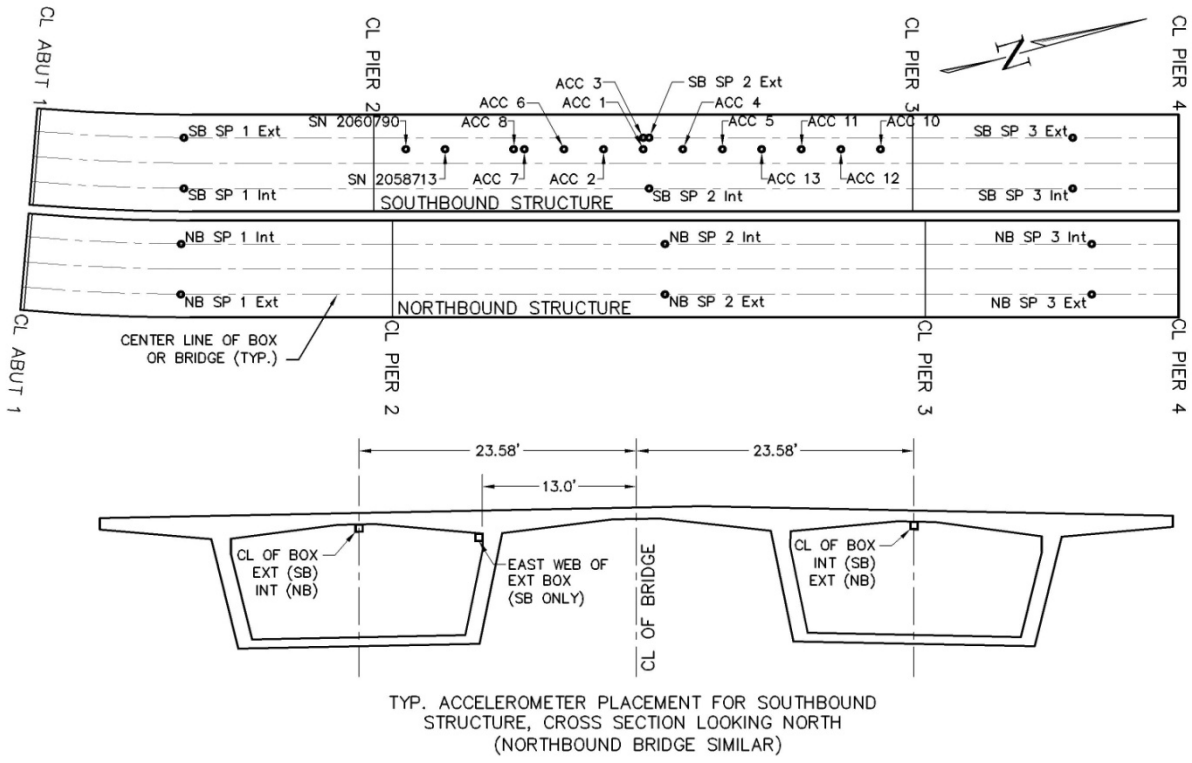

TYP. ACCELEROMETER PLACEMENT FOR SOUTHBOUND STRUCTURE, CROSS SECTION LOOKING NORTH (NORTHBOUND BRIDGE SIMILAR)

Figure 2.45: Long-term accelerometer layout used from September 17, 2008 until May 10, 2010

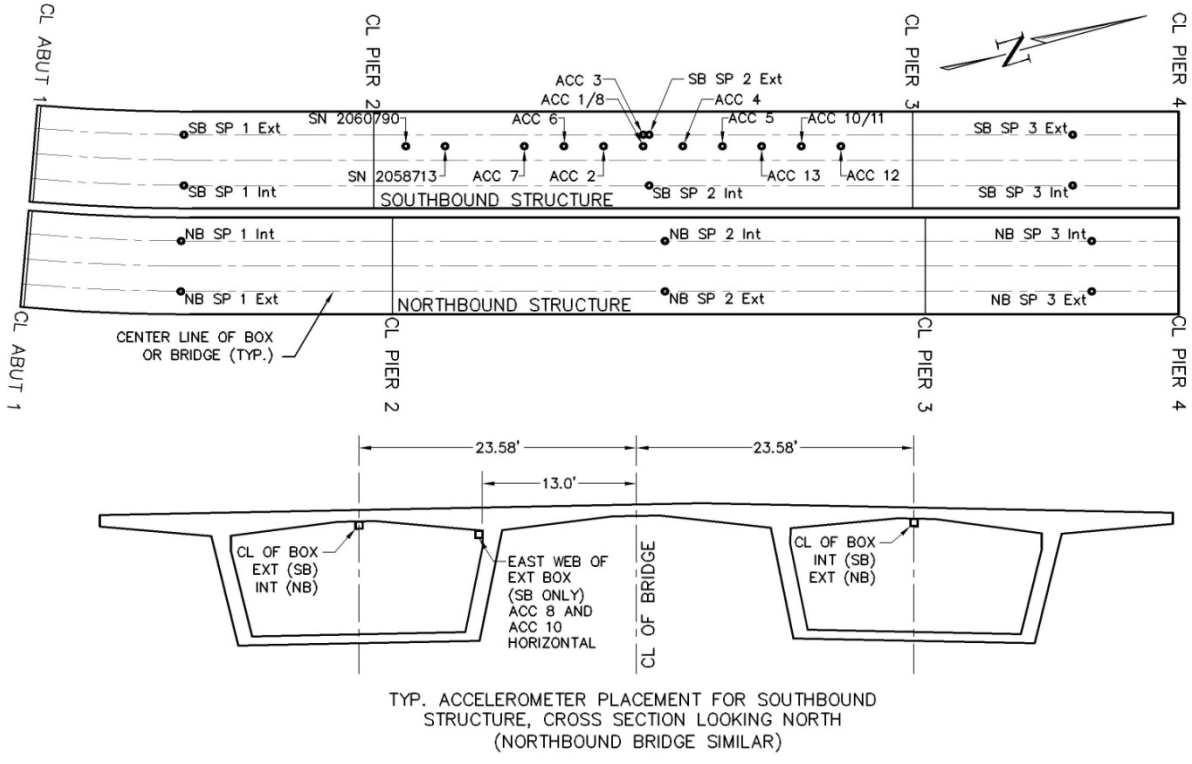

TYP. ACCELEROMETER PLACEMENT FOR SOUTHBOUND STRUCTURE, CROSS SECTION LOOKING NORTH (NORTHBOUND BRIDGE SIMILAR)

Figure 2.46: Long-term accelerometer layout used from May 11, 2010 until present

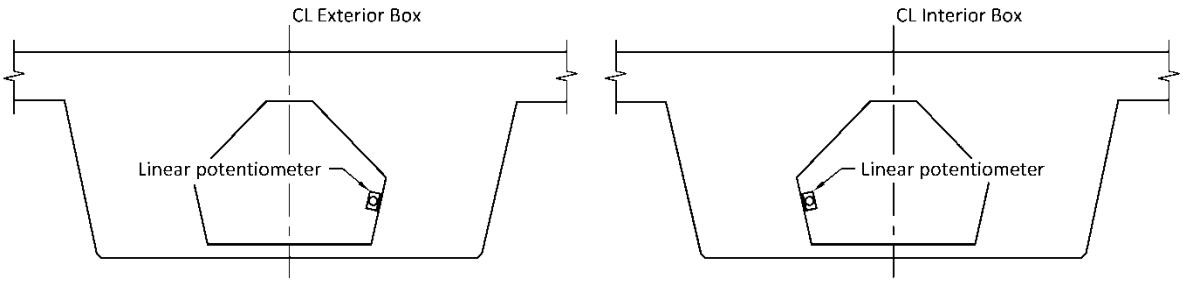

Figure 2.47: Linear potentiometer layout at the south end of Span 1 for the southbound bridge (northbound bridge and north end of Span 3 similar) looking upstation (i.e., north)

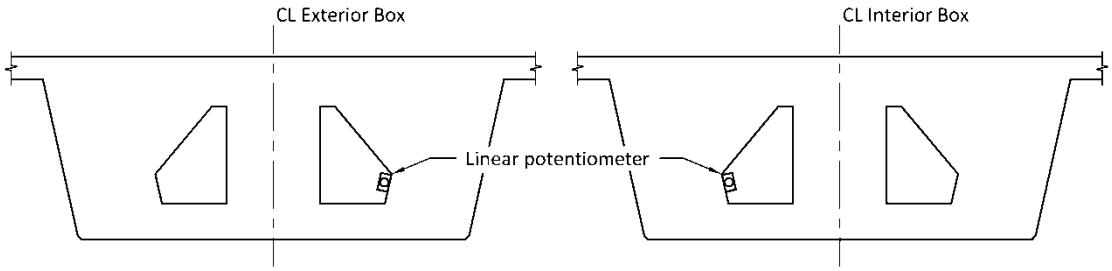

Figure 2.48: Linear potentiometer layout at the south end of Span 4 for the southbound bridge looking upstation (i.e., north)

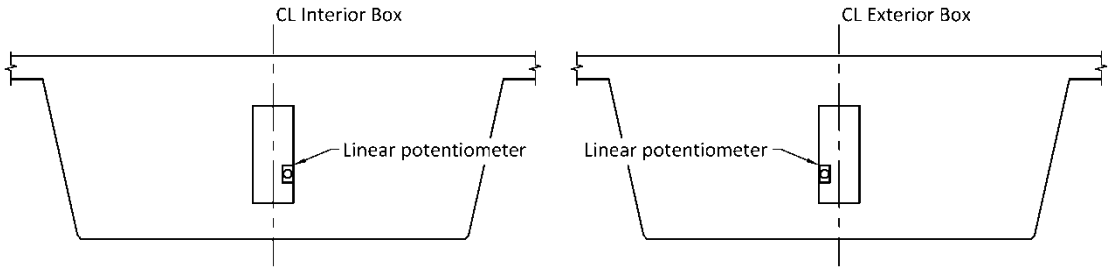

Figure 2.49: Linear potentiometer layout at the south end of Span 4 for the northbound bridge looking upstation (i.e., north)

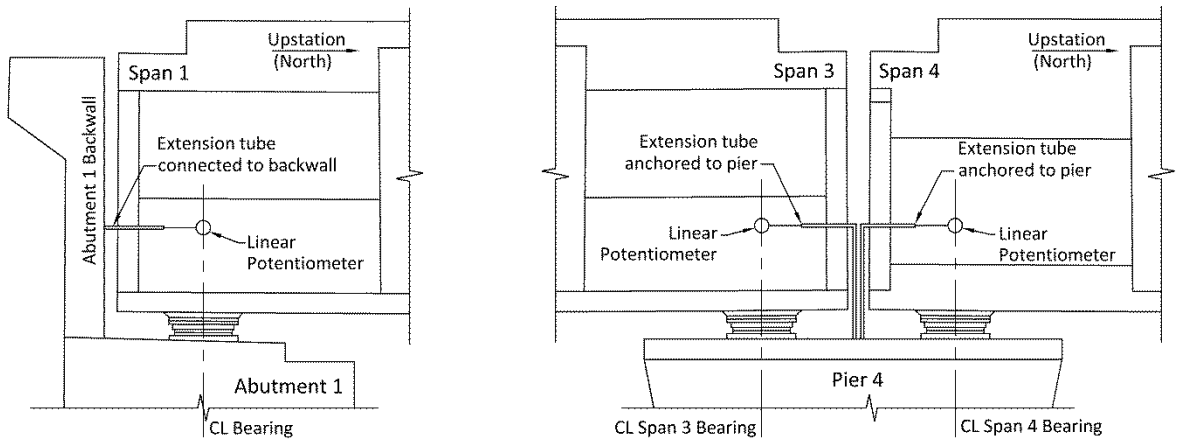

Figure 2.50: Typical linear potentiometer installations at Abutment 1 and Pier 4

Figure 2.51: Typical Corsensys CS-040 sensor installation. Photo from Corsensys datasheet. Sensor shown is not actual sensor in bridge.

Figure 2.52: Typical Corsensys CS-402 sensor installation. Photo from Corsensys datasheet. Sensor shown is not actual sensor in bridge.

Figure 3.1: Modulus of elasticity sample in Forney concrete testing machine with compressometer attached

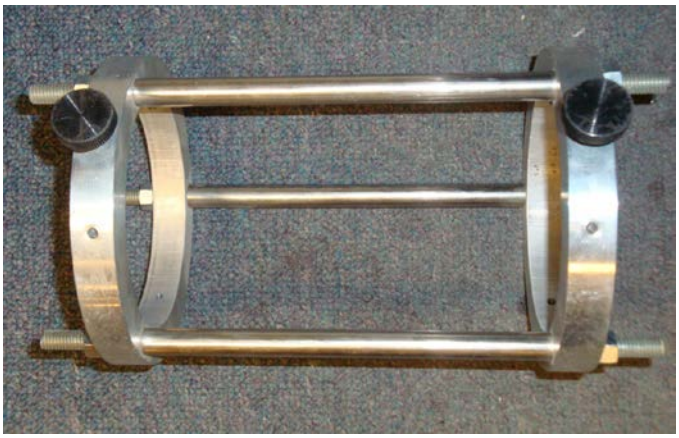

Figure 3.2: Fixture used for creating creep and shrinkage specimen molds

Figure 3.3: Creep and shrinkage specimen mold

Figure 3.4: Whittemore gage

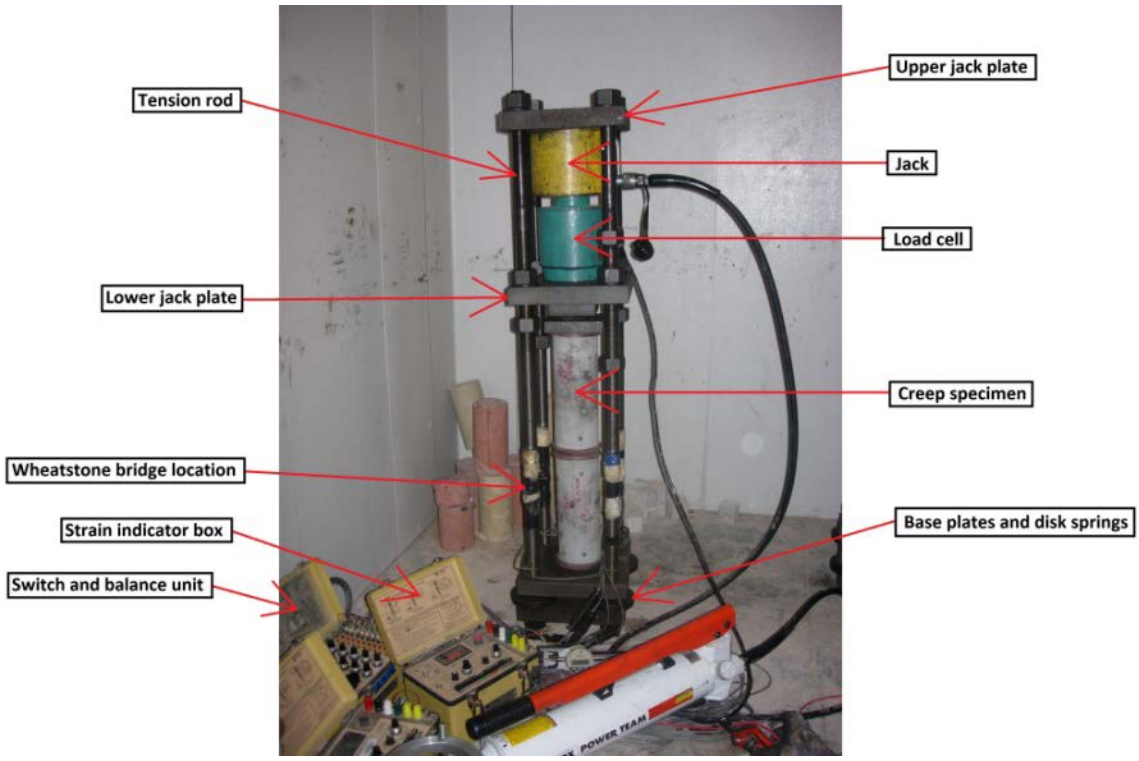

Figure 3.5: Frame used for monitoring creep

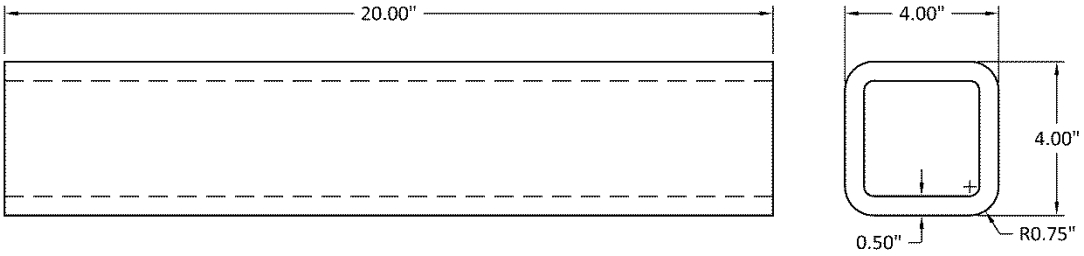

Figure 3.6: Creep calibration sample

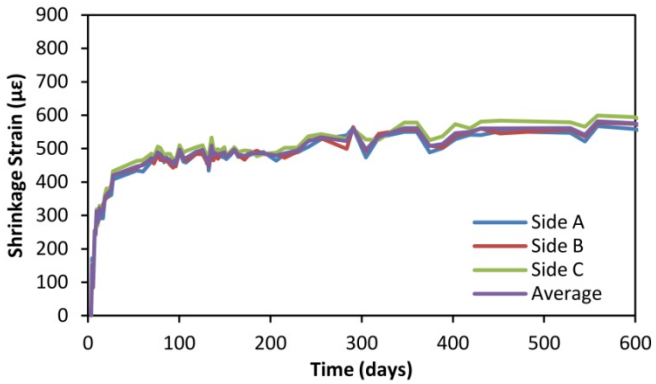

Figure 3.7: Southbound bridge first sample (S4SB1) shrinkage strains

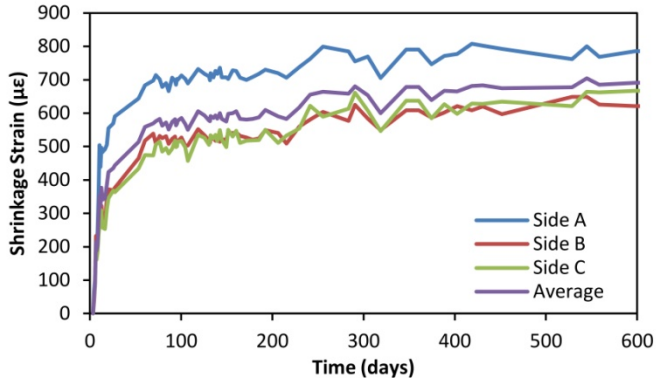

Figure 3.8: Southbound bridge second sample (S4SB2) shrinkage strains

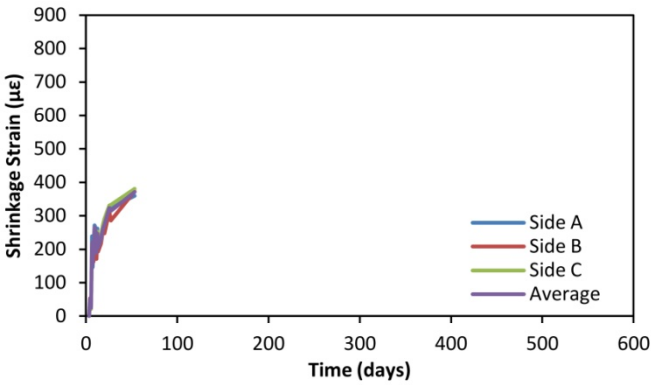

Figure 3.9: Southbound bridge third sample (S4SB3) shrinkage strains. Transferred to Frame #2 for creep measurements on October 5, 2008 (age 57 days).

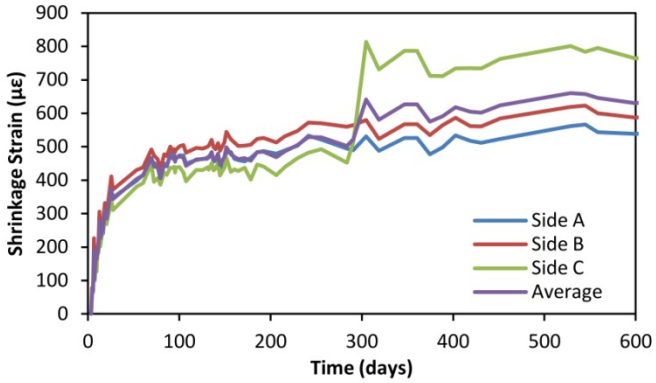

Figure 3.10: Southbound bridge fourth sample (S4SB4) shrinkage strains

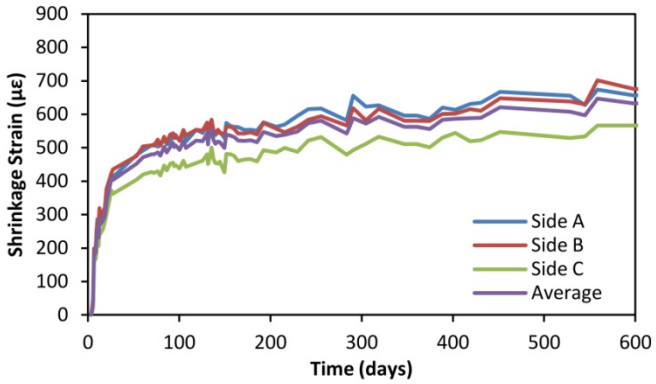

Figure 3.11: Southbound bridge fifth sample (S4SB5) shrinkage strains

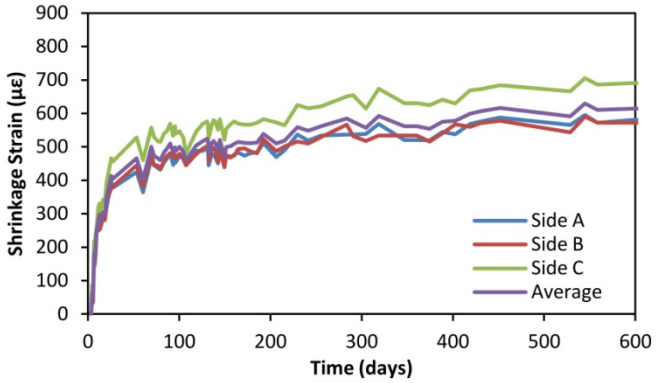

Figure 3.12: Southbound bridge sixth sample (S4SB6) shrinkage strains

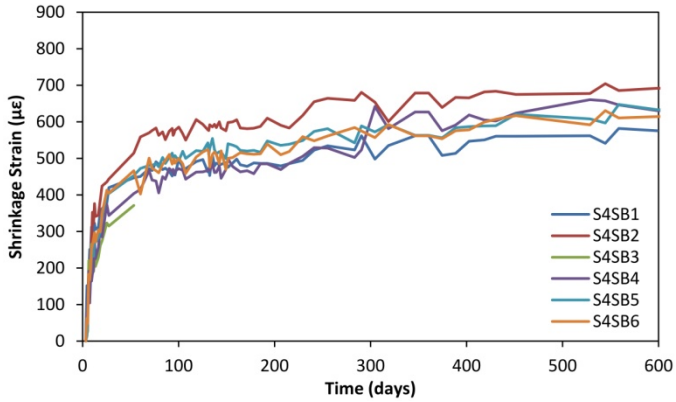

Figure 3.13: Southbound bridge average sample shrinkage strains

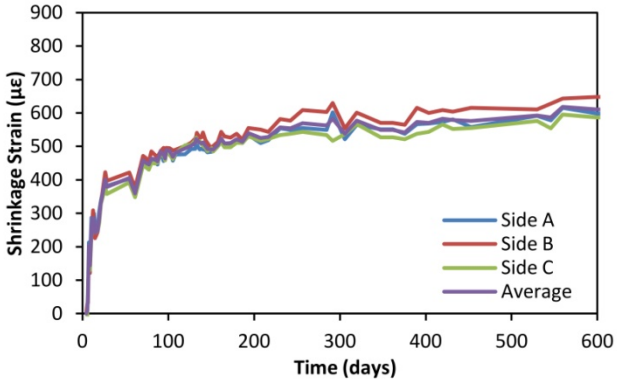

Figure 3.14: Northbound bridge first sample (S4NB1) shrinkage strains

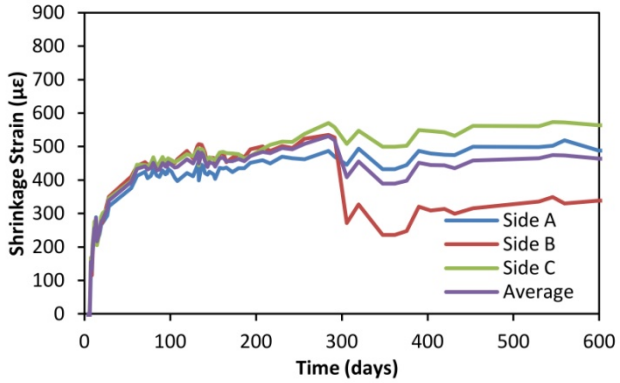

Figure 3.15: Northbound bridge second sample (S4NB2) shrinkage strains

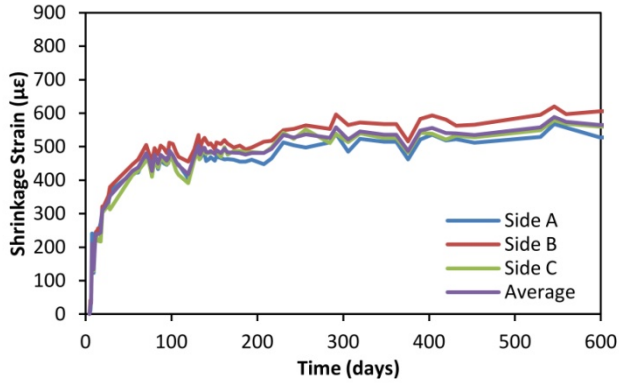

Figure 3.16: Northbound bridge third sample (S4NB3) shrinkage strains

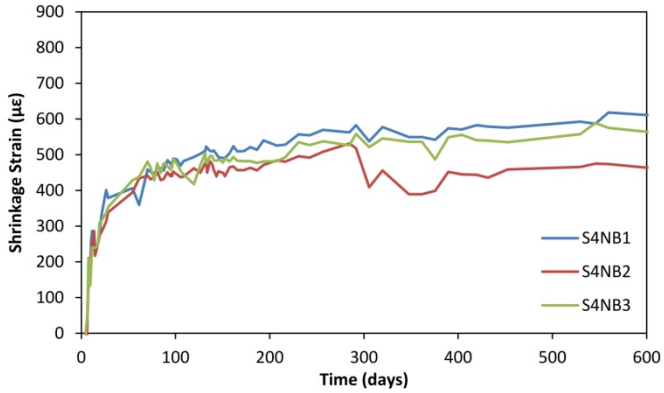

Figure 3.17: Northbound bridge average sample shrinkage strains

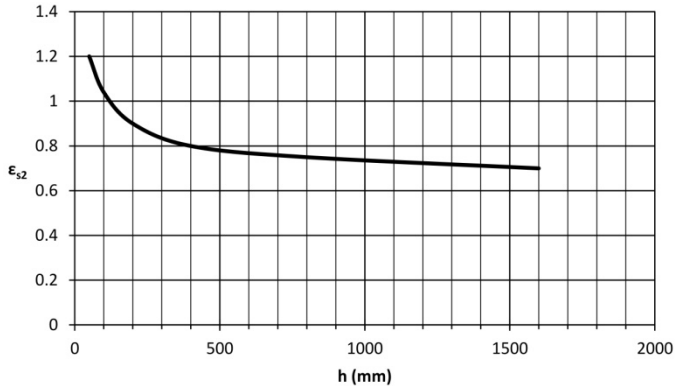

Figure 3.18: Shrinkage constant ε_{s2} from 1978 CEB/FIP Model Code

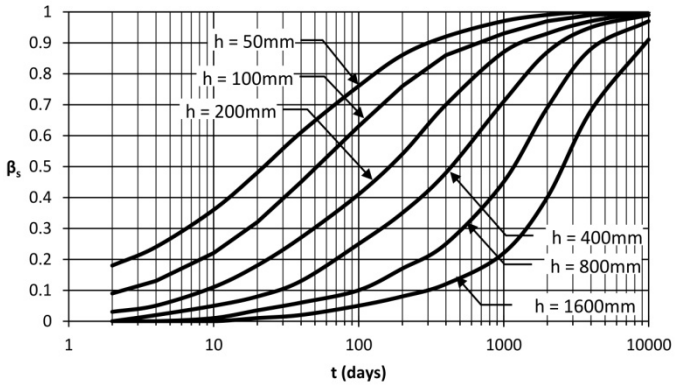

Figure 3.19: Shrinkage function $\beta_s(t)$ from 1978 CEB/FIP Model Code

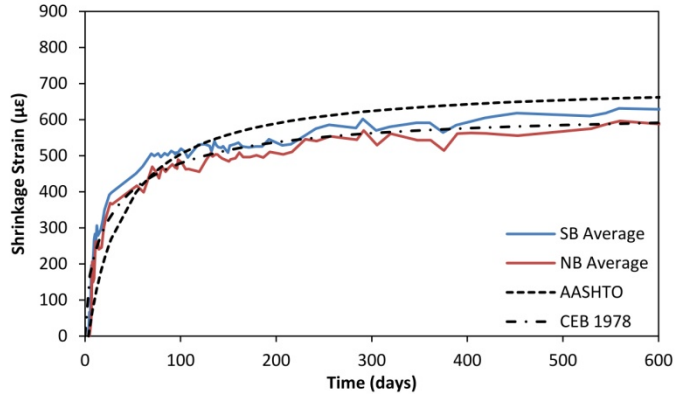

Figure 3.20: Average sample shrinkage strains from southbound and northbound bridge samples compared to predictions from AASHTO LRFD (2010) and 1978 CEB/FIP Model Code

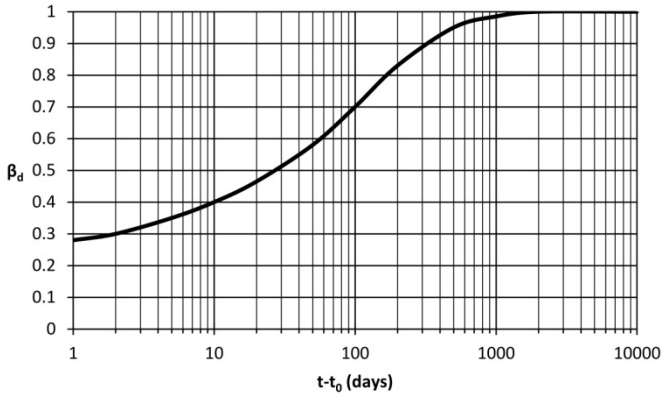

Figure 3.21: Recoverable deformation coefficient β_d(t-t0) from 1978 CEB/FIP Model Code

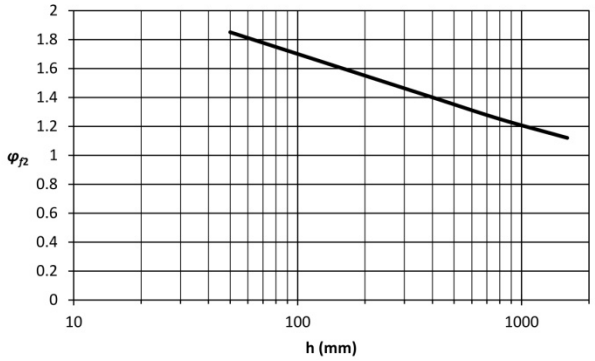

Figure 3.22: Shape dependent creep flow coefficient φ_{f2} from 1978 CEB/FIP Model Code

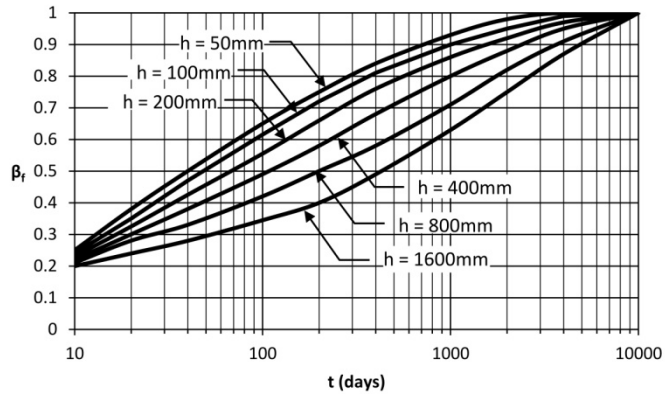

Figure 3.23: Unrecoverable deformation coefficient $\beta_f(t)$ from 1978 CEB/FIP Model Code

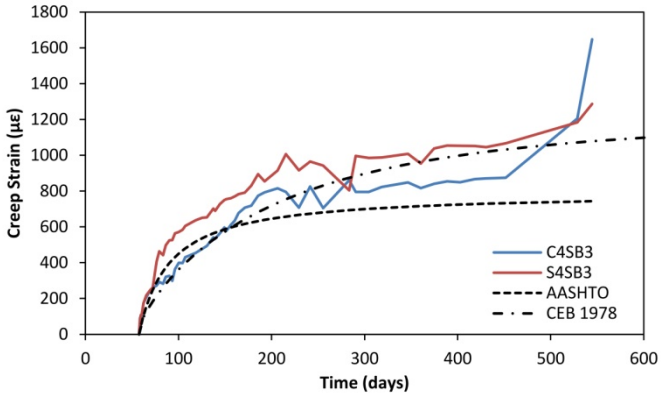

Figure 3.24: Creep strains for Frame #2 stressed at 0.45*f'_c (36.8 kip load) at 57 days old compared to AASHTO LRFD (2010) and 1978 CEB/FIP Model Code predictions. Only two of the three DEMEC point sides were used for computing strain in samples C4SB3 and S4SB3.

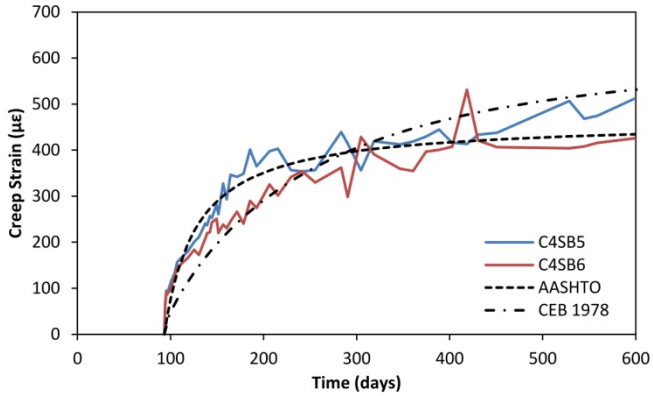

Figure 3.25: Creep strains for Frame #4 stressed at 275ksf (24.0 kip load) at 93 days old compared to AASHTO LRFD (2010) and 1978 CEB/FIP Model Code predictions.

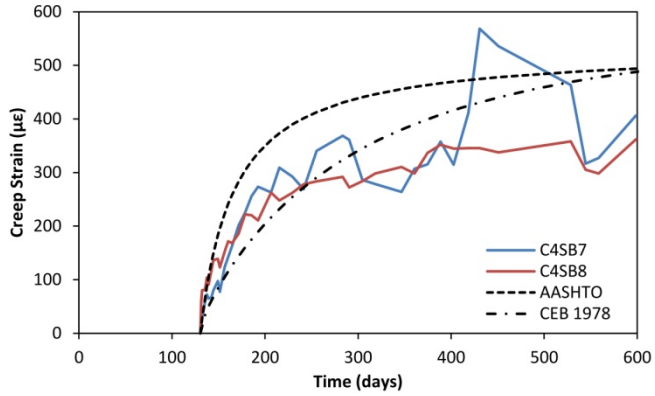

Figure 3.26: Creep strains for Frame #3 stressed at 275ksf (24.0 kip load) at 130 days old compared to AASHTO LRFD (2010) and 1978 CEB/FIP Model Code predictions.

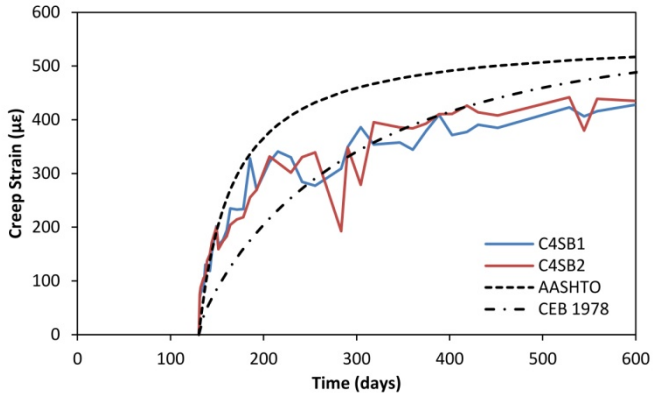

Figure 3.7: Creep strains for Frame #1 restressed at 275ksf (24.0 kip load) at 130 days old compared to AASHTO LRFD (2010) and 1978 CEB/FIP Model Code predictions.

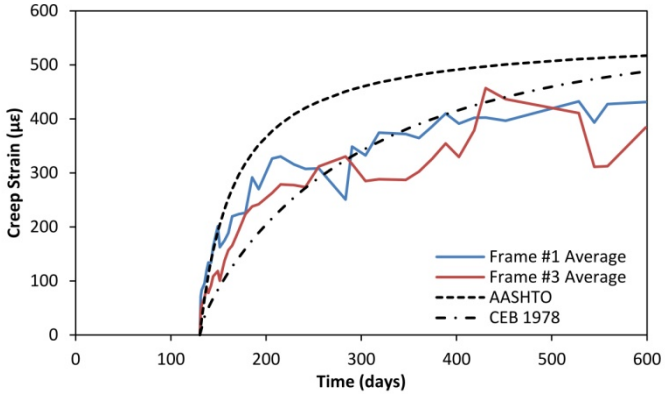

Figure 3.28: Creep strains for Frame #1 and Frame #3 stressed at 275ksf (24.0 kip load) at 130 days old compared to AASHTO LRFD (2010) and 1978 CEB/FIP Model Code predictions.

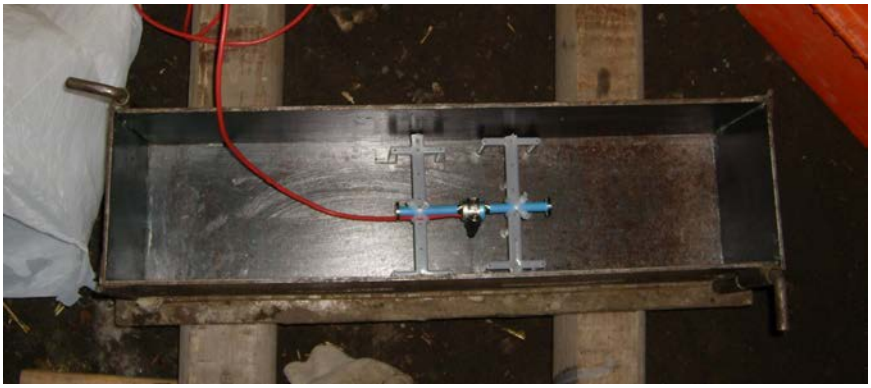

Figure 3.29: Coefficient of thermal expansion 6 x 6 x 24 in. specimen mold with VWSG

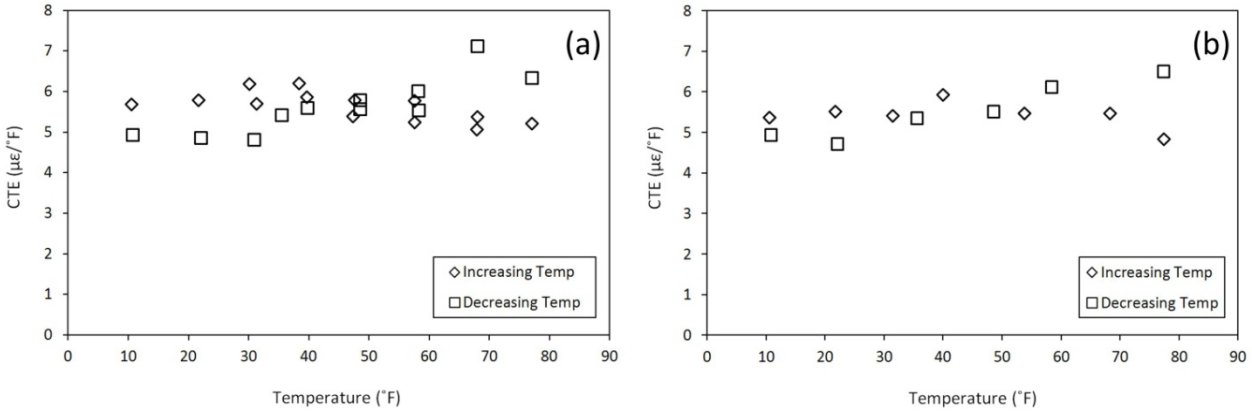

Figure 3.30: Incremental coefficient of thermal expansion for superstructure laboratory specimens plotted against temperature averaged over (a) all Roctest Model EM-5 gages and (b) all Geokon Model VCE-4200 gages.

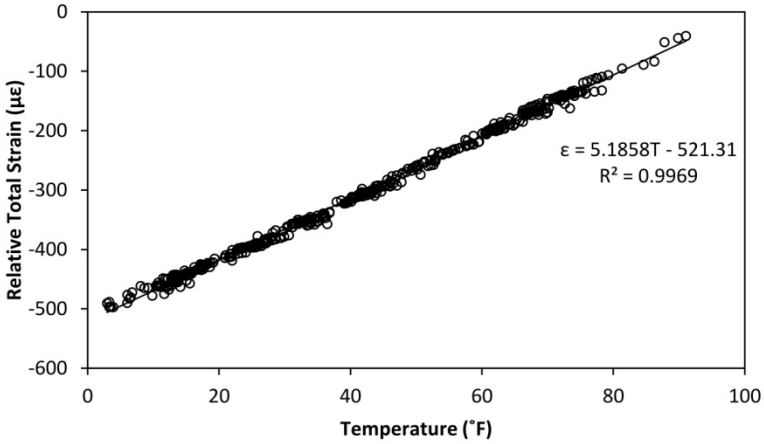

Figure 3.31: Gage VS03TEL2 total strain data plotted with respect to temperature from January 1, 2011 to June 30, 2011. Total strain was assumed zero at 6:00 AM on September 2, 2008.

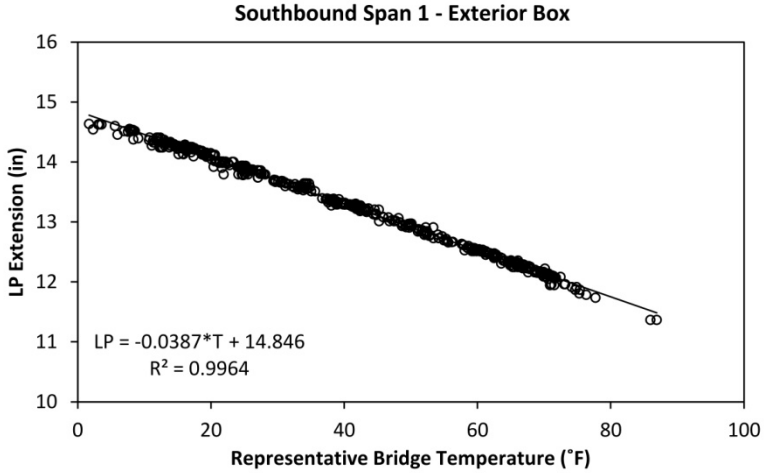

Figure 3.32: Linear potentiometer elongation from the exterior box of the southbound structure at Abutment 1 plotted with respect to temperature from January 1, 2011 until June 30, 2011.

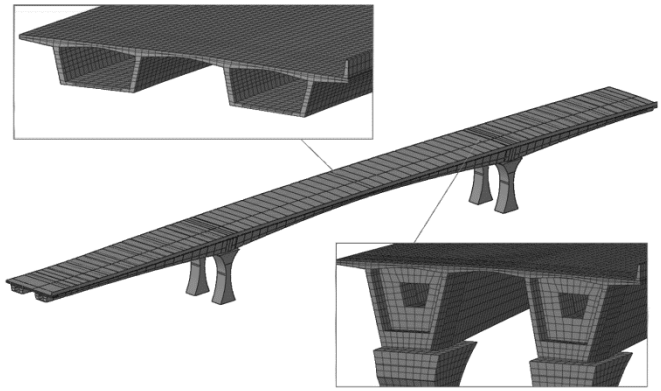

Figure 4.1: Three-dimensional finite element model of southbound bridge, Spans 1 through 3.

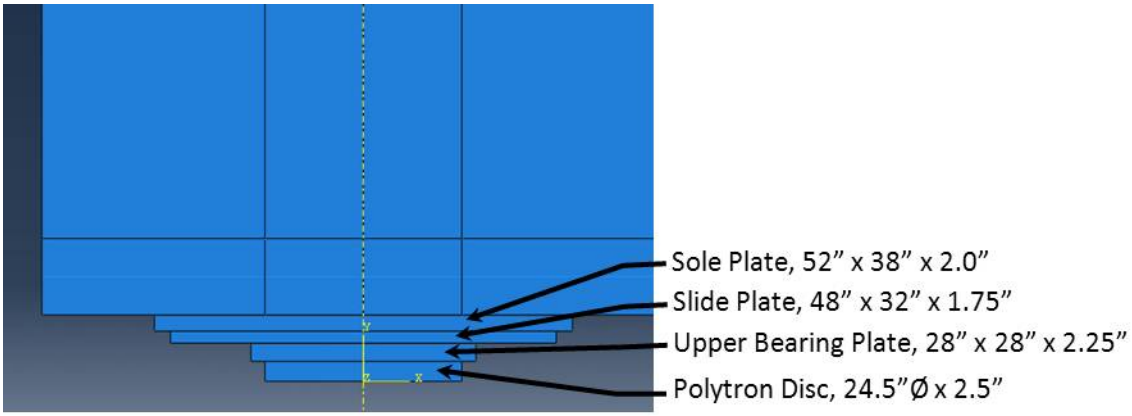

Figure 4.2: Abutment 1 bearing detail for the two-dimensional finite element model

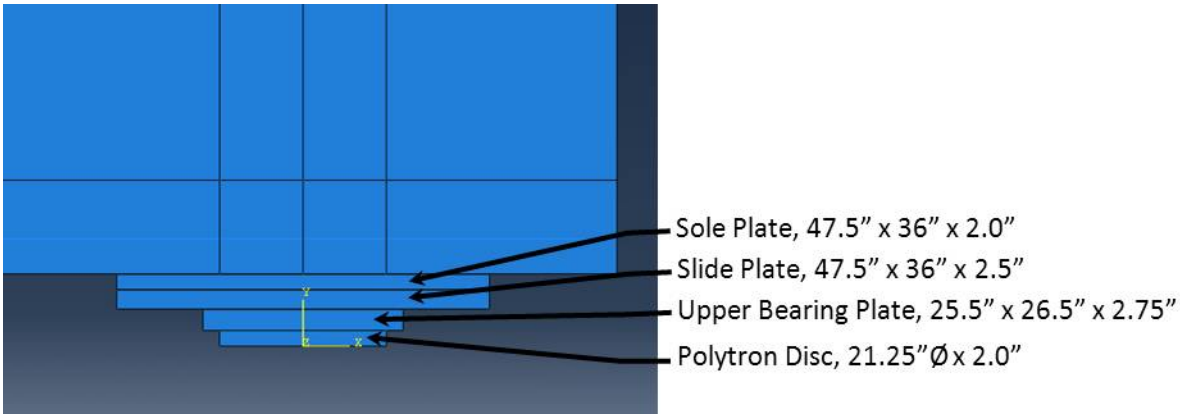

Figure 4.3: Pier 4 bearing detail for the two-dimensional finite element model

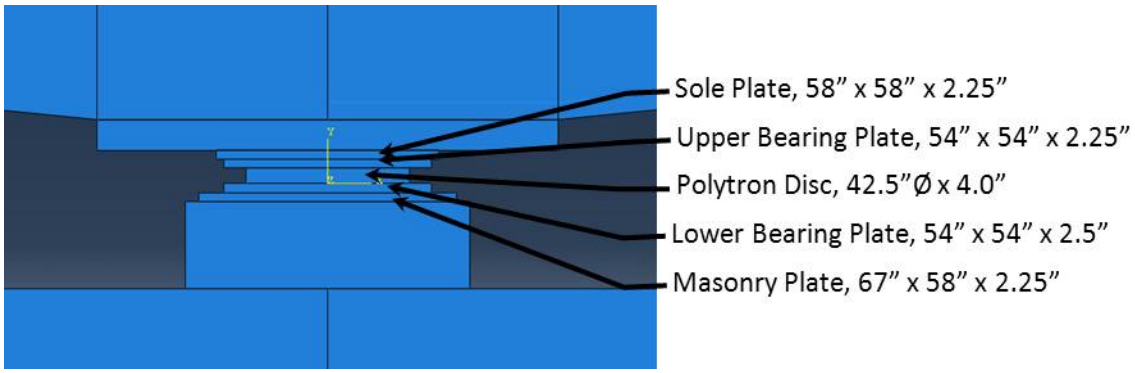

Figure 4.4: Pier 2 and Pier 3 bearing detail for the two-dimensional finite element model

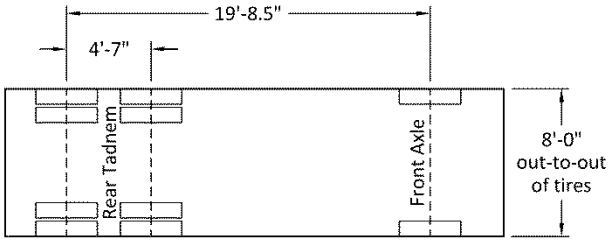

Figure 5.1: Typical dimensions of trucks used in truck tests

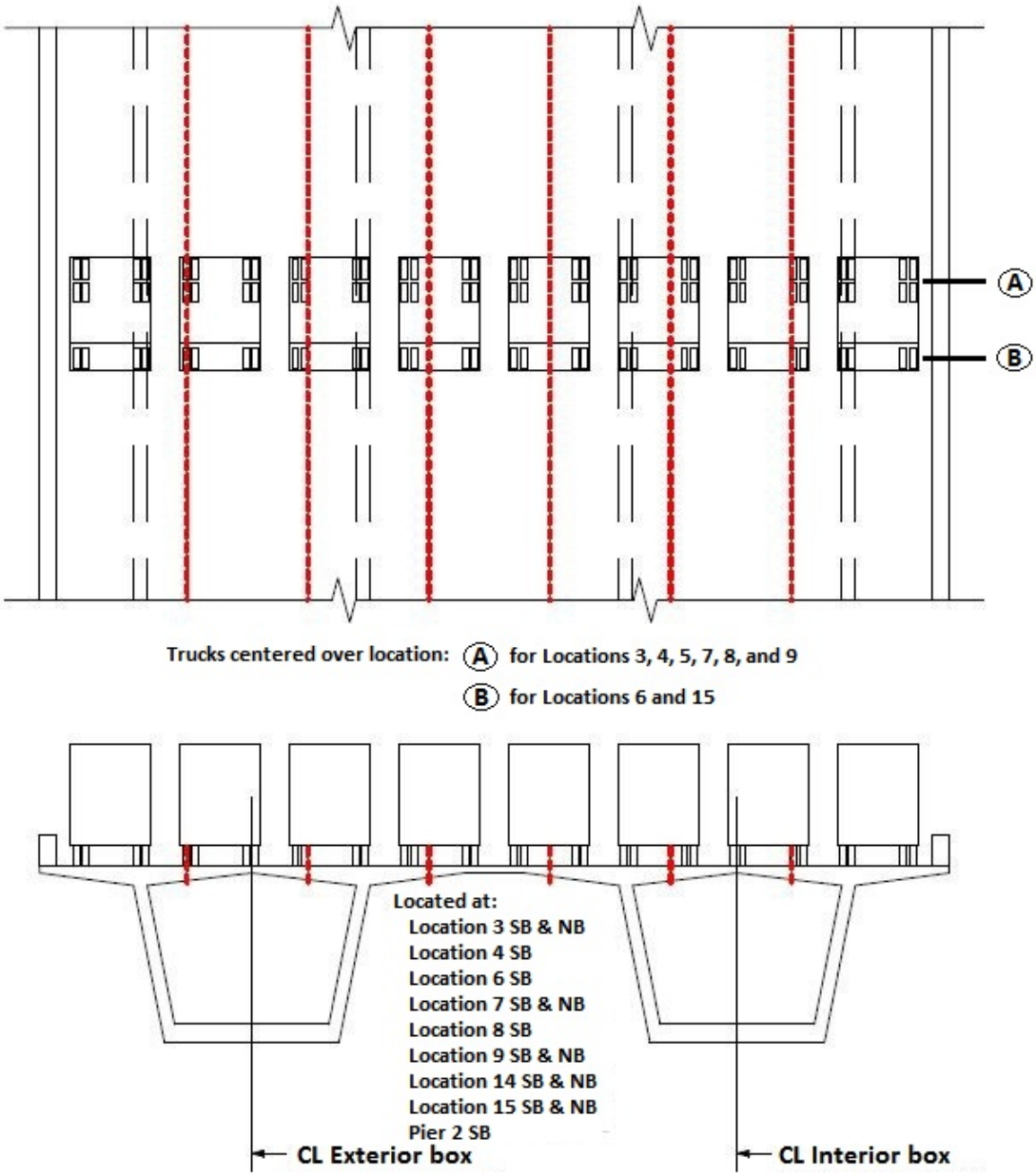

Figure 5.2: Truck orientation ST I

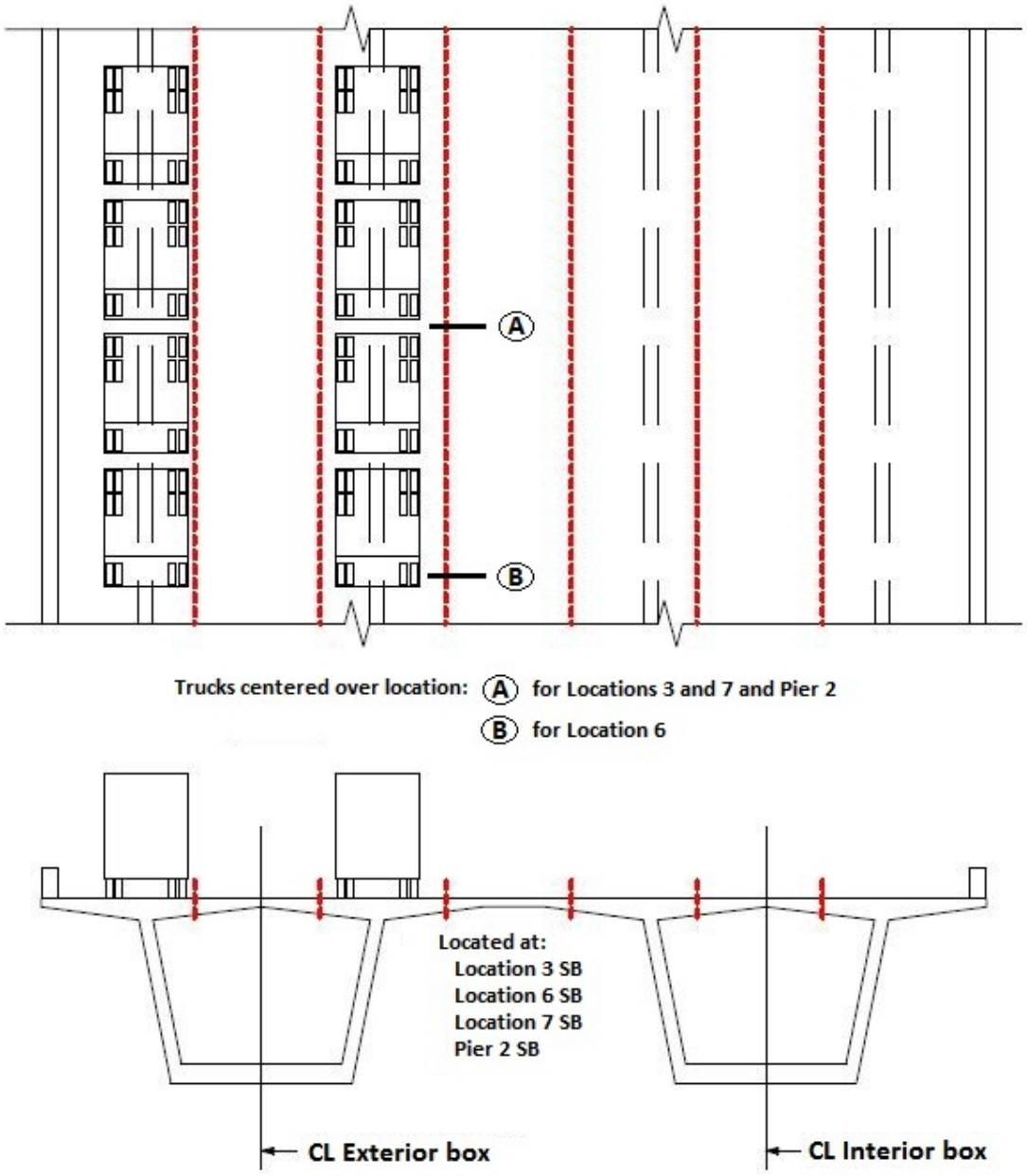

Figure 5.3: Truck orientation ST II

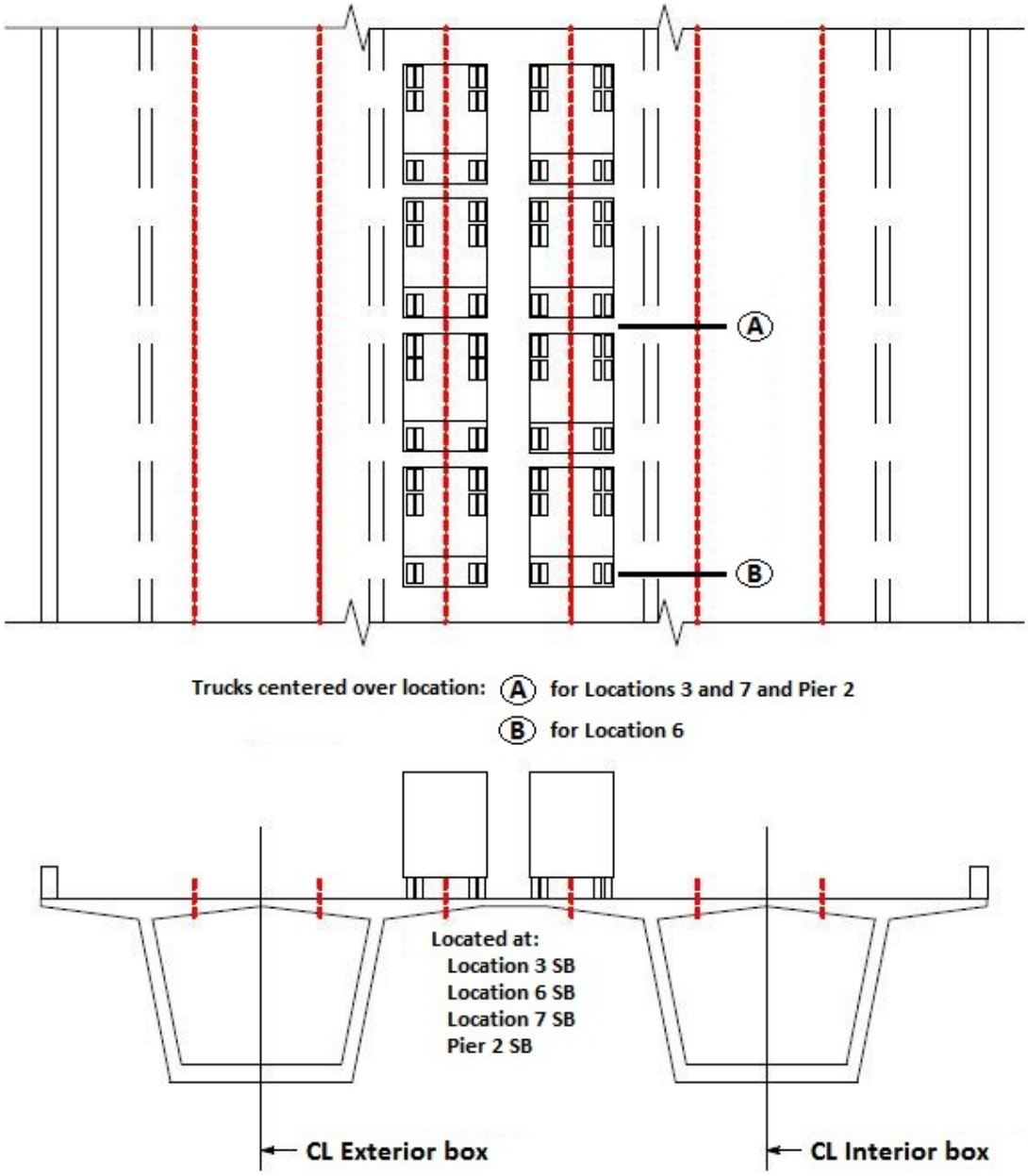

Figure 5.4: Truck orientation ST III

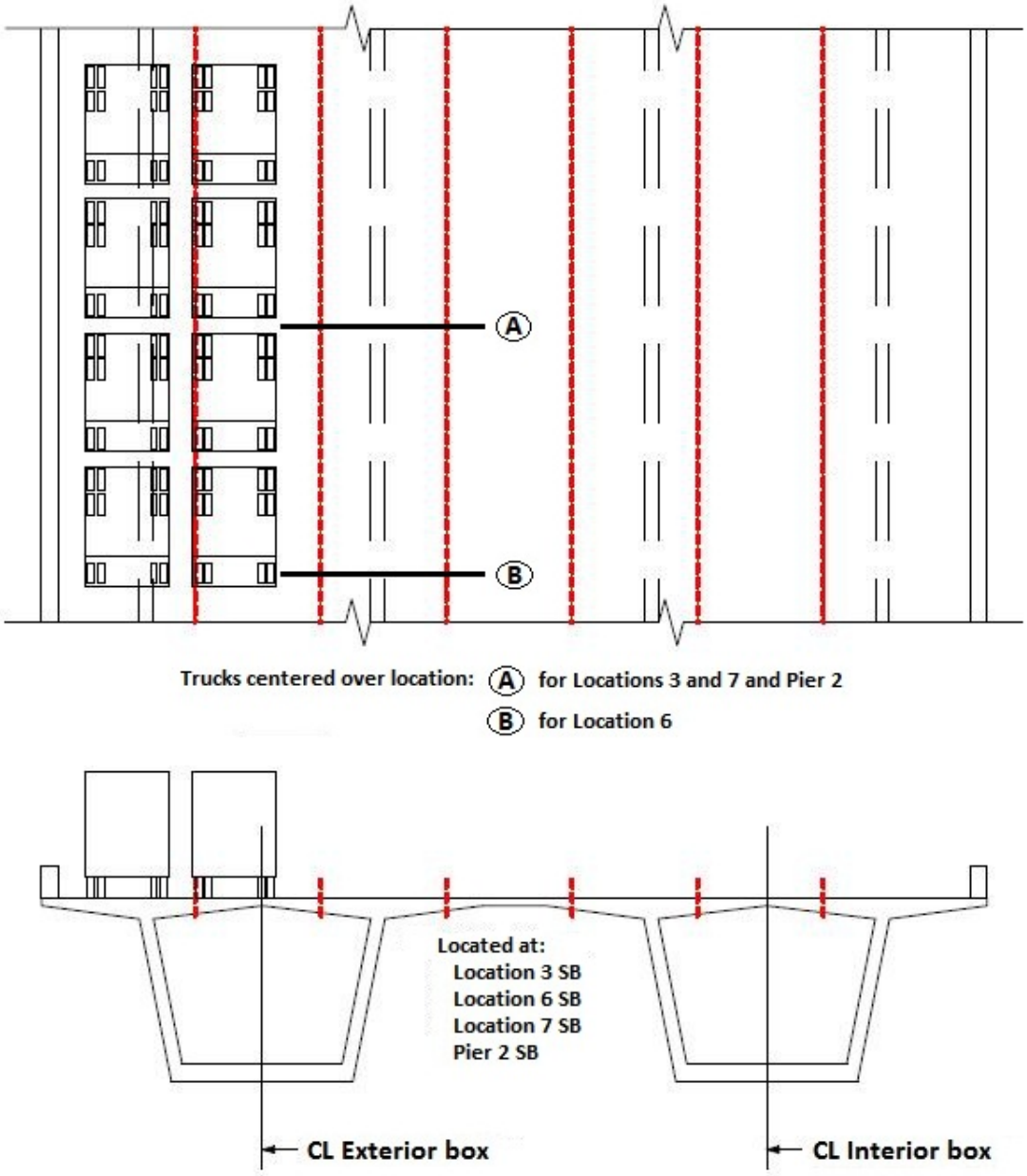

Figure 5.5: Truck orientation ST IVa

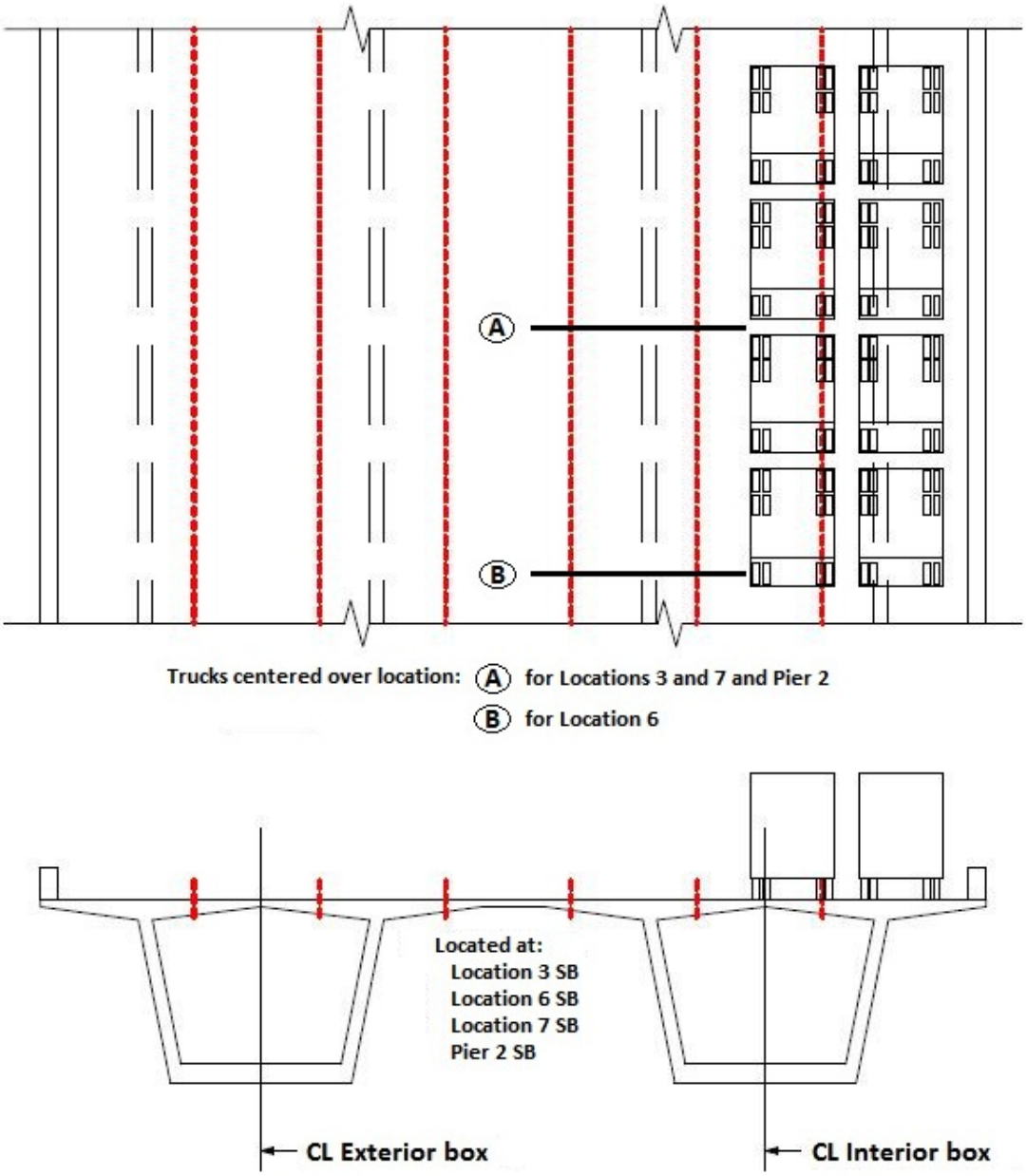

Figure 5.6: Truck orientation ST IVb

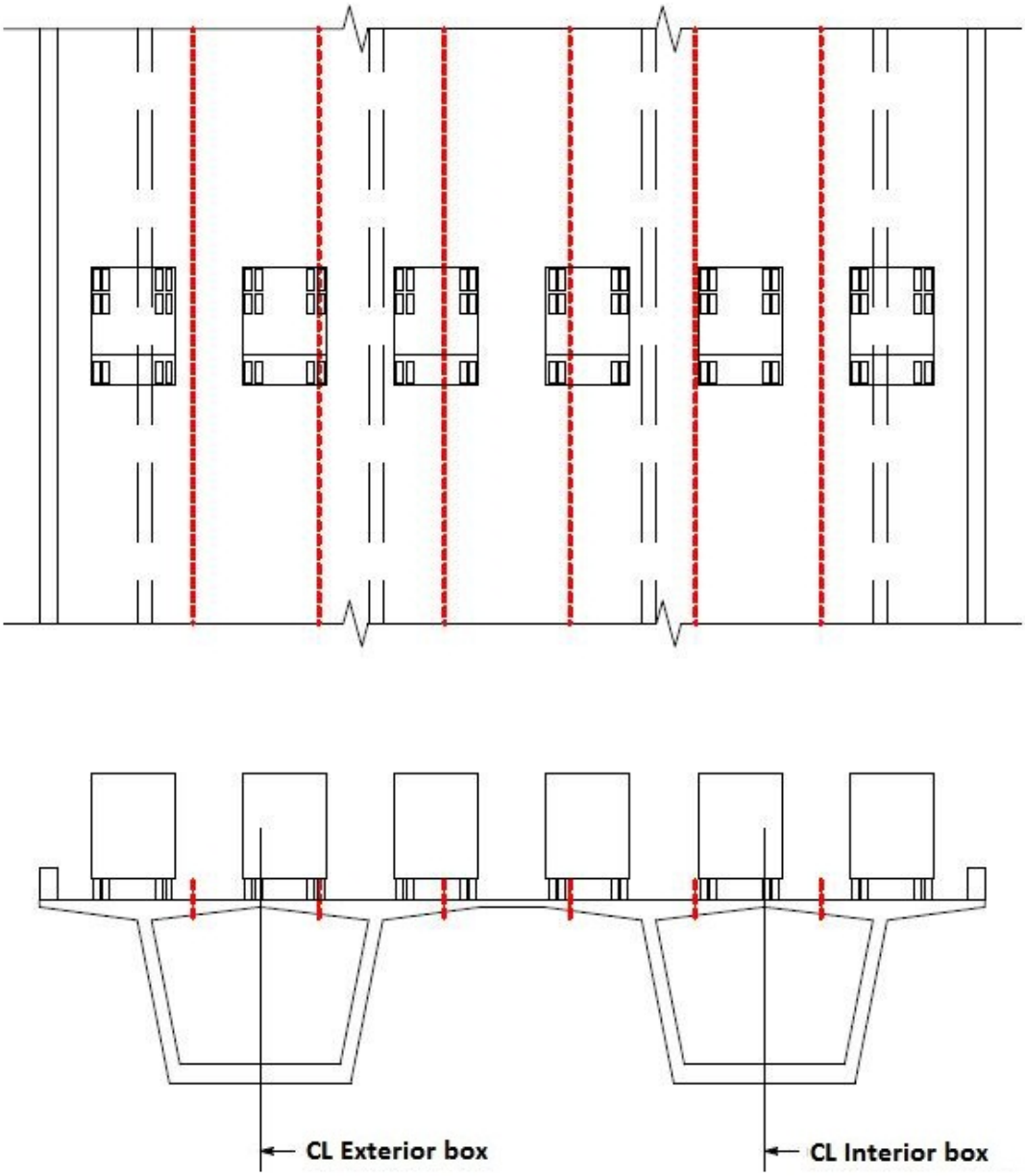

Figure 5.7: Truck orientation ST V

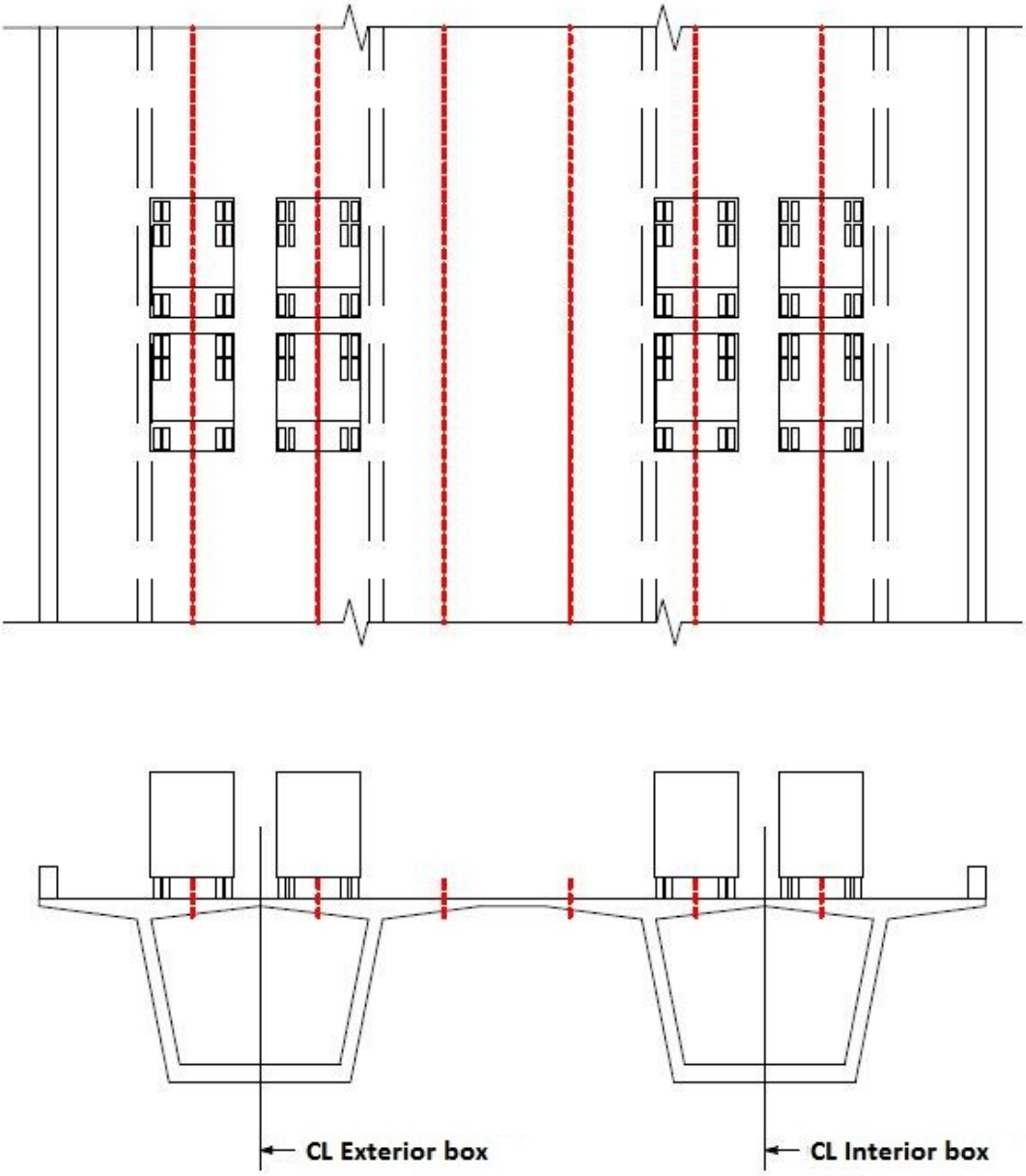

Figure 5.8: Truck orientation ST VI

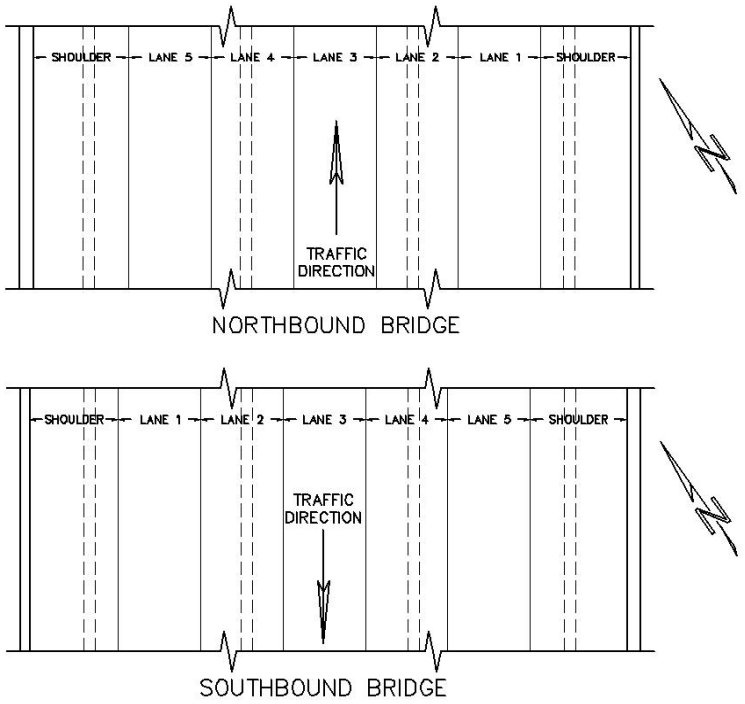

Figure 5.9: Lane labeling for dynamic testing on northbound and southbound structures for October 2010 truck tests

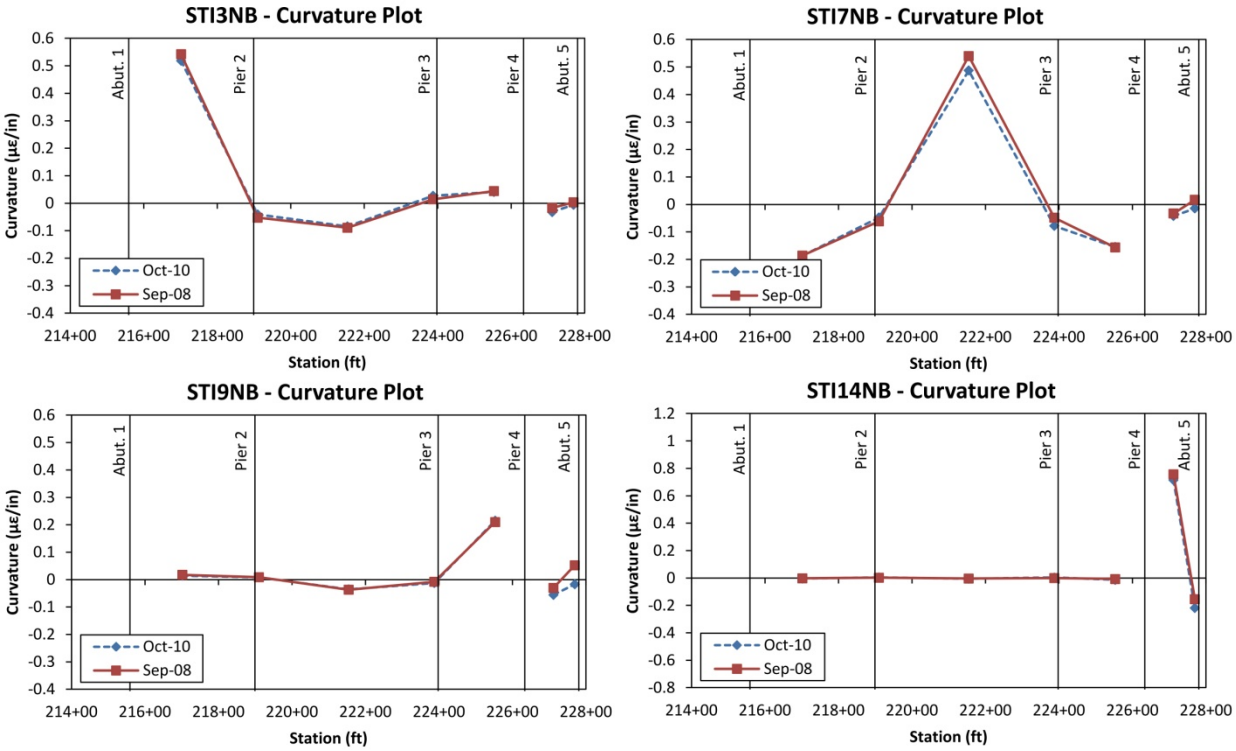

Figure 6.1: Curvature plot comparisons of October 2010 truck tests to September 2008 tests on northbound bridge.

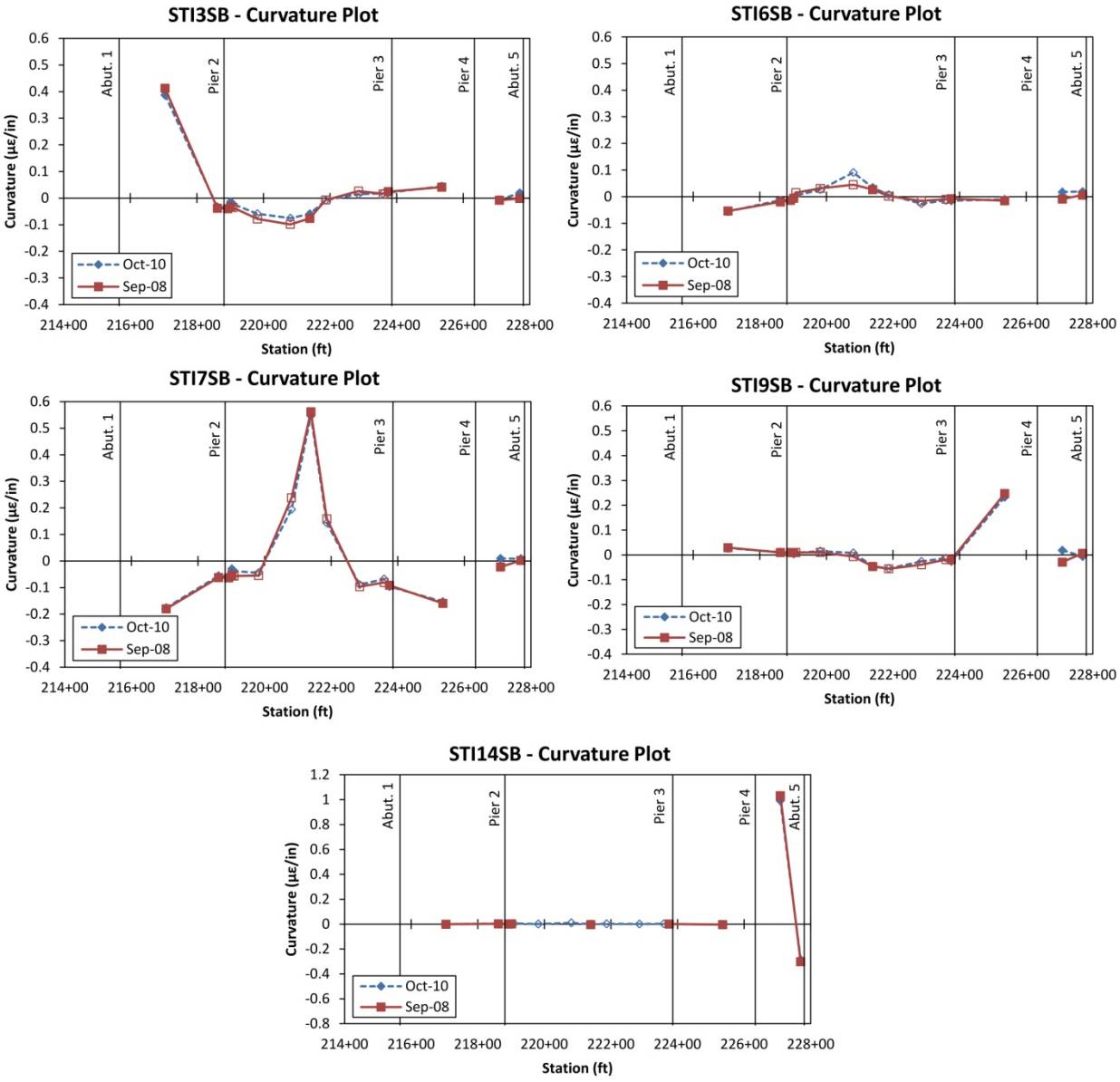

Figure 6.2: Curvature plot comparisons of October 2010 truck tests to September 2008 tests on southbound bridge. Note that for the STI9SB plot, the October 2010 line uses the 9-ft offset test from Location 9 (test STI9(-9)SB), whereas the September 2008 line uses the tandem centered over Location 9 (test STI9SB).

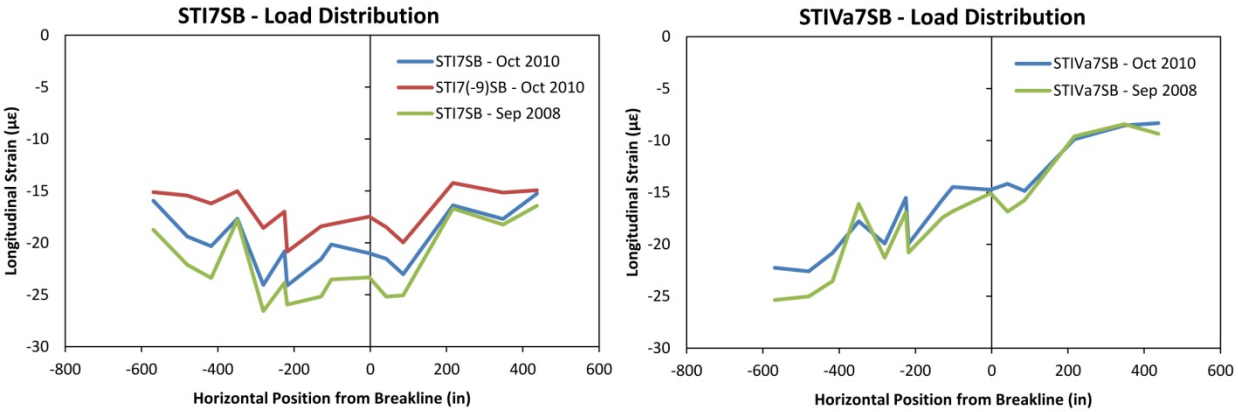

Figure 6.3: Load distribution (plotted as longitudinal strains across width of top flange) at southbound Location 7 comparing October 2010 truck tests to September 2008 tests.

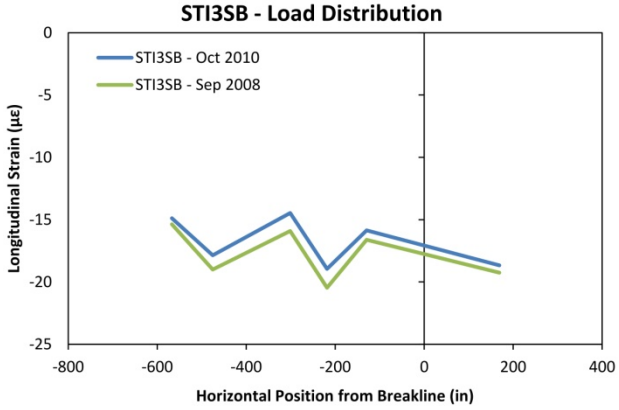

Figure 6.4: Load distribution (plotted as longitudinal strains across width of top flange) at southbound Location 3 comparing October 2010 truck tests to September 2008 tests.

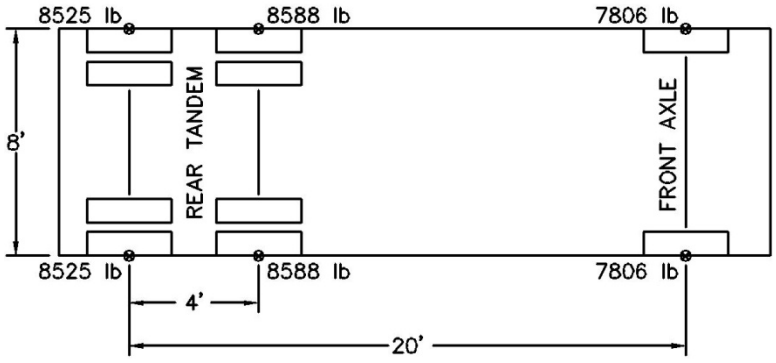

Figure 6.5: Idealized point loads per truck used for FEM analysis

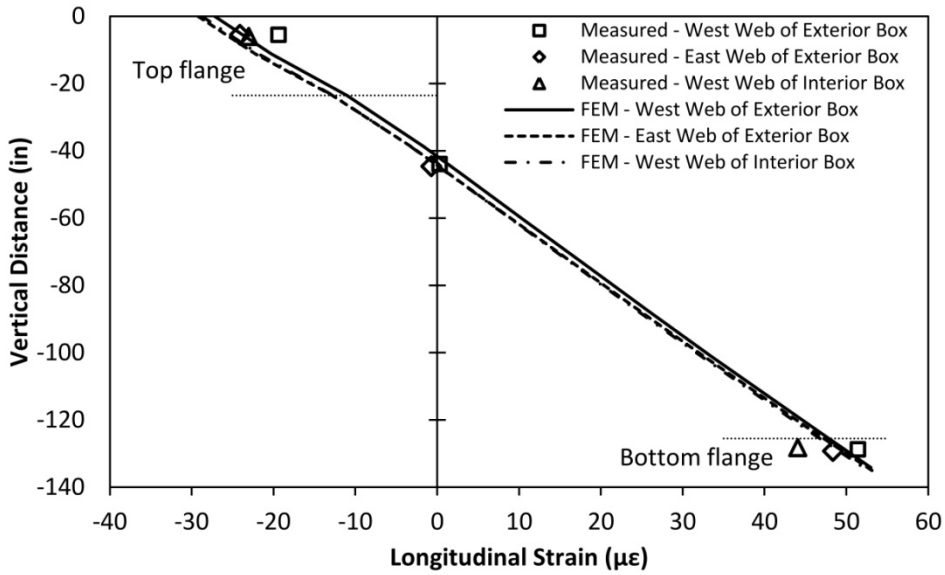

Figure 6.6: Comparison of measured and computed longitudinal strain through the webs at Location 7 due to truck test STI7SB. Measured data represents strain readings from October 2010 truck test results.

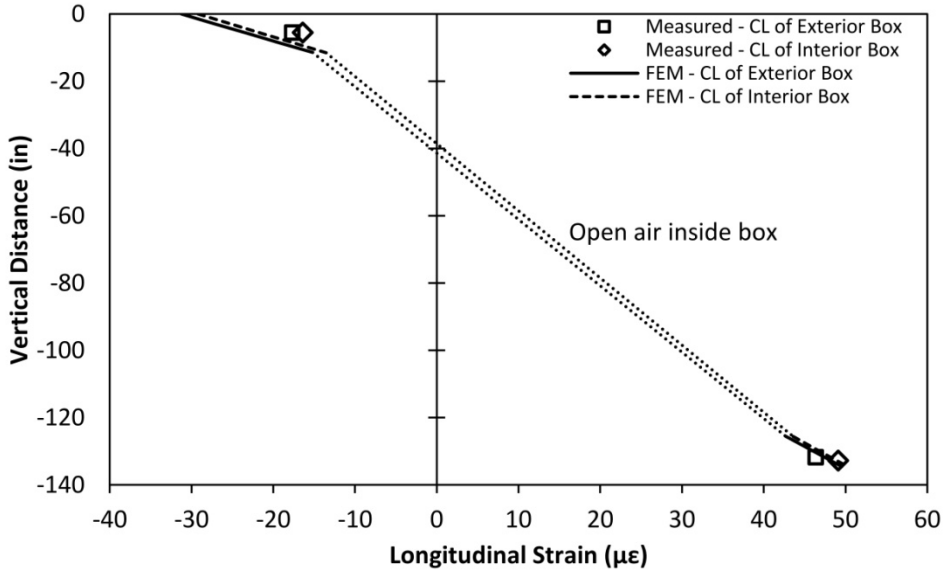

Figure 6.7: Comparison of measured and computed longitudinal strain through centerlines of boxes at Location 7 due to truck test STI7SB. Measured data represents strain readings from October 2010 truck test results.

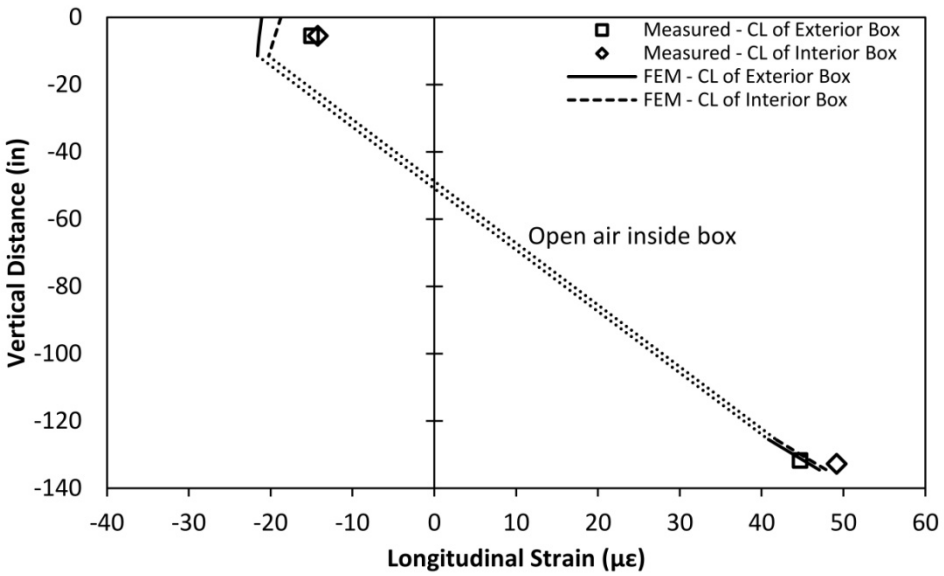

Figure 6.8: Comparison of measured and computed longitudinal strain through centerlines of boxes at Location 7 due to truck test STI7(-9)SB (Offset Test). Measured data represents strain readings from October 2010 truck test results.

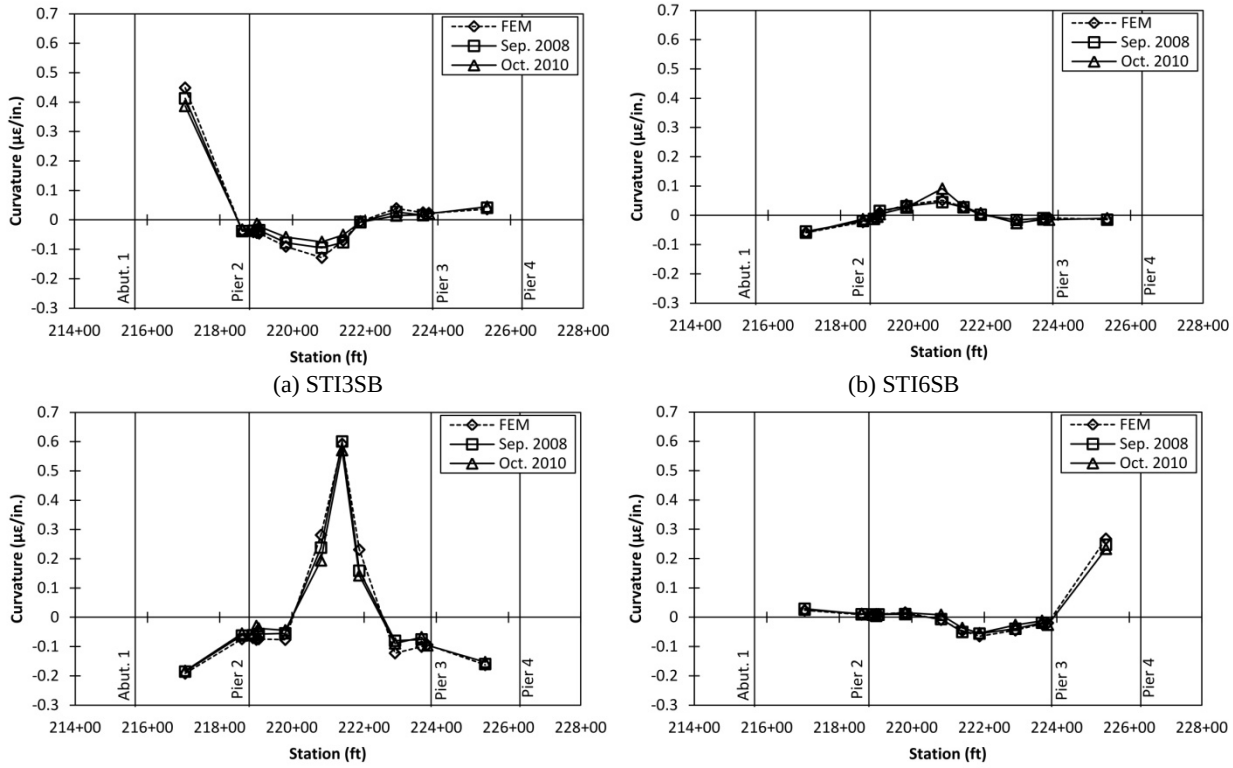

(a) STI3SB (b) STI6SB

(c) STI7SB (d) STI9SB

Figure 6.9: Comparison of measured to computed curvature along length of the southbound bridge. Note that for the STI9SB plot, the October 2010 line uses the 9-ft offset test from Location 9 (test STI9(-9)SB), whereas the September 2008 line uses the tandem centered over Location 9 (test STI9SB).

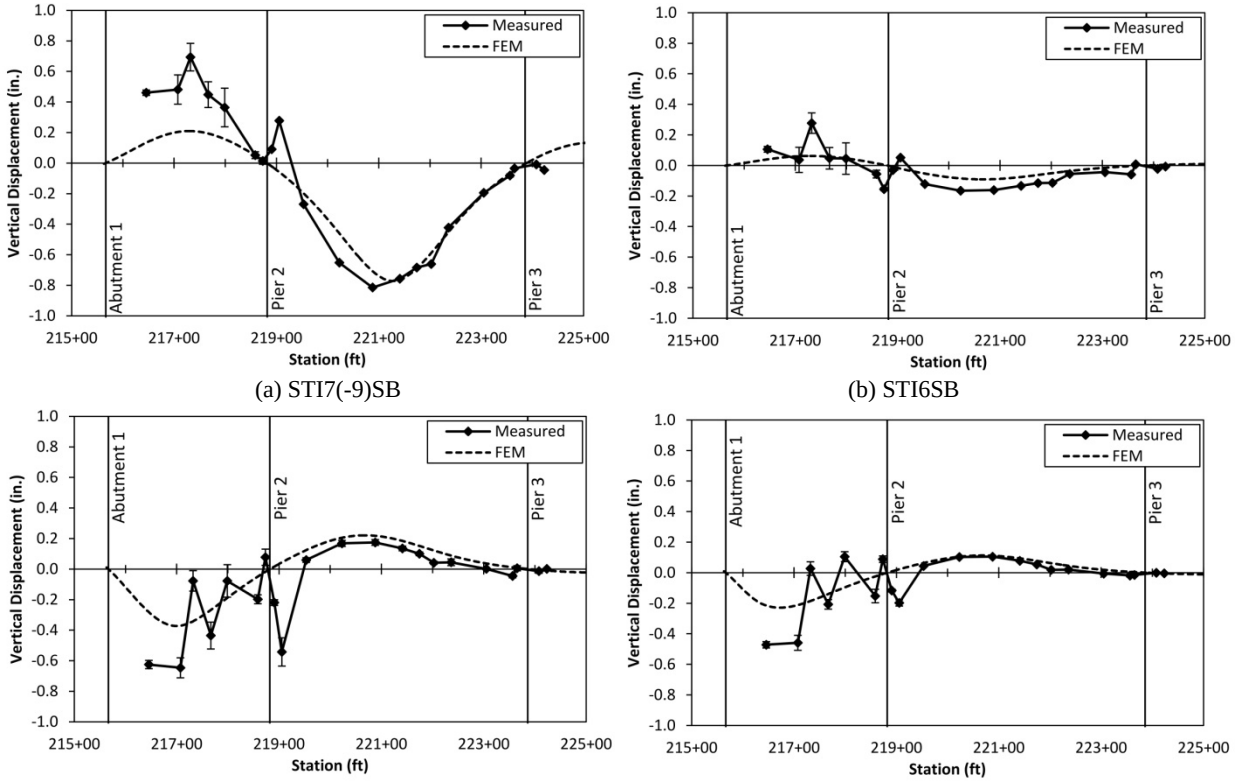

(a) STI7(-9)SB (b) STI6SB

(c) STI3SB (d) STI3(-70)SB

Figure 6.10: Comparison of measured (using IBIS-S provided by Olson Engineering) to computed deflections along Spans 1 and 2 of the southbound bridge. Measured data from October 2010 truck tests only.

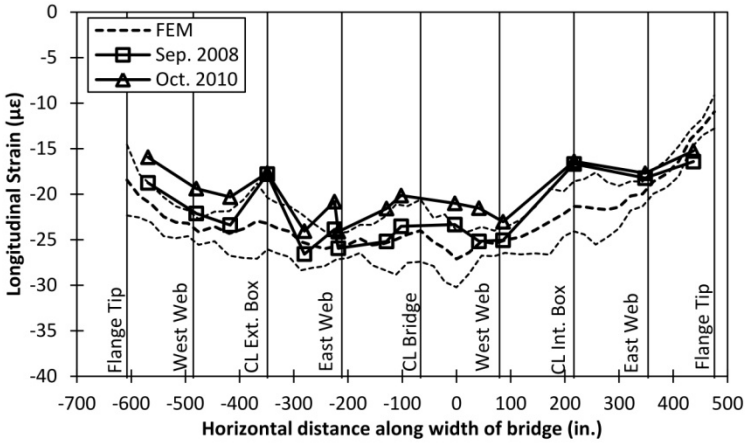

Figure 6.11: Comparison of measured and computed longitudinal strain across deck at Location 7 due to truck test STI7SB. Dotted lines represent ±2-in. gage positional errors for the modeled results.

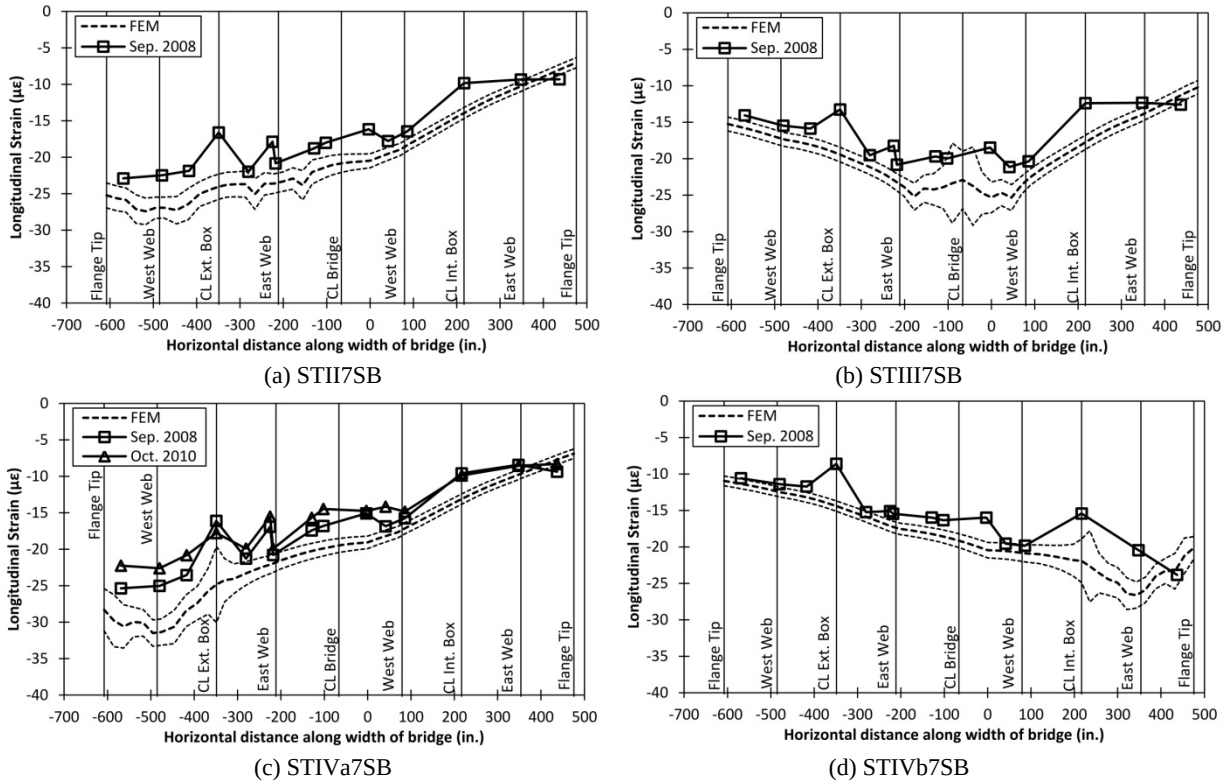

(a) STII7SB (b) STIII7SB

(c) STIVa7SB (d) STIVb7SB

Figure 6.12: Comparison of measured and computed longitudinal strain across deck at Location 7. Dotted lines represent ±2-in. gage positional errors for the computed results.

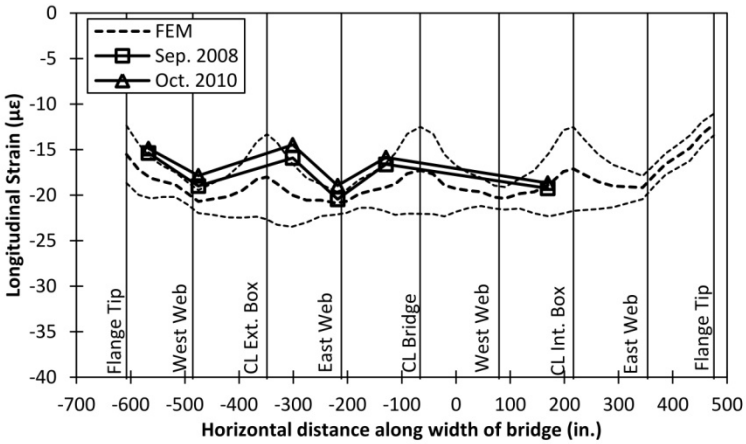

Figure 6.13: Comparison of measured and computed longitudinal strain across deck at Location 3 due to truck test STI3SB. Dotted lines represent ±2-in. gage positional errors for the modeled results.

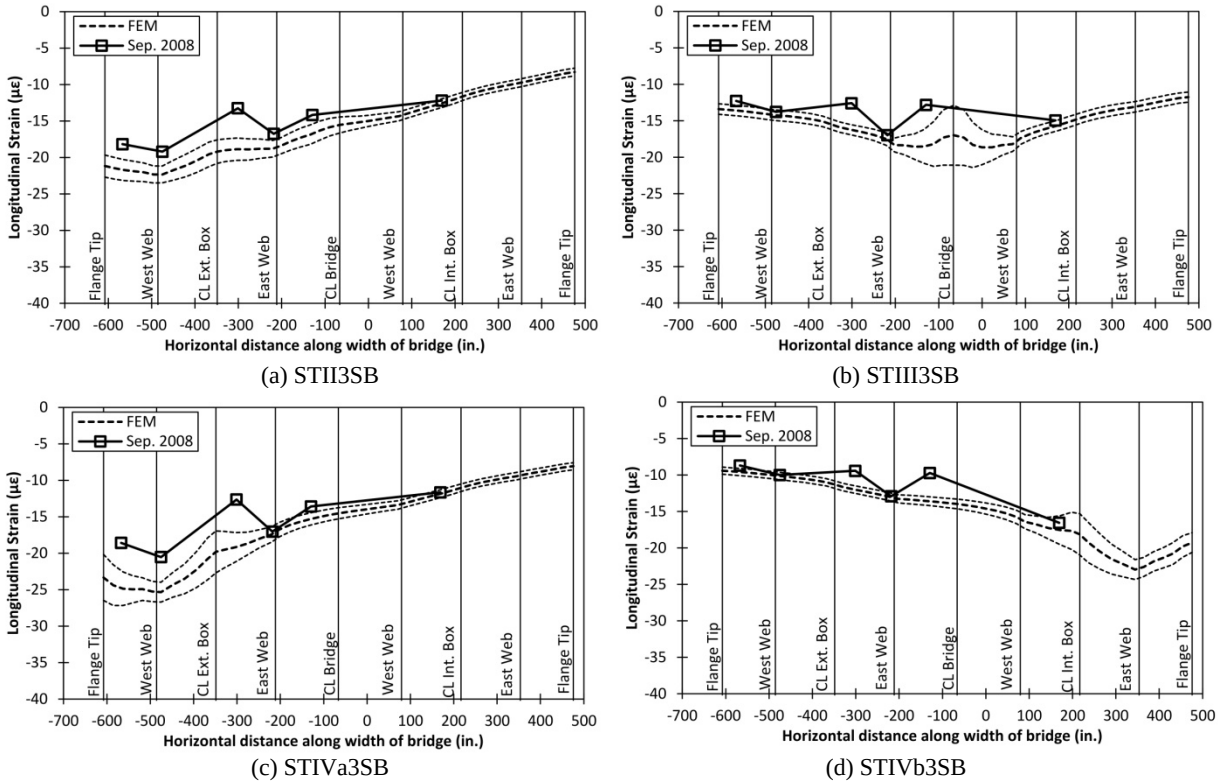

(a) STII3SB (b) STIII3SB

(c) STIVa3SB (d) STIVb3SB

Figure 6.14: Comparison of measured and computed longitudinal strain across deck at Location 3. Dotted lines represent ±2-in. gage positional errors for the computed results.

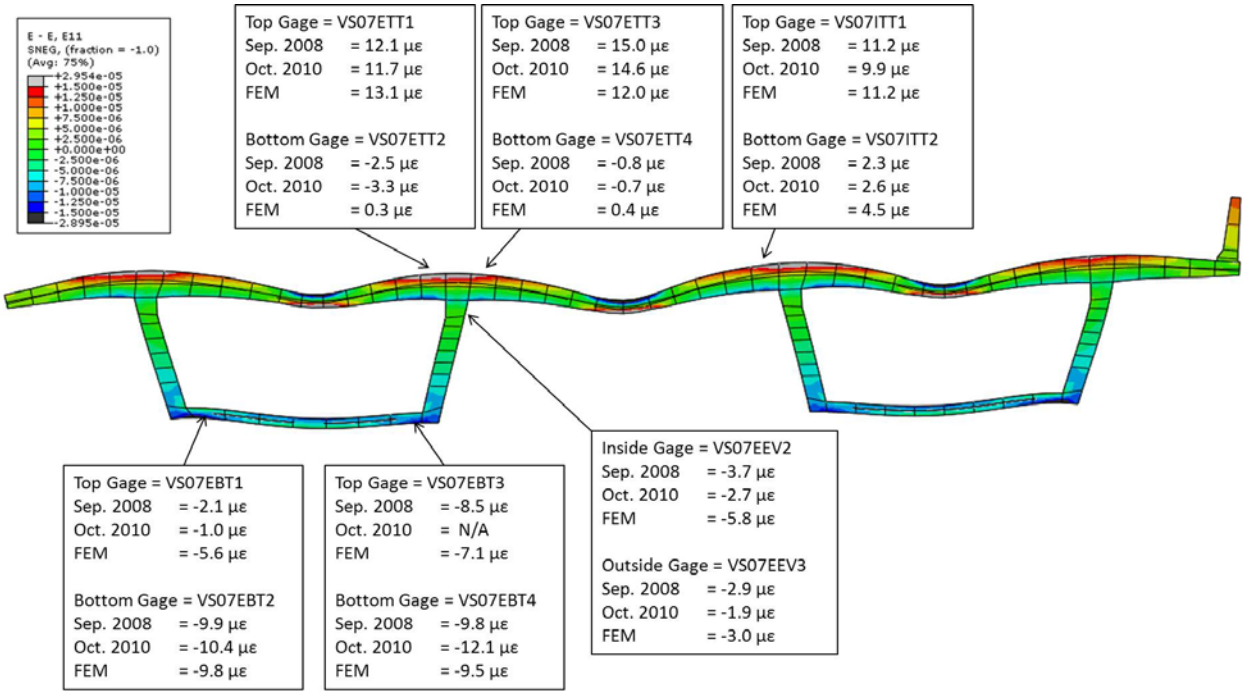

Figure 6.15: Deformed shape of box section at Location 7 due to test STI7SB. Color contours represent transverse strain. Deflections are magnified 2,500 times.

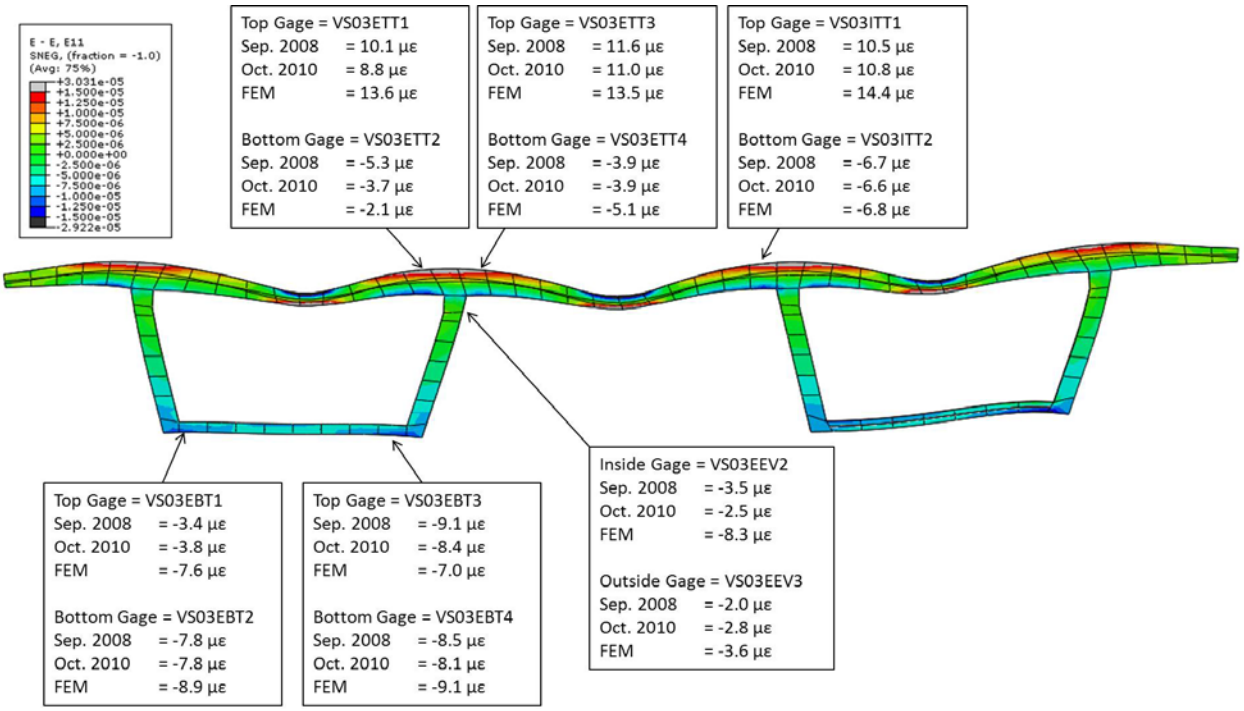

Figure 6.16: Deformed shape of box section at Location 3 due to test STI3SB. Color contours represent transverse strain. Deflections are magnified 2,500 times.

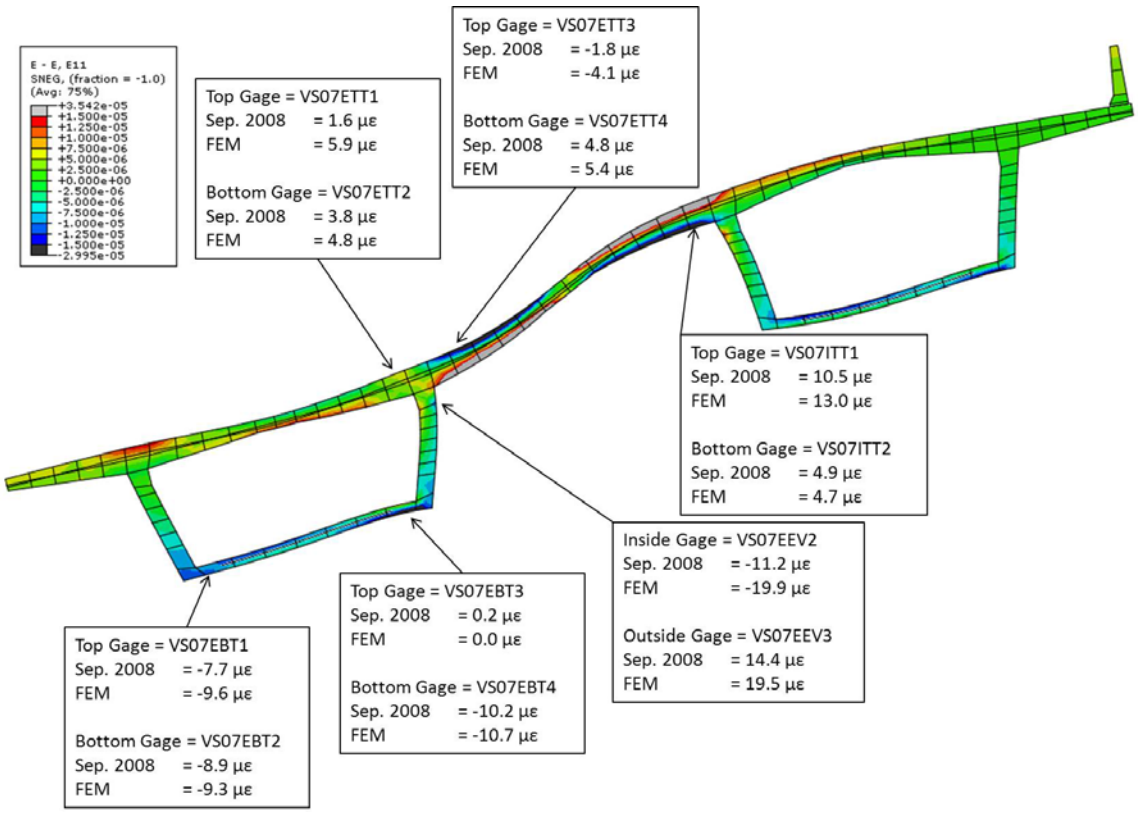

Figure 6.17: Deformed shape of box section at Location 7 due to test STII7SB. Color contours represent transverse strain. Deflections are magnified 1,000 times.

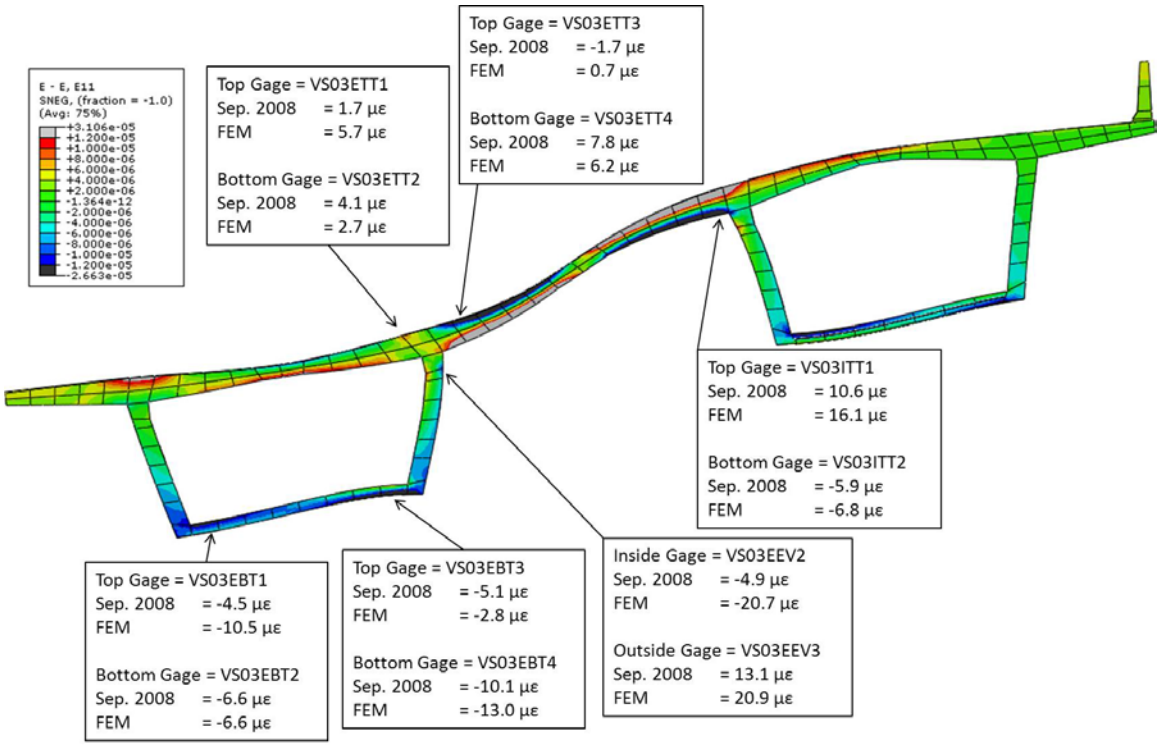

Figure 6.18: Deformed shape of box section at Location 3 due to test STII3SB. Color contours represent transverse strain. Deflections are magnified 1,000 times.

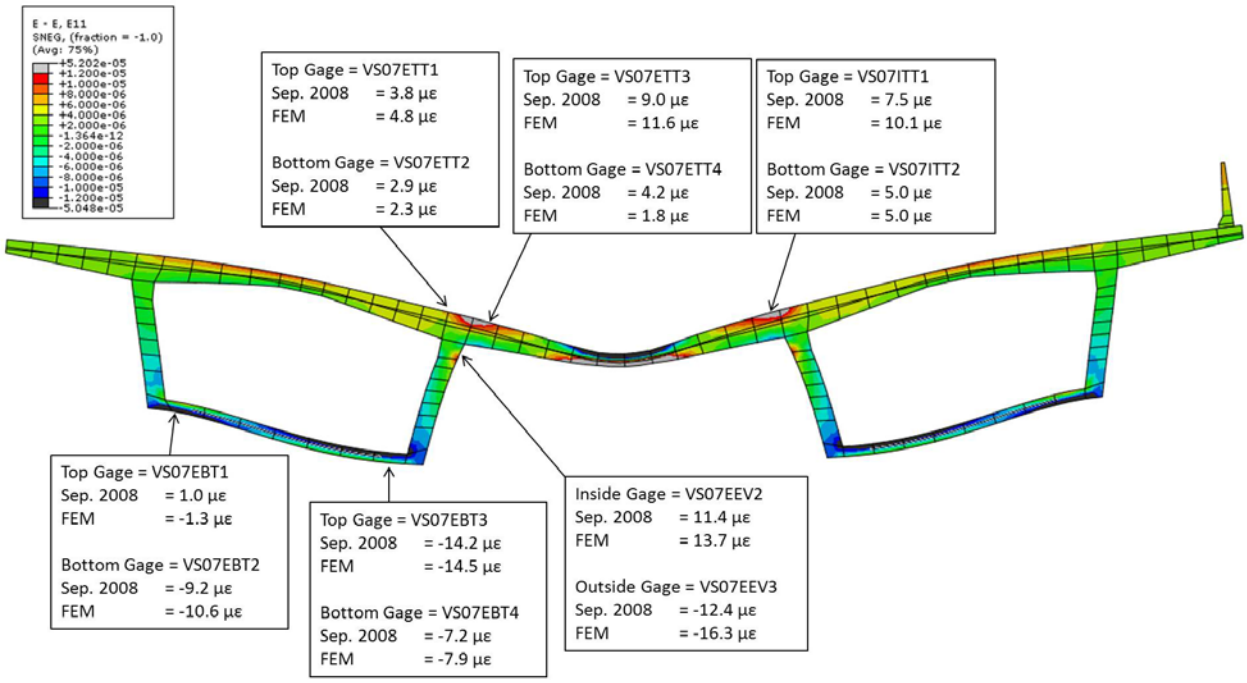

Figure 6.19: Deformed shape of box section at Location 7 due to test STIII7SB. Color contours represent transverse strain. Deflections are magnified 1,000 times.

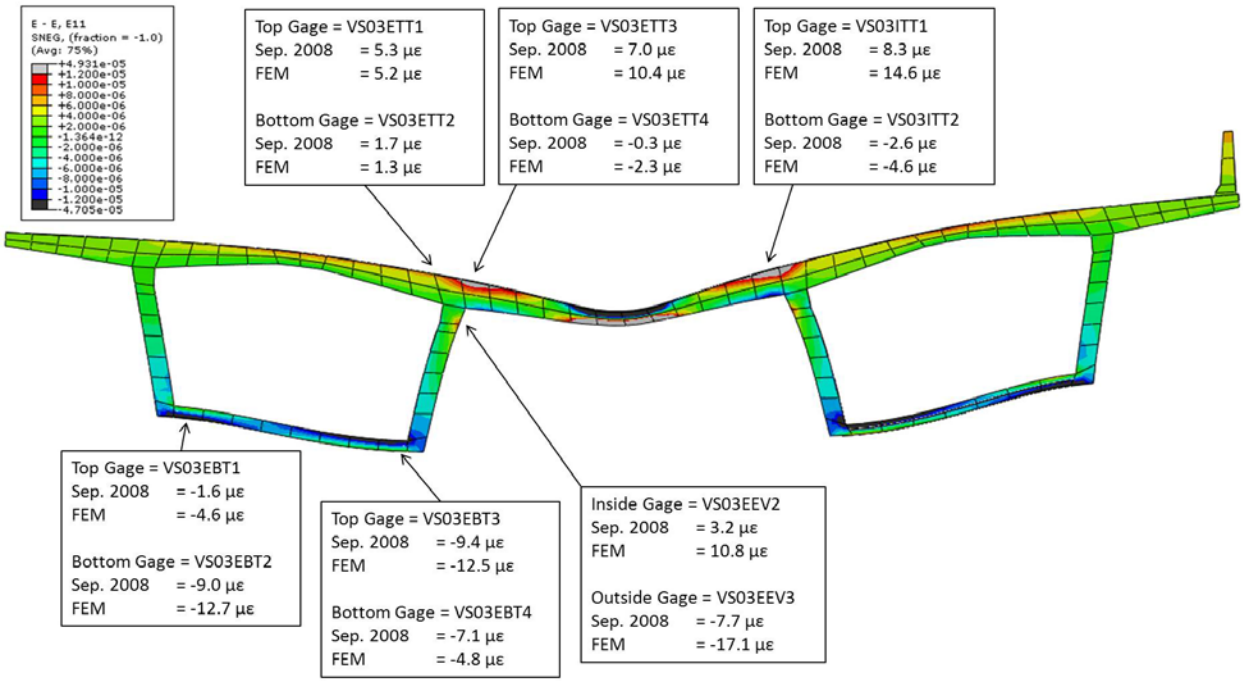

Figure 6.20: Deformed shape of box section at Location 3 due to test STIII3SB. Color contours represent transverse strain. Deflections are magnified 1,000 times.

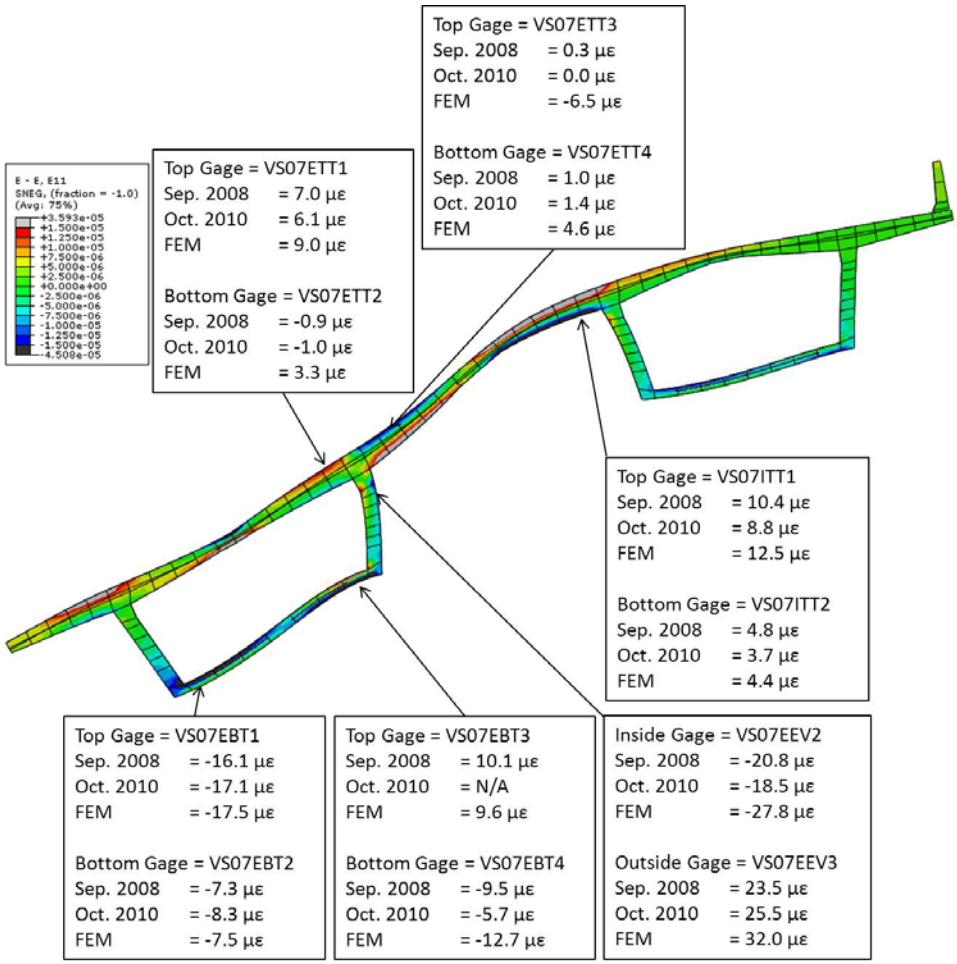

Figure 6.21: Deformed shape of box section at Location 7 due to test STIVa7SB. Color contours represent transverse strain. Deflections are magnified 1,000 times.

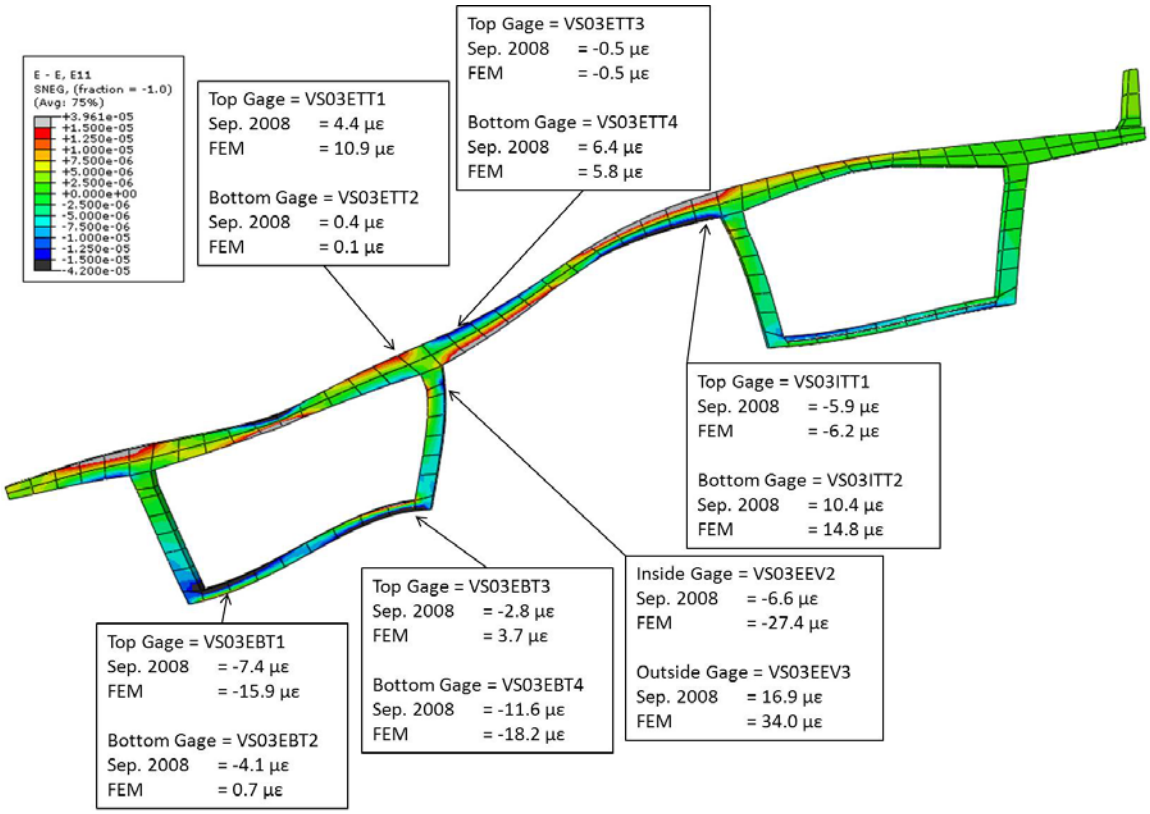

Figure 6.22: Deformed shape of box section at Location 3 due to test STIVa3SB. Color contours represent transverse strain. Deflections are magnified 1,000 times.

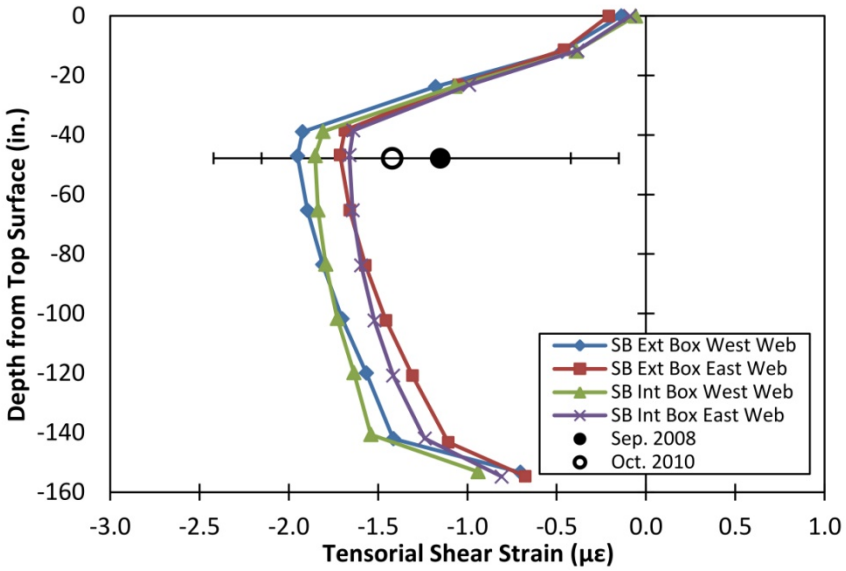

Figure 6.23: FEM tensorial shear strain through webs at Location 3 for test STI7SB. Rosettes located only in the east web of the southbound exterior box at Location 3.

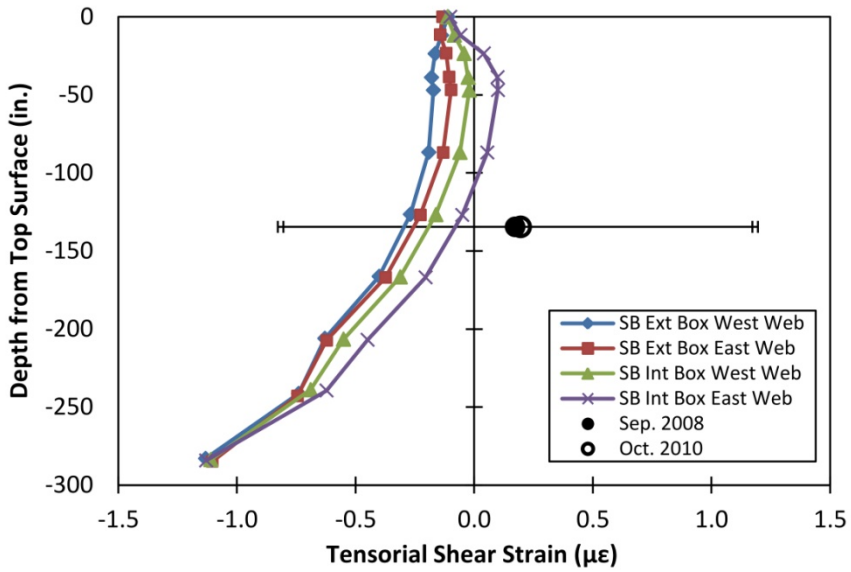

Figure 6.24: FEM tensorial shear strain through webs at Location 4 for test STI7SB. Measured results from west web of the southbound exterior box at Location 4; rosettes in east web of the southbound exterior box provided inconsistent results.

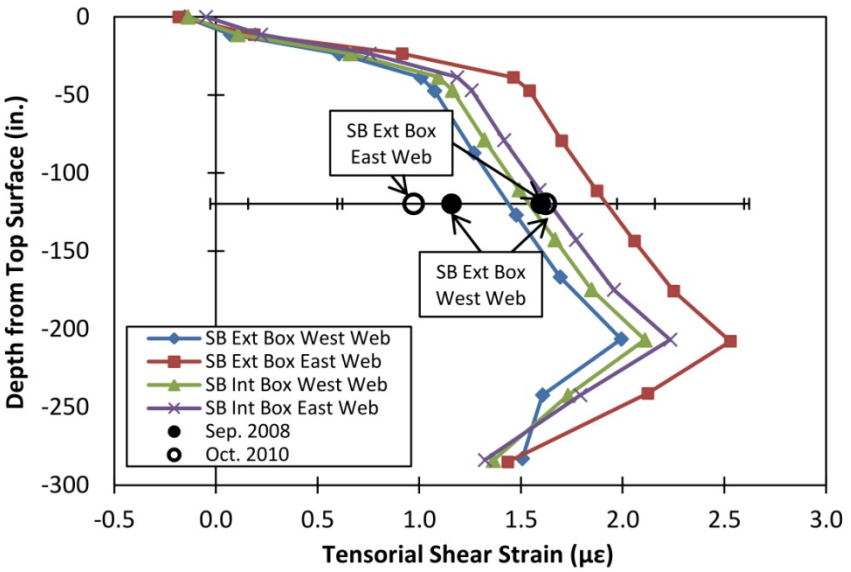

Figure 6.25: FEM tensorial shear strain through webs at Location 6 for test STI7SB.

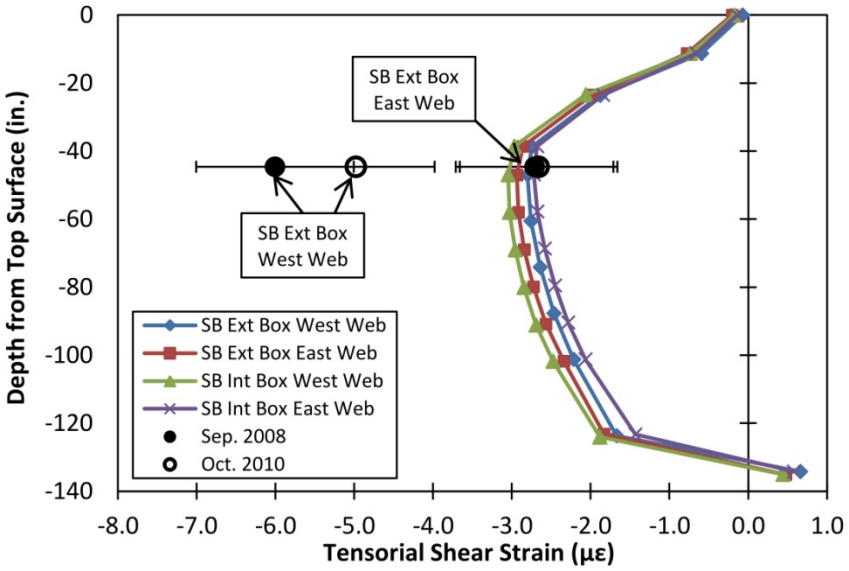

Figure 6.26: FEM tensorial shear strain through webs at Location 7 for test STI7SB.

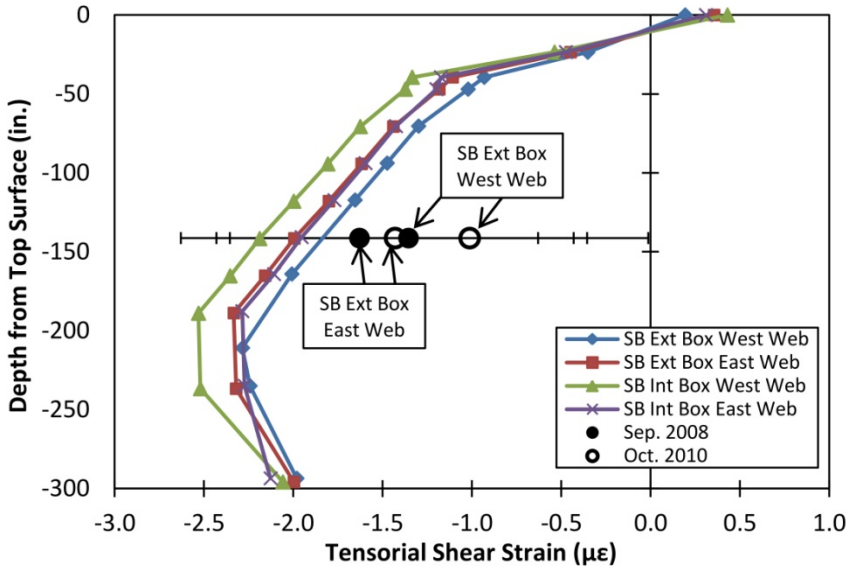

Figure 6.27: FEM tensorial shear strain through webs at Location 8 for test STI7SB.

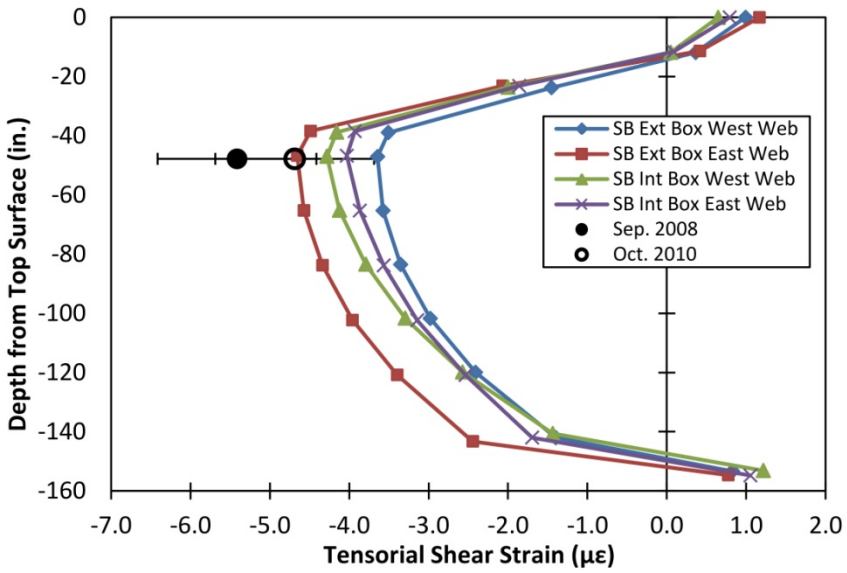

Figure 6.28: FEM tensorial shear strain through webs at Location 3 for test STI3SB. Rosettes located only in the east web of the southbound exterior box at Location 3.

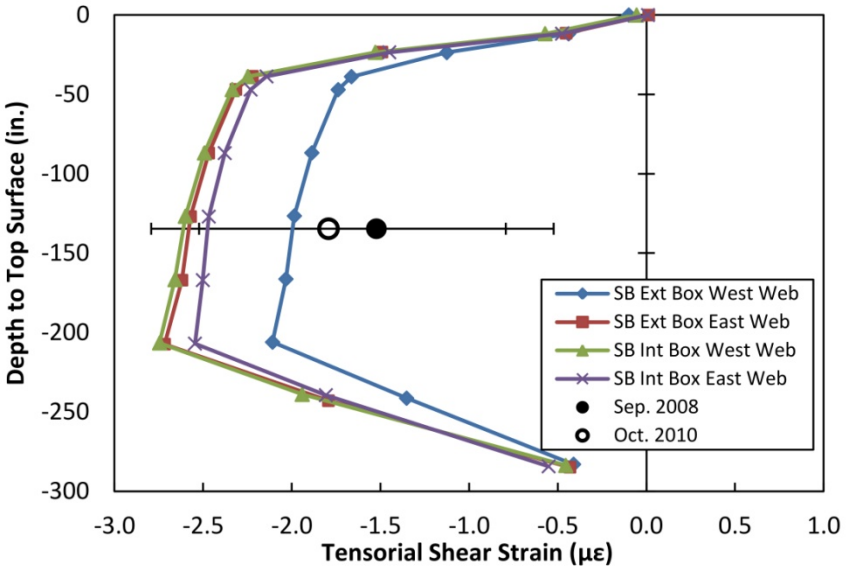

Figure 6.29: FEM tensorial shear strain through webs at Location 4 for test STI3SB. Measured results from west web of the southbound exterior box at Location 4; rosettes in east web of the southbound exterior box provided inconsistent results.

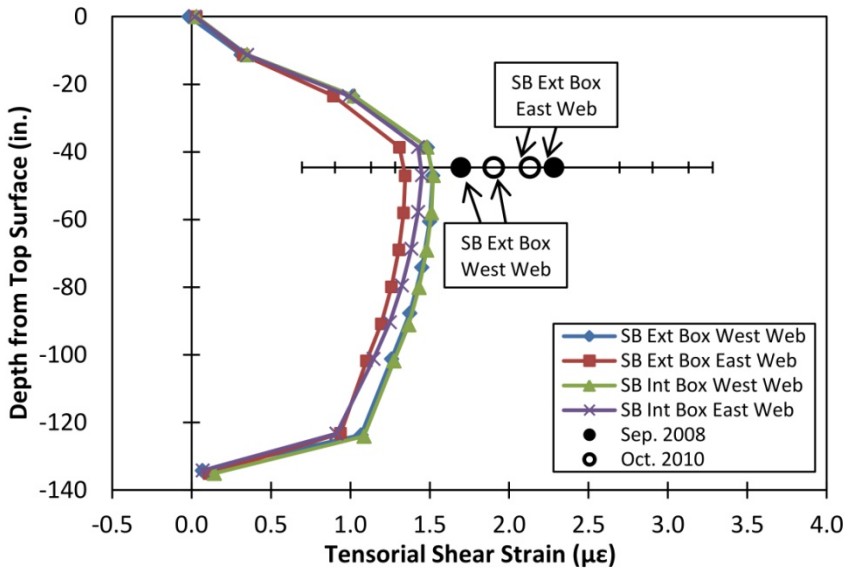

Figure 6.30: FEM tensorial shear strain through webs at Location 7 for test STI3SB.

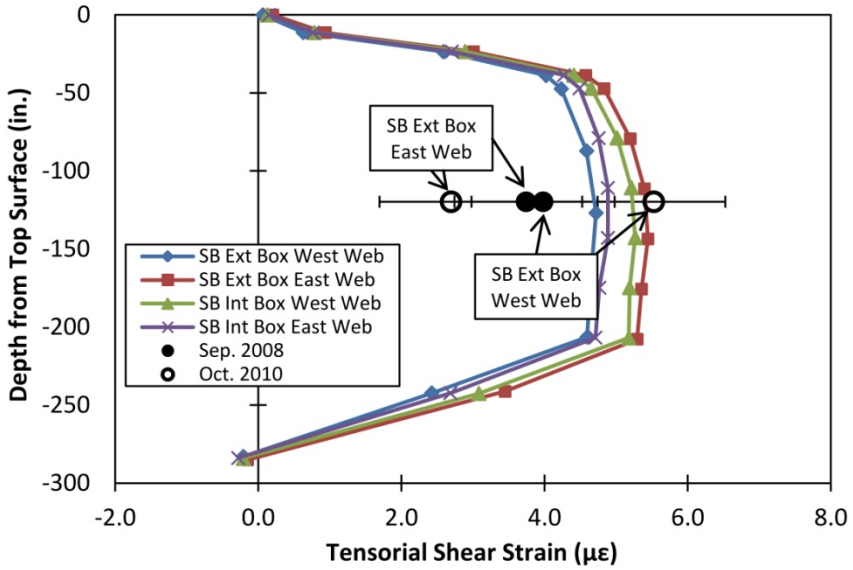

Figure 6.31: FEM tensorial shear strain through webs at Location 6 for test STI6SB.

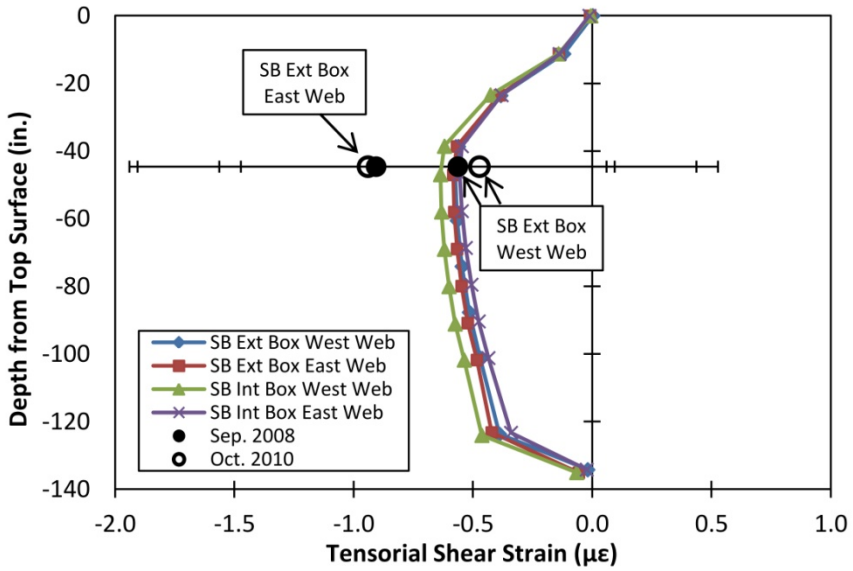

Figure 6.32: FEM tensorial shear strain through webs at Location 7 for test STI6SB.

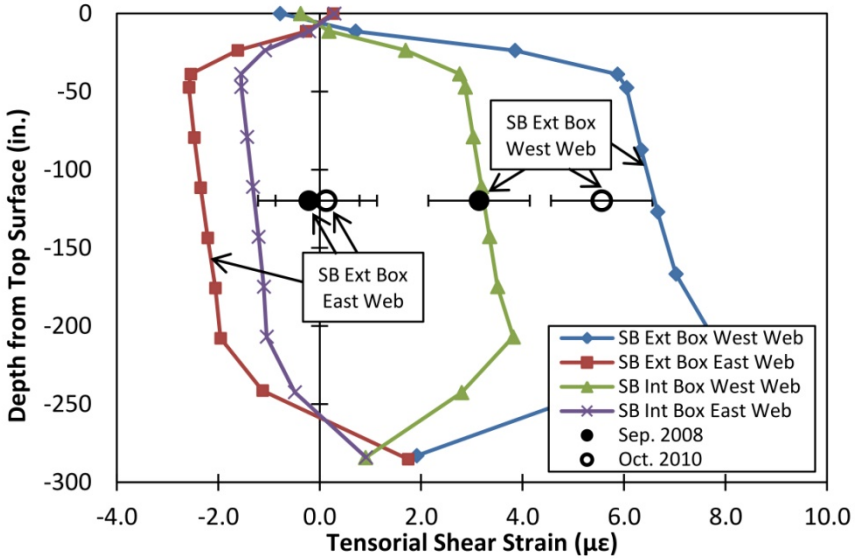

Figure 6.33: FEM tensorial shear strain through webs at Location 6 for test STIVa7SB.

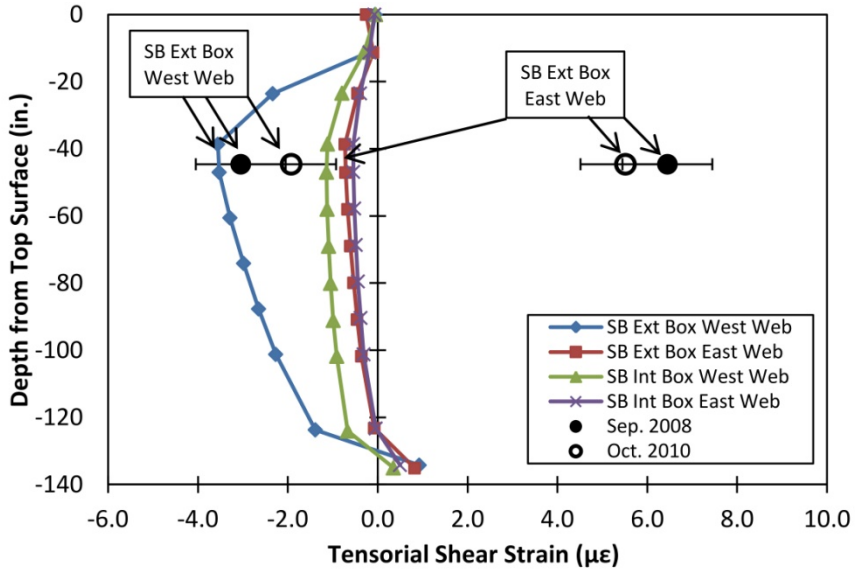

Figure 6.34: FEM tensorial shear strain through webs at Location 7 for test STIVa7SB.

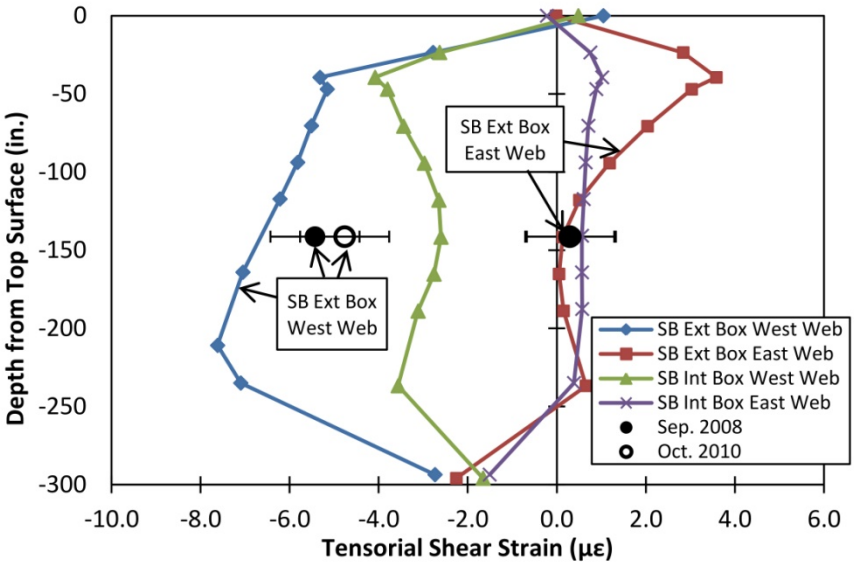

Figure 6.35: FEM tensorial shear strain through webs at Location 8 for test STIVa7SB.

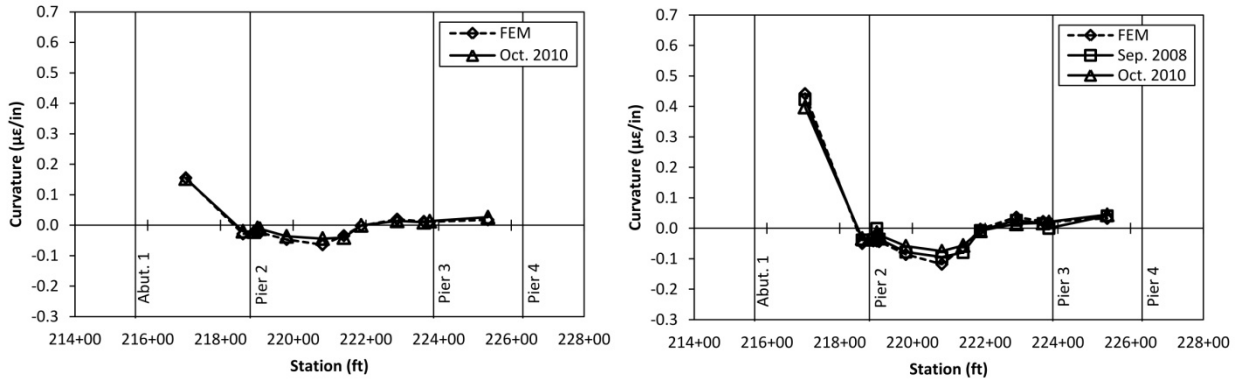

(a) STI3(-70)SB

(b) STI3SB

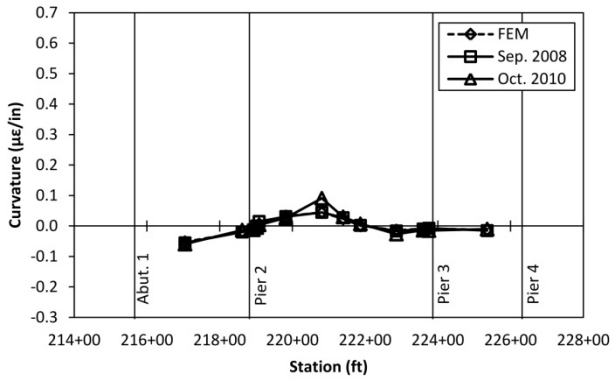

(c) STI6SB

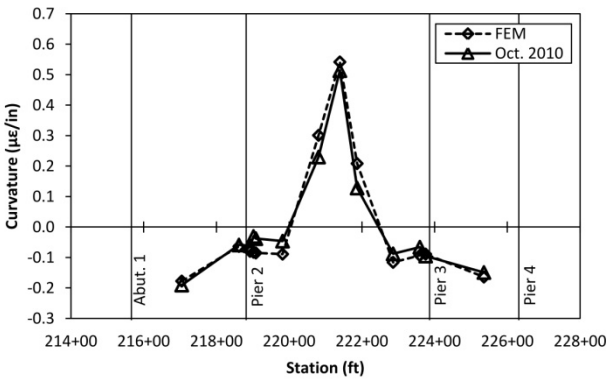

(d) STI7(-9)SB

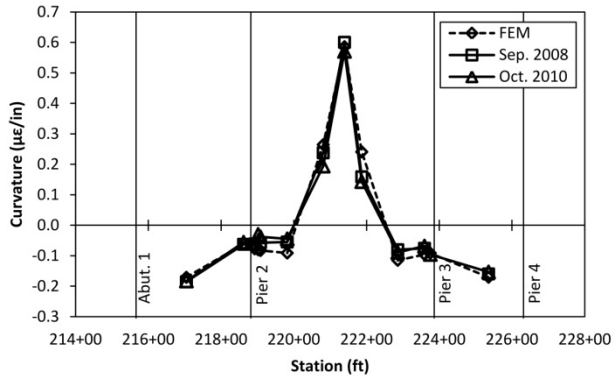

(e) STI7SB

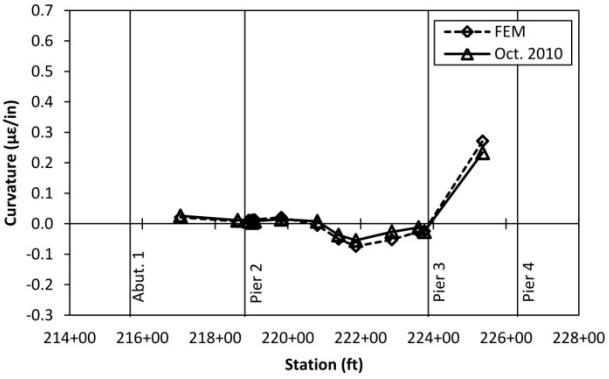

(f) STI9(-9)SB

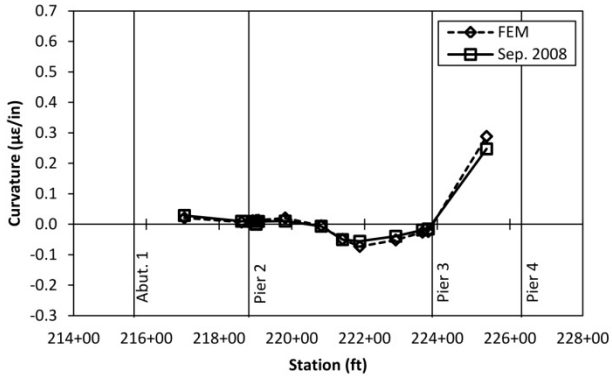

(g) STI9SB

Figure 6.36: Curvature comparisons for two-dimensional finite element model validation with measured truck test results.

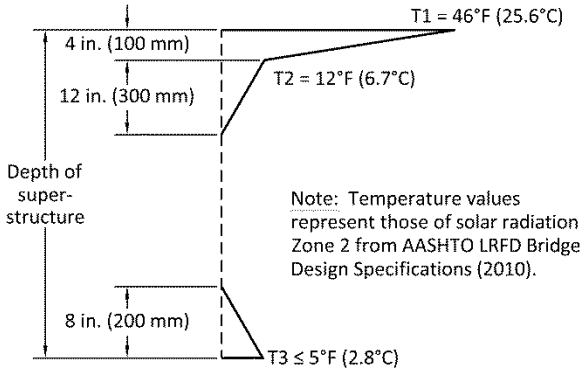

Figure 7.1: AASHTO LRFD Bridge Design Specifications (2010) design positive thermal gradient.

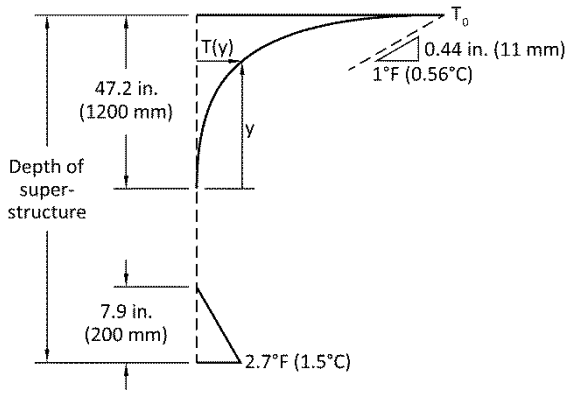

Figure 7.2: New Zealand Code design positive thermal gradient as presented in Priestley (1978).

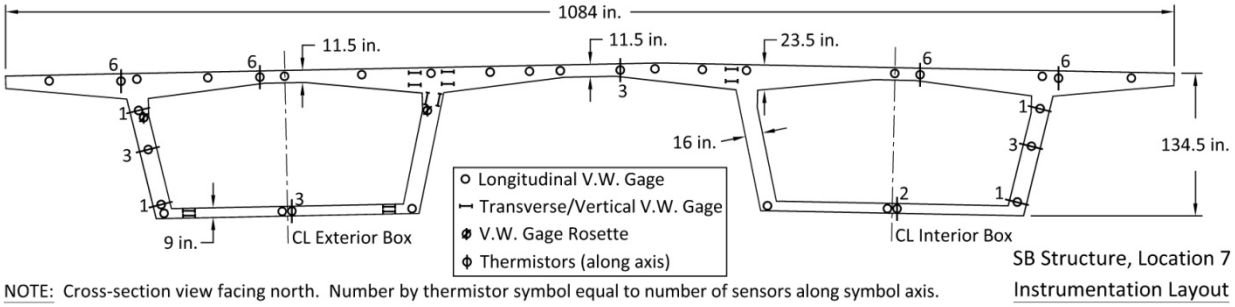

Figure 7.3: Characteristic section dimensions and instrumentation layout in southbound structure Location 7.

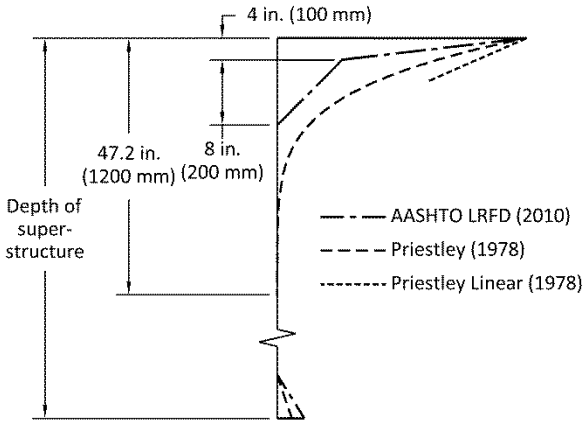

Figure 7.4: Comparison of AASHTO LRFD (2010) and New Zealand (Priestley, 1978) design gradients.

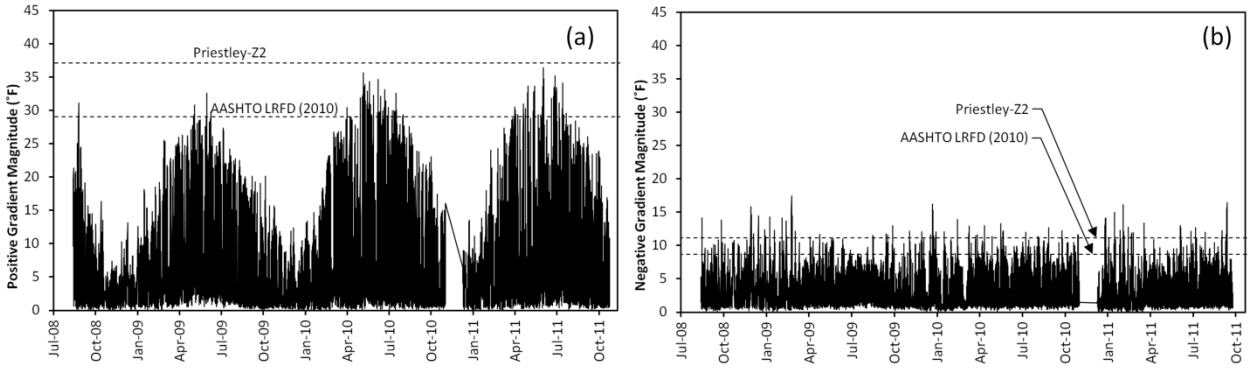

Figure 7.5: Measured (a) positive and (b) negative gradient magnitudes. Design gradient magnitudes considered at a depth of 2 in. (51 mm) below the deck surface for comparison against measured gradients.

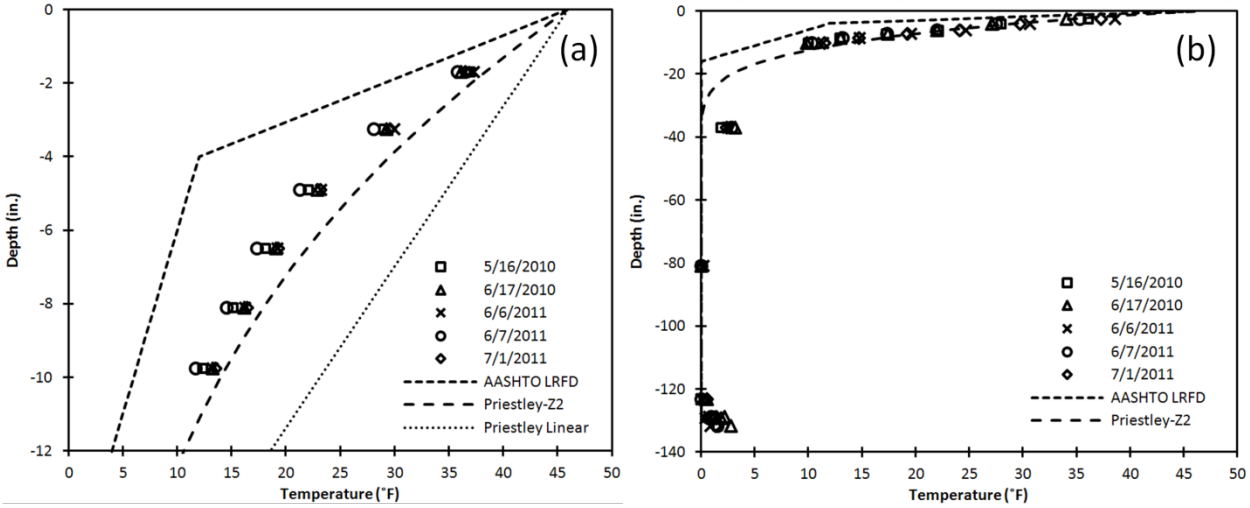

Figure 7.6: Maximum measured positive gradients at Location 7 compared to design gradients through (a) centerline of exterior box, top flange only, and (b) along centerline of west web of exterior box.

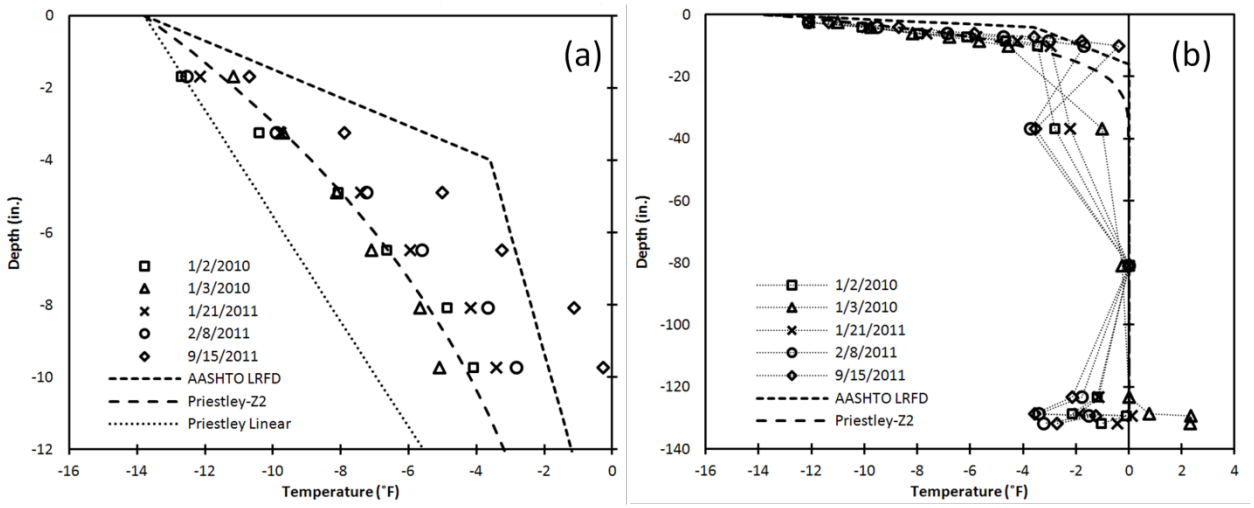

Figure 7.7: Maximum measured negative gradients at Location 7 compared to design gradients through (a) centerline of exterior box, top flange only, and (b) along centerline of west web of exterior box.

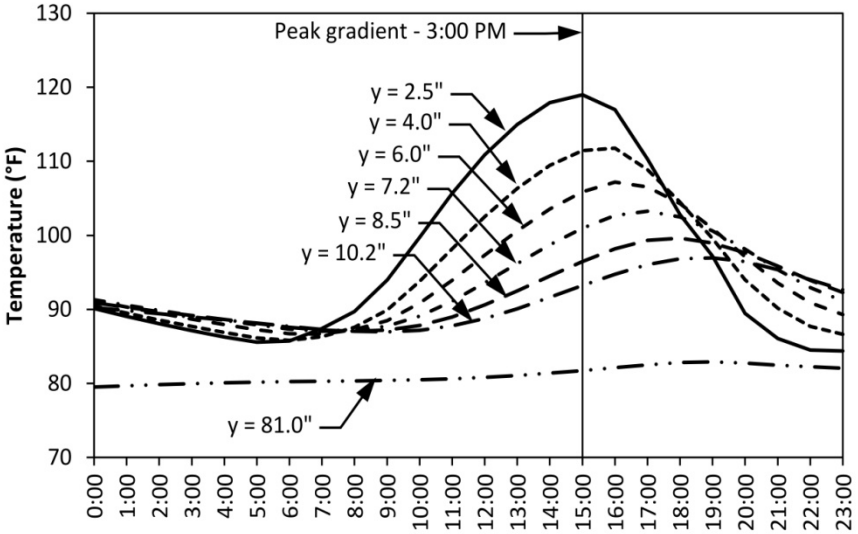

Figure 7.8: Development of temperatures over 24 hours during a maximum measured positive thermal gradient on July 1, 2011. Temperatures were measured along centerline of west web of exterior box at Location 7. Given *y*-values correspond to the nominal depth from the top surface of the deck.

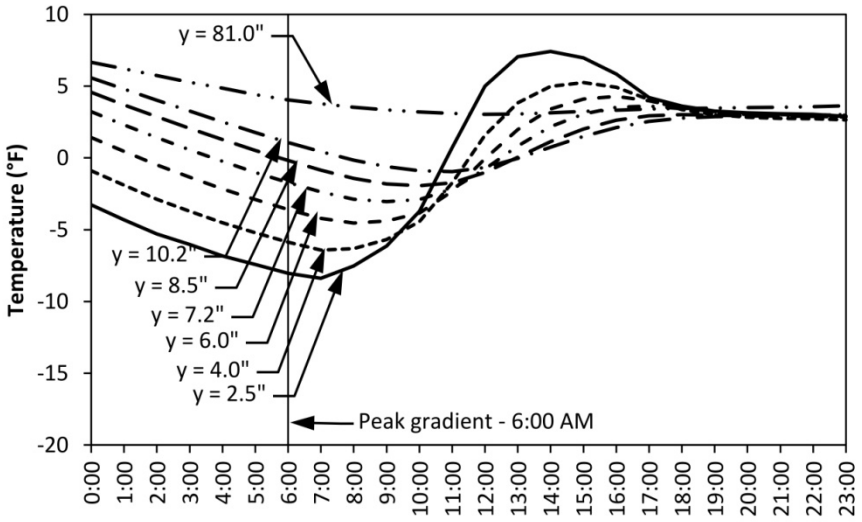

Figure 7.9: Development of temperatures over 24 hours during a maximum measured negative thermal gradient on January 21, 2011. Temperatures were measured along centerline of west web of exterior box at Location 7. Given *y*-values correspond to the nominal depth from the top surface of the deck.

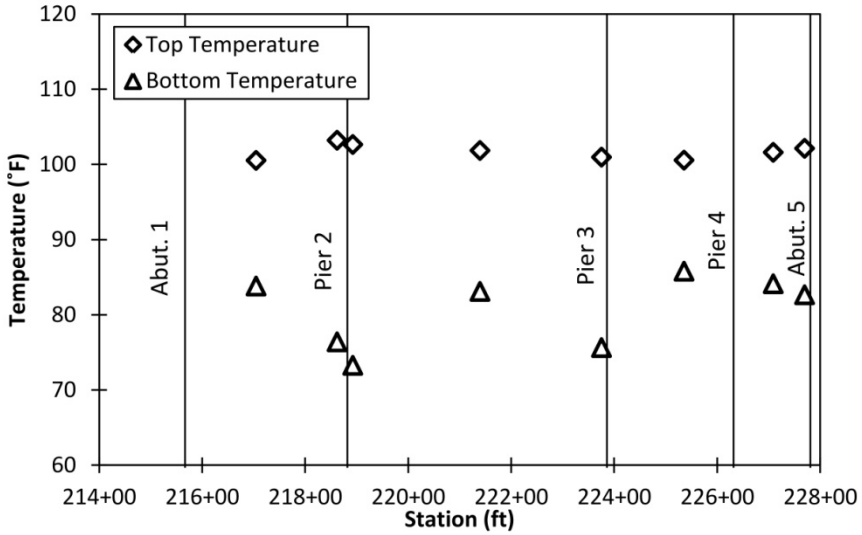

Figure 7.10: Measured temperatures in top and bottom flanges along the length of the southbound superstructure from maximum measured positive gradient on July 1, 2011 at 3:00 PM.

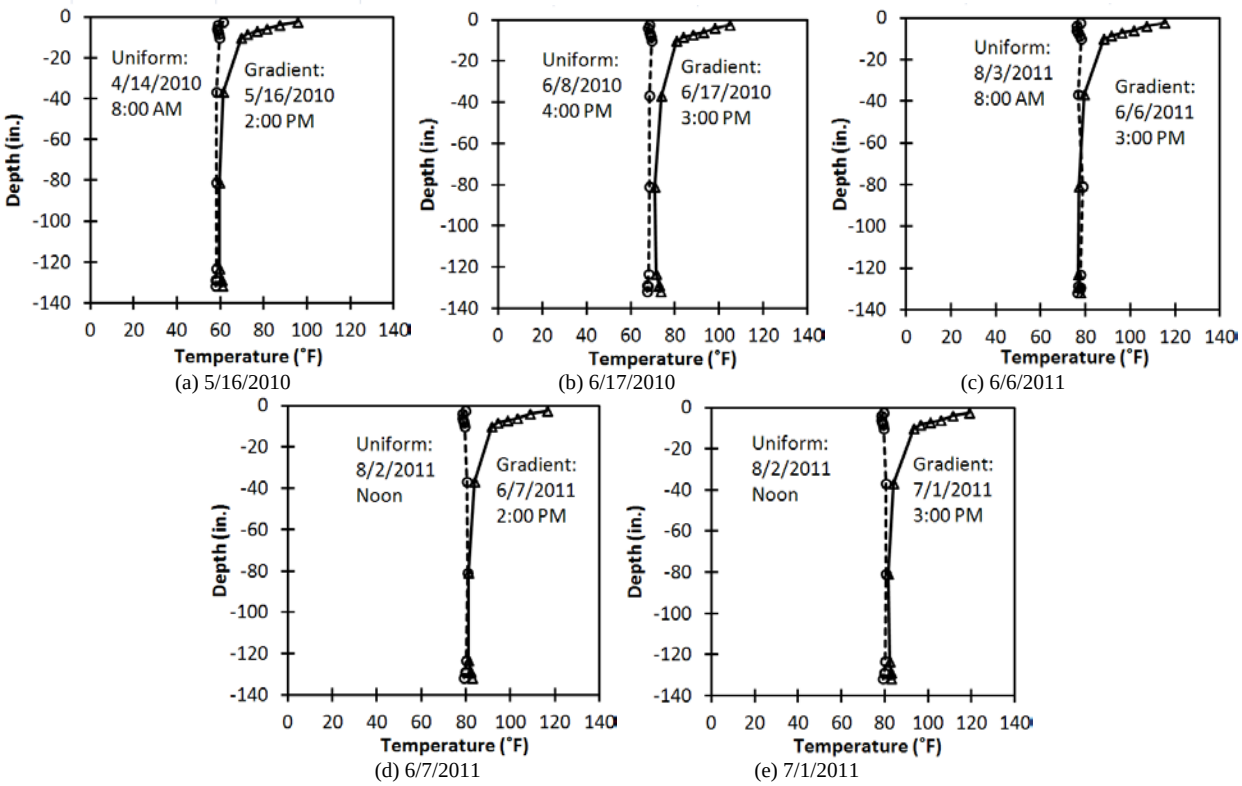

(a) 5/16/2010 (b) 6/17/2010 (c) 6/6/2011

(d) 6/7/2011 (e) 7/1/2011

Figure 7.11: Temperature profiles through the depth of the west web of the exterior box at Location 7 in the southbound structure both at the time of the maximum measured positive gradient and during the associated initial (uniform temperature) strain reading.

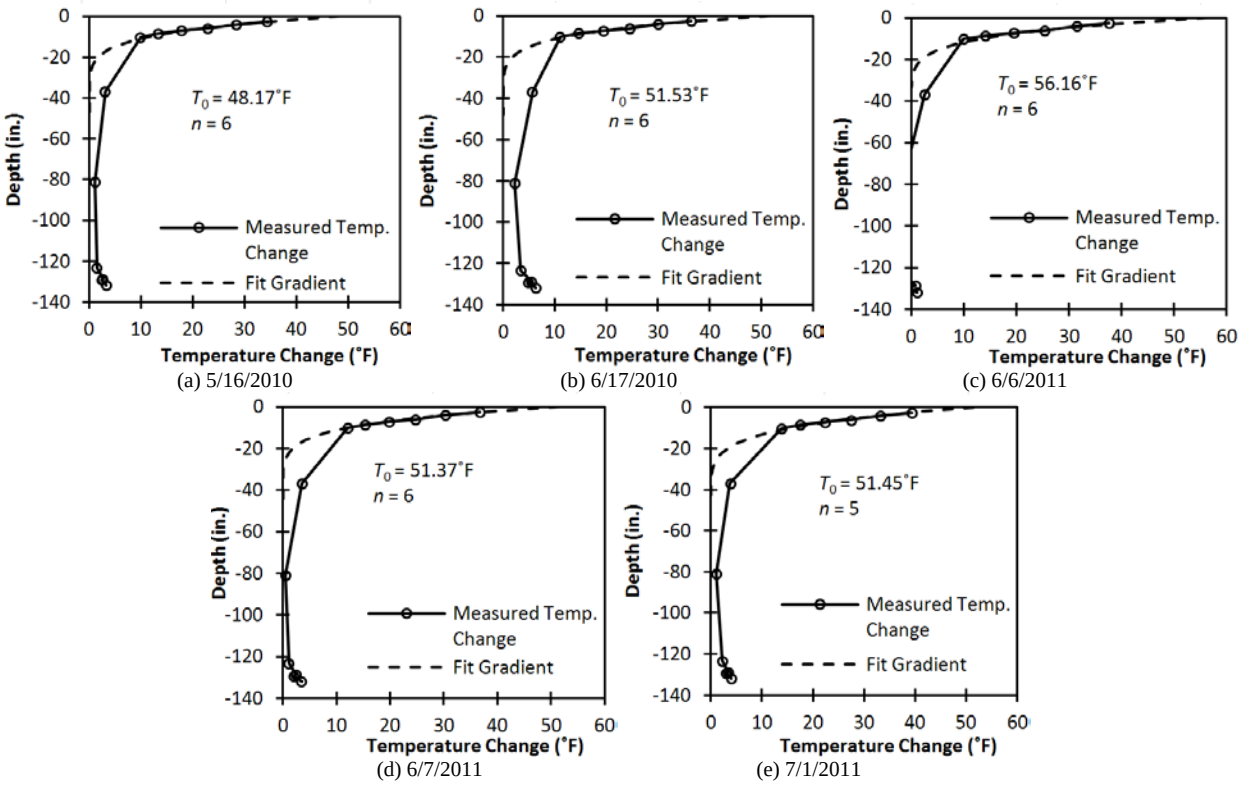

Figure 7.12: Change in temperature profiles through the depth of the west web of the exterior box at Location 7 in the southbound structure between time of the maximum measured positive gradient and time of initial (uniform temperature) strain reading compared to fitted baseline gradients using to Eqn. (7-2).

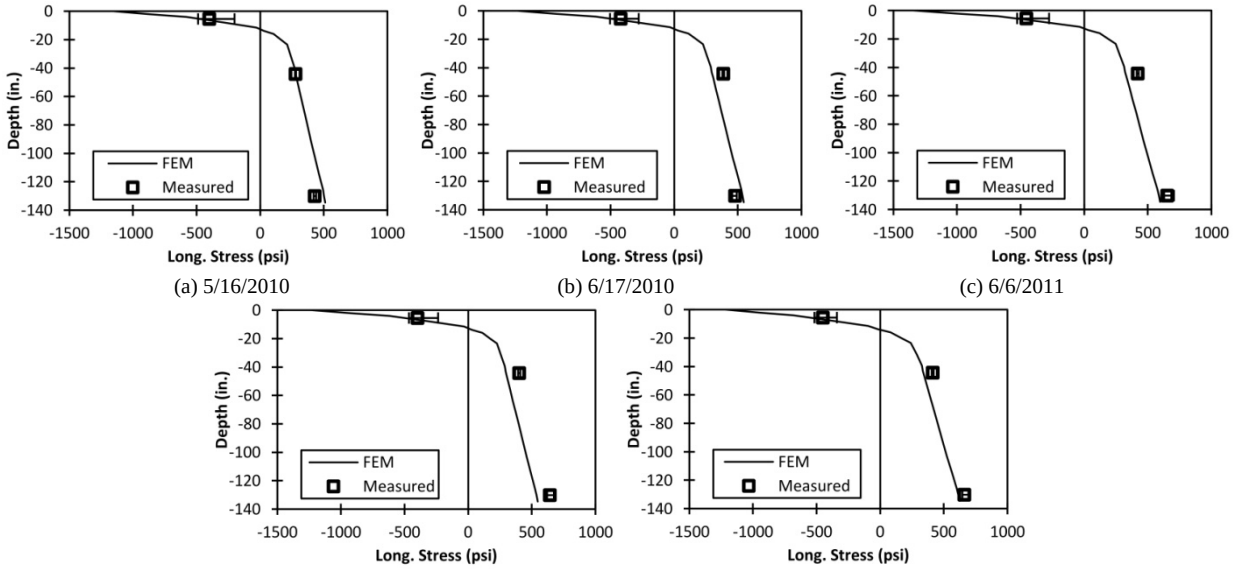

(a) 5/16/2010 (b) 6/17/2010 (c) 6/6/2011

(d) 6/7/2011 (e) 7/1/2011

Figure 7.13: Comparison of changes in longitudinal stresses approximated from measured strains (averaged at each depth, errors bars depict measured range at each depth) at southbound Location 7 caused by five maximum measured positive thermal gradients to stresses computed from finite element model using baseline fitted thermal gradients (no adjustment to top 2 in. (51 mm) of gradient).

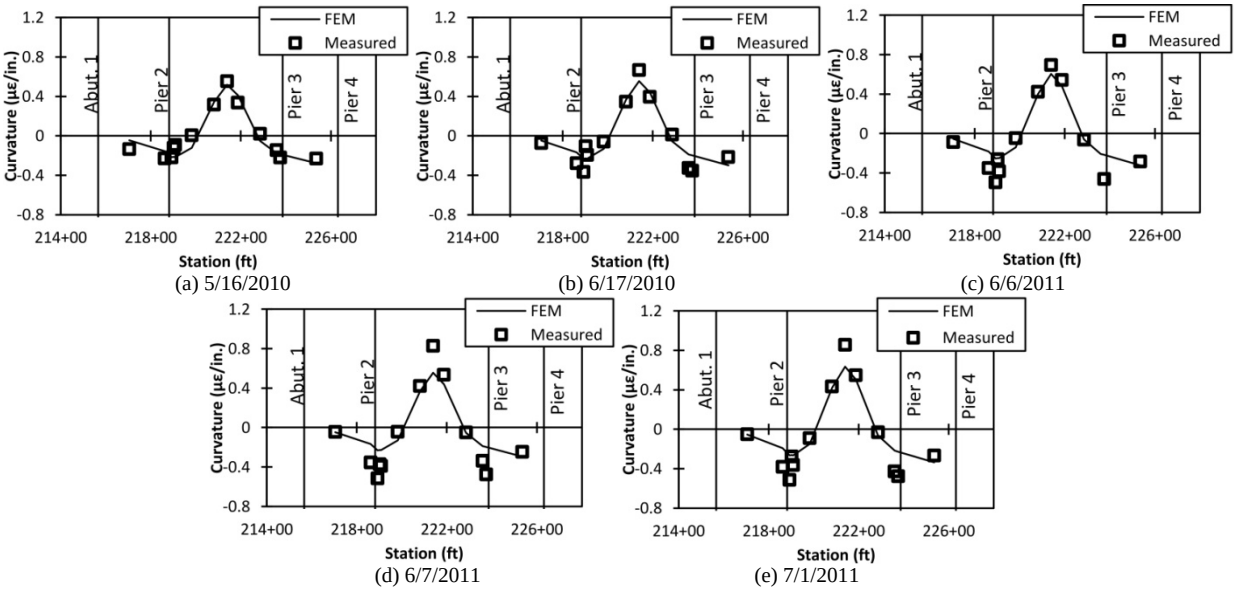

(a) 5/16/2010 (b) 6/17/2010 (c) 6/6/2011

(d) 6/7/2011 (e) 7/1/2011

Figure 7.14: Comparison of changes in longitudinal curvature along southbound bridge caused by five maximum measured positive thermal gradients to curvatures computed from finite element model using baseline fitted thermal gradients (no adjustment to top 2 in. (51 mm) of gradient).

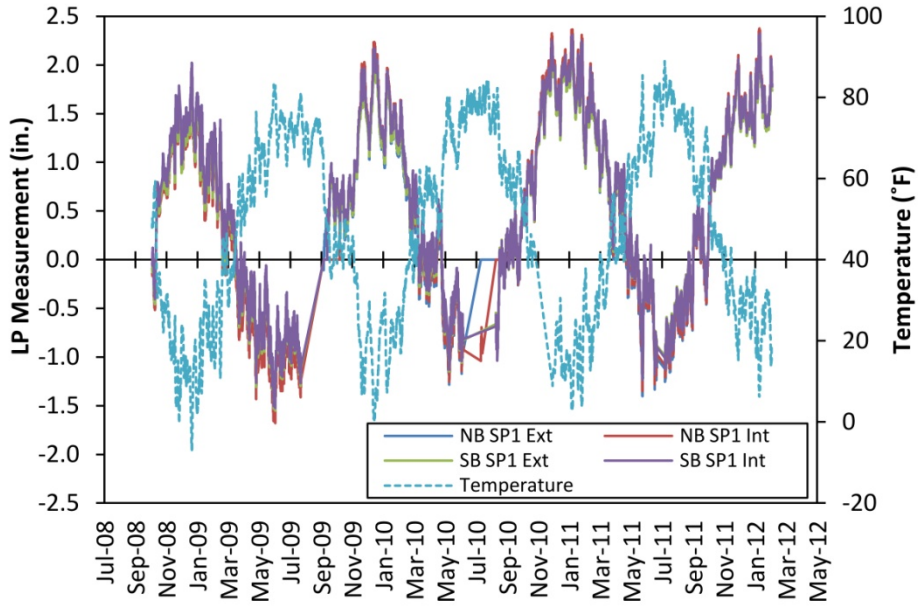

Figure 7.15: Linear potentiometer data for Span 1 attached to Abutment 1 from October 31, 2008 until February 12, 2012.

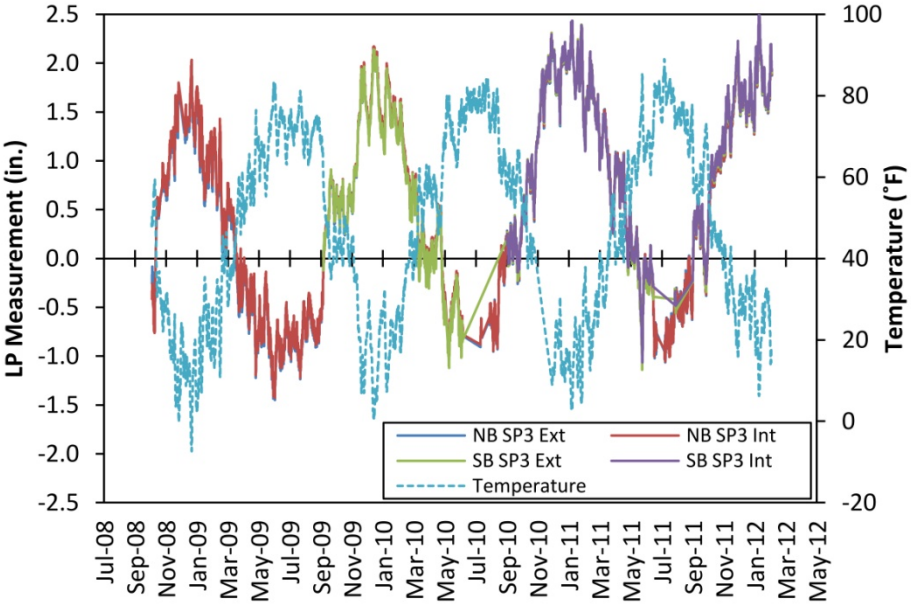

Figure 7.16: Linear potentiometer data for Span 3 attached to Pier 4 from October 31, 2008 until February 12, 2012.

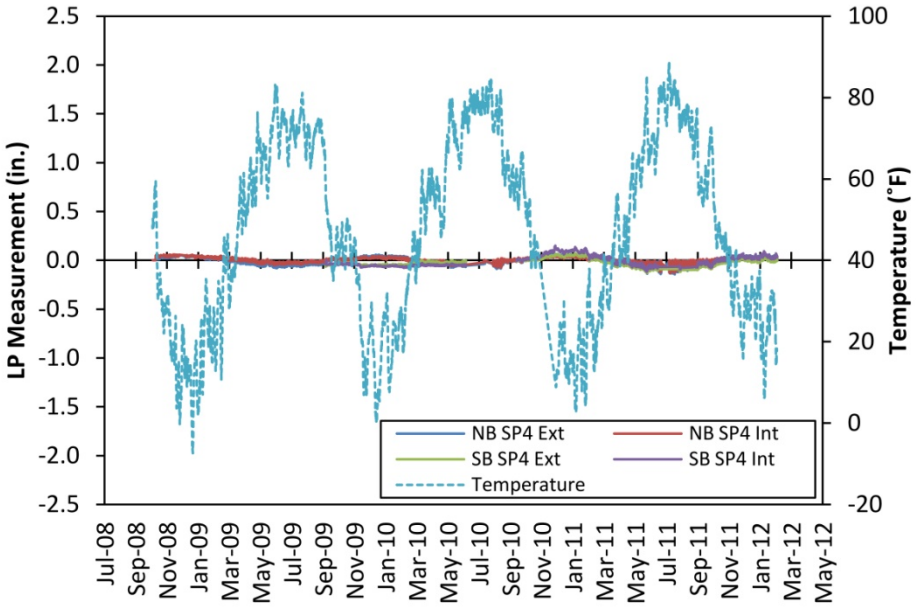

Figure 7.17: Linear potentiometer data for Span 4 attached to Pier 4 from October 31, 2008 until February 12, 2012.

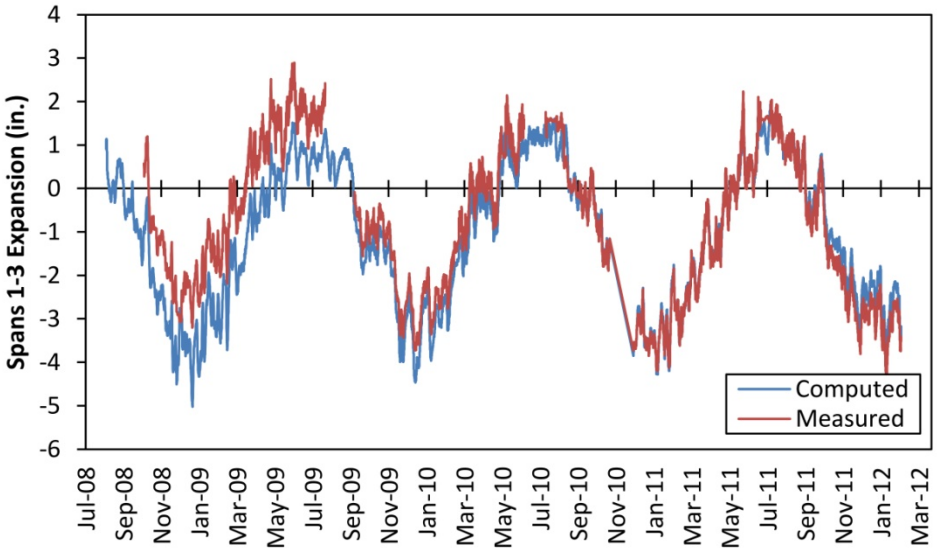

Figure 7.18: Approximations of the total elongation of Spans 1 through 3 of the northbound bridge. "Computed" represents the elongation computed from measured temperatures and assuming only longitudinal elongation (no time-dependence or thermal gradients). "Measured" represents the LP measurements at the ends of Spans 1 and 3, minus the assumed elongation of Span 4.

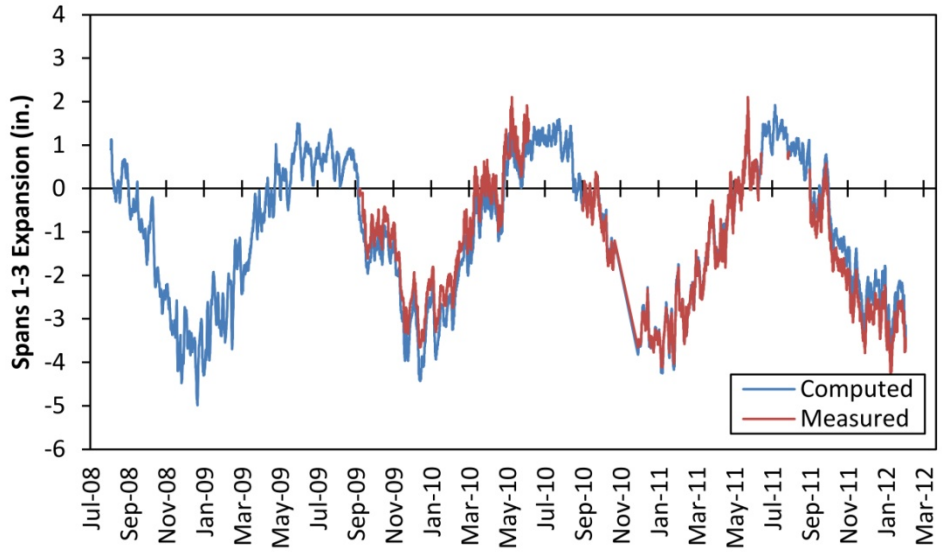

Figure 7.19: Approximations of the total elongation of Spans 1 through 3 of the southbound bridge. "Computed" represents the elongation computed from measured temperatures and assuming only longitudinal elongation (no time-dependence or thermal gradients). "Measured" represents the LP measurements at the ends of Spans 1 and 3, minus the assumed elongation of Span 4.

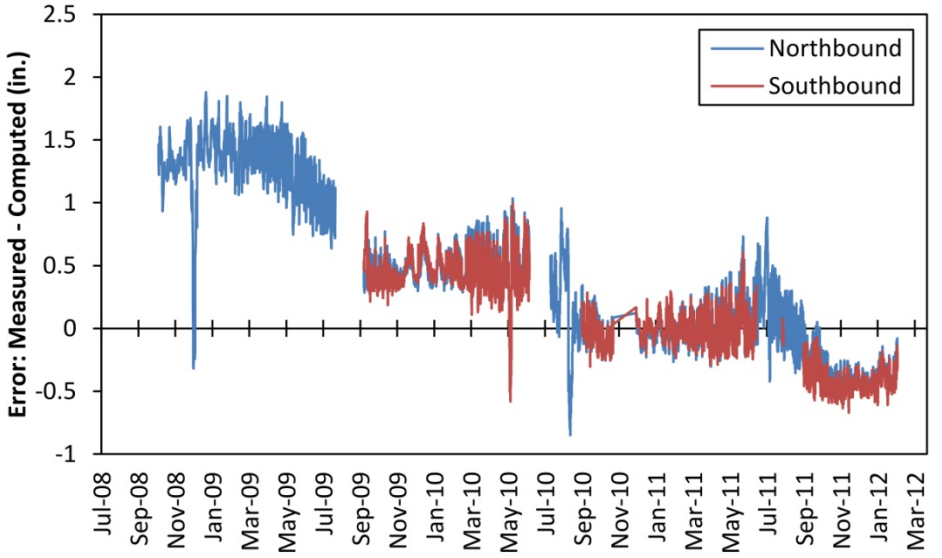

Figure 7.20: Difference between "Measured" and "Computed" estimates for the total elongation of the northbound and southbound bridges.

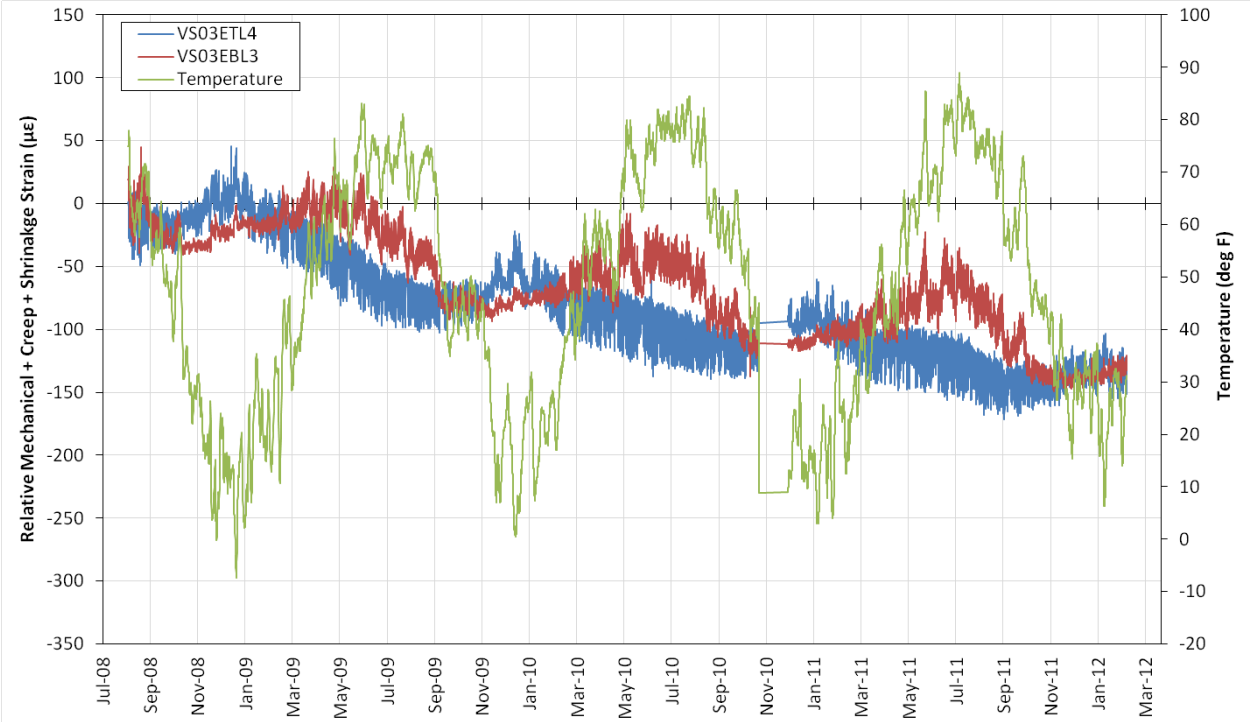

Figure 7.21: Relative mechanical strain plus creep and shrinkage strains for gages VS03ETL4 (blue; top flange at southbound Location 3) and VS03EBL3 (red; bottom flange at southbound Location 3).

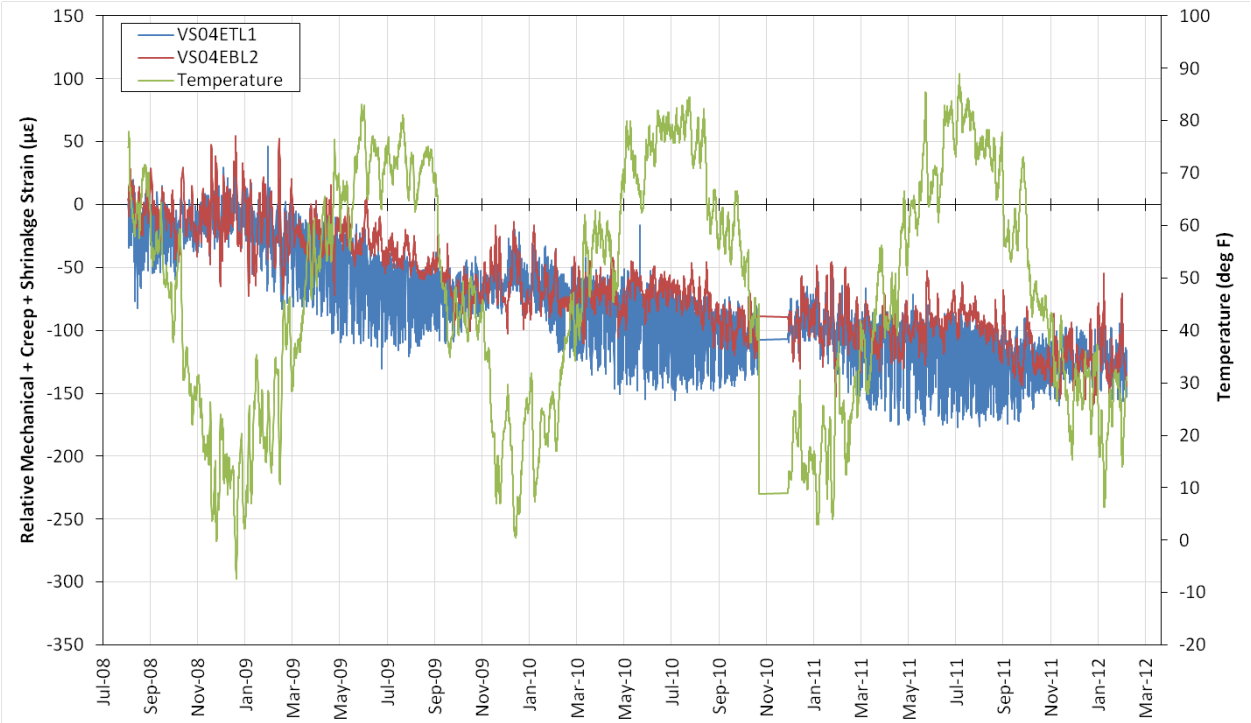

Figure 7.22: Relative mechanical strain plus creep and shrinkage strains for gages VS04ETL1 (blue; top flange at southbound Location 4) and VS04EBL2 (red; bottom flange at southbound Location 4).

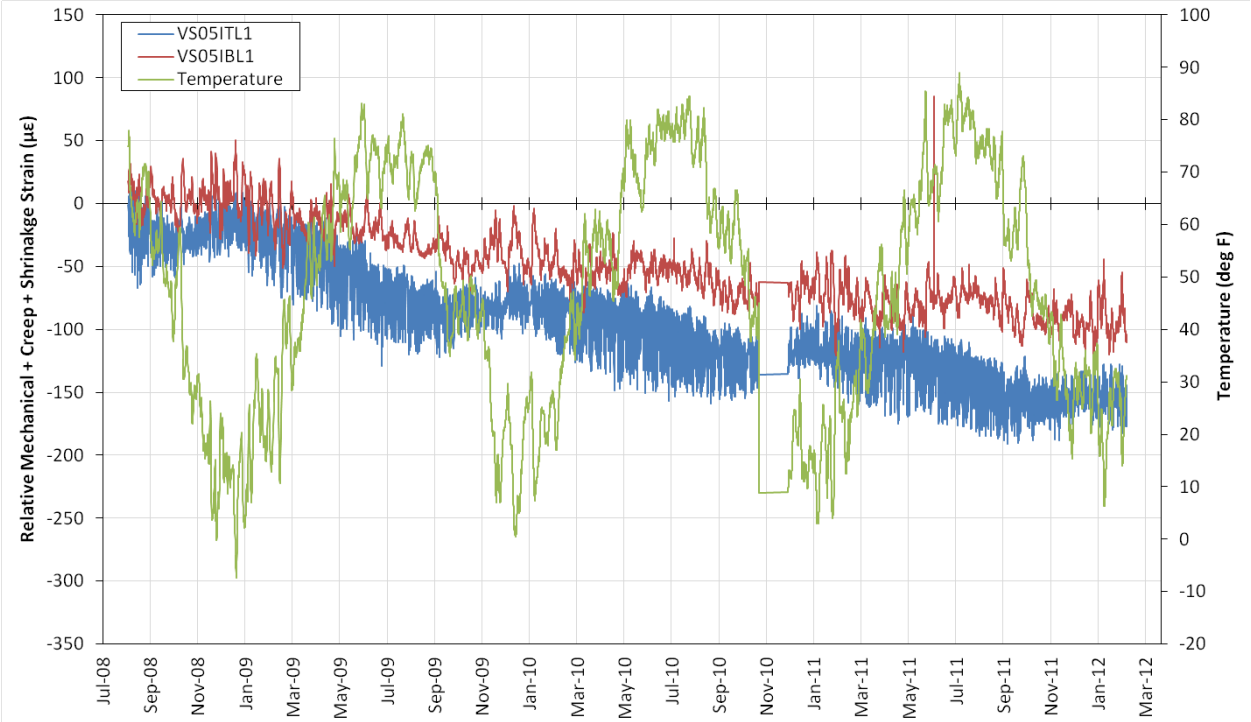

Figure 7.23: Relative mechanical strain plus creep and shrinkage strains for gages VS05ITL1 (blue; top flange at southbound Location 5) and VS05IBL1 (red; bottom flange at southbound Location 5).

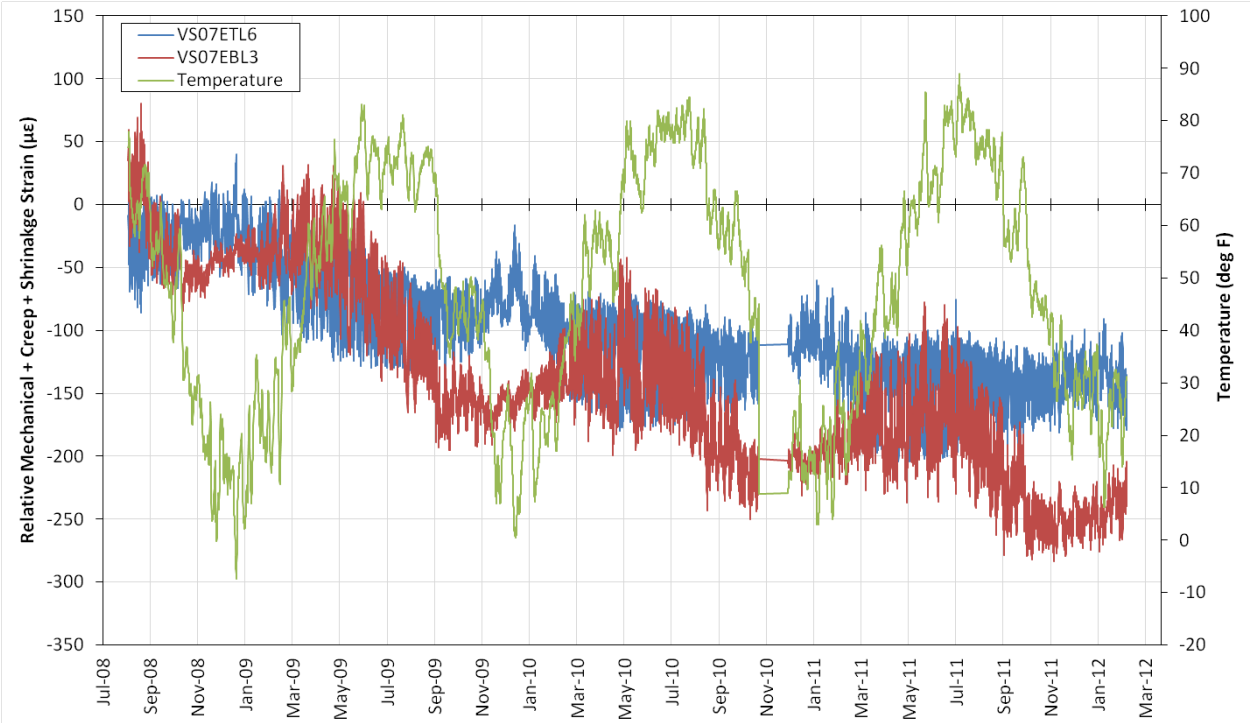

Figure 7.24: Relative mechanical strain plus creep and shrinkage strains for gages VS07ETL6 (blue; top flange at southbound Location 7) and VS07EBL3 (red; bottom flange at southbound Location 7).

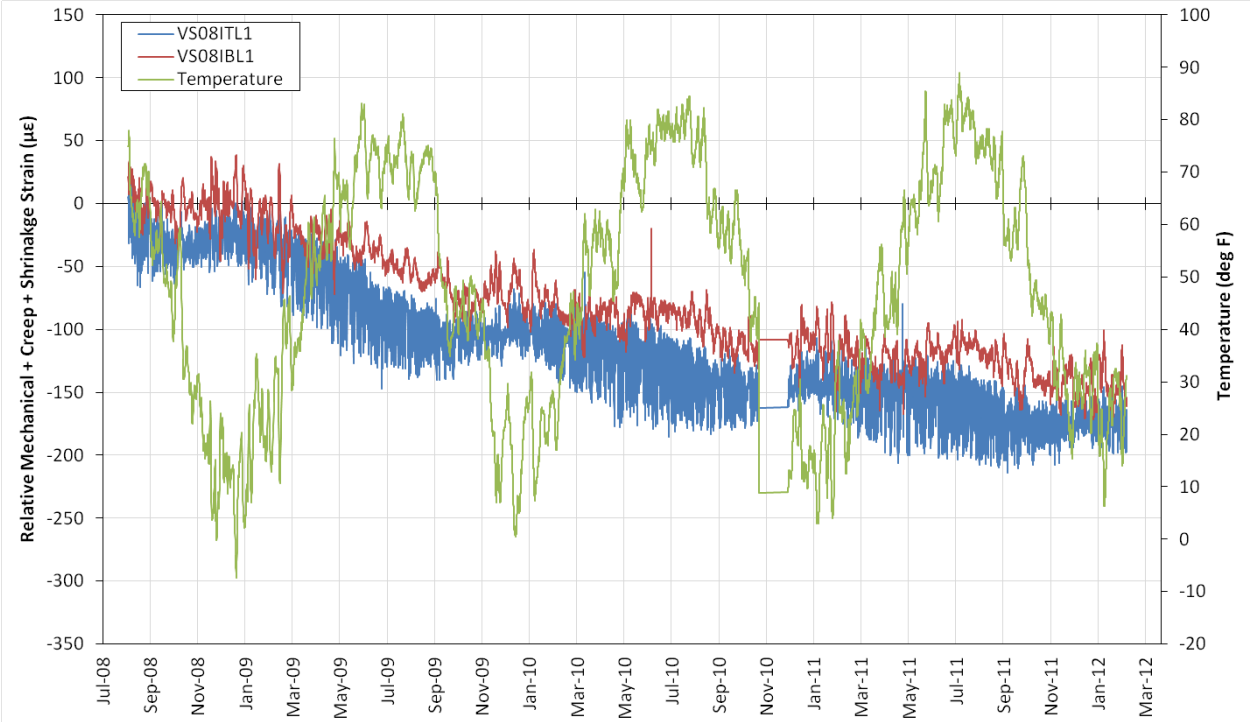

Figure 7.25: Relative mechanical strain plus creep and shrinkage strains for gages VS08ITL1 (blue; top flange at southbound Location 8) and VS08IBL1 (red; bottom flange at southbound Location 8).

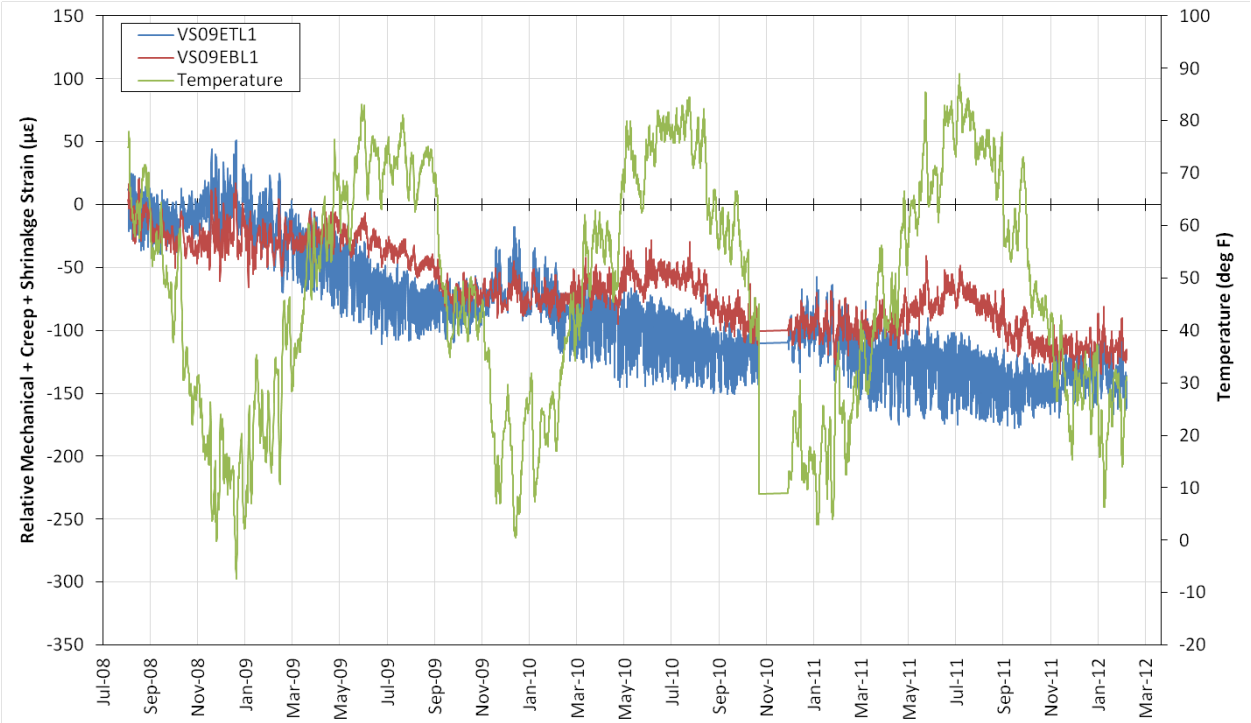

Figure 7.26: Relative mechanical strain plus creep and shrinkage strains for gages VS09ETL1 (blue; top flange at southbound Location 9) and VS09EBL1 (red; bottom flange at southbound Location 9).

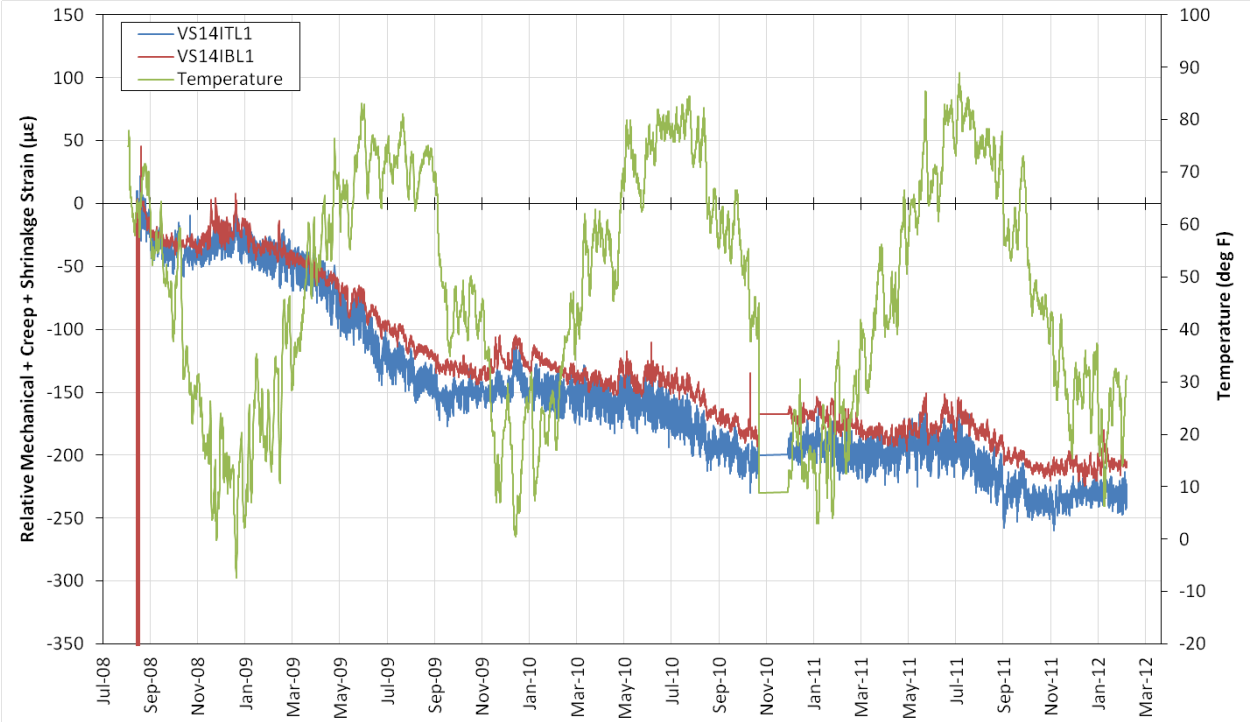

Figure 7.27: Relative mechanical strain plus creep and shrinkage strains for gages VS14ITL1 (blue; top flange at southbound Location 14) and VS14IBL1 (red; bottom flange at southbound Location 14).

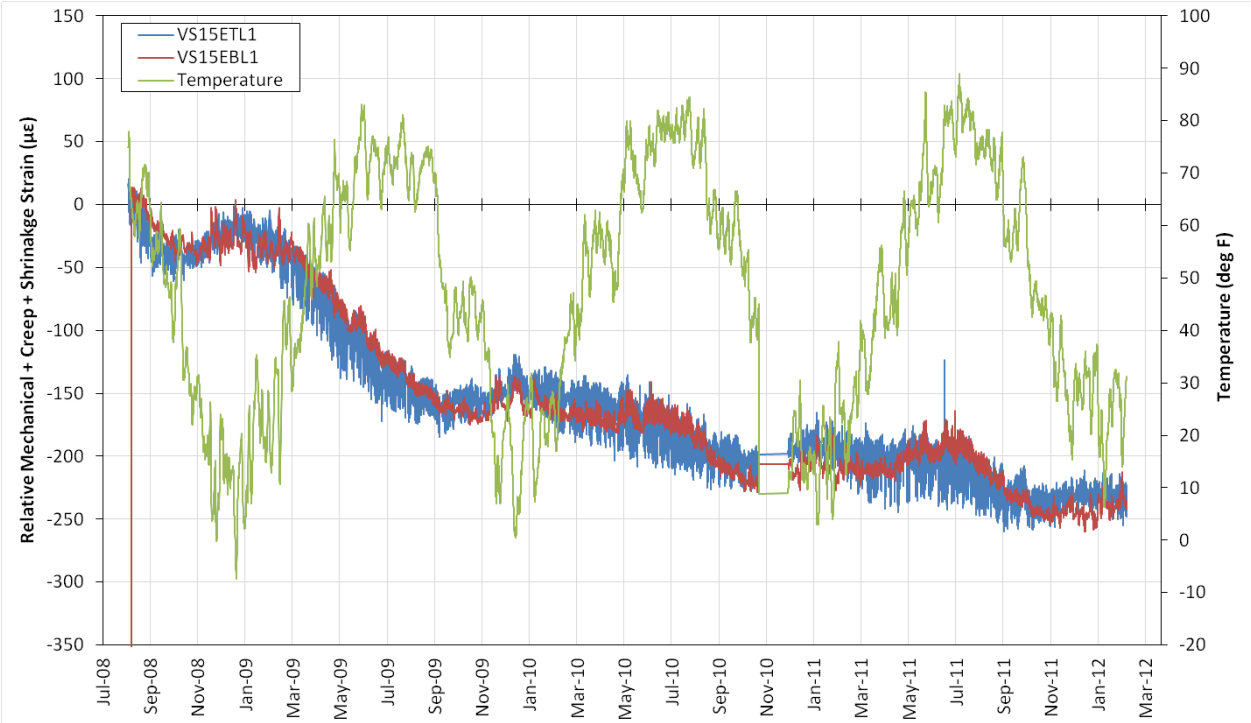

Figure 7.28: Relative mechanical strain plus creep and shrinkage strains for gages VS15ETL1 (blue; top flange at southbound Location 15) and VS15EBL1 (red; bottom flange at southbound Location 15).

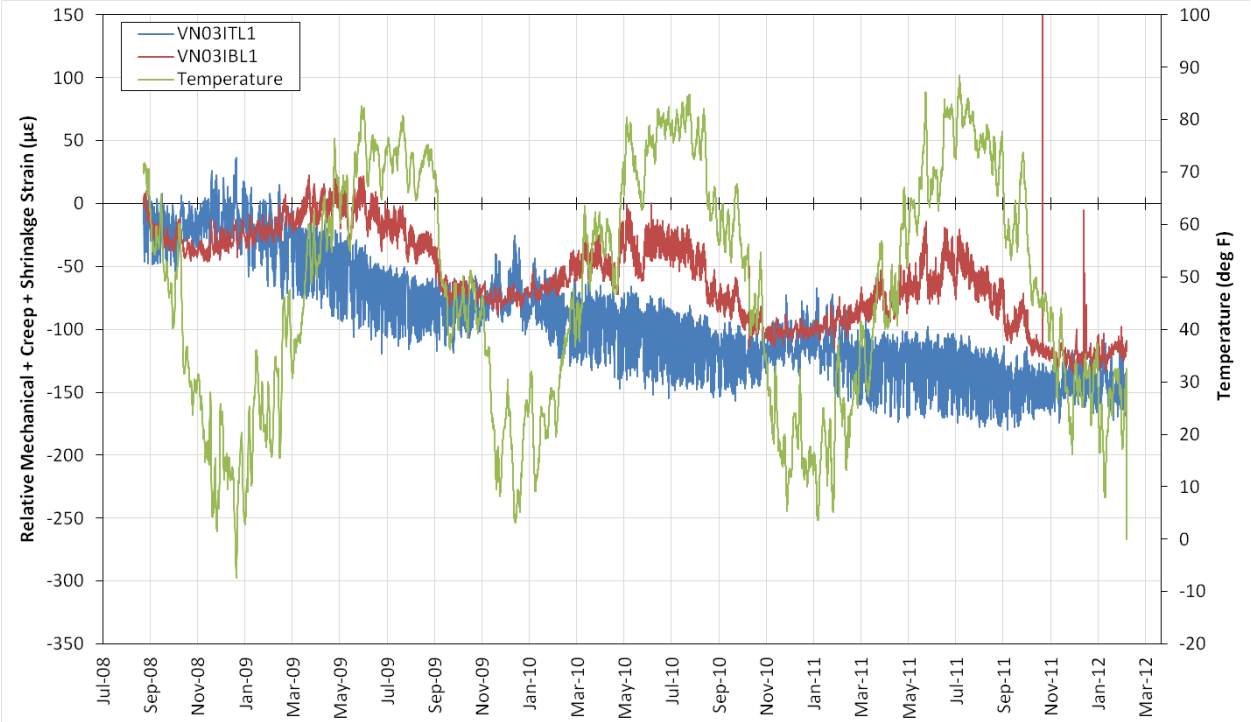

Figure 7.29: Relative mechanical strain plus creep and shrinkage strains for gages VN03ITL1 (blue; top flange at northbound Location 3) and VN03IBL1 (red; bottom flange at northbound Location 3).

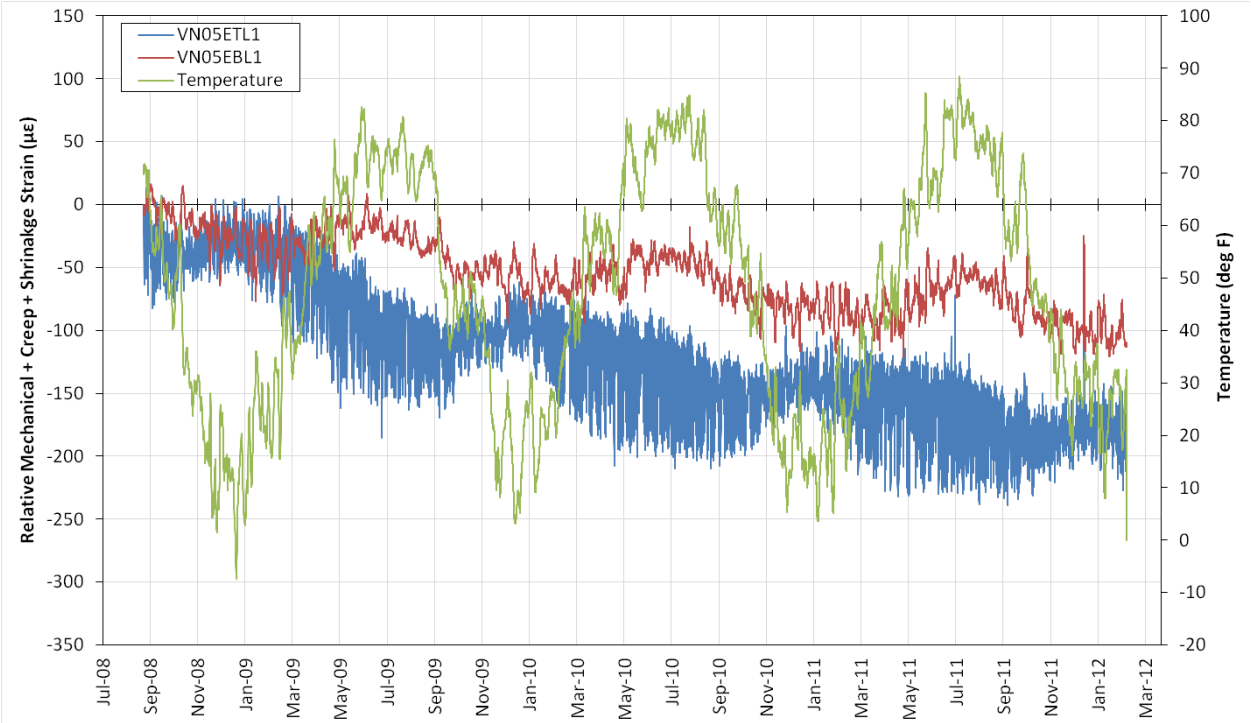

Figure 7.30: Relative mechanical strain plus creep and shrinkage strains for gages VN05ETL1 (blue; top flange at northbound Location 5) and VN05EBL1 (red; bottom flange at northbound Location 5).

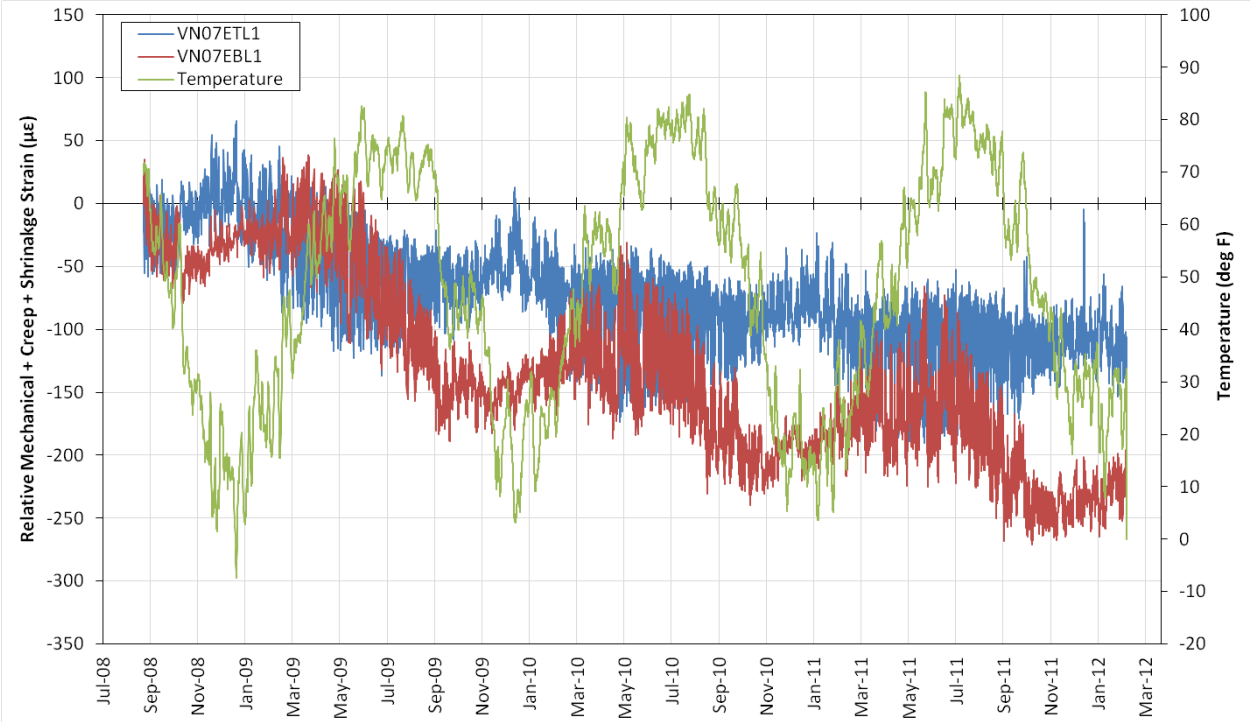

Figure 7.31: Relative mechanical strain plus creep and shrinkage strains for gages VN07ETL1 (blue; top flange at northbound Location 7) and VN07EBL1 (red; bottom flange at northbound Location 7).

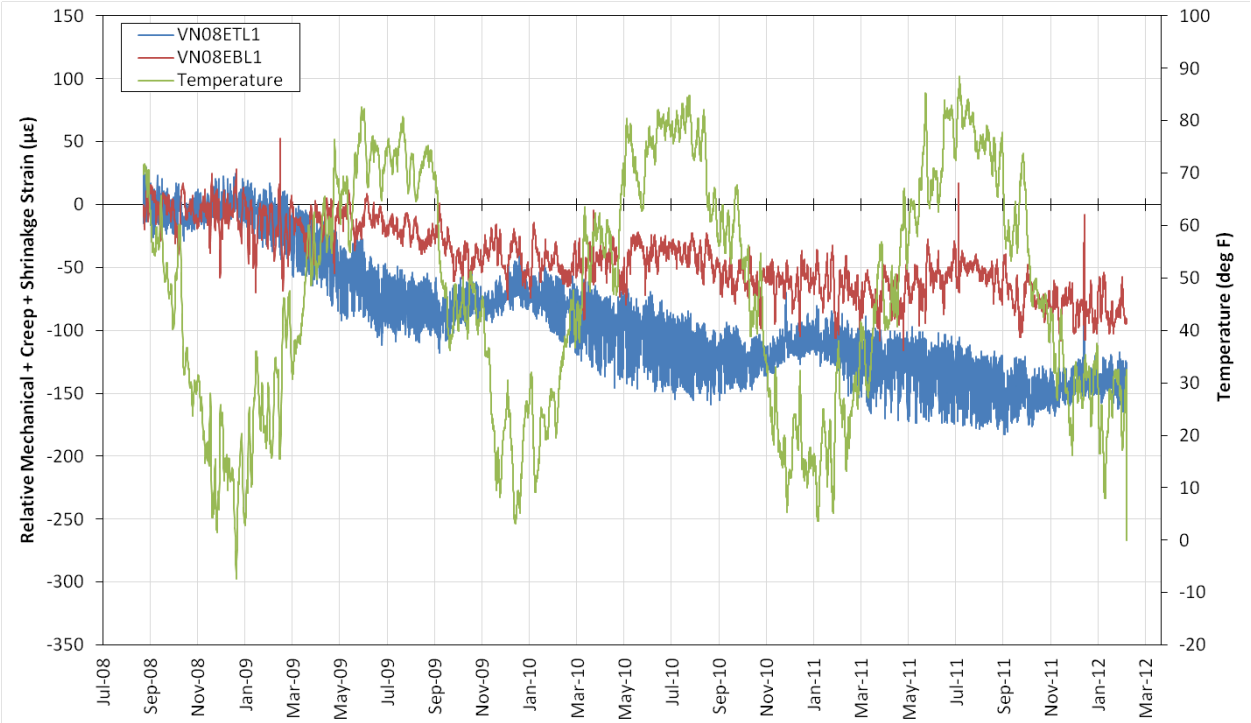

Figure 7.32: Relative mechanical strain plus creep and shrinkage strains for gages VN08ETL1 (blue; top flange at northbound Location 8) and VN08EBL1 (red; bottom flange at northbound Location 8).

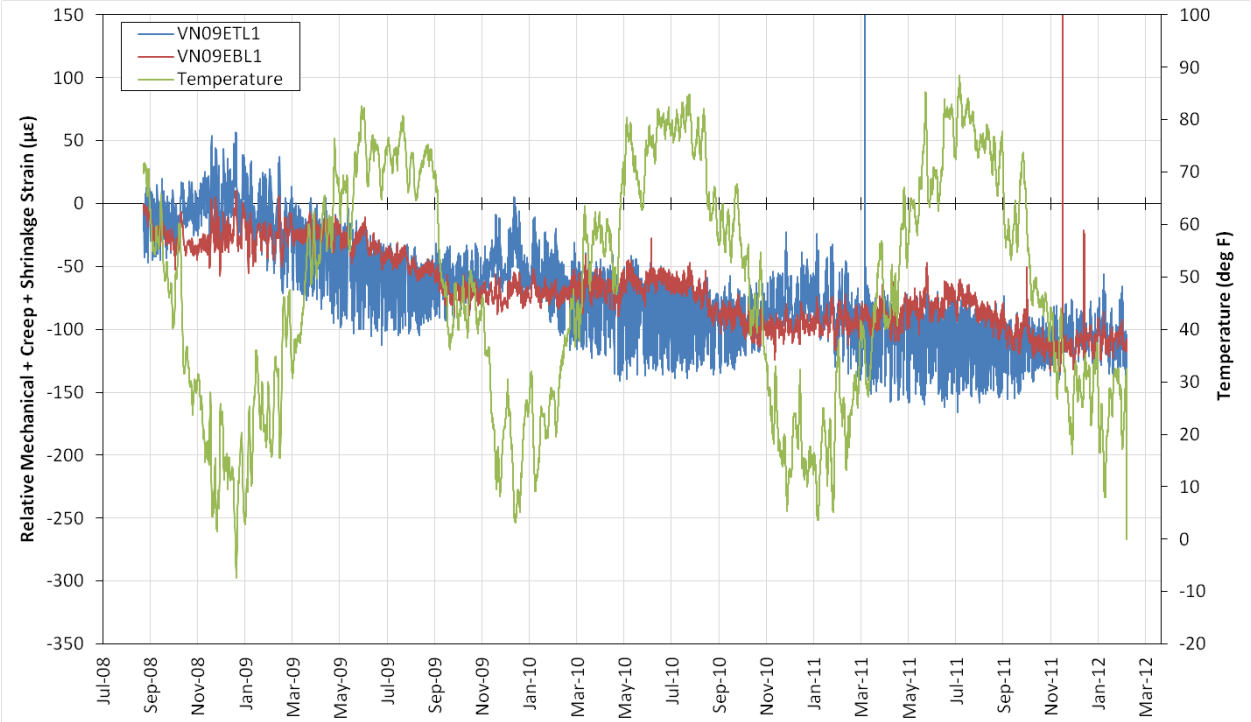

Figure 7.33: Relative mechanical strain plus creep and shrinkage strains for gages VN09ETL1 (blue; top flange at northbound Location 9) and VN09EBL1 (red; bottom flange at northbound Location 9).

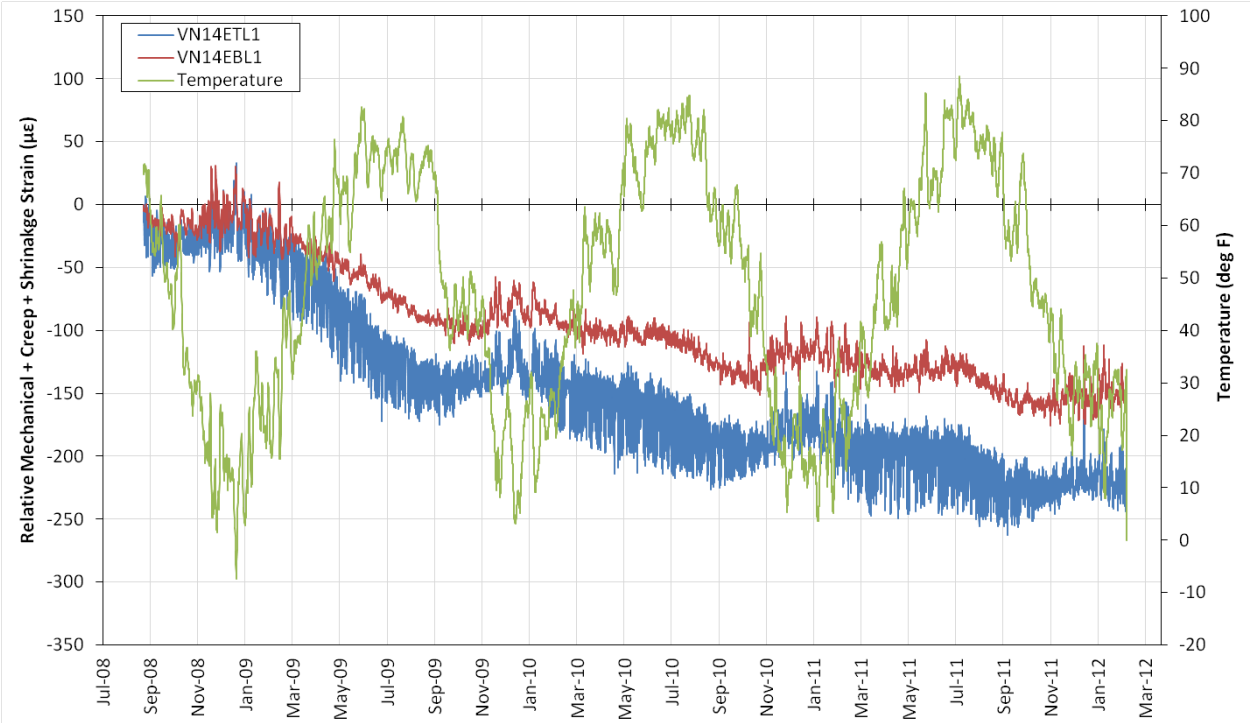

Figure 7.34: Relative mechanical strain plus creep and shrinkage strains for gages VN14ETL1 (blue; top flange at northbound Location 14) and VN14EBL1 (red; bottom flange at northbound Location 14).

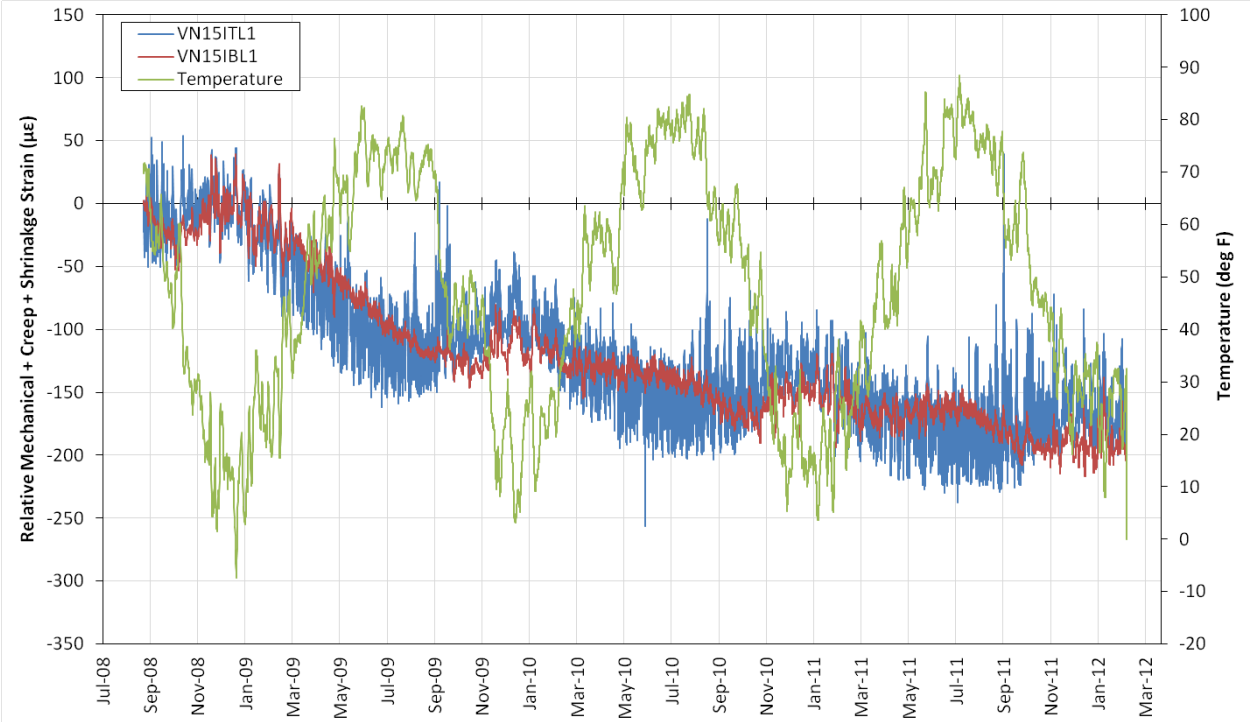

Figure 7.35: Relative mechanical strain plus creep and shrinkage strains for gages VN15ITL1 (blue; top flange at northbound Location 15) and VN15IBL1 (red; bottom flange at northbound Location 15).

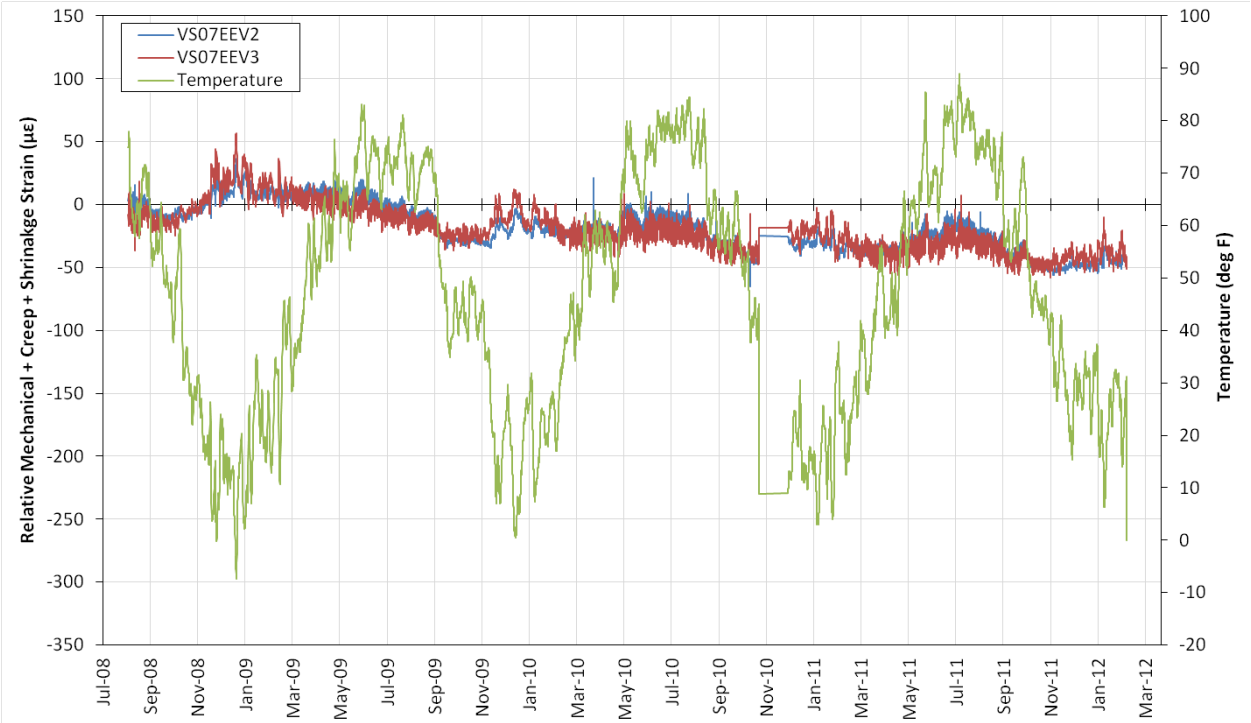

Figure 7.36: Relative mechanical strain plus creep and shrinkage strains for gages VS07EEV2 (blue; vertical gage at interior face of east web of exterior box, southbound Location 7) and VS07EEV3 (red; vertical gage at exterior face of east web of exterior box, southbound Location 7).

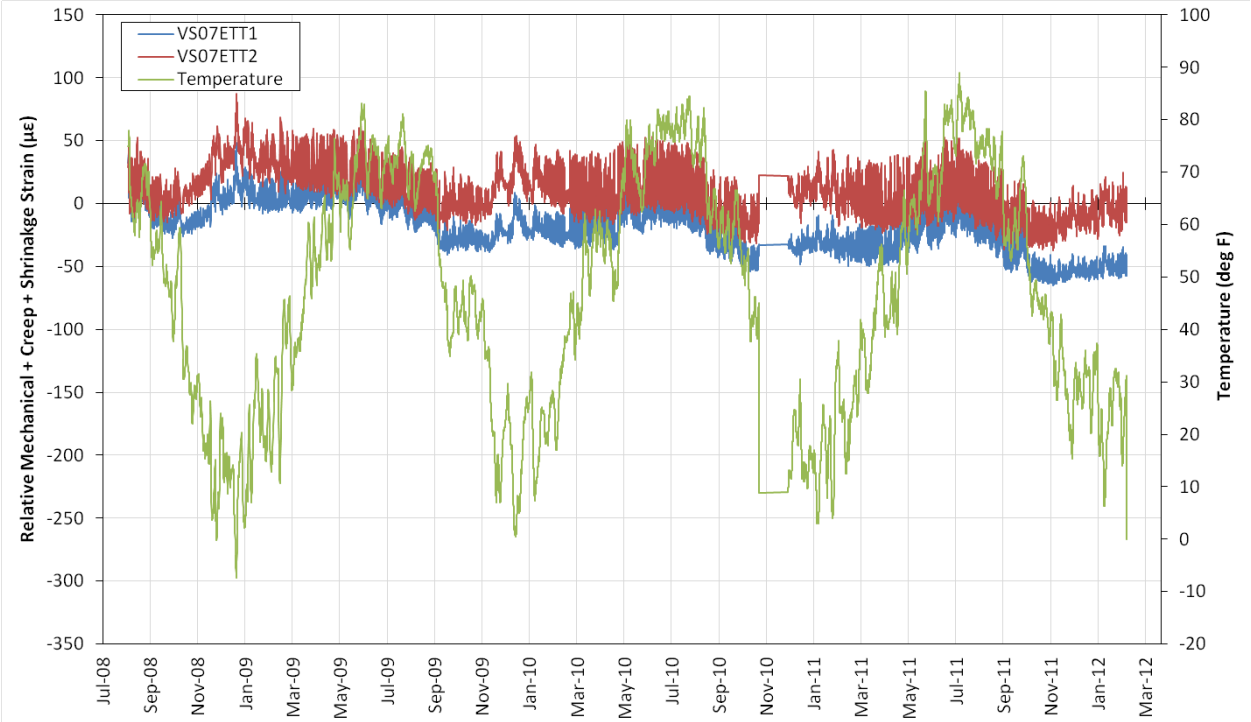

Figure 7.37: Relative mechanical strain plus creep and shrinkage strains for gages VS07ETT1 (blue; top transverse gage in top flange of southbound Location 7) and VS07ETT2 (red; bottom transverse gage in top flange of southbound Location 7).

Figure 7.38: Relative mechanical strain plus creep and shrinkage strains for gages VS07EBT1 (blue; top transverse gage in bottom flange of southbound Location 7) and VS07EBT2 (red; bottom transverse gage in bottom flange of southbound Location 7).

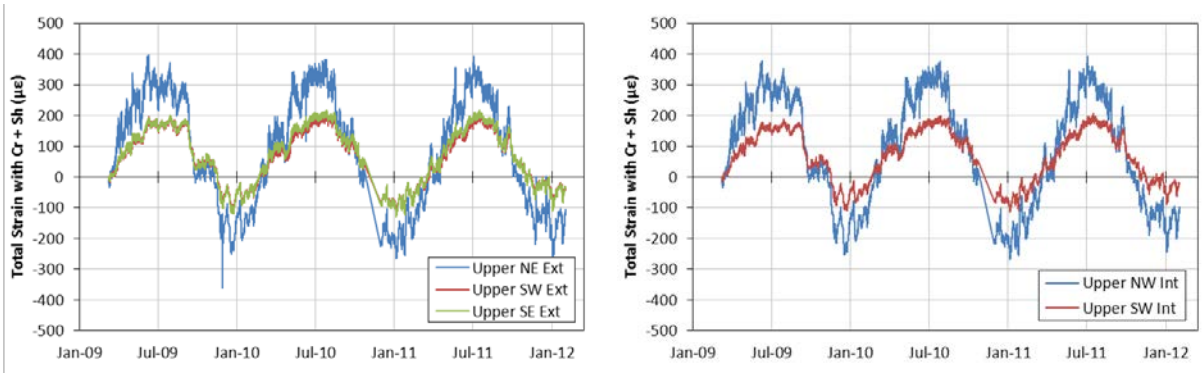

(a) Exterior (west) Pier (b) Interior (east) Pier

Figure 7.39: Relative total strain plus creep and shrinkage strains measured at midheights of interior and exterior columns of Southbound Pier 2.

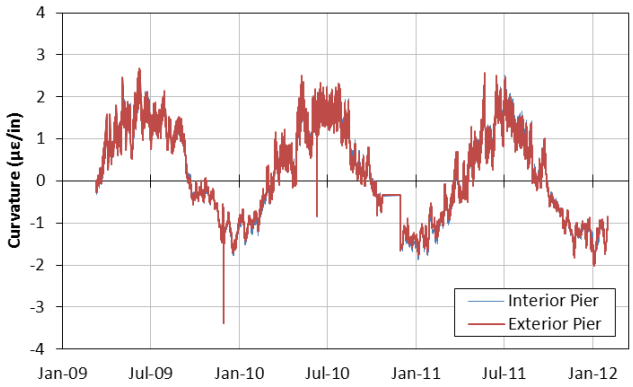

Figure 7.40: Relative curvatures measured at midheights of interior and exterior columns of Southbound Pier 2.

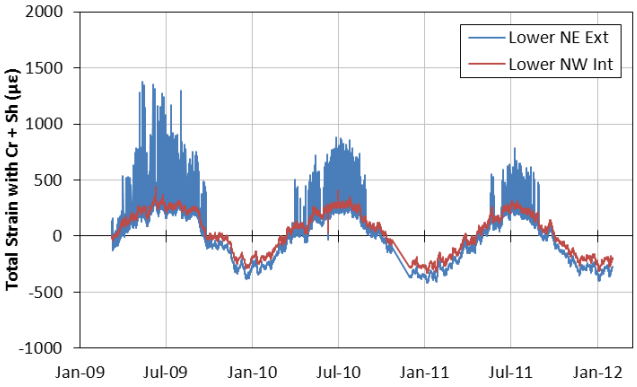

Figure 7.41: Relative total strain plus creep and shrinkage strains measured from UMN gages below midheight of interior and exterior columns of Southbound Pier 2.

Mode Number	Southbound	Northbound
Mode 1 – Bending	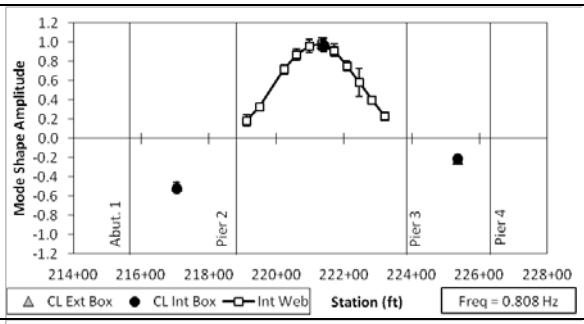	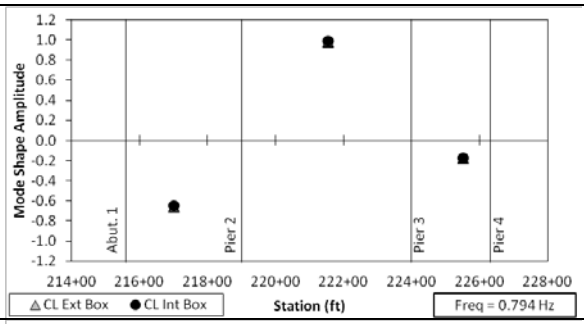
Mode 2 – Bending	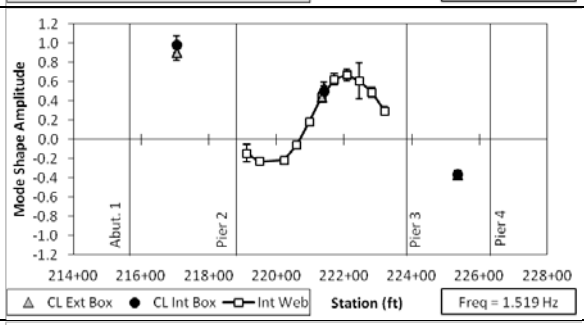	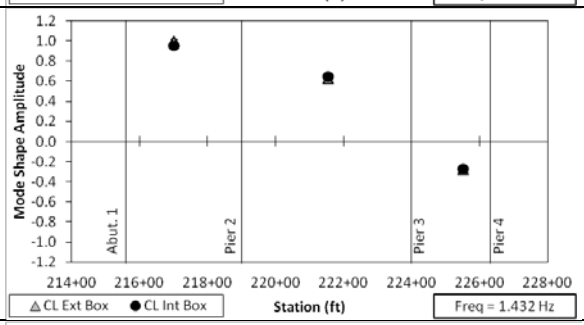
Mode 3 – Bending	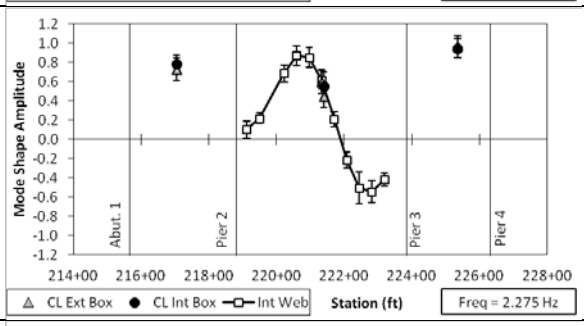	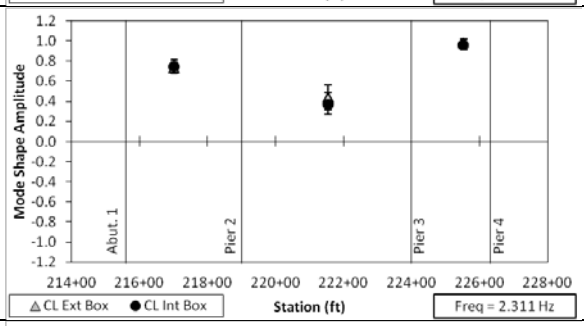
Mode 4 – Torsion	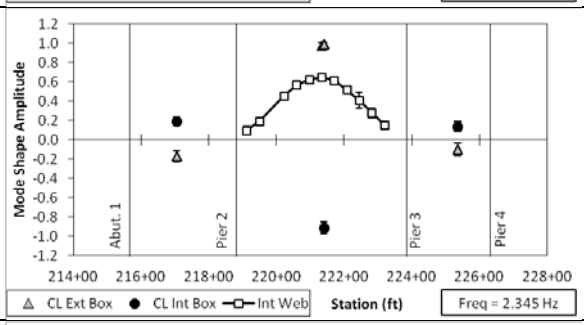	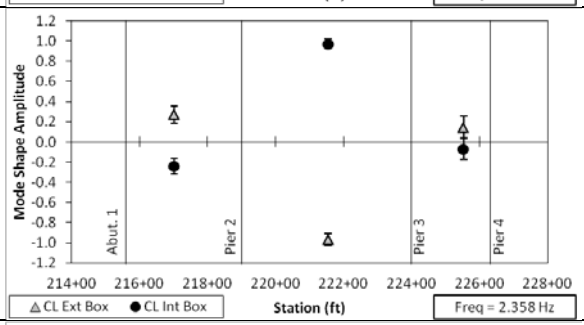
Mode 5 – Torsion Span 1	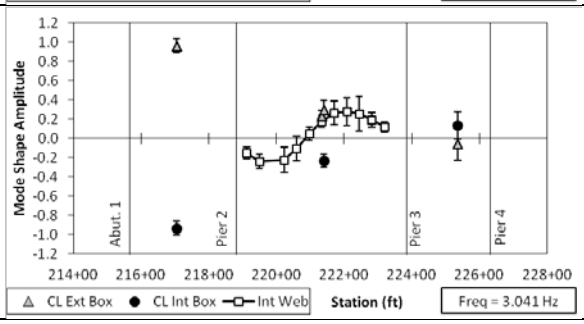	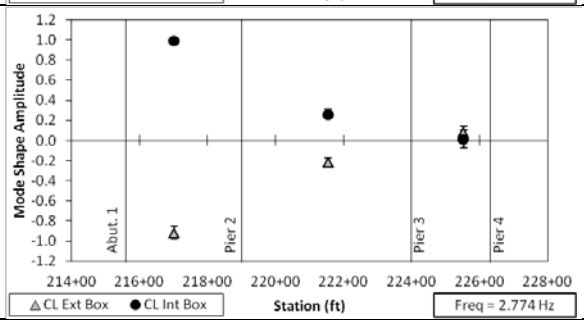

Figure 8.1: Estimated mode shapes 1 through 5 using NExT-ERA/DC

Mode Number	Southbound	Northbound
Mode 6-1 – Torsion Span 1	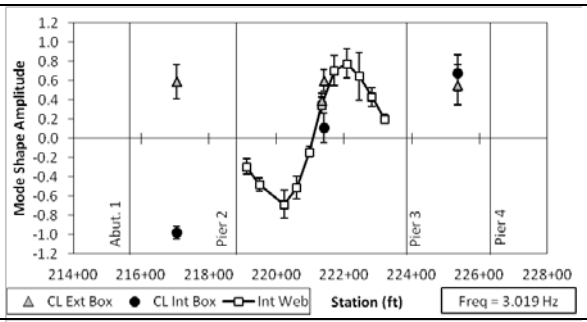	Not captured by NExT-ERA/DC
Mode 6-2 – Torsion Span 1	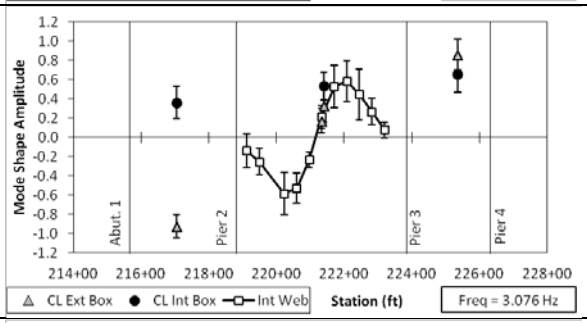	Not captured by NExT-ERA/DC
Mode 6-3 – Bending	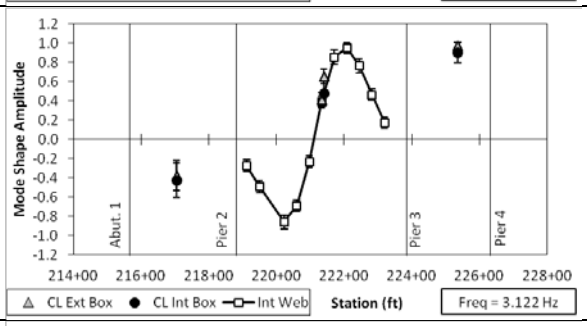	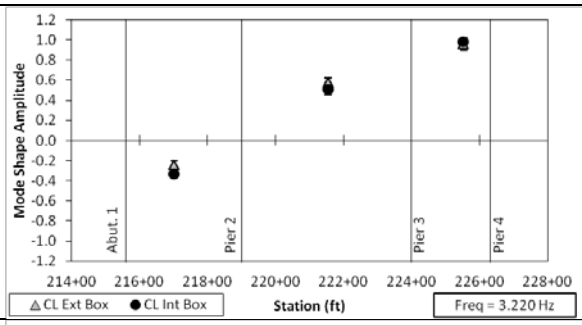
Mode 7 – Torsion Span 3	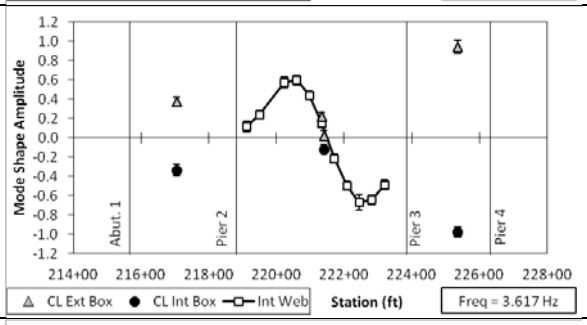	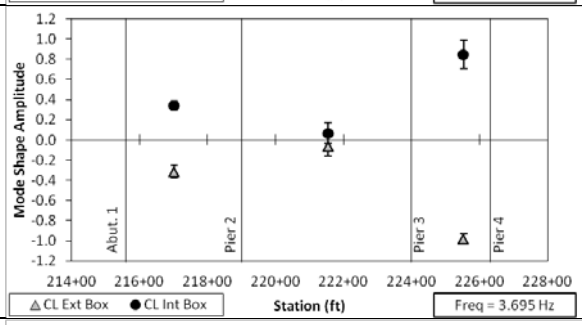
Mode 8 – Torsion Span 3	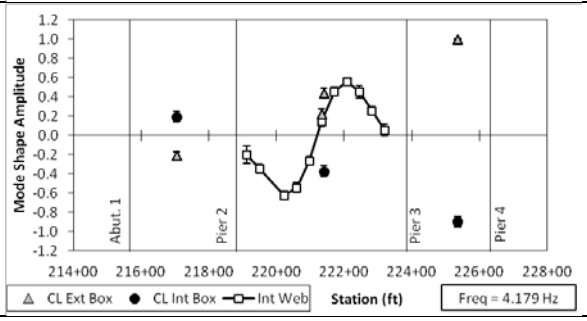	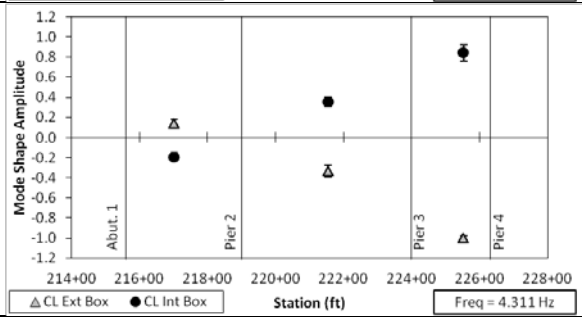

Figure 8.2: Estimated mode shapes 6-8 using NExT-ERA/DC

Mode Number	Southbound	Northbound
Mode 9 – Bending	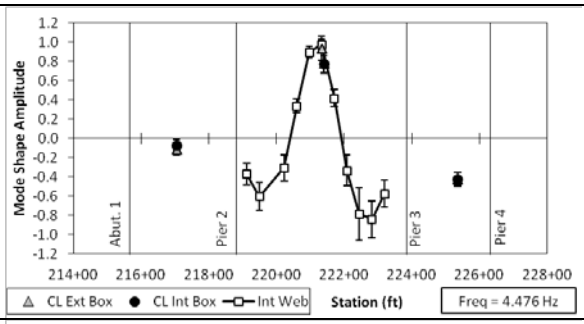	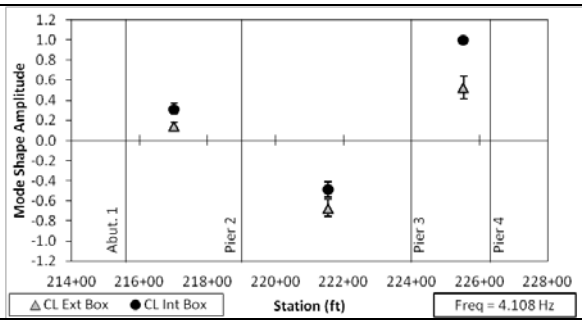
Mode 10 – Opposed Twisting	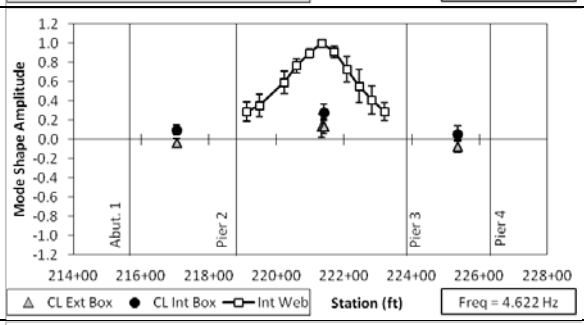	Not captured by NExT-ERA/DC
Mode 11 – Bending	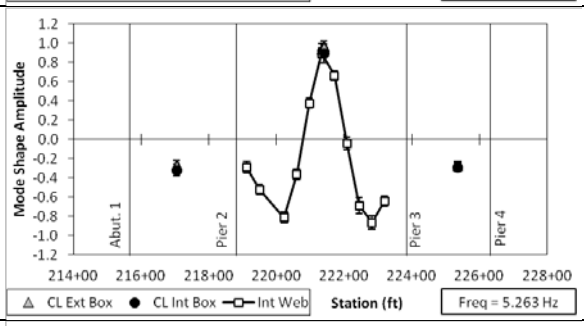	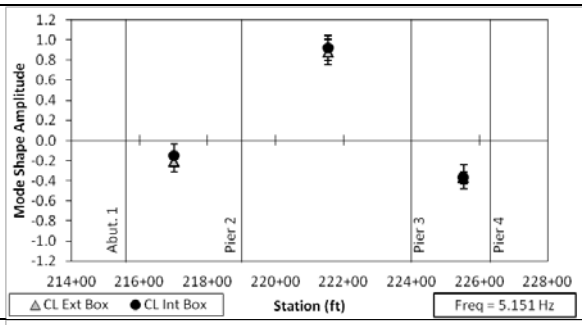
Mode 12 – Torsion	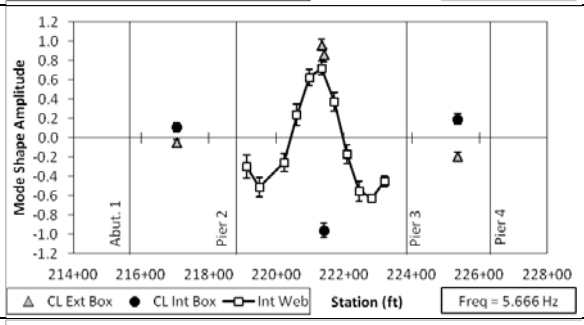	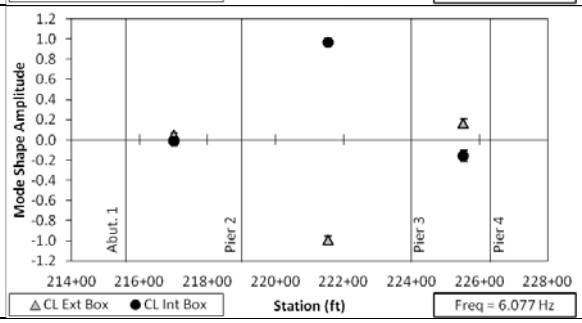
Mode 13 – Torsion	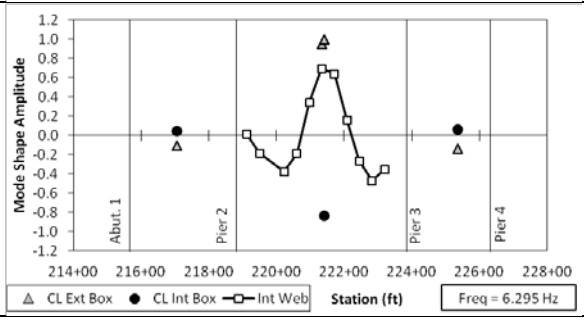	Not captured by NExT-ERA/DC

Figure 8.3: Estimated mode shapes 9-13 using NExT-ERA/DC

Mode Number	Southbound	Northbound
Mode 14 – Opposed Twisting	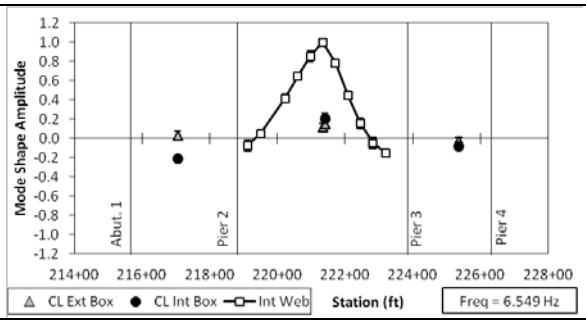	Not captured by NExT-ERA/DC
Mode 15 – Bending	Not captured by NExT-ERA/DC in ambient data. Mode captured in Truck Test SS9 data (see Figure 8.13 for mode shape)	Not captured by NExT-ERA/DC
Mode 16 – Torsion and Transverse Bending	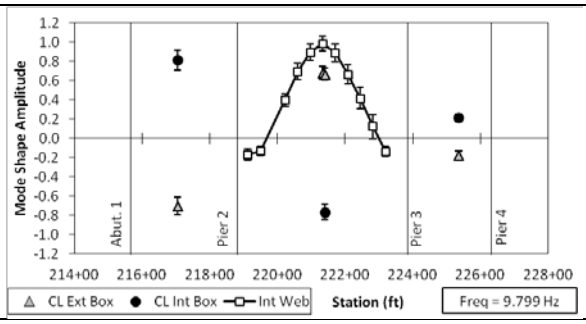	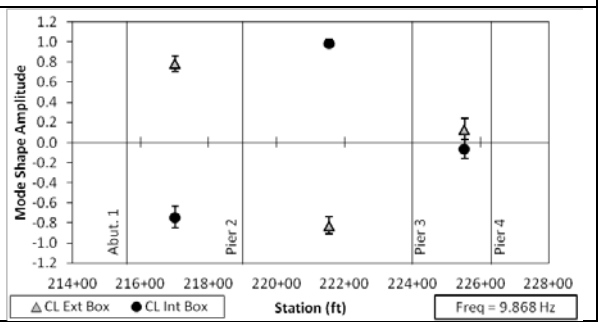

Figure 8.4: Estimated mode shapes 14 and 16 using NExT-ERA/DC

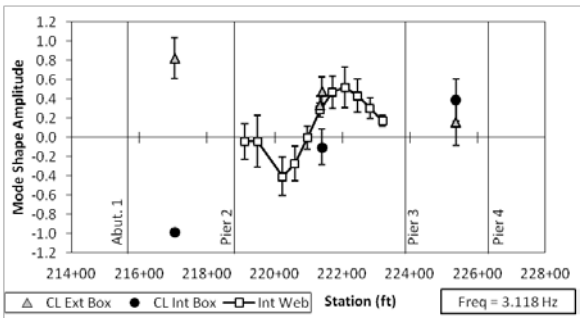

(a) February 1: Mode 5, Example 1

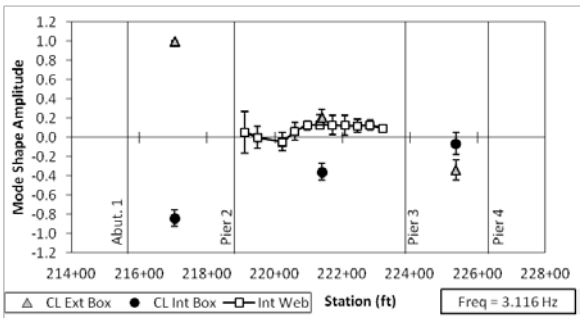

(b) February 1: Mode 5, Example 2

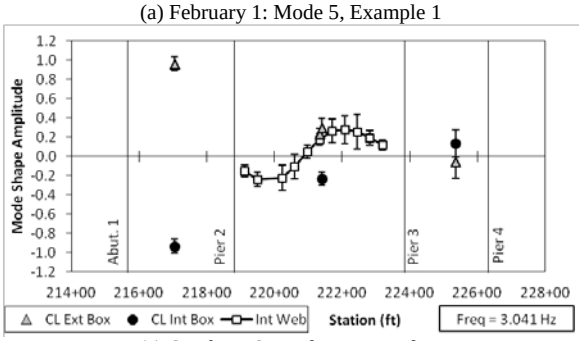

(c) October 26: Mode 5, Example 1

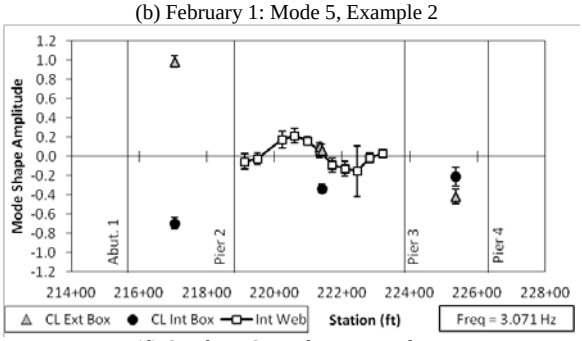

(d) October 26: Mode 5, Example 2

Figure 8.5: Examples of variability for calculated mode shape 5

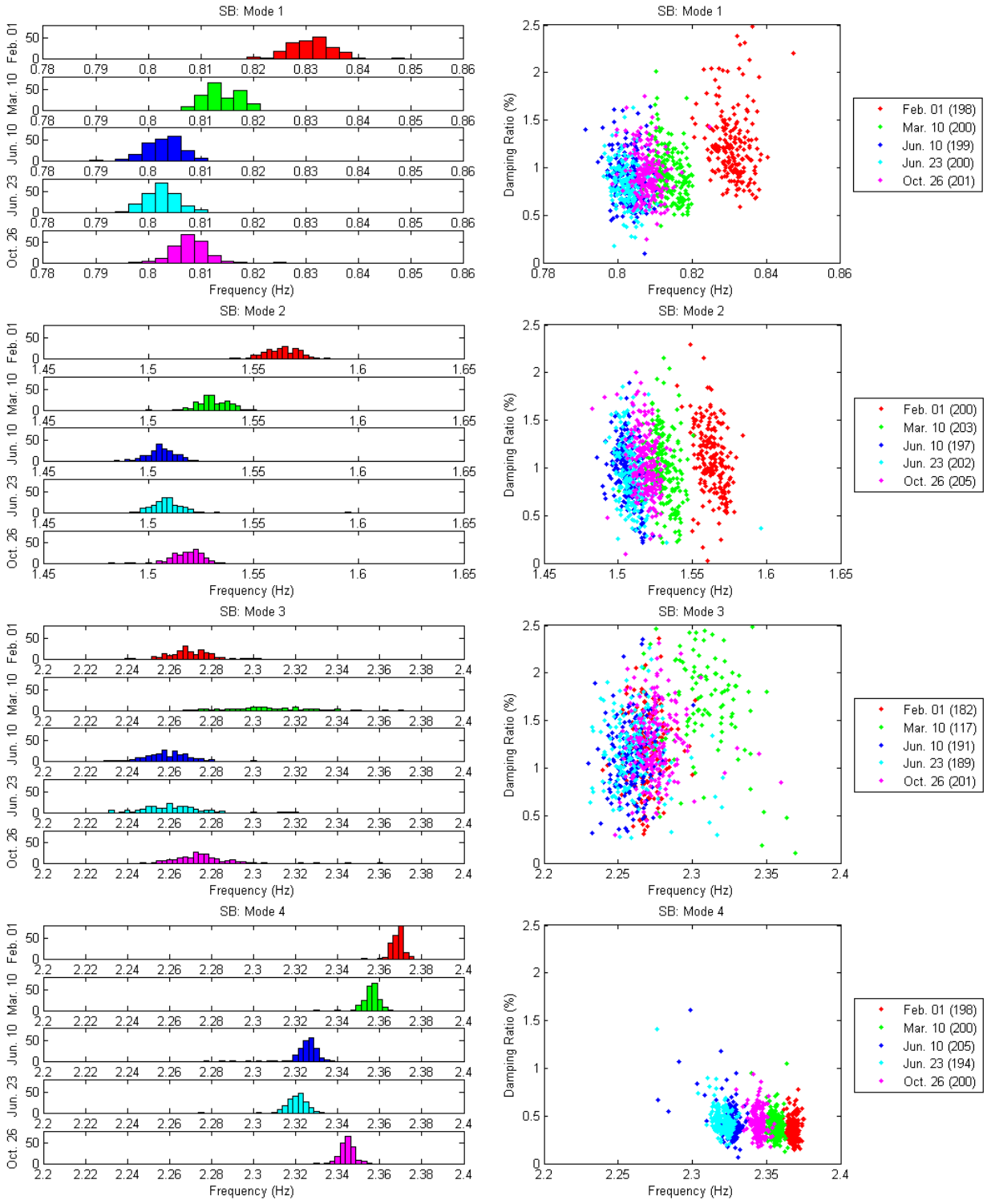

Figure 8.6: Comparisons of the frequency and damping ratio estimates identified from the ambient vibration data of the five days for the SB structure using NExT-ERA/DC

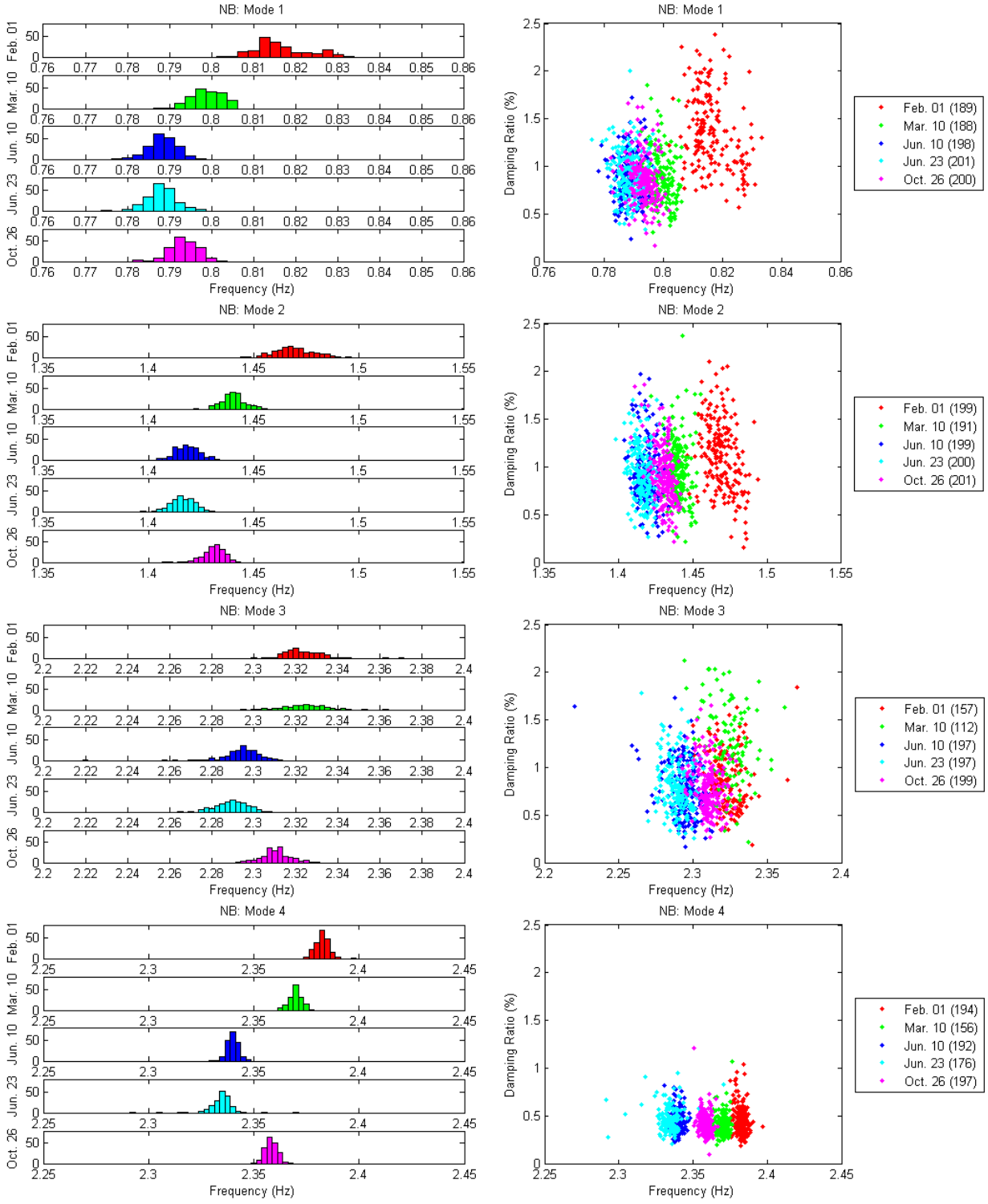

Figure 8.7: Comparisons of the frequency and damping ratio estimates identified from the ambient vibration data of the five days for the NB structure using NExT-ERA/DC

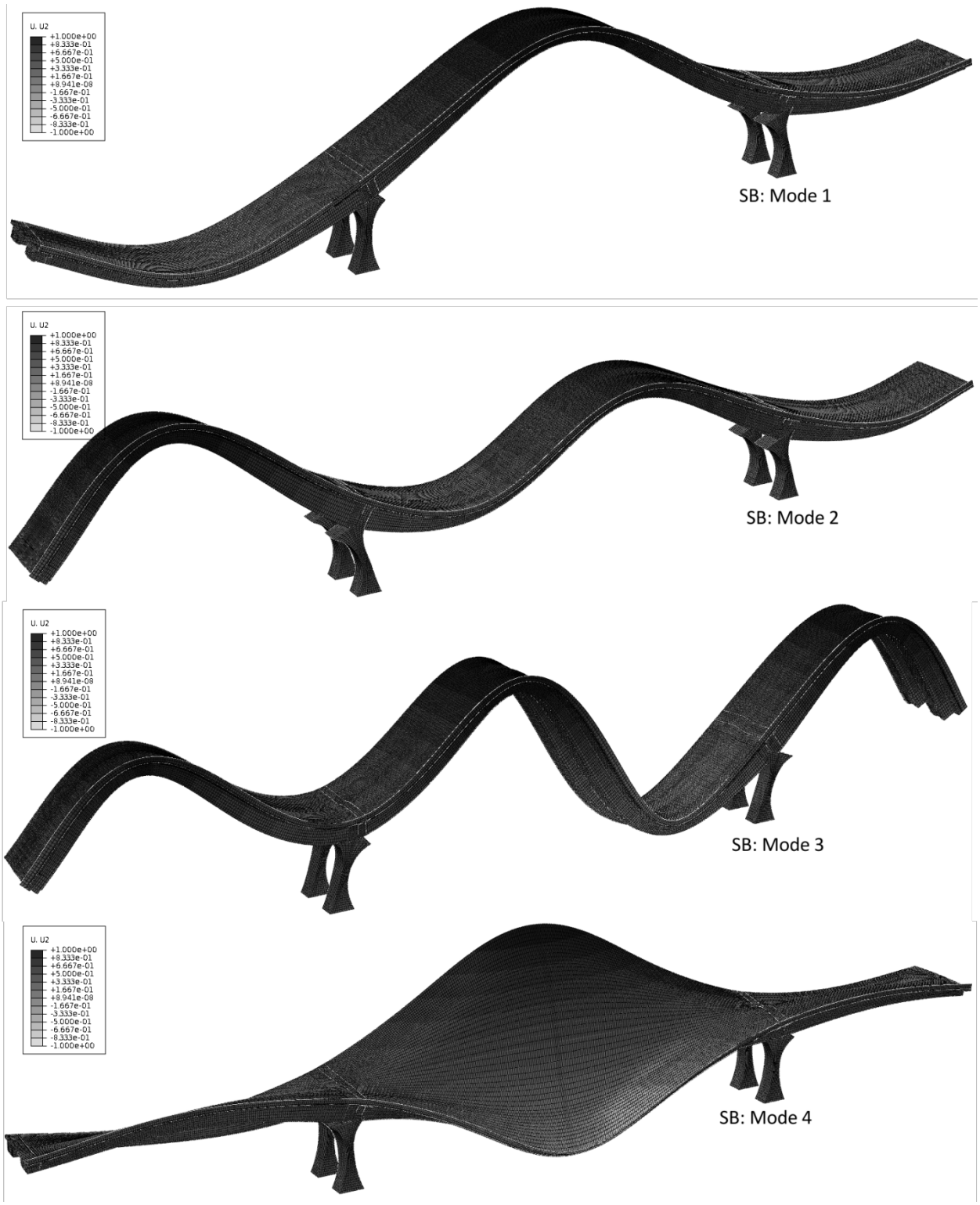

Figure 8.8: Southbound estimated mode shapes 1 through 4 (modeled modes A, D, F, and G, respectively) as extracted from finite element model.

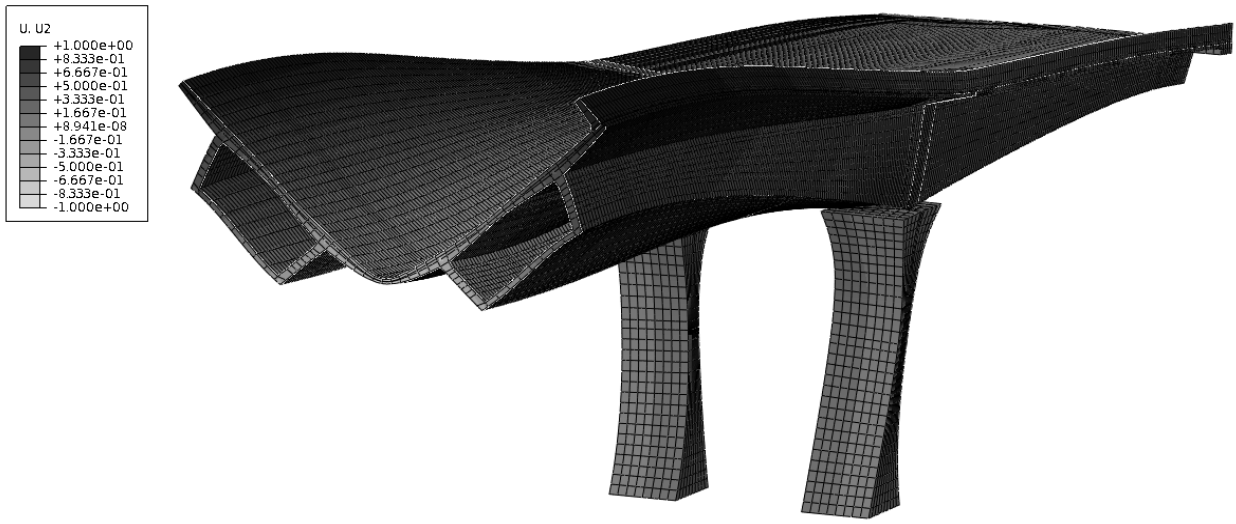

Figure 8.9: Southbound estimated mode shape 10 (modeled mode shape N), representing opposed twisting of the boxes, as extracted from finite element model. Model sliced at midspan of Span 2 for clarity with view towards Span 3.

Southbound Estimated Mode	FEM Mode	Mode Shape Comparison (FEM vs. NExT-ERA/DC Estimation)
Mode 1 – Bending	A	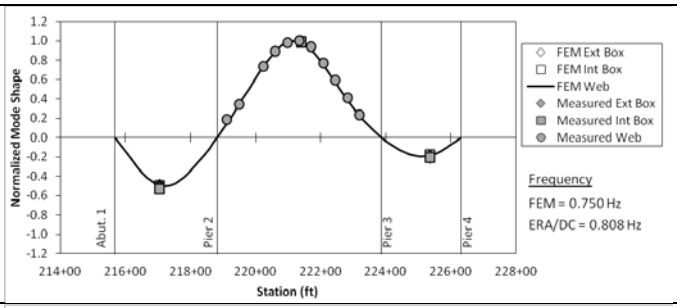
Mode 2 – Bending	D	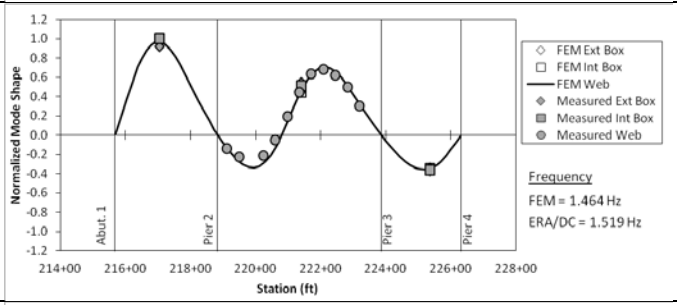
Mode 3 – Bending	F	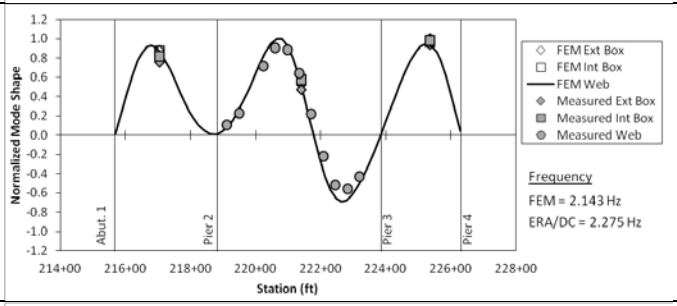
Mode 4 – Torsion	G	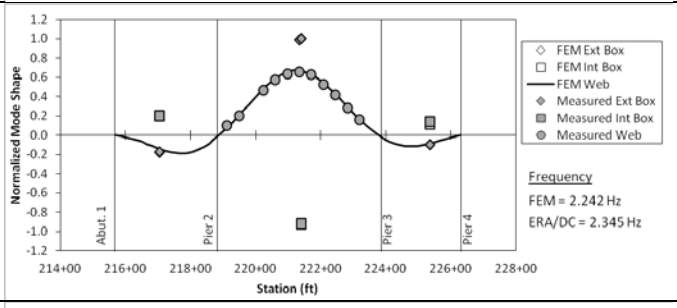
Mode 5 – Torsion Span 1	H	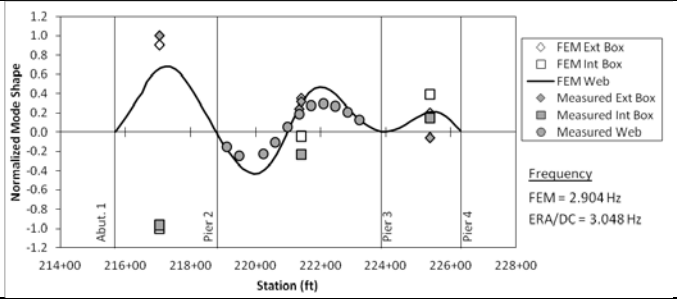

Figure 8.10: Comparison between mean estimated southbound mode shapes 1 through 5 using NExT-ERA/DC and modeled mode shapes from finite element model.

Southbound Estimated Mode	FEM Mode	Mode Shape Comparison (FEM vs. NExT-ERA/DC Estimation)
Mode 6-1 – Torsion Span 1	H	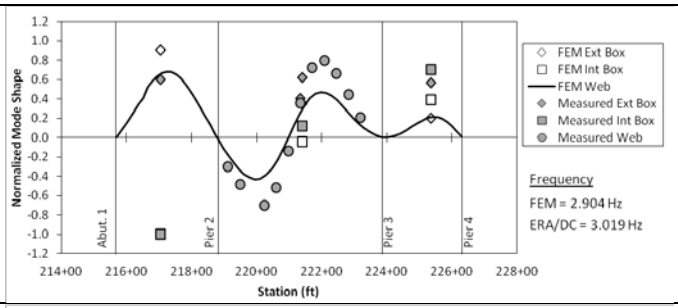
Mode 6-2 – Torsion Span 1	I	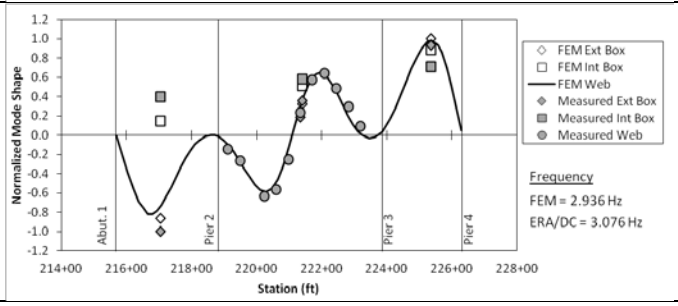
Mode 6-3 – Bending	-	Measured mode not matched with any extracted FEM mode
Mode 7 – Torsion Span 3	K	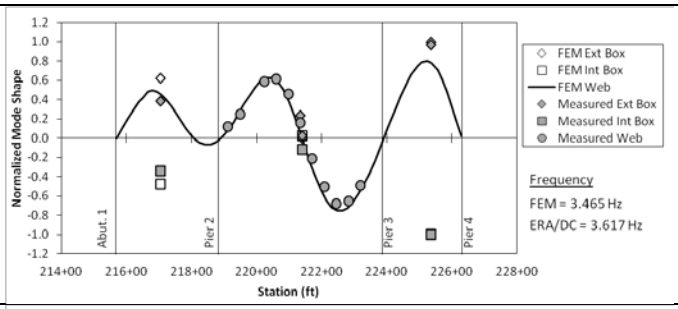
Mode 8 – Torsion Span 3	L	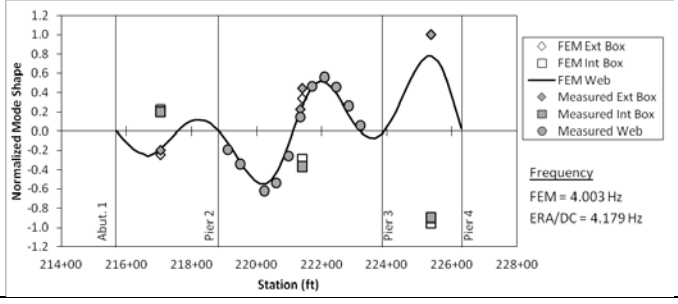

Figure 8.11: Comparison between mean estimated southbound mode shapes 6 through 8 using NExT-ERA/DC and modeled mode shapes from finite element model.

Southbound Estimated Mode	FEM Mode	Mode Shape Comparison (FEM vs. NExT-ERA/DC Estimation)
Mode 9 – Bending	M	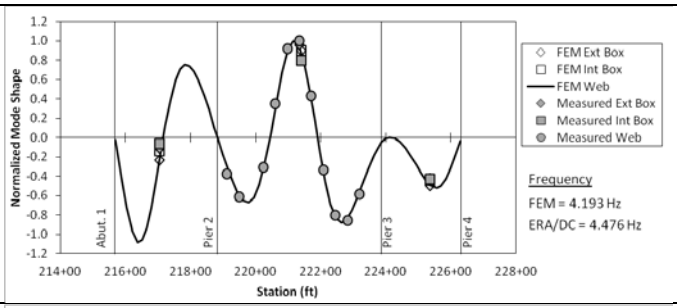
Mode 10 – Opposed Twisting	N	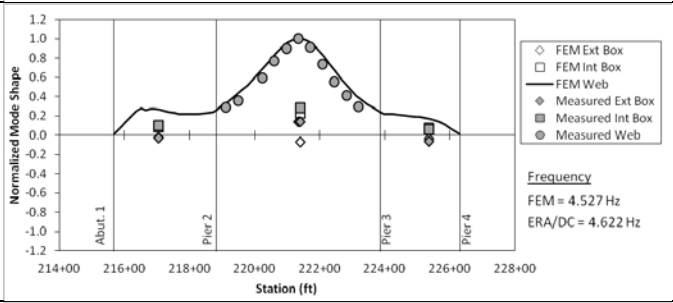
Mode 11 – Bending	O	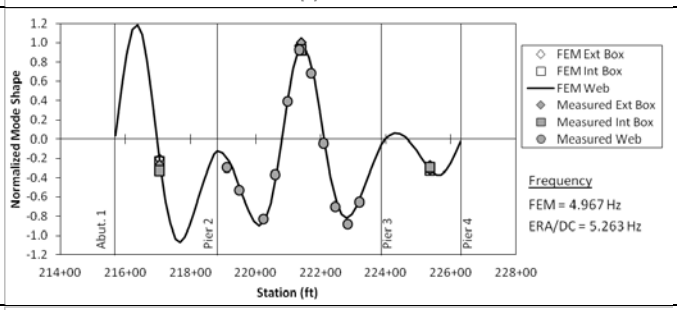
Mode 12 – Torsion	P	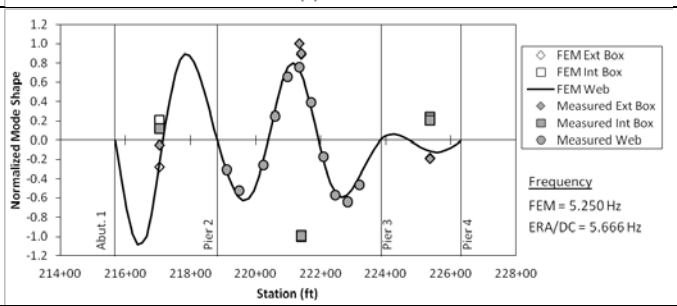
Mode 13 – Torsion	T	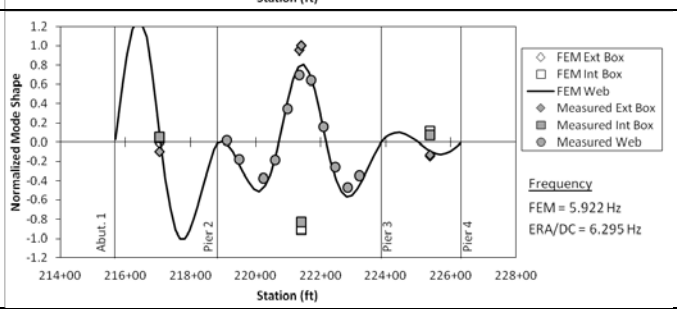

Figure 8.12: Comparison between mean estimated southbound mode shapes 9 through 13 using NExT-ERA/DC and modeled mode shapes from finite element model.

Southbound Estimated Mode	FEM Mode	Mode Shape Comparison (FEM vs. NExT-ERA/DC Estimation)
Mode 14 – Opposed Twisting	U	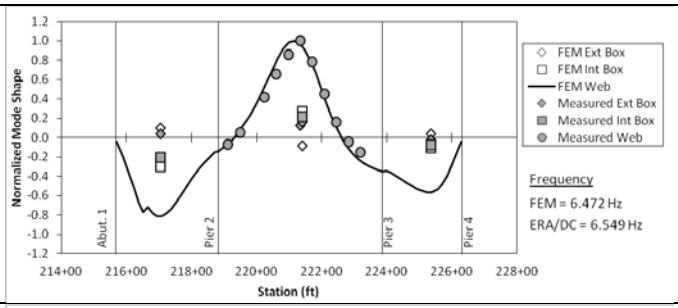
Mode 15 – Bending*	V	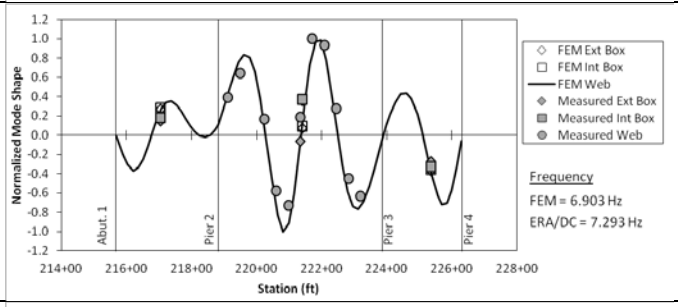
Mode 16 – Torsion + Transverse Bending	AF	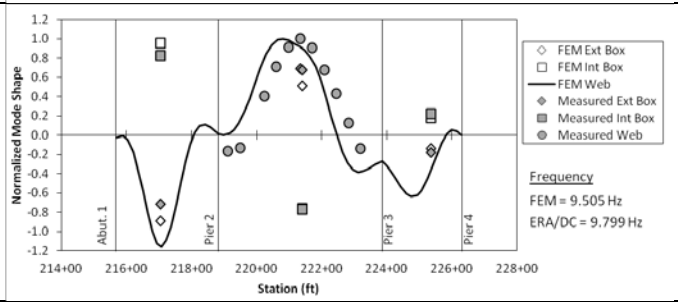
* Mode 15 “measured” mode shape and frequency taken from Truck Test SS9 analysis		

Figure 8.13: Comparison between mean estimated southbound mode shapes 14 through 16 using NExT-ERA/DC and modeled mode shapes from finite element model.

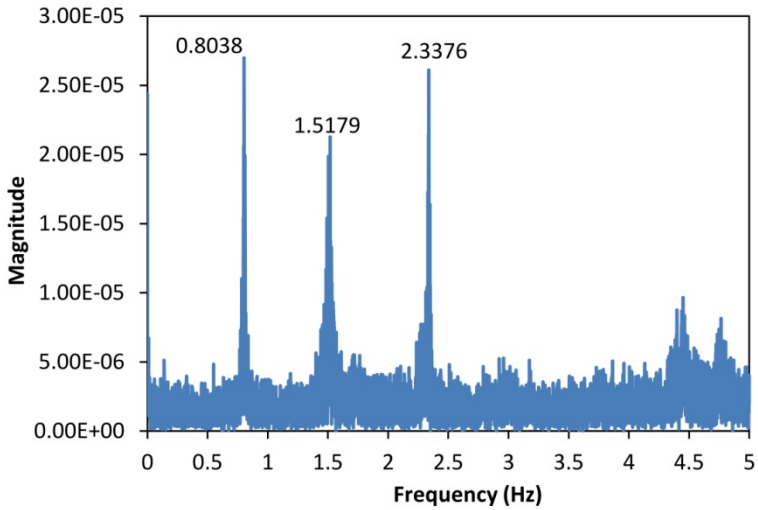

Figure 8.14: Frequency spectrum taken at midspan of SB Span 2 on November 1, 2008

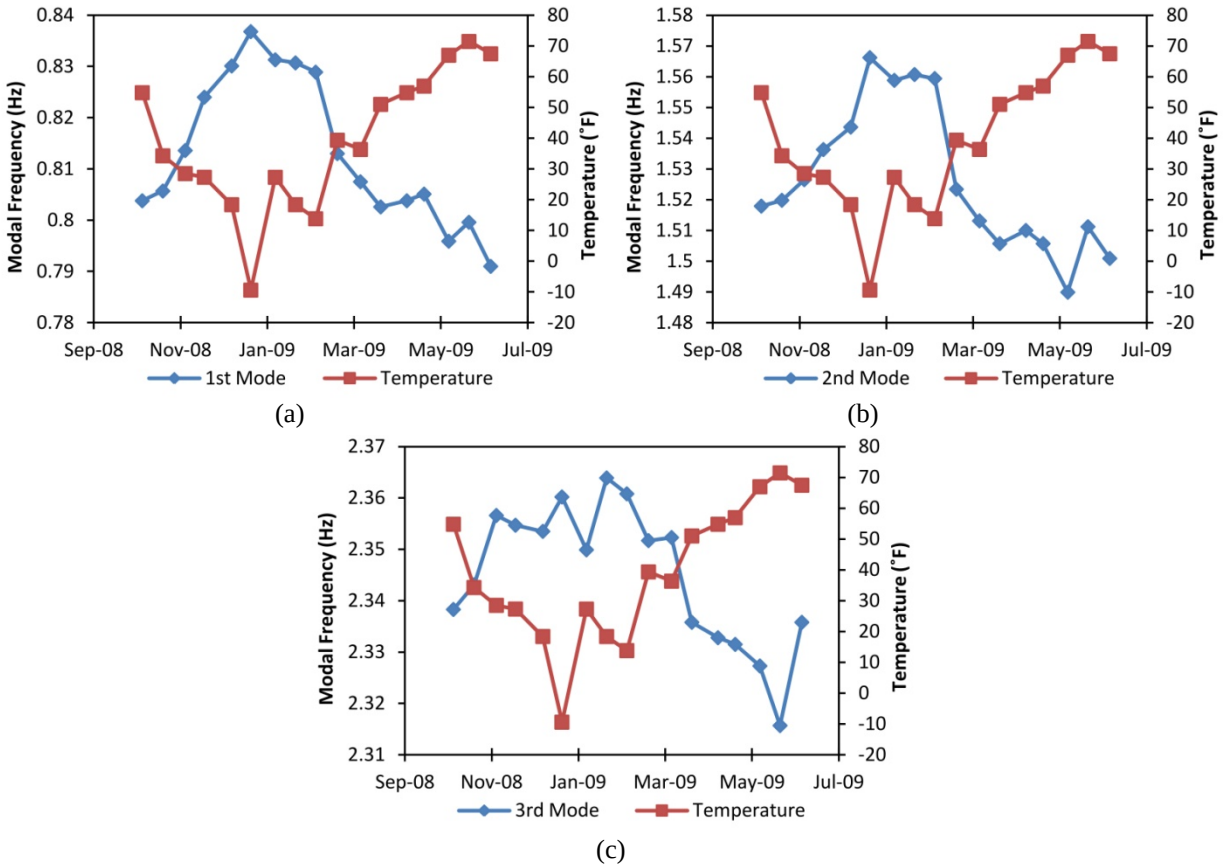

Figure 8.15: Variation of (a) first mode, (b) second mode and (c) third mode from FFT data at midspan of SB Span 2 over eight-month period from November 2008 to the end of June 2009.

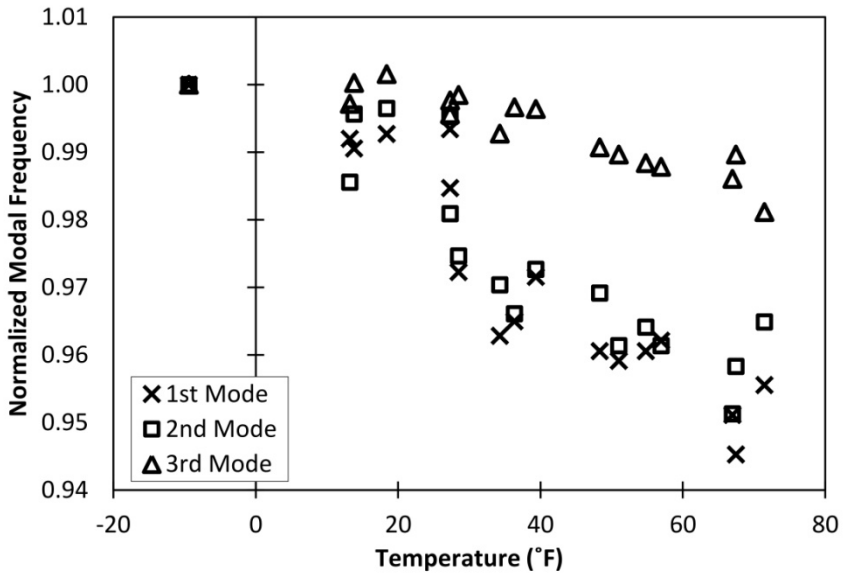

Figure 8.16: Normalized modal frequencies (extracted using FFT) against temperature variation at midspan of SB Span 2 for eight-month period

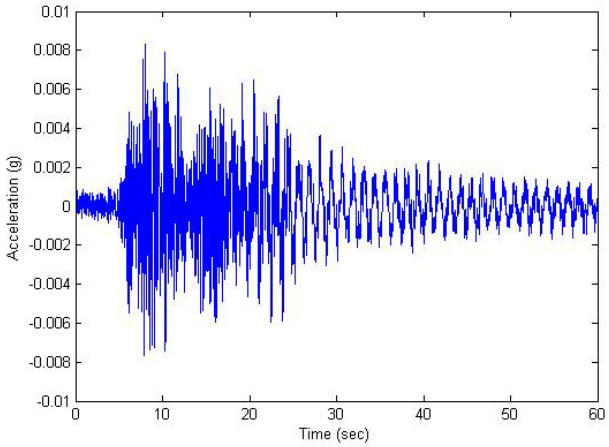

Figure 8.17: Measured acceleration at centerline of the exterior box at midspan of Span 2 of the southbound bridge during dynamic truck test SB Bridge Closed SS9.

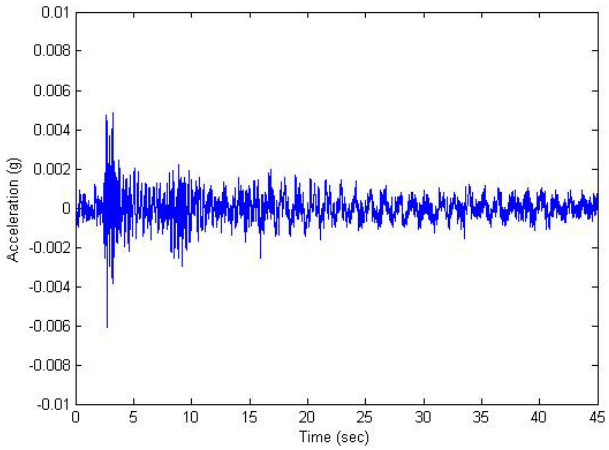

Figure 8.18: Measured acceleration at centerline of the exterior box at midspan of Span 2 of the southbound bridge during dynamic truck test SB Bridge Closed SS10, Wave 8.

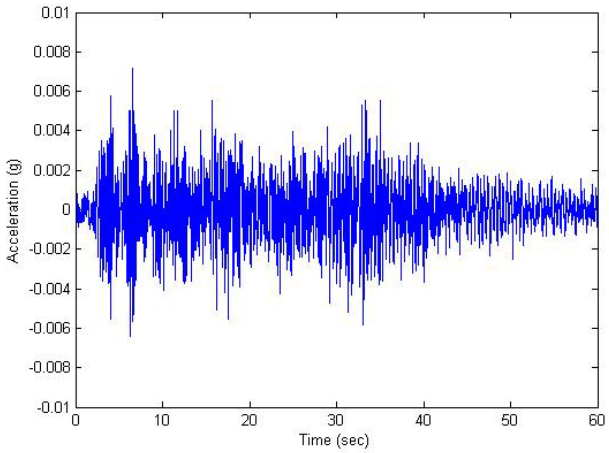

Figure 8.19: Measured acceleration at centerline of the exterior box at midspan of Span 2 of the southbound bridge during dynamic truck test SB Bridge Open S4, Wave 2.

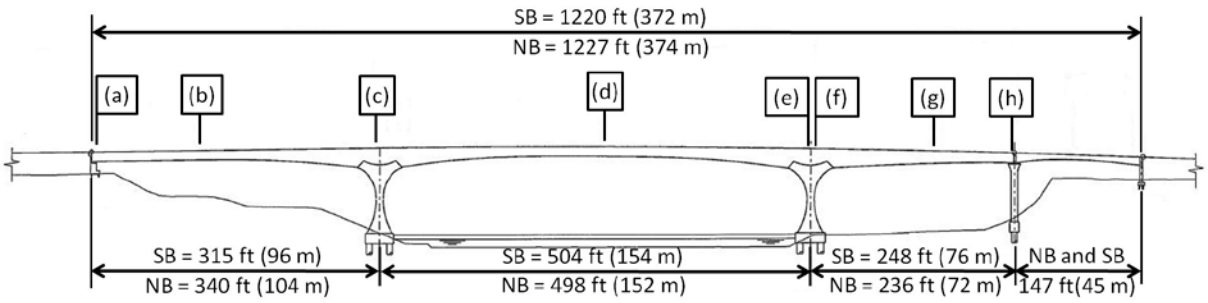

Figure 9.1: Bridge positions (a) through (h) plotted for moment and shear influence lines.

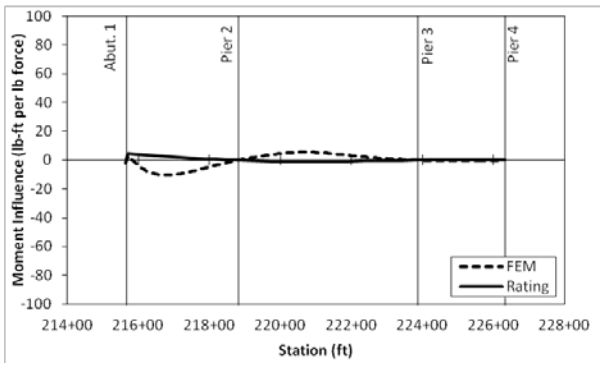

(a) 4.9 ft north of Abutment 1 (Station 215+71.4)

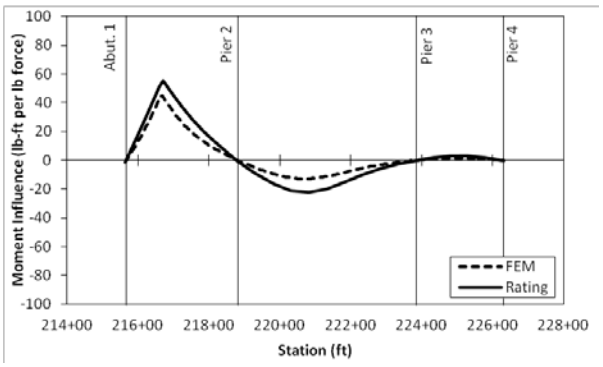

(b) 103.8 ft north of Abutment 1 (Station 216+70.3)

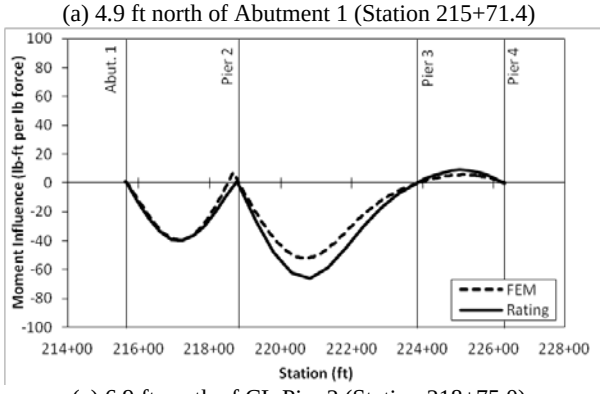

(c) 6.9 ft south of CL Pier 2 (Station 218+75.0)

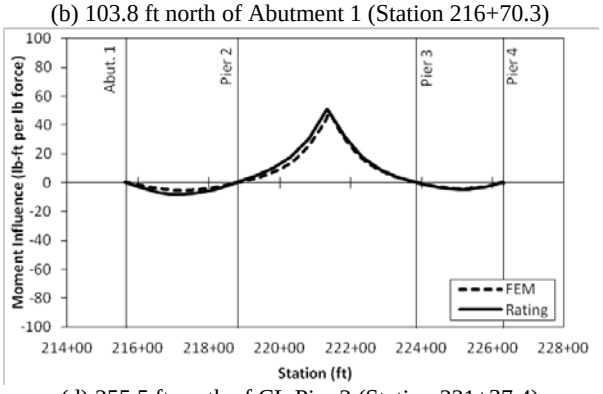

(d) 255.5 ft north of CL Pier 2 (Station 221+37.4)

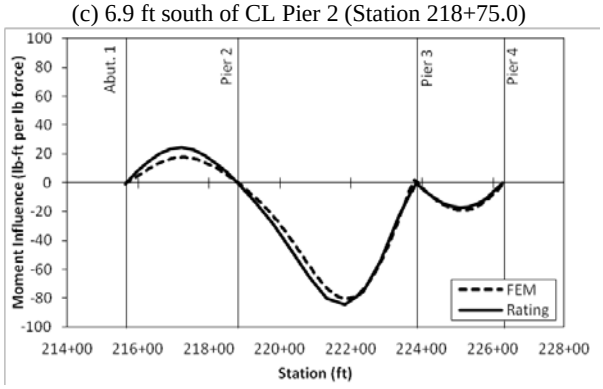

(e) 13.0 ft south of CL Pier 3 (Station 223+72.9)

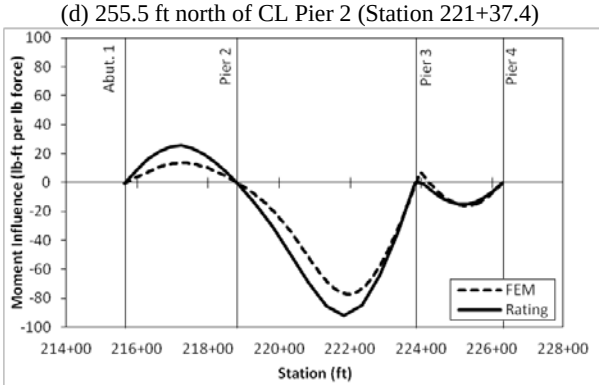

(f) 5.0 ft north of CL Pier 4 (Station 223+90.9)

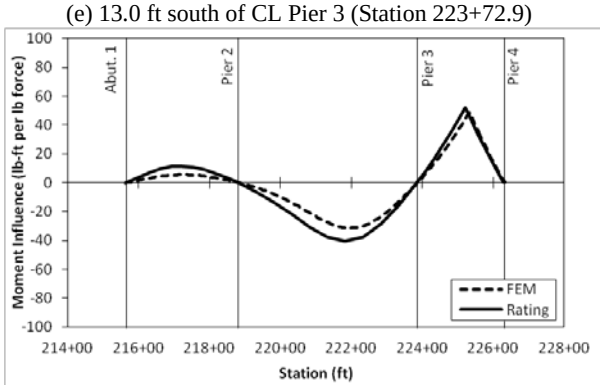

(g) 137.7 ft north of CL Pier 3 (Station 225+23.6)

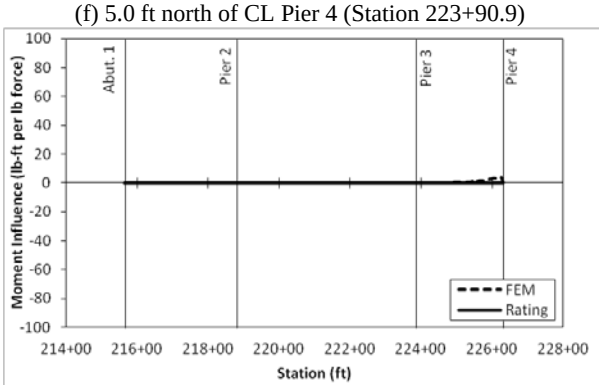

(h) 4.3 south of CL Pier 4 (Station 226+29.6)

Figure 9.2: Load Rating Manual ("Rating") and validated FEM moment influence lines

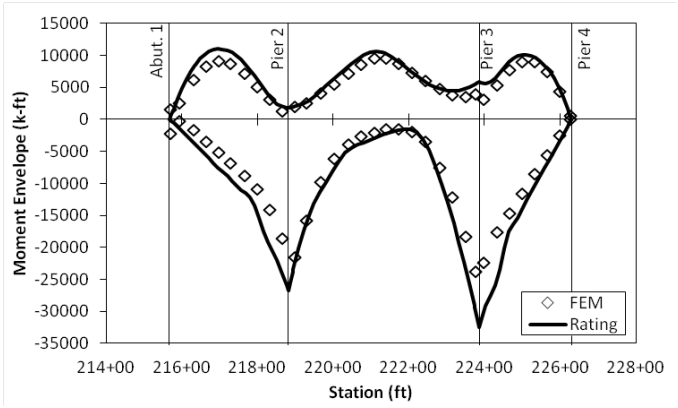

Figure 9.3: Comparison of HL-93 moment envelope for validated FEM and Load Rating Manual ("Rating") values

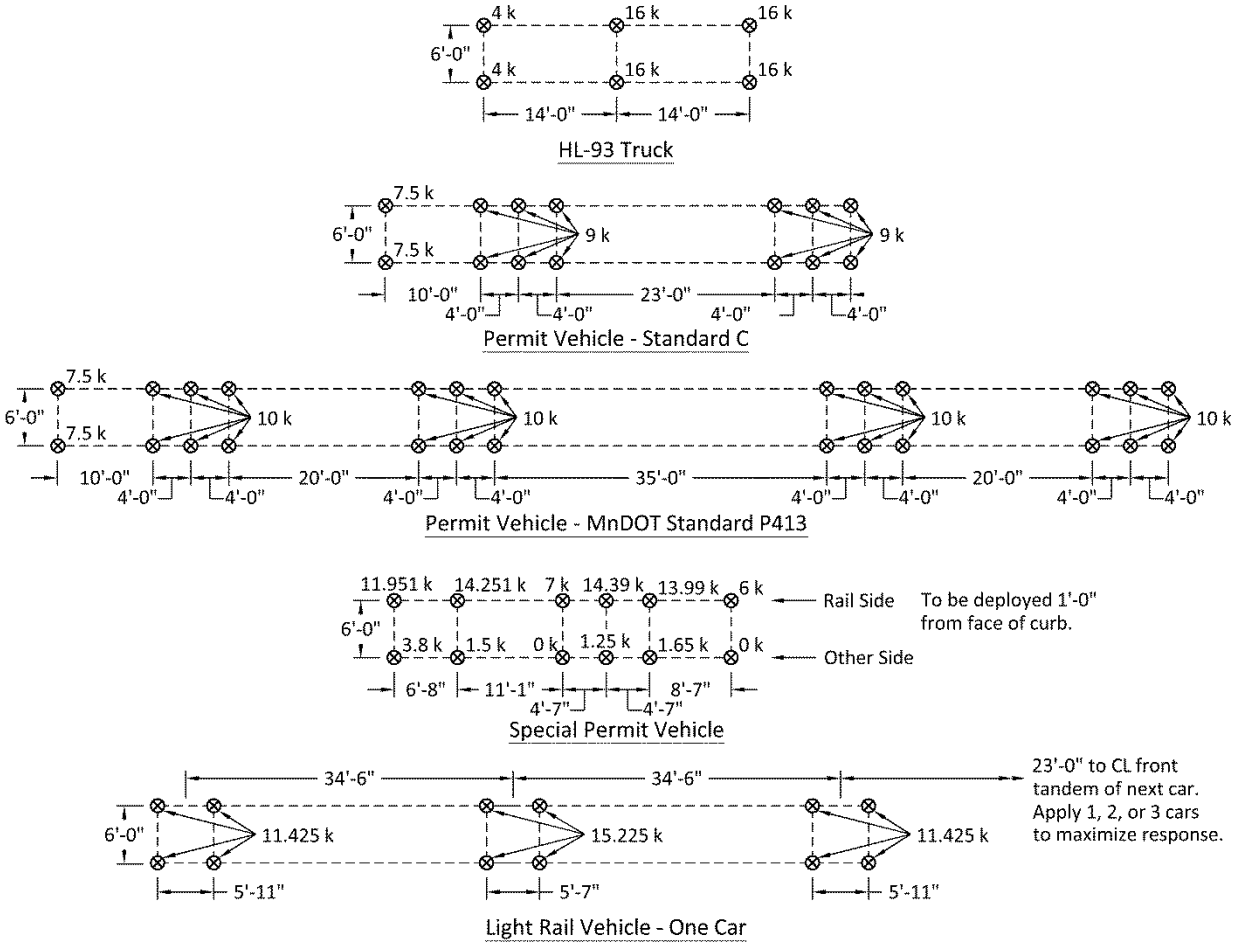

Figure 9.4: HL-93, permit and light-rail vehicle live loads

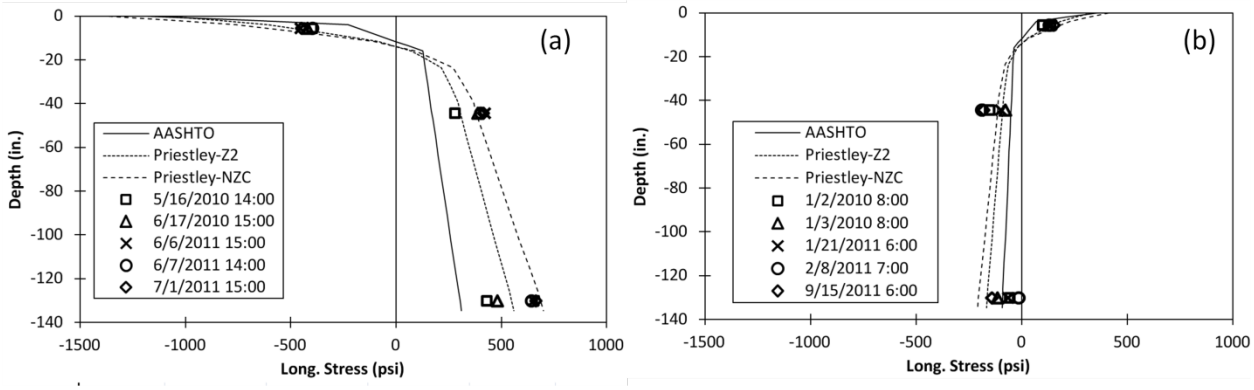

Figure 9.5: Changes in longitudinal stresses approximated from measured strains (averaged at each depth) at Location 7 caused by five maximum measured (a) positive and (b) negative thermal gradients compared to FEM-computed stresses from design gradients.

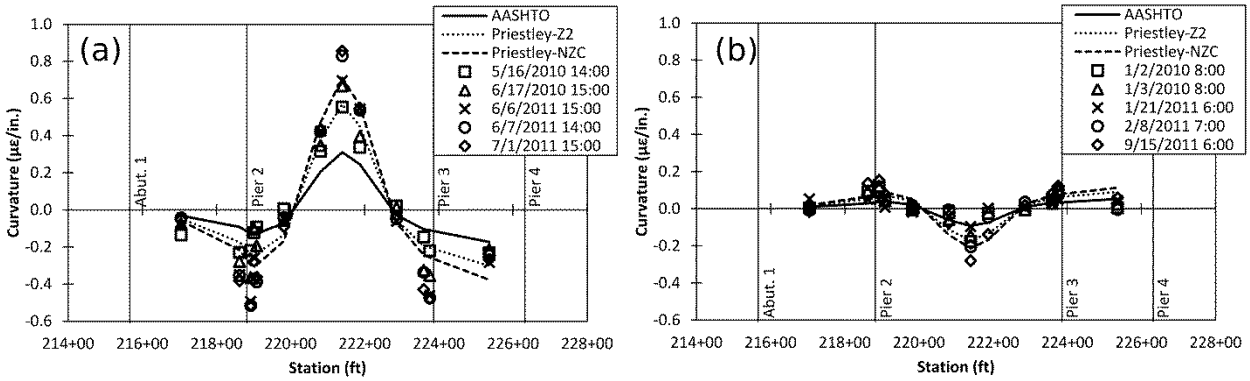

Figure 9.6: Comparison of measured curvatures caused by five maximum measured (a) positive and (b) negative thermal gradients compared to FEM-computed curvatures from design gradients.

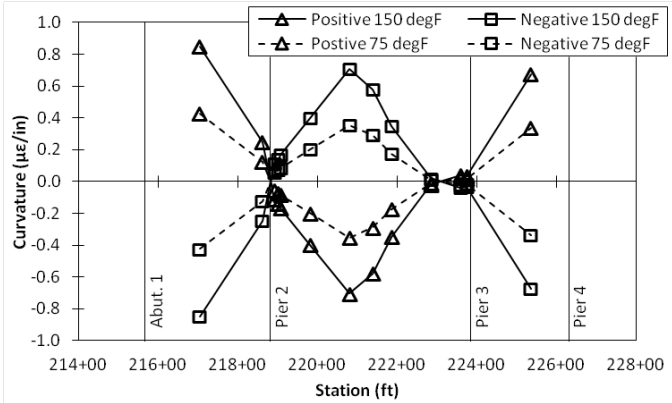

Figure 9.7: Curvature along length of southbound structure from FEM results for ±150°F and ±75°F uniform temperature changes

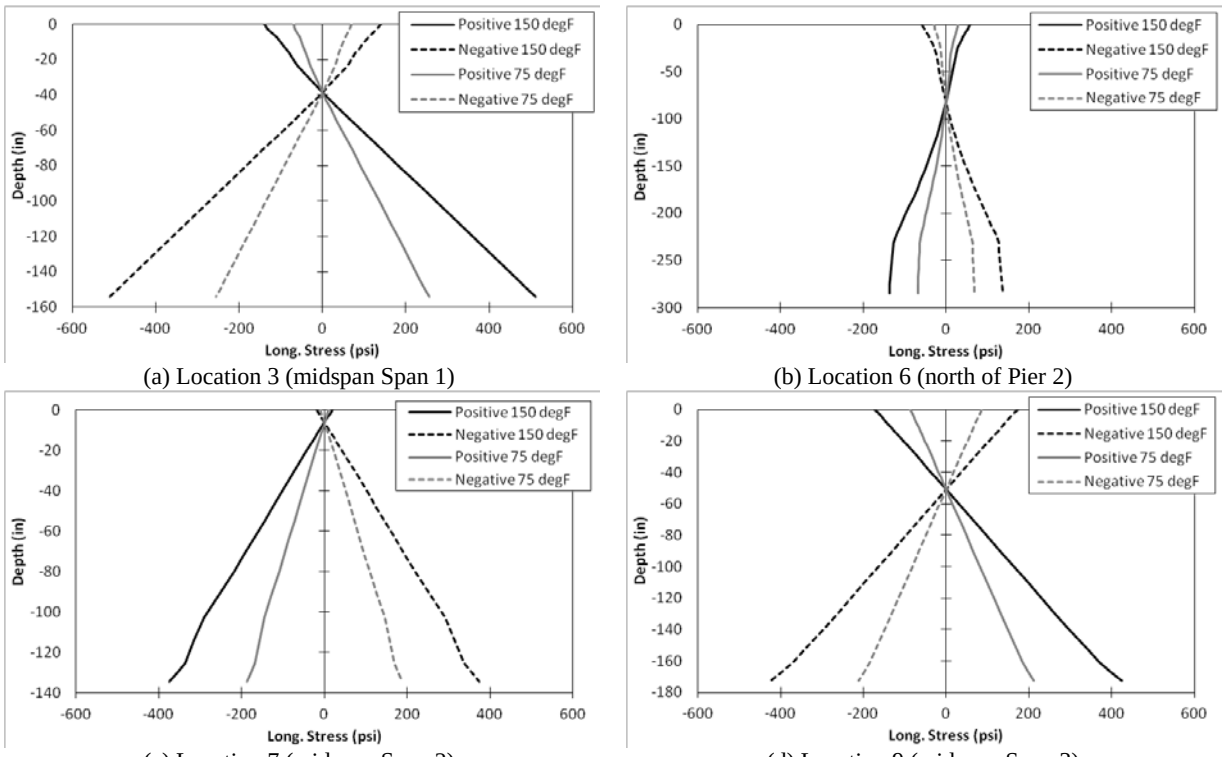

(a) Location 3 (midspan Span 1)

(b) Location 6 (north of Pier 2)

(c) Location 7 (midspan Span 2)

(d) Location 9 (midspan Span 3)

Figure 9.8: Stress profile at instrumented locations of southbound structure from FEM results for ±150°F and ±75°F uniform temperature changes

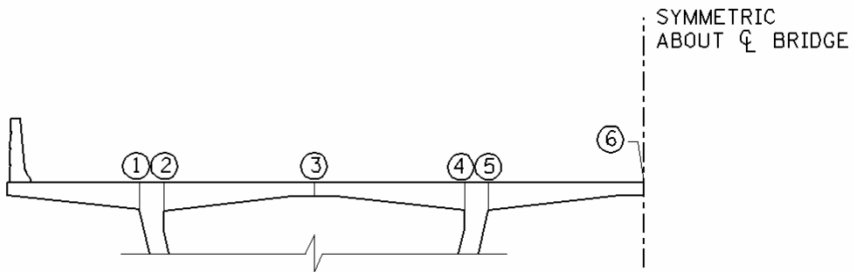

Figure 9.9: Critical points in top flange of Spans 1 though 3 of the northbound and southbound structures for transverse moments (Figg 2008, image reproduced with permission from Figg Bridge Engineers, Inc.)

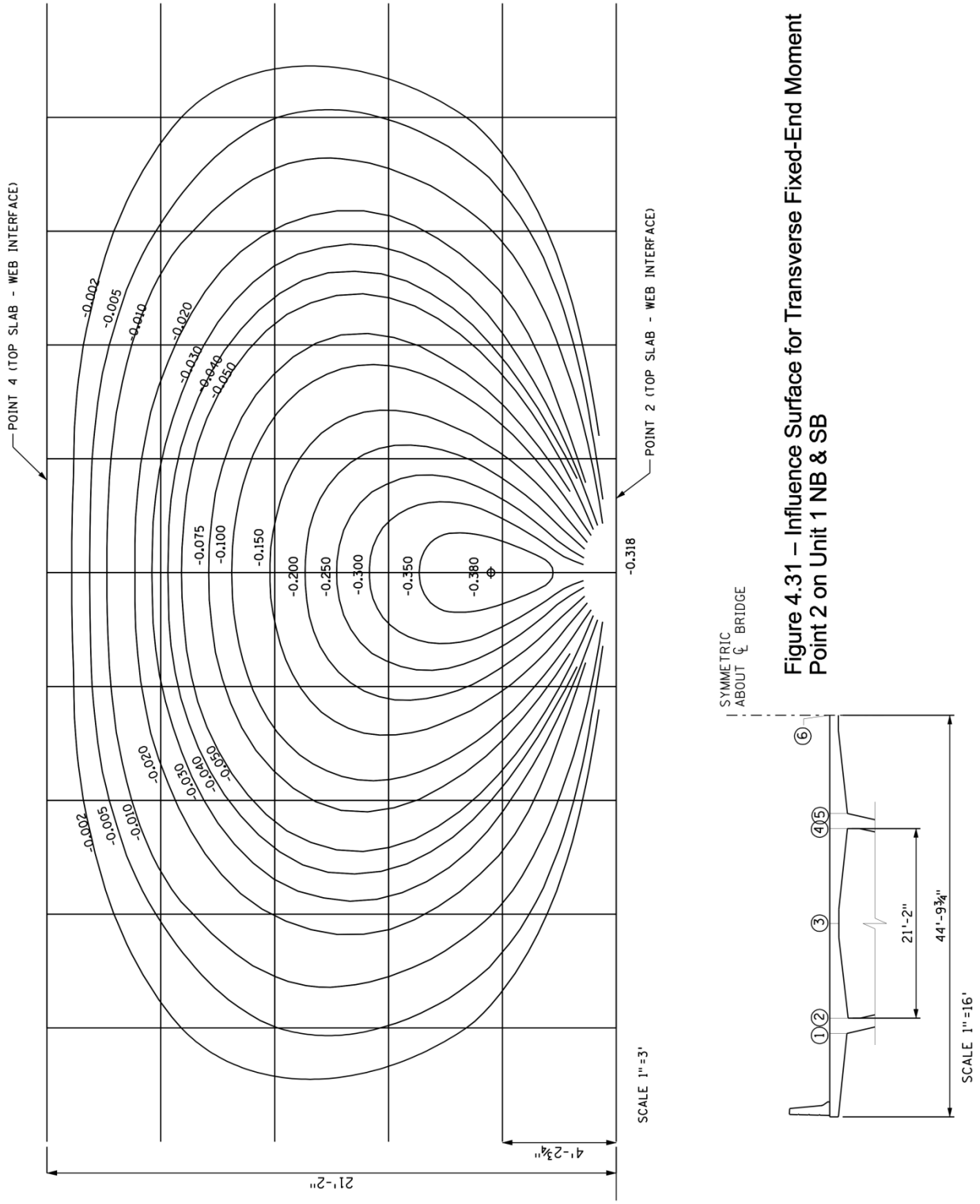

Figure 9.10: Fixed-end-moment influence surface for Point 2 (not to scale). Contour values are unitless. Loads applied to the surface are multiplied by the contour values to calculate the moment at Point 2 in force-length/length (Figg 2008, image reproduced with permission from Figg Bridge Engineers, Inc.).

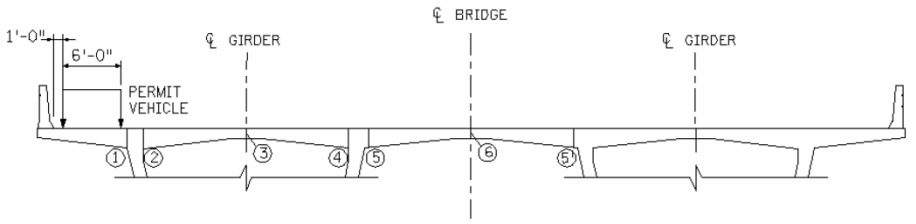

(a) Load Case 1 (negative moment for Point 1) and Load Case 4 (negative moment for Point 3)

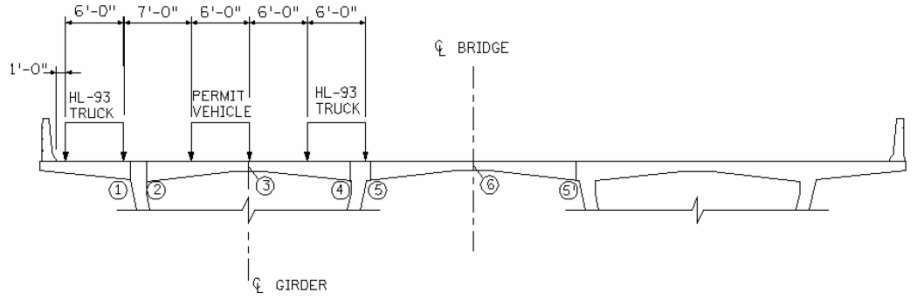

(b) Load Case 2 (negative moment for Point 2)

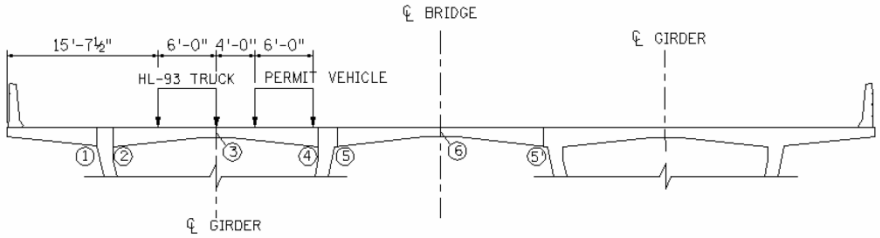

(c) Load Case 3 (positive moment for Point 3) and Load Case 8 (negative moment for Point 6)

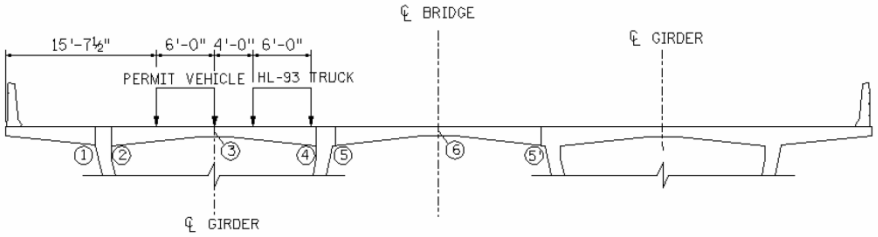

(d) Load Case 5 (negative moment for Point 4)

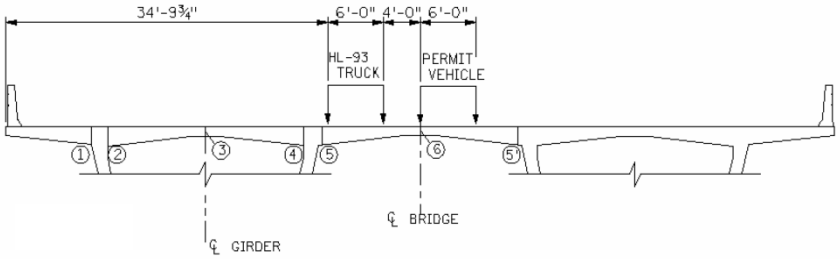

(e) Load Case 6 (negative moment for Point 5) and Load Case 7 (positive moment for Point 6)

Figure 9.11: Sample load configurations from Load Rating Manual (Figg 2008, images reproduced with permission from Figg Bridge Engineers, Inc.)

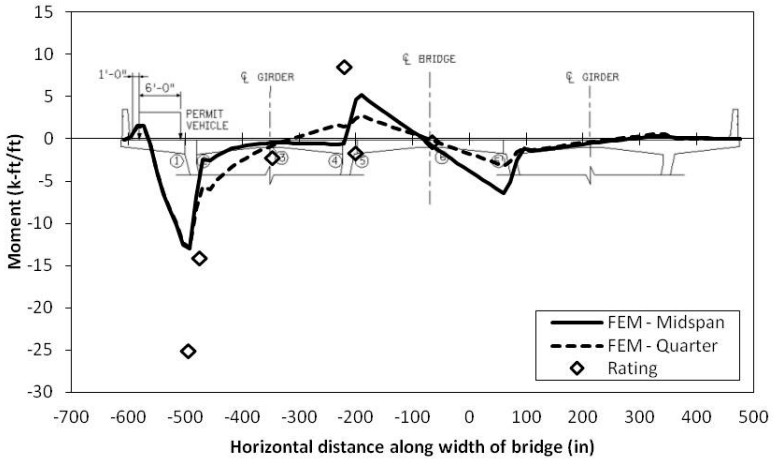

Figure 9.12: Comparison of transverse Load Rating Manual ("Rating") moments and FEM computed moments for Load Case 1 (negative moment at Point 1).

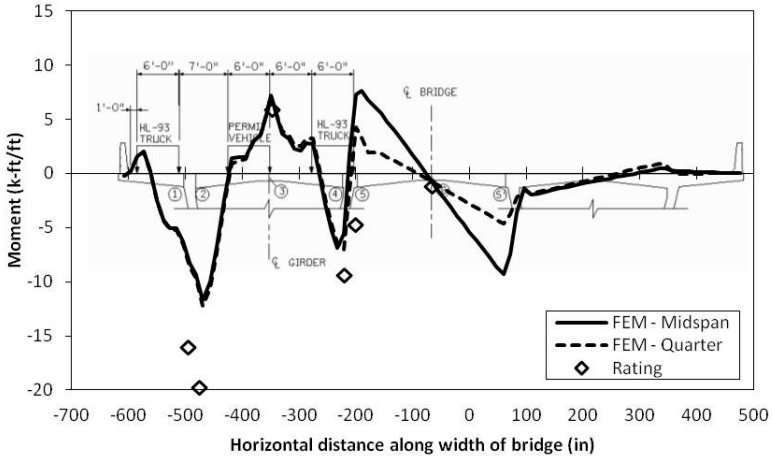

Figure 9.13: Comparison of transverse Load Rating Manual ("Rating") moments and FEM computed moments for Load Case 2 (negative moment for Point 2).

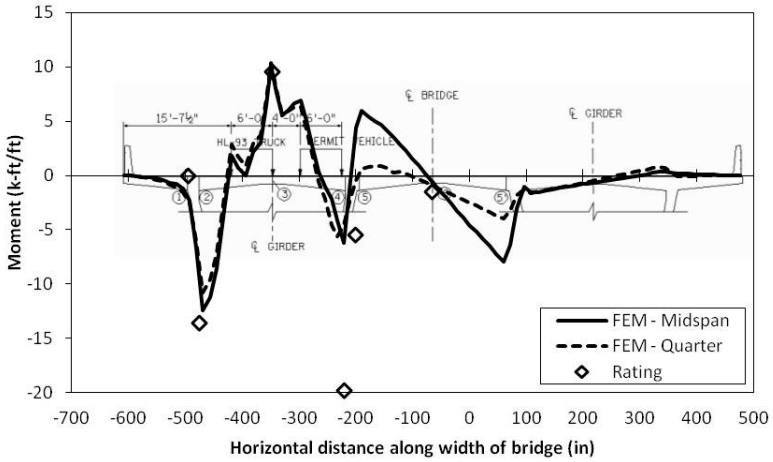

Figure 9.14: Comparison of transverse Load Rating Manual ("Rating") moments and FEM computed moments for Load Case 3 (positive moment for Point 3) and Load Case 8 (negative moment for Point 6).

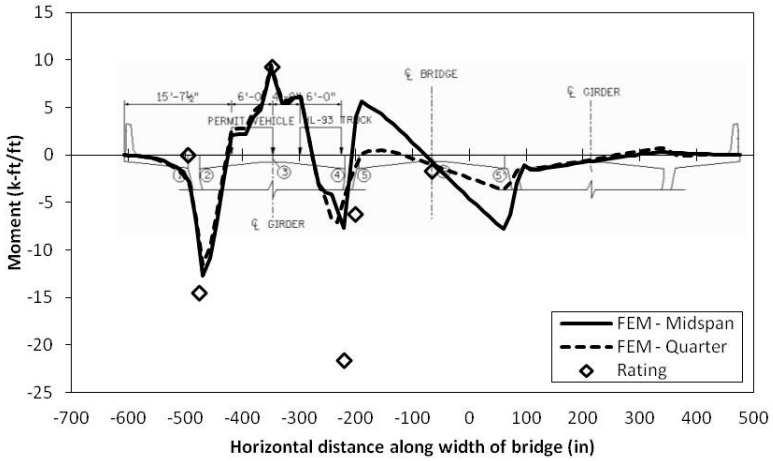

Figure 9.15: Comparison of transverse Load Rating Manual ("Rating") moments and FEM computed moments for Load Case 5 (negative moment for Point 4).

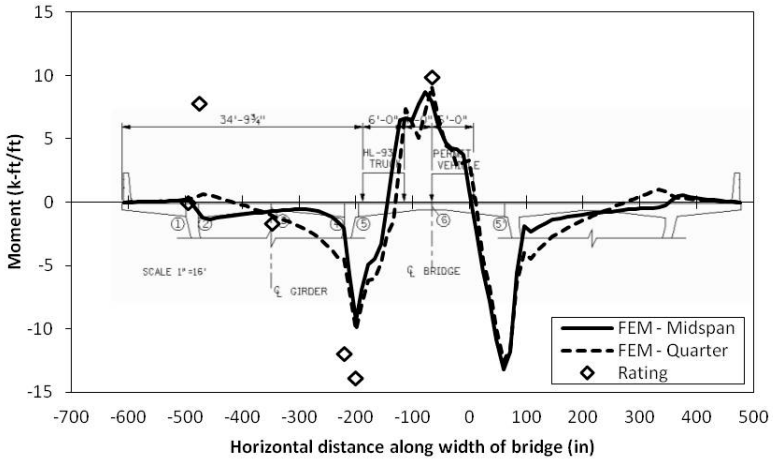

Figure 9.16: Comparison of transverse Load Rating Manual ("Rating") moments and FEM computed moments for Load Case 6 (negative moment for Point 5) and Load Case 7 (positive moment for Point 6)

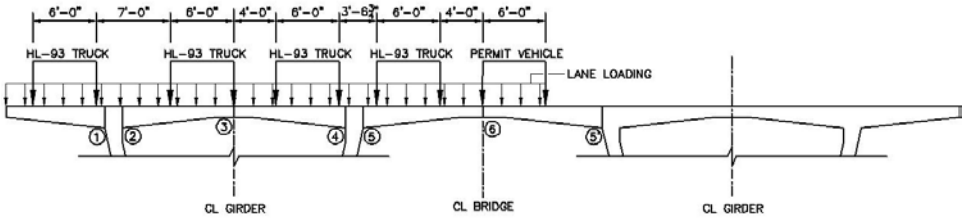

Figure 9.17: Load configuration for maximizing negative moment at Point 5'.

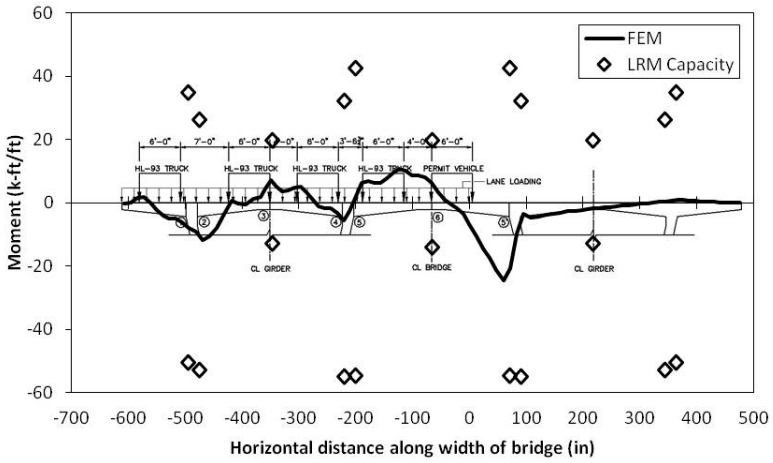

Figure 9.18: Comparison of FEM computed transverse moments for load case from Figure 9.20 (case for maximizing negative moments at Point 5') with transverse live-load moment capacity as listed in the Load Rating Manual.

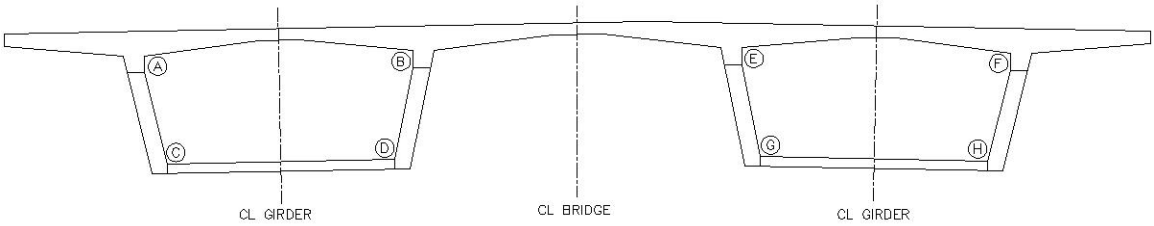

Figure 9.19: Additional critical sections for Spans 1 through 3 of the northbound and southbound structures for moments outside of top flange.

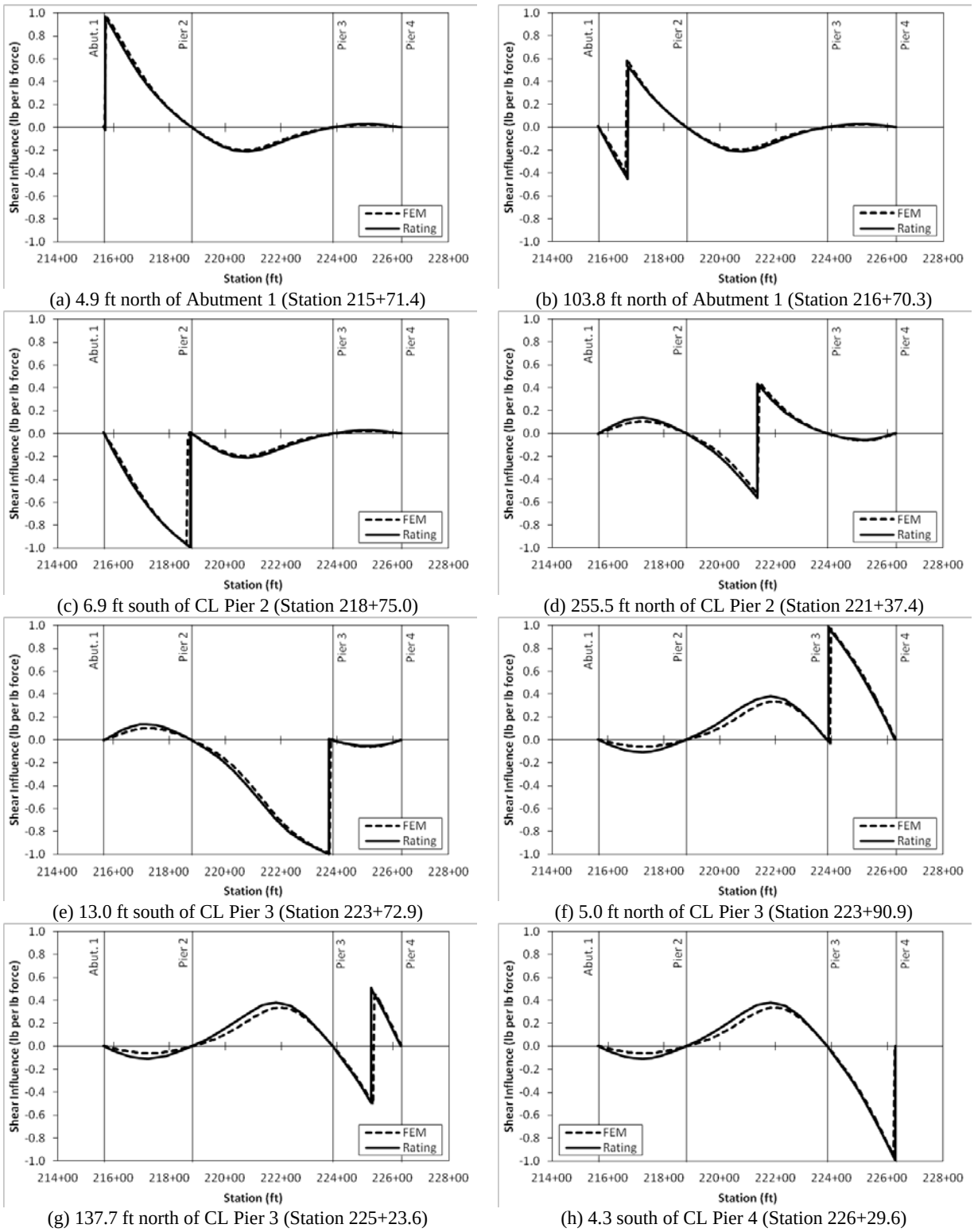

(a) 4.9 ft north of Abutment 1 (Station 215+71.4)

(b) 103.8 ft north of Abutment 1 (Station 216+70.3)

(c) 6.9 ft south of CL Pier 2 (Station 218+75.0)

(d) 255.5 ft north of CL Pier 2 (Station 221+37.4)

(e) 13.0 ft south of CL Pier 3 (Station 223+72.9)

(f) 5.0 ft north of CL Pier 3 (Station 223+90.9)

(g) 137.7 ft north of CL Pier 3 (Station 225+23.6)

(h) 4.3 south of CL Pier 4 (Station 226+29.6)

Figure 9.20: Load Rating Manual and validated FEM shear influence lines

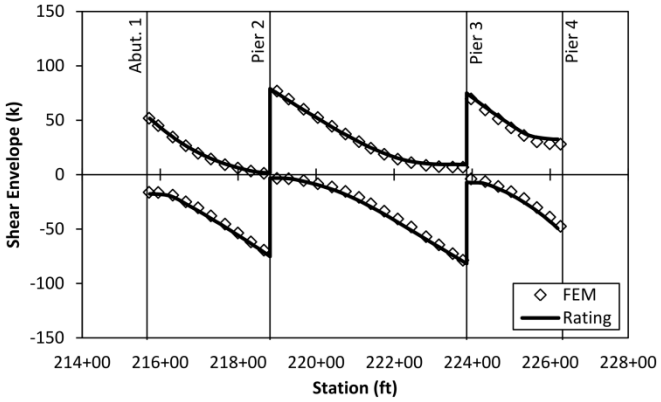

Figure 9.21: Comparison of HL-93 shear envelope for validated FEM and Load Rating Manual values. FEM values incorporate Load Rating Manual inconsistencies (i.e. impact factor of 1.33 applied to both lane loading and vehicle loading, and shear divided between all four webs of section).

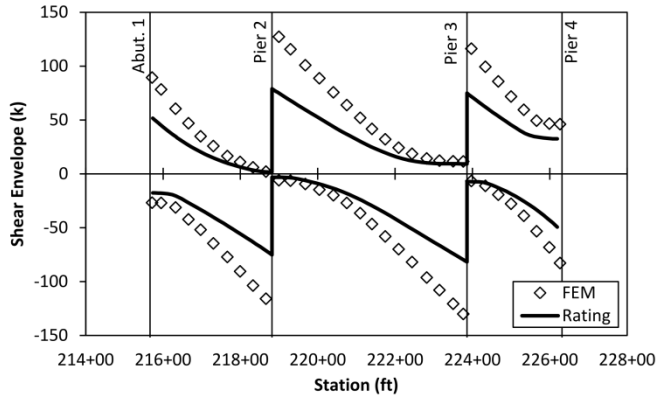

Figure 9.22: Comparison of HL-93 shear envelope for validated FEM and Load Rating Manual values. FEM values represent assumptions consistent with AASHTO LRFD (2010) (i.e. no impact factor for lane loading and shear divided by two webs instead of four).

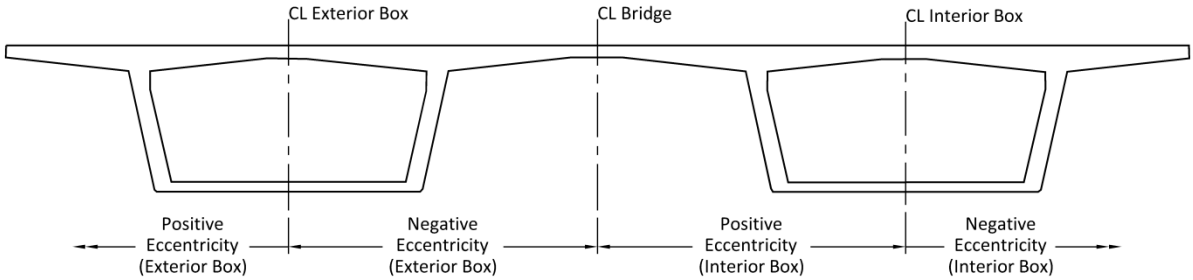

Figure 9.23: Eccentric loading convention from original Load Rating Manual

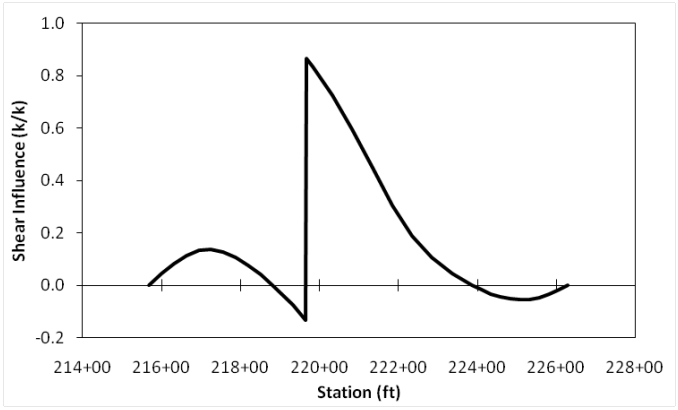

Figure 9.24: Load Rating Manual shear influence diagram for Southbound Span 2 - Abscissa 83.5 ft (station 219+65.4)

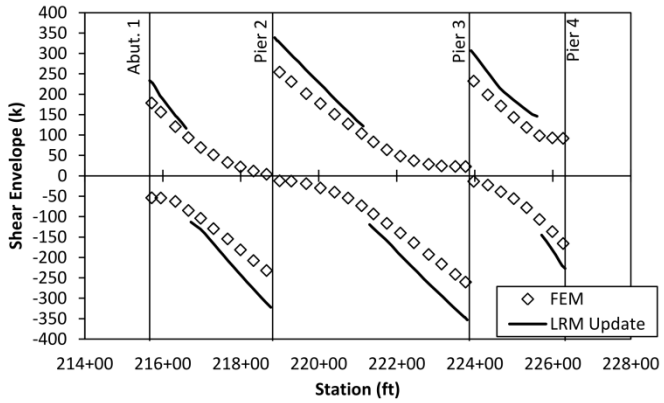

Figure 9.25: Comparison of HL-93 total-section undistributed shear envelope for validated FEM and updated Load Rating Manual values. FEM values represent assumptions consistent with AASHTO LRFD (2010).

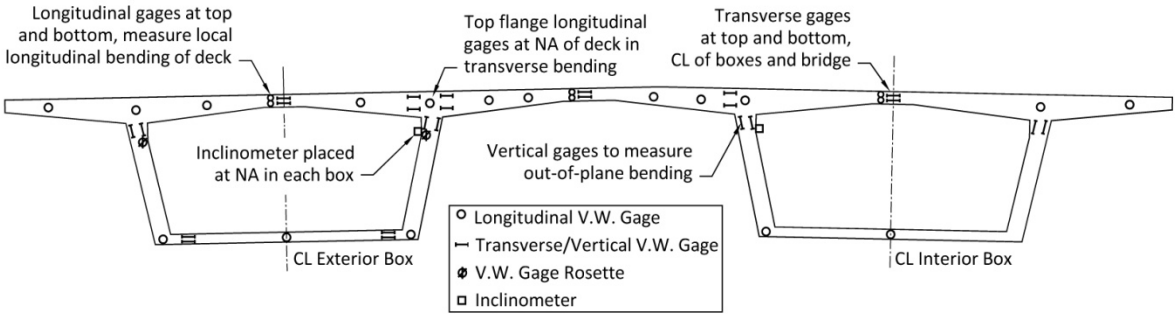

Figure 10.1: Recommendations for static instrumentation

Appendix A: VWSG and Thermistor Figures

List of Figures - Appendix A

This appendix provides figures to illustrate the locations of the VWSG and thermistor gages within the cross sections of the bridge with their assigned labels annotated in the same figures. In addition, figures showing the typical installation of gages are provided. Some of these figures give nominal dimensions for the spacing of gages. Table 2.2 provides the measured locations of the gages within the bridge.

The gages were installed by Polyphase, an electrical contractor hired by Flatiron/Manson. During installation, Polyphase used their own naming scheme. Roctest was hired by Flatiron/Manson to connect the VWSG gages to the dataloggers. When setting up the datalogger, Roctest used their own naming scheme, which was different from the Polyphase naming scheme. After determining the final locations of the gages, the University of Minnesota (UMN) assigned new names to the gages to better associate each gage with its type and location. In Figure A.1 through A.14, the labels are shown as "UMN gage label (installation gage number) (connection gage number)." The installation gage number refers to the number assigned by Polyphase during construction of the bridge. The connection gage number refers to the number assigned by Roctest during the connection of the system to the dataloggers.

The VWSG label assigned by the UMN consisted of eight characters. The first character denoted whether the strain (V) or temperature (T) of the gage was being measured. In other words, each VWSG gage had two labels, one for strain and one for temperature. Only the strain labels are provided in this appendix, though the temperature labels for each VWSG are identical to those shown with the substitution of T for V. The second character in the label denoted whether the gage was located in the northbound (N) bridge or southbound (S) bridge. The third and fourth characters denoted the location of the gage along the length of the bridge (i.e., 03, 04, 05, 06, 07, 08, 09, 14, or 15). The fifth character in the label specified whether the gage was located in the interior (I) box or the exterior (E) box. The sixth character specified whether the gage was located within the top flange (T), the bottom flange (B), the east web (E) (i.e., on the interior side of the bridge for the southbound bridge and exterior side for the northbound bridge), the west web (W) (i.e., on the exterior side of the bridge for the southbound bridge and interior side for the northbound bridge), or the middle web (M) (i.e., in the case of Span 4) of the box. The seventh character denoted whether the orientation of the gage was longitudinal (L), transverse (T), vertical (V), or at 45° (A). Finally, the eighth character was a number assigned to the gage to separate it from the other gages with the same first seven characters in their label. The eighth character typically increased from exterior to interior and from the top of the section down. For example, the gage labeled "VS07EEA1" represented the 45° strain gage of the rosette in the east (interior web) of the exterior (west) box near midspan of Span 2 of the southbound bridge. All labels are eight digits by default. If a sensor's first seven digits were unique to that sensor, the eighth digit was "1."

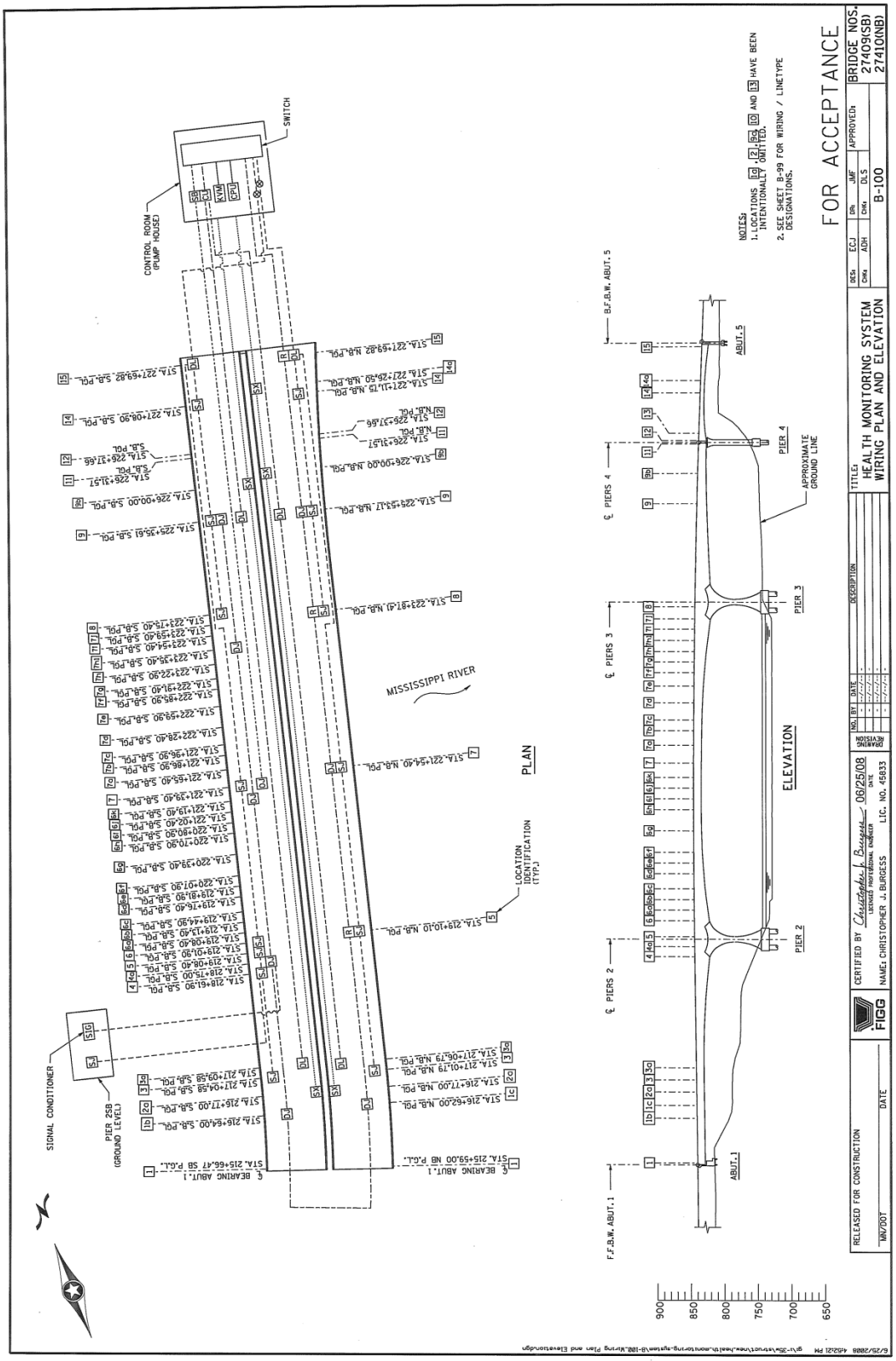

Figure A.1: Overall bridge view showing instrumented locations

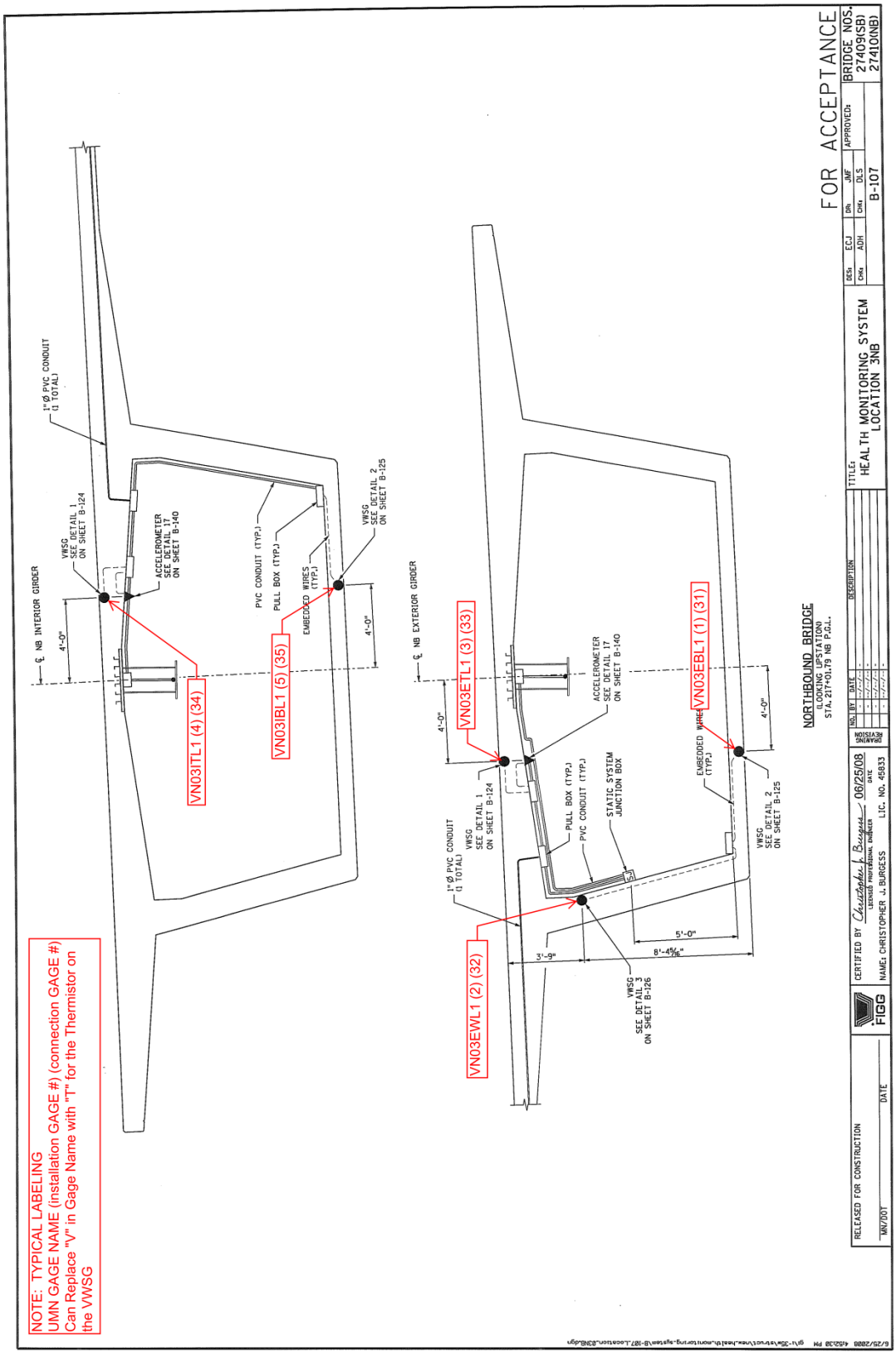

Figure A.2: Location 3NB instrumentation

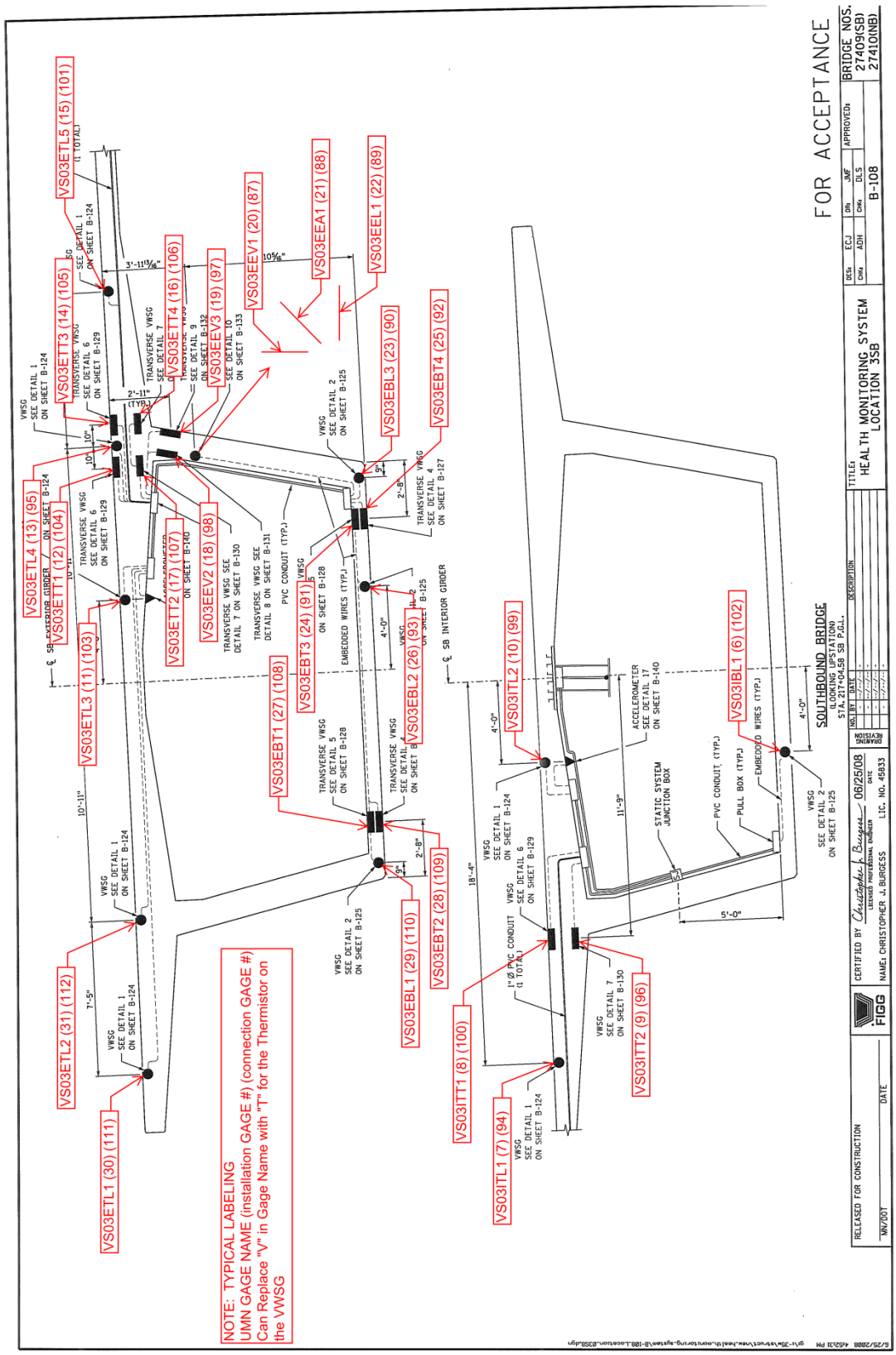

Figure A.3: Location 3SB instrumentation

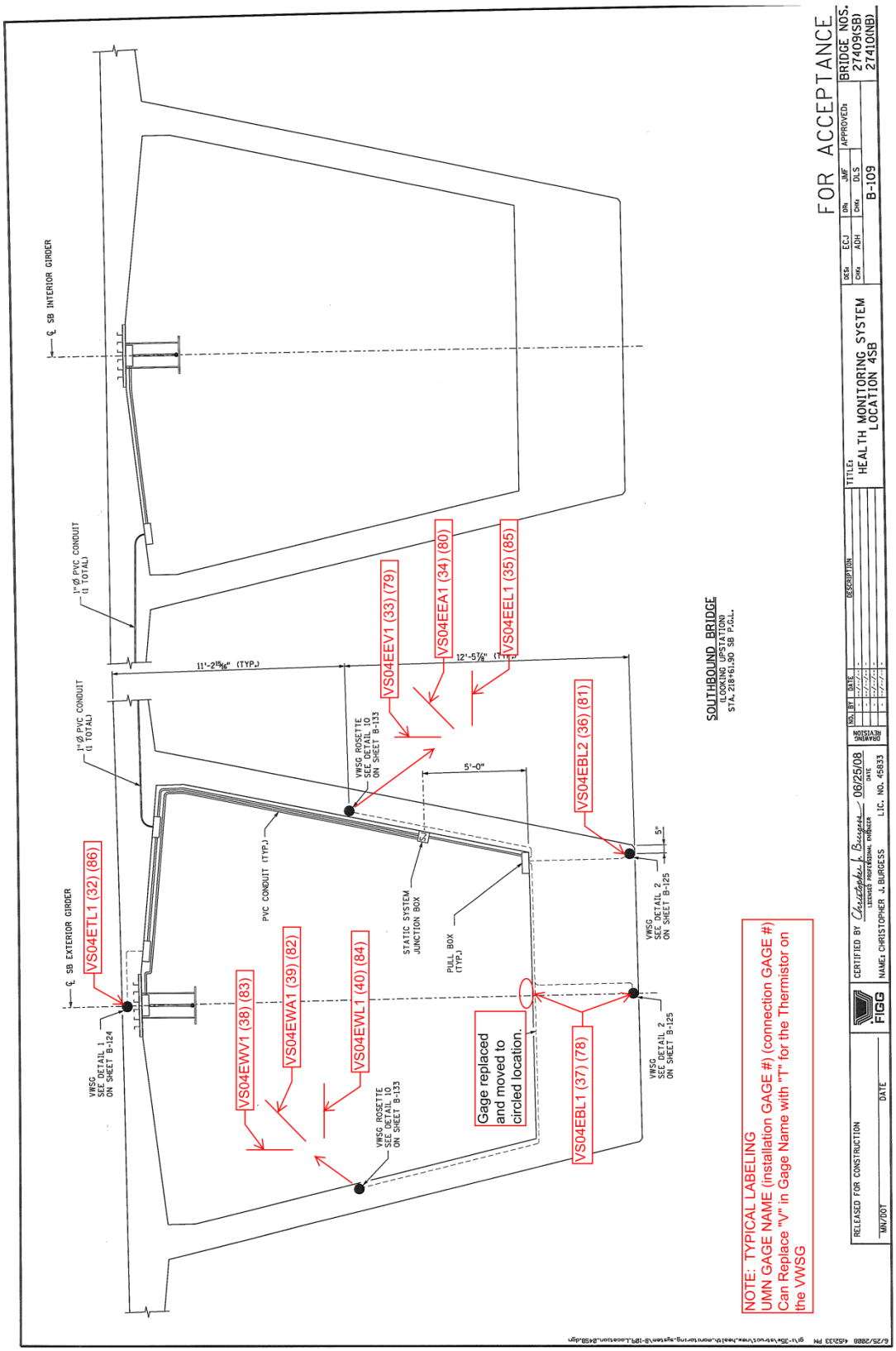

Figure A.4: Location 4SB instrumentation

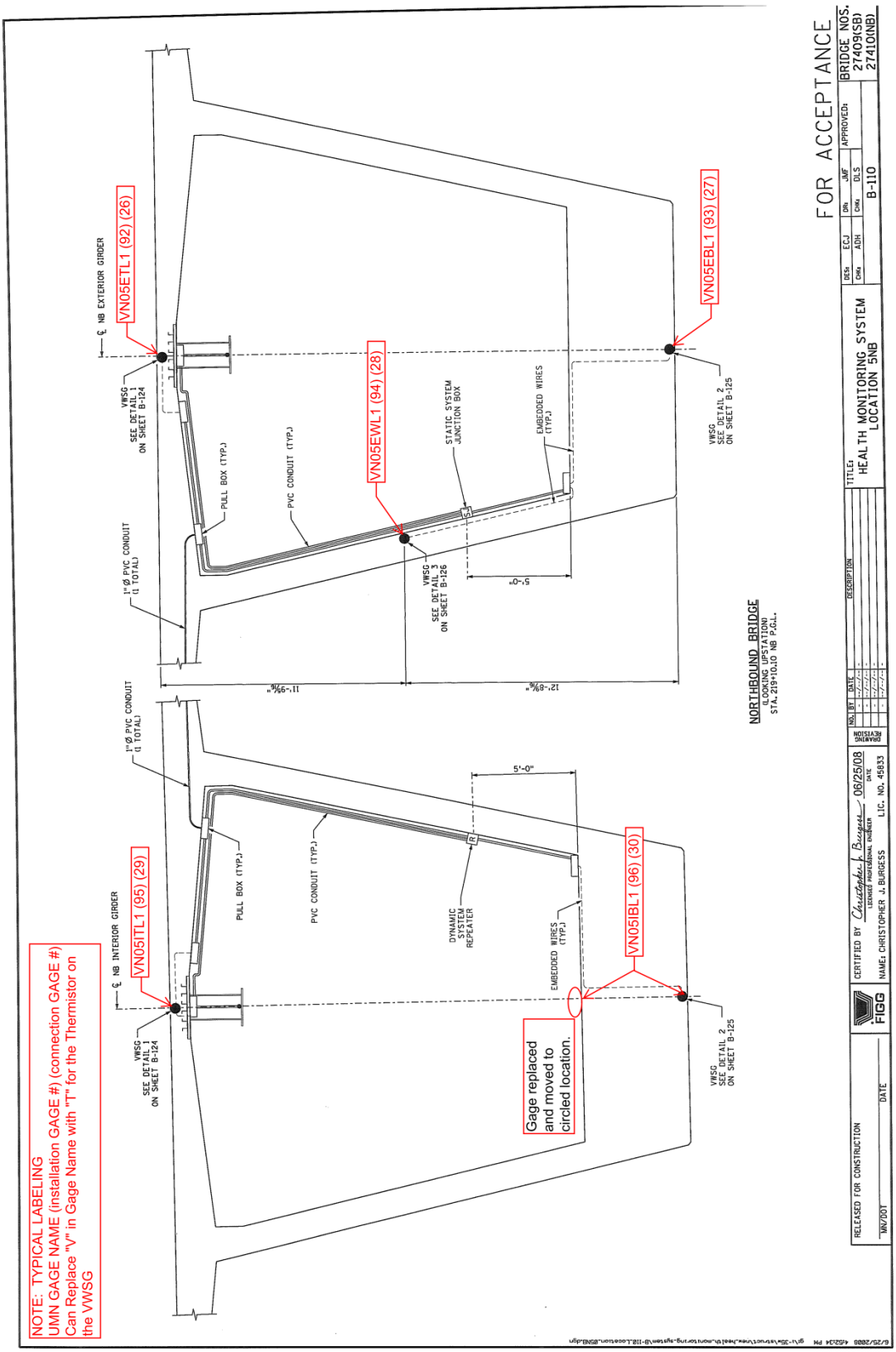

Figure A.5: Location 5NB instrumentation

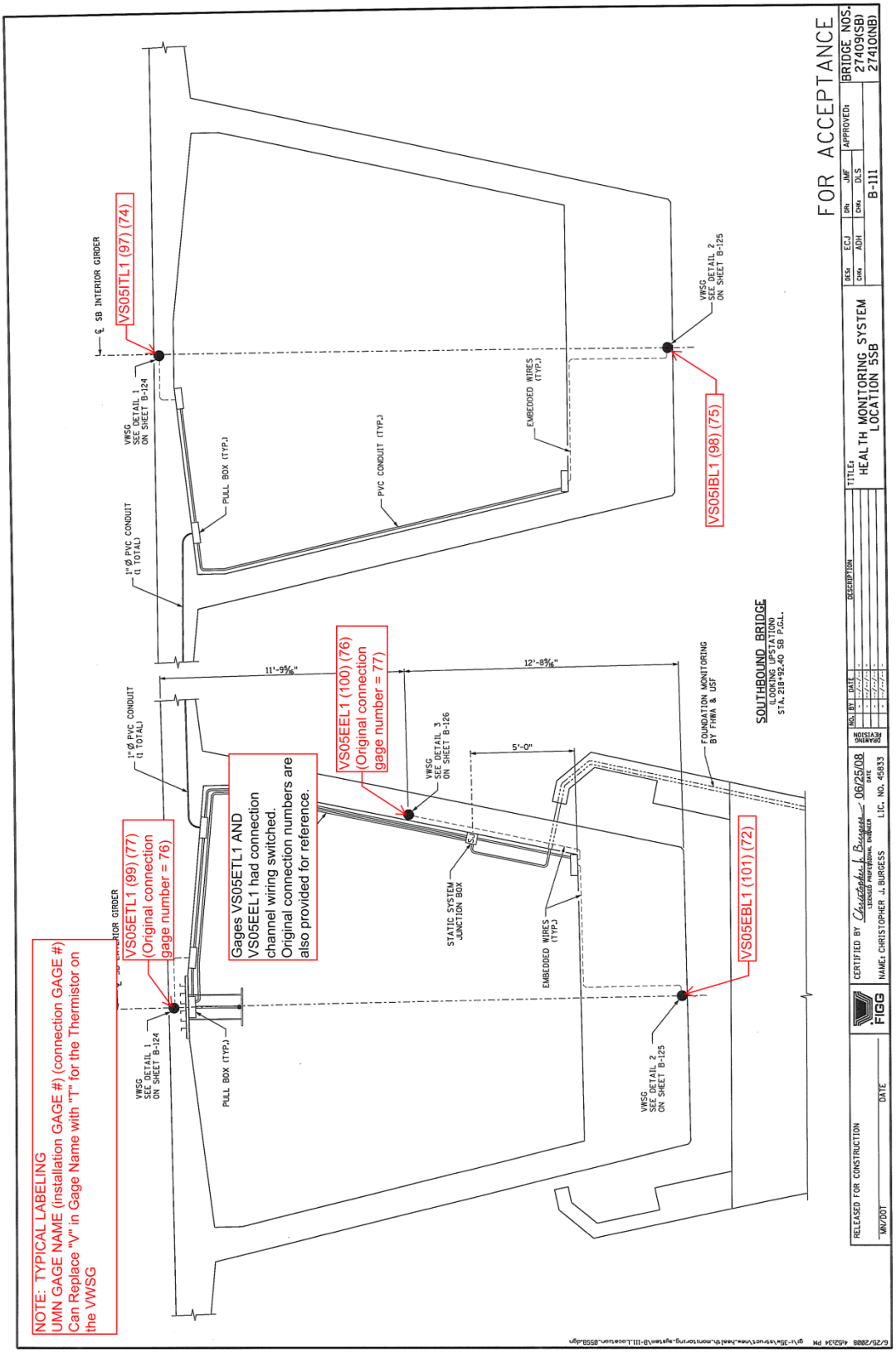

Figure A.6: Location 5SB instrumentation

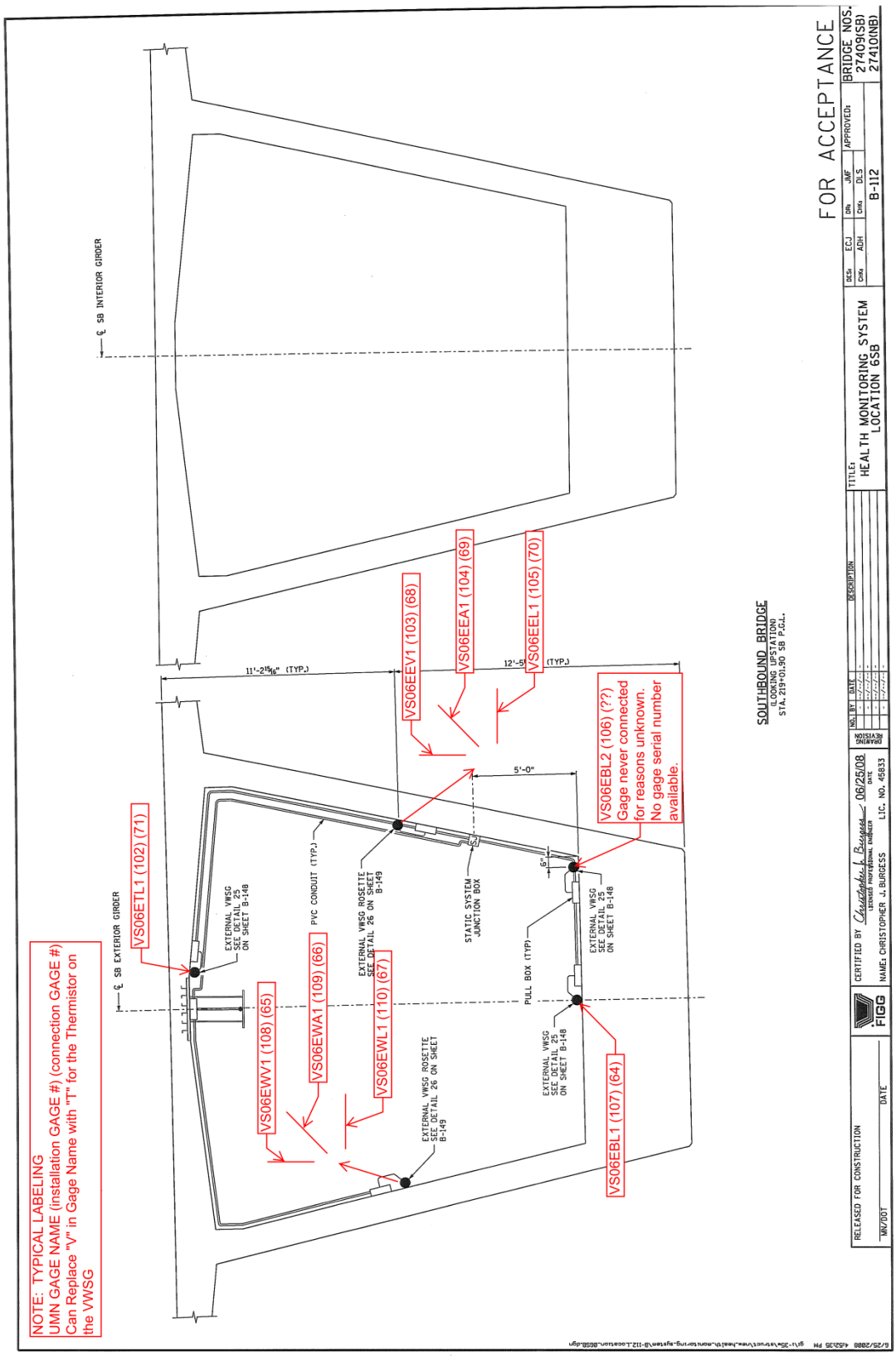

Figure A.7: Location 6SB instrumentation

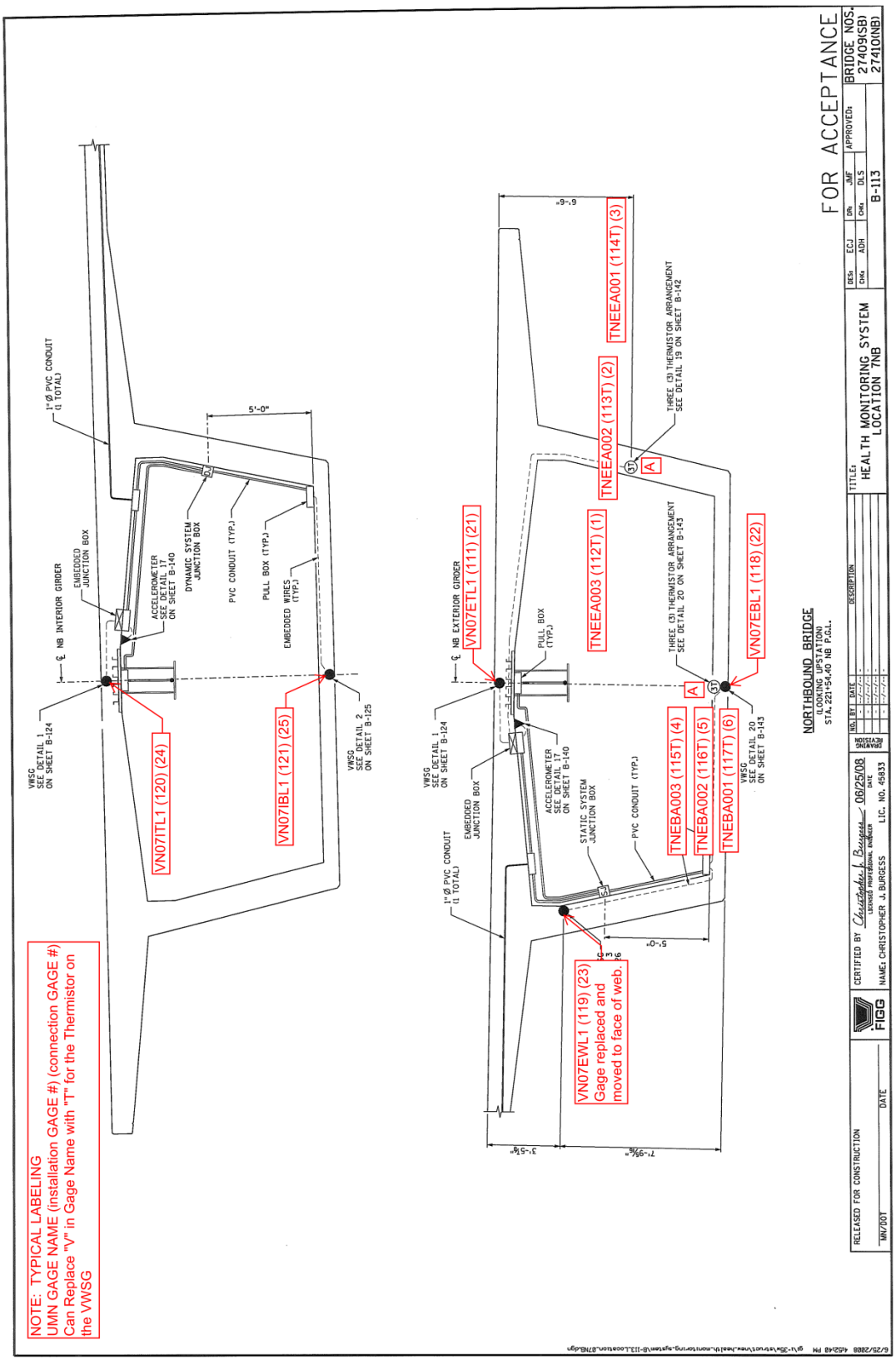

Figure A.8: Location 7NB instrumentation

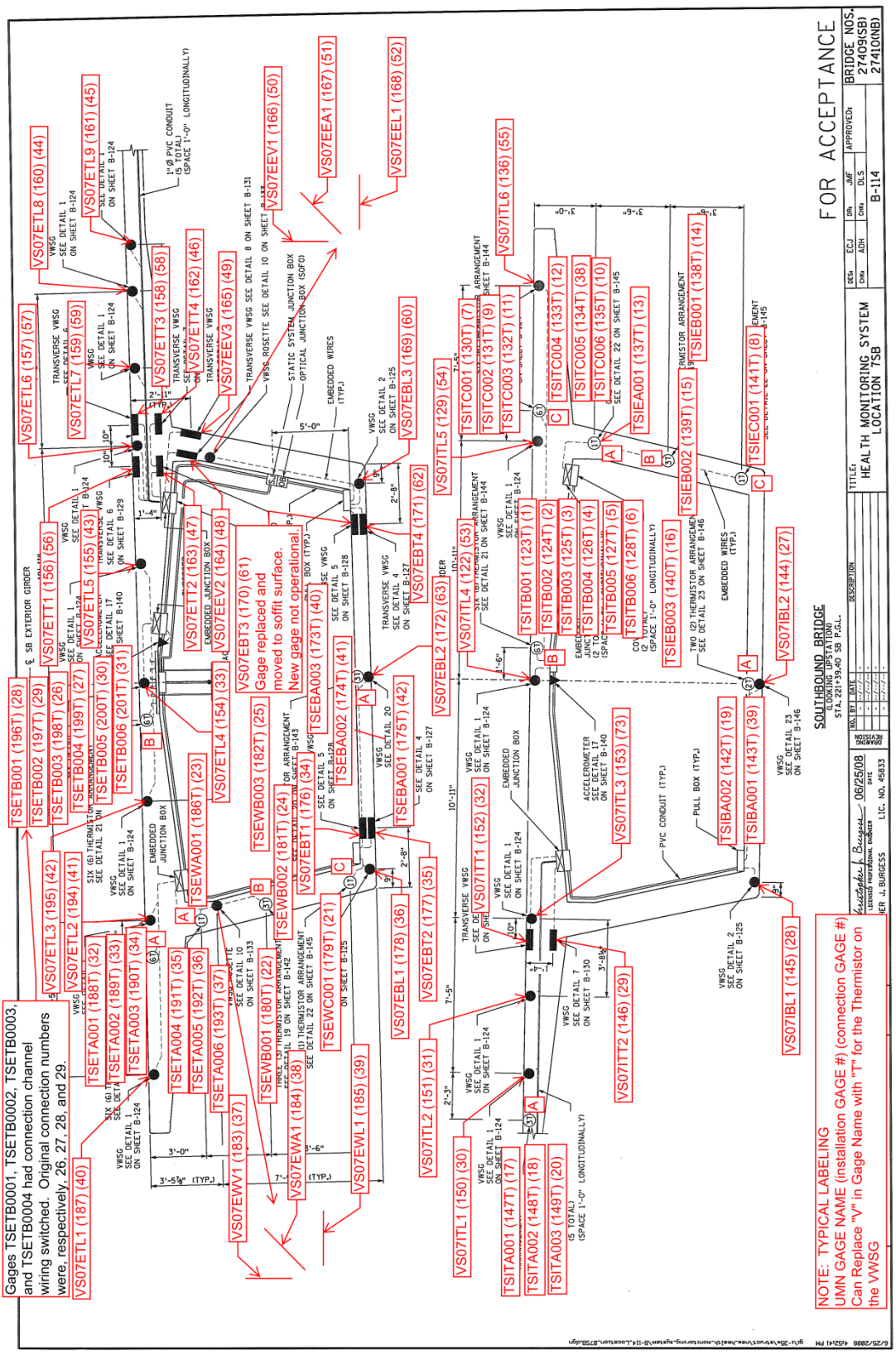

Figure A.9: Location 7SB instrumentation

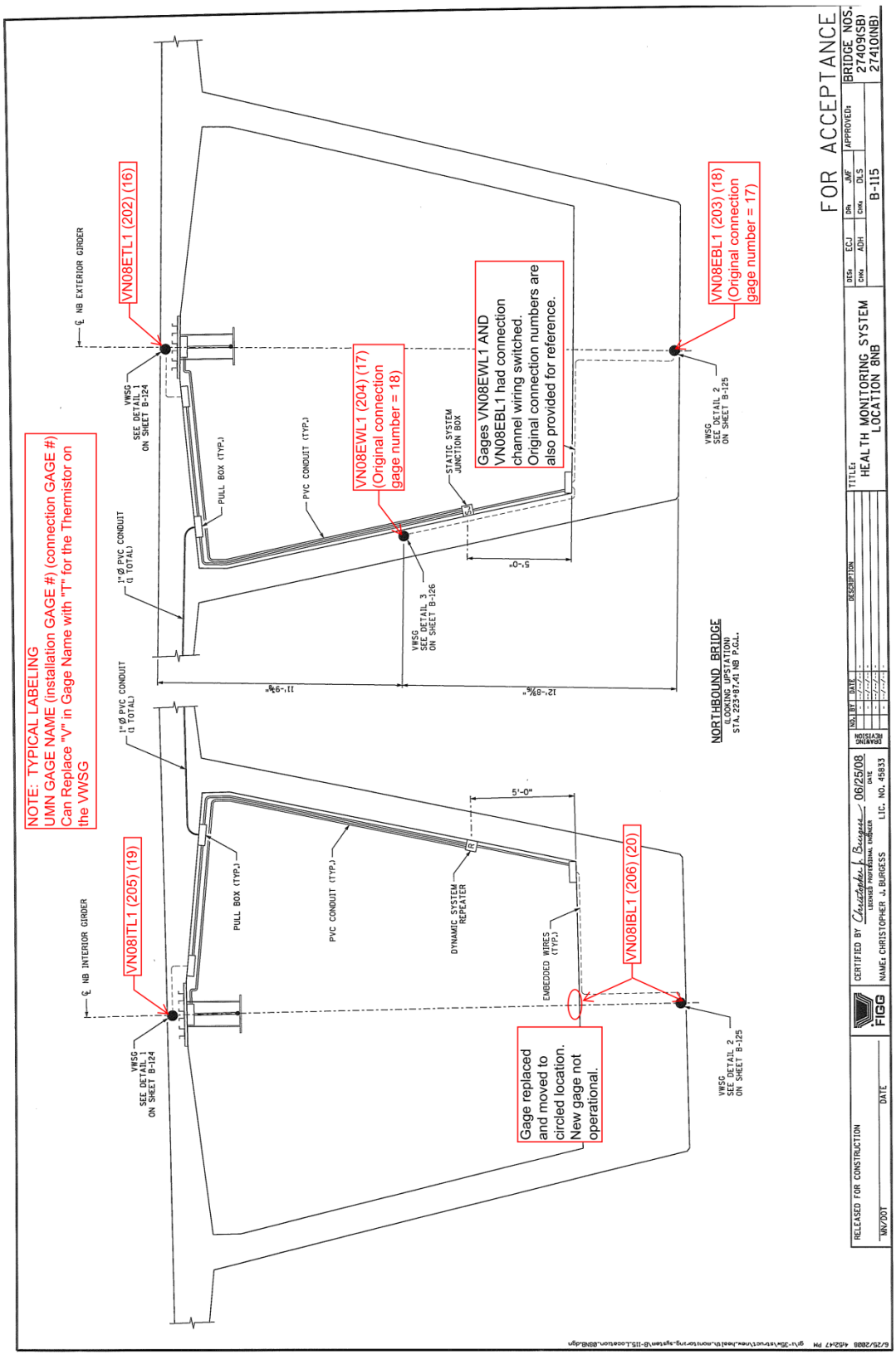

Figure A.10: Location 8NB instrumentation

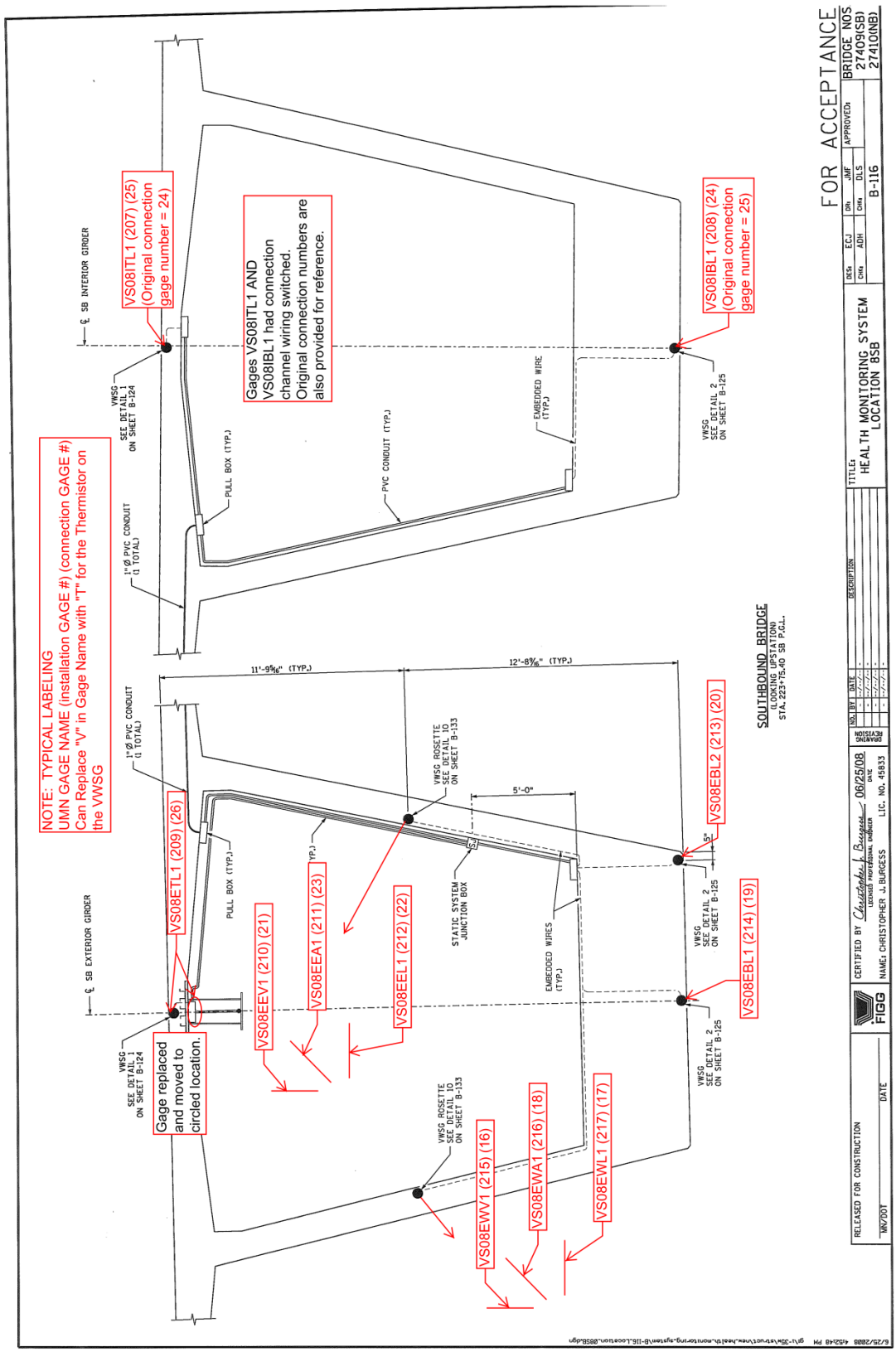

Figure A.11: Location 8SB instrumentation

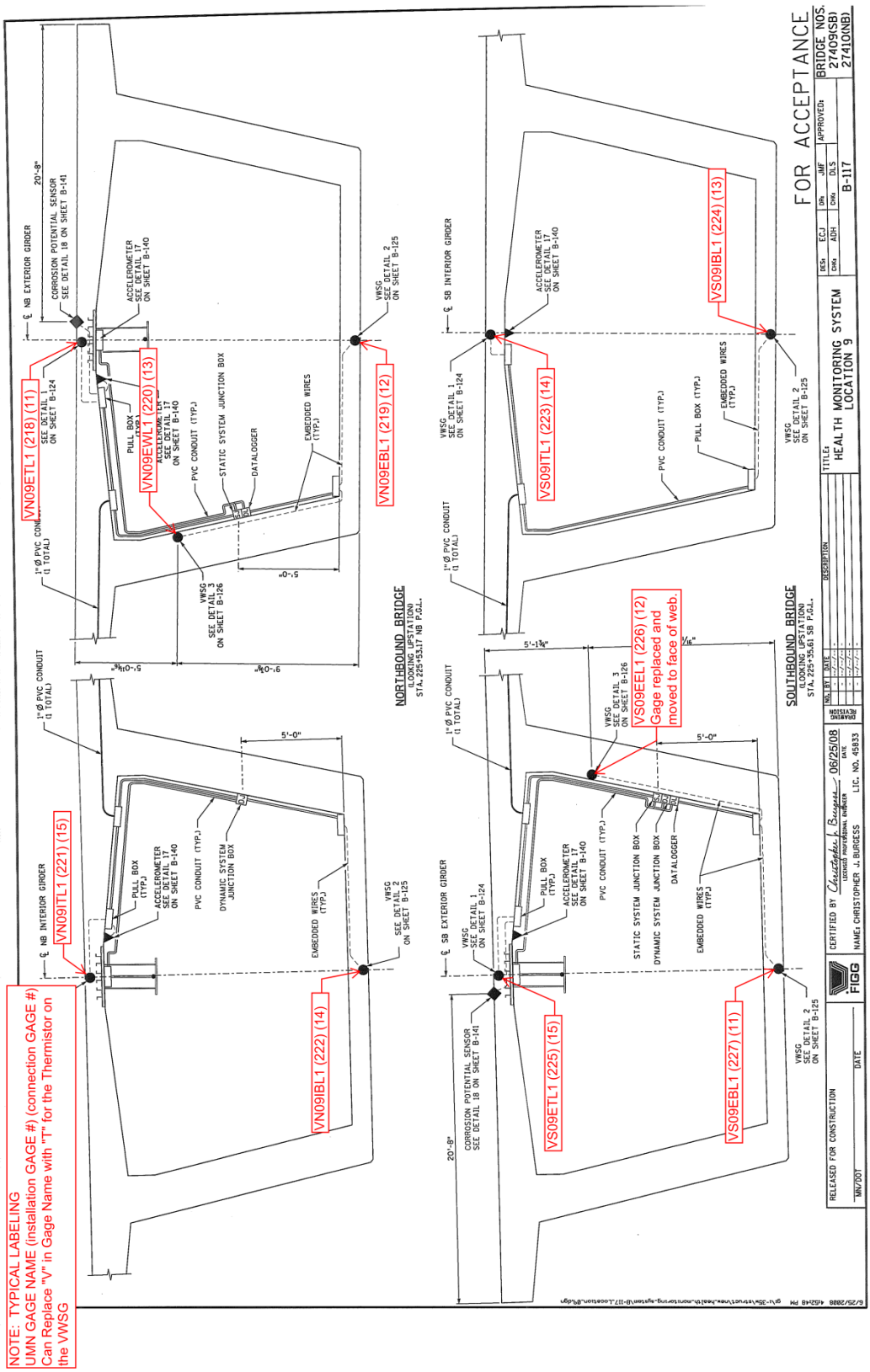

Figure A.12: Location 9NB and 9SB instrumentation

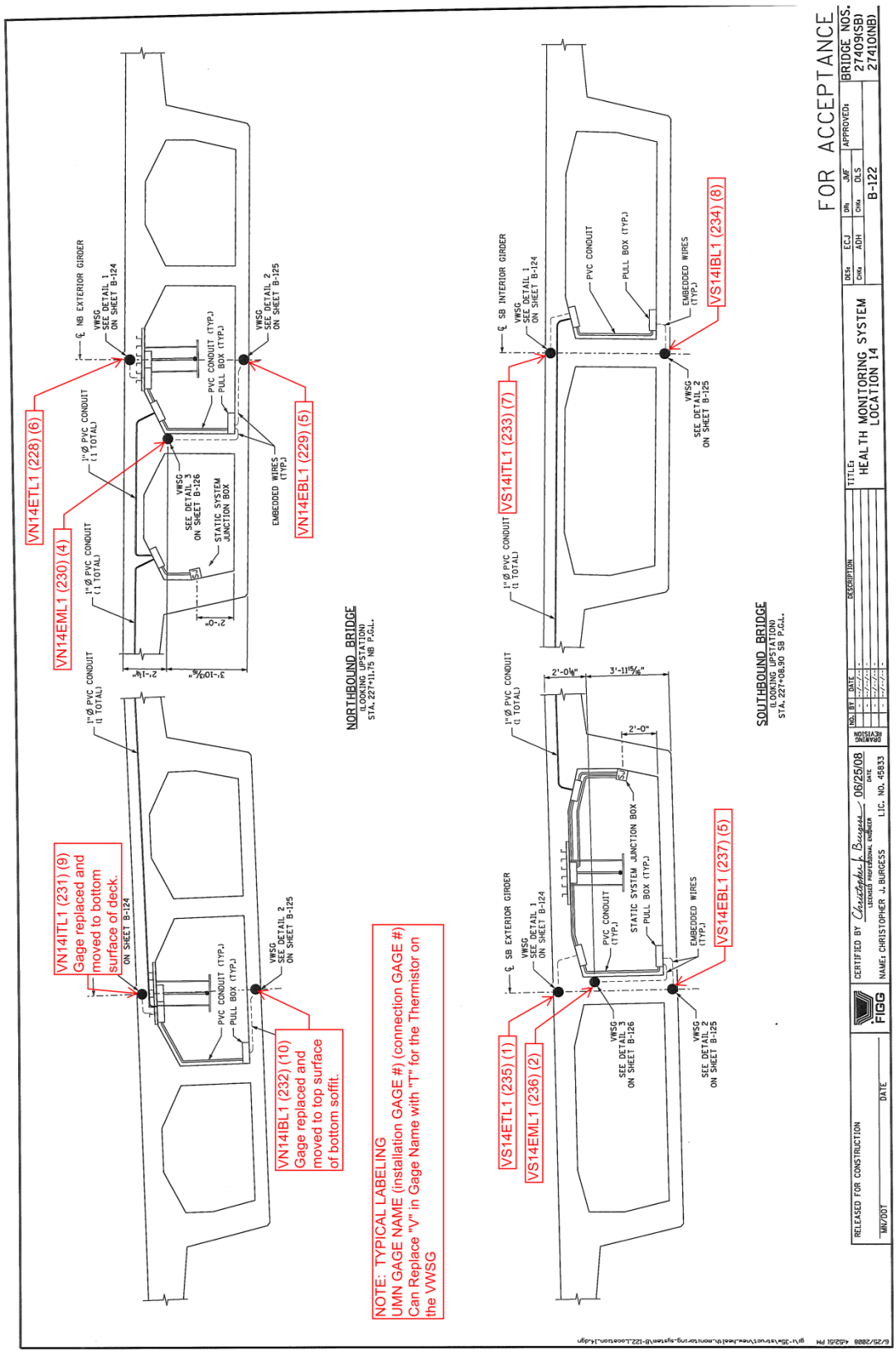

Figure A.13: Location 14NB and 14SB instrumentation

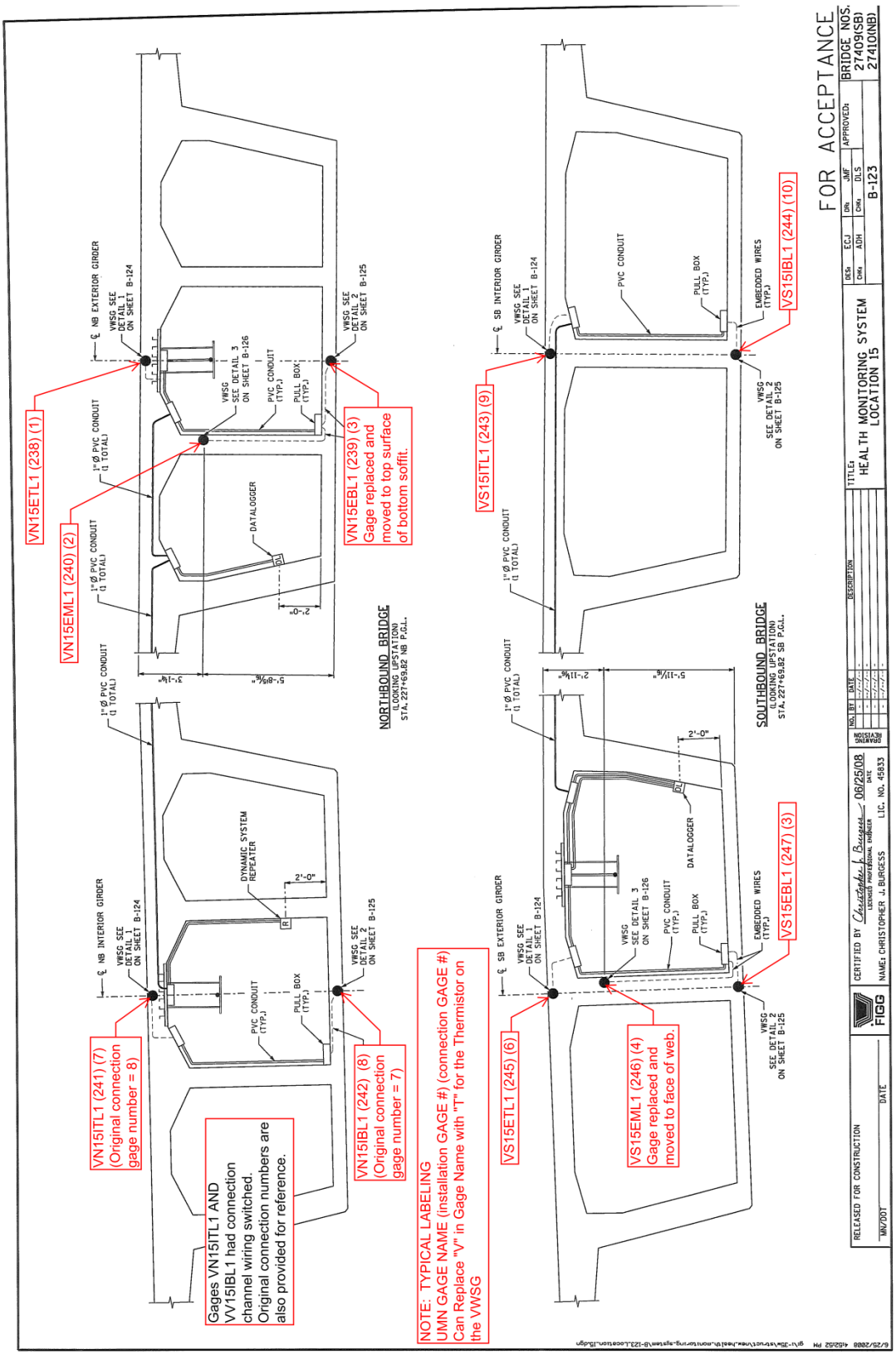

Figure A.14: Location 15NB and 15SB instrumentation

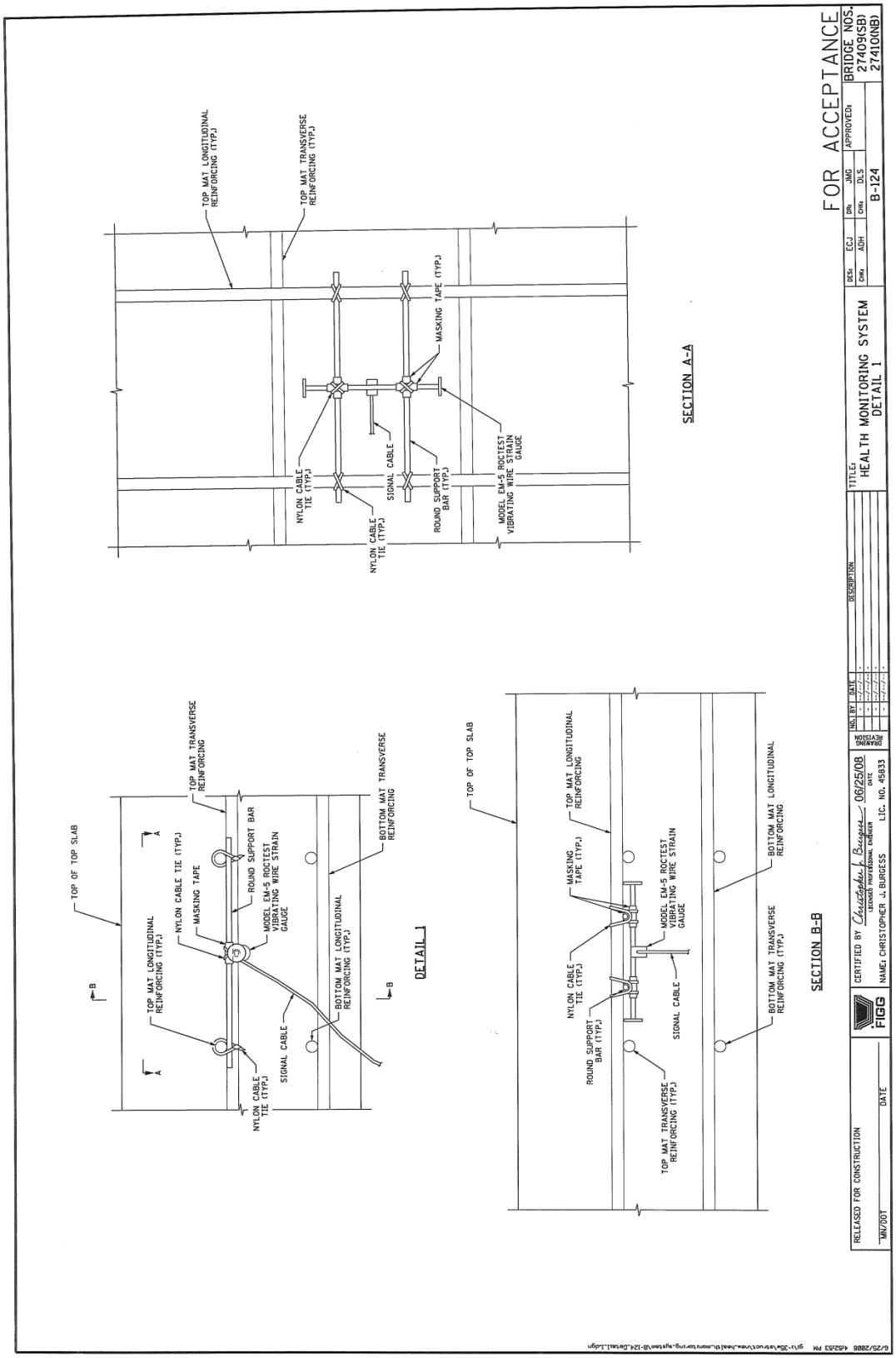

Figure A.15: VWSG Detail 1

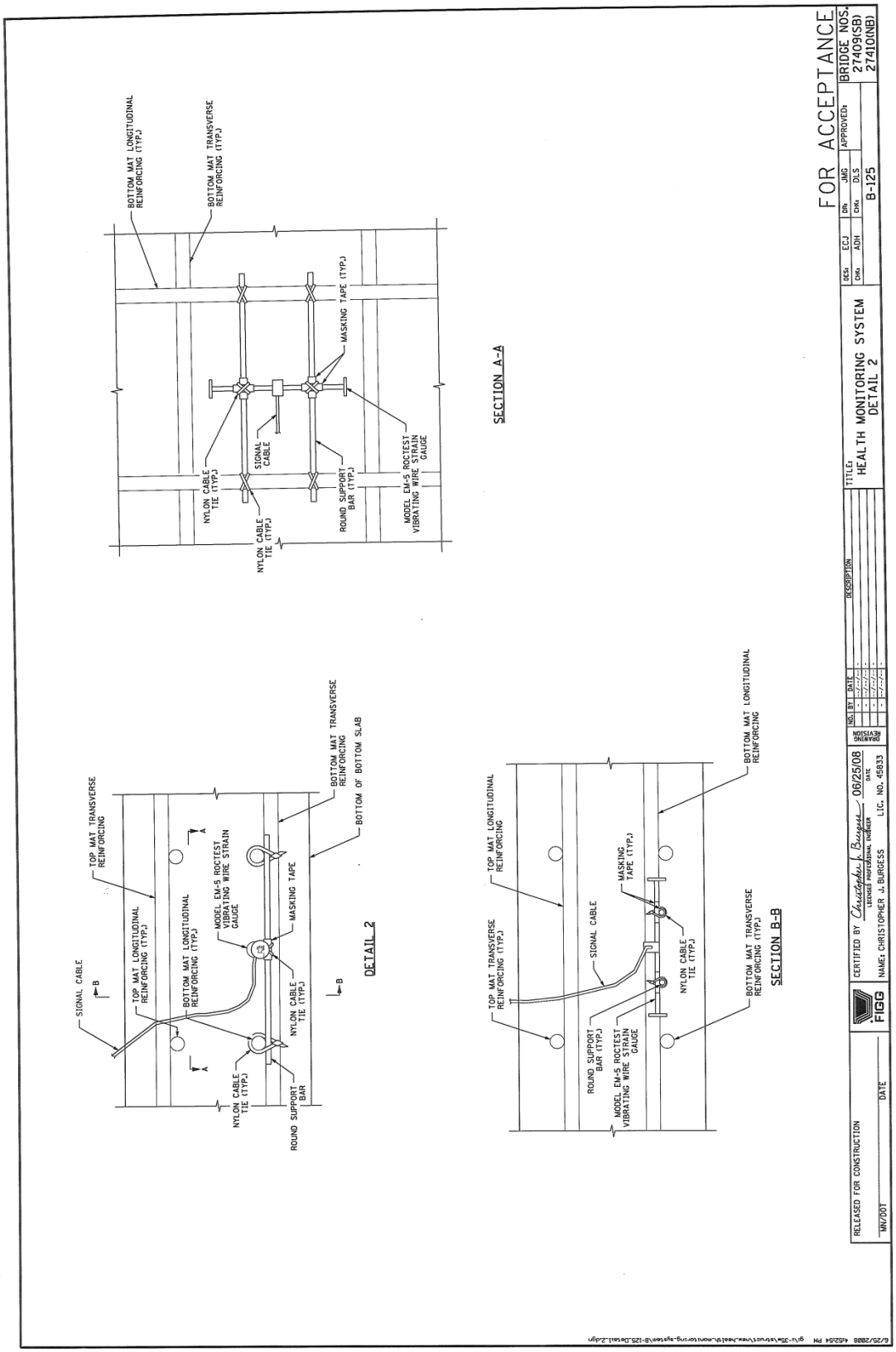

Figure A.16: VWSG Detail 2

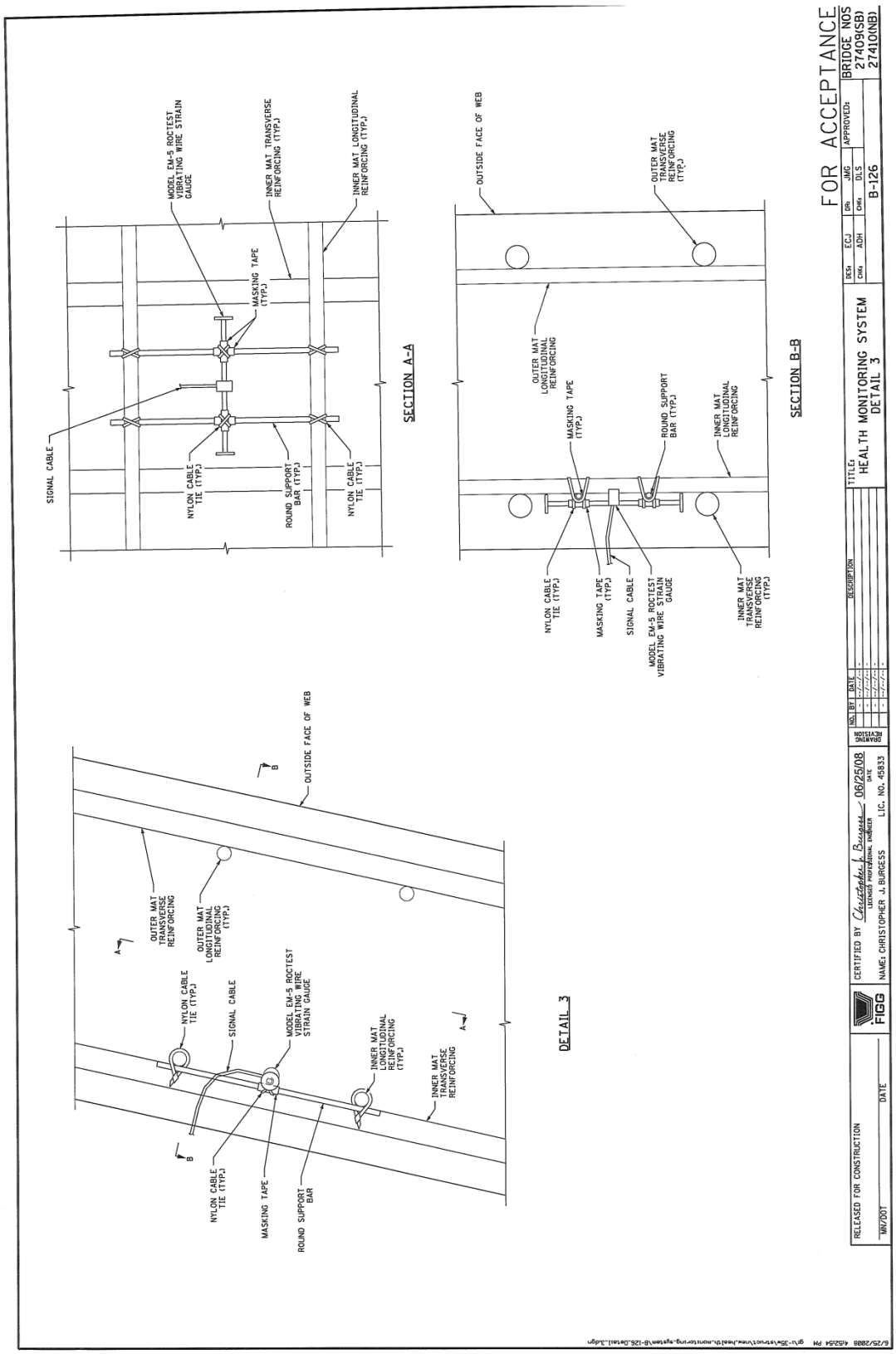

Figure A.17: VWSG Detail 3

Figure A.18: VWSG Detail 4

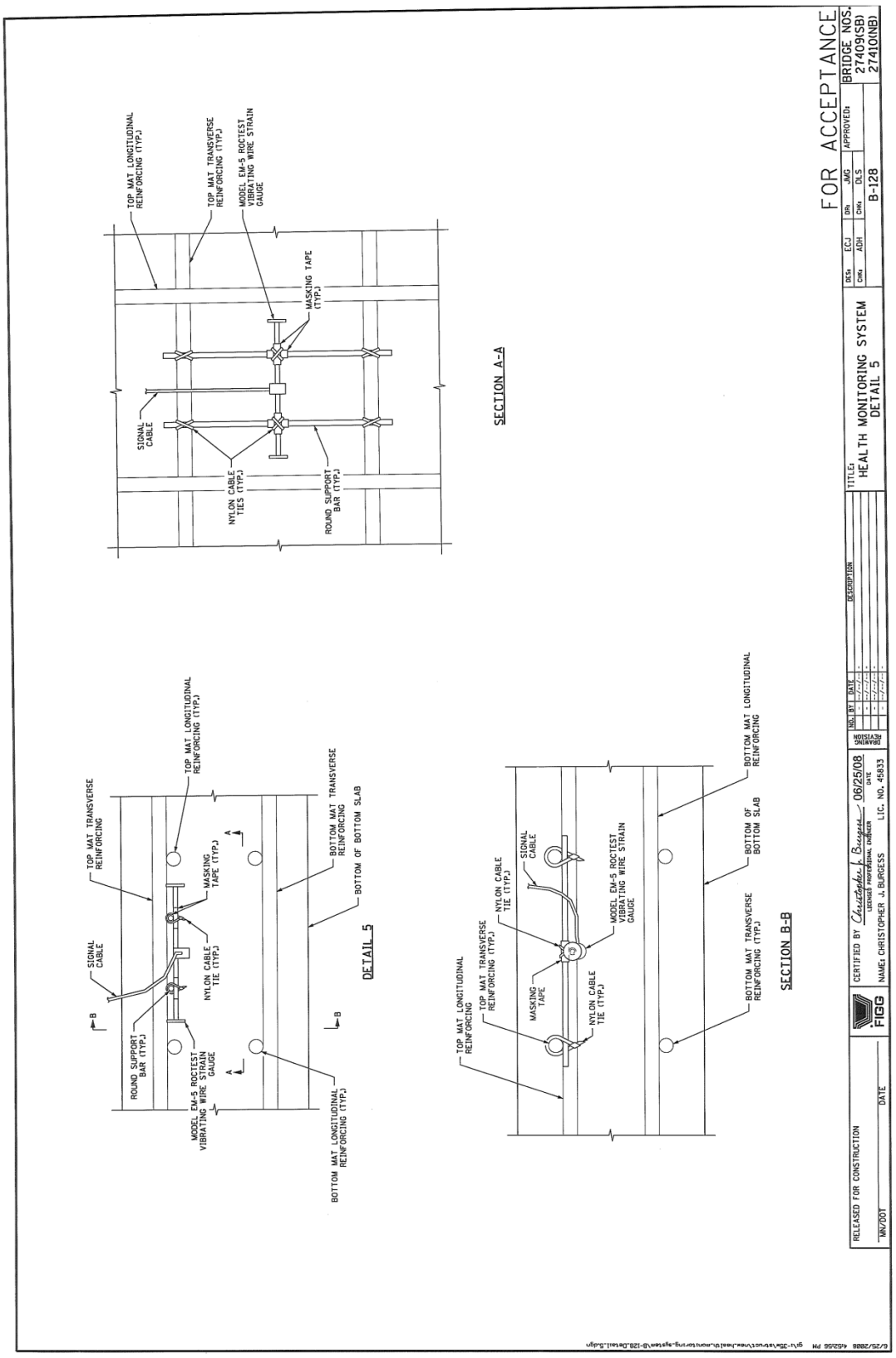

Figure A.19: VWSG Detail 5

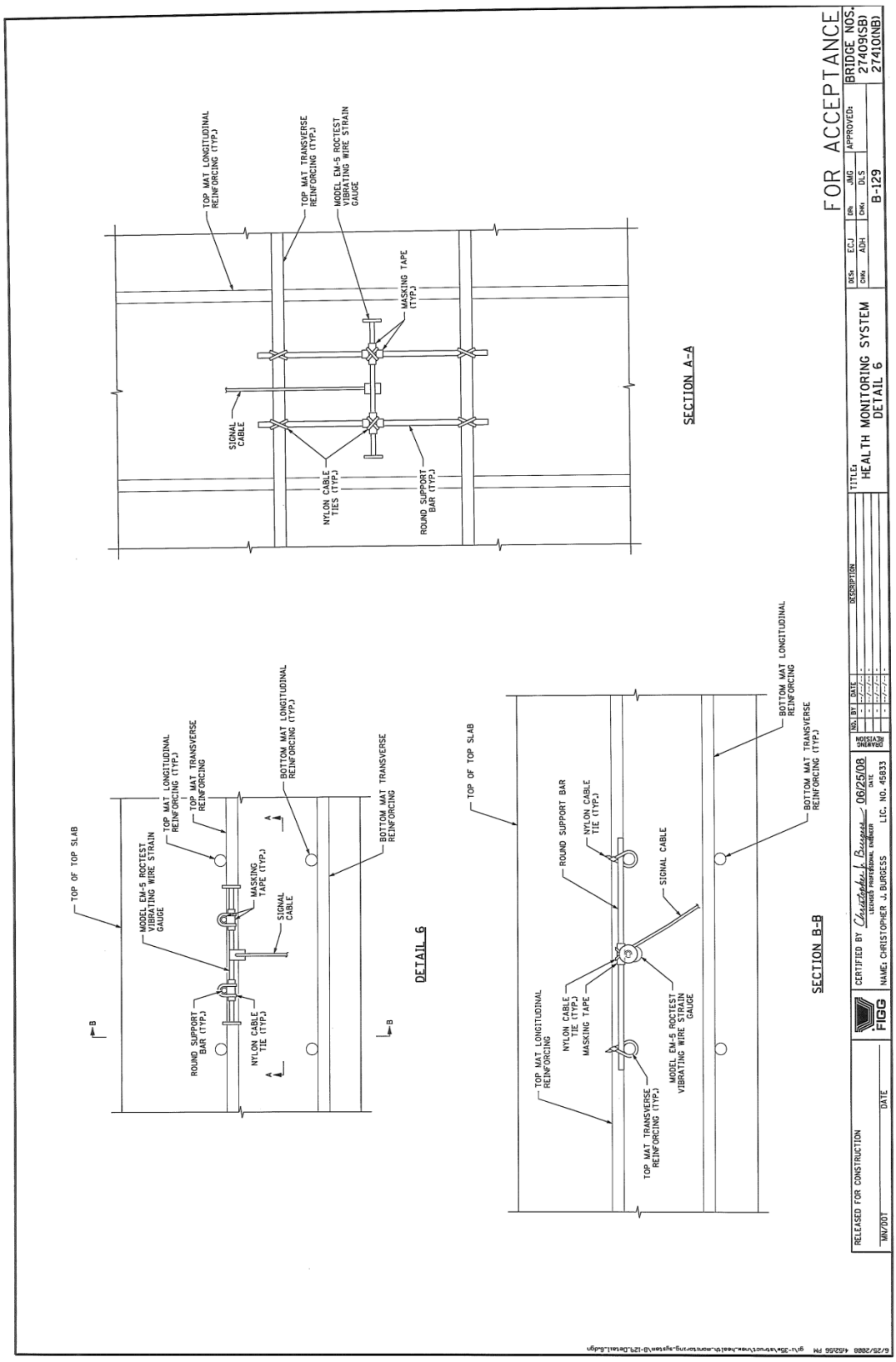

Figure A.20: VWSG Detail 6

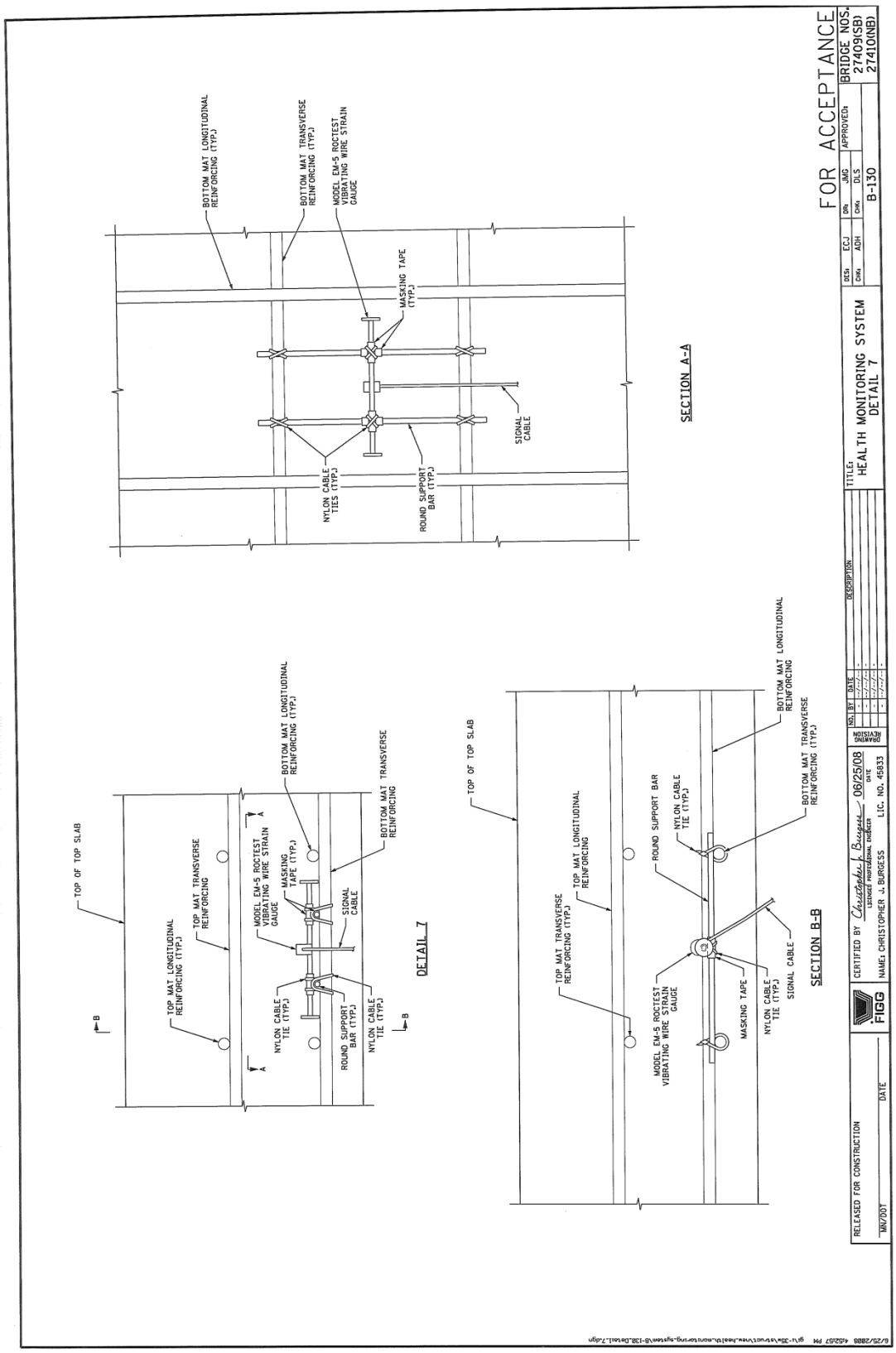

Figure A.21: VWSG Detail 7

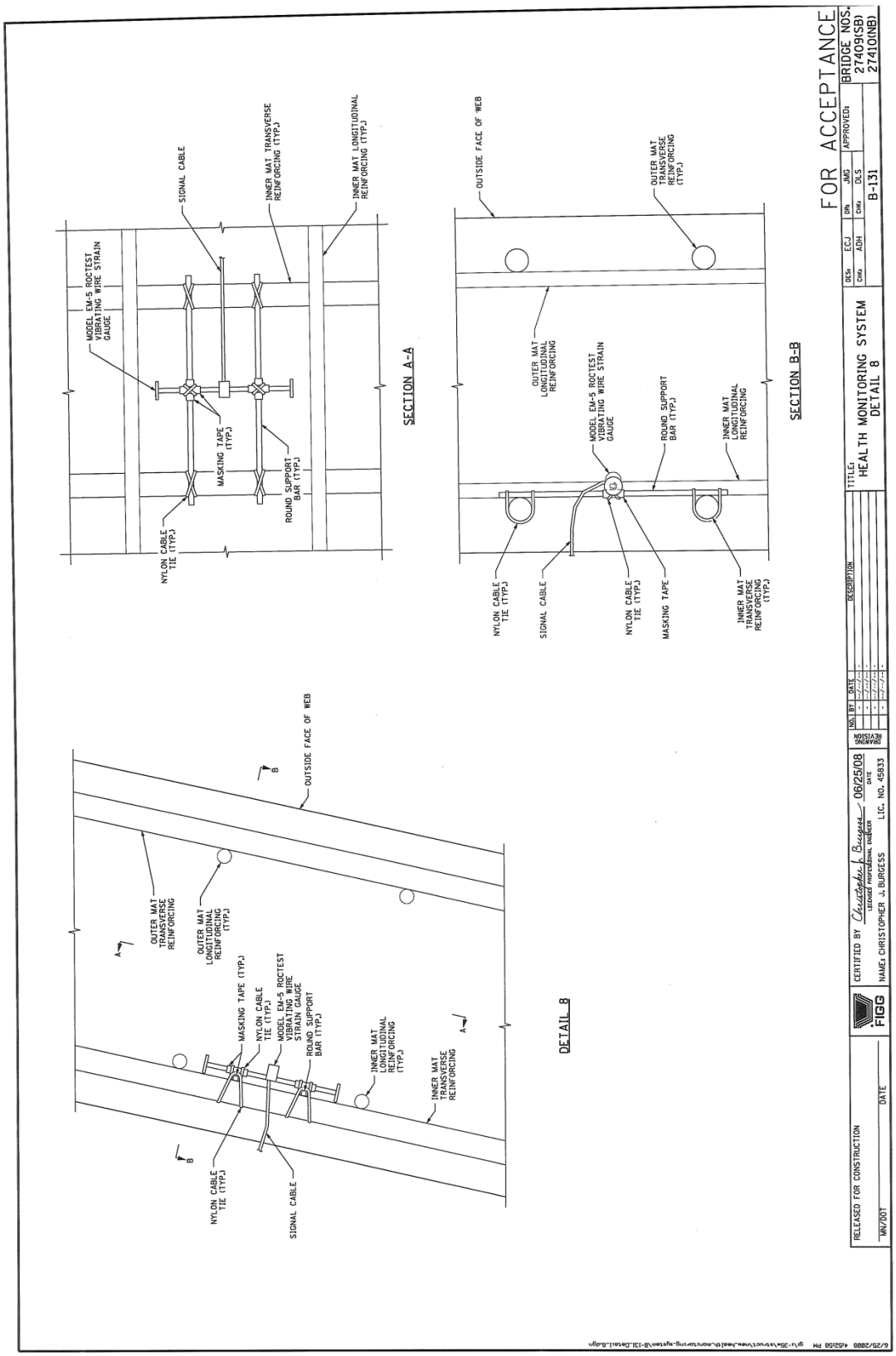

Figure A.22: VWSG Detail 8

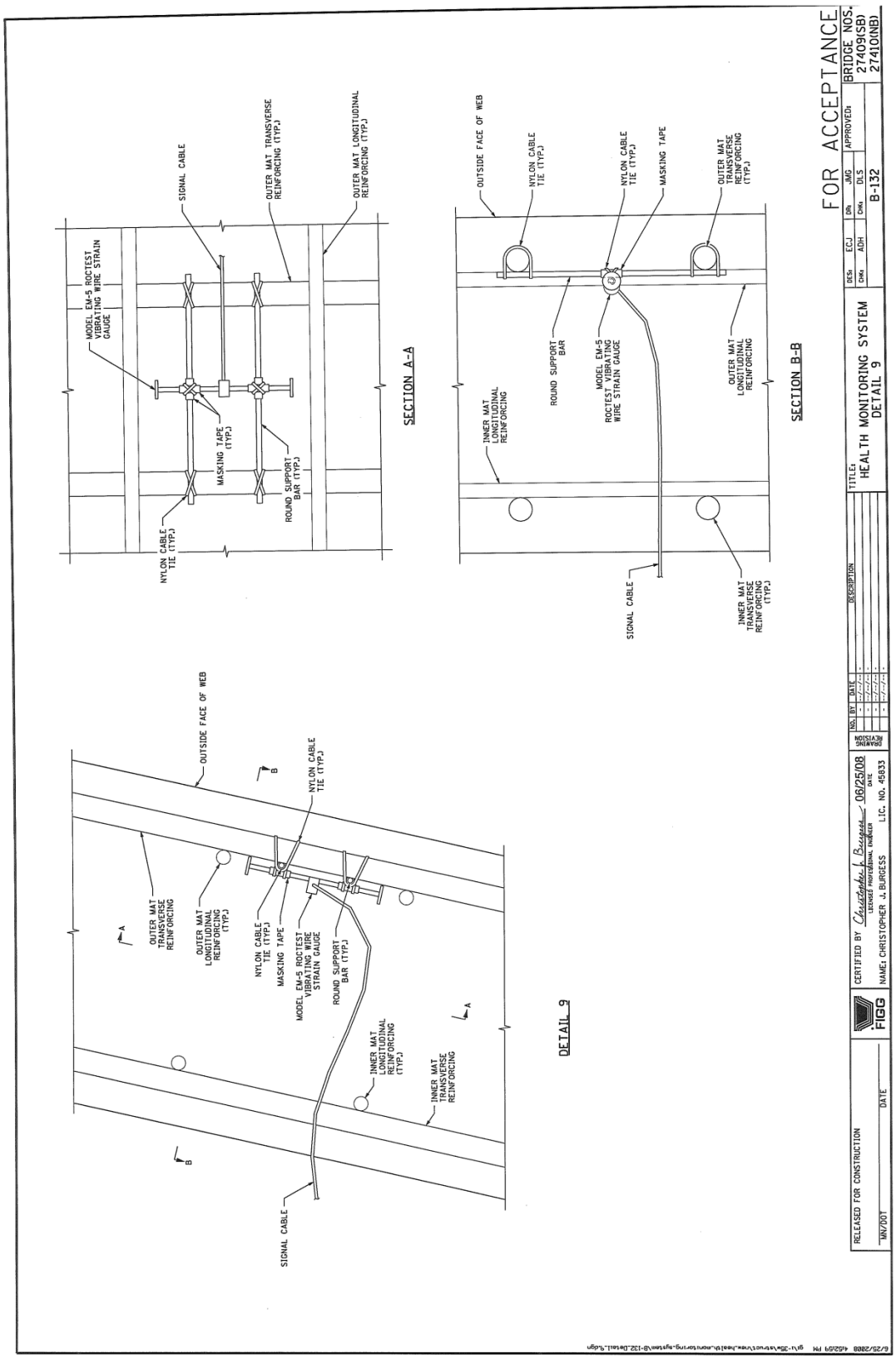

Figure A.23: VWSG Detail 9

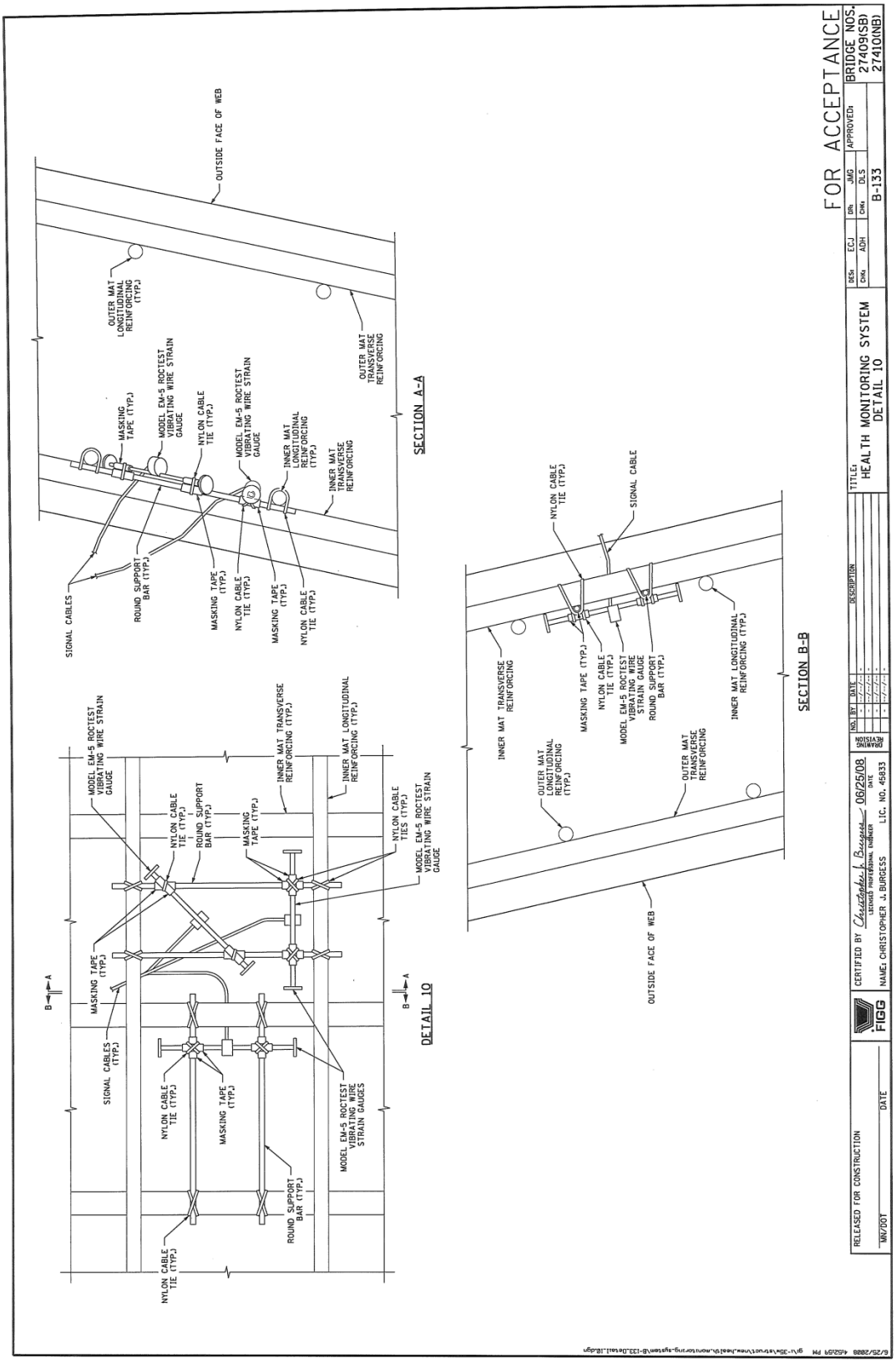

Figure A.24: VWSG Detail 10

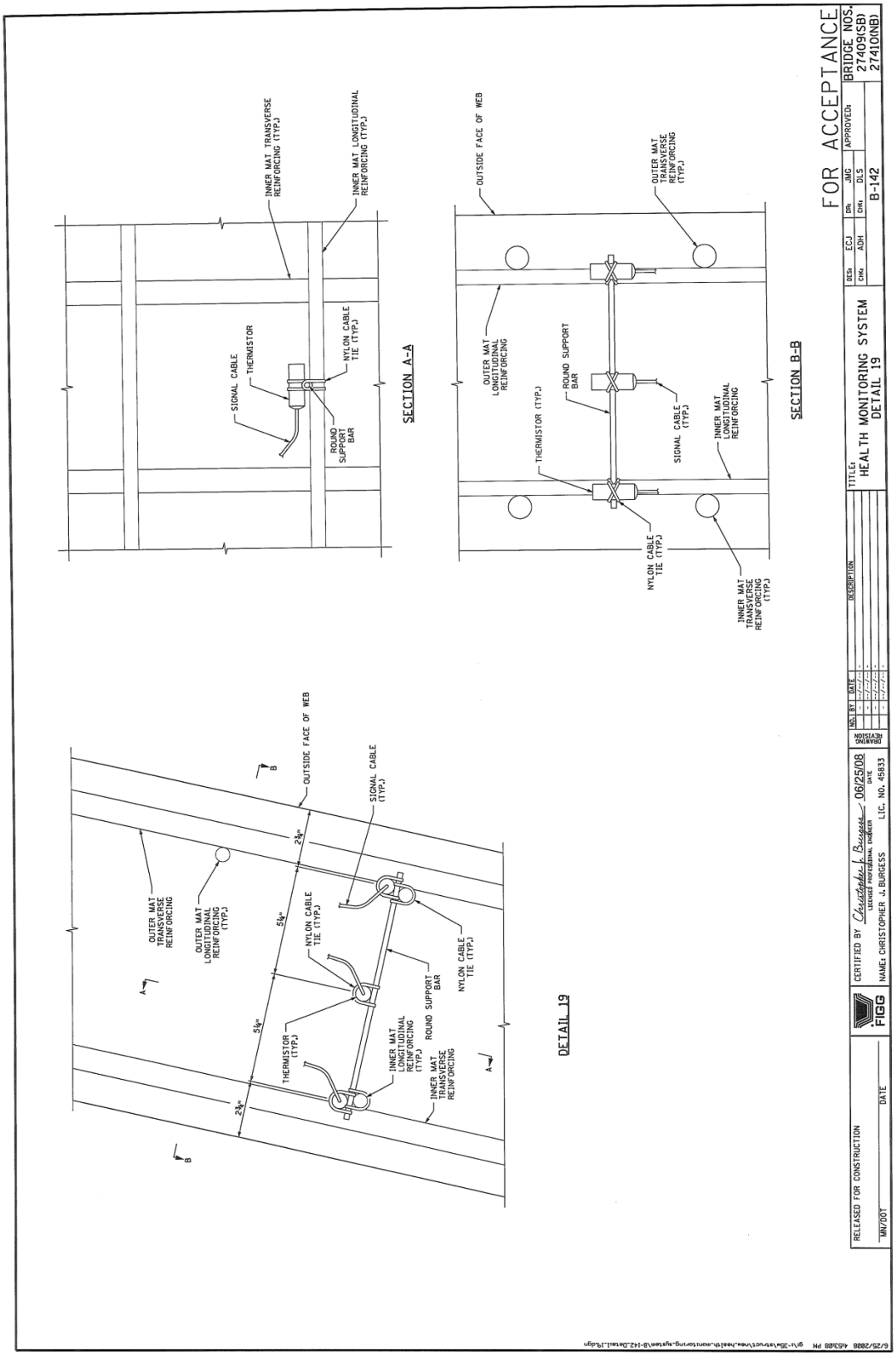

Figure A.25: Thermistor Detail 19

Figure A.26: Thermistor Detail 20

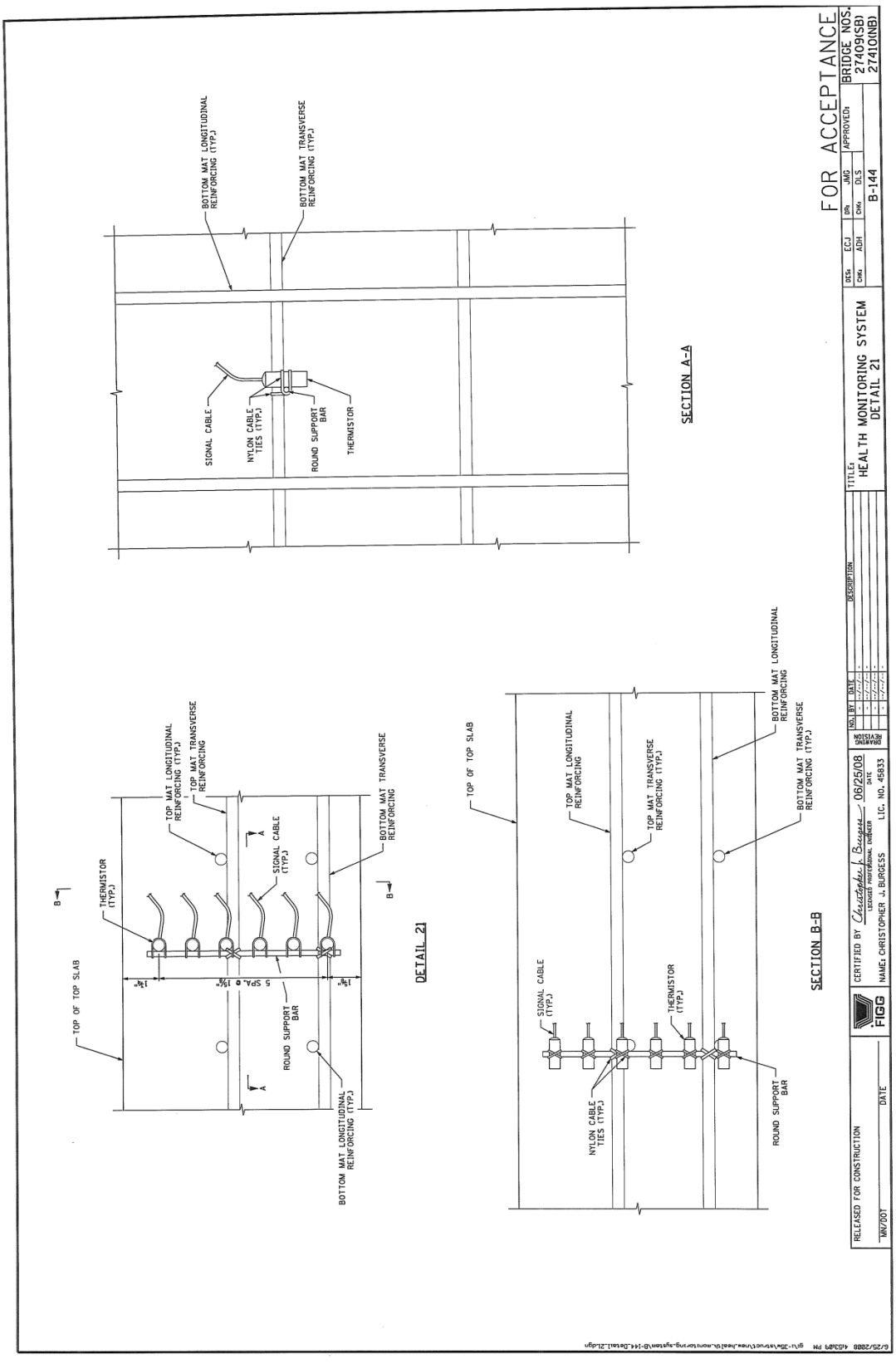

Figure A.27: Thermistor Detail 21

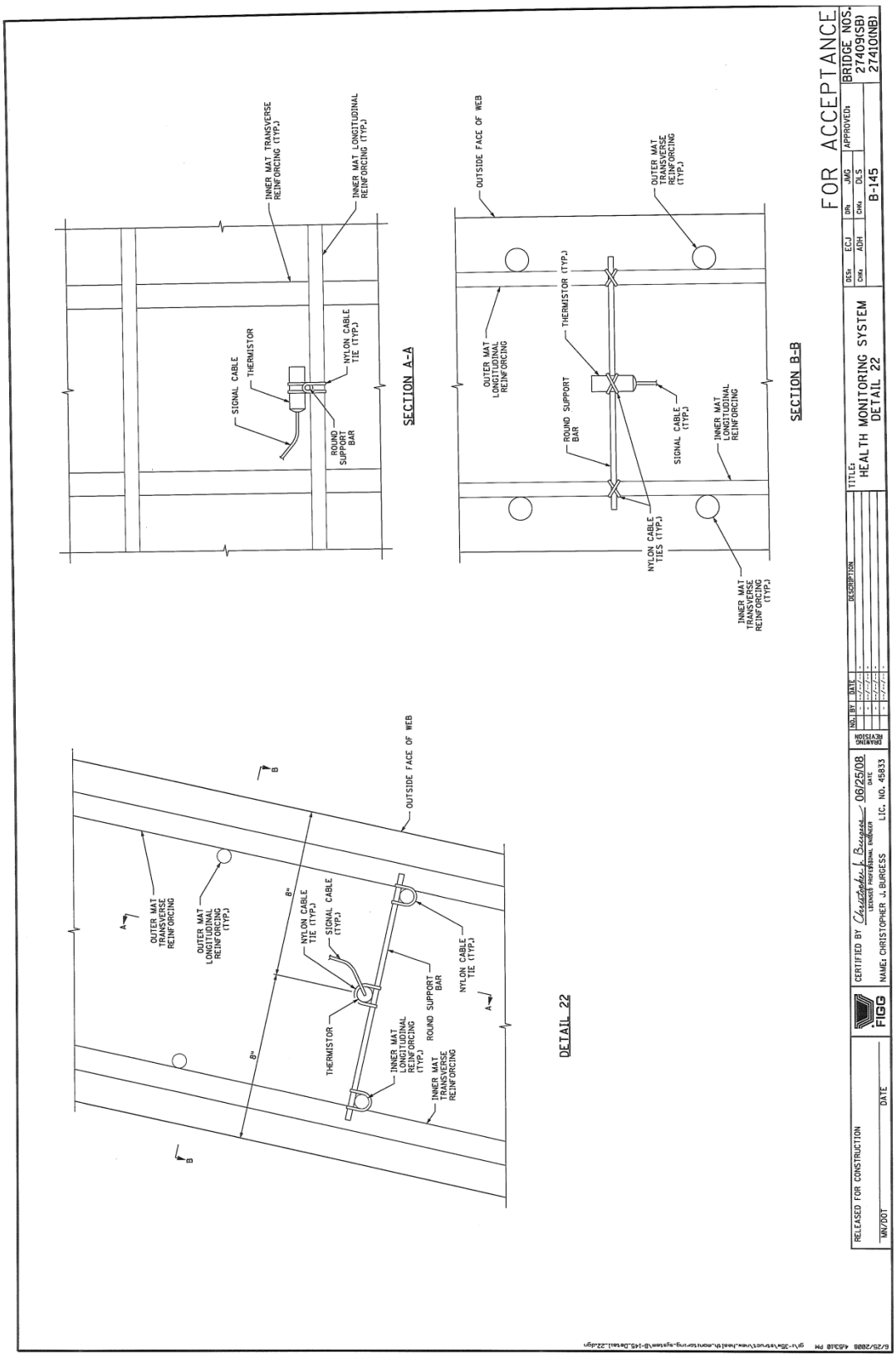

Figure A.28: Thermistor Detail 22

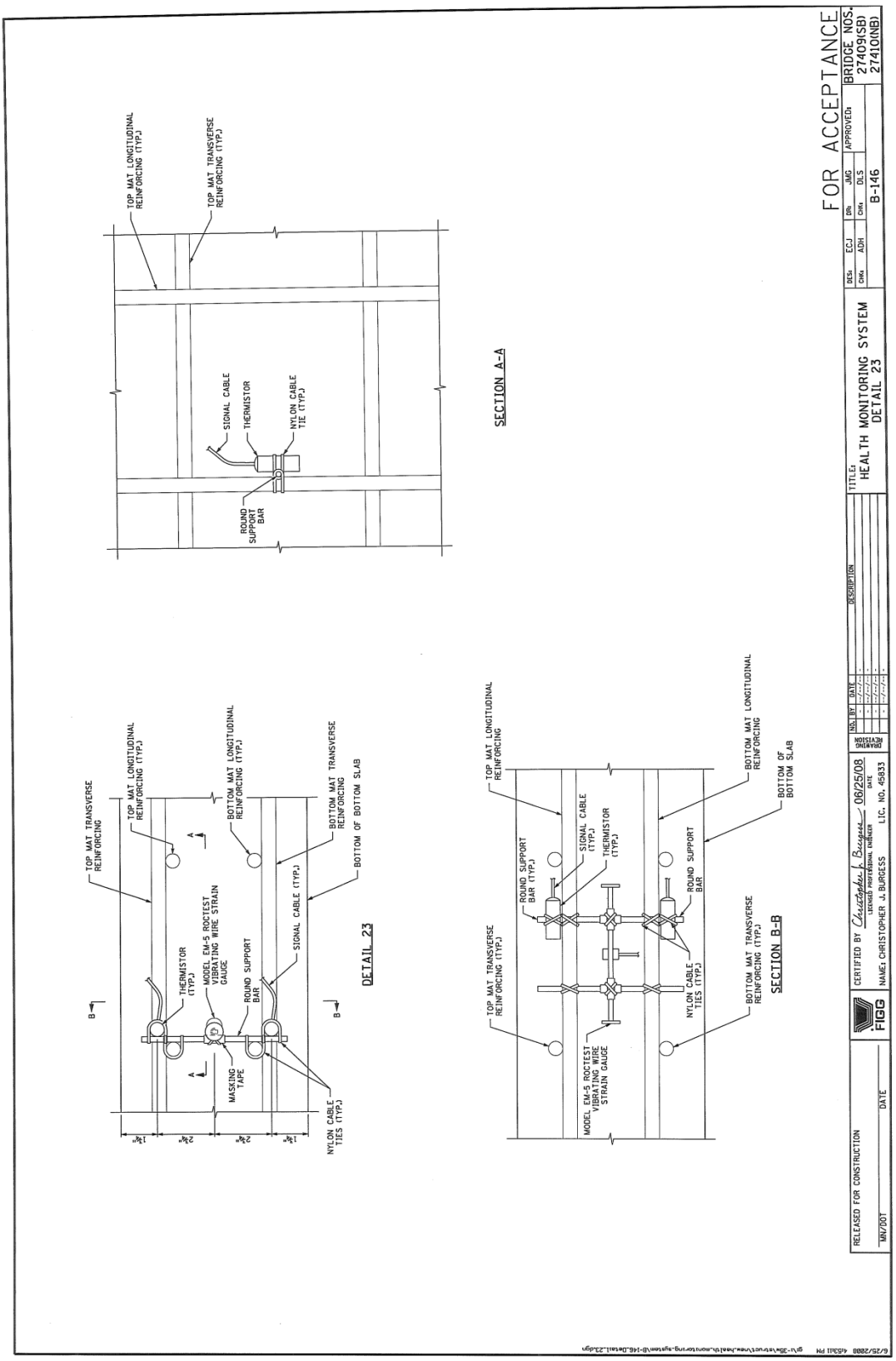

Figure A.29: VWSG and thermistor Detail 23

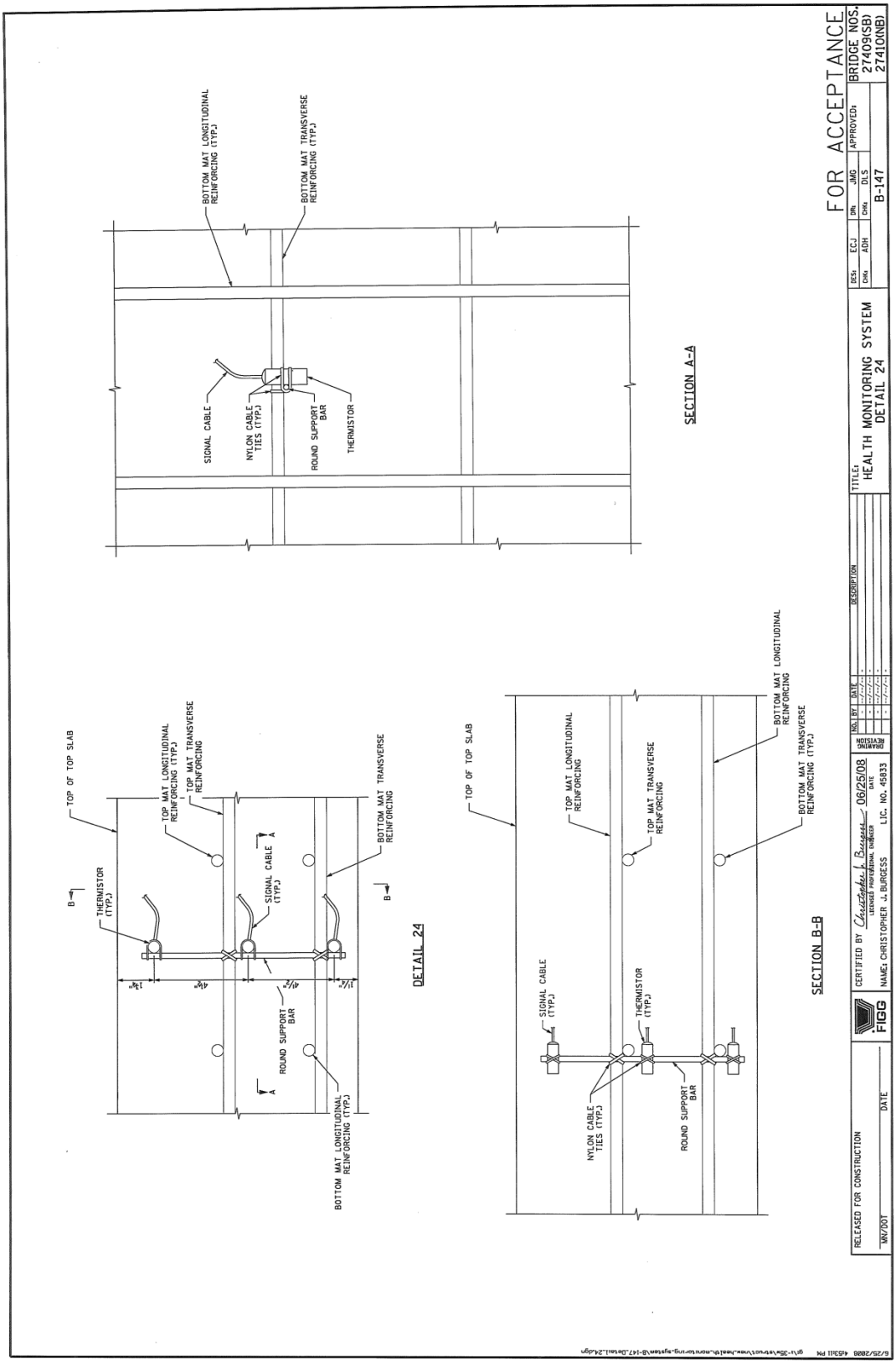

Figure A.30: Thermistor Detail 24

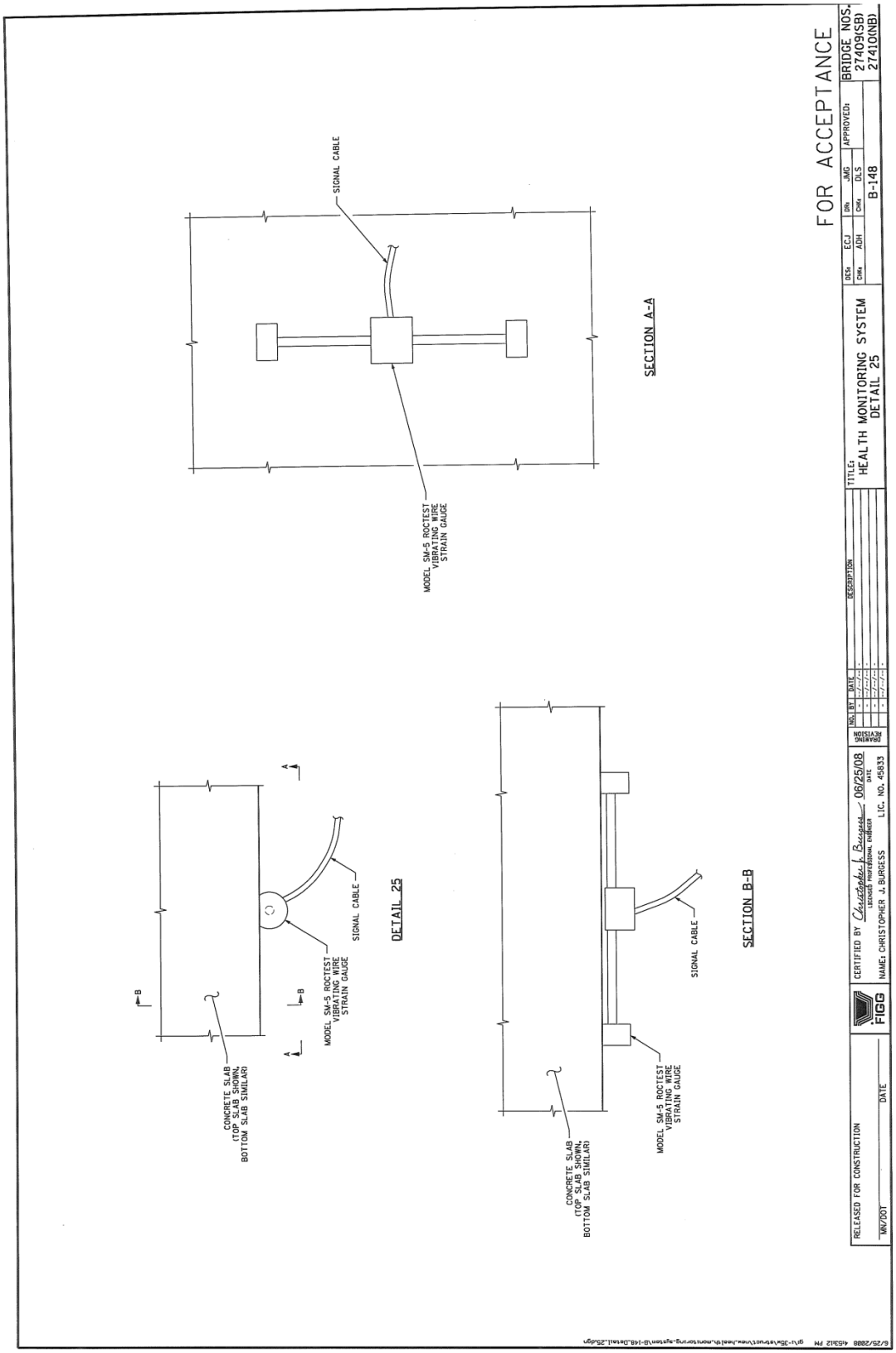

Figure A.31: External VWSG Detail 25

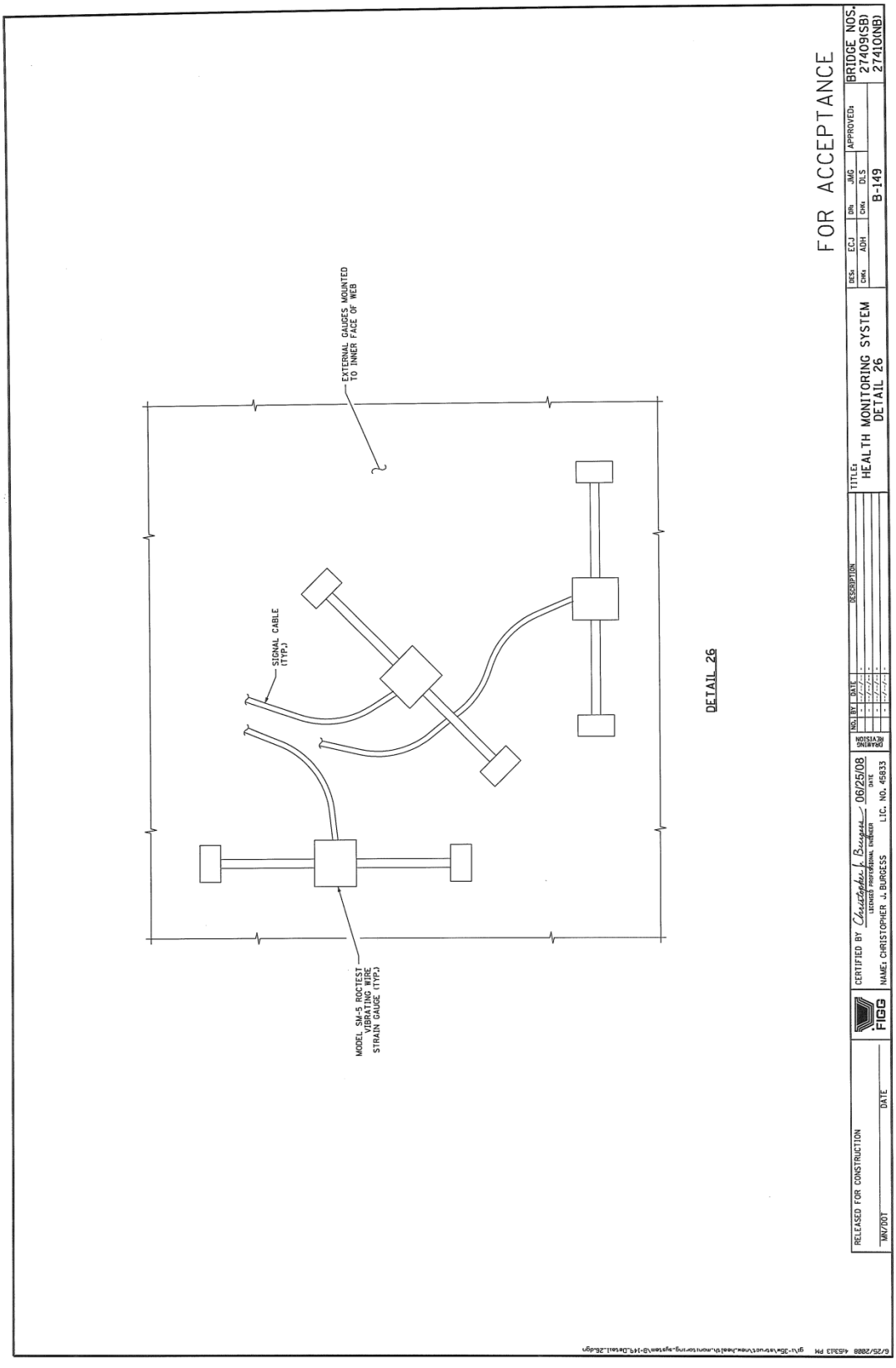

Figure A.32: External VWSG Detail 26

Appendix B: Manufacturer Shop Drawings for Bearing Pad Assemblies

List of Figures - Appendix B

Bearing pad assemblies for the I-35W St. Anthony Falls Bridge were supplied by R.J. Watson, Inc. Shop drawings detailing the construction and dimensions of the bearing pads are presented on the following pages of this appendix. These dimensions were integrated in the finite element models, as documented in Chapter 4.

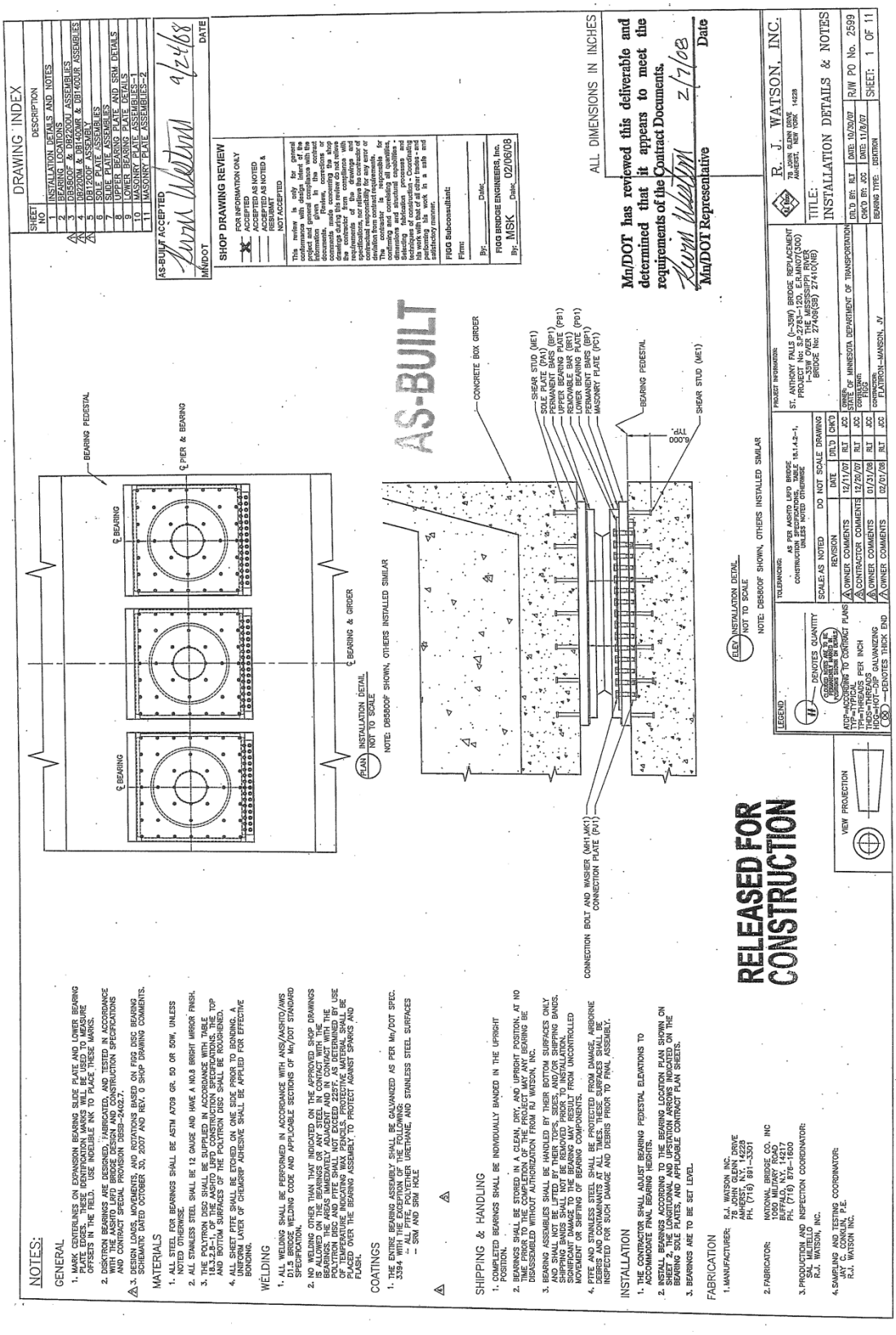

Figure B.1: Manufacturer Shop Drawing Sheet 1 – Installation Details and Notes

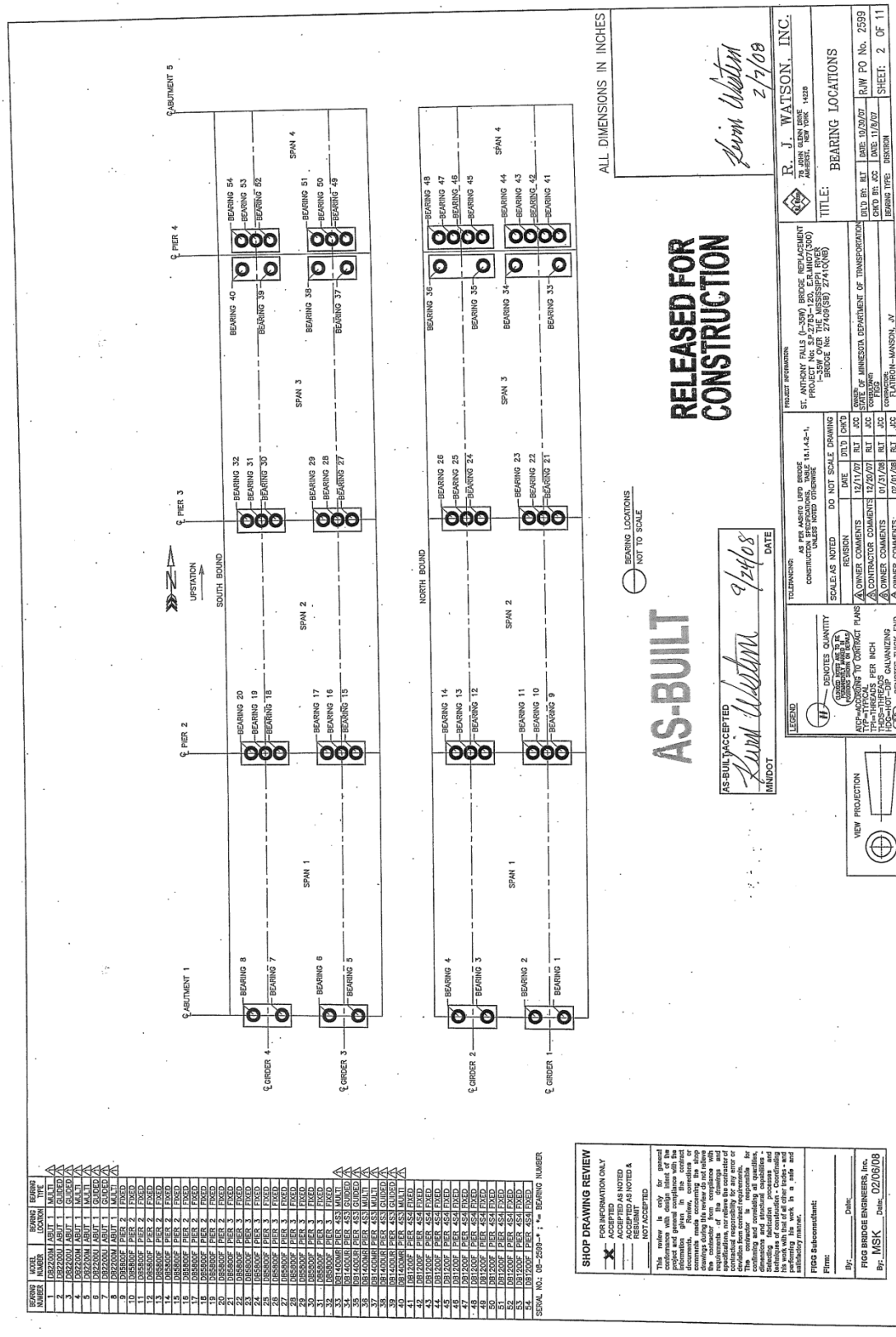

Figure B.2: Manufacturer Shop Drawing Sheet 2 – Bearing Locations

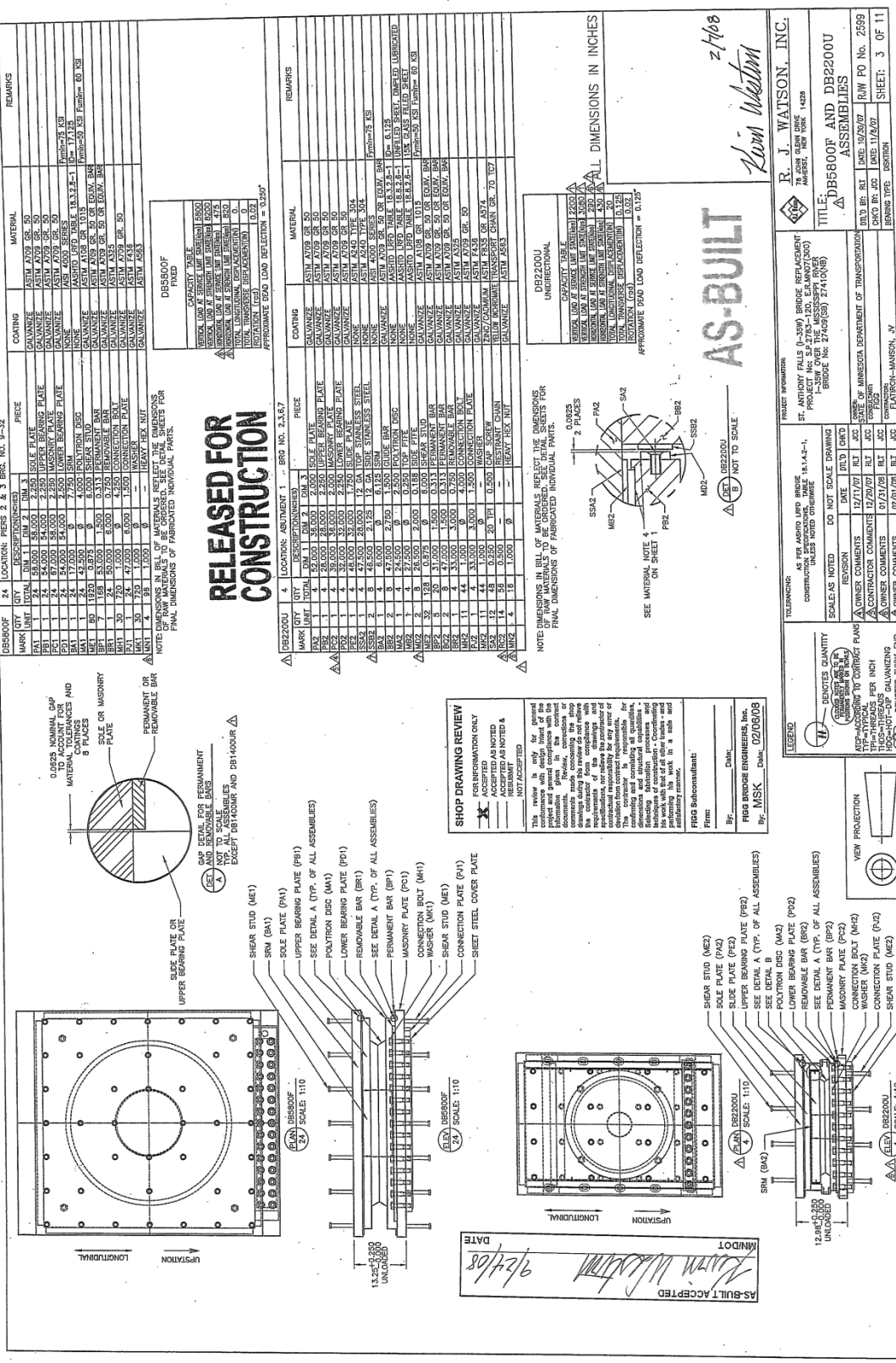

Figure B.3: Manufacturer Shop Drawing Sheet 3 – DB5800F (Fixed – Piers 2 and 3) and DB2200U (Guided – Abutment 1)

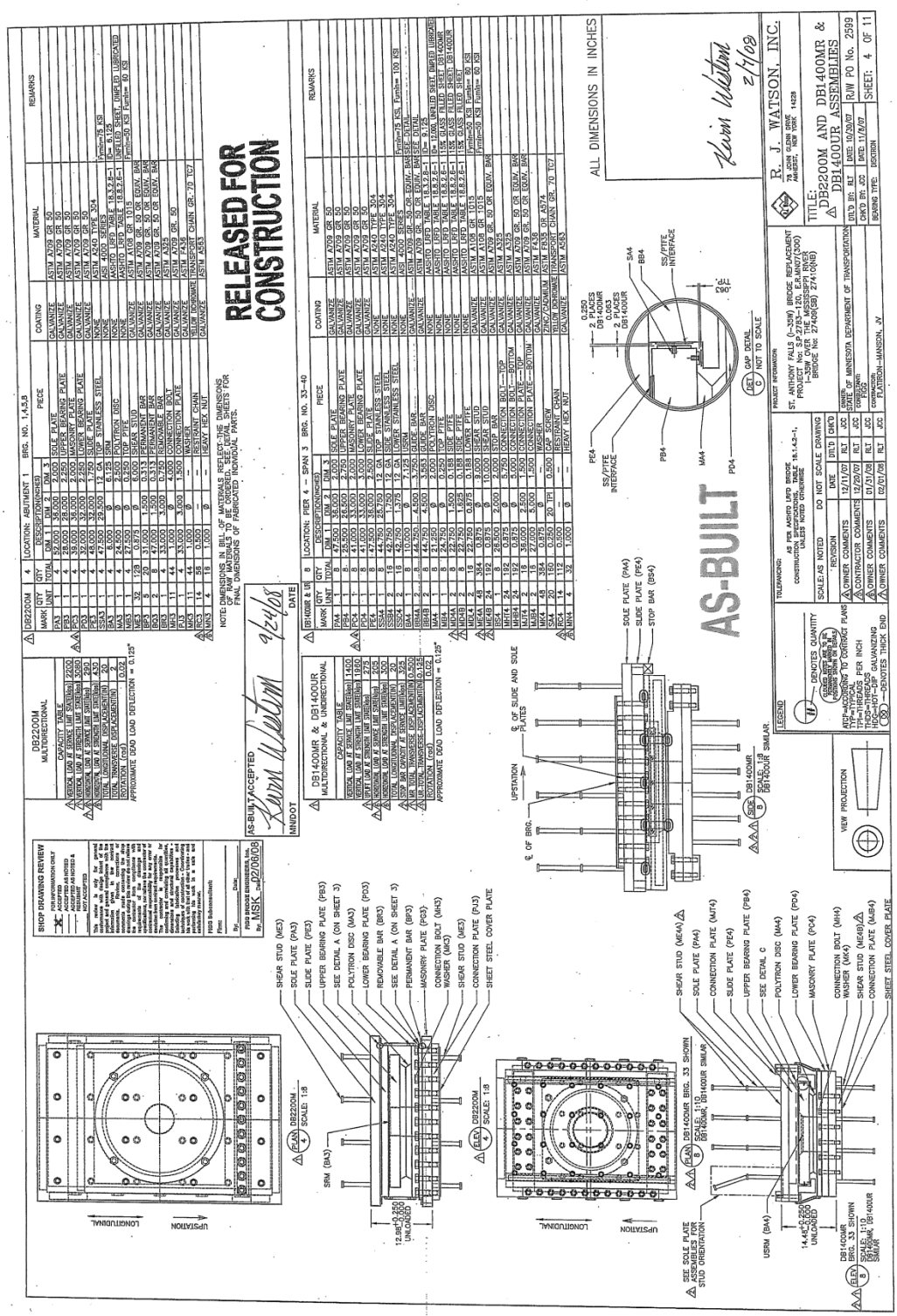

Figure B.4: Manufacturer Shop Drawing Sheet 4 – DB2200M (Multidirectional – Abutment 1) and DB1400MR/DB1400UR (Multidirectional/Guided – Pier 4, Span 3)

Note that DB1400MR and DB1400UR are effectively the same, except for the size of the gap between the guide rails and the upper bearing plate: 0.25 in. (6.4 mm) for DB1400MR (multidirectional) and 0.063 in. (1.6 mm) for DB1400UR (guided).

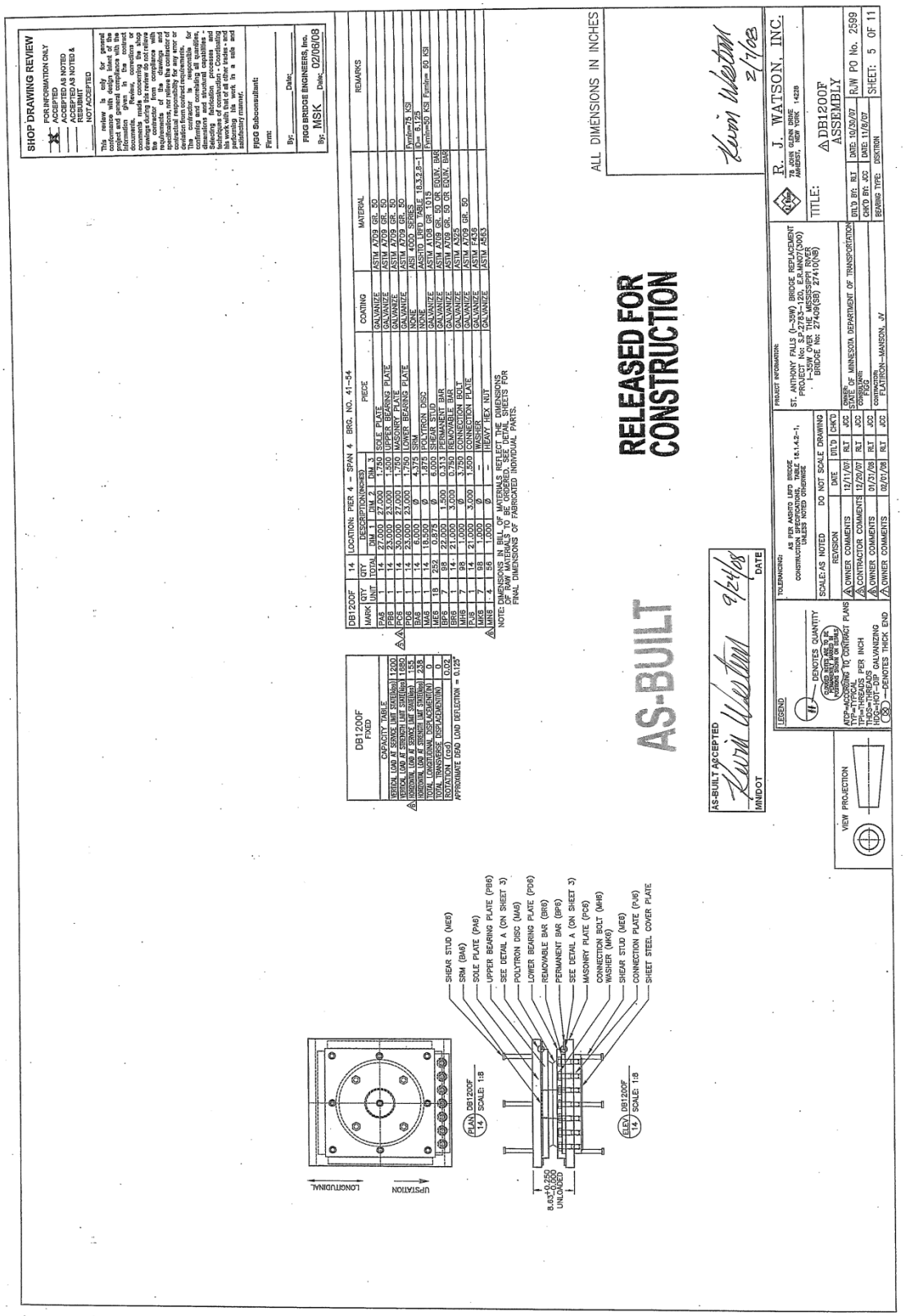

Figure B.5: Manufacturer Shop Drawing Sheet 5 – DB1200F (Fixed – Pier 4, Span 4)

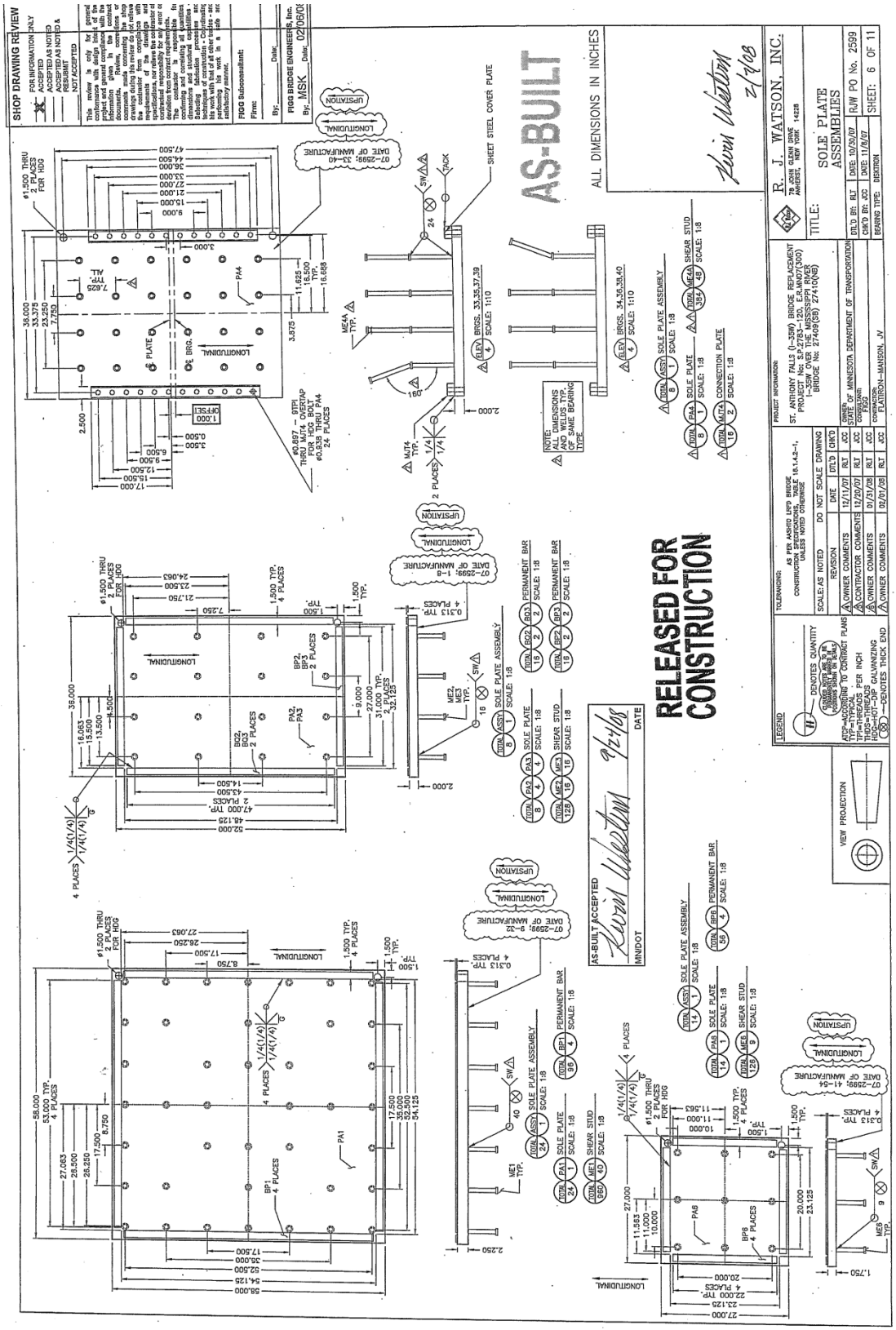

Figure B.6: Manufacturer Shop Drawing Sheet 6 – Sole Plate Assemblies

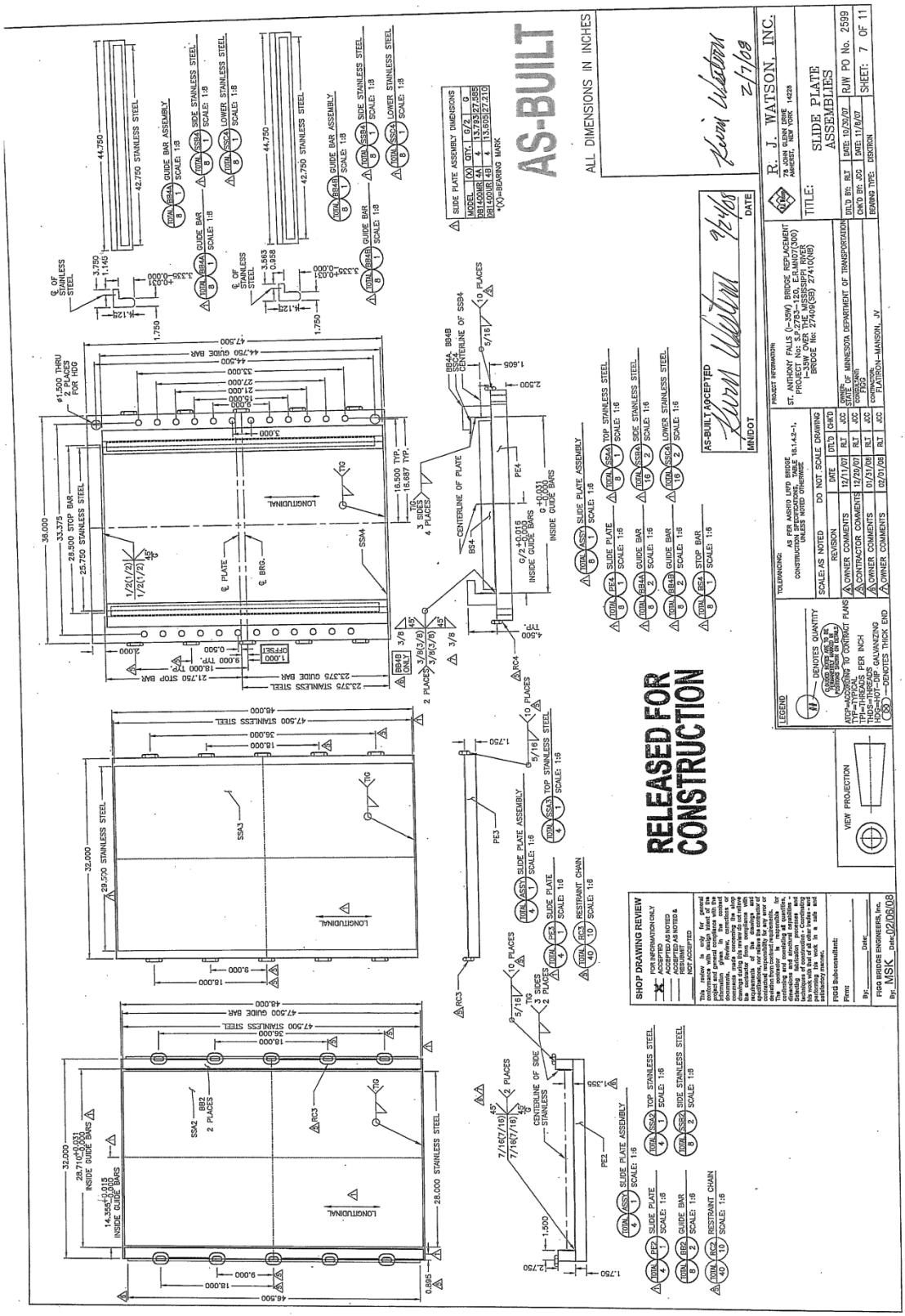

Figure B.7: Manufacturer Shop Drawing Sheet 7 – Slide Plate Assemblies

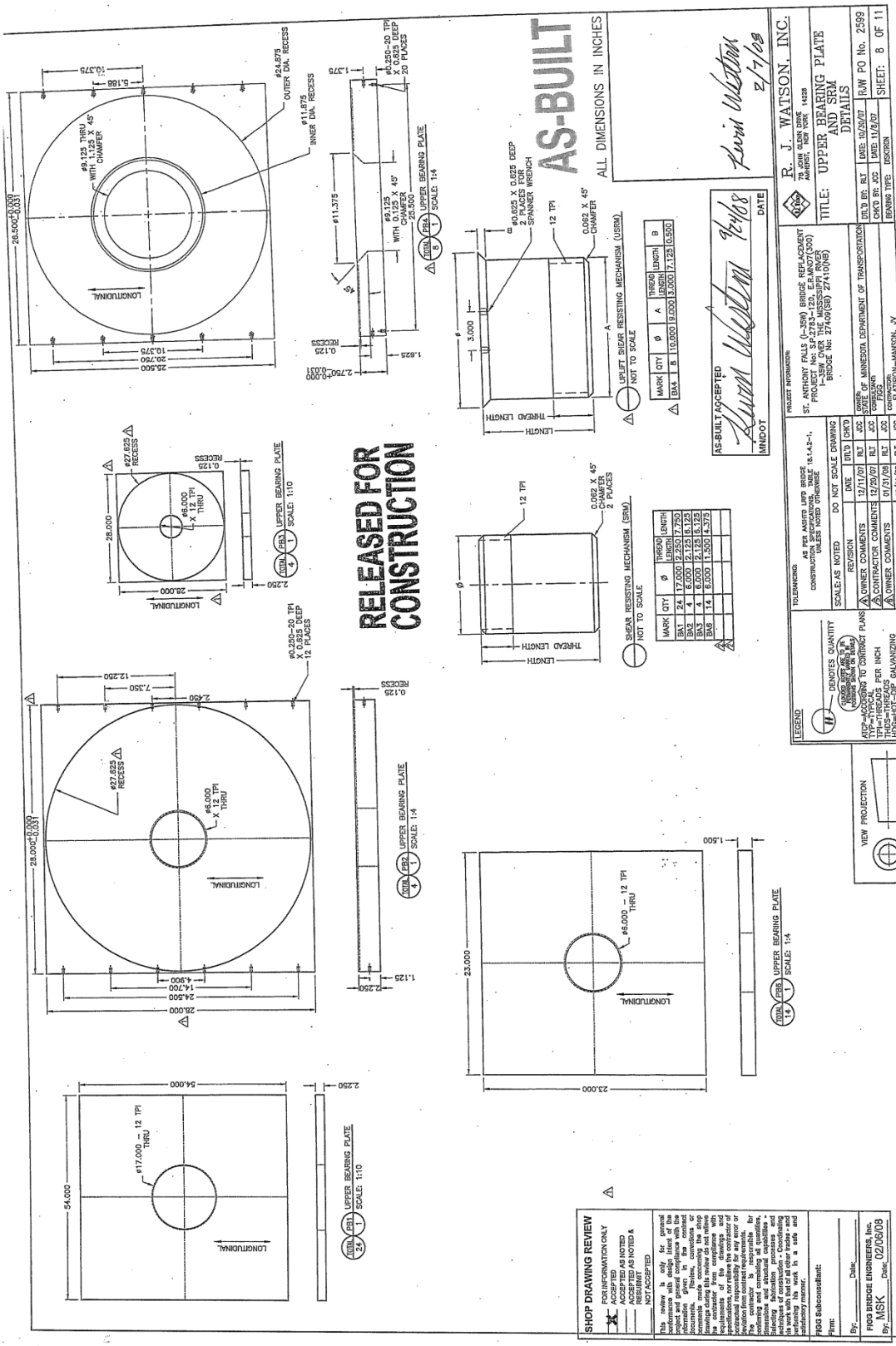

Figure B.8: Manufacturer Shop Drawing Sheet 8 – Upper Bearing Plate and SRM Assemblies

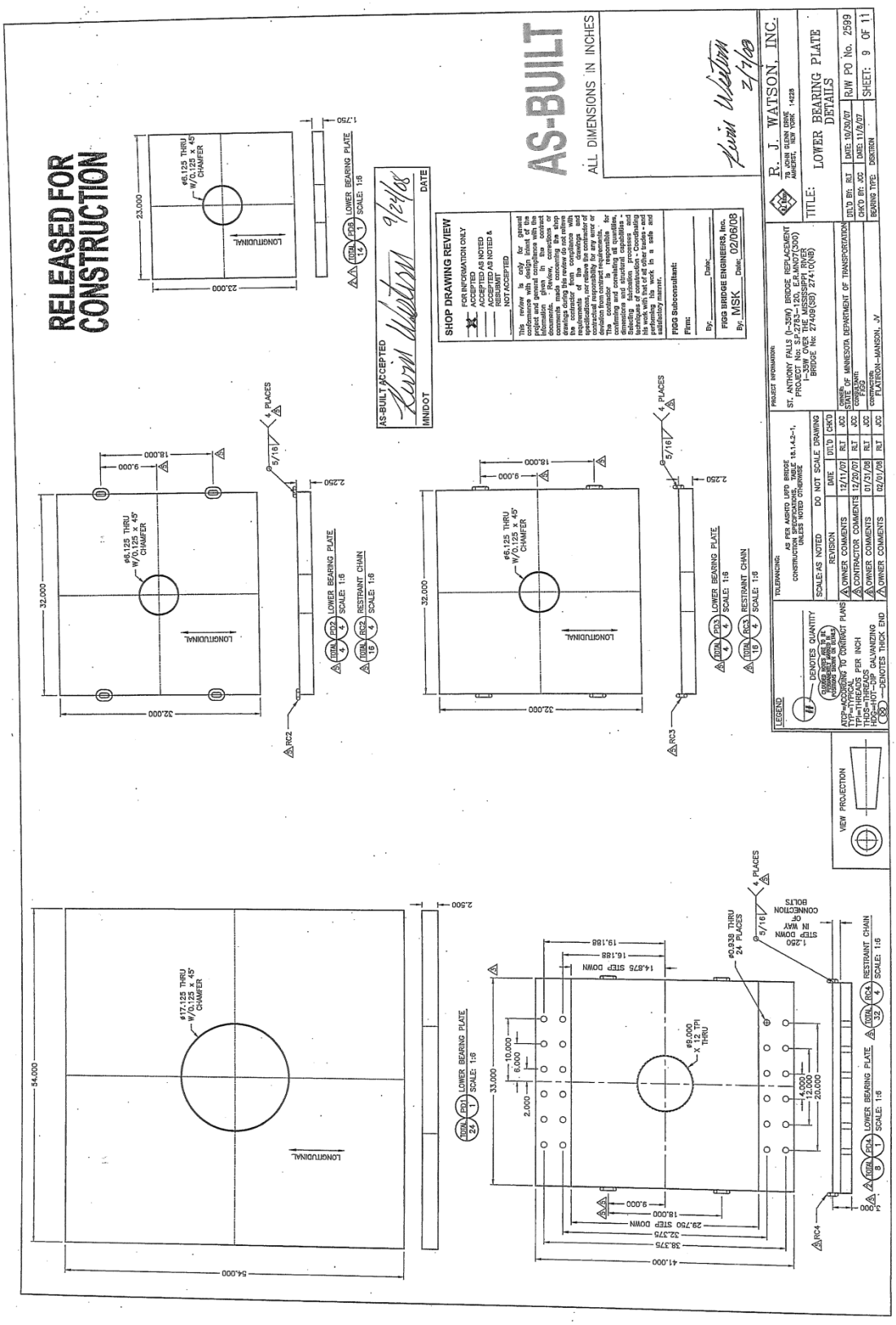

Figure B.9: Manufacturer Shop Drawing Sheet 9 – Lower Bearing Plate Assemblies

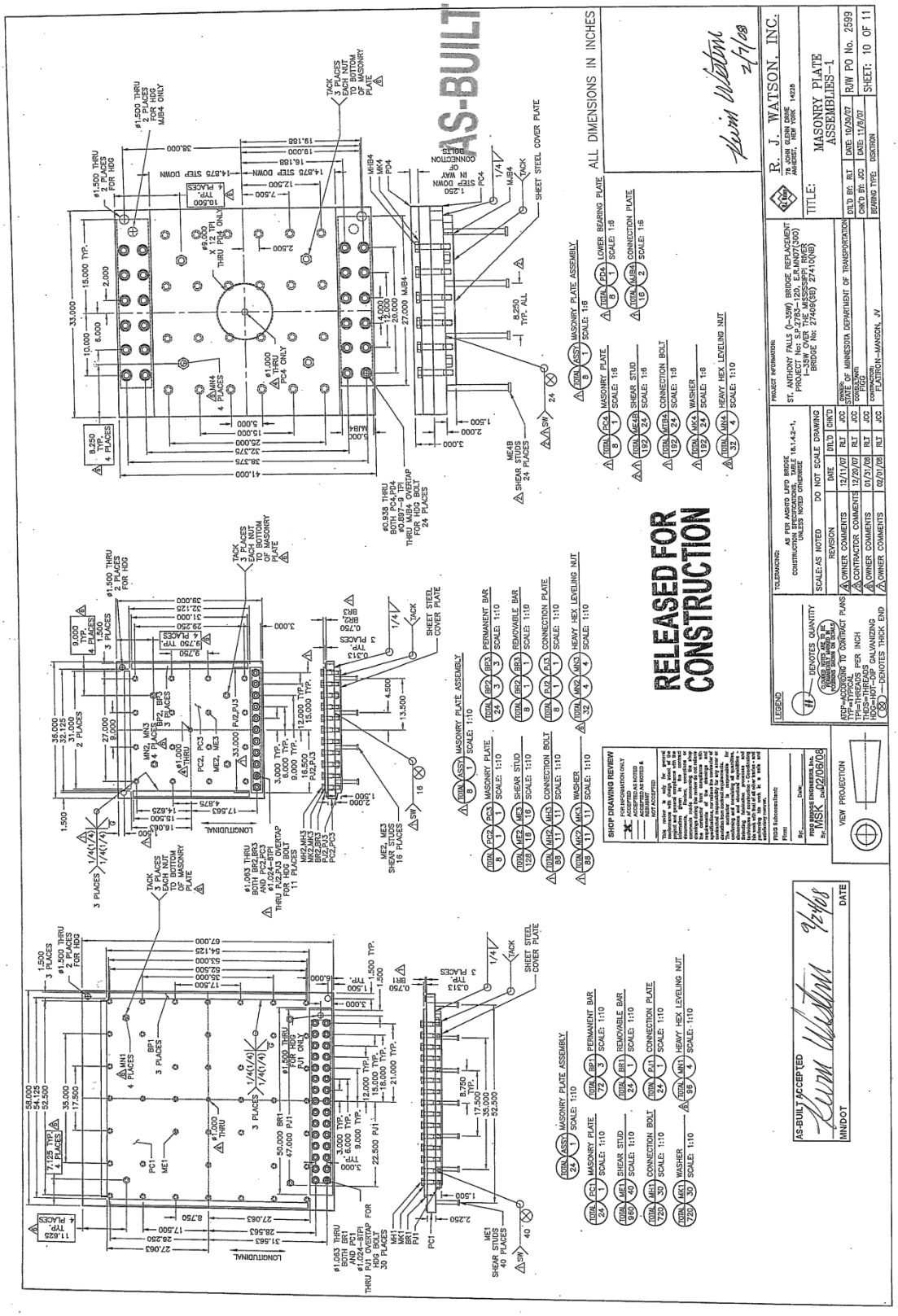

Figure B.10: Manufacturer Shop Drawing Sheet 10 – Masonry Plate Assemblies page 1

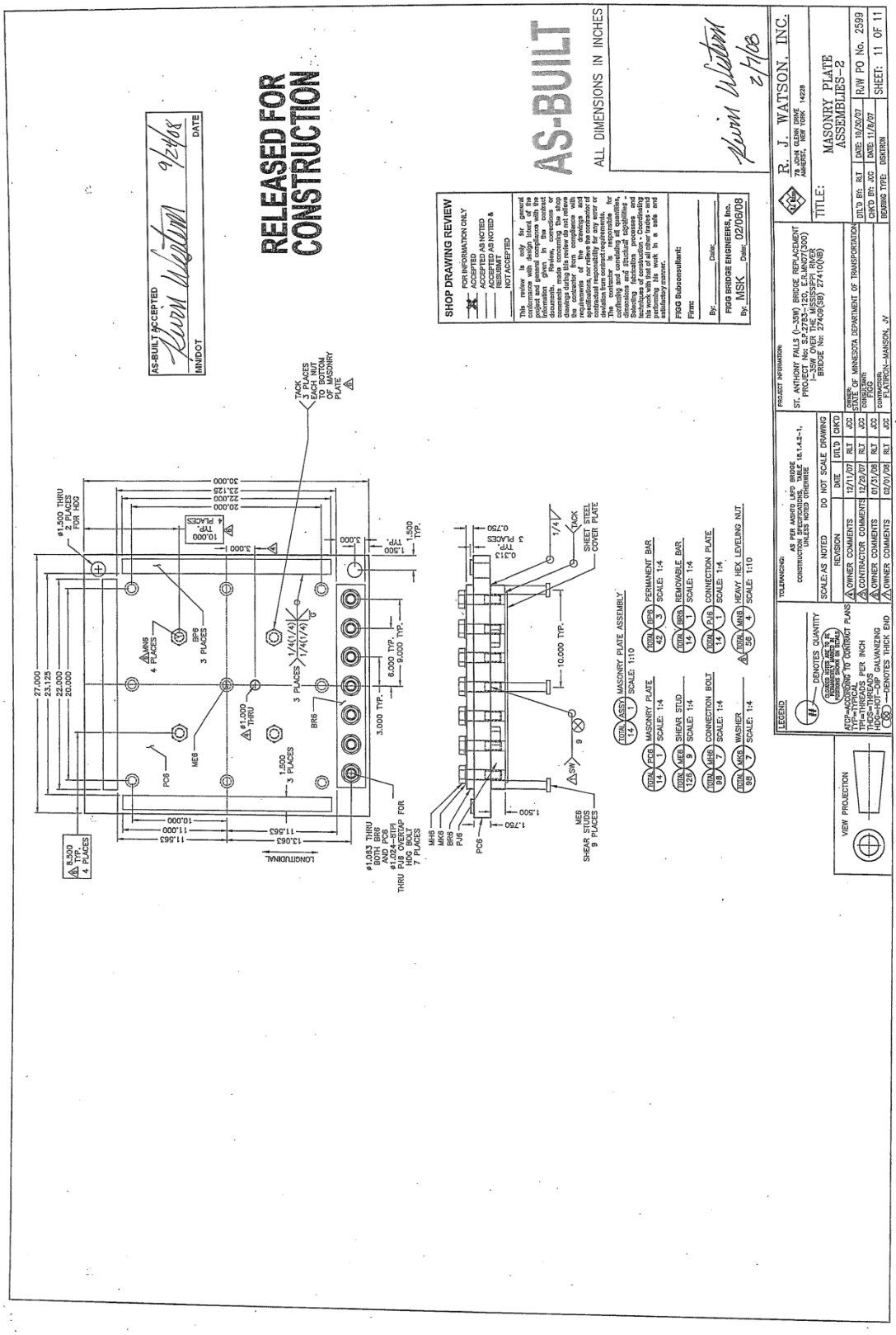

Figure B.11: Manufacturer Shop Drawing Sheet 11 – Masonry Plate Assemblies page 2

Figure B.12: Northbound Bridge Pier 3 Bearing Pad Assemblies

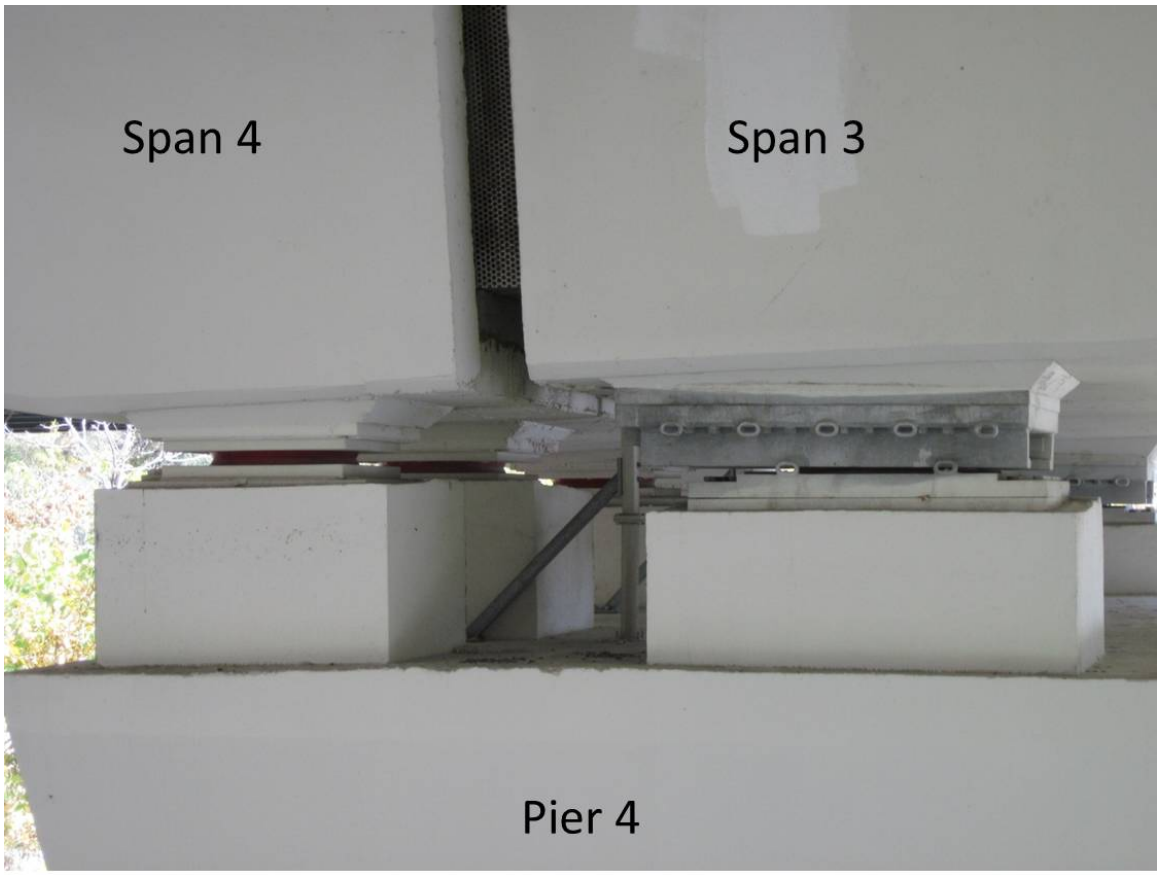

Figure B.13: Northbound Bridge Pier 4 Bearing Pad Assemblies